# Electroweak-boson production in p-Pb collisions at $\sqrt{sNN} = 8.16$ TeV with ALICE

Guillaume Taillepied

ÉCOLE DOCTORALE DES SCIENCES FONDAMENTALES

UNIVERSITÉ Clermont Auvergne

LPC Particules pLasmas Univers applicationS — Laboratoire de Physique de Clermont

Thèse de doctorat présentée pour l'obtention du grade de

Docteur d'Université
Spécialité : Particules, Interactions, Univers

par

**Guillaume Taillepied**

# Mesure de la production de bosons électrofaibles dans les collisions p–Pb à $\sqrt{s_{\mathrm{NN}}} = 8.16$ TeV avec ALICE

soutenue le 24 septembre 2021 à Clermont-Ferrand

**Jury**:

| | |
|---|---|
| Rapporteurs : | M. Gagliardi |
| | E. Gonzalez Ferreiro |
| | M. Ploskon |
| Examinateurs : | N. Bastid |
| | J. Castillo Castellanos |
| | S. Monteil |
| Directeur de thèse : | X. Lopez |

# Contents

**Acknowledgments** **v**

**Abstract** **vii**

**Résumé détaillé** **ix**

**Introduction** **1**

**I High-energy nuclear physics** **5**

**1 Nuclear matter in particle physics** **7**
1.1 Fundamentals of QCD . . . 7
1.1.1 Quark model and the colour charge . . . 7
1.1.2 QCD Lagrangian . . . 9
1.1.3 Perturbative QCD and the asymptotic freedom . . . 11
1.1.4 Chiral symmetry breaking . . . 13
1.1.5 QCD phase diagram . . . 16
1.2 Structure of nuclei . . . 19
1.2.1 The parton model . . . 19
1.2.2 QCD-improved parton model . . . 22
1.2.3 The PDF framework . . . 27
1.2.4 Nuclear effects and nPDFs . . . 31

**2 Heavy-ion collisions** **37**
2.1 History of a collision . . . 37
2.2 Heavy-ion accelerators . . . 41
2.3 The Glauber model . . . 42
2.4 Small systems . . . 46
2.4.1 Small systems as benchmarks for heavy-ions . . . 47
2.4.2 Collectivity in small systems(?) . . . 49

**3 Weak bosons in heavy-ion collisions** **53**
3.1 Carriers of the weak force . . . 53
3.1.1 Historical perspective . . . 53
3.1.2 $W^{\pm}$ and $Z^0$ bosons in the Standard Model . . . 58
3.1.3 Properties of the $W^{\pm}$ and $Z^0$ bosons . . . 60
3.2 Production and decay . . . 62
3.2.1 The Drell-Yan process . . . 62
3.2.2 Higher order corrections . . . 65
3.2.3 Muonic decay channel . . . 66
3.2.4 Production and study in proton–lead collisions . . . 67
3.3 Measurements at the LHC . . . 70
3.3.1 Production in Pb–Pb collisions at midrapidities . . . 70
3.3.2 Production in Pb–Pb collisions at large rapidities . . . 72
3.3.3 Production in p–Pb collisions at midrapidities . . . 73
3.3.4 Production in p–Pb collisions at large rapidities . . . 76

**II A Large Ion Collider Experiment** **79**

**4 The ALICE detector** **81**
4.1 The Large Hadron Collider . . . 81
4.1.1 LHC at CERN . . . 81
4.1.2 Injection and beams . . . 83
4.2 Overview of ALICE . . . 84
4.3 Global detectors . . . 87
4.3.1 Constituents . . . 87
4.3.2 V0-based triggering and beam-gas rejection . . . 89
4.3.3 Luminosity and visible cross sections . . . 90
4.3.4 Centrality determination . . . 91
4.4 Central barrel . . . 93
4.4.1 Detector layout . . . 95
4.4.2 Primary vertex reconstruction . . . 96
4.4.3 Charged track reconstruction . . . 98
4.4.4 Particle identification . . . 100

**5 Forward muon spectrometer** **107**
5.1 Overview . . . 107
5.2 Composition . . . 110
5.2.1 Tracking system . . . 110
5.2.2 Trigger stations . . . 111
5.2.3 Absorbers . . . 112
5.3 Track reconstruction . . . 113
5.3.1 Reconstruction algorithm . . . 113

5.3.2 Alignment of the tracking chambers . . . 114
5.3.3 Reconstruction efficiency . . . 115
5.4 Muon triggering . . . 116

**6 Data taking in ALICE** **119**
6.1 Online Control System . . . 119
6.1.1 Trigger . . . 120
6.1.2 Data AcQuisition (DAQ) . . . 122
6.1.3 High-Level Trigger (HLT) . . . 127
6.1.4 Detector and Experiment Control Systems (DCS and ECS) . . . 130
6.2 ALICE Offline . . . 132
6.2.1 The LHC computing grid . . . 132
6.2.2 ROOT and AliRoot . . . 133
6.2.3 Simulation and reconstruction . . . 135

**7 ALICE in the LHC Run 3** **137**
7.1 Physics motivation . . . 137
7.2 Central barrel and global detectors . . . 140
7.2.1 Inner Tracking System . . . 140
7.2.2 Time Projection Chamber . . . 141
7.2.3 Readout and trigger . . . 142
7.3 Muon spectrometer . . . 147
7.3.1 Motivation for the upgrade . . . 147
7.3.2 Muon identifier and tracking system . . . 148
7.3.3 Muon Forward Tracker . . . 149
7.4 Software upgrade . . . 151
7.4.1 The Online-Offline framework . . . 151
7.4.2 Data Quality Control . . . 154
7.4.3 MID raw data QC . . . 157

**III $Z^0$- and $W^{\pm}$-boson measurements in p–Pb collisions at $\sqrt{s_{NN}}$ = 8.16 TeV** **161**

**8 Data analysis** **163**
8.1 Data samples and selection . . . 163
8.1.1 Collision system and LHC periods . . . 163
8.1.2 Event selection . . . 165
8.1.3 Luminosity . . . 167
8.1.4 Centrality . . . 171
8.1.5 Track selection . . . 172
8.2 Signal extraction . . . 173
8.2.1 Overview . . . 173

8.2.2 MC simulations . . . 175
8.2.3 $Z^0$-boson signal extraction . . . 179
8.2.4 $W^{\pm}$-boson signal extraction . . . 184
8.3 Efficiency correction . . . 192
8.4 Differential studies . . . 193
8.5 Summary of systematic uncertainties . . . 195

**9 Results and physics interpretation** **197**
9.1 $Z^0$ and $W^{\pm}$ production cross sections in p–Pb collisions . . . 197
9.1.1 Measured production . . . 197
9.1.2 Comparison with measurements at $\sqrt{s_{\mathrm{NN}}} = 5.02$ TeV . . . 199
9.1.3 Comparison with theoretical calculations . . . 200
9.1.4 Comparison with CMS measurement at midrapidity . . . 202
9.2 Lepton charge asymmetry . . . 204
9.3 Nuclear modification factor . . . 208
9.4 Binary scaling . . . 211

**Conclusion** **213**

**List of figures** **215**

**List of tables** **221**

**Bibliography** **223**

# Acknowledgments

First and foremost I would like to deeply thank my thesis supervisor, Prof. Xavier Lopez, for the time I shared with him during this thesis. His involvement, his scientific skills and his rigour provided me with the perfect working environment. Thank you Xavier for your kindness and your patience. I would like to thank as well Nicole Bastid, Javier Castillo, Martino Gagliardi, Elena Gonzalez, Mateusz Ploskon and Stéphane Monteil for agreeing to be part of my jury. All the comments, discussions and suggestions were very much appreciated.

The ALICE group at the LPC has been a warm and welcoming environment, making my life in the laboratory interesting and pleasant. This naturally extends to the whole laboratory, from the colleagues of the other groups to the administration and IT departments.

During my work I had the pleasure to publish with very kind and competent persons. Thank you Ophélie, Sizar, Nicolo and Mingrui for our writing and discussion sessions, I hope we will stay in touch and wish you all the best in your future endeavours. Being part of a CERN Collaboration such as ALICE leads one to meet way too many people for allowing me to list and thank everyone who had a scientific and/or personal impact on me and my work.

I am very grateful to Silvia Masciocchi, Andrea Dubla and Ralf Averbeck, and all the people at the GSI institute, for giving me the opportunity to pursue my journey in heavy-ion physics. I am very much looking forward to start working with you.

This experience would not have been the same without all the other students I had the chance to meet here. Jonathan, Siyu, Boris, Yannick, Manon, Florian, Sofia, Cédric, Henri, Emmanuelle, Théo, Mélissa, Ioan, Chandan, Chun-Lu, Damien, Lina, Mark, Nazlim, Lenhart, Zhuman, Louis, Cristina, Arthur, and all the others, it was a pleasure eating, drinking, climbing, playing, discussing, and simply being with you all.

My family and friends have been more crucial for the completion of this thesis that they will probably ever realise. I am both happy for all we gained and sorry for all we lost during these peculiar times.

To my mother and my sister, for their unconditional, although not always deserved, support.

# Abstract

**Electroweak-boson production in p–Pb collisions at $\sqrt{s_{\mathrm{NN}}}$ = 8.16 TeV with ALICE.**

The matter that surrounds us is made of quarks, forming bound states through the exchange of the bosons mediating the strong nuclear force, the gluons. The interaction between quarks and gluons is described theoretically by means of quantum chromodynamics (QCD). Similarly to ordinary matter, the quark matter can be found in various states that one can depict in a phase diagram. Experimentally, these phases can be created by performing heavy-ion collisions (HIC), such as the ultra-relativistic lead-lead collisions delivered at the Large Hadron Collider (LHC). Such a collision leads to the creation of a Quark-Gluon Plasma (QGP), a near-perfect fluid which study sheds light on the first moments of the Universe, as the standard model of cosmology predicts that the Universe was a QGP a few microseconds after the Planck wall. In the experimental study of HIC, the measurements are often a sum of effects occuring at various stages of the history of the collision, and can be related to the initial state, the existence and evolution of the QGP phase, if any, or the hadronisation phase in which the partons that were released in the QGP form bound states as the confinment mechanism sets in.

This thesis aims at providing information on the initial state through the measurement of electroweak-boson production in proton-lead (p–Pb) collisions. The parton model allows to describe the internal structure of the nucleus by means of the nuclear Parton Distribution Functions (nPDFs), representing the distribution of the hadron momentum among its constituent partons at a given energy scale. The nPDFs are used as input for theoretical calculations of the production cross section of a given process in hadronic collisions, replacing the long-distance, non-perturbative part of the factorised expression. The nPDFs are determined from a global QCD analysis of data, which are fitted with phenomenological functional forms that can be extrapolated to all energy scales, with the DGLAP evolution equations, and to all chemical species with the $A$ dependence of the nPDFs themselves. Their determination thus relies on the amount of available experimental data.

The $\mathrm{Z}^0$ and $\mathrm{W}^{\pm}$ bosons are colourless particles, produced at the very early stages of the collision, in the so-called hard scattering processes, and decaying very rapidly due to their large masses and widths. Their production cross section is directly proportional to the momentum of the colliding parton. Moreover, they have a probability to decay into muons in the $\mathrm{Z}^0 \to \mu^+\mu^-$ and $\mathrm{W}^{\pm} \to \mu^{\pm}\nu$ processes, with a branching fraction of 3% and 10%, respectively. The lepton themselves are also insensitive to the strong force, and their energy loss in the medium by brehmsstrahlung can be

shown to be negligible. The leptonic decay of electroweak bosons thus provides medium-blind processes which production cross section is directly proportional to the nPDFs of the colliding hadrons, and this information will travel through the following stages of the collision history without being affected until their detection.

In the following, the measurements of the $Z^0$- and $W^{\pm}$-boson productions in p–Pb collisions at $\sqrt{s_{NN}} = 8.16$ TeV are measured in the muonic decay channels, using the ALICE muon spectrometer. The analysis is based on data collected in 2016 in two configurations called p-going and Pb-going, depending on whether the proton beam moves towards the spectrometer or away from it, respectively. The measurements are performed on the dimuon invariant mass spectrum for the $Z^0$ and through a fit of the single-muon $p_T$ distribution for the $W^{\pm}$. The production cross sections for the three processes are reported and compared with theoretical calculations relying on various parametrisations of the nPDF, as well as calculations performed from free-nucleon PDF as to evaluate the modification of the production from the nuclear effects themselves. The two charges of the $W^{\pm}$ boson allow for the evaluation of the lepton-charge asymmetry as well, a quantity sensitive to the down-to-up ratio in the nucleus. The nuclear modification factor is presented, computed using pQCD calculations of the reference pp cross section. Finally, the production of hard processes is expected to scale with the number of binary collisions, assuming an unbiased estimation of the centrality of the events. Measurements of the cross section, scaled to the average number of binary collisions in several centrality classes, are thus also shown.

The ALICE detector is currently undergoing an upgrade in preparation for the Run 3 of the LHC. Part of this upgrade aims at transforming the trigger system of the muon spectrometer into the Muon IDentifer (MID), as to cope with the continuous readout mode and the higher collision rate foreseen. Besides the upgrade of the detector, a new software framework, $O^2$, has been developped to replace the one used during Run 1 and 2 (AliRoot). A new software for the Quality Control of the MID, aiming at monitoring the detector status and quality of the data during data taking, is developped in this new framework and according to the new experimental conditions. The contribution to the MID Quality Control that constituted the service work of this thesis is detailed.

**Keywords**: heavy-ion collisions, quantum chromodynamics, initial state, nuclear parton distribution functions, electroweak bosons, $Z^0$, $W^{\pm}$, ALICE, LHC.

# Résumé détaillé

Dans ce manuscrit, la mesure de la production des bosons électrofaibles dans les collisions proton-plomb (p–Pb) à une énergie dans le centre de masse $\sqrt{s_{\rm NN}} = 8.16$ TeV avec ALICE est reportée. Ce résumé commence par une présentation du contexte théorique sous-jacent à cette analyse, en montrant en quoi ces mesures peuvent aider à la détermination des fonctions de distributions partoniques qui décrivent la structure interne du noyau. Il se poursuit par une description du détecteur ALICE, centrée sur le spectromètre à muons qui a servi à collecter les données utilisées. Enfin, la stratégie d'analyse est détaillée et les résultats obtenus sont reportés et discutés.

## Chromodynamique quantique et les collisions d'ions lourds

La matière hadronique est faite de quarks, particules élémentaires de spin 1/2. Le Modèle Standard de la physique des particules [1] contient six quarks regroupés en trois doublets : *up* et *down*, *charm* et *strange*, *top* et *bottom*. Les principales caractéristiques des quarks sont indiquées dans le Tableau 1. Ces quarks portent une charge dîte de couleur pouvant prendre trois valeurs, rouge ($r$), bleu ($b$) ou verte ($g$). Dans le modèle des quarks, indépendamment proposé par Murray Gell-Man et Georges Zweig en 1964 [2, 3], les hadrons sont en conséquence interprétés comme étant des assemblages de quarks. Il est naturel de décrire la transformation de couleur à l'aide du groupe de symmétrie SU(3), celui-ci menant à la prédiction des états baryoniques (contenant trois quarks) et mésoniques (contenant deux quarks) observés dans la nature. Le recourt au groupe de symmétrie SU(3) entraîne également la prédiction de huit bosons médiateurs de l'interaction dîte forte, dont la couleur constitue la charge. Ces bosons de masse nulle et de spin 1 sont appelés gluons, et sont responsables du confinement des quarks en paquets d'au moins deux quarks ayant une charge totale de couleur nulle.

La chromodynamique quantique (QCD) est la théorie de l'interaction forte. Sous sa formluation Lagrangienne, elle s'exprime comme :

$$\mathcal{L}_{\rm QCD} = \overline{\psi}_a \left( i\gamma^\mu \partial_\mu \delta_{ab} - m\delta_{ab} - g_s \gamma^\mu t^A_{ab} \mathcal{A}^A_\mu \right) \psi_b - \frac{1}{4} F^A_{\mu\nu} F^{\mu\nu}_A, \tag{1}$$

où $a = (1, 2, 3) = (r, g, b)$ et $A = (1, ..., 8)$ indiquent respectivement les indices de couleur des quarks et gluons[1]. L'une des caractéristiques fondamentales de la QCD provient du fait que les gluons portent une charge de couleur, et sont donc eux-mêmes sensibles à l'interaction forte (à l'inverse

[1] Voir la Section 1.1.2 pour une description détaillée des termes présents dans le Lagrangien.

| Quark | Charge | Isospin | $\mathcal{B}$ | $S$ | $C$ | $B$ | $T$ | Masse (MeV/$c^2$) |
|---|---|---|---|---|---|---|---|---|
| $d$ – down | $-\frac{1}{3}$ | $-\frac{1}{2}$ | $\frac{1}{3}$ | 0 | 0 | 0 | 0 | $4.7^{+0.5}_{-0.3}$ |
| $u$ – up | $+\frac{2}{3}$ | $+\frac{1}{2}$ | $\frac{1}{3}$ | 0 | 0 | 0 | 0 | $2.2^{+0.5}_{-0.4}$ |
| $s$ – strange | $-\frac{1}{3}$ | 0 | $\frac{1}{3}$ | $-1$ | 0 | 0 | 0 | $95^{+9}_{-3}$ |
| $c$ – charm | $+\frac{2}{3}$ | 0 | $\frac{1}{3}$ | 0 | $+1$ | 0 | 0 | $(1.275^{+25}_{-35}) \times 10^3$ |
| $b$ – bottom | $-\frac{1}{3}$ | 0 | $\frac{1}{3}$ | 0 | 0 | $-1$ | 0 | $(4.18^{+0.04}_{-0.03}) \times 10^3$ |
| $t$ – top | $+\frac{2}{3}$ | 0 | $\frac{1}{3}$ | 0 | 0 | 0 | $+1$ | $(173.2 \pm 0.9) \times 10^3$ |

**Table 1:** Charge, isospin, nombres quantiques et masse des quarks du Modèle Standard. Les nombres quantiques sont le nombre baryonique $\mathcal{B}$, et les nombres de saveur : étrangeté $S$, charme $C$, beauté $B$ and vérité $T$. La masse indiquée pour le quark top est celle rapportée par le Tevatron Electroweak Working Goup, estimée d'après l'analyse des mesures au Tevatron et au LHC. Informations tirées de la Ref. [4].

par exemple du photon, de charge nulle et donc insensible à l'interaction électromagnétique). En effet, développer le tenseur $F^A_{\mu\nu}$ donne l'expression :

$$F^A_{\mu\nu} = \partial_\mu \mathcal{A}^A_\nu - \partial_\nu \mathcal{A}^A_\mu - \frac{\alpha_s}{4\pi} f_{ABC} \mathcal{A}^B_\mu \mathcal{A}^C_\nu , \tag{2}$$

dont le dernier terme décrit l'interaction du gluon avec lui-même.

La QCD possède deux régimes particuliers selon l'énergie à laquelle on se place. À basse énergie, l'interaction liant les particules colorées est importante et entraîne le confinement des quarks en hadrons. À haute énergie en revanche, la force de cette interaction décroît dans un régime nommé la liberté asymptotique. Cette évolution de l'interaction forte est illustrée par sa "constante" de couplage $\alpha_s$, comme indiquée par la Figure 1 (gauche). Un paramètre fondamental de la QCD est $\Lambda_{\mathrm{QCD}}$, l'échelle d'énergie en dessous de laquelle la force de l'interaction empêche l'utilisation des techniques perturbatives dans les calculs.

Ces différents régimes entraînent l'apparition de phases de la matière forte, qui peuvent être étudiées à travers l'exploration d'un diagramme de phase tel que celui de la Figure 1 (droite). Différentes régions peuvent être isolées sur ce diagramme, correspondant aux différentes phases de la matière forte. À faible énergie, le phénomène de confinement entraîne l'apparition de la matière nucléaire ordinaire, dans laquelle les quarks sont regroupés en hadrons, eux-mêmes formant des assemblages composites plus lourds, les noyaux atomiques. Une élevation de l'energie empêchera la formation de noyaux, sans pour autant casser les hadrons, formant de ce fait une phase de gaz hadronique. À très haute température, le couplage $\alpha_s$ devient trop faible pour entretenir l'existence des hadrons eux-mêmes, et les quarks et gluons qui les constituent sont relachés et deviennent libres. Cette phase, appelées le Plasma de Quarks et Gluons (QGP), est un important objet d'étude dans le cadre de la physique des particules, donnant un accès unique à des spécificités de la QCD

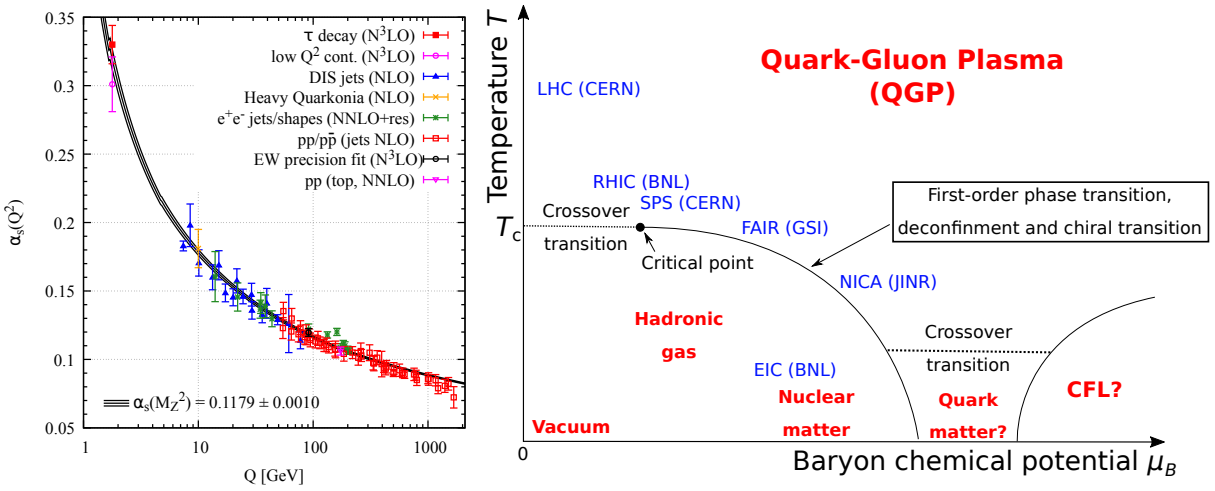


**Figure 1: Gauche** : mesures du couplage $\alpha_s(Q^2)$ en fonction de l'échelle d'énergie $Q$. Figure tirée de la Ref. [4]. **Droite** : diagramme de phase de la matière forte dans l'espace ($\mu_B$, $T$) correspondant respectivement au potentiel baryonique et à la température. Voir la Section 1.1.5 pour une description détaillée du diagramme.

absente des autres phases.

La création d'un QGP dans le laboratoire nécessite une densité d'énergie très importante, qui n'est atteinte qu'auprès des plus puissants accélérateurs de particules, tels que le Grand Collisionneur de Hadrons (LHC) au CERN [5]. Le LHC est un anneau de 27 kilomètres de circonférence, permettant d'accélérer jusqu'à des vitesses ultra-relativistes (plus de 99% de la vitesse de la lumière) deux faisceaux de particules circulant dans des sens opposés. Ces faisceaux se rencontrent en quatre points de collisions autour desquels sont installées les quatre principales expériences du LHC : ALICE, ATLAS, CMS et LHCb. Bien que le mode de fonctionnement ordinaire du LHC consiste en l'accélération de faisceaux de protons, un certain temps est chaque année dédié à l'accélération et la collision d'ions lourds, tels que des noyaux de plomb. Dans l'histoire d'une collision d'ions lourds, plusieurs étapes peuvent être distinguées [6] :

1. **État initial** : les deux noyaux sont accélérés à des vitesse proches de celle de la lumière, et subissent en conséquence une importante contraction de Lorentz.

2. **Collision** : les noyaux entrent en collision, et de nombreuses collisions partoniques (entre quarks et gluons) ont lieu. Ces intéractions partoniques initiales entraînent les procédés dits durs, lors desquels de grandes quantités d'impulsion ($> 10$ GeV) sont échangées en des temps très courts ($\sim 1/Q$). Ces processus donnent naissance aux particules dures parmi lesquelles on trouve les gerbes hadroniques, des photons, paires d'electrons, quarks lourds et les bosons vecteurs.

3. **Procédés semi-durs** : suite à la production de particules dures, des procédés impliquant de plus faibles transferts d'énergie prennent place. Lors de cette étape, les consituants des noyaux sont libérés, les gluons de l'état initial se fragmentent et s'hadronisent, produisant la majeure partie de la multiplicité de l'évènement.

4. **Phase hors-équilibre** : la densité de particules créées lors d'une collision d'ions lourds entraine des interactions entre celles-ci, ces interactions pouvant être détectées et étudiées à travers des effets collectifs tels que le flux elliptique ou les phénomènes de co-déplacement.

5. **Plasma de Quark et Gluons** : les interactions lors de la phase hors-équilibre entraîne la thermalisation du système, qui continue cependant de s'étendre et se refroidir. Cette étape peut être efficacement décrite par des modèles hydrodynamiques.

6. **Hadronisation et gel** : lorsque le refroidissement progressif du système ramène la temperature sous une valeur critique, le confinement rassemble les partons dans des états hadroniques. Deux phases de gel sont par la suite distinguées : le gel thermique, après lequel les hadrons peuvent encore subir des interactions inélastiques, et le gel chimique après lequel la composition chimique de l'etat final n'évolue plus, alors que seules des interactions elastiques peuvent encore survenir.

Cette description schématique n'est évidemment pas fixe, et l'histoire d'une collision d'ions lourds reste une question essentiellement ouverte, faisant l'object d'intenses efforts de recherche. Ces étapes se déroulent en un temps très courts, environ 20 fm/$c$, empêchant l'accès expérimental direct. Le produit d'une collision d'ions lourds, tel qu'il est détécté expérimentalement, est donc la somme de tous les effets intervenant aux différentes étapes de la collision. Il est donc d'une importance cruciale, pour les expérimentateurs, de trouver des sondes et observables spécifiques à l'étude de chaque étape, afin d'en distinguer les effets. À ce titre, les collisions proton-plomb (p–Pb) réalisées au LHC apportent un éclairage supplémentaire. Dans de telles collisions, l'apparition d'un QGP n'est en effet pas attendue, de telle sorte que seuls les effets nucléaires dits froids[2] entrent en action. La comparaison des mesures faites dans les collisions p–Pb et plomb-plomb (Pb–Pb) permet donc de distinguer ces effets des effets nucléaires chauds.

## Fonctions de distribution partoniques

Les fonctions de distribution partoniques (PDF) décrivent la probabilité de trouver un parton portant une fraction $x$, appelée $x$ de Bjorken, de l'impulsion totale du hadron à une énergie donnée. Elle permettent donc une description de l'état initial de la collision en terme de répartition de l'énergie dans le noyau. Par le théorème de factorisation, il est possible d'exprimer la section efficace de production $\sigma$ d'un état final générique $H$ dans une collision hadronique comme :

$$\sigma_{pp\to H}(s,\mu_F^2,\mu_R^2) = \sum_{i,j}\int \mathrm{d}x_1\mathrm{d}x_2 f_i(x_1,\mu_F^2,\mu_R^2) f_j(x_2,\mu_F^2,\mu_R^2)\hat{\sigma}_{ij\to X}(x_1,x_2,s;\mu_F^2,\mu_R^2), \qquad (3)$$

[2]Par convention, on désigne comme effects nucléaires chauds les effets faisant suite à la présence d'un QGP, et comme effets froids ceux qui n'en dépendent pas.

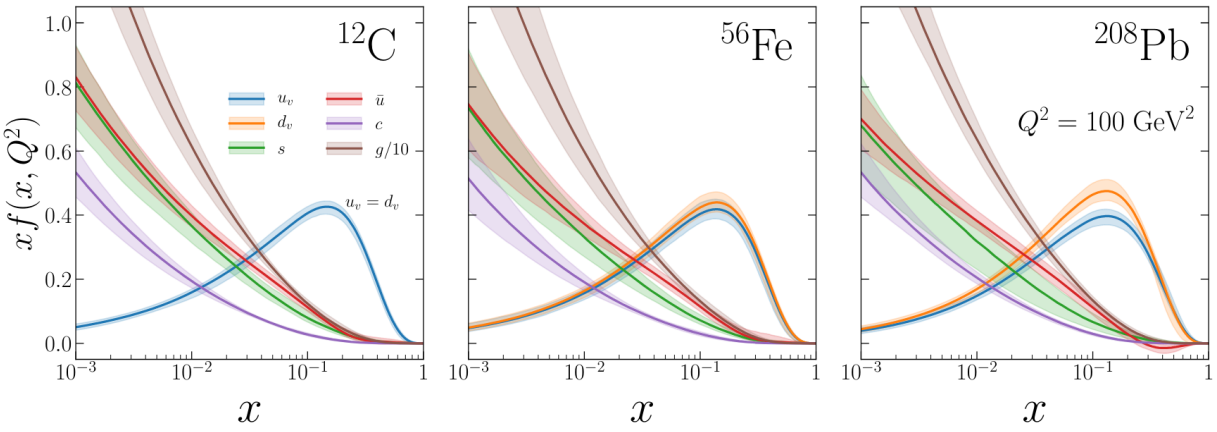


**Figure 2:** Les PDF nucléaires du carbone $^{12}$C, du fer $^{56}$Fe et du plomb $^{208}$Pb à l'énergie $Q^2 = 100$ GeV$^2$ dans le modèle nNNPDF2.0. Figure tirée de la Ref. [7].

où $s$ représente l'énergie, $x_1$ et $x_2$ sont les $x$ de Bjorken des partons 1 et 2 respectivement, et $\mu_F$ et $\mu_R$ sont les échelles de factorisation et de renormalisation. Dans cette expression, $\hat{\sigma}$ est la section efficace partonique, calculable par l'application de techniques perturbatives. Les termes $f_i$ et $f_j$ représentent les PDF des partons $i$ et $j$. Ces fonctions sont non-perturbatives, rendant impossible leur détermination par le calcul, elles peuvent en revanche être estimée depuis les mesures expérimentales. Pour cela, une paramétrisation initiale de la PDF est établie de manière phénoménologique à une échelle d'énergie initiale arbitraire $Q_0$. À l'aide des équations d'évolution de DGLAP, cette paramétrisation initiale est ensuite extrapolée à l'énergie requise, correspondant à celle du jeu de donné considéré, permettant l'évaluation des observables. Cette étape est réalisée pour tous les jeux de données disponibles. Enfin, les paramètres libres du modèles à $Q_0$ sont ajustés afin de déterminer ceux qui permettent de reproduire au mieux l'ensemble des mesures expérimentales.

La paramétrisation typique d'une PDF se présente comme :

$$f(x, Q_0, \{a_i\}) = x^{a_1}(1-x)^{a_2} C(x, \{a_{i>2}\}), \tag{4}$$

où les termes $a_i$ sont les paramètres libres du modèle. Les termes en $x$ et $1-x$ vont respectivement contraindre la distribution dans les limites où $x$ tend vers 0 et 1. La fonction $C$ est la fonction d'interpolation, qui détermine le comportement de la PDF entre ces deux limites. Dans le cas d'une PDF nucléaire (nPDF), les paramètres libres porteront la dépendance en $A$. Les nPDF de quelques éléments dans le modèle nNNPDF2.0 [7] sont données par la Figure 2. La différence de comportement entre les quarks de valence $u_V$ et $d_V$ et ceux de mer est particulièrement visible, les quarks de valence dominant la distribution à de grandes valeurs de $x$. La détermination d'une nPDF peut également suivre une approche alternative, reposant sur la paramétrisation de la fonction de modification nucléaire. Il est en effet possible de relier une nPDF à la PDF du proton libre par :

$$f_i^{p/A}(x, Q^2) = R_i^A(x, Q^2) f_i^p(x, Q^2), \tag{5}$$

où $f_i^{p/A}(x, Q^2)$ est la PDF du parton $i$ dans un proton du noyau $A$, $f_i^p$ celle de ce même parton dans un proton libre, et $R_i^A$ est la fonction de modification nucléaire. Cette dernière peut donc également se définir comme le rapport entre la nPDF et la PDF. Suite à la quantité et la précision des données récoltées dans les collisions pp, les PDF du proton libre sont connues avec une plus grande précision que celle du proton lié, permettant d'utiliser les premières comme réferences dans la détermination des secondes. Ces deux approches, ainsi que la variété des paramétrisations et méthodes de détermination possibles, entraine l'existence de nombreux jeux de nPDF. La Figure 3 montre la forme typique d'une fonction de modification nucléaire en fonction du $x$ de Bjorken. Plusieurs régions peuvent y être distinguées, selon les effets nucléaires entrant en action :

- l'effet de shadowing, pour des petites valeurs de $x$, entraîne une diminution de la PDF suite aux interférences destructives créées par les diffusions multiples entre partons dans le noyau,
- l'effet d'antishadowing, homologue de l'effet de shadowing, entraîne une augmentation de la PDF suite aux interférences constructives,
- l'effet EMC, du nom de la European Muon Collaboration qui l'a mis en avant, est une observation de la diminution des PDF pour des valeurs proches de $x = 1$ dont l'interprétation est encore en cours.

Les paramètres $x_a$, $x_e$, $y_a$ et $y_e$ représentent des paramètres libres supplémentaires du modèle, permettant de déterminer pour chaque nPDF la position des extrema dans les régions d'antishadowing et d'effet EMC.

Les résultats présentés dans cette thèse sont comparés à trois modèles récents de nPDF : nCTEQ15 [9], EPPS16 [8] et nNNPDF2.0 [7]. Ces trois modèles suivent diverses approches phénomenologiques et methodologiques pour la détermination des distributions. Dans le modèle nCTEQ15, une paramétrisation directe des nPDF est réalisée, avec une fonction d'interpolation exprimée sous forme polynômiale. Le modèle comporte 35 paramètres libres, dont la détermination est faite sur environ 700 points expérimentaux dans sa version initiale. En 2021, une extension de ce modèle a été publiée, contenant la version nCTEQ15WZ [10]. Celle-ci se distingue du modèle initial par l'inclusion de 120 points expérimentaux supplémentaires provenant de mesures de la production des bosons $W^{\pm}$ et $Z^0$ effectuées au LHC lors du Run 1. Le modèle EPPS16 repose sur la détermination de la fonction de modification nucléaire, prenant la PDF libre CT14 comme base. Ici également, la fonction d'interpolation est un polynôme. Ce modèle contient plus de 1800 points expérimentaux, permettant une paramétrisation indépendante du quark $s$, en conséquence de quoi le modèle contient également plus de paramètres libres (52). Le modèle nNNPDF2.0 se distingue des deux précédents par le choix d'utiliser un réseau de neurones pour la fonction d'interpolation, permettant d'atteindre une précision équivalente aux modèles nCTEQ et EPPS avec 256 paramètres libres. Le modèle nNNPDF connaît une évolution rapide, portée par l'inclusion de nouveaux points expérimentaux. À ce jour, environ 1500 points sont utilisés pour la détermination de la version 2.0. La Table 2 résume les principales caractéristiques des modèles utilisés dans ce travail de thèse.

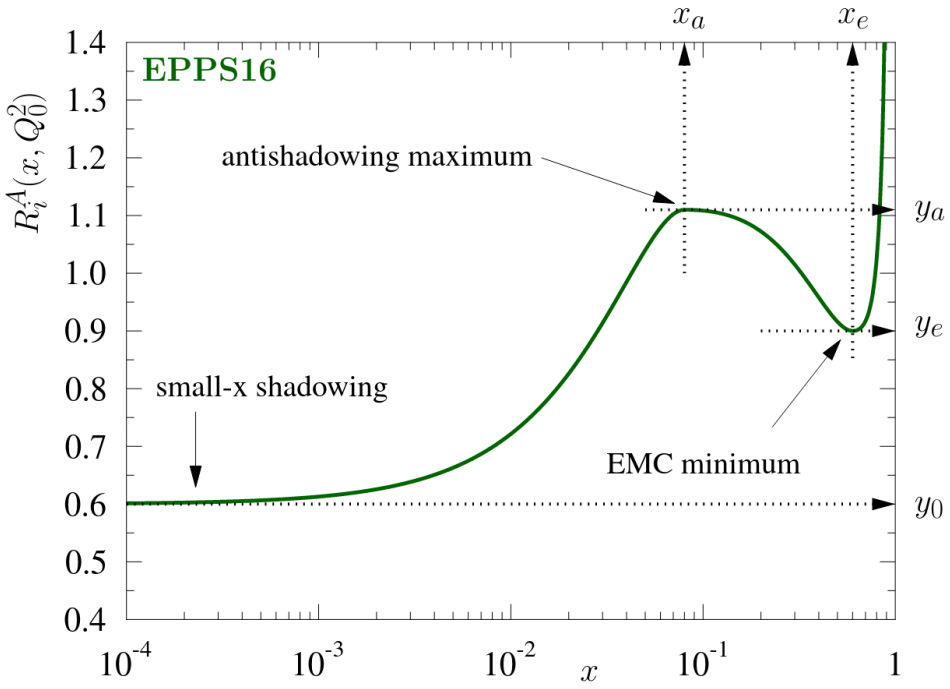


**Figure 3:** Illustration de la fonction de modification nucléaire dans le modèle EPPS16. Figure tirée de la Ref. [8].

## Bosons électrofaibles dans les collisions d'ions lourds

L'étude de la production des bosons $W^{\pm}$ et $Z^0$ dans les collisions d'ions lourds fournit une manière efficace de sonder l'état initial de la collision. Depuis leur découverte au Super Proton Synchrotron (SPS) dans les années 1980, ces bosons ont été largement étudiés auprès d'expériences et par des collaborations dédiées. La Table 3 donne les principales caractéristiques des bosons $W^{\pm}$ et $Z^0$: leur masse, largeur, et rapport d'embranchement $BR$ hadronique et leptonique.

L'énergie atteinte par le LHC dans les collisions d'ions lourds a rendu possible l'étude des bosons électrofaibles pour la première fois. Comme ils ne portent pas de charge de couleur, ils sont insensibles à l'interaction forte, et leur propagation ne sera donc pas affectées par la présence éventuelle de matière forte dans l'histoire de la collision. Comme indiqué dans la Table 3, ils possèdent une certaine probabilité de se désintégrer en leptons, particules également insensibles à l'interaction forte. Il est possible de montrer que suite à leur impulsion importante, les muons provenant de la désintégration des bosons électrofaibles ont des interactions électromagnétiques négligeables avec le plasma, de sorte que le procédé dans son ensemble n'est pas affecté par le QGP. La grande masse des bosons en fait des particules dures, dont la production lors des tous premiers instants de la collision a été montrée comme étant proportionnelle aux nPDF des ions entrant en collision. Cette information cruciale sur l'état initial sera donc portée par les bosons, puis par leurs

| Modèle | nCTEQ15 | EPPS16 | nNNPDF2.0 |
|---|---|---|---|
| Ordre | NLO | NLO | NLO |
| Séparation des saveurs | quarks de valence | quarks de valence et mer | quarks de valence et mer |
| PDF libre de référence | CTEQ6M modifiée | CT14NLO | NNPDF3.1 |
| Points expérimentaux | 708 | 1811 | 1467 |
| Échelle $Q_0$ | 1.30 GeV | 1.30 GeV | 1 GeV |
| Paramètres libres | 35 | 52 | 256 |
| Paramétrisation | polynôme | polynôme | réseau de neurones |
| Incertitudes | Hessienne | Hessienne | Monte Carlo |

**Table 2:** Caractéristiques principales des modéles nCTEQ15 [9], EPPS16 [8] et nNNPDF2.0 [7]. Les informations pour le modèle nCTEQ15 valent pour sa version originale.

| Boson | Masse (GeV/$c^2$) | Largeur (GeV/$c^2$) | $BR$ hadronique (%) | $BR$ leptonique (%) |
|---|---|---|---|---|
| $W^{\pm}$ | 80.379 ± 0.012 | 2.085 ± 0.042 | 67.41 ± 0.27 | 10.86 ± 0.09 |
| $Z^0$ | 91.1876 ± 0.0021 | 2.4952 ± 0.0041 | 69.911 ± 0.056 | 3.3658 ± 0.0023 |

**Table 3:** Masse, largeur, et rapport d'embranchement hadronique et leptonic des bosons $W^{\pm}$ et $Z^0$. Informations tirées de la Ref. [4].

produits de désintégration, jusqu'aux détecteur où elle pourra être collectée directement.

L'intérêt d'une telle étude est illustrée par la Figure 4, montrant des prédictions sur la production des bosons $Z^0$, $W^-$ et $W^+$ en collisions p–Pb à l'énergie nominale du LHC. Ces calculs théoriques ont été réalisés avec et sans inclure les modifications nucléaires des PDF. Sans ces modifications, la production du boson $Z^0$ est symmétrique en fonction de la rapidité, alors qu'une large asymmétrie entre les productions à rapidité positive et négative est observée lors de leur inclusion. Les mêmes conclusions sont dérivables des distributions pour les bosons $W^-$ et $W^+$. Il est également intéressant de considerer les incertitudes sur les prédictions. Même lorsque les valeurs centrales sont significativement différentes, la taille des intervalles d'erreur entraine un recouvrement important des distributions avec et sans modifications nucléaires. Il est donc important de fournir davantage de données précises pour la détermination des nPDF, afin d'aider à réduire les incertitudes sur les modèles.

La Figure 4 permet d'identifier les observables d'intérêt, fournissant des informations et contraintes importantes pour la détermination des nPDF. La section efficace de production est la première d'entre elles, par sa dépendance directe aux nPDF. La taille des effets nucléaires peut être évaluée par le facteur de modification nucléaire $R_{\mathrm{pPb}}$, défini comme le rapport entre les sections efficaces de production dans les collisions p–Pb et pp, cette dernière étant corrigée pour le nombre de nucléons dans le noyau :

$$R_{\mathrm{pPb}} = \frac{1}{208}\frac{\mathrm{d}\sigma_{\mathrm{pPb}}}{\mathrm{d}\sigma_{\mathrm{pp}}}. \tag{6}$$

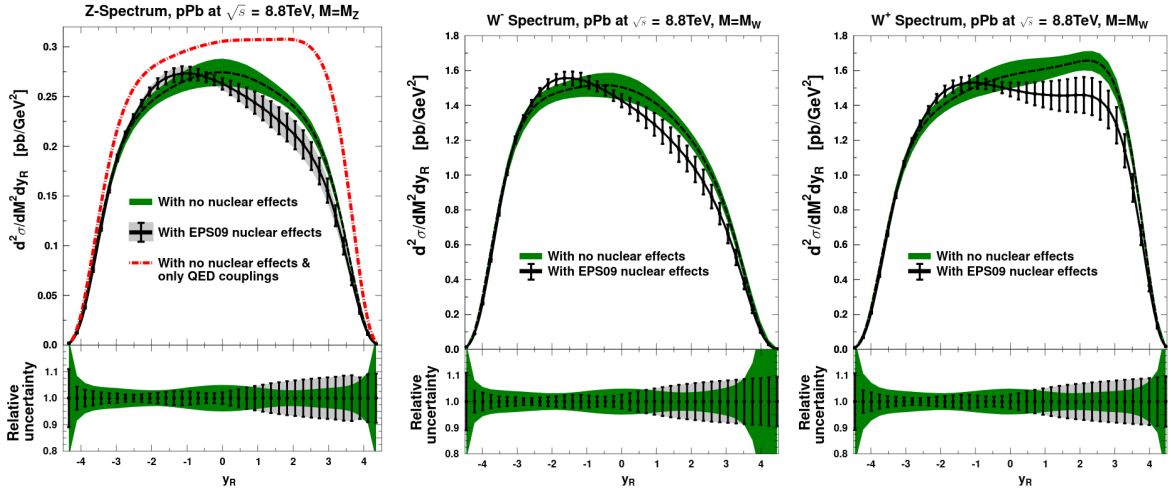


**Figure 4:** Section efficace de production des bosons $Z^0$ (gauche), $W^-$ (milieu) et $W^+$ (droite) dans les collisions p–Pb à $\sqrt{s_{NN}} = 8.8$ TeV. La ligne en pointillés correspond aux prédictions réalisées avec le modèle de PDF libre CTEQ6.6 [11], sans inclusion de modifications nucléaires. La ligne pleine correspond aux prédictions avec CTEQ6.6 combiné avec le modèle EPS09 [12] de modification nucléaire. Les panneaux inférieurs montrent les incertitudes relatives pour chaque distribution. Figure tirée de la Ref. [13].

Il est important de noter que le dénominateur dans l'expression représente une somme de collisions pp. Le facteur de modification nucléaire, calculé ou mesuré pour les bosons électrofaibles, ne sera donc pas égal à 1 en l'absence d'effets nucléaires, puisque la production dans des collisions p–Pb est également impactée par l'effet d'isospin. Enfin, il est possible de bénéficier des deux charges possibles du boson $W^{\pm}$ pour définir le ratio de charge $R$ :

$$R = \frac{N_{\mu^+ \leftarrow W^+}}{N_{\mu^- \leftarrow W^-}}, \tag{7}$$

où $N_{\mu^+ \leftarrow W^+}$ et $N_{\mu^- \leftarrow W^-}$ représentent le nombre de muons provenant de la désintégration de $W^+$ et $W^-$ respectivement. Cette observable permet de contraindre les PDF des quarks légers à travers sa sensibilité au rapport entre le nombre de quarks $d$ et $u$ dans le noyau. Il est possible d'augmenter cette sensibilité en définissant l'asymmétrie de charge $A_{ch}$ comme :

$$A_{ch} = \frac{N_{\mu^+ \leftarrow W^+} - N_{\mu^- \leftarrow W^-}}{N_{\mu^+ \leftarrow W^+} + N_{\mu^- \leftarrow W^-}} = \frac{R-1}{R+1}. \tag{8}$$

Ces quantités étant des rapports, et étant calculés à partir du nombre de muons détectés, et non de la section efficace de production, ils permettent d'enlever certaines sources d'incertitudes sur la mesure finale.

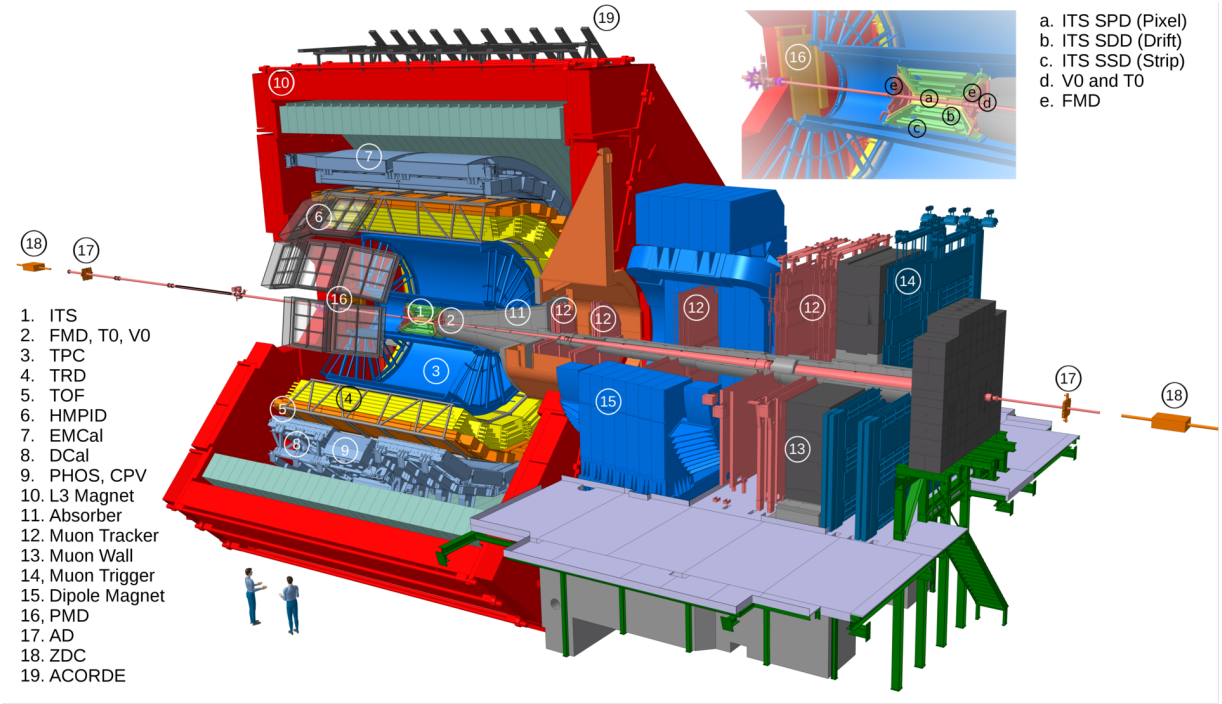


**Figure 5:** Illustration shématique du détecteur ALICE. La région autour du point de collision est détaillée dans le panneau en haut à droite.

# Le détecteur ALICE

L'expérience ALICE (A Large Ion Collider Experiment) [14] est l'une des quatre principales expériences du LHC, la seule dédiée à l'étude des collisions d'ions lourds. La Collaboration ALICE comporte 1975 membres, venant de 170 instituts répartis dans 40 pays. La Collaboration utilise un détecteur de 10 000 tonnes, long de 26 mètres, large et haut de 16 mètres, enterré 56 mètres sous terre à l'un des points d'interaction du LHC. Le détecteur a été spécialement conçu pour supporter les importantes multiplicités de particules attendues dans les collisions d'ions lourds les plus centrales, pouvant produire jusqu'à 8 000 particules chargées par unité de rapidité, tout en conservant des capacités de trajectographie et de reconstruction de traces sur un large intervalle d'impulsion.

Le détecteur est schématisé sur la Figure 5. Il contient trois principaux groupes de sous-détecteurs :

- les détecteurs dits globaux fournissent des informations générales sur les collisions, telles que la multiplicité et la centralité de chaque évènement. Ils participent au déclenchement et à l'analyse du bruit de fond,
- le tonneau central, centré autour du point de collision, est utilisé pour la reconstruction

du vertex primaire, la trajectographie des particules chargées, l'identification des électrons, photons et hadrons, ainsi que la détection des gerbes hadroniques,

- le spectromètre à muons, conçu pour la détection des produits de désintégration muonique des mésons légers ($\rho$, $\eta$, $\omega$), quarkonia, hadrons de saveurs lourdes et bosons électrofaibles à grande rapidité.

Plusieurs de ces détecteurs ont servi aux analyses présentées dans ce manuscrit.

Le V0 contient deux tuiles de scintillateurs, découpées en 4 cercles creux concentriques et placées à 340 cm et -90 cm du point de collision. Les fonctions principales du V0 sont de fournir un signal de déclenchement à travers la coincidence de signaux dans les deux tuiles, ainsi que de fournir des capacités de rejet du bruit de fond. L'amplitude totale du signal enregistré par les tuiles est utilisée pour l'évaluation de la centralité de l'évènement, et le V0 contribue à la mesure de la section efficace visible par balayage van der Meer [15, 16].

Le calorimètre à zero degré (Zero Degree Calorimeter, ZDC) contient deux ensemble identiques de deux calorimètres chacun, pour la détection de protons et neutrons le long de la ligne des faisceaux. Les deux ensembles sont placés de part et d'autre du point de collision, à 113 m de celui-ci. Le ZDC fournit un évaluateur de la centralité de l'évènement grâce à la détection des nucléons spectateurs.

Le système de trajectographie interne (Inner Tracking System, ITS) est un cylindre composé de six couches de détecteurs en silicone, placé symmétriquement autour du point de collision. Étant le détecteur le plus proche du point de collision, avec une couche interne à 3.9 cm de celui-ci, l'ITS vise à évaluer les vertex primaires et secondaires, et assiste la chambre à projection temporelle (Time Projection Chamber, TPC) dans la trajectographie des particules chargées.

Le spectromètre à muons [17, 18] constitue le principal détecteur utilisé pour réaliser les mesures présentées dans cette thèse. Il fournit une couverture azimuthale totale pour des angles polaires compris entre 170° et 178°. La composition du spectromètre est indiquée sur la Figure 6. Il est composé d'un système de trajectographie, d'un système de déclenchement et d'un ensemble d'absorbeurs.

Le système de trajectographie contient cinq stations, chacune comprenant deux plans de chambres cathodiques. Les prérequis en terme de résolution ont conduit à l'utilisation de chambres proportionnelles multifils pour les stations de trajectographie, permettant d'atteindre une précision spatiale de 100 $\mu$m nécessaire à la résolution des différents états d'excitation du bottomonium. La troisième station est située à l'intérieur d'un aimant dipolaire, dont les bobines résistives fournissent un champ magnétique intégré de 3 Tm dans le plan horizontal, perpendiculairement à l'axe des faisceaux. La déviation induite par ce champ permet la mesure de la charge et de l'impulsion des muons traversant le trajectographe.

Le déclencheur à muons est composé de quatre plans regroupés en deux stations, chaque plan contenant 18 chambres à plaques résistives (Resistive Plate Chamber, RPC). Une évaluation bidimensionnelle de la position d'un muon frappant le déclencheur est fournie par un système de bandes de lecture orthogonales découpant les plans en 234 zones de détection. Chaque RPC est faite de deux électrodes en Bakelite de haute résistivité séparées de 2 mm. Le signal est créé par

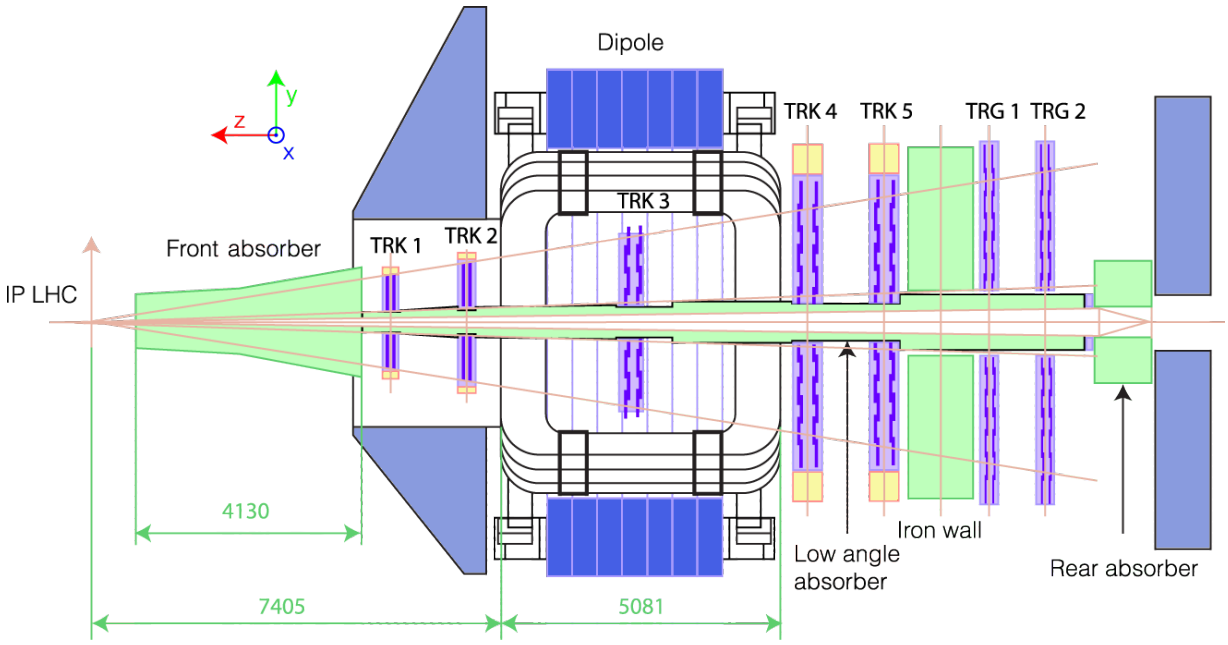


**Figure 6:** Coupe transversale, dans le plan longitudinal, du spectromètre à muon d'ALICE.

l'avalanche d'électrons déclenchée par le passage d'une particule chargée à travers le gaz contenu dans l'espace entre les deux électrodes. Le système fournit des signaux de déclenchement selon des configurations pré-programmées, afin par exemple de sélectionner les évènements contenant un muon de basse ou haute impulsion transverse, une paire de muons de signes opposés, etc.

Le spectromètre est protégé du bruit de fond par la présence de plusieurs absorbeurs. Entre le point de collision et la première station de trajectographie se trouve l'absorbeur avant, un cône de ciment et de carbone de 37 tonnes visant à absorber les particules de faible impulsion provenant du point d'interaction. Les stations du déclencheur sont situées derrière un mur de fer d'une épaisseur de 1,2 m, qui filtre les hadrons et les particules passant à travers l'absorbeur avant ou étant produites dans celui-ci. Le spectromètre dans son ensemble est protégé de l'important bruit de fond produit par les interactions entre le tube du faisceau et les particules émises à très faible rapidité par l'absorbeur à petit angle, un tuyau de tungstène, de plomb et d'acier entourant le tuyau du faisceau sur tout la longueur du spectromètre. Enfin, un second mur de fer protège l'arrière du déclencheur des particules produites lors des interactions entre le faisceau et le gaz rémanant présent dans le tuyau du faisceau.

# Upgrade d'ALICE pour le Run 3 au LHC

Depuis 2018, le LHC est à l'arrêt afin de préparer les prises de données du Run 3. Cet arrêt long, le deuxième depuis le démarrage du LHC en 2009, permet aux collaborations d'améliorer leurs détecteurs. L'amélioration du LHC lui-même vise à augmenter la luminosité délivrée par le

collisioneur. Le programme d'amélioration du détecteur ALICE [19] vise à renforcer les capacités de détection et d'analyse dans trois domaines principaux.

- **Saveurs lourdes** : l'amélioration de la précision et des possibilités de mesures de la production des quarks $c$ et $b$ constitue l'une des principales motivations pour l'amélioration du détecteur ALICE. Ces études se feront principalement à travers les mesures de la thermalisation des saveurs lourdes dans le QGP, par la détermination du rapport entre baryons et mésons pour chaque saveur, les anisotropies azimuthales et la possible production thermique du quark $c$ à l'intérieur du QGP ; ainsi que par l'évaluation de la dépendance aux masses partoniques et charges de couleur de la perte d'énergie dans le QGP. Ces études nécessitent notamment une importante précision dans la détermination des vertex secondaires, et la capacité de fonctionner en lecture continue afin de pleinement bénéficier de la luminosité offerte par le LHC.

- **Quarkonia** : la mesure de la production des quarkonia, états liés de quark-antiquark $c$ ou $b$, devrait apporter une réponse définitive à la question de la production de ces saveurs dans le QGP. Les données des Runs 1 et 2 ont notamment fait ressortir l'importance de réaliser de telles mesures à de très faibles impulsions transverses. Plusieurs modèles ont été proposés pour reproduire les productions observées des mésons $J/\psi$ et $\Upsilon$, tels que l'hadronisation statistique, l'écrantage de Debye ou les modèles de transport. L'amélioration devrait également permettre des mesures précises de la production des états excités de ces mésons.

- **Dileptons de basse masse invariante** : ces mesures apporteront un éclairage sur l'évolution spatio-temporelle de la matière forte lors des collisions d'ions lourds. Elles permettront en particulier d'étudier la brisure spontanée de la symétrie chirale, l'évolution de la température du système, et le temps de vie des différentes phases d'évolution de la collision. Ici encore les capacités de détermination des vertex de production et les mesures à basses impulsions transverses sont cruciales.

À ceci s'ajoute un intérêt certain pour la mesure des gerbes hadroniques et des états exotiques.

Ces objectifs seront autant réalisés par l'amélioration des détecteurs existants que par l'ajout de nouveaux détecteurs. Le spectromètre à muons se verra amélioré par l'addition du trajectographe à muons à l'avant (Muon Forward Tracker, MFT) [20]. Le MFT se situe entre le point de collision et l'absorbeur à l'avant. Il est composé de deux demi-cônes, chacun comportant cinq demi-disques faits de détecteurs en silicone. Le MFT apporte des capacités de détermination de vertex au spectromètre et, couplé au trajectographe, améliore la reconstruction des traces. Il devrait notamment permettre une mesure précise de la production du $\psi(2S)$ afin de tester les modèles de dissociation et (re)combinaison.

L'électronique de lecture du trajectographe sera améliorée afin d'assumer le taux de lecture attendu dans le mode continu. Le déclencheur à muons sera transformé pour devenir l'identificateur à muons (Muon Identifier, MID). Le vieillissement des RPC sera diminué par l'utilisation de cartes à plus faible gain, couplée à des puces électroniques appelées FEERIC fournissant une amplification du signal. Les RPC les plus proches du faisceau, ayant soutenu une charge plus importante lors des Runs 1 et 2, seront remplacées.

Enfin, un nouveau logiciel d'analyse est développé afin de remplacer AliRoot, le logiciel utilisé précedemment par la Collaboration ALICE. Ce nouveau logiciel, appelé O2 (Online-Offline) [21], vise notamment à assurer la possibilité de lire, analyser et stocker les données aux taux du Run 3, s'élevant à 50 kHz dans les collisions Pb–Pb et 200 kHz pour les collisions p–Pb et pp.

Lors de ce travail de thèse, j'ai contribué à l'amélioration du détecteur par la participation au développement du logiciel de contrôle qualité (Quality Control, QC) du MID. Le QC vise à fournir un retour instantané sur la qualité des données et le fonctionnement du détecteur lors des campagnes de prise de données. Il surveille également les premières étapes du traitement des données et leur enregistrement. Un module du QC, attaché à un détecteur, comprend typiquement une série de tâches effectuées sur les données, ou un fraction d'entre elles, produisant des résultats affichés sous la forme d'histogrammes régulièrement mis à jour dans la salle de contrôle de l'expérience. Ces objets de sortie permettent de surveiller en temps réel l'état de fonctionnement, une information cruciale pour les analystes lors notamment de l'évaluation de l'efficacité du détecteur. Ces objets peuvent aussi, en cas de besoin, être conservés pour référence.

Un module du QC s'organise autour de fichiers pour les tâches définies par l'utilisateur, et d'un fichier de configuration au format `json`. Ce dernier contient des informations telles que les fichiers et bibliothèques devant être chargées lors du lancement du module, ou les instructions d'échantillonnage des données lorsqu'une lecture de la totalité de celles-ci n'est pas possible ou souhaitable. Ma participation a consisté à l'inclusion de tâches de vérfication des données brutes dans le module du MID. Le module a éte testé sur des données simulées, en forçant l'apparition d'erreurs aléatoires. Les données sont lues par le module au fil de l'eau, et une série de tests automatisés s'assurent de leur qualité. Une erreur détectée par le module se trouve affichée sous la forme :

```
BCid: 0x71c Orbit: 0xf   [in  page: 542  (line: 277505)  ]
loc-reg inconsistency: fired locals (00010000) != expected from reg (00000000);
Crate ID: 15  Loc ID:  4  status: 0xc0  trigger: 0x 0 firedChambers: [...]
```

La première ligne permet d'identifier l'évènement, la seconde fourni une description de l'erreur détectée (ici une incohérence entre les réponses de cartes à différentes étapes de la chaîne de traitement). La troisième ligne permet enfin de localiser spatialement l'erreur à travers les identifiants uniques attribués à chaque RPC du MID. Un histogramme est rempli pour chaque évènement lu et chaque erreur détectée.

## Mesure de la production des bosons électrofaibles dans les collisions p–Pb à $\sqrt{s_{\mathrm{NN}}} = 8.16$ TeV

Les données analysées lors de ce travail de thèse ont été collectées lors de collisions p–Pb effectuées en 2016 à une énergie dans le centre de masse $\sqrt{s_{\mathrm{NN}}} = 8.16$ TeV. Les collisions ont été effectuées dans deux configurations différentes, l'une avec le faisceau de proton dirigé vers le spectromètre (p–Pb), l'autre avec le faisceau de proton pointant à son opposé (Pb–p). Les collisions entre protons et noyaux de plomb etant asymétriques, la rapidité dans le centre de masse se retrouve

| Système | Période | Nb de runs | Rapidité | $N_{\texttt{CMSH}}$ | $N_{\texttt{CMUL}}$ |
|---|---|---|---|---|---|
| p–Pb | LHC16r | 57 | $2.03 < y_{\rm cms} < 3.53$ | $18.5 \times 10^6$ | $25.8 \times 10^6$ |
| Pb–p | LHC16s | 80 | $-4.46 < y_{\rm cms} < -2.96$ | $35.1 \times 10^6$ | $72.0 \times 10^6$ |

**Table 4:** Caractéristiques des deux périodes analysées dans cette thèse, correspondant à des collisions p–Pb à $\sqrt{s_{\rm NN}} = 8.16$ TeV.

décalée par rapport à la rapidité dans le référentiel du laboratoire par $\Delta y \approx 0.465$. La couverture en rapidité du spectromètre, $-4 < y_{\rm lab} < -2.5$, correspond donc à :

- p–Pb collisions : $2.03 < y_{\rm cms} < 3.53$,
- Pb–p collisions : $-4.46 < y_{\rm cms} < -2.96$,

avec le faisceau de protons se dirigeant vers les rapidités positives, par convention. La rapidité peut être reliée au $x$ de Bjorken par :

$$x_{1,2} = \frac{M_{\rm Z,W}}{\sqrt{s_{\rm NN}}} \exp\left(-y\right). \tag{9}$$

Les configurations p–Pb et Pb–p correspondent donc à de faibles ($\sim 10^{-4}- \sim 10^{-3}$) et fortes ($\sim 0.1- \sim 1$) valeurs de $x$ respectivement.

Les évènements sont dans un premier temps sélectionné par la `PhysicsSelectionTask` qui applique une série de tests basiques portant sur la qualité des données, rejetant par exemple les évènements classés comme bruit de fond par le V0. La tâche rejette également les évènements pile-up, ceux pour lesquelles deux collisions ou plus ont eu lieu lors du croisement de deux paquets des faisceaux. Une sélection portant sur la qualité du vertex s'assure qu'au moins une trace ait été détecté par l'ITS, et que le vertex primaire se trouve à moins de 10 cm du point d'interaction. Les classes de déclenchement permettent ensuite de sélectionner les évènements utiles à l'analyse. Pour ce travail, deux classes ont principalement été utilisées:

- **Dimuon Unlike-sign low** (`MUL`) : demandant une paire de muons de signes opposés avec un impulsion transverse ($p_{\rm T}$) d'au moins 0.5 GeV/$c$, servant à la mesure du boson $\rm Z^0$,
- **Single Muon High** (`MSH`) : demandant un muon avec $p_{\rm T} \gtrsim 4.2$ GeV/$c$ pour la mesure du boson $\rm W^{\pm}$.

La Table 4 résume les caractéristiques des deux périodes et indiquent le nombre d'évènements sélectionnés pour les deux classes de déclenchement. Le calcul de la luminosité pour les deux analyses diffère, la mesure du boson $\rm Z^0$ ayant été effectuée avant l'inclusion de la sélection sur le pile-up dans la `PhysicsSelectionTask`. Les luminosités correspondant à chaque configurations ont été évaluées à :

- sans rejet du pile-up (boson $\rm Z^0$) :

$$\mathcal{L}_{\rm int} = \begin{cases} 8.40 \pm 0.01\ (\text{stat}) \pm 0.17\ (\text{syst})\ \text{nb}^{-1} & \text{collisions p–Pb}, \\ 12.74 \pm 0.01\ (\text{stat}) \pm 0.26\ (\text{syst})\ \text{nb}^{-1} & \text{collisions Pb–p}, \end{cases} \tag{10}$$

- avec rejet du pile-up (boson $W^{\pm}$) :

$$\mathcal{L}_{\text{int}} = \begin{cases} 6.81 \pm 0.01\ (\text{stat}) \pm 0.15\ (\text{syst})\ \text{nb}^{-1} & \text{collisions p–Pb,} \\ 10.2 \pm 0.01\ (\text{stat}) \pm 0.28\ (\text{syst})\ \text{nb}^{-1} & \text{collisions Pb–p.} \end{cases} \tag{11}$$

Les évènements sélectionnés ont ensuite été lus pour en extraire les traces pouvant correspondre aux signaux des bosons $Z^0$ et $W^{\pm}$. Une sélection est appliquée afin de s'assurer de la qualité des traces et rejeter une partie du bruit de fond. Cette sélection comporte :

- la coincidence entre le trajectographe et le déclencheur, afin de s'assurer que la trace reconstruite dans le trajectographe correspond à un segment de trace reconstruit dans le déclencheur,
- le rejet des traces ayant un angle polaire mesuré à l'extrémité de l'absorbeur à l'avant hors de $170^{\circ} < \theta_{\text{abs}} < 178^{\circ}$ afin de ne pas conserver des traces ayant subit des diffusions multiples dans l'absorbeur,
- une sélection sur le produit de l'impulsion de la trace avec sa distance de plus proche approche ($p \times DCA$), c'est-à-dire la distance entre le vertex et la trace projetée dans le plan perpendiculaire au faisceau et contenant le vertex. Cette sélection vise à réduire drastiquement le bruit de fond en ne sélectionnant que des traces provenant du vertex d'interaction.

Une région fiducielle est de plus définie pour chaque analyse, d'après les capacités du détecteur et afin de maximiser l'efficacité de l'extraction du signal. Ces régions sont définies par :

- la couverture angulaire du spectromètre, $-4 < y_{\text{lab}} < -2.5$,
- une sélection sur l'impulsion transverse ($p_{\text{T}}$) de la trace, avec $p_{\text{T}} > 20$ GeV/$c$ pour l'analyse du boson $Z^0$ et $p_{\text{T}} > 10$ GeV/$c$ pour l'analyse du boson $W^{\pm}$,
- une sélection sur la masse invariante de la paire de muons pour l'analyse du boson $Z^0$, qui doit être dans l'intervalle $60 < m_{\mu\mu} < 120$ GeV/$c^2$ afin d'enlever les paires ayant une masse invariante irréaliste avec celle du boson $Z^0$.

L'extraction de signal du boson $Z^0$ repose sur l'analyse de la distribution en masse invariante des paires de muons reconstruites dans les évènements et à partir des traces sélectionnés. L'application de ces sélections permet d'obtenir les distributions indiquées par la Figure 7, sur laquelle un pic de production autour d'une masse invariante d'environ 90 GeV/$c^2$ est nettement visible. Le comptage des candidats dans la région fiducielle donne $64 \pm 8$ candidats pour le $Z^0$ dans les collisions p–Pb et $34 \pm 6$ dans les collisions Pb–p.

La sélection présentée précedemment vise à réduire au maximum le bruit de fond. Il peut cependant rester des contributions non négligeables, provenant de la décroissance muonique des hadrons de saveur lourde, de paires de quarks top, du procéde $Z \to \tau\tau \to \mu\mu$ ou du bruit de fond combinatoriel. Ces contributions potentielles ont été estimées par le biais de simulations Monte

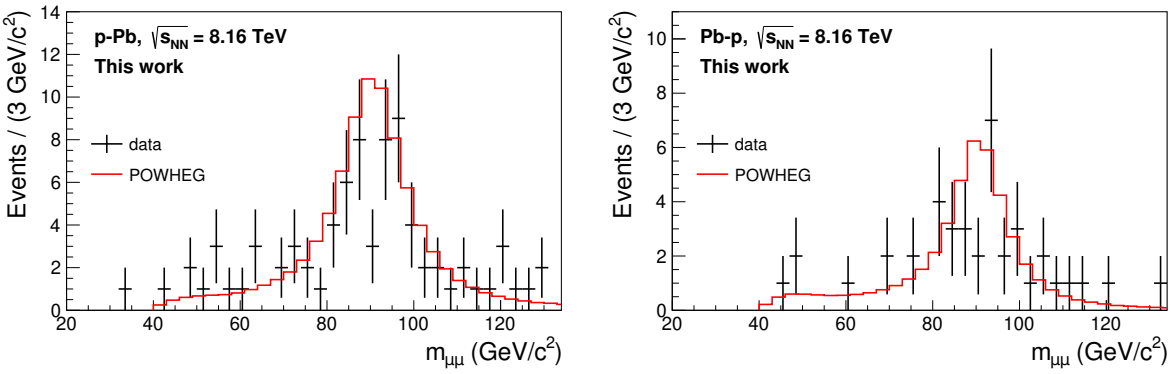


**Figure 7:** Distribution en masse invariante des paires de muons reconstruites dans les collisions p–Pb (gauche) et Pb–p (droite) à $\sqrt{s_{\mathrm{NN}}} = 8.16$ TeV. Les lignes sur chaque figure correspondent à des simulations du procédé $\mathrm{Z}^0 \to \mu^+\mu^-$ avec le générateur POWHEG, et CT10 et EPS09 comme modèles de PDF et nPDF, respectivement. Les simulations incluent la réponse du détecteur et sont normalisées au nombre d'évènements dans les données.

Carlo ou de l'analyse des paires de signes similaires pour le bruit combinatoriel. Le bruit de fond total a été estimé à 1% pour la configuration p–Pb, il est négligeable pour la configuration Pb–p. Ce faible niveau de bruit de fond permet de prendre le résultat du comptage comme extraction de signal, avec une erreur systématique de 1% dans les collisions p–Pb.

L'extraction de signal du boson $\mathrm{W}^{\pm}$ est compliquée par la présence d'un neutrino dans l'état final du procédé $\mathrm{W} \to \mu\nu$. Ce neutrino ne peut pas être reconstruit à travers l'énergie manquante, ALICE n'étant pas un détecteur hermétique. L'extraction de signal repose donc sur l'étude de la distribution en $p_{\mathrm{T}}$ des muons, qui est ajustée par une combinaison de gabarits obtenus par simulations Monte Carlo. Ces gabarits visent à reproduire les contributions participant au spectre inclusif. L'ajustement est réalisé par la formule :

$$f(p_{\mathrm{T}}) = N_{\mathrm{bkg}} \cdot f_{\mathrm{bkg}}(p_{\mathrm{T}}) + N_{\mu^{\pm}\leftarrow \mathrm{W}^{\pm}} \cdot \left( f_{\mu^{\pm}\leftarrow \mathrm{W}^{\pm}}(p_{\mathrm{T}}) + R \cdot f_{\mu^{\pm}\leftarrow \mathrm{Z}^0}(p_{\mathrm{T}}) \right), \tag{12}$$

où :

- $f_{\mathrm{bkg}}$, $f_{\mu^{\pm}\leftarrow \mathrm{W}^{\pm}}$ et $f_{\mu^{\pm}\leftarrow \mathrm{Z}^0}$ représente les gabarits pour les muons provenant de la décroissance des hadrons de saveur lourde, des bosons $\mathrm{W}^{\pm}$ et des bosons $\mathrm{Z}^0$ respectivement,
- $N_{\mathrm{bkg}}$ et $N_{\mu^{\pm}\leftarrow \mathrm{W}^{\pm}}$ sont les paramètres libres de l'ajustement, représentant le nombre de muons provenant de la décroissance des hadrons de saveur lourde et des bosons $\mathrm{W}^{\pm}$ respectivement,
- $R$ est un paramètre fixe, forçant le nombre du muons provenant de la décroissance de bosons $\mathrm{Z}^0$ à être proportionnel à celui provenant de la décroissance de bosons $\mathrm{W}^{\pm}$ suivant le rapport de leurs sections efficaces de production évalué par le générateur POWHEG [22].

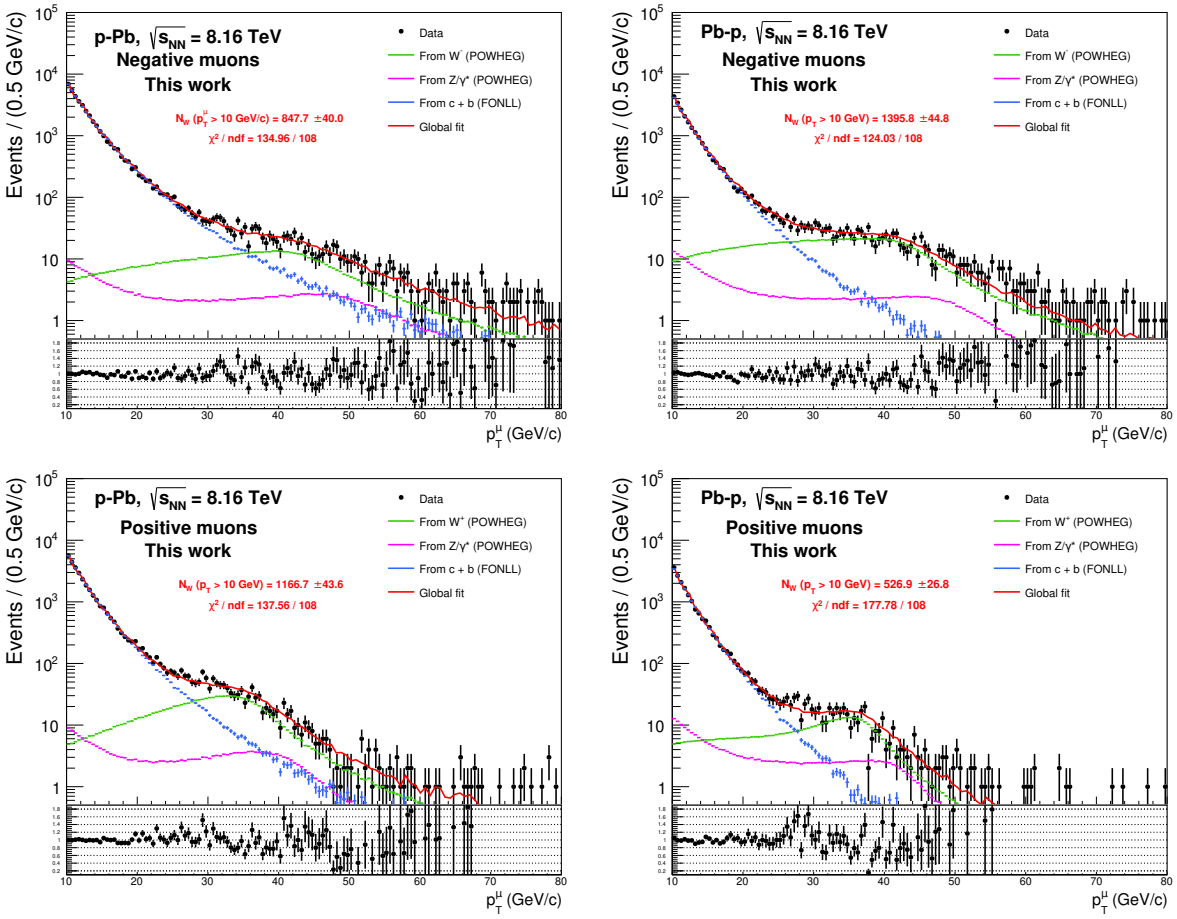


**Figure 8:** Ajustement de la distribution en $p_{\mathrm{T}}$ des muons simples dans les collisions p–Pb (haut) et Pb–p (bas) pour les muons chargés négativement (gauche) et positivement (droite). Le panneau inférieur de chaque figure montre le rapport entre les données et le résultat de l'ajustement.

Le résultat de cette procédure est illustré par la Figure 8. Pour les quatre configurations de collision et de charge considérées, le résultat de l'ajustement est en bon accord avec les données. Cette procédure repose sur l'utilisation intensive de simulations, elle est donc dépendante de la paramétrisation de celles-ci, ainsi que de celle de la méthode d'ajustement. Afin d'evaluer l'incertitude associée, ces paramètres ont été variés afin de refaire l'ajustement dans des conditions différentes. Les variations considérées comportent : l'intervalle dans lequel l'ajustement est réalisé, la valeur du couplage et l'ordre auquel les gabarits sont simulés, les modèles de PDF et nPDF utilisés pour la génération des gabarits des bosons, l'incertitude sur la section efficace de production des hadrons de saveur lourde, l'incertitude sur la résolution des clusters, qui doit être dégradée dans les simulations, et la reproduction d'un potentiel misalignement du spectromètre dans son ensemble. Toutes ces variations sont combinées de toutes les manières possibles, donnant 1290

| Collision | $\mathbf{N_{W-}}$ | $\mathbf{N_{W^+}}$ | $\mathbf{N_{Z^0}}$ |
|---|---|---|---|
| p–Pb | $824.1 \pm 43.9 \pm 72.8$ | $1105.8 \pm 47.3 \pm 65.4$ | $64 \pm 8 \pm 1$ |
| Pb–p | $1388.4 \pm 48.5 \pm 53.3$ | $493.0 \pm 28.3 \pm 35.8$ | $34 \pm 6$ |

**Table 5:** Nombres de muons provenant de la décroissance des bosons $Z^0$ et $W^{\pm}$ dans les collisions p–Pb et Pb–p à $\sqrt{s_{NN}} = 8.16$ TeV.

configurations utilisées pour l'ajustement. Une sélection sur la qualité de ce dernier assure que la configuration considérée est capable de reproduire les données de manière satisfaisante. Ces ajustements donnent une distribution de $N_{\mu^{\pm}\leftarrow W^{\pm}}$, dont la moyenne fournit le résultat final de l'extraction de signal et la déviation standard est prise comme erreur systématique associée. Le Tableau 5 résume les extractions de signal pour les deux analyses. Ces valeurs sont finalement corrigées pour l'efficacité du détecteur au cours de la période avec POWHEG, incluant une simulation de la réponse du détecteur avec le code GEANT3 [23]. La Table 6 résume les sources et valeurs des erreurs systématiques considérées pour les deux analyses.

| *in %* | Collisions p–Pb | | | Collisions Pb–p | | |
|---|---|---|---|---|---|---|
| | $W^-$ | $W^+$ | $Z^0$ | $W^-$ | $W^+$ | $Z^0$ |
| Extraction du signal | 8.8 | 5.9 | 1.0 | 3.8 | 7.3 | — |
| – vs rapidité | 4.4 – 14.3 | 3.9 – 10.7 | — | 2.5 – 9.5 | 3.9 – 21.6 | — |
| – vs centralité | 3.6 – 12.8 | 3.6 – 12.8 | — | 3.6 – 12.8 | 3.6 – 12.8 | — |
| Efficacité du trajectographe | 0.5 | | 1.0 | 1.0 | | 2.0 |
| Efficacité du déclencheur | 0.5 | | 1.0 | 0.5 | | 1.0 |
| Coincidence | 0.5 | | 1.0 | 0.5 | | 1.0 |
| Clusters et misalignement | 0.7 | 0.6 | 7.7 | 0.7 | 0.3 | 5.7 |
| Facteur de normalisation | 1.1 | | 0.7 | 1.9 | | 0.2 |
| Section visible V0 | 1.9 | | 1.9 | 2.0 | | 2.0 |
| $\langle N_{\rm coll}^{\rm mult} \rangle$ | 2.8 – 4.3 | | — | 2.8 – 4.3 | | — |

**Table 6:** Résumé des sources d'incertitudes systématiques affectant les mesures des bosons $Z^0$ et $W^{\pm}$ dans les collisions p–Pb et Pb–p à $\sqrt{s_{NN}} = 8.16$ TeV. Des intervalles sont indiquées pour les études différentielles, un barre horizontale indique que la source n'est pas appliquable ou est négligeable.

# Résultats

La section efficace de production est évaluée comme :

$$\frac{\mathrm{d}\sigma_{\mu^+\mu^-\leftarrow Z^0}}{\mathrm{d}y} = \frac{N_{\mu^+\mu^-\leftarrow Z^0}}{\Delta y \times \mathcal{L}_{\rm int} \times \varepsilon}, \qquad \frac{\mathrm{d}\sigma_{\mu^{\pm}\leftarrow W^{\pm}}}{\mathrm{d}y} = \frac{N_{\mu^{\pm}\leftarrow W^{\pm}}}{\Delta y \times \mathcal{L}_{\rm int} \times \varepsilon}, \tag{13}$$

avec $N_{\mu^+\mu^-\leftarrow \mathrm{Z}^0}$ et $N_{\mu^\pm\leftarrow \mathrm{W}^\pm}$ le nombre du muons venant de bosons $\mathrm{Z}^0$ et $\mathrm{W}^\pm$ respectivement, $\Delta y$ la largeur de l'intervalle en rapidité, $\mathcal{L}_{\mathrm{int}}$ la lumosité intégrée et $\epsilon$ l'efficacité du détecteur.

La section efficace du boson $\mathrm{Z}^0$ est montrée par la Figure 9, où elle est comparée à des prédictions théoriques obtenues avec les modèles nucléaires EPPS16 [8] et nCTEQ15 [9] et le modèle libre CT14 [24]. À des rapidités négatives, on constate la faible différence qu'il existe entre les prédictions avec et sans modifications nucléaires. En effet, cette région correspondant à des valeurs du $x$ de Bjorken entre $\sim 10^{-1}$ et $\sim 1$, la production y est affectée à la fois par l'antishadowing et par l'effet EMC, les deux effets tendant à s'annuler l'un l'autre. À rapidité positive, en revanche, l'inclusion des modifications nucléaires a un effet significatif sur les prédictions, puisqu'ici seul le shadowing entre en action et baisse la production attendue. Il est également important de noter la taille des incertitudes sur les modèles nucléaires. Cette région correspond à de basses valeurs du $x$ de Bjorken, et à ce titre elle souffre du manque de données disponibles pour contraindre les modèles théoriques. En comparant ces modèles avec les points expérimentaux, on constate que les mesures sont bien reproduites par les calculs théoriques, mais qu'aucune conclusion sur les modifications nucléaires elles-mêmes ne peut être tirée. En effet, les points expérimentaux sont en accord avec les prédictions incluant ou non les modifications nucléaires des PDF.

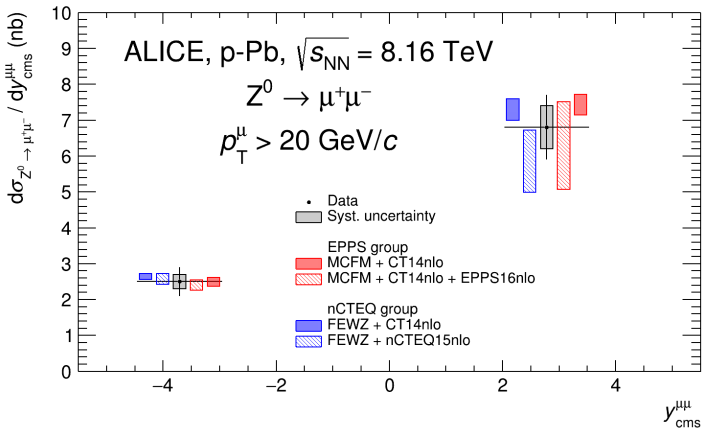


**Figure 9:** Section efficace de production du procédé $\mathrm{Z}^0 \rightarrow \mu^+\mu^-$ dans les collisions p–Pb à $\sqrt{s_{\mathrm{NN}}} = 8.16$ TeV, comparée avec des prédiction théoriques avec les modèles de nPDF EPPS16 et nCTEQ15, ainsi qu'avec des prédiction du modèle de PDF libre CT14, incluant l'effet d'isospin mais modifications nucléaires. Les barres et boîtes autour des points expérimentaux correspondent respectivement aux incertitudes statistiques et systématiques. Les points théoriques ont été décalés verticalement pour assurer la lisibilité.

La section efficace de production des bosons $\mathrm{W}^\pm$ est montrée par la Figure 10. Le signal du boson $\mathrm{W}^\pm$ étant plus fort que celui du $\mathrm{Z}^0$, il a ici été possible de couper l'intervalle en rapidité en plusieurs sous-intervalles, pour une évaluation différentielle de la section efficace. Les mesures sont comparées avec des prédictions obtenues avec les modèles EPPS16, nCTEQ15, nCTEQ15WZ [10] et nNNPDF2.0 [7]. On peut dériver les mêmes conclusions que pour la Figure 9 sur la faible amplitude des effects nucléaires à rapidité négative, et leur forte amplitude et incertitudes aux rapidités

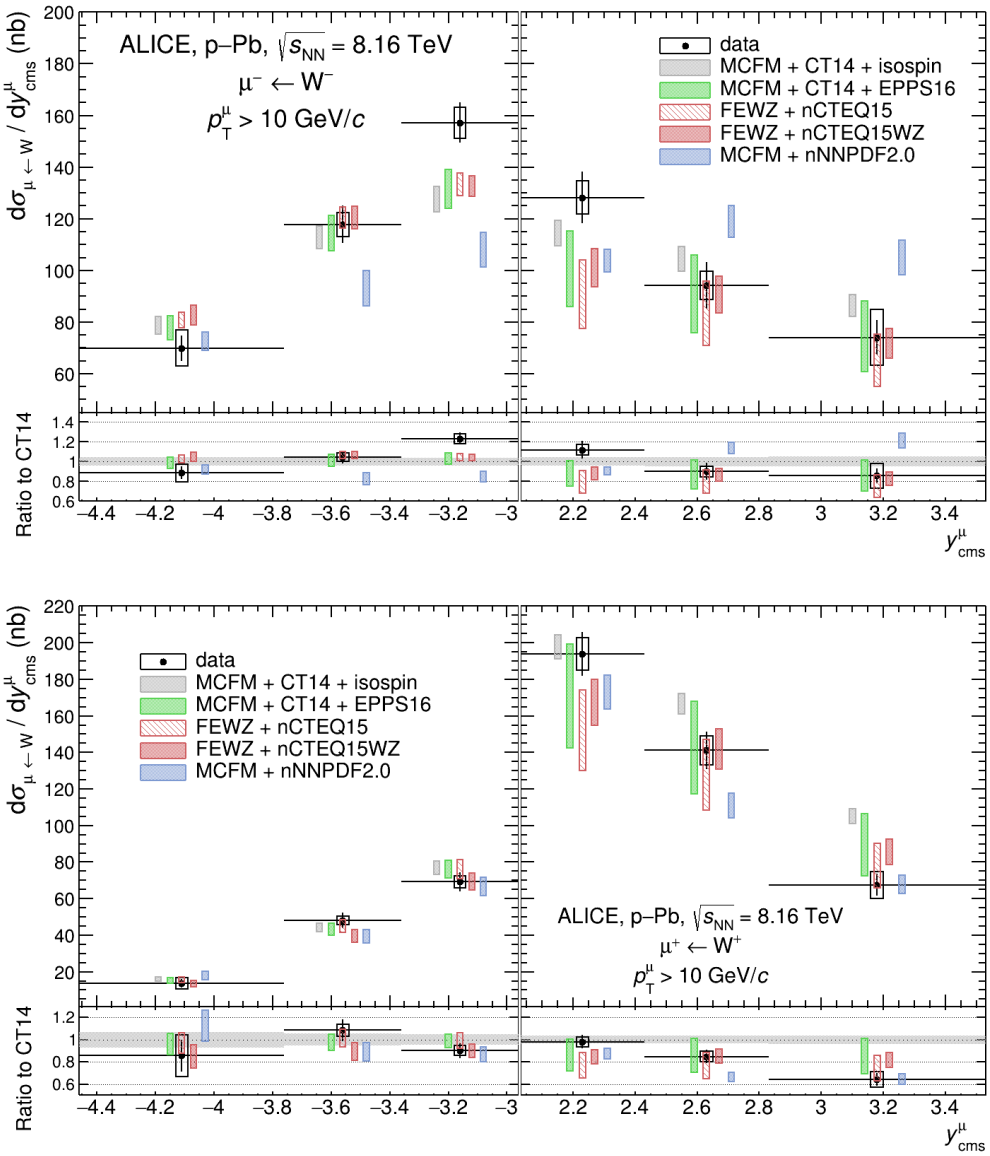


**Figure 10:** Section efficace de production du procédé $W^\pm \to \mu^\pm \nu_\mu$ pour les bosons $W^-$ (haut) et $W^+$ (bas) en fonction de la rapidité, dans les collisions p–Pb à $\sqrt{s_{NN}} = 8.16$ TeV. Les mesures sont comparées avec des prédictions obtenues en utilisant plusieurs modèles de nPDF, ainsi qu'avec des prédictions obtenues avec le modèle de PDF libre CT14, incluant l'effet d'isospin mais sans modifications nucléaires. Les panneaux inférieurs de chaque figure indiquent le rapport entre les mesures et prédictions nucléaires, et les prédictions CT14. Les barres et boîtes autour des points expérimentaux correspondent respectivement aux incertitudes statistiques et systématiques, la bande grise dans les panneaux inférieurs indique l'incertitude sur les prédictions CT14. Les points expérimentaux sont centrés dans les intervalles en rapidité, les points théoriques sont décalés horizontalement pour une meilleure visibilité.

positives. On observe un bon accord entre les prédictions des modèles EPPS16 et nCTEQ15. Il est également intéressant de comparer les deux versions du modèle nCTEQ15, on constate alors que l'inclusion de données supplémentaires pour la détermination de nCTEQ15WZ s'est traduite par une réduction significative de l'incertitude associée à ce modèle, reflétant l'intérêt de fournir de nouvelles données. Le modèle nNNPDF montre un certain désaccord avec EPPS16 et nCTEQ15 pour les prédictions du boson $W^-$, avec une section efficace plus faible à rapidité négative et un comportement plat à rapidité positive. L'accord de nNNPDF2.0 avec les autres modèles est en revanche plus satisfaisant dans le cas du boson $W^+$. Les mesures de la production du boson $W^-$ montrent une évolution plus importante de la section efficace que celle prédite par les modèles, entrainant notamment une différence significative pour les bins les plus centraux des deux intervalles en rapidité. Ces mesures pourront donc permettre de mieux contraindre les modèles nucléaires. L'accord entre la mesure et les prédictions est meilleur dans le cas du boson $W^+$. Dans ce second cas, il faut particulièrement noter l'intervalle à plus grande rapidité pour une rapidité positive. Ici la section efficace mesurée est bien reproduite par les modèles incluant les modifications nucléaires, mais pas par le modèle CT14 qui prédit une section efficace à 3.5 $\sigma$ de celle mesurée. Ce point constitue la plus forte observation de modifications nucléaires des PDF dans ce travail de thèse. Pour les deux bosons, il est également important de souligner que la taille des incertitudes expérimentales est généralement plus faible que celle des modèles. Ainsi, même en cas d'accord entre la théorie et l'expérience, ces mesures peuvent apporter un contrainte certaine et aider à réduire les incertitudes accompagnant les calculs théoriques.

Les sections efficaces de production mesurées à grande rapidité avec le spectromètre à muons d'ALICE sont complémentaires avec des mesures similaires effectuées par des détecteurs couvrant des rapidités centrales. La Figure 11 compare les mesures du boson $W^\pm$ obtenues lors de ce travail de thèse avec celles obtenues par la Collaboration CMS [25] depuis les mêmes systèmes de collision. La combinaison de ces mesures permet de couvrir quasi-intégralement le domaine en pseudorapidité $|\eta^\mu_{\rm lab}| < 4$, correspondant à des $x$ de Bjorken sur quatre ordres de grandeur. Les mesures de la Collaboration CMS sont effectuées dans une région fiducielle différente de celle des mesures ALICE, avec une sélection sur l'impulsion transverse à 25 GeV/$c$, ce qui empêche une comparaison directe. Il est en revanche possible de comparer les deux analyses à travers leur rapport avec des prédictions théoriques calculées dans les régions fiducielles adéquates. On note ici un bon accord entre les mesures provenant des deux analyses, le comportement observé aux bords de l'intervalle couvert par le détecteur CMS étant confirmé par les mesures à grandes rapidités. La précision apportée par le LHC sur les mesures de bosons électrofaibles dans les collisions p–Pb est largement mise en avant par la comparaison des incertitudes des points expérimentaux et théoriques. Ainsi, même si le modèle EPPS16 montre un très bon accord avec les mesures, l'inclusion de ces dernières fournira des contraintes importantes pour augmenter la précision des calculs.

Dans le modèle de Glauber, on s'attend à ce que la production des particules dures, telles que les bosons électrofaibles, soit directement proportionnelle avec le nombre de collisions binaires (collisions nucléon-nucléon). Ceci peut être vérifié par l'étude de la production en fonction de la centralité de la collision. La Figure 12 montre la section efficace de production du boson $W^\pm$ en fonction de la centralité exprimée par le nombre moyen de collisions binaires $\langle N^{\rm mult}_{\rm coll}\rangle$ pour quatre

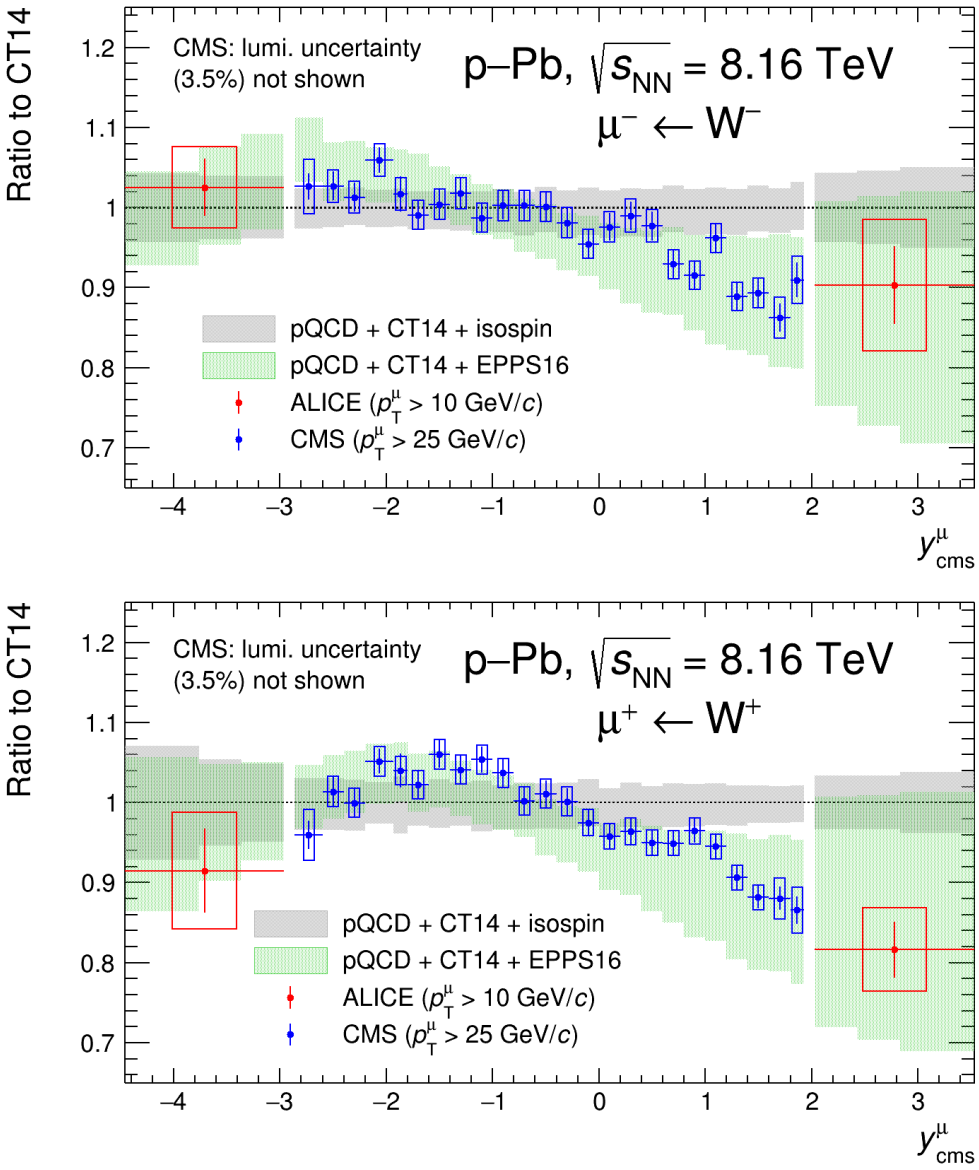


**Figure 11:** Rapport aux prédictions CT14 des sections efficaces de production des bosons $W^-$ (haut) et $W^+$ (bas) mesurées par les Collaborations ALICE (cette thèse) et CMS [25] dans les collisions p–Pb à $\sqrt{s_{NN}} = 8.16$ TeV. Ce rapport est comparé avec le rapport à CT14 de prédictions obtenues avec le modèles EPPS16. Tous les calculs théoriques tiennent compte de l'effet d'isospin. La bande grises correspond à l'incertitude sur les prédiction CT14, les barres et boîtes autour des points expérimentaux indiquent les incertitudes statistiques et systématiques, respectivement.

classes de centralité. Afin d'augmenter la précision sur la mesure, les productions des bosons $W^-$ et $W^+$ sont ici combinées. On observe effectivement la mise à l'échelle attendue sur les deux distributions. Il est important de noter que la ligne en pointillés sur les figures n'est pas le résultat d'un ajustement des données par une fonction constante, mais le résultat de l'évaluation de la section efficace normalisée sur l'intervalle en centralité 0–100%.

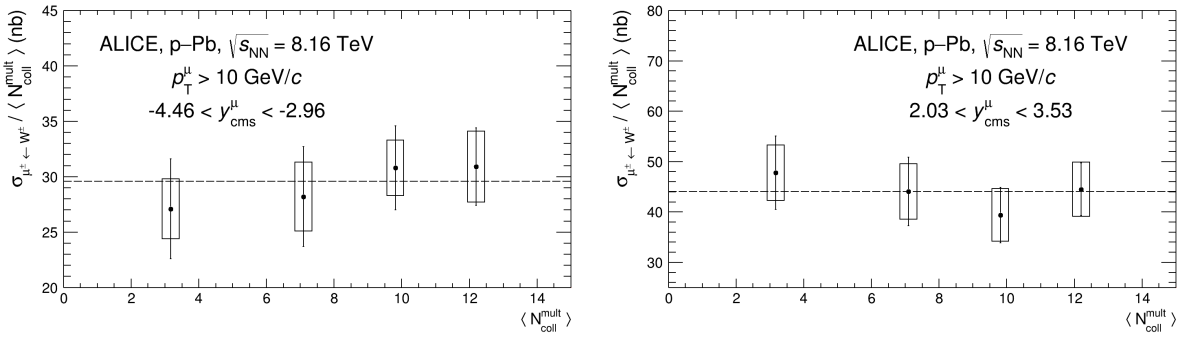


**Figure 12:** Section efficace de production des bosons $W^\pm$ en fonction de la centralité, normalisée au nombre moyen de collisions binaires $\langle N_{\rm coll}^{\rm mult} \rangle$, dans les collisions Pb–p (gauche) et p–Pb (droite) à $\sqrt{s_{\rm NN}} = 8.16$ TeV. Les barres et boîtes autour des points indiquent respectivement les incertitudes statistiques et systématiques. La ligne en pointillés correspond à la même observable évaluée pour une centralité de 0–100%.

# Conclusion

Les mesures de production des bosons $Z^0$ et $W^\pm$ dans les collisions p–Pb à $\sqrt{s_{\rm NN}} = 8.16$ TeV ont été présentées. Les bosons sont détectés à travers leur canal de désintégration muonique, en utilisant les données collectées par le spectromètre à muons du détecteur ALICE. Les mesures ont été effectuées dans les régions fiducielles :

$$\mathrm{Z}^0 : \quad \begin{cases} -4 < \eta_\mu < -2.5, \\ p_{\rm T}^\mu > 20 \text{ GeV}/c, \\ 60 < m_{\mu^+\mu^-} < 120 \text{ GeV}/c^2, \end{cases} \qquad \mathrm{W}^\pm : \quad \begin{cases} -4 < \eta_\mu < -2.5, \\ p_{\rm T}^\mu > 10 \text{ GeV}/c. \end{cases}$$

La couverture en rapidité du spectromètre, et les deux configurations de collision disponibles, permettent d'accéder à de basses ($\sim 10^{-4} - 10^{-3}$) et hautes ($\sim 10^{-1} - \sim 1$) valeurs du $x$ de Bjorken. Les mesures expérimentales ont été comparées à celles faites par la Collaboration CMS à des rapidités centrales, montrant l'accord entre les deux analyses et la complémentarité des expériences du LHC en terme de couverture de l'espace des phases. Les mesures ont également été comparées à des prédictions théoriques avec et sans modifications nucléaires des PDF. La section efficace de production du boson $Z^0$ est bien reproduite par les mesures, mais les incertitudes théoriques et expérimentales empêchent de conclure sur les modifications nucléaires. Des tensions sont observées

dans le cas du boson $W^-$ pour les rapidités les plus centrales, et ce avec l'ensemble des modèles théoriques considérés. Ces modèles sont en revanche en bon accord avec les mesures de la production du boson $W^+$ lorsqu'ils incluent les modifications nucléaires, alors qu'une déviation de 3.5 $\sigma$ d'une prédiction basée sur le modèle de PDF libre CT14 est observée à grande rapidité positive.

Cette étude apporte d'importantes contraintes pour la détermination des nPDF, particulièrement pour des valeurs du $x$ de Bjorken pour lesquelles les données expérimentales sont rares. La précision des mesures est souvent meilleure que celle des modèles, indiquant la possibilité d'utiliser les résultats pour diminuer les incertitudes théoriques même en cas d'accord entre les modèles et l'expérience. Les effets significatifs de l'inclusion de telles données dans les modèles ont pu être observés dans la comparaison entre les deux versions disponibles du modèle nCTEQ15. La haute luminosité attendue après le redémarrage du LHC en 2022 entraînera une nouvelle augmentation de la précision de telles mesures. Celles-ci permettront de poursuivre les itérations entre les communautés théoriques et expérimentales vers une détermination toujours plus précise des nPDF.

# Bibliography


[1] M. D. Schwartz, *Quantum Field Theory and the Standard Model*. Cambridge University Press, Cambridge, 2014.

[2] M. Gell-Mann, "A schematic model of baryons and mesons," *Physics Letters* **8** (1964) 214–215.

[3] G. Zweig, "An $SU_3$ model for strong interaction symmetry and its breaking,". `https://cds.cern.ch/record/570209`. Published in: *Developments in the Quark Theory of Hadrons. Vol. 1: 1964 - 1978*, ed. D. Lichtenberg and S. Rosen, Hadronic Press, Nonantum MA, 1980. pp. 22-101.

[4] **Particle Data Group**, P. Zyla, *et al.*, "Review of Particle Physics," *Progress of Theoretical and Experimental Physics* **2020** (2020) 083C01. `https://pdg.lbl.gov/`. Updated in 2021.

[5] L. Evans and P. Bryant, "LHC Machine," *Journal of Instrumentation* **3** (2008) S08001.

[6] W. Busza, K. Rajagopal, and W. van der Shee, "Heavy Ion Collisions: The Big Picture and the Big Questions," *Annual Review of Nuclear and Particle Science* **68** (2018) 339–376, `arXiv:1802.04801 [hep-ph]`.

[7] R. A. Khalek, J. J. Ethier, J. Rojo, and G. van Weelden, "nNNPDF2.0: Quark Flavor Separation in Nuclei from LHC Data," *Journal of High-Energy Physics* **09** (2020) 183, `arXiv:2006.14629 [hep-ph]`.

[8] K. J. Eskola, P. Paakkinen, H. Paukkunen, and C. A. Salgado, "EPPS16: Nuclear parton distributions with LHC data," *The European Physics Journal C* **77** (2017) 163, `arXiv:1612.05741 [hep-ph]`.

[9] K. Kovarik, A. Kusina, T. Jezo, D. B. Clark, C. Keppel, F. Lyonnet, J. G. Morfin, F. I. Olness, J. F. Owens, I. Schienbein, and J. Y. Yu, "nCTEQ15 - Global analysis of nuclear parton distributions with uncertainties in the CTEQ framework," *Physical Review D* **93** (2016) 085037, `arXiv:1509.00792 [hep-ph]`.

[10] A. Kusina, T. Jezo, D. B. Clark, P. Duwentäster, E. Godat, T. J. Hobbs, J. Kent, M. Klasen, K. Kovarík, F. Lyonnet, K. F. Muzaffa, F. I. Olness, I. Schienben, and J. Y. Yu, "Impact of LHC vector boson production in heavy ion collisions on strange PDFs," *The European Physical Journal C* **80** (2020) 968, `arXiv:2007.09100 [hep-ph]`.

[11] P. M. Nadolsky, H.-L. Lai, Q.-H. Cao, J. Huston, J. Pumplin, D. Stump, W.-K. Tung, and C.-P. Yuan, "Implications of CTEQ global analysis for collider observables," *Physical Review D* **78** (2008) 013004, arXiv:0802.0007 [hep-ph].

[12] K. J. Eskola, H. Paukkunen, and C. A. Salgado, "EPS09 – A new generation of NLO and LO nuclear parton distribution functions," *Journal Of High Energy Physics* **04** (2009) 065, arXiv:0902.4154 [hep-ph].

[13] H. Paukkunen and C. A. Salgado, "Constraints for the nuclear parton distributions from $Z$ and $W^{\pm}$ production at the LHC," *Journal of High Energy Physics* **03** (2011) 71, arXiv:1010.5392 [hep-ph].

[14] **ALICE** Collaboration, K. Aamodt *et al.*, "The ALICE experiment at the CERN LHC," *Journal of Instrumentation* **3** (2008) S08002. http://cds.cern.ch/record/1129812. Also published by CERN Geneva in 2010.

[15] S. van der Meer, "Calibration of the effective beam height in the ISR," Tech. Rep. CERN-ISR-PO-68-31. ISR-PO-68-31, CERN, Geneva, 1968. https://cds.cern.ch/record/296752.

[16] V. Balagura, "Notes on van der Meer Scan for Absolute Luminosity Measurement," *Nuclear Instruments and Methods in Physics Research A* **654** (2011) 634–638, arXiv:1103.1129 [physics.ins-det].

[17] **ALICE** Collaboration, G. Dellacasa *et al.*, "Technical Design Report of the Dimuon Forward Spectrometer," Tech. Rep. CERN-LHCC-99-022. ALICE-TDR-5, CERN, Aug, 1999. http://cds.cern.ch/record/401974.

[18] **ALICE** Collaboration, G. Dellacasa *et al.*, "ALICE dimuon forward spectrometer: addendum to the Technical Design Report," Tech. Rep. CERN-LHCC-2000-046. ALICE-TDR-5-add-1, CERN, Dec, 2000. http://cds.cern.ch/record/494265.

[19] **ALICE** Collaboration, B. Aabelev *et al.*, "Upgrade of the ALICE Experiment: Letter Of Intent," *Journal of Physics G* **41** (2014) 087001.

[20] **ALICE** Collaboration, J. Adam *et al.*, "Technical Design Report for the Muon Forward Tracker," Tech. Rep. CERN-LHCC-2015-001. ALICE-TDR-018, CERN, Jan, 2015. https://cds.cern.ch/record/1981898.

[21] **ALICE** Collaboration, J. Adam *et al.*, "Technical Design Report for the Upgrade of the Online-Offline Computing System," Tech. Rep. CERN-LHCC-2015-006. ALICE-TDR-019, CERN, Apr, 2015. https://cds.cern.ch/record/2011297.

[22] S. Aioli, P. Nason, C. Oleari, and E. Re, "A general framework for implementing NLO calculations in shower Monte Carlo programs: the POWHEG BOX," *JHEP* **06** (2010) 43, arXiv:1002.2581 [hep-ph].

[23] R. Brun, F. Bruyant, M. Maire, A. C. McPherson, and P. Zanarini, "GEANT3: user's guide Geant 3.10, Geant 3.11 rev. version," 1987. https://cds.cern.ch/record/1119728. CERN-DD-EE-84-01.

[24] S. Dulat, T. J. Hou, J. Gao, M. Guzzi, J. Huston, P. Nadolsky, J. Pumplin, C. Schmidt, D. Stump, and C. P. Yuan, "New parton distribution functions from a global analysis of quantum chromodynamics," *Physical Review D* **93** (2016) 033006, arXiv:1506.07443 [hep-ph].

[25] **CMS** Collaboration, A. M. Sirunyan *et al.*, "Observation of nuclear modifications in $W^{\pm}$ boson production in pPb collisions at $\sqrt{s_{NN}} = 8.16$ TeV," *Physics Letters B* **800** (2020) 135048, arXiv:1905.01486 [hep-ex].

# Introduction

The study of the constituents and behaviour of nuclear matter under different thermodynamical conditions is the quest of heavy-ion physics. It relies on the theory of quantum chromodynamics (QCD) that describes the quark sector of the Standard Model of particle physics. QCD predicts that, similarly to normal matter, the nuclear matter can be found in various states depending on macroscopic conditions such as the temperature and baryonic density. One of the central objective of heavy-ion collisions is then to enable the characterisation of the nuclear matter phase diagram. The transitions between the states of nuclear matter demand a tremendous amount of energy, such that their realisation requires powerful particle accelerators, the collision of heavy ions at very high rates, and sizeable experimental apparatus to collect and process the data.

A collision between two ultrarelativistic ions, such as performed at the European Organisation for Nuclear Research (CERN) using the Large Hadron Collider (LHC), is a complex process of huge entropy production. It allows to bring the system up to large temperatures at low baryonic density, fusing the ion constituents into a strongly-coupled, near-perfect fluid called the Quark-Gluon Plasma (QGP). The study of the QGP sheds light on the first moments of the Universe, as the standard model of cosmology predicts that the Universe was a QGP a few microseconds after the Planck wall. The lifetime of a QGP in the evolution of a heavy-ion collision is feeble, as the system quickly expands and cools down. The study of the QGP, arguably the main goal of high-energy nuclear physics, relies on a precise knowledge of the initial state of the collision, such that the so-called hot nuclear effects, related to the QGP, can be disentangled from the cold effects, among which one finds the modification of the inner structure of nucleons when they are bound inside a nucleus. These nuclear modifications are theoretically reproduced by means of nuclear parton distribution functions (nPDF), describing the repartition of the nucleon total energy among its constituents quarks and gluons by means of the Bjorken-$x$ variable, the fraction of the total momentum carried by a given parton. The determination of the nPDF is based on global analyses of the available experimental data.

In this thesis, measurements of the $W^{\pm}$- and $Z^0$-boson production in p–Pb collisions are reported. Due to their large masses, these electroweak bosons are produced early during the collision, in hard processes of high momentum exchange. Their production is significantly dependent on the inner structure of the colliding hadrons, providing a valuable probe of the nPDF. Moreover, one can detect the bosons through their leptonic decay, in order to have a full decay chain of particles that do not interact strongly, therefore being blind to the QGP phase. Studies in p–Pb collisions constitute an intermediate step in between measurements in pp and Pb–Pb collisions, and the

asymmetry of the collision system can be used for extracting additional information.

The measurements are performed with data from p–Pb collisions at $\sqrt{s_{\mathrm{NN}}} = 8.16$ TeV, collected using the detector of ALICE (A Large Ion Collider Experiment). ALICE is one of the four main experiments at the LHC, and is the only one dedicated to heavy-ion physics. The ALICE Collaboration regroups 1975 members from 170 institutes over 40 countries. The detector is composed of a central barrel for the detection of electrons, hadrons and photons at midrapidities, and a muon spectrometer lying at large rapidities. The latter provided the data samples used for this work. Combining the rapidity acceptance of the spectrometer and the large centre-of-mass energy delivered by the LHC enables the access to a very low Bjorken-$x$ region, where experimental data are scarce and the nPDF models show large uncertainties. This study then provides specific and valuable inputs for the determination of nPDF models.

This document is organised in nine chapters regrouped in three parts. The first part describes the theoretical context of the analysis in three chapters.

- **Chapter 1** exposes the theoretical description of nuclear matter from particle physics. It starts with a presentation of fundamental aspects of QCD by detailing its Lagrangian formulation, the running of the coupling strength $\alpha_s$ from which originate the regimes of perturbative QCD and asymptotic freedom, the chiral symmetry breaking mechanism, and the nuclear matter phase diagram and its various regions. In a second section, the representation of the inner structure of hadrons is described, through the improved parton model that gives rise to the PDF framework for free nucleons and nPDFs for the bound ones.

- **Chapter 2** gives a selection of topics about heavy-ion collisions relevant for this thesis. The current understanding of the history of a heavy-ion collision is described, followed by a presentation of the Glauber model, the standard description of a hadronic collision used for the determination of its geometrical parameters. The specific topic of small systems, that is, collision systems (such as p–Pb) in which the creation of a QGP is a priori not foreseen, is discussed. Recent observations in such systems have significantly impacted the vision of heavy-ion collisions, and constitute a strong motivation for this study.

- **Chapter 3** concludes the first part with a discussion on the $\mathrm{Z}^0$ and $\mathrm{W}^{\pm}$ boson production. Their prediction and discovery at the CERN SPS is recalled, followed by a presentation of their current status within the Standard Model and the most recent knowledge on their mass, width and decay probabilities. The theoretical description of the boson production and decay through the Drell-Yan mechanism is then presented, with an emphasis on p–Pb collisions. The chapter ends with a state-of-the-art of $\mathrm{Z}^0$ and $\mathrm{W}^{\pm}$ studies at the LHC.

The second part, containing four chapters, presents the experimental context of this work.

- **Chapter 4** offers a description of the LHC at CERN, presenting the accelerator complex and detailing the generation and acceleration of the proton and ion beams. Then the ALICE detector is described, starting with the so-called global detectors that aim at characterising the collision, followed by the central barrel that provides means of detection of electrons, photons and hadrons, and participates to the determination of the primary vertex.

- **Chapter 5** introduces the muon spectrometer, with which the data samples used in this analysis were obtained. Its composition is presented in details. The tracking and triggering procedures are then described.

- **Chapter 6** presents the online and offline systems of ALICE, constituting the two steps of the data treatment chain. The online system runs during data taking, and is composed of the trigger system, data acquisition, high-level trigger and detector and experiment control systems. The offline system performs the full reconstruction of the events, and provides the AliRoot framework used for data analysis and simulation.

- **Chapter 7** summarises the ongoing upgrade of the experiment, in preparation for the LHC restart scheduled for 2022. The physics motivations, and the foreseen physics program, are briefly recapped. The upgrade itself is then presented, starting with the ameliorations concerning the central barrel and global detectors, followed by that concerning the muon spectrometer, and concluding with the upgrade of the software system. In this last section, the outcome of my service task, on the software for the quality control of the muon identifier, is presented.

The two chapters of the last part present the data analyses constituting the core of my PhD work.

- **Chapter 8** details the analysis procedure enabling the measurement of the $Z^0$- and $W^{\pm}$-boson production. The data samples are presented, with a description of how the events and muon tracks are selected, and how the luminosity and centrality are evaluated. The procedure for the signal extraction and correction for the efficiency of the detector are then described. The evaluation of the systematic uncertainties is discussed.

- **Chapter 9** presents the results of the $Z^0$ and $W^{\pm}$ measurements, through the integrated and differential production cross sections, lepton charge asymmetry and nuclear modification factor. The measurements are compared with theoretical predictions and similar measurements performed at the LHC. The normalised yield is also presented as a function of centrality.

A conclusion summarises the results and main outcomes of the comparison with models, and discusses the future potentialities offered by this study.

# Part I

# High-energy nuclear physics

# Chapter 1

# Nuclear matter in particle physics

This chapter presents the theoretical context underlying this thesis. The Standard Model of particle physics [1] describes the interaction between quarks and gluons by means of quantum chromodynamics (QCD), whose fundamental characteristics are briefly recalled in Section 1.1. The aim of the analyses presented in this work is to probe a subspace of the phase diagram, featuring the liquid phase. It corresponds to the "ordinary" nuclear matter, that is the one found under everyday thermodynamical conditions under which the quarks and gluons are confined into hadrons. This state can be described in terms of the Parton Distribution Functions (PDF) and their nuclear counterparts, the so-called nuclear PDF (nPDF). This framework is detailed in Section 1.2.

## 1.1 Fundamentals of QCD

### 1.1.1 Quark model and the colour charge

The most fundamental tenet of QCD is that hadronic matter is made of quarks. The so-called quark model, independently proposed by Murray Gell-Man and George Zweig in 1964 [2, 3] is an organisational scheme for hadrons in terms of their valence quarks, which underlies the SU(3) symmetry group that dictates the strong interaction. The six known quarks are listed in Table 1.1 along with their quantum numbers and masses. Quarks are strongly interacting fermions of spin 1/2, having positive parities by convention and the baryon number 1/3. The quantum numbers are related to the charge $Q$ (in terms of the elementary charge $e$) through the generalised Gell-Mann-Nishijima formula [4, 5]:

$$Q = I + \frac{\mathcal{B} + S + C + B + T}{2}, \tag{1.1}$$

where $I$, $\mathcal{B}$, $S$, $C$, $B$, $T$ correspond to the quark isospin, baryon number, strangeness, charm, bottomness and topness, respectively. To each quark is associated an antiquark by sign conjugation of the parity, charge, baryon and flavour numbers.

In the quark model, baryons such as protons and neutrons are interpreted in terms of three-quark states $|q_1 q_2 q_3\rangle$. As to account for the observed spins of the low-mass baryons, quarks

| Quark | Charge | Isospin | $\mathcal{B}$ | $S$ | $C$ | $B$ | $T$ | Mass (MeV/$c^2$) |
|---|---|---|---|---|---|---|---|---|
| $d$ – down | $-\frac{1}{3}$ | $-\frac{1}{2}$ | $\frac{1}{3}$ | 0 | 0 | 0 | 0 | $4.7^{+0.5}_{-0.3}$ |
| $u$ – up | $+\frac{2}{3}$ | $+\frac{1}{2}$ | $\frac{1}{3}$ | 0 | 0 | 0 | 0 | $2.2^{+0.5}_{-0.4}$ |
| $s$ – strange | $-\frac{1}{3}$ | 0 | $\frac{1}{3}$ | $-1$ | 0 | 0 | 0 | $95^{+9}_{-3}$ |
| $c$ – charm | $+\frac{2}{3}$ | 0 | $\frac{1}{3}$ | 0 | $+1$ | 0 | 0 | $(1.275^{+25}_{-35}) \times 10^3$ |
| $b$ – bottom | $-\frac{1}{3}$ | 0 | $\frac{1}{3}$ | 0 | 0 | $-1$ | 0 | $(4.18^{+0.04}_{-0.03}) \times 10^3$ |
| $t$ – top | $+\frac{2}{3}$ | 0 | $\frac{1}{3}$ | 0 | 0 | 0 | $+1$ | $(173.2 \pm 0.9) \times 10^3$ |

**Table 1.1:** Charge, isospin, additive quantum numbers and mass of the known quarks. The quantum numbers are the baryon number $\mathcal{B}$, and the flavour numbers strangeness $S$, charm $C$, bottomness (beauty) $B$ and topness (truth) $T$. The mass given for the top quark is the mass reported by the Tevatron Electroweak Working Group from a global analysis of published measurements from Tevatron and LHC data. More information can be found in Ref. [6] from which this table is adapted.

are forced to be fermions of half-integer spins. Quarks in the spin-3/2 baryons, such as the $|\Delta^{++}\rangle = |u^{\uparrow}u^{\uparrow}u^{\uparrow}\rangle$, are then in a symmetrical state of space, spin and SU(3) degrees of freedom. However, being fermions the quarks follow the Fermi-Dirac statistics and therefore must obey the spin-statistics theorem [7] requiring the total antisymmetry of the wave function. The contradiction is solved if one introduces a supplementary degree of freedom for the quarks, with three possible values [8]. Under this new indexing, the baryon wave function becomes totally antisymmetric. This degree of freedom is known as the colour charge $C$, with possible values $C \in \{red, green, blue\} = \{r, g, b\}$ by analogy with the real colours. In order to avoid the emergence of a proliferation of new states, and to cope with the invisibility of colour in hadronic matter, the colour hypothesis has to be supplemented by the requirement that only colour singlet states can exist in nature. The SU(3) group is a natural candidate for the colour transformation. Indeed, if the quarks transform under the fundamental $3 \times 3$ unitary matrix and the antiquarks under its complex conjugate, the basic colour singlet states are precisely the mesons $|q_a\overline{q}^a\rangle$ and the baryons $|\epsilon^{abc}q_aq_bq_c\rangle$, where $a$, $b$ and $c$ indicate the quark colour and $\epsilon^{abc}$ is the totally antisymmetric tensor. Similarly to the electric charge, colours come with their associated charge conjugation dubbed anticolours $\overline{C} \in \{\overline{r}, \overline{g}, \overline{b}\}$.

The strong interaction then relies on the non-abelian SU(3) group. One can use the colour charge to define a local symmetry. Each such symmetry requires a number of gauge bosons equal to the number of generators of the group, eight in this case. There are thus eight different types of bosons of the strong interaction, the massless spin-1 gluons, forming an SU(3) octet:

$$r\overline{g}, \quad r\overline{b}, \quad g\overline{r}, \quad g\overline{b}, \quad b\overline{r}, \quad b\overline{g}, \quad \frac{1}{\sqrt{2}}(r\overline{r} - g\overline{g}), \quad \frac{1}{\sqrt{6}}(r\overline{r} + g\overline{g} - 2b\overline{b}),$$

from which follows a peculiarity of the strong interaction: as the mediator gluons carry a colour

charge, they can self-interact. The symmetric single state $\frac{1}{\sqrt{3}}(r\overline{r}+b\overline{b}+g\overline{g})$, corresponding the colour (in fact colourless) singlet, does not exist. Indeed, a colour singlet gluon would be unconfined, behaving as a strongly interacting photon, thus giving the strong force an infinite range.

### 1.1.2 QCD Lagrangian

Quantum chromodynamics (QCD) is a non-abelian gauge theory based on a special unitary group (i.e. a Yang-Mills theory) [1, 9, 10] describing the interaction of coloured quarks and gluons. It forms the SU(3) components of the SU(3) $\otimes$ SU(2) $\otimes$ U(1) Standard Model [1]. Denoting $a = (1, 2, 3) = (r, g, b)$ the quark colour indices and $A = (1, ..., 8)$ the gluon colour indices, its Lagrangian reads[1]:

$$\mathcal{L}_{\mathrm{QCD}} = \overline{\psi}_a \left( i\gamma^\mu \partial_\mu \delta_{ab} - m\delta_{ab} - g_s \gamma^\mu t^A_{ab} \mathcal{A}^A_\mu \right) \psi_b - \frac{1}{4} F^A_{\mu\nu} F^{\mu\nu}_A, \tag{1.2}$$

where repeated indices are summed over and $\delta$ is the Kroenecker delta. The fundamental parameters of QCD are the quark masses $m$ and the strong coupling $g_s$, often expressed as $\alpha_s = g_s^2/4\pi$.

$\psi_a$ and $\psi_b$ are the quark-field spinors, dynamical functions of spacetime in the fundamental representation of the SU(3) gauge group. The $\gamma^\mu$ are the Dirac covariant matrices connecting the spinor representation to the vector representation of the Lorentz group:

$$\gamma^0 = \begin{pmatrix} 1 & 0 & 0 & 0 \\ 0 & 1 & 0 & 0 \\ 0 & 0 & -1 & 0 \\ 0 & 0 & 0 & -1 \end{pmatrix}, \qquad \gamma^1 = \begin{pmatrix} 0 & 0 & 0 & 1 \\ 0 & 0 & 1 & 0 \\ 0 & -1 & 0 & 0 \\ -1 & 0 & 0 & 0 \end{pmatrix},$$

$$\gamma^2 = \begin{pmatrix} 0 & 0 & 0 & -i \\ 0 & 0 & i & 0 \\ 0 & i & 0 & 0 \\ -i & 0 & 0 & 0 \end{pmatrix}, \qquad \gamma^3 = \begin{pmatrix} 0 & 0 & 1 & 0 \\ 0 & 0 & 0 & -1 \\ -1 & 0 & 0 & 0 \\ 0 & 1 & 0 & 0 \end{pmatrix}.$$

The $\mathcal{A}^A_\mu$ terms correspond to the eight gluon field. The $t^A_{ab}$ denote the fundamental representation of the SU(3) Lie algebra, the eight $3 \times 3$ matrices forming the generators of the group. One has:

$$t^A = \frac{1}{2}\lambda^A, \tag{1.3}$$

that is, a representation of the generators $t^A$ is given by the hermitian and traceless Gell-Mann matrices $\lambda^A$:

$$\lambda^1 = \begin{pmatrix} 0 & 1 & 0 \\ 1 & 0 & 0 \\ 0 & 0 & 0 \end{pmatrix}, \qquad \lambda^2 = \begin{pmatrix} 0 & -i & 0 \\ i & 0 & 0 \\ 0 & 0 & 0 \end{pmatrix}, \qquad \lambda^3 = \begin{pmatrix} 1 & 0 & 0 \\ 0 & -1 & 0 \\ 0 & 0 & 0 \end{pmatrix}, \qquad \lambda^4 = \begin{pmatrix} 0 & 0 & 1 \\ 0 & 0 & 0 \\ 1 & 0 & 0 \end{pmatrix},$$

[1]The Lagrangian given here is not fully complete, and so-called gauge-fixing terms and ghost fields must be introduced in order to make the theory consistent. More details one this topic can be found in Ref. [9].

$$\lambda^5 = \begin{pmatrix} 0 & 0 & -i \\ 0 & 0 & 0 \\ i & 0 & 0 \end{pmatrix}, \qquad \lambda^6 = \begin{pmatrix} 0 & 0 & 0 \\ 0 & 0 & 1 \\ 0 & 1 & 0 \end{pmatrix}, \qquad \lambda^7 = \begin{pmatrix} 0 & 0 & 0 \\ 0 & 0 & -i \\ 0 & i & 0 \end{pmatrix}, \qquad \lambda^8 = \frac{1}{\sqrt{3}} \begin{pmatrix} 1 & 0 & 0 \\ 0 & 1 & 0 \\ 0 & 0 & -2 \end{pmatrix},$$

The field tensor $F^A_{\mu\nu}$ is given by:

$$F^A_{\mu\nu} = \partial_\mu \mathcal{A}^A_\nu - \partial_\nu \mathcal{A}^A_\mu - \frac{\alpha_s}{4\pi} f_{ABC} \mathcal{A}^B_\mu \mathcal{A}^C_\nu, \tag{1.4}$$

with the structure constants of the SU(3) group $f_{ABC}$ following from the commutation relation of the SU(3) generators, yielding the algebra of the group:

$$\left[t^A, t^B\right] = i f_{ABC} t^C. \tag{1.5}$$

The structure constant are antisymmetric in the exchange of two indices, the non-zero ones are:

$$f^3_{12} = 1, \tag{1.6}$$

$$f^7_{14} = f^5_{16} = f^6_{24} = f^7_{25} = f^5_{34} = f^6_{37} = \frac{1}{2}, \tag{1.7}$$

$$f^8_{45} = f^8_{67} = \frac{1}{2}\sqrt{3}. \tag{1.8}$$

The last, non-abelian term on the right-hand side of Equation 1.4 makes a fundamental dynamical difference between QCD and quantum electrodynamics (QED) as it describes the gluon self-interaction, which eventually leads to the phenomenon called asymptotic freedom.

Useful colour-algebra relations include:

$$t^A_{ab} t^A_{bc} = C_F \delta_{ac}, \qquad C_F \equiv \frac{N_C^2 - 1}{2N_C} = \frac{4}{3}, \tag{1.9}$$

$$f_{ACD} f_{BCD} = C_A \delta_{AB}, \qquad C_a \equiv N_C = 3, \tag{1.10}$$

$$t^A_{ab} t^B_{ab} = T_R \delta_{AB}, \qquad T_R = \frac{1}{2}, \tag{1.11}$$

which introduce the SU(3) group invariants $C_F$ and $C_A$, the Casimir colour factors associated with the gluon emission from a quark and a gluon, respectively, and $T_R$ the colour factor for a gluon to split into a $q\bar{q}$ pair.

Developing the QCD Lagrangian, and multiplying out the field tensor contraction $F^A_{\mu\nu} F^{A,\mu\nu}$, one gets the elements of a QCD Feynman diagram:

- Quark propagator: 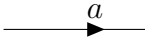

$= \overline{\psi}_a \left(i\gamma^\mu \partial_\mu - m_q\right) \psi_a,$

- Gluon propagator: 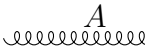

$= (\partial^\mu \mathcal{A}^\nu_A - \partial^\nu \mathcal{A}^\mu_A)(\partial_\mu \mathcal{A}^A_\nu - \partial_\nu \mathcal{A}^A_\mu),$

- Quark-gluon vertex: 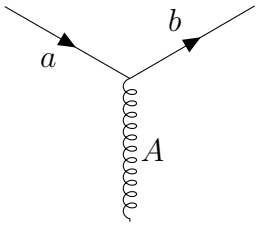

$= g_s \overline{\psi}_a \lambda^A_{ab} \psi_b \gamma^\mu \mathcal{A}^A_\mu ,$

- 3-gluons vertex: 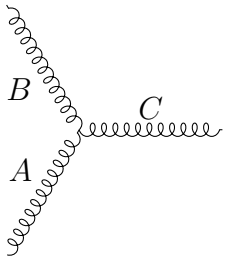

$= g_s \left(\partial^\mu \mathcal{A}^\nu_A - \partial^\nu \mathcal{A}^\mu_A\right) f_{ABC} \mathcal{A}^B_\mu \mathcal{A}^C_\nu ,$

- 4-gluons vertex: 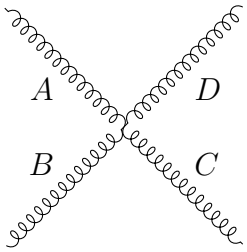

$= g_s^2 f_{EAB} \mathcal{A}^\mu_A \mathcal{A}^\nu_B f_{ECD} \mathcal{A}^C_\mu \mathcal{A}^D_\nu .$

### 1.1.3 Perturbative QCD and the asymptotic freedom

In field theories, the quantum corrections (loops) calculated in perturbation theory have ultraviolet divergences originating from the intermediate states with high momenta [9]. In renormalisable field theories, such as QCD, these divergences can always be combined with the bare parameters of the Lagrangian and are absorbed in the renormalised parameters. The renormalisation procedure requires to introduce a mass scale $\mu$ (often denoted $\mu_R$) at which the subtractions removing the ultraviolet divergences are performed. The value of $\mu$ is arbitrary, and this parameter does not show up in the QCD Lagrangian of Equation 1.2. A dimensionless observable $R(Q^2, x_f)$, where $x_f$ represents any dimensionless kinematic variables, must then be independent of the arbitrary value of $\mu$. This independence is given by the Callan-Symanzik relation for QCD [11, 12, 13]:

$$\frac{\mathrm{d}}{\mathrm{d}\ln(\mu^2)} R(Q^2/\mu^2, \alpha_s, x_f) = \mu^2 \frac{\mathrm{d}}{\mathrm{d}\mu^2} R(Q^2/\mu^2, \alpha_s, x_f) \tag{1.12}$$

$$= \left(\mu^2 \frac{\partial}{\partial \mu^2} + \mu^2 \frac{\partial \alpha_s}{\partial \mu^2} \frac{\partial}{\partial \alpha_s}\right) R(Q^2/\mu^2, \alpha_s, x_f) \tag{1.13}$$

$$= 0. \tag{1.14}$$

If one defines:

$$\beta(\alpha_s) = \mu^2 \frac{\partial \alpha_s}{\partial \mu^2}, \qquad t = \ln\left(\frac{Q^2}{\mu^2}\right), \tag{1.15}$$

Equation 1.14 becomes

$$\left(-\frac{\partial}{\partial t}+\beta(\alpha_s)\frac{\partial}{\partial \alpha_s}\right)=R\left(e^t,\alpha_s,x_f\right)=0. \tag{1.16}$$

Expressing the observable as a perturbative series now in $\alpha_s(Q^2)$ defined by:

$$t=\int_{\alpha_s}^{\alpha_s(Q^2)}\frac{\mathrm{d}x}{\beta(x)}, \qquad\qquad \alpha_s(\mu^2)\equiv\alpha_s, \tag{1.17}$$

one has:

$$R(e^t,\alpha_s,x_f)=\sum_{n=0}^{n_{max}\sim\pi/\alpha_s} r_n(1,\alpha_s,x_f)\left(\frac{\alpha_s(\mu^2)}{\pi}\right)^n, \tag{1.18}$$

which can be checked to be a solution of Equation 1.17. Setting $e^t=1$, that is, setting the physical scale $Q$ equal to the renormalisation scale $\mu$, makes the coefficients $r_n$ independent of $Q^2/\mu^2$. When one takes $\mu$ close to the scale of the momentum transfer $Q$ in a given process, then $\alpha_s(\mu^2\simeq Q^2)$ is indicative of the effective strength of the strong interaction for that process.

The coupling satisfies the renormalisation group equation:

$$Q^2\frac{\partial\alpha_s}{\partial Q^2}=\beta(\alpha_s). \tag{1.19}$$

In QCD, the $\beta$ function has the perturbative expansion:

$$\beta(\alpha_s)=-(b_0\alpha_s^2+b_1\alpha_s^3+b_2\alpha_s^4+\mathcal{O}(\alpha_s^5)), \tag{1.20}$$

with $b_0$, $b_1$ and $b_2$ being the 1-, 2- and 3-loop $\beta$-function coefficients:

$$\begin{aligned} b_0&=\frac{11C_A-4n_fT_R}{12\pi}=\frac{33-2n_f}{12\pi},\\ b_1&=\frac{17C_A^2-n_fT_R(10C_A+6C_F)}{24\pi^2}=\frac{153-19n_f}{24\pi^2},\\ b_2&=\frac{2857-\frac{5033}{9}n_f+\frac{325}{27}n_f^2}{128\pi^3}, \end{aligned} \tag{1.21}$$

for the SU(3) values of $C_A$ and $C_F$ and with $n_f$ the number of active quarks (i.e. satisfying $m_q\ll\mu$). Starting from $b_2$, the coefficients are renormalisation-scheme dependent and the formula given here is obtained in the widely-used modified minimal subtraction ($\overline{\mathrm{MS}}$) scheme [14]. The minus sign in Equation 1.20 is the origin of the asymptotic freedom, i.e. the fact that the strong coupling becomes weak for processes involving large momentum transfers (so-called hard processes). In the 100 GeV – 1 TeV range the coupling amounts to $\sim 0.1$.

If one works within an energy range where the number of flavours is constant, an analytic solution of Equation 1.14 can be found by neglecting all but the $b_0$ term, giving:

$$\alpha_s(\mu_R^2) = \frac{1}{b_0 \ln\left(\frac{\mu_R^2}{\Lambda_{\mathrm{QCD}}^2}\right)} = \frac{12\pi}{(33 - 2n_f)\ln\left(\frac{\mu_R^2}{\Lambda_{\mathrm{QCD}}^2}\right)}, \tag{1.22}$$

where $\Lambda_{\mathrm{QCD}}$ is a constant of integration, corresponding to the scale at which the perturbatively-defined coupling would diverge. Its value is then indicative of the energy range where non-perturbative dynamics dominates. The definition of $\Lambda_{\mathrm{QCD}}$ can vary, and it depends on e.g. the number of active flavours, such that its value may differ following the various approaches, but it lies in the neighbourhood of 200 MeV $\sim$ 1 fm$^{-1}$. Its determination relies on the experimental measurement of $\alpha_s$, based on a wealth of available data from various experiments and combining several physics channels. All the available data are combined and a reasonably stable world average can be extracted, as illustrated in Figure 1.1.

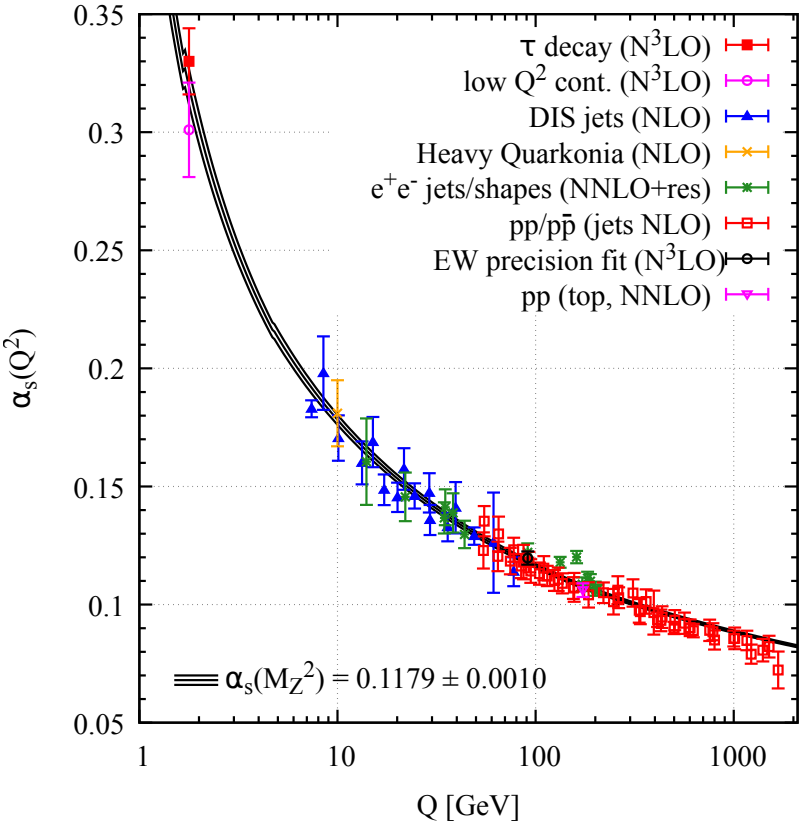


**Figure 1.1:** Summary of measurements of $\alpha_s(Q^2)$ as a function of the energy scale $Q$. The respective degree of QCD perturbation theory used in the extraction of $\alpha_s$ is indicated in parentheses (NLO: next-to-leading order, NNLO: next-to-NLO, NNLO+res.: NNLO matched to a resummed calculation, N$^3$LO: next-to-NNLO). Figure taken from Ref. [6].

The world average clearly features the running of the coupling strength versus the energy scale. As $\alpha_s$ becomes large, perturbation theory breaks down and the attractive strong force binds the

quarks and gluons into confined and colourless states, whence the name of confinement for the low-$Q$ regime. On the contrary, for large energy scales the coupling becomes weaker, yielding the asymptotic freedom. For very large energies the weakening is so important that quarks and gluons are not bounded anymore and start to move freely. These various regimes are at the origin of the phases of nuclear matter, which are discussed in Section 1.1.5.

### 1.1.4 Chiral symmetry breaking

In the Standard Model, the mass of quarks is generated via Yukawa coupling to the Higgs field. As they are the constituents of the hadrons, one would expect that in the ground state, the hadron mass should correspond to the one of its valence quarks. However, taking as an example the proton $\mathrm{p} = |uud\rangle$ with $m_\mathrm{p} \sim 938$ MeV/$c^2$, one sees that the sum of the masses of two up quarks and one down is far from amounting to $m_\mathrm{p}$: $2m_u + m_d \sim 9.1$ MeV/$c^2$, the mass of the valence quarks only account for about 1% of the proton mass. As it is shown below, this difference is explained by the chiral symmetry breaking in QCD. Chirality indicates the lack of identity of a phenomenon to its mirror image. In particle physics, the so-called handedness is defined from the spin of the particle through the helicity, the projection of the spin along the direction of motion. A particle is right-handed if the helicity points towards the direction of motion, left-handed otherwise. Helicity allows one to define the parity as the symmetry transformation between right- and left-handed particles. Chiral symmetry is then the invariance under parity.

Considering the QCD Lagrangian of Equation 1.2, for the first two flavours, one gets:

$$\begin{aligned}\mathcal{L} &= \sum_{q=u,d} \overline{\psi}_{q,a}(i\gamma^\mu \partial_\mu \delta_{ab} - m\delta_{ab} - g_s \gamma^\mu t^A_{ab} \mathcal{A}^A_\mu)\psi_{q,b} - \frac{1}{4} F^A_{\mu\nu} F^{\mu\nu}_A \\ &= \overline{q}\left(i\gamma^\mu D_\mu - M\delta_{ab}\right) q - \frac{1}{4} F^A_{\mu\nu} F^{\mu\nu}_A, \end{aligned} \tag{1.23}$$

where we introduced a notation for the gauge covariant derivative $D_\mu$ and a matrix notation for the quark field $q$ and the mass $M$ as:

$$D_\mu = \partial_\mu \delta_{ab} - i g_s t^A_{ab} \mathcal{A}^A_\mu, \qquad q = \begin{pmatrix} u \\ d \end{pmatrix}, \qquad M = \begin{pmatrix} m_u & 0 \\ 0 & m_d \end{pmatrix}. \tag{1.24}$$

Assuming that $m_u - m_d$ is much less than the hadronic mass scale, one can approximate $M$ as a multiple of the unit matrix. This Lagrangian is then invariant under the chiral transformation:

$$q \to \exp\left(\sum_{i=0}^{3} \alpha_i \sigma_i\right) q,$$

where $\sigma_0$ is the unit matrix and $\sigma_i, i = (1, 2, 3)$ are the Pauli matrices. This $\mathrm{U}(2)_V$ symmetry ($V$ standing for vector) can be decomposed into the product $\mathrm{U}(1)_V \otimes \mathrm{SU}(2)_V$. The $\mathrm{U}(1)_V$ symmetry corresponds to the quark number symmetry, while $\mathrm{SU}(2)_V$ is the isospin symmetry that emerges when considering the $u$ and $d$ quarks to be degenerated in mass. Note here that as the gluon fields are not affected by chiral transformation the gluon degrees of freedom can be neglected throughout this discussion [15].

One can furthermore take the massless limit where $m_u$ and $m_d$ are negligible, and hence $M \equiv 0$. Considering the left- and right-handed projectors:

$$\gamma_L = \frac{1}{2}\left(1 - \gamma_5\right), \qquad \gamma_R = \frac{1}{2}\left(1 + \gamma_5\right), \qquad \text{with } \gamma^5 \equiv i\gamma^0\gamma^1\gamma^2\gamma^3, \tag{1.25}$$

satisfying the relations $\gamma_L^2 = \gamma_L$, $\gamma_R^2 = \gamma_R$ and $\gamma_L\gamma_R = 0$, one can decompose the quark fields into left- and right-handed components:

$$q_L = \gamma_L q, \qquad q_R = \gamma_R q. \tag{1.26}$$

The quark sector of the Lagrangian of Equation 1.23 then becomes:

$$\mathcal{L} = \overline{q}_L i\gamma^\mu D_\mu q_L + \overline{q}_R \gamma^\mu D_\mu q_R. \tag{1.27}$$

As no term connects the left- and right-handed fields, independent left and right rotations are permitted, yielding a $U(2)_L \otimes U(2)_R$ symmetry:

$$q_L \to \exp\left(\sum_{i=0}^{3} \alpha_i \sigma_i\right) q_L, \qquad q_R \to \exp\left(\sum_{i=0}^{3} \beta_i \sigma_i\right) q_R,$$

and constitutes a chiral symmetry as it acts separately on left- and right-handed fields (in this case a chiral SU(2)). According to Noether's theorem [16], each of these symmetries has an associated conserved current:

$$L_\mu^i = \overline{q}\gamma_\mu\gamma_L\sigma^i q, \tag{1.28}$$

$$R_\mu^i = \overline{q}\gamma_\mu\gamma_R\sigma^i q. \tag{1.29}$$

If chiral symmetry was exact, the QCD spectrum would show that every hadron comes with a partner of same mass and opposite parity, which is not observed. Chiral symmetry is explicitely broken by the non-zero masses of the quarks. Looking e.g. at the triplets $\rho(770)$ and $a_1(1260)$, which are chiral partners, one sees by their masses $m_{\rho(770)} \sim 755$ MeV/$c^2$ and $m_{a_1(1260)} \sim 1230$ MeV/$c^2$ that the chiral symmetry is in fact strongly broken. This indicates that the masses of the $u$ and $d$ quarks are not as small as their current mass in the QCD vacuum[2]. Due to the strong coupling between quarks, the QCD vacuum is non-vanishing, it is defined by the chiral condensation [17]:

$$\langle\overline{q}q\rangle = \langle 0|\overline{q}_L q_R + \overline{q}_R q_L|0\rangle \neq 0. \tag{1.30}$$

Equation 1.30 denotes the chiral spontaneous symmetry breaking in the QCD vacuum, and describes the flip of chirality as for example a right-handed particle annihililates via $q_R$, leaving $\overline{q}_L$ to create a left-handed particle of same momentum. The chiral condensation $\langle\overline{q}q\rangle$ explains the

[2]Defining the mass of the quarks is an arduous topic which comes with a lot of caveats. For the light quarks $u$, $d$ and $s$, the so-called current mass is the one acquired through the Higgs mechanism. An extensive discussion can be found in Ref. [6] ("Quark Masses") and references herein.

energy gap between the physics and QCD vacua, which generates an additional constituent mass for the quarks, even at vanishing current masses [18]:

$$M(p^2) \overset{\text{large}-p^2}{=} \frac{2}{3}\pi^2\gamma_m \frac{-\langle\bar{q}q\rangle}{\left(\frac{1}{2}\ln\frac{p^2}{\Lambda^2_{\text{QCD}}}\right)^{1-\gamma_m}}, \tag{1.31}$$

where $p$ is the quark momentum in the propagator and $\gamma_m = 12/(33-2n_f) = \pi/b_0$. This can be extended by also neglecting the $s$ quark mass, yielding a chiral SU(3) symmetry spontaneously broken to $\text{SU}(3)_V$, with eight pseudoscalar Goldstone bosons corresponding to the flavour SU(3) octet: $\pi^0$, $\pi^\pm$, $K^0$, $\overline{K}^0$, $K^\pm$ and $\eta$. The fact that they constitute the lightest hadrons allows one to apply chiral SU(3) perturbation theory for the three lightest quarks [19] while other techniques are needed for the heavy quarks [10].

Figure 1.2 shows the constituent mass as a function of the squared momentum for several flavours. One can see that about 99% of the $u$ and $d$ mass are generated by the chiral spontaneous symmetry breaking, and that chiral symmetry is restored at very large momentum transfer. As the visible matter in the Universe is constituted by the nucleons (the proton $|uud\rangle$ and neutron $|udd\rangle$), almost all the mass of the visible Universe comes from the chiral spontaneous symmetry breaking mechanism.

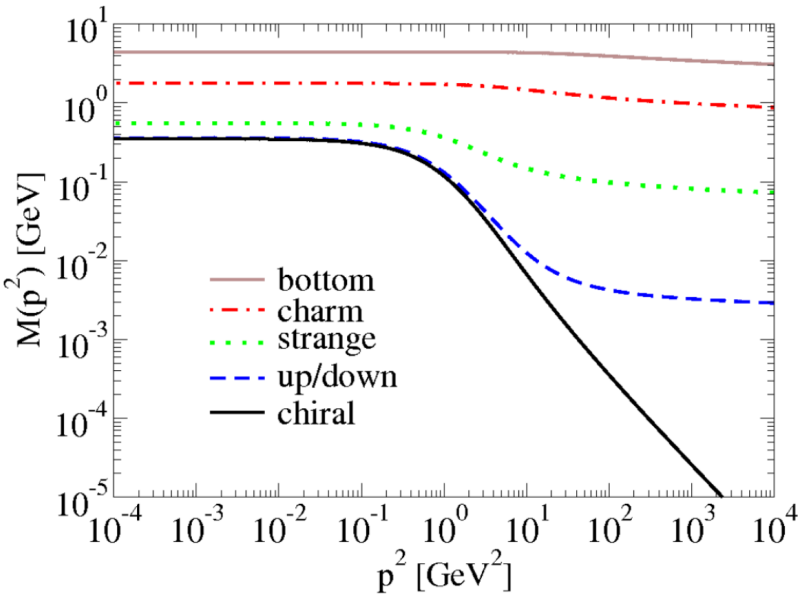


**Figure 1.2:** Constituent quark masses as a function of the squared momentum for the $u/d$, $s$, $c$ and $b$ quarks. Figure taken from Ref. [20], adapted from Ref. [21].

### 1.1.5 QCD phase diagram

As established above, the peculiarities of QCD lead to the existence of several phases for matter made of quarks and gluons. At low energy, quarks and gluons are confined into colourless bound

states, while at high energy QCD indicates that the strongly interacting matter undergoes a phase transition to a state where quarks and gluons are not confined anymore, the Quark-Gluon Plasma (QGP). Similarly to the standard matter, the phases of the QCD matter can be depicted and studied through a phase diagram. A common choice is the $(\mu_B, T)$ space to do so, where $T$ is the temperature and $\mu_B$ is the baryon-chemical potential. In QCD, a $|qqq\rangle$ baryon is always created or annihilated pairwise with an antibaryon $|\overline{qqq}\rangle$. Said otherwise, one can define a conserved quantity, the so-called baryon number $\mathcal{B}$ presented in Section 1.1.1, as:

$$\mathcal{B} = N_B - N_{\overline{B}}, \tag{1.32}$$

where $N_B$ and $N_{\overline{B}}$ are the numbers of baryons and antibaryons respectively. For systems in which the baryon number is allowed to vary, the most convenient thermodynamic potential to consider is the grand potential:

$$\Omega(T, V, \mu) = E - TS - \mu_B \mathcal{B}. \tag{1.33}$$

Reaching the thermodynamic equilibrium requires the minimisation of $\Omega$, and for a system at equilibrium one recognises $\mu_B$ as the increase in $E$ when $B$ increases by one. When systems are analysed using the grand canonical ensemble of statistical physics, $\mu_B$ is kept as a control parameter, and the baryon density $n_B = \mathcal{B}/V$ is a derived quantity whose value depends on the details of the equation of state $n_B = n_B(T, \mu_B)$. A schematic view of the QCD phase diagram in the $(\mu_B, T)$ plane is given in Figure 1.3. It must be stressed that the current knowledge of the QCD phase diagram is mostly conjectural, and as such it must be considered with care.

The QCD vacuum in which we live, having the hadrons as its excitations, lies at the bottom left of the diagram. As established in Section 1.1.4, this region features a strong breaking of the chiral symmetry, providing the hadrons with most of their mass. The phase coined "nuclear matter" corresponds to the nuclei that we observe under Earth-like thermodynamical conditions. One of the first successful model at describing the baryons is the bag model developed at the Massachusetts Institute of Technology (MIT) in 1974 [22, 23, 24]. This model visualises the hadron as a bag of radius $R$ in which the quarks evolve freely. In its simplest form, the quarks are massless, that is to say ultra-relativistic. The boundary condition at the surface is chosen to prevent the colour flux to leave the confining region. In the fundamental state, the size of the bag is such that the pressure applied by the quarks on the surface is equilibrated by the confinement pressure due to the QCD vacuum, pointing inwards and counter-acting the kinetic energy of the inner quarks. The vacuum pressure is the bag constant, usually denoted $B$. The model has been successful in obtaining some properties of the nucleons, such as the radii and magnetic moments. In order to fit the data, however, the bag has to have a radius $R \sim 1$ fm, which leaves little room for pions and other mesons. The model was then extended into the chiral bag model [25, 26] in which pions are coupled to the surface of the bag.

Ordinary nuclear matter is a mixed phase, consisting of droplets (the nuclei) surrounded by the vacuum. The transition between vacuum and nuclear matter is expected to take place at low $T$, for $\mu_B \sim 300$ MeV. Moving along the horizontal axis of the diagram, and augmenting the baryon potential while staying at low temperature, one moves towards matter of higher and higher density which starts to correspond to the expected state inside a neutron star. At even higher densities,

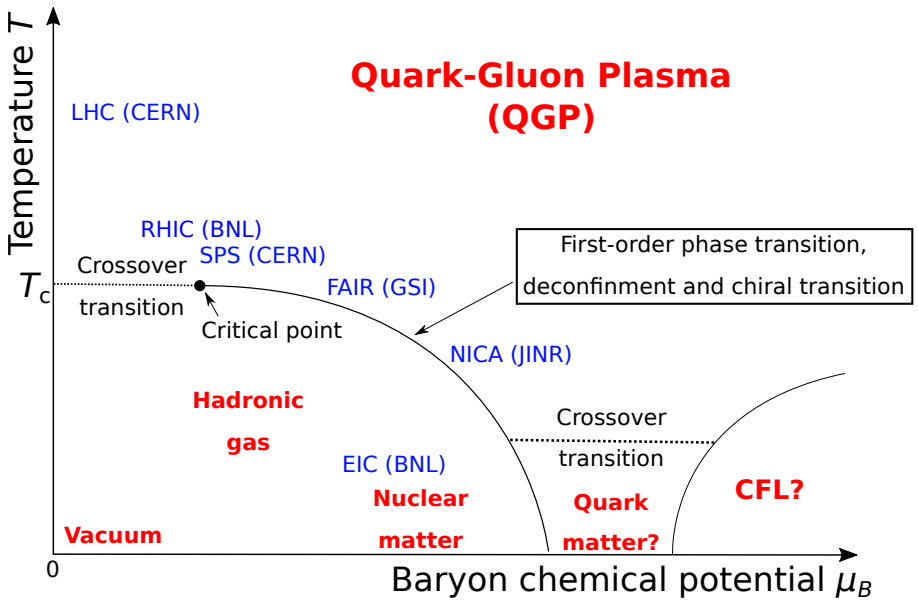


**Figure 1.3:** Schematic view of the phases of the QCD matter in the plane of temperature $T$ and baryon-chemical potential $\mu_B$. The various phases, observed or predicted, are reported on the figure. The lines indicate the phase transitions, while the critical point is reported as a circle. The dashed lines correspond to expected crossovers. LHC, RHIC, SPS, FAIR, NICA, and EIC are the acronyms of the heavy-ion collision experiments described in Section 2.2.

a phase called Colour-Flavour-Locking (CFL) [27] is expected. Matter under those extreme conditions is expected to be a colour superconductor, a form of quark matter where the quarks form Cooper pairs. Quark matter (to which CFL belongs) is not well known, both on the theoretical and experimental sides. It is distinguished from the ordinary nuclear matter in that the degrees of freedom are not the nucleons but the quarks themselves, and is foreseen to behave as a Fermi liquid.

Going back at low baryonic potential and heating up the system, we move along the vertical axis. At first, the confinement mechanism is still present and the nuclear matter is found in the form of an hadronic gas, mostly composed of pions. At sufficiently high temperature one expects a crossover towards a deconfined phase: the inner structure of the hadrons breaks up from thermal fluctuations, and the quarks and gluons form a gas of themselves along with other light particles such as photons and electrons. This phase transition is of particular interest as the matter at very-high temperature and low $\mu_B$ is expected to be the state of the early Universe, a fraction of a second after the Big-Bang ($\sim 10^{-5} - 10^{-4}$ s). The crossover transition is then a stage through which the Universe underwent, and its study sheds new lights on the early cosmology and the formation of the matter we see today.

The temperature at which this transition occurs can be obtained from lattice QCD (lQCD) calculations [28]. Due to long distance particle correlations during the phase transition, and since the chiral symmetry comes from the non-perturbative properties of the QCD vacuum, perturbative

QCD (pQCD) cannot be applied in the study of the phase transition. In order to solve QCD from first principles in the non-perturbative regime, one can introduce the QCD Lagrangian onto a discrete, Euclidean space-time lattice. The lattice is a mesh in which quarks are located on the vertices, while gluons travel along the lines between them. This framework allows for applying the Feynman path integral technique to deal with the propagators, while the temperature of the system is treated by statistical physics. Varying the size of the lattice space, one can extrapolate to the infinitesimal case, i.e. the continuum limit. lQCD is a rapidly-growing field of theoretical physics, mostly challenged by computing power and bandwidth issues as realistic calculations require a sizeable amount of numerical integrations. Nonetheless, several predictions have already been obtained under this framework for what concerns the QCD transition at high temperature and low baryonic potential. One of the most recent evaluation of the critical temperature $T_c$ at which the transition occurs is shown in Figure 1.4. The extrapolation from several values of the lattice volume $N_\tau$ up to the continuum limit yields a critical temperature at $T_c = (156.5 \pm 1.5)$ MeV [29]. A recent review of the lQCD results concerning the exploration of the phase diagram can be found in Ref. [30].

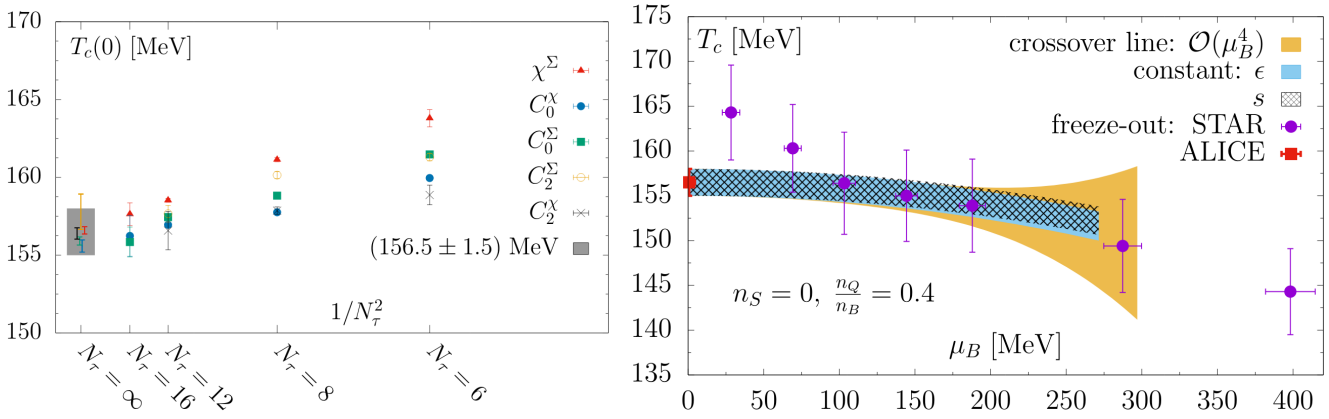


**Figure 1.4: Left**: pseudo-critical temperature $T_c(0)$ as a function of the lattice volume $N_\tau$ using several parametrisation of the chiral order parameter $C^\Sigma$, the disconnected chiral susceptibility $C^\chi$ and the susceptibility of the chiral order parameter $\chi^\Sigma$. The solid grey band depicts the continuum extrapolated value. **Right**: phase boundary of $2+1$ flavour QCD compared with the line of constant energy density $\varepsilon = (0.42 \pm 0.06)$ GeV/fm$^3$ and the line of constant entropy $s = (3.7 \pm 0.5)$ fm$^{-3}$ in the $T - \mu_B$ plane. It is also compared with the chemical freeze-out parameters extracted from grand canonical ensemble based fits to hadron yields within 0–10% centrality class from ALICE and 0–5% centrality class from STAR. Figures taken from Ref. [29] where more details can be found.

At the top of the diagram, at high temperature, one finds the Quark-Gluon Plasma (QGP) phase [31], a state of matter in which the elementary particles constituting the hadrons of baryonic matter are released from their strong attraction towards one another due to the extremely high energy density. Initially expected to be a gas of almost-free quarks and gluons, it was found to be a strongly interacting liquid. The study of the QGP is of relevance for cosmology, as it helps

pinpointing the conditions underwent by the Universe shortly after the Big Bang. In this regard, a sizeable amount of resources is dedicated to QGP studies, which can be done with a collider of sufficiently high energy such that the necessary thermodynamical conditions for a QGP to be created are met. Reference [32] provides a recent overview of the phenomenology of the QGP.

## 1.2 Structure of nuclei

### 1.2.1 The parton model

The parton model was originally proposed by Richard Feynman in 1969 as a way to analyse high-energy hadronic collisions [33, 34]. It was immediately applied to deep inelastic scattering (DIS) of electrons on protons by Bjorken and Paschos [35]. Later on, after the development of QCD and its experimental confirmation through the observation of the Bjorken scaling and asymptotic freedom, partons came to be matched with the quarks and gluons constituting the hadrons.

The most convenient way to experimentally study the inner structure of hadrons is by DIS. In this process, illustrated in Figure 1.5, a lepton $\ell$ of very-high energy scatters off a hadron $h$ which breaks apart and fragment into a final state $X$ containing many particles of large invariant mass $m_x \gg m_h$. In the perturbative approximation, the interaction occurs by means of the exchange of a virtual photon $\gamma^*$ emitted by the lepton and absorbed by the target hadron, transferring energy to one of its constituent quark. Historically, the process provided the first convincing evidence of the reality of quarks, which until that point were considered as a purely mathematical object. In the Target Rest Frame (TRF), the four-momentum transfer from the lepton to the hadron is:

$$q \overset{\text{TRF}}{=} (E - E')(\boldsymbol{k} - \boldsymbol{k'}), \tag{1.34}$$

where $E$ ($E'$) and $\boldsymbol{k}$ ($\boldsymbol{k'}$) are respectively the energy and the three-momenta of the lepton $\ell$ ($\ell'$), and its square is given in terms of the initial- and final-state lepton energies and the scattering angle $\theta$ of the final-state lepton $\ell'$ by:

$$Q^2 = -q^2 \overset{\text{TRF}}{=} 2EE'(1 - \cos\theta). \tag{1.35}$$

One can introduce the Lorentz-invariant Bjorken variables $x$ and $y$:

$$x = \frac{Q^2}{2P \cdot q} \overset{\text{TRF}}{=} \frac{Q^2}{2M(E - E')}, \qquad y = \frac{P \cdot q}{P \cdot k} \overset{\text{TRF}}{=} 1 - \frac{E'}{E}, \tag{1.36}$$

where $P \overset{\text{TRF}}{=} (M, 0, 0, 0)$ is the four-momentum of the hadron. The $x$ variable, commonly known as Bjorken-$x$, represents the fraction of the total momentum of the nucleon carried by a given parton, while the elasticity $y$ denotes the fraction of energy lost by the lepton in the process, defining the so-called elasticity of the event. With these, the unpolarised double-differential cross section of the DIS process reads:

$$\frac{\mathrm{d}^2\sigma}{\mathrm{d}Q^2\mathrm{d}x} = \frac{4\pi\alpha_{\text{em}}^2}{Q^4}\frac{y^2}{2Q^2}L_{\mu\nu}(k, k')W^{\mu\nu}(P, q), \tag{1.37}$$

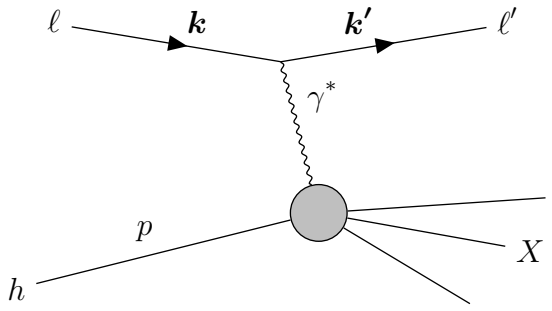


**Figure 1.5:** Feynman diagram for the deep inelastic lepton-hadron scattering.

where $\alpha_{\text{em}} = e^2/4\pi$ is the electromagnetic fine-structure constant and $L_{\mu\nu}$ and $W^{\mu\nu}$ are the leptonic and hadronic tensors, respectively. For a neutral-current electromagnetic scattering, the leptonic tensor reads:

$$L_{\mu\nu}(k, k') = 2(k_\mu k'_\nu + k'\mu k_\nu - k \cdot k' g_{\mu\nu}), \tag{1.38}$$

and the hadronic tensor can be obtained from the conservation of current as [36]:

$$W^{\mu\nu}(P, q) = -\left(g^{\mu\nu} - \frac{q^\mu q^\nu}{q^2}\right) F_1(x, Q^2) + \frac{1}{P \cdot q}\left(P^\mu - \frac{P \cdot q}{q^2} q^\mu\right)\left(P^\nu - \frac{P \cdot q}{q^2} q^\nu\right) F_2(x, Q^2), \tag{1.39}$$

where $F_1$ and $F_2$ are the structure functions of the hadron. In these terms, the cross section can be written as:

$$\frac{\mathrm{d}\sigma}{\mathrm{d}Q^2 \mathrm{d}x} = \frac{4\pi\alpha_{\text{em}}^2}{Q^4}\frac{1}{x}\left[xy^2 F_1(x, Q^2) + \left(1 - y - x^2 y^2 \frac{M^2}{Q^2}\right) F_2(x, Q^2)\right]. \tag{1.40}$$

One can go further by considering the infinite-momentum frame (IMF) (the Breit frame), in which the hadron moves at high velocity, and assuming $Q^2 \gg M^2$ one gets:

$$P \overset{\text{IMF}}{=} \left(\frac{Q}{2x}, 0, 0, \frac{Q}{2x}\right), \qquad q \overset{\text{IMF}}{=} (0, 0, 0, -Q). \tag{1.41}$$

That is to say, the hadron is highly boosted, and the interaction times between partons are dilated. One can then consider these interactions to be frozen over the timescale in which the interaction with the lepton takes place, and the lepton can scatter incoherently from the individual partons. The parton involved in the interaction can then be considered to be effectively free. In this original version of the parton model, the high-energy hadron can be seen as a collection of point-like constituents moving colinearly. One can thus define

$$f_i(\xi) = \text{the probability density of finding a parton } i \text{ within the hadron carrying a fraction } \xi \text{ of the hadron momentum.}$$

The function $f_i(\xi)$ is the parton distribution function (PDF).

The photon couples only to electrically charged particles, the Leading Order (LO) of the hadronic tensor reads:

$$W^{\mu\nu} = \sum_{i=q,\bar{q}} \int \frac{\mathrm{d}\xi}{\xi} f_i(\xi) \hat{W}_i^{\mu\nu}(p,q) + \mathcal{O}\left(\frac{1}{Q^2}\right), \tag{1.42}$$

where $p = \xi P \overset{\text{IMF}}{=} (\xi Q/2x, 0, 0, \xi Q/2x)$ and $\hat{W}_i^{\mu\nu}$ denotes a so-called partonic tensor. At the perturbative scales $Q^2 \gg M^2$ the higher orders can be neglected. In this LO approximation, called the Born approximation, the quark-initiated partonic tensor is:

$$\hat{W}_{q,\text{Born}}^{\mu\nu}(p,q) = \frac{x}{2Q^2} \frac{e_q^2}{2} \text{Tr}\left[\gamma^\mu p \gamma^\nu \gamma^\nu n \gamma^\mu\right] \delta(\xi - x), \tag{1.43}$$

where $e_q$ is the quark fractional charge, $\delta$ is the Dirac-delta function and:

$$n = q + xP \overset{\text{IMF}}{=} (Q/2, 0, 0, -Q/2), \qquad n^2 = 0. \tag{1.44}$$

The delta function in Equation 1.43 arises from integrating over the final-state quark momentum $p'$ and shows that, to LO perturbative accuracy, the Bjorken-$x$ measures the momentum fraction of the parton. Using Equations 1.42 and 1.43, one rewrites the cross section as:

$$\left(\frac{\mathrm{d}\sigma}{\mathrm{d}Q^2\mathrm{d}x}\right)_{\text{LO}} = \sum_{q,\bar{q}} e_q^2 f_q(x) \left(\frac{\mathrm{d}\hat{\sigma}}{\mathrm{d}Q^2\mathrm{d}x}\right)_{\text{Born}}, \qquad \left(\frac{\mathrm{d}\hat{\sigma}}{\mathrm{d}Q^2\mathrm{d}x}\right)_{\text{Born}} = \frac{4\pi\alpha_{\text{em}}^2}{Q^4}\left[\frac{y^2}{2} + \left(1 - y - x^2y^2\frac{M^2}{Q^2}\right)\right]. \tag{1.45}$$

If expressed in terms of the structure functions, one has:

$$2xF_1(x) = F_2(x) = x\sum_{q,\bar{q}} e_q^2 f_q(x). \tag{1.46}$$

The relation $F_2 = 2xF_1$ is known as the Callan-Gross relation [37]. Notably, it defines the $F_2(x)$ structure function as the charge-weighted sum of the parton densities $xf_q(x)$. Equation 1.46 shows that, in the naive parton model, the structure functions depend only on $x$ and not on the scale, a phenomenon referred to as the Bjorken scaling.

### 1.2.2 QCD-improved parton model

In the naive parton model, gluons show up as missing momentum, but they are not treated as dynamical quantities. Incorporating the effects of gluon radiation by quarks leads to the definition of the QCD-improved parton model. The diagram of such a radiation is shown in Figure 1.6. Here a quark that carries a fraction $y$ of the proton momentum radiates a gluon with a fraction $(1 - z)$ of its momentum. After the radiation, the quark, carrying a momentum fraction $yz$, scatters off the virtual photon. The momentum fraction seen by the photon is thus $x = yz$ which implies $z = x/y$.

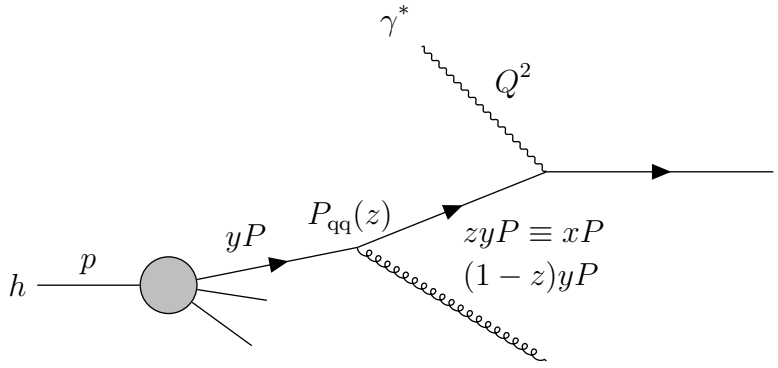


**Figure 1.6:** Feynman diagram for the deep inelastic lepton-hadron scattering, preceded by a gluon radiation.

Taking the gluon radiation into account, the $F_2$ structure function is found to be:

$$\frac{F_2(x,Q^2)}{x} = \sum_i e_i^2 \int_x^1 \frac{\mathrm{d}y}{y} f_i(y) \left[ \delta\left(1-\frac{x}{y}\right) + \frac{\alpha_s}{2\pi} P_{\rm qq}\left(\frac{x}{y}\right) \ln\frac{Q^2}{m^2} \right], \tag{1.47}$$

where $m^2$ is a lower transverse momentum cut-off to regularise the divergence when the gluon is collinear with the quark, and $P_{\rm qq}$ is the splitting function given by:

$$P_{\rm qq} = \frac{4}{3}\left(\frac{1+z^2}{1-z}\right). \tag{1.48}$$

The splitting function represents the probability for the parent quark to emit a gluon with the daughter quark retaining a fraction $z$ of the parent momentum. An infrared divergence shows up when $(1-z) \to 0$ where the gluon becomes so soft that the parent and daughter quarks cannot be resolved anymore. In order to simplify the notation, one can set:

$$I_{\rm qq}(x) = \frac{\alpha_s}{2\pi} \int_x^1 \frac{\mathrm{d}y}{y} f(y) P_{\rm qq}\left(\frac{x}{y}\right), \tag{1.49}$$

and get:

$$\frac{F_2(x,Q^2)}{x} = \sum_i e_i^2 \underbrace{\left[ \underbrace{f_i(x) + I_{\rm qq}(x)\ln\frac{\mu^2}{m^2}}_{f_i(x,\mu^2)} + I_{\rm qq}(x)\ln\frac{Q^2}{\mu^2} \right]}_{f_i(x,Q^2)}. \tag{1.50}$$

Here are defined the renormalised quark distribution $f_i(x,\mu^2)$ at the factorisation scale $\mu$ where are separated the singular factor, which depends on $m$ but not on $Q^2$, from the calculable factor which depends on $Q^2$ but not on $m$. Substituting the renormalised distribution for the bare distribution in $I_{\rm qq}$ one obtains:

$$f_i(x,Q^2) = f_i(x,\mu^2) + \frac{\alpha_s}{2\pi} \int_x^1 \frac{\mathrm{d}y}{y} f_i(y,\mu^2) P_{\rm qq}\left(\frac{x}{y}\right) \ln\frac{Q^2}{\mu^2} + \mathcal{O}(\alpha_s^2). \tag{1.51}$$

The expression of $F_2$ up to $\mathcal{O}(\alpha_s^2)$ then becomes:

$$\frac{F_2(x,Q^2)}{x} = \sum_i e_i^2 \left[ f_i(x,\mu^2) + \frac{\alpha_s}{2\pi} \int_x^1 \frac{\mathrm{d}y}{y} f_i(y,\mu^2) P_{\mathrm{qq}}\left(\frac{x}{y}\right) \ln \frac{Q^2}{\mu^2} \right]. \tag{1.52}$$

The structure function $F_2$ should not depend on the choice of the factorisation scale, which leads to the renormalisation group equation:

$$\frac{1}{2e^2 x} \frac{\partial F_2(x,Q^2)}{\partial \ln \mu^2} = \frac{\partial f(x,\mu^2)}{\partial \ln \mu^2} + \frac{\alpha_s}{2\pi} \int_x^1 \frac{\mathrm{d}y}{y} \left[ \frac{\partial f(y,\mu^2)}{\partial \ln \mu^2} \ln\left(\frac{Q^2}{\mu^2}\right) - f(y,\mu^2) \right] P_{\mathrm{qq}}\left(\frac{x}{y}\right) \tag{1.53}$$

$$= 0. \tag{1.54}$$

One sees from this equation that the term $(\partial f / \partial \ln \mu^2)$ is of the order $\alpha_s$, then the first term in the above integral is of the order of $\alpha_s^2$. Neglecting this term, one obtains the evolution equation for the quark:

$$\frac{\partial f(x,\mu^2)}{\partial \ln \mu^2} = \frac{\alpha_s}{2\pi} \int_x^1 \frac{\mathrm{d}y}{y} f(y,\mu^2) P_{\mathrm{qq}}\left(\frac{x}{y}\right) + \mathcal{O}(\alpha_s^2), \tag{1.55}$$

which is known as the Dokshitzer-Gribov-Lipatov-Altarelli-Parisi (DGLAP) equation [38, 39, 40]. It can be numerically solved once $f(x,\mu_0^2)$ is given as an input at some starting scale $\mu_0^2$.

Introducing the gluon distribution requires to consider all the splitting graphs, each yielding a splitting function:

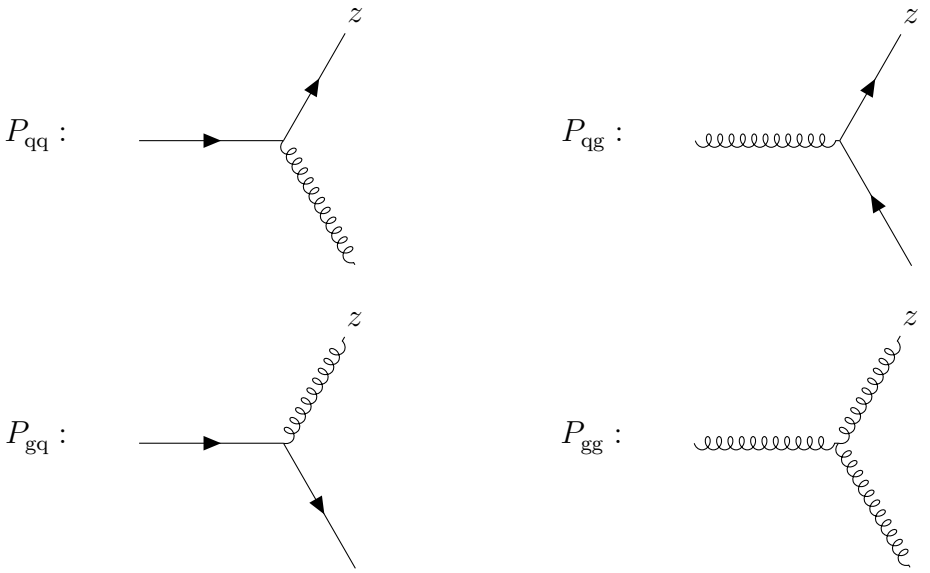


In the $P_{\mathrm{qg}}$ and $P_{\mathrm{gq}}$ cases, no singularity develops since the daughter and parent can always be distinguished. For the two other graphs a singularity develops in the soft limit $(1-z) \to 0$. The

leading order splitting functions read:

$$
\begin{aligned}
P_{\mathrm{qq}}^{(0)}(z) &= \frac{4}{3}\left[\frac{1+z^2}{(1-z)_+} + \frac{3}{2}\delta(1-z)\right], \\
P_{\mathrm{qg}}^{(0)}(z) &= \frac{1}{2}\left[z^2 + (1-z)^2\right], \\
P_{\mathrm{gq}}^{(0)}(z) &= \frac{4}{3}\left[\frac{1+(1-z)^2}{z}\right], \\
P_{\mathrm{gg}}^{(0)}(z) &= 6\left[\frac{z}{(1-z)_+} + \frac{1-z}{z} + z(1-z) + \left(\frac{11}{12} - \frac{n_f}{18}\right)\delta(1-z)\right].
\end{aligned}
\tag{1.56}
$$

The singularities showing up in $P_{\mathrm{qq}}$ and $P_{\mathrm{gg}}$ in the soft limit are regulated by the so-called "plus" prescription, denoted by the subscript + and defined as:

$$
\left[f(x)\right]_+ = f(x) - \delta(1-x)\int_0^1 f(z)\mathrm{d}z, \tag{1.57}
$$

or equivalently:

$$
\int_x^1 f(z)\left[g(z)\right]_+ \mathrm{d}z = \int_x^1 \left[f(z) - f(1)\right] g(z)\mathrm{d}z - f(1)\int_0^x g(z)\mathrm{d}z. \tag{1.58}
$$

The prescription guarantees that the integral from $x$ to 1 of the splitting function multiplied by the parton density function exists, provided that the PDF goes to zero as $x$ goes to 1. The $qq$, $qg$, $gq$ and $gg$ transitions lead to a set of $2n_f + 1$ coupled evolution equations that can be written as:

$$
\frac{\partial f_i(x,\mu^2)}{\partial \ln \mu^2} = \sum_{j=-n_f}^{n_f} \frac{\alpha_s}{2\pi}\int_x^1 \frac{\mathrm{d}y}{y} P_{ij}\left(\frac{x}{y}\right) f_j(y,\mu^2), \tag{1.59}
$$

where $P_{ij}(z)$ is the splitting function for a daughter $i$ with momentum fraction $z$ of a parent $j$. The indexing denotes:

$$
i,j = \begin{cases} -n_f, ..., -1 & \text{antiquarks} \\ 0 & \text{gluon} \\ 1, ..., n_f & \text{quarks} \end{cases}
$$

The expressions for the evolution equations can be simplified by writing the so-called Mellin convolution in short-hand notation as:

$$
P \otimes f \equiv \int_x^1 \frac{\mathrm{d}y}{y} P\left(\frac{x}{y}\right) f(y,\mu^2), \tag{1.60}
$$

allowing to rewrite the set of coupled equations as:

$$
\frac{\partial f_i}{\partial \ln \mu^2} = \sum_{j=-n_f}^{n_f} \frac{\alpha_s}{2\pi} P_{ij} \otimes f_j. \tag{1.61}
$$

In LO QCD, the splitting functions read:

$$P_{\overline{\mathrm{q}}_i\overline{\mathrm{q}}_j} = P_{\mathrm{q}_i\mathrm{q}_j} \equiv P_{\mathrm{qq}}\delta_{ij}, \qquad P_{\overline{\mathrm{q}}_i g} = P_{\mathrm{q}_i g} \equiv P_{\mathrm{qg}}, \qquad P_{g\overline{\mathrm{q}}_i} = P_{g\mathrm{q}_i} \equiv P_{\mathrm{gq}} \tag{1.62}$$

Exploiting these symmetries, the set of $2n_f + 1$ coupled equations can be, to a large extend, decoupled by defining the singlet distribution $q_{\mathrm{s}}$, which is the sum over all flavours of the quark and antiquark distributions:

$$q_{\mathrm{s}} \equiv \sum_{i=1}^{n_f}(q_i + \overline{q}_i). \tag{1.63}$$

One can show that the evolution of this distribution is coupled to that of a gluon:

$$\frac{\partial q_{\mathrm{s}}}{\partial \ln \mu^2} = \frac{\alpha_s}{2\pi}\left[P_{\mathrm{qq}} \otimes q_{\mathrm{s}} + 2n_f P_{\mathrm{qg}} \otimes g\right], \tag{1.64}$$

$$\frac{\partial g}{\partial \ln \mu^2} = \frac{\alpha_s}{2\pi}\left[P_{\mathrm{gq}} \otimes q_{\mathrm{s}} + P_{\mathrm{gg}} \otimes g\right], \tag{1.65}$$

which is often written in compact matrix notation:

$$\frac{\partial}{\partial \ln \mu^2}\begin{pmatrix} q_{\mathrm{s}} \\ g \end{pmatrix} = \frac{\alpha_s}{2\pi}\begin{pmatrix} P_{\mathrm{qq}} & 2n_f P_{\mathrm{qg}} \\ P_{\mathrm{gq}} & P_{\mathrm{gg}} \end{pmatrix} \otimes \begin{pmatrix} q_{\mathrm{s}} \\ g \end{pmatrix}. \tag{1.66}$$

Likewise it can be shown that non-singlet distributions:

$$q_{\mathrm{ns}} \equiv \sum_{i=1}^{n_f}(C_i q_i + D_i \overline{q}_i), \qquad \text{with} \qquad \sum_{i=1}^{n_f}(C_i + D_i) = 0, \tag{1.67}$$

evolve independently from the gluon and from each other:

$$\frac{\partial q_{\mathrm{ns}}}{\partial \ln \mu^2} = \frac{\alpha_s}{2\pi} P_{\mathrm{qq}} \otimes q_{\mathrm{ns}}. \tag{1.68}$$

An example of a non-singlet is the valence distribution $q_i - \overline{q}_i$. In practice, one does not evolve the quark distributions $u$, $\overline{u}$, $d$, $\overline{d}$, ... but, instead, the singlet distribution, coupled to the gluon, and a well chosen set of $2n_f - 1$ non-singlet distributions.

At this point, three different scales were considered:

- the factorisation scale $\mu_F^2$ at which the short and long distance physics are separated, and on which the PDFs evolve,
- the renormalisation scale $\mu_R^2$ on which the strong coupling strength $\alpha_s$ evolve,
- the hard scattering scale $Q^2$ which, in DIS, is the square of the 4-momentum transfer from the electron to the proton.

Exposing the different scales, one can write the (non-singlet) evolution equation and the expression for $F_2$ at LO as:

$$\frac{\partial q_{\rm ns}(x,\mu_F^2)}{\partial \ln \mu_F^2} = \frac{\alpha_s(\mu_R^2)}{2\pi}\int_x^1 \frac{{\rm d}y}{y} P_{\rm qq}\left(\frac{x}{y}\right) q_{\rm ns}(y,\mu_F^2), \tag{1.69}$$

$$F_2(x,Q^2) = \sum_{i=1}^{n_f} e_i^2 x\left[q_i(x,\mu_F^2) + \overline{q}_i(x,\mu_F^2)\right] + \mathcal{O}(\alpha_s). \tag{1.70}$$

Usually, one sets $\mu_F^2 = \mu_R^2 = Q^2$. This choice yields a theoretical uncertainty on the predictions, which is evaluated by varying the scales within a certain range. A typical choice for the variations is

$$\frac{1}{4}\mu_F^2 \leq \mu_R^2 \leq 4\mu_F^2 \qquad \text{and} \qquad \frac{1}{4}Q^2 \leq \mu_F^2 \leq 4Q^2. \tag{1.71}$$

One should note, however, that $F_2(x,Q^2)$ in Equation 1.70 depends only on $\mu_F^2$ which, for a given $Q^2$, is arbitrary. It follows that the LO perturbative stability is poor, and that LO pQCD has limited predictive power. This issue is remedied when higher order terms are included, as they are functions of both $Q^2$ and $\mu_F^2$. The scale dependence rapidly decreases as higher orders of corrections are added, driving a significant effort towards the evaluation of the splitting functions, and currently the knowledge of $F_2$ goes up to NNLO.

### 1.2.3 The PDF framework

The factorisation theorem can be applied to a wide class of processes in order to separate them into a universal long distance piece (which is non-perturbative, but process independent) and a short distance piece that is calculable in pQCD. For the hadroproduction of a generic final state $X$ in unpolarised pp collisions, the corresponding factorised expression reads [41]:

$$\sigma_{pp\to X}(s,\mu_F^2,\mu_R^2) = \sum_{i,j}\int {\rm d}x_1,{\rm d}x_2 f_i(x_1,\mu_F^2,\mu_R^2) f_j(x_2,\mu_F^2,\mu_R^2)\hat{\sigma}_{ij\to X}(x_1,x_2,s;\mu_F^2,\mu_R^2), \tag{1.72}$$

The unpolarised hard cross section $\hat{\sigma}_{ab\to X}$ can be calculated perturbatively as an expansion in the QCD and electroweak running couplings. A common procedure is to set the factorisation ($\mu_F$) and renormalisation ($\mu_R$) scales equal to the energy scale of the process: $\mu_F = \mu_R \equiv \mu = Q$. The PDFs $f_i$ and $f_j$ are process-independent, but they are not perturbative. They can, however, be estimated from measurements, and extrapolated to the necessary scales with the DGLAP equations. It is convenient to define the valence and sea distributions by

$$\begin{aligned} &u_{\rm V} = u - \overline{u}, && d_{\rm V} = v - \overline{v}, && s_{\rm V} = s - \overline{s} = 0, && \ldots \\ &u_{\rm S} = 2\overline{u}, && d_{\rm S} = 2\overline{d}, && s_{\rm S} = 2\overline{s}, && \ldots \end{aligned}$$

so that $q_i + \overline{q}_i = q_{i,{\rm V}} + q_{i,{\rm S}}$ for all flavours $i$. As the quantum numbers of the proton must be carried by the surplus of quarks over antiquarks, one gets the counting rules:

$$\int_0^1 u_{\rm V}(x){\rm d}x = 2, \qquad \int_0^1 d_{\rm V}(x){\rm d}x = 1 \qquad \int_0^1 s_{\rm V}(x){\rm d}x = 0, \tag{1.73}$$

the latter holding also for $c$, $b$ and $t$ quarks. The momentum distributions $xf_i(x)\mathrm{d}x$ give the probability that a quark carries a momentum fraction between $x$ and $x + \mathrm{d}x$. Summing over all the quark flavours in experimental data, leads to a deficit in the total probability, which is solved by introducing a gluon momentum distribution $xg(x)$. Then:

$$\sum_i \int_0^1 xf_i(x)\mathrm{d}x + \int_0^1 xg(x)\mathrm{d}x = 1. \tag{1.74}$$

The universality of the PDF is ensured by the isospin symmetry, which states that the $u$ (anti)quark distribution in the proton is equal to the $d$ (anti)quark distribution in the neutron, and vice versa. All these physics requirements are used as constraints during the PDF determination.

The PDFs are determined from a global QCD analysis (see Refs. [42, 43] for recent reviews, and references herein) of data from both colliders and fixed-target experiments. Various collaborations and working groups provide PDFs and their associated error sets, as well as regular updates following from theoretical developments or the availability of new data. Several hundreds of PDF sets are now available, among which some of the most recent are ABMP16[3] [44], CT18[4] [46], JAM19[5] [47], MSHT20[6] [48] and NNPDF3.1[7] [49] (the given references correspond to the last standard release of the sets, note that the names can greatly vary between versions, especially when it is based on the authors' names). The PDF determination usually relies on a parametrisation at an arbitrary input scale $Q_0$, typically around 1 GeV, from which the PDF is derived at any relevant scale by means of DGLAP evolution. In the process, the parameters at $Q_0$ are optimised to fit the variety of experimental data that are used. The contribution of heavy-quark flavours is power-suppressed at scales below their threshold production, with most models going up to five active flavours.

A typical parametrisation for each flavour or flavour combination is of the form:

$$f(x, Q_0, \{a_i\}) = x^{a_1}(1 - x)^{a_2} C(x, \{a_i\}), \tag{1.75}$$

with different parameters $\{a_i\}$ for each flavour. The $a_1$ and $a_2$ coefficients control the asymptotic behaviour of $f(x, Q_0, \{a_i\})$ in the limits $x \to 0$ and 1. For example, the $(1 - x)^{a_2}$ term, with $a_2 > 0$, ensures that the PDFs vanish in the elastic limit $x \to 1$. The $C(x)$ function, called the interpolating function, affects the behaviour of the PDFs outside of the asymptotic limits, and can be parametrised in several way. A typical choice is to take a basic polynomial:

$$C(x) = 1 + a_2 y(x) + a_3 [y(x)]^2 + ..., \tag{1.76}$$

[3] Alekhin–Blümlein–Moch–Placakyte, the authors.

[4] CT: CTEQ-TEA. CTEQ stands for Coordinated Theoretical-Experimental Project on QCD [45], a regroupment of theoreticians and experimentalists around QCD-centered research projects and collaborative works. TEA refers to the Tung Et Al. group which takes care of the determination and update of the CTEQ PDF sets, with the late Wu-Ki Tung as co-founder of CTEQ and former group leader.

[5] JLab Angular Momentum, the name of the collaboration, based at the Jefferson Laboratory.

[6] Martin–Stirling–Harland-Lang–Thorne, the authors.

[7] Neural-Network PDF, from the methodology used for the determination.

where $y$ can be any function of $x$, such as $y = x$, $y = \sqrt{x}$, and so on. The gluon PDF is determined in the same manner, often with a lower order polynomial and different mapping of $y$ in order to account for the fewer existing constraints on the gluonic distributions in the data. In their most recent releases the CT and MSHT groups respectively used a basis of Bernstein and Chebyshev polynomials instead of basic ones, as it allows for a larger number of free parameters while staying formally equivalent to the simple polynomial expansion.

An alternative approach to the PDF parametrisation is adopted by the NNPDF collaboration. The interpolating function $C(x)$ is modelled using a multi-layered feed-forward neural network, which allows for a much larger number of free parameters (typically higher by one order of magnitude) than in the sets of the other groups. The form of Equation 1.75 is still assumed, but with $C(x) = \mathrm{NN}(x)$, where NN is a neural network. The $x^{a_1}(1-x)^{a_2}$ term is now a preprocessing factor that speeds up the minimisation procedure and is determined by iteration. In order to avoid overfitting, the data are splitted into a training and a validation sets, the best fit being determined by cross-validation.

After the choice of parametrisation, the best-fit parameters and associated uncertainties are determined via a fitting methodology and the minimisation of a suitable statistical estimator such as $\chi^2$. The definition of the $\chi^2$ may vary from one group to the other and each choice is detailed in the corresponding publication. A standard choice is of the form:

$$\chi^2 = \sum_{i,j}^{N_{\mathrm{data}}} \left[T_i(\{a_k\}) - D_i\right] (M_{\mathrm{cov}}^{-1})_{ij} \left[T_j(\{a_k\}) - D_j\right], \tag{1.77}$$

where $N_{\mathrm{data}}$ is the number of data points from a given experiment, $T_i$ and $D_i$ are the corresponding theoretical predictions and experimental measurements, and $(M_{\mathrm{cov}}^{-1})_{ij}$ is the inverse of the experimental covariance matrix. The theoretical prediction $T_i$ depends on the set of parameters $\{a_k\}$ via the PDF parametrisation of Equation 1.75, such that the $\chi^2$ defined above assesses the agreement between data and theory.

Determining the best-fit parameters is not sufficient, it needs to be accompanied by a determination of the associated uncertainty as to enable the evaluation of the uncertainty on predictions from the PDFs. Two main methods are used for this, the so-called Hessian and Monte Carlo (MC) methods.

The Hessian method [50] is based on the parabolic expansion of the $\chi^2$ in the vicinity of its minimum:

$$\Delta\chi^2 \equiv \chi^2 - \chi^2_{\mathrm{min}} = \sum_{i=1,j}^{n_{\mathrm{par}}} H_{ij} \left(a_i - a_i^0\right) \left(a_j - a_j^0\right), \tag{1.78}$$

where $n_{\mathrm{par}}$ is the number of parameters of the PDF and $a_{i,j}^0$ denotes the best-fit values determined by $\chi^2$ minimisation. The Hessian matrix is defined as:

$$H_{ij} \equiv \frac{1}{2} \frac{\partial^2 \chi^2}{\partial a_i \partial a_j}\bigg|_{\{\vec{a}\}=\{\vec{a}^0\}}. \tag{1.79}$$

The diagonalisation of the Hessian matrix enables the representation of the PDF uncertainties in terms of orthogonal eigenvectors within a fixed tolerance $T = \sqrt{\Delta\chi^2}$. These eigenvectors can then be used to estimate the PDF uncertainty for arbitrary cross sections, using the master formula of Hessian PDF sets for the uncertainty of a cross section $\mathcal{F}$:

$$\sigma_{\mathcal{F}} = \frac{1}{2}\left(\sum_{i}^{n_{\rm par}} \left[\mathcal{F}(S_i^+) - \mathcal{F}(S_i^-)\right]^2\right)^{1/2}, \tag{1.80}$$

where $S_i^{\pm}$ corresponds to the $i$-th eigenvector associated with positive and negative variations with respect to the best fit value.

The MC method relies on the construction of a representation of the probability distribution in terms of a large number of replicas $N_{\rm rep}$, encoding all the information on central values, variances and correlations provided by the experiments. Specifically, given an experimental measurement of a hard-scattering observable $\mathcal{F}_I^{(\rm exp)}$ with total uncorrelated uncertainty $\sigma_I^{(\rm stat)}$, a number $N_{\rm syst}$ of fully correlated systematic uncertainties $\sigma_{I,c}^{(\rm corr)}$ and a number $N_a$ ($N_r$) of absolute (relative) normalisation uncertainties $\sigma_{I,n}^{(\rm norm)}$, the MC replicas are constructed using the expression:

$$\mathcal{F}_I^{(\rm art)(k)} = S_{I,N}^{(k)}\mathcal{F}_I^{(\rm exp)}\left(1 + \sum_{c=1}^{N_{\rm syst}} r_{I,c}^{(k)}\sigma_{I,c}^{(\rm corr)} + r_I^{(k)}\sigma_I^{(\rm stat)}\right), \qquad k = 1, ..., N_{\rm rep}, \tag{1.81}$$

where $S_{I,N}^{(k)}$ is a normalisation prefactor. The variables $r_{I,c}^{(k)}$, $r_I^{(k)}$ are univariate Gaussian random numbers. The PDFs are then individually fitted on each of the MC replicas. The resulting set of PDFs scans the probability density in the space of PDFs. The expectation function of a generic observable $\mathcal{F}(\{f\})$, depending on the fitted set of PDFs $\{f\}$, is estimated as the average over the replica sample,

$$\langle\mathcal{F}(\{f\})\rangle = \frac{1}{N_{\rm rep}}\sum_{k=1}^{N_{\rm rep}}\mathcal{F}(\{f\}). \tag{1.82}$$

The corresponding uncertainty is determined as the variance of the MC sample:

$$\sigma_{\mathcal{F}} = \left(\frac{1}{N_{\rm rep}-1}\sum_{k=1}^{N_{\rm rep}}\left[\mathcal{F}(\{f^{(k)}\}) - \langle\mathcal{F}(\{f\})\rangle\right]^2\right)^{1/2}. \tag{1.83}$$

The PDF sets determined by the various groups are distributed as numerical tables in the standard Les Houches Accord PDF (LHAPDF) format [51] and can be accessed from a public repository [52]. An example of PDF sets, NNPDF3.1, is shown in Figure 1.7. The PDF4LHC working group now regularly provides and updates a set of recommendations [53] for the determination, publication and usage of PDF sets and the assessment of PDF and PDF+$\alpha_s$ uncertainties, focusing on applications for the Large Hadron Collider (LHC).

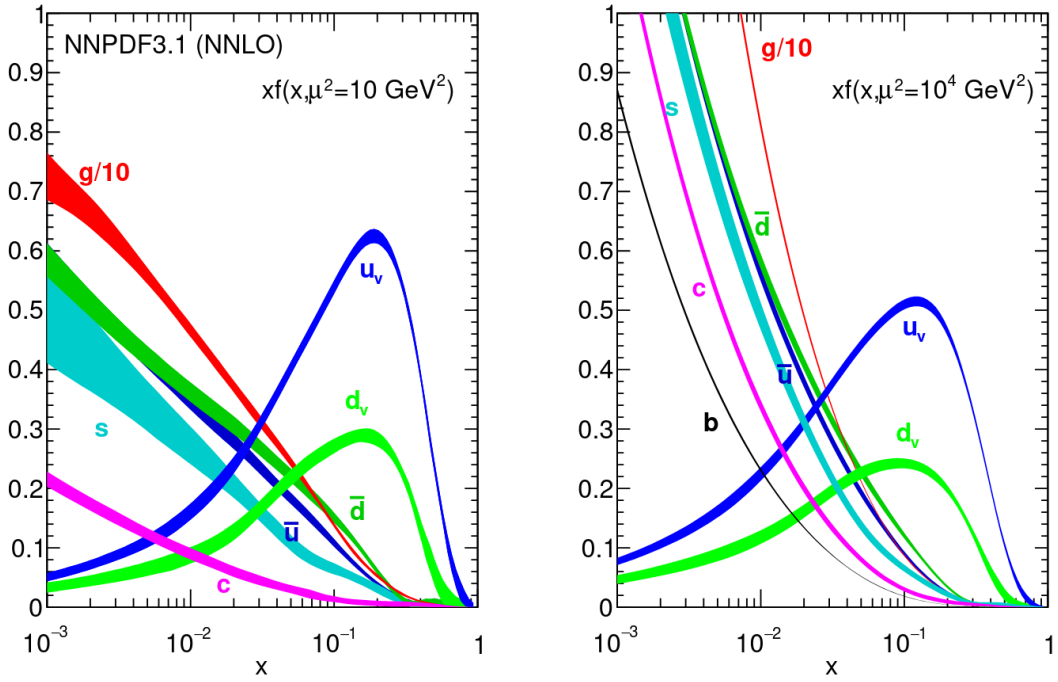


**Figure 1.7:** The NNPDF3.1 NNLO PDF set evaluated at $\mu^2 = 10$ GeV$^2$ (left) and $\mu^2 = 10^4$ GeV$^2$ (right). The gluon distribution is scaled by a factor 1/10 for better visibility. Figure taken from Ref. [49].

### 1.2.4 Nuclear effects and nPDFs

The concepts presented up to now focused on the determination of the proton PDF and the neutron one through the isospin symmetry. What has been discussed is also relevant for studying the partonic content of heavier nuclei, by means of the determination of nuclear PDF (nPDF) sets. Although still limited, the amount of available data from heavy-ion collisions (HIC) is rapidly growing and nPDF models are becoming more and more precise. Here as well, several models are available, among which one can cite the recent EPPS16[8] [54], nCTEQ15[9] [55], nNNPDF2.0[10] [56], DSSZ[11] [57], and KA15[12] [58]. An interesting recent set is TUJU19[13] [59], which was derived using the open source xFitter (formerly HERAFitter) tool [60]. In the following, we shall focus on the EPPS, nCTEQ and nNNPDF models are they are the ones to which the results presented in this thesis are compared.

It is, in principle, possible to extract the nPDF $f_i^A$ for the parton $i$ in a nucleus of atomic number $A$ independently for each chemical species, without having to rely on a comprehensive

[8] Eskola–Paakkinen–Paukkunen–Salgado, the authors.
[9] Nuclear-CTEQ, as it based on the CTEQ framework for free-PDF determination.
[10] Nuclear Neural-Network PDF, from the methodology.
[11] De Florian–Sassot–Stratmann–Zurita, the authors.
[12] Khanpour–Atashbar Tehrani, the authors.
[13] Tübingen–Jyvaskyla, the hosting Universities of the authors.

model for nuclear effects[14]. This requires, however, a large amount of data for each species, while the current set of available data is barely sufficient to determine the nPDFs of the most commonly used nuclei in experiments (lead and gold). Thus, as it was needed to extrapolate for the energy scale in the determination of the proton PDF, an extrapolation for $A$ is required in the nPDF case. In order to assemble all the available data, performed over a wide range of collision systems, geometrical coverages, physics channels, etc., a number of simplifying assumptions can be made:

- one can assume that the nuclear modifications in the bound-proton PDF are small, such that one can take the free-proton PDF as a baseline for the parametrisation of $f^A$,
- the bulk of the nuclear corrections is expected to depend on nothing but $A$, enabling the use of the full set of available data.

From here, two main approaches can be followed, that of nuclear correction factors or of full parametrisation of the nPDF.

The nuclear correction factor $R_i^A(x, Q_0^2)$ is defined as the proportionality factor between the free- and bound-nucleon PDF:

$$f_i^A(x, A, Q^2) = R_i^A(x, Q_0^2) \times f_i(x, Q^2) \qquad \Leftrightarrow \qquad R_i^A(x, Q_0^2) = \frac{f_i^A(x, A, Q^2)}{f_i(x, Q^2)}, \tag{1.84}$$

with $i$ denoting the parton flavour or flavour combination, $i = u_\mathrm{V}, d_\mathrm{V}, g, \overline{u} + \overline{d}, s, \overline{s}, \overline{u}/\overline{d}$ being a common choice in recent models. In Equation 1.84, the free-proton PDF (so-called baseline) is held fixed, and as for the free-PDF case the PDF of a bound neutron $f_{i/n}^A$ is related to that of a bound proton $f_{i/p}^A$ by isospin symmetry. All the $A$-dependent free parameters are then contained in the correction factor $R$, for which a dedicated parametrisation is built. This choice of implementing the nuclear corrections by means of a nuclear modification factor is followed by the EPPS group. Figure 1.8 shows the typical shape of the $R$ factor as a function of the Bjorken-$x$. The shape of the nuclear modification function is mainly driven by the combination of three effects:

- the shadowing effect, with a depletion originating from destructing interferences of amplitudes arising for multiple scatterings between partons in the nucleus [61],
- the anti-shadowing effect, counterpart of the shadowing effect (typically, a gluon fusion will deplete the low-$x$ region and fill the high-$x$ region by destroying two gluons with low momenta and create one of high momentum),
- the EMC effect, which is yet to be fully understood [62].

The parametrisation of the nuclear modification function in the EPPS16 analysis uses the following piecewise expression:

$$R_i^A(x, Q_0^2) = \begin{cases} a_0 + a_1(x - x_a)^2 & x \leq x_a \\ b_0 + b_1 x^\alpha + b_2 x^{2\alpha} + b_3 x^{3\alpha} & x_a \leq x \leq x_e \\ c_0 + (c_1 - c_2 x)(1 - x)^{-\beta} & x_e \leq x \leq 1, \end{cases} \tag{1.85}$$

[14]It is conventional, when speaking of nuclear effects, to exclude the isospin effect following from the nucleon content of the nucleus. We adopt this convention here.

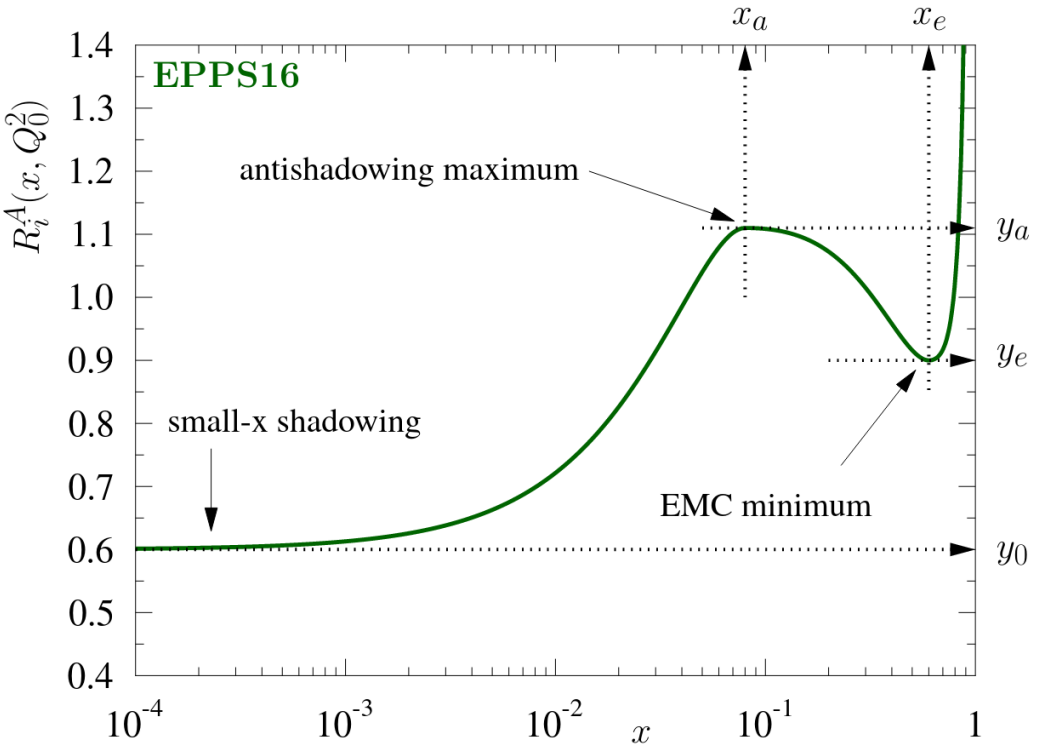


**Figure 1.8:** Illustration of the EPPS16 fit function $R_i^A(x, Q_0^2)$. See the text for more details about the nuclear effects and the meaning of the $x_k$ and $y_k$. Figure taken from Ref. [54].

where $\alpha = 10x_a$, and all the parameters $a_k$, $b_k$ and $c_k$ have implicit $i$ and $A$ dependencies. These parameters are fully determined by the asymptotic small-$x$ limit $y_0 = R_i^A(x \to 0, Q_0^2)$, the antishadowing maximum $y_a = R_i^A(x_a, Q_0^2)$ and the EMC minimum $y_e = R_i^A(x_e, Q_0^2)$, as well as requirements for continuity and vanishing first derivatives at the matching points $x_a$ and $x_e$. The $A$ dependency of the $y_k$ points is parametrised as:

$$y_k(A) = y_k(A_{\text{ref}}) \left( \frac{A}{A_{\text{ref}}} \right)^{\gamma_k [y_k(A_{\text{ref}}) - 1]} , \tag{1.86}$$

with $\gamma_k \geq 0$ and $A_{\text{ref}} = 12$. In the EPPS16 model the input scale $Q_0^2$ is set at the charm pole mass $Q_0^2 = m_c^2 = (1.3 \text{ GeV})^2$ and the value of the strong coupling strength is set at the PDG value [6] by $\alpha_s(M_Z) = 0.118$, with $M_Z$ the mass of the $Z$ boson. The CT14 PDF set [63] serves as baseline, and the error sets are determined by means of the Hessian matrix method.

The second approach, followed in the nCTEQ global analysis [55], does not operate with a nuclear correction factor. It is instead a full parametrisation of the whole nPDF for bound proton

$f^A(x,Q_0)$[15]. In the nCTEQ15 analysis the functional form mimics that of the CTEQ6 PDF [64]:

$$xf_i^A(x,Q_0) = c_0 c^{c_1}(1-x)^{c_2} e^{c_3 x}(1+e^{c_4}x)^{c_5}, \tag{1.87}$$

for $i = u_V, d_V, g, \overline{u}+\overline{d}, s+\overline{s}, s-\overline{s}$. A specific parametrisation of the down-to-up quark ratio is chosen as:

$$\frac{\overline{d}(x,Q_0)}{\overline{u}(x,Q_0)} = c_0 x^{c_1}(1-x)^{c_2} + (1+c_3 x)(1-x)^{c_4}. \tag{1.88}$$

The $A$ dependence is directly embedded into the $c_k$ coefficients:

$$c_k(A) \equiv c_{k,0} + c_{k,1}\left(1 - A^{-c_{k,2}}\right). \tag{1.89}$$

The coefficient $c_{k,0} = c_k(A=1)$ is the underlying proton coefficient. It is held fixed during the nCTEQ analysis, and set at the value determined in the study of Ref. [65]. Here as well the input scale corresponds to the charm pole mass, $Q_0 = 1.3$ GeV and the method for the determination of the error sets is the Hessian matrix method.

The same choice was taken for the nNNPDF2.0 analysis. The parametrisation scale is chosen as $Q_0 = 1$ GeV, where the evolution basis (the one given by the eigenvectors of the DGLAP evolution equations) is given by $\Sigma, T_3, T_8, V, V_3$ and $g$. Expressed in terms of the elements of the flavour basis, composed of the active flavours, the evolution basis reads:

$$\begin{aligned}
\Sigma(x,Q^0) &= (u^+ + d^+ + s^+)(x,Q^0), && \text{total quark singlet,}\\
T_3(x,Q^0) &= (u^+ - d^+)(x,Q^0), && \text{quark triplet,}\\
T_8(x,Q^0) &= (u^+ + d^+ - 2s^+)(x,Q^0), && \text{quark octet,}\\
V(x,Q^0) &= (u^- + d^-)(x,Q^0), && \text{total valence quark,}\\
V_3(x,Q^0) &= (u^- - d^-)(x,Q^0), && \text{valence quark triplet,}\\
g(x,Q^0) & && \text{gluon,}
\end{aligned} \tag{1.90}$$

with $q^\pm = q \pm \overline{q}$ and $s = \overline{s}$ is assumed. Six PDF combinations are independently parametrised as:

$$xf_i(x,Q^0) = B_i x^{\alpha_i}(1-x)^{\beta_i}\mathrm{NN}_i(x,A), \tag{1.91}$$

with $i = (\Sigma, T_3, T_8, V, V_3, g)$ the flavour combination, $B_\Sigma = B_{T_3} = B_{T_8} = 1$ and the three other $B$ coefficients are fixed by the sum rules. $\mathrm{NN}_i(x,A)$ is the value yielded by the neuron of the output layer of the neural network associated to each specific distribution. The neural network consists in one input layer, one hidden layer with sigmoid activation function and one output layer with linear activation function. In the nNNPDF2.0 analysis the uncertainty on the nPDFs is estimated with the MC method, using a number of replicas $N_{\mathrm{rep}} = 1000$. Figure 1.9 shows the results of the nNNPDF2.0 determination for three nucleus species, carbon, iron and lead.

Table 1.2 summarises the key specifications of the three nPDF models discussed in this section.

[15] It should be noted that baselines are still used here, as to help the global fits by providing e.g. reference values and boundary conditions.

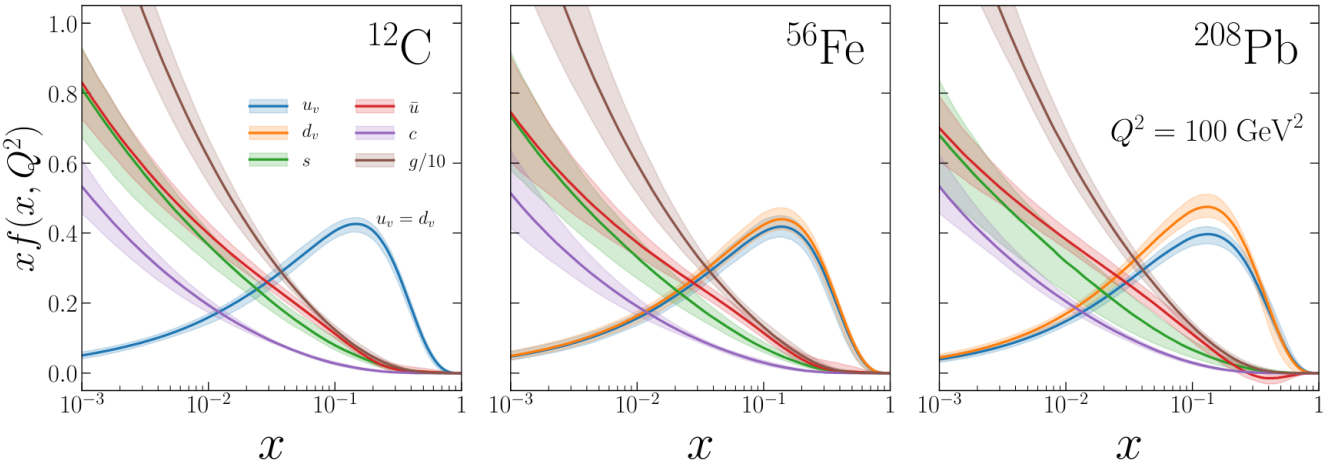


**Figure 1.9:** The nNNPDF2.0 set of nuclear PDF for $^{12}$C, $^{56}$Fe and $^{208}$Pb at the energy scale $Q^2 = 100$ GeV$^2$. The uncertainty band correspond to the 90% confidence level. Figure taken from Ref. [56].

| nPDF set | nCTEQ15 | EPPS16 | nNNPDF2.0 |
|---|---|---|---|
| Order | NLO | NLO | NLO |
| Flavour separation | valence quarks | valence + sea quarks | valence + sea quarks |
| Proton baseline | CTEQ6M-like | CT14NLO | NNPDF3.1 |
| Data points | 708 | 1811 | 1467 |
| Input scale $Q_0$ | 1.30 GeV | 1.30 GeV | 1 GeV |
| Free parameters | 35 | 52 | 256 |
| Parametrisation | polynomial | polynomial | neural network |
| Error determination | Hessian | Hessian | MC |

**Table 1.2:** Key specifications of the nCTEQ15 [55], EPPS16 [54] and nNNPDF2.0 [56] nPDF sets.

# Chapter 2

# Heavy-ion collisions

In this chapter, a selection of topics relevant for the analyses presented in this manuscript are briefly reviewed. The first section sets the stage by summarising the current view of the evolution of a heavy-ion collisions (HIC). It is followed by a short introduction to the main present and future heavy-ion colliders in Section 2.2. Section 2.3 describes the theoretical side of the Glauber model, the common picture for modelling a hadronic collision and through which key quantities for the characterisation of the event can be obtained. Finally, Section 2.4 presents the motivation behind the study of small systems as a mean to acquire more inputs for the interpretation of data from HIC, and provides some details on peculiar recent observations.

## 2.1 History of a collision

The requirements, in terms of thermodynamical conditions, for the creation of a quark-gluon plasma (QGP) prevent its systematic study in the laboratory, outside of large scale experiments able to bring beams of particles up to relativistic speed before colliding them. Up to now HIC are the only known way to create a QGP, with one caveat: a hadronic collision is a complex process, in which the QGP only represents a fraction of the physics involved. Over the years, a standard model of ultrarelativistic HIC (URHIC) has emerged, which is depicted in Figure 2.1. Every stage of the evolution features a different form of QCD matter with specific active degrees of freedom. One can isolate several steps, described below, all defined in terms of the Lorentz-invariant proper time $\tau \equiv \sqrt{t^2 - z^2}$, which parametrises the hyperbolic curves in the figure, and defining $\tau = 0$ as the collision time. The indicated times are of course not firm boundaries, but rather indications of our current understanding of the phenomena and their temporal evolution. More information can be found in Ref. [66].

**1: Initial state** ($\tau < 0$ fm/$c$):

Before the collision, setting oneself in the centre-of-mass (cms) frame, one sees the incoming nuclei as being highly contracted, with a longitudinal extent smaller by a factor $\gamma = \sqrt{s_{\mathrm{NN}}}/2m_{\mathrm{N}} \sim 10^3$ at the LHC energies (the Lorentz boost factor) to that of the radial extent in the transverse plane. The system here is described by the QCD-improved parton model presented in Section 1.2

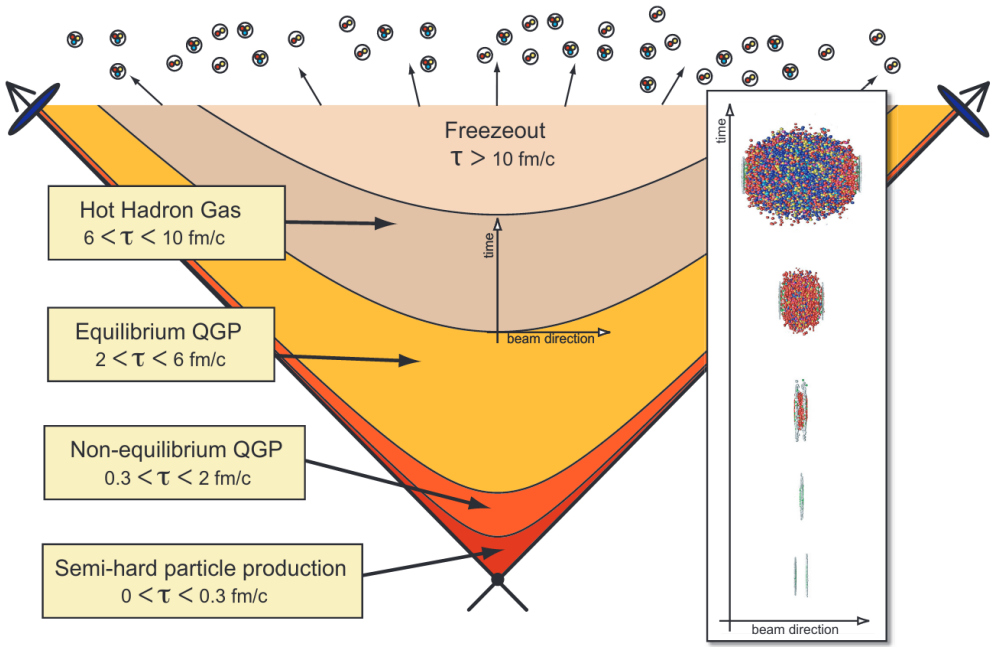


**Figure 2.1:** Light cone and space-time evolution of a HIC, with the typical proper times $\tau$ indicated for the energies attained at the Large Hadron Collider (LHC). The overlay shows a simulation as seen in the laboratory frame. Figure taken from Ref. [67].

as a wall of partons travelling along colinear trajectories. At high energy, the nuclei are mostly composed of gluons as seen in the low-$x$ gluon distribution function of Figure 1.9. The higher we go in energies, the higher the gluon density becomes. However, the longitudinal extension of the nucleus has a lower limit and the rapid increase of the number of gluons cannot continue forever. Having a typical transverse size of $1/Q$, the gluons will eventually overlap each other and saturate [68, 69]. The gluons form a classical coherent field configuration called the Colour Glass Condensate (CGC) [70]. The saturation scale, $Q_s$, is proportional to the gluon distribution, the radius of the hadron and the coupling:

$$Q_s \sim \alpha_s(Q_s^2)\frac{xg(x,Q_s^2)}{\pi R^2}, \tag{2.1}$$

where $R$ is the radius of the mother hadron. The saturation scale for a nucleus follows the same expression, with the corresponding nuclear gluon distribution and radius: $g(x,Q_s^2) \to g_{\rm A}(x,Q_s^2)$ and $R \to RA^{1/3}$, meaning that the gluon saturation effect will be more significant in heavy nuclei than in protons. The CGC approach is an alternative to the nPDF framework described in Section 1.2 for the description of the initial state.

**2: Collision** ($\tau \sim 0$ fm/$c$):

At $\tau = 0$, the two nuclei hit each other and the interactions start developing. The central collision of ultra-relativistic heavy nuclei is a process of huge entropy production. Hard processes

involving large momentum transfers $Q > 10$ GeV are the first to occur, within a time $\tau \sim 1/Q$ by the uncertainty principle. These processes lead to the production of hard particles, i.e. particles carrying transverse energies and momenta of the order of $Q$. The hard processes include (hadronic) jets, direct photons, dilepton pairs, heavy quarks and vector bosons. They are often used to characterise the event (e.g. "di-jet event").

This stage is efficiently described by the framework presented in Chapter 1, by means of the QCD-improved parton model. The nucleus is seen as a stream of partons, with partonic interactions being frozen over the timescale at which the collision happens. The high energy of the collision allows one to use pQCD and the factorisation theorem to depict the interactions and calculate the cross sections. The non-perturbative part of the cross section is estimated from global QCD analysis of experimental data, from which the nPDF is derived. Hard processes are therefore of particular interest for the study of HIC, as their production is theoretically rather well known, and they experience the whole history of the system from which information on the various stages can be obtained.

**3: Semi-hard particle production** $(0 < \tau < 0.3$ fm/$c)$:

At this stage are produced the so-called semi-hard processes, with a corresponding transverse momentum scale of about 1 GeV/$c$. The bulk of the partonic content of the colliding nuclei, which constituted the CGC, is now liberated by the collision. Most of the multiplicity of the event is generated here, as most of the hadrons eventually seen in the detectors are produced via the fragmentation and hadronisation of the initial-state gluons after their liberation. Right after being liberated, they form a relatively dense medium, with an average density estimated as $\epsilon \sim 15$ GeV/fm$^3$ in Pb–Pb collisions at the LHC energies. This density is about one order of magnitude higher than that in nuclear matter. This out-of-equilibrium state of partonic matter is known as the glasma [71].

**4: Out-of-equilibrium state** $(0.3 < \tau < 2$ fm/$c)$:

If the produced partons could not interact with each other, they would rapidly separate and independently evolve (via fragmentation and hadronisation) towards the final state hadrons. This situation corresponds, roughly speaking, to what happens in pp collisions, where the density is low enough to neglect the interaction mentioned above (although the situation is more complex and will be addressed in Section 2.4). In URHIC, collective phenomena are observed, such as the particle anisotropic flow [32] and comovers interactions [72], indicating that the particles liberated and created during the collision do interact. A direct consequence is that the system quickly reaches thermal equilibrium: data are consistent with a very short thermalisation time $\tau_{th} \sim 1$ fm/$c$. It is a striking feature, as it requires a strong interaction between the partons, able to compete with the medium expansion: these interactions have to redistribute energy and momentum among the partons despite the fact that the latter separate quite fast from each other. Such a rapid thermalisation is not consistent with perturbative calculations at weak coupling, driving the emergence of a new paradigm: the dense partonic matter produced at the intermediate stages of a HIC may

actually be a strongly coupled, near perfect fluid.

**5: Quark-Gluon Plasma** $(2 < \tau < 6$ fm/$c)$:

The outcome of the thermalisation process is the high-temperature phase of QCD matter known as the QGP. The existence of this phase is well established from theoretical calculations on the lattice, but its production during a HIC is at best ephemeral: the partonic matter keeps expanding and cooling down (this implies in particular that the temperature is space and time dependent, such that the thermal equilibrium is only reached locally) until the hadronisation phase, in which the coloured quarks and gluons recombined into colour-singlet hadrons. During the time of existence of the QGP, its description can be achieved by means of relativistic hydrodynamics [31]. The fundamental equations are the conservation of the energy-momentum tensor and the baryon number:

$$\partial_\mu \langle T^{\mu\nu} \rangle = 0, \qquad \partial_\mu \langle j^\mu_{\mathcal{B}} \rangle = 0, \tag{2.2}$$

where the expectation value is taken with respect to the time-dependent state in local thermal equilibrium. Arguably one the main objective of heavy-ion programs is the characterisation of the QGP through the determination of its physical properties, such as the temperature, density, or shear viscosity to entropy ratio. The precise nature of the QGP is still an open question. If the system can be approximated by a perfect fluid, the expectation values are parametrised solely by the local density $\varepsilon$ and the local pressure $P$. If the fluid is not perfect, extra information are required, such as the viscosity or the heat conductivity. A recent review of the phenomenology of the QGP can be found in Ref. [32].

**6: Hadronic phase and freeze-out** $(\tau > 6$ fm/$c)$:

Hadronisation occurs when the local temperature reaches the order of the critical temperature of the phase transition $T_c \simeq 155$ MeV. This hadronic system is still relatively dense, such that the local thermal equilibrium is preserved during the expansion. One then speaks of hot hadron gas, with decreasing temperature and density. Inelastic interactions keep occuring until the so-called chemical freeze-out. From this point on, the relative abundances of hadrons are fixed, and the only interactions that still happen are elastic. The properties of the medium at this stage, as a function of the beam energy, is shown in Figure 2.2. Around $\tau \sim 20$ fm, the elastic collisions stop as well, at the thermal freeze-out. The momenta of the formed particles are set, and they stream freely towards the detectors.

It should be mentioned that this picture is not fixed, and the actual behaviour of the QCD matter during a HIC remains an open question. Recent works on the application of hydrodynamics, for example, indicate that the system may never come close to equilibrium [74, 75, 76]. In this alternative picture, the transition between the fourth and fifth phases should be considered in terms of hydrodynamisation instead of reach of an equilibrium state, and the boundary between the two set at the point where hydrodynamics becomes applicable. Then the so-called "pre-equilibrium state" is wrongly named, and one should speak of pre-hydrodynamisation instead.

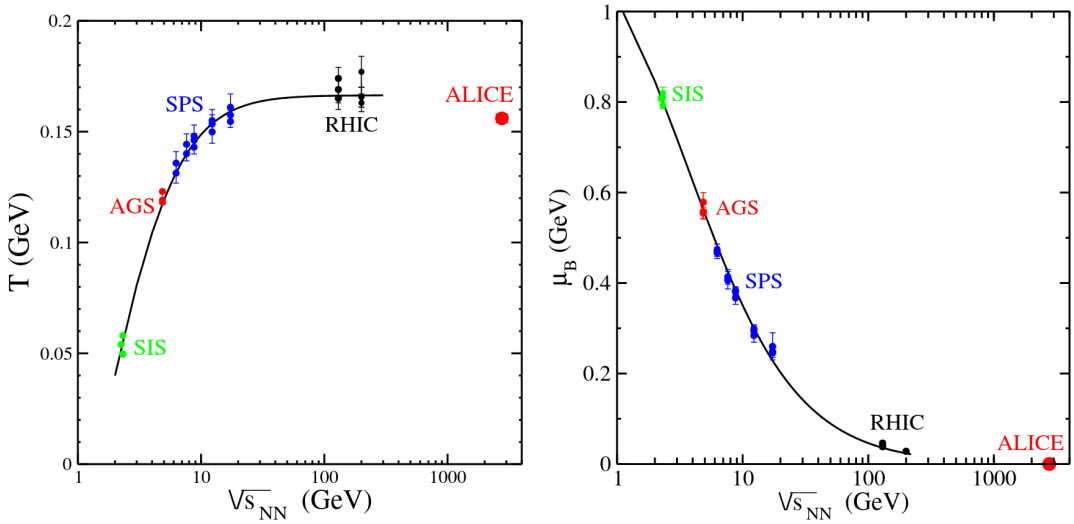


**Figure 2.2:** Temperature $T$ and baryon chemical potential $\mu_B$ as a function of the beam energy. The energy reach of various heavy-ion experiments is shown. Figures taken from Ref. [73].

## 2.2 Heavy-ion accelerators

The study of HIC is a vivid field in rapid expansion. It relies on the ability to perform a large variety of collision configurations over a vast range of energies. This motivates the current existence, building and planification of several experiments fully or partially dedicated to HIC. The main facilities currently running or planned for the near future are:

- the Super Proton Synchrotron (SPS) and the Large Hadron Collider (LHC) [77] at the European Organisation for Nuclear Research (CERN) in Geneva, Switzerland,
- the Relativistic Heavy Ion Collider (RHIC) [78] at Brookhaven National Laboratory (BNL) in Upton, New York,
- the Nuclotron-based Ion Collider fAcility (NICA) [79] at the Joint Institute for Nuclear Research (JINR) in Dubna, Russia,
- the Facility for Antiproton and Ion Research (FAIR) [80] at the GSI Helmholtz Centre for Heavy Ion Research in Darmstadt, Germany,
- the Electron-Ion Collider (EIC) [81] at BNL, as an extension of RHIC.

As depicted in Figure 1.3, these accelerators are designed to run with various energies, collision types (colliders or fixed targets) and chemical species, enabling the exploration of a large region of the phase diagram. The SPS was the first facility to observe signals in favour of the QGP formation in HIC collisions, such as the $J/\psi$ anomalous suppression [82]. It provides now beams for the NA61/SHINE experiment [83] and serves as injector for the LHC (see Section 4.1). An extension of its heavy-ion physics program has been recently proposed in Ref. [84]. RHIC and the LHC aim at exploring the low-$\mu_B$, high-$T$ region. FAIR and NICA assess the line of first order

phase transition, the former aiming at the critical point, the latter being designed for reaching the largest $\mu_B$ accessible in a laboratory. With its peculiar e–A collision system, the EIC will provide precise measurements of the internal structure of nuclei. The key characteristics of the accelerators are summarised in Table 2.1. As the measurements presented in this thesis were performed using LHC data, the accelerator will be presented in more details in Chapter 4.

| | SPS | RHIC | LHC | NICA | FAIR (SIS100) | EIC |
|---|---|---|---|---|---|---|
| Starting year | 1976 | 2000 | 2009 | 2022 | 2025 | 2025 |
| Ions | O, S, In, Pb | Al, Au, Cu, Zr, Ru, U | Pb, Xe | up to Au | up to U | up to U |
| $E_{\text{max}}$ per nucleon | 177 GeV | 100 GeV | 2.76 TeV | 4.5 GeV | 11 GeV | 100 GeV |

**Table 2.1:** Starting year, accelerated ions and maximum energy $E_{\text{max}}$ per nucleon for the five main present and future heavy-ion accelerators. The energy per nucleon correspond to the maximal energy attained or foreseen for the heavy-ion beams. The information for FAIR are given for SIS100, the accelerator of the complex dedicated to heavy ions.

## 2.3 The Glauber model

When studying HIC, pp collisions come as a natural reference, being the simplest hadronic collision system. In order to draw the comparison, one needs to know precisely the geometry of the collision, as to know the overlap area between the two nuclei, from which is derived the amount of nucleons participating in the collision. Such information is of particular interest when performing measurements as a function of the event multiplicity, and provide information on the temperature reached during the collision, a key point for QGP studies. In experiments, the Glauber modelling [85] of HIC has come to be the standard way to calculate geometrical quantities on the collision, typically expressed as the impact parameter $b$, the number of participating nucleons $N_{\text{part}}$ or the number of binary nucleon-nucleon collisions $N_{\text{coll}}$. At sufficiently high energies one reaches the optical limit [86], in which nucleons have high momenta such that they will be undeflected as the nuclei pass through each other (i.e. they are transparent to each other). This is the so-called ultra-relativistic regime, in which the densities reached around the collision point are low. Besides calculations in the optical limit, one can combine the Glauber model with Monte Carlo techniques as an efficient framework through the use of more realistic particle production codes (see Refs. [87, 88] for early examples).

Glauber calculations start from a parametrisation of the nucleon density, for which a Fermi distribution (also known as the Wood-Saxon nucleon density) is generally used:

$$\rho(r) = \rho_0 \frac{1 + w(r/R)^2}{1 + \exp\left(\frac{r-R}{a}\right)}, \tag{2.3}$$

where $\rho_0$ is the nucleon density at the centre of the nucleus ($\rho_0 = \rho(r = 0)$), and $R$ the nucleus radius. $a$ is the skin thickness of the nucleus, denoting how quickly the nuclear density falls off

near the edges. The additional parameter $w$ is needed to describe deviations from a spherical shape ($w = 0$ for Pb, in which case a 2-parameter Fermi is sufficient). The collisions are assumed to be inelastic, with a number of charged particles produced to be the same on average for each nucleon-nucleon collision. As the cross section involves soft processes (processes of low momentum transfer), it is not possible to calculate it in pQCD. The measured inelastic nucleon-nucleon cross section $\sigma_{\mathrm{NN}}^{\mathrm{inel}}$ is then used as an input, providing the only non-trivial dependence of the Glauber calculation to the beam energy. Typical values for $\sigma_{\mathrm{NN}}^{\mathrm{inel}}$ used by the ALICE Collaboration at the LHC energies are [89]:

$$\sigma_{\mathrm{NN}}^{\mathrm{inel}} = \begin{cases} 61.8 \pm 0.9 \text{ mb}, & \sqrt{s_{\mathrm{NN}}} = 2.76 \text{ TeV}, \\ 67.6 \pm 0.6 \text{ mb}, & \sqrt{s_{\mathrm{NN}}} = 5.02 \text{ TeV}, \\ 64.8 \pm 0.5 \text{ mb}, & \sqrt{s_{\mathrm{NN}}} = 5.44 \text{ TeV}, \\ 72.5 \pm 0.5 \text{ mb}, & \sqrt{s_{\mathrm{NN}}} = 8.16 \text{ TeV}. \end{cases}$$

The collision geometry foreseen by the Glauber model in the optical limit is depicted in Figure 2.3.

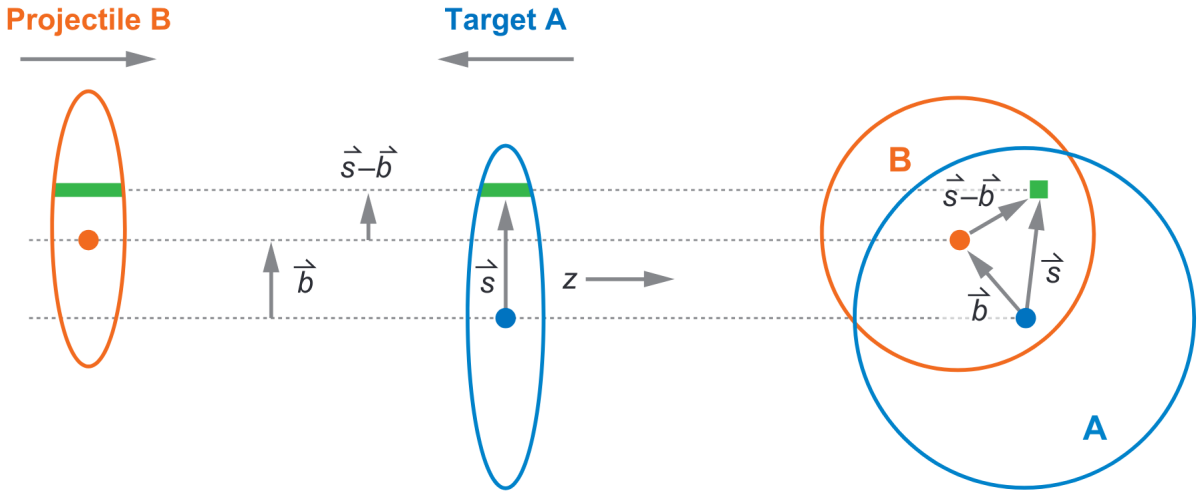


**Figure 2.3:** Schematic representation of the optical-limit Glauber geometry in the longitudinal (left) and transverse (right) views. Figure taken from Ref. [85].

In Figure 2.3, two heavy ions, denoted as target A and projectile B[1], are shown colliding at relativistic velocities at an impact parameter $\vec{b}$. One can consider two flux tubes located at a displacement $\vec{s}$ with respect to the centre of the target nucleus, and hence at a distance $\vec{s}-\vec{b}$ from the centre of the projectile. During the collision, these tubes overlap. The probability, per unit of transverse area, for a given nucleon to be located in the target flux tube is:

$$T_{\mathrm{A}}(\vec{s}) = \int \rho_{\mathrm{A}}(\vec{s}, z_{\mathrm{A}}) \mathrm{d}z_{\mathrm{A}}, \tag{2.4}$$

[1] At colliders, the choice of the nucleus considered as the target or the projectile is of course purely a matter of convenience or convention.

where $\rho_{\mathrm{A}}(\vec{s}, z_{\mathrm{A}})$ is the probability per unit volume, normalised to unity, of finding the nucleon at the location $(\vec{s}, z_{\mathrm{A}})$. Similarly, the corresponding equation for the projectile follows:

$$T_{\mathrm{B}}(\vec{s}) = \int \rho_{\mathrm{B}}(\vec{s}, z_{\mathrm{B}}) \mathrm{d}z_{\mathrm{B}}. \tag{2.5}$$

The information for both $\rho_{\mathrm{A}}(\vec{s}, z_{\mathrm{A}})$ and $\rho_{\mathrm{B}}(\vec{s}, z_{\mathrm{B}})$ is given by the nuclear density profile of Equation 2.3. The joint probability per unit area of nucleons being located in the respective overlapping projectile and target flux tubes of differential area $\mathrm{d}^2 s$ is then given by the product:

$$T_{\mathrm{A}}(\vec{s}) T_{\mathrm{B}}(\vec{s} - \vec{b}) \mathrm{d}^2 s. \tag{2.6}$$

Integrating this product over all the possible values of $s$ leads to define the nuclear thickness function, or nuclear overlap, $T_{\mathrm{AB}}(\vec{b})$:

$$T_{\mathrm{AB}}(\vec{b}) = \int T_{\mathrm{A}}(\vec{s}) T_{\mathrm{B}}(\vec{s} - \vec{b}) \mathrm{d}^2 s, \tag{2.7}$$

which has the unit of inverse area. The thickness function can be interpreted as the effective overlap area for which a specific nucleon in nucleus A can interact with a given nucleon in nucleus B. The probability $P_{\mathrm{NN}}$ for such a nucleon-nucleon to occur is then:

$$P_{\mathrm{NN}}(\vec{b}) = T_{\mathrm{AB}}(\vec{b}) \sigma_{\mathrm{NN}}^{\mathrm{inel}}, \tag{2.8}$$

where $\sigma_{\mathrm{NN}}^{\mathrm{inel}}$ is the inelastic nucleon-nucleon cross section. As elastic processes lead to very small energy loss, they are not considered in the Glauber-model calculation. From the probability of a given nucleon-nucleon interaction to take place, one derives the probability of having $n$ such interactions between the nucleus A (with $A$ nucleons) and nucleus B (with $B$ nucleons) by means of a binomial distribution:

$$P(n, \vec{b}) = \binom{AB}{n} \left[ T_{\mathrm{AB}}(\vec{b}) \sigma_{\mathrm{NN}}^{\mathrm{inel}} \right]^n \left[ 1 - T_{\mathrm{AB}}(\vec{b}) \sigma_{\mathrm{NN}}^{\mathrm{inel}} \right]^{AB-n}, \tag{2.9}$$

where the first term between brackets is the probability of having exactly $n$ collisions, the second one the probability of exactly $AB - n$ collisions to miss, and one has the binomial coefficient

$$\binom{AB}{n} = \frac{(AB)!}{n!(AB-n)!} \tag{2.10}$$

describing the number of combinations yielding $n$ collisions out of $AB$ possible nucleon-nucleon interactions.

From this probability distribution, one can derive useful reaction quantities, starting with the total probability of an interaction between A and B:

$$\frac{\mathrm{d}^2 \sigma_{\mathrm{AB}}^{\mathrm{inel}}}{\mathrm{d}b^2} = \sum_{i=1}^{AB} P(n, \vec{b}) = 1 - \left[ 1 - T_{\mathrm{AB}}(\vec{b}) \sigma_{\mathrm{NN}}^{\mathrm{inel}} \right]^{AB}. \tag{2.11}$$

In the case where the nuclei are not polarised, the vectorial impact parameter can be replaced by a scalar distance, and the cross section reads:

$$\sigma_{\mathrm{AB}}^{\mathrm{inel}} = \int_0^\infty 2\pi b \mathrm{d}b \left\{ 1 - \left[ 1 - T_{\mathrm{AB}}(b)\sigma_{\mathrm{NN}}^{\mathrm{inel}} \right]^{AB} \right\}. \tag{2.12}$$

The total number of nucleon-nucleon collisions is then:

$$N_{\mathrm{coll}}(b) = \sum_{i=1}^{AB} nP(n,b) = (AB)T_{\mathrm{AB}}(b)\sigma_{\mathrm{NN}}^{\mathrm{inel}}, \tag{2.13}$$

using the result for the mean of a binomial distribution.

The number of nucleons in the target and projectile nuclei that interact is called the number of participants $N_{\mathrm{part}}$, also known as the number of wounded nucleons. At impact parameter $b$ it is given by:

$$N_{\mathrm{part}}(\vec{b}) = A \int T_{\mathrm{A}}(\vec{s}) \left\{ 1 - \left[ 1 - T_{\mathrm{B}}(\vec{s} - \vec{b})\sigma_{\mathrm{NN}}^{\mathrm{inel}} \right]^{B} \right\} \mathrm{d}^2 s + \tag{2.14}$$

$$B \int T_{\mathrm{B}}(\vec{s} - \vec{b}) \left\{ 1 - \left[ 1 - T_{\mathrm{A}}(\vec{s})\sigma_{\mathrm{NN}}^{\mathrm{inel}} \right]^{A} \right\} \mathrm{d}^2 s \tag{2.15}$$

where it can be noted that the integral over the bracketed terms gives the respective inelastic cross sections for nucleon-nucleon collisions:

$$\sigma_{\mathrm{A(B)}}^{\mathrm{inel}} = \int \mathrm{d}^2 s \left\{ 1 - \left[ 1 - T_{\mathrm{A(B)}}(\vec{s})\sigma_{\mathrm{NN}}^{\mathrm{inel}} \right]^{A(B)} \right\}. \tag{2.16}$$

The Monte Carlo approach of Glauber modelling, so-called Glauber Monte Carlo (Glauber-MC) provides an efficient and simple way to calculate geometry-related quantities such as $\langle N_{\mathrm{part}} \rangle$ and $\langle N_{\mathrm{coll}} \rangle$, the average numbers of participants and nucleon-nucleon binary collisions, respectively. Moreover, it enables the possibility to simulate experimentally observable quantities such as the charged-particle multiplicity, which allows for the use of similar analysis methods (e.g. centrality cuts) to that for real data. In the Glauber-MC procedure, the two colliding nuclei are numerically assembled by distributing $A$ nucleons for nucleus A and $B$ nucleons for nucleus B in a three-dimensional coordinate system, according to their respective nuclear density profiles. A random impact parameter $b$ is then drawn as to parametrise the centrality of the collision. The AB collision is then treated as a sequence of independent nucleon-nucleon collisions by having them travelling along straight-line trajectories. An example of collision simulated with the Glauber-MC method is shown in Figure 2.4. By simulating many nucleus-nucleus collisions, one can build a distribution similar to that of data taking, from which the geometrical quantities can be derived.

In the optical limit approach, it is assumed that the scattering amplitude can be described by an eikonal approach, where the incoming nucleons see the target as a smooth density. It captures many features of the collision process, but does not feel the full physics behind the total cross section, leading to distortions in the $N_{\mathrm{part}}$ and $N_{\mathrm{coll}}$ distributions, while the Glauber-MC approach

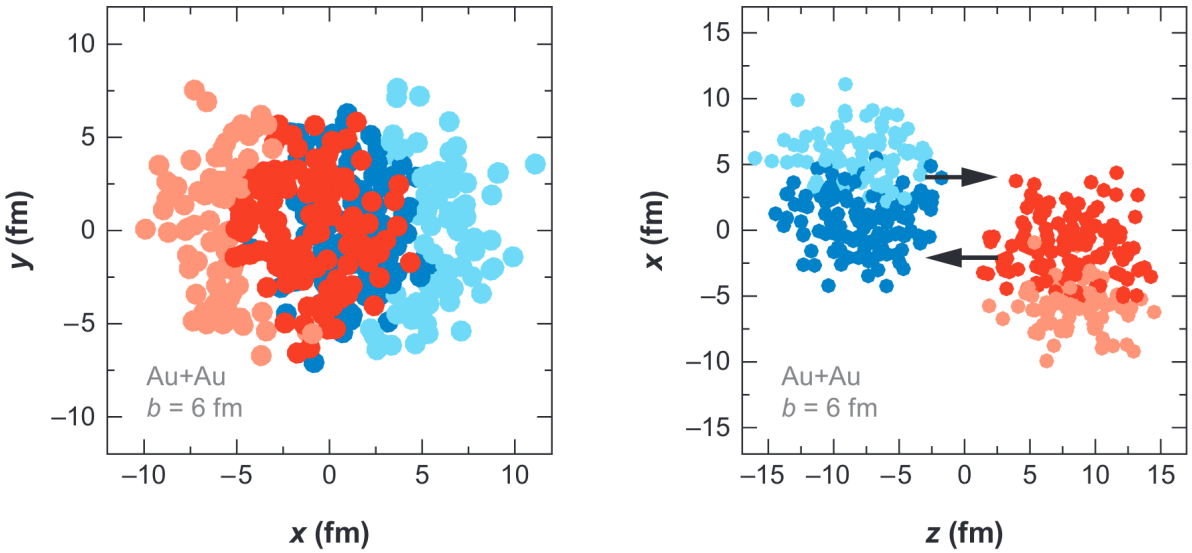


**Figure 2.4:** Glauber-MC event simulated in Au–Au collisions at $\sqrt{s_{\mathrm{NN}}}$ 200 GeV with impact parameter $b = 6$ fm, viewed in the transverse (left) and longitudinal (right) planes. Darker disks represent the participating nucleons. Figure taken from Ref. [85].

does not suffer from these flaws. The full integral to calculate the total cross section is [86]:

$$\begin{aligned}\sigma_{\mathrm{AB}} = \int \mathrm{d}^2 b \int \mathrm{d}^2 s_1^{\mathrm{A}} ... \mathrm{d}^2 s_A^{\mathrm{A}} \mathrm{d}^2 s_1^{\mathrm{B}} ... \mathrm{d}^2 s_B^{\mathrm{B}} \\ \times T_{\mathrm{A}}(\vec{s}_1^{\,\mathrm{A}}) ... T_{\mathrm{A}}(\vec{s}_A^{\,\mathrm{A}}) T_{\mathrm{B}}(\vec{s}_1^{\,\mathrm{B}}) ... T_{\mathrm{B}}(\vec{s}_B^{\,\mathrm{B}}) \\ \times \left\{ 1 - \prod_{j=1}^{B} \prod_{i=1}^{A} \left[ 1 - \hat{\sigma}(\vec{b} - \vec{s}_i^{\,\mathrm{A}} + \vec{s}_j^{\,\mathrm{B}}) \right] \right\},\end{aligned} \tag{2.17}$$

to be compared with the formula obtained in the optical limit of Equation 2.12. Many terms are missing in the optical limit formula, which are the terms describing local density fluctuations event-by-event. Despite this difference, the two approaches are in very good agreement when it comes to evaluate simple geometrical quantities such as $N_{\mathrm{part}}$ and $N_{\mathrm{coll}}$ as a function of the impact parameter.

## 2.4 Small systems

In the HIC community, small collision systems[2] have long been used to study initial- and final-state effects in the so-called cold nuclear matter (that is, without passing through a phase of QGP), in order to establish a baseline for the interpretation of heavy-ion (A+A) results. Subtracting these

[2]Broadly speaking, small systems designate all collision systems where one does not expect to see the apparition of a QGP phase during the evolution of the system. As it is discussed in this section, recent observations of collectivity-like phenomena in small systems might have rendered this definition obsolete.

cold effects from A+A measurements leads to establish the hot effects, expected to be signatures of the creation and evolution of the QGP, such as jet quenching, quarkonia suppression and regeneration, strangeness enhancement or collective flow. At the starting time of the LHC, only pp and Pb–Pb collisions were firmly scheduled, and operational plans for p–Pb collisions were only preliminary, although strongly advocated for by both theoreticians and the experimental community [90]. Three of the four main LHC experiments (ALICE, ATLAS and CMS), included p+A collisions in their performance studies and have discussed their importance. At that time, a p–Pb program at the LHC was foreseen to satisfy two main interests, by providing benchmarks for Pb–Pb results and offering new scientific opportunities for studies related to e.g. saturation, ultra-peripheral collisions or astrophysics-related processes. As it turned out, the study of small systems by the HIC community revealed one of the most striking discovery of the LHC era, namely the presence of QGP-like behaviour (collective effects) in systems where they were not expected.

### 2.4.1 Small systems as benchmarks for heavy-ions

The usage of small systems as a benchmark for A+A studies has been essential for the interpretation of A+A results at RHIC. A key example is the absence of suppression in the transverse momentum spectrum of the inclusive hadron production [91, 92], which proved the jet quenching hypothesis as the genuine final-state effect at work to explain the observed deficit of high-$p_{\mathrm{T}}$ hadrons in Au–Au collisions [93, 94]. A few years before, at the CERN SPS, data from several p+A systems at different energies were already found to be fundamental for the interpretation of results on the $J/\psi$ suppression in Pb–Pb collisions [82].

Equation 1.72 shows the importance of precisely knowing the PDFs such that models are able to reproduce the data. The proton PDF is well constrained by a wealth of data, and is extracted from global fits performed at LO, NLO and NNLO. In the nuclear case, the precision on the PDF determination suffers from the lack of data available in the perturbative region, and most of these data are covering the range $x > 0.01$, above the kinematical reach of the LHC where the PDF uncertainties then remain sizeable. This situation is illustrated in Figure 2.5 showing the nuclear modification functions $u_{\mathrm{V}}$, $d_{\mathrm{V}}$ and $g$ from the EPPS16 analysis [54], where one can observe the large uncertainty bands at low-$x$ and in the EMC region. One of the central conceptual insight expected from the heavy-ion program at the LHC is the transition from cold nuclear matter to hot partonic matter. For all dynamical model of this evolution, a control over the initially-produced particle density is crucial. This density, however, varies with the uncertainty on the nPDF, whose reduction is a decisive step in addressing one of the central issues in the dynamics of heavy-ion collisions.

The medium properties in HIC is characterised through processes which couple to the medium in a theoretically well-controlled manner, among which we find heavy flavours (HF). The description of the heavy quark (charm and bottom) production is provided by the Fixed-Order Next-to-Leading-Log (FONLL) resummation approach [95, 96]. In the left panel of Figure 2.6, the nuclear modification factor $R_{\mathrm{pPb}}$ (i.e. the ratio of the production in p–Pb collisions to that in pp collisions scaled by the atomic number of Pb) of charm and bottom is shown, with the nuclear modifications

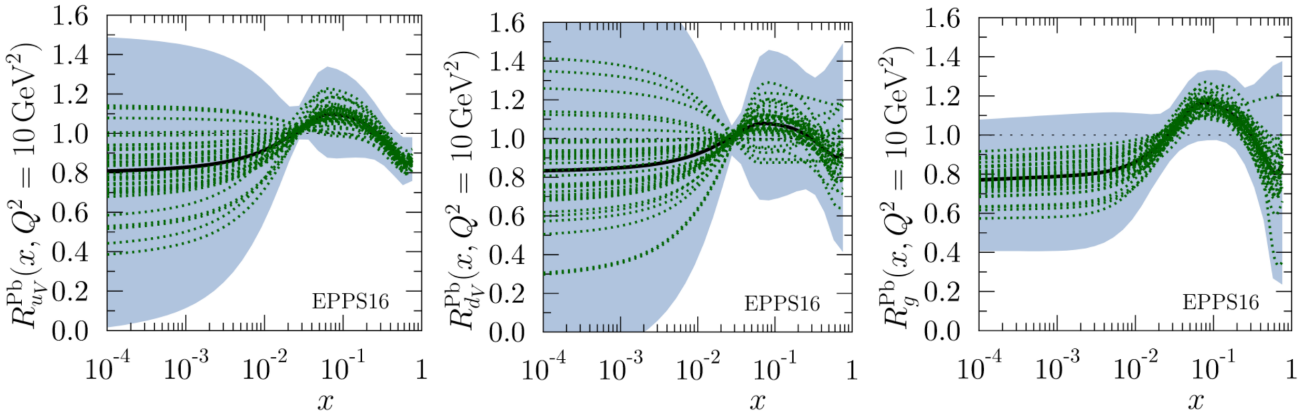


**Figure 2.5:** EPPS16 nuclear modifications for Pb at the parametrisation scale $Q_0^2 = 10$ GeV$^2$, for the $u_{\mathrm{V}}$, $d_{\mathrm{V}}$ and $g$ PDFs. The black curves correspond to the central fits, the dashed green lines to the error sets. The total uncertainties are shown as blue bands. Figures taken from Ref. [54].

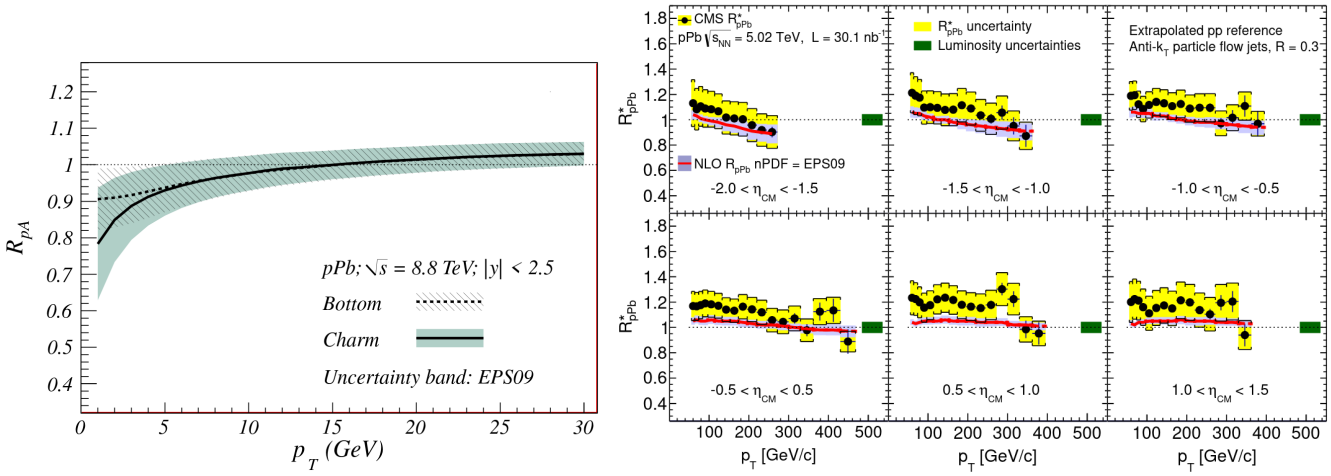


**Figure 2.6: Left**: nuclear modification factors for the charm and bottom quarks in p–Pb collisions at $\sqrt{s_{\mathrm{NN}}} = 8.8$ TeV, and the corresponding uncertainties from the EPS09 parametrisation of the nuclear modifications. Figure taken from Ref. [90]. **Right**: inclusive jet nuclear modification factor $R^*_{\mathrm{pPb}}$ as a function of the jet $p_{\mathrm{T}}$, in p–Pb collisions at $\sqrt{s_{\mathrm{NN}}} = 5.02$ TeV, measured by the CMS collaboration [97]. The measurements are compared with calculations using the EPS09 parametrisation of the nuclear modifications. The $^*$ exponent indicates that the pp reference cross section is not directly measured, but extrapolated (see Ref. [97] for more details).

implemented using the EPS09 [98] parametrisation. The nuclear effects tend to be small, and one should particularly notice that their size is of the same order as the size of the uncertainties of the predictions, showing the importance of increasing our knowledge on the cold nuclear effects for the purpose of understanding the hot ones.

The modification of the spectrum of particles produced at large transverse momentum, the so-called jet quenching effect, is one of the main probes of the properties of the hot and dense matter

formed in HIC. Here as well, it is of utmost importance to disentangle cold and hot effects in order to interpret the results in Pb–Pb collisions. In the right panel of Figure 2.6, the measurement of the $R_{\mathrm{pPb}}$ for jets in p–Pb collisions at $\sqrt{s_{\mathrm{NN}}} = 5.02$ TeV by the CMS collaboration [97] is reported. The ratio shows that there is little sensitivity (although non-zero) of the jet production to cold nuclear effects, indicating that the modifications observed in Pb–Pb can majoritarily be interpreted in terms of parton energy loss in the medium. Reference [99] gives a recent overview of jet quenching measurements in HIC.

Electroweak bosons constitute an other important probe in p–Pb collisions. As they are the main topic of this thesis, their importance will be developed in a dedicated section in Chapter 3.

### 2.4.2 Collectivity in small systems(?)

In the classical picture of hadronic collisions, pp, p+A and A+A collisions are well separated, the first providing a reference, the second probing the cold nuclear effects and the third assessing both hot and cold effects. But recent years have witnessed a surprising development in multiparticle dynamics of high multiplicity pp and p+A collisions. This started with the observation of a ridge-like structure by the CMS experiment in pp collisions [100], and has been confirmed since them. The surprise came from the fact that a few years before, a very similar effect was observed in HIC, in Au+Au collisions at $\sqrt{s_{\mathrm{NN}}} = 200$ GeV at RHIC [101, 102].

Measurements of azimuthal particle correlations in small collision systems have drawn a lot of interest. In HIC, the measurements of flow coefficients, through which is quantified the degree of azimuthal anisotropy, are understood as the propagation, via the hydrodynamic expansion, of the initial spatial anisotropy to the final state particles. Similar observations in small collision systems do not necessarily have the same origin, and one must carry a careful comparison between data and theory in order to understand the experimental observations. The correlations are often parametrised via the particles relative azimuthal angle $\Delta\phi$ in the transverse plane, and their relative longitudinal pseudorapidity $\Delta\eta$. The typical shape of correlations between pairs of charged particle, displayed in the $\Delta\phi - \Delta\eta$ space and for Pb–Pb collisions, is shown in the top panels of Figure 2.7. The distribution shows a clear ridge-like structure in the near side ($\Delta\phi \sim 0$), considered to be the consequence of the collective expansion of the matter during the QGP phase. In the middle left panel of the Figure, the same two-particle correlation function is shown in low-multiplicity p–Pb collisions. Here the ridge is not seen. However, looking at high multiplicity events (middle right panel), the ridge is present, although not as pronounced as in Pb–Pb data. The situation is reproduced when looking at pp collisions, in the bottom panels of Figure 2.7. Here again, when selecting high multiplicity events, the ridge appears. It is interesting to notice that the magnitude of the ridge is highly dependent on the collision system. The full interpretation of this effect is yet to be derived. One has to carefully account for the non-flow background, which can create the same pattern in the data while not being a sign of collective behaviour.

These new results triggered a global analysis, or re-analysis, of the data in small and large systems, as well as a vast theoretical effort towards the interpretation of these observations. A recent review of the experimental and theoretical status of this topic can be found in [106]. The

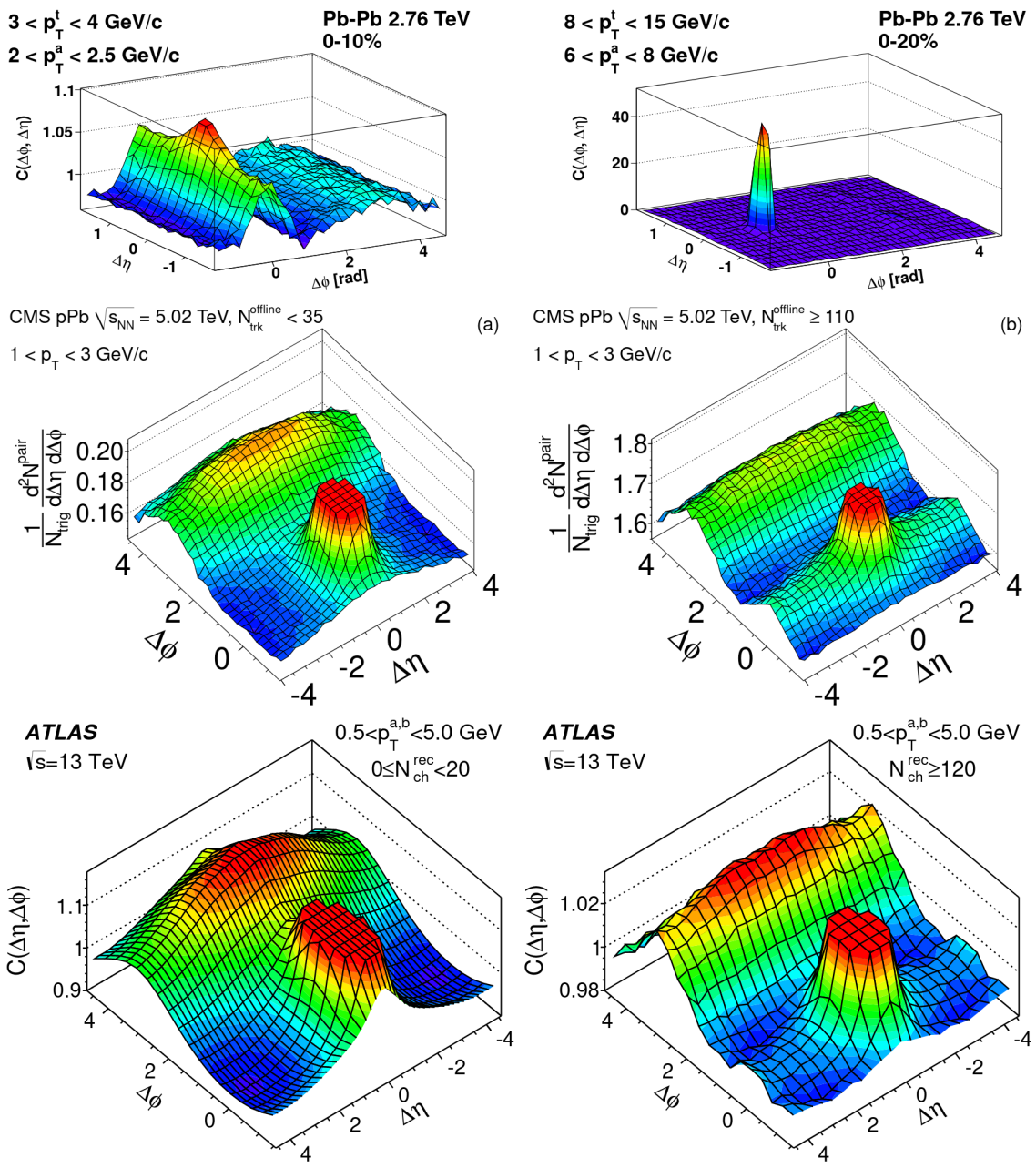


**Figure 2.7: Top**: two-particle correlation function $C(\Delta\phi, \Delta\eta)$ measured by ALICE for central Pb–Pb collisions at $\sqrt{s_{\rm NN}}$ = 2.76 TeV, at low to intermediate transverse momenta (left) and high $p_{\rm T}$ (right). Note the large difference in vertical scale between the panels. Figure taken from Ref. [103]. **Middle**: two-particle correlation function measured by CMS in p–Pb collisions at $\sqrt{s_{\rm NN}}$ = 5.02 TeV for low (left) and high (right) multiplicities. Figure taken from Ref. [104]. **Bottom**: two-particle correlation function measured by ATLAS in pp collisions at $\sqrt{s_{\rm NN}}$ = 13 TeV for low (left) and high (right) multiplicities. Figure taken from Ref. [105].

fact that small systems is an ever-growing field of interest in the heavy-ion community, due to the new insights it can provide for the interpretation of HIC data, is a central motivation of the work presented in this thesis, which aims at studying reference processes in p–Pb collisions.

# Chapter 3

# Weak bosons in heavy-ion collisions

This chapter focuses on the $Z^0$- and $W^{\pm}$- boson production, with an emphasis on p–Pb collisions as a context. The first section provides a quick history of the prediction and discovery of the bosons, leading to their current status within the Standard Model and the knowledge of their properties. Section 3.2 presents the theoretical framework for the description and understanding of the production and decay of weak bosons in hadronic collisions. The chapter ends by a review of the measurements performed at the Large Hadron Collider (LHC) in Section 3.3.

## 3.1 Carriers of the weak force

### 3.1.1 Historical perspective

The history of the $Z^0$ and $W^{\pm}$ bosons can be traced back to 1933, when Enrico Fermi published his landmark theory for beta decay [107], where he applied the principles of quantum mechanics to matter particles, assuming that they can be created and annihilated just like light quanta in atomic transitions. Hideki Yukawa [108] introduced the idea of an intermediate massive boson exchanged between the nucleons that would generate the nucleon interaction. It turned out later that Yukawa's bosons are the Lattes, Occhialini and Powell pions [109], and that Yukawa's intention to describe both the strong interaction and the weak coupling did not meet with success regarding the weak interaction. The form of the weak interaction was established as a special combination of a vector current $V$ and an axial-vector current $A$, namely $V - A$, in interaction with itself, after proposals from R. Feynman and M. Gell-Mann [110], E. Sudarshan and R. Marshak [111], and J. J. Sakurai [112]. Shortly after, Brazilian physicist J. L. Lopes devised in 1958 an equation [113] showing the analogy of the weak nuclear interactions with electromagnetism, and predicted that the weak interaction would feature both charged and neutral currents through the exchange of very massive bosons. A really firm prediction of the masses would be obtained with the emergence of the electroweak unified theory of Glashow [114], Salam and Ward [115], and Weinberg [116]. The formula obtained by Weinberg in 1967 features a parameter $\theta_W$, so-called weak mixing angle, whose value was not known. Weinberg could thus only establish boundaries for the masses: $m_{W^{\pm}} \geq 37$ GeV/$c^2$ and $m_{Z^0} \geq 75$ GeV/$c^2$. In the 15 years separating the prediction of the $W^{\pm}$ and $Z^0$ bosons

from their discovery, this angle was measured by a variety of experiment such that in 1982 the masses were calculated to be:

$$m_{\mathrm{W}^{\pm}} = 82 \pm 2 \text{ GeV}/c^2, \qquad m_{\mathrm{Z}^0} = 92 \pm 2 \text{ GeV}/c^2.$$

The ideal machine to produce the weak bosons in the most convenient experimental conditions is an $e^+e^-$ collider. Indeed, the Large Electron-Positron (LEP) program at CERN would demonstrate that by providing precise measurements of the $\mathrm{W}^{\pm}$ and $\mathrm{Z}^0$ masses. However, the starting of the LEP collider was still in the far future, leading Rubbia, Cline and McIntyre [117] to propose the transformation of an existing high-energy proton accelerator into a proton-antiproton collider as a fast and inexpensive way to achieve collisions above the energy threshold for weak-boson production. The proposal was accepted as an evolution of the CERN super proton synchrotron (SPS) in 1978, and the first $\mathrm{p\overline{p}}$ collisions at an energy of $\sqrt{s_{\mathrm{NN}}} = 540$ GeV were delivered in July 1981.

The production of $\mathrm{W}^{\pm}$ and $\mathrm{Z}^0$ bosons at a $\mathrm{p\overline{p}}$ collider is expected to occur mainly as the results of quark-antiquark annihilation:

$$\mathrm{\overline{d}u} \to \mathrm{W}^+, \qquad \mathrm{d\overline{u}} \to \mathrm{W}^-, \qquad \mathrm{u\overline{u}} \to \mathrm{Z}^0, \qquad \mathrm{d\overline{d}} \to \mathrm{Z}^0.$$

In the parton model, about half of the momentum of a high-energy proton is carried, on average, by the three valence quarks, which then individually carry 1/6 of the proton momentum. Weak boson production thus requires a total centre-of-mass energy equal to about 6 times the mass of the bosons. The $\mathrm{W}^{\pm}$ boson predominantly decay into quark-antiquark pairs, which appear as two hadronic jets, but this detection channel is overwhelmed by two-jet production from hard parton scatterings. It was thus chosen to detect the $\mathrm{W}^{\pm}$ bosons by identifying their leptonic decays. The minimal luminosity is determined by the need to detect $\mathrm{Z}^0 \to e^+e^-$, with a cross section of $\sim 1$ nb at $\sqrt{s} \sim 600$ GeV. Considering the branching fraction of the process, amounting to about 3%, one gets that a luminosity of the order $10^{-29}$ cm$^{-2}$ s$^{-1}$ would yield one event per day. These requirements drove the design of the antiproton source and beam collimation and acceleration at the SPS. Table 3.1 summarises the running conditions of the collider during its nine years of operation time. The collider was shut down at the end of 1990 as it was no longer competitive with the 1.8 TeV proton-antiproton collider at Fermilab which started to run in 1987.

Two experiments, UA1 and UA2[1] were conceived to collect SPS data, both approved in 1978. UA1 is a general-purpose magnetic detector [118, 119], a 6-chamber cylindrical assembly of 5.8 m in length and 2.3 m in diameter, making it the largest imaging drift chamber at that time. Its almost complete solid-angle coverage made it effective in the reconstruction of the undetected neutrino in the $\mathrm{W}^{\pm} \to \mathrm{e}^{\pm}\nu$. The UA2 [120] was on the contrary optimised for the detection of electrons from $\mathrm{W}^{\pm}$ and $\mathrm{Z}^0$ decays, relying on calorimetry of high granularity. By ignoring some of the physics, being for example blind to muons, UA2 was easier to design and only costed a third of UA1, a strong argument towards its approval. The calorimeter had 24 slices of 4 tons each,

[1] UA stands for Underground Area, as the SPS is built in an underground tunnel at an average depth of 100 meters.

| Year | Collision energy (GeV) | Peak luminosity ($cm^{-2}$ $s^{-1}$) | Integrated luminosity ($cm^{-2}$) |
|---|---|---|---|
| 1981 | 546 | $\sim 10^{27}$ | $2 \times 10^{32}$ |
| 1982 | 546 | $5 \times 10^{28}$ | $2.8 \times 10^{34}$ |
| 1983 | 546 | $1.7 \times 10^{29}$ | $1.5 \times 10^{35}$ |
| 1984–1985 | 630 | $3.9 \times 10^{29}$ | $1.0 \times 10^{36}$ |
| 1987–1990 | 630 | $3 \times 10^{30}$ | $1.6 \times 10^{37}$ |

**Table 3.1:** Centre-of-mass energy, instantaneous and integrated luminosity delivered by the CERN proton-antiproton collider from 1981 to 1990.

arranged circularly around the collision point. By focusing on the detection of $W^{\pm}$ and $Z^0$ bosons, UA2 was able to measure their masses with a higher accuracy than UA1. The calorimetry system enabled the measurement of hadron jets.

The signal of $W^{\pm} \to \ell^{\pm}\nu_{\ell}$ is characterised by the presence of a high $p_T$ isolated lepton, a peak in the lepton $p_T$ distribution at around half of the $W^{\pm}$ mass (the Jacobian peak), and a large missing $p_T$ in the event due to the undetected neutrino. The missing transverse momentum vector $\vec{p}_T^{\,\text{miss}}$ is defined as

$$\vec{p}_T^{\,\text{miss}} = -\sum_{\text{cells}} \vec{p}_T, \tag{3.1}$$

where $\vec{p}_T$ is the transverse component of the vector associated with each calorimeter cell, with direction from the event vertex to the cell centre and length equal to the energy deposition in the cell. The sum runs over all cells with a non-zero energy deposition. Assuming a perfect and hermetic detector, it follows from momentum conservation that $\vec{p}_T^{\,\text{miss}}$ correspond to the neutrino transverse momentum.

The left panel of Figure 3.1 shows the $|\vec{p}_T^{\,\text{miss}}|$ distribution measured by the UA1 Collaboration from 1982 data [121]. The component decreasing approximately as $|\vec{p}_T^{\,\text{miss}}|^2$ is due to resolution effects in the calorimeter, from events without significant missing $p_T$. It is followed by a flat component with genuine $|\vec{p}_T^{\,\text{miss}}|$. In the latter, six events contain a high-$p_T$ electron. Further study of these events showed that the $\vec{p}_T^{\,\text{miss}}$ vector is almost back-to-back with the electron $\vec{p}_T$ vector, such as these signals are interpreted as $W^{\pm} \to e^{\pm}\nu_e$ decays. The right panel of Figure 3.1 shows six events containing a high-$p_T$ electron measured by the UA2 Collaboration in the 1982 data. In these events, four are showing a $|\vec{p}_T^{\,\text{miss}}|$ value comparable to the electron $p_T$, a property expected in the leptonic decay of $W^{\pm}$ bosons. These two results were presented on January 20 and 21, 1983, and provided the first experimental observation of the $W^{\pm}$ boson.

Both collaborations also searched for a signal characteristic of the $Z^0$ leptonic decay. As the production of $Z^0$ boson is rarer than that of $W^{\pm}$, it took an supplementary year of data taking. The left panel of Figure 3.2 illustrates the search for the $Z^0 \to e^+e^-$ process in UA1 [123]. The first selection required the presence of two calorimeter clusters consistent with electrons having a transverse energy $E_T > 25$ GeV. 152 events were retained from the 1982-83 data. A further selection required the presence of an isolated track with $p_T > 7$ GeV/$c$ pointing to one of the two clusters. This selection already isolates events around the expected mass of the $Z^0$ boson. Finally,

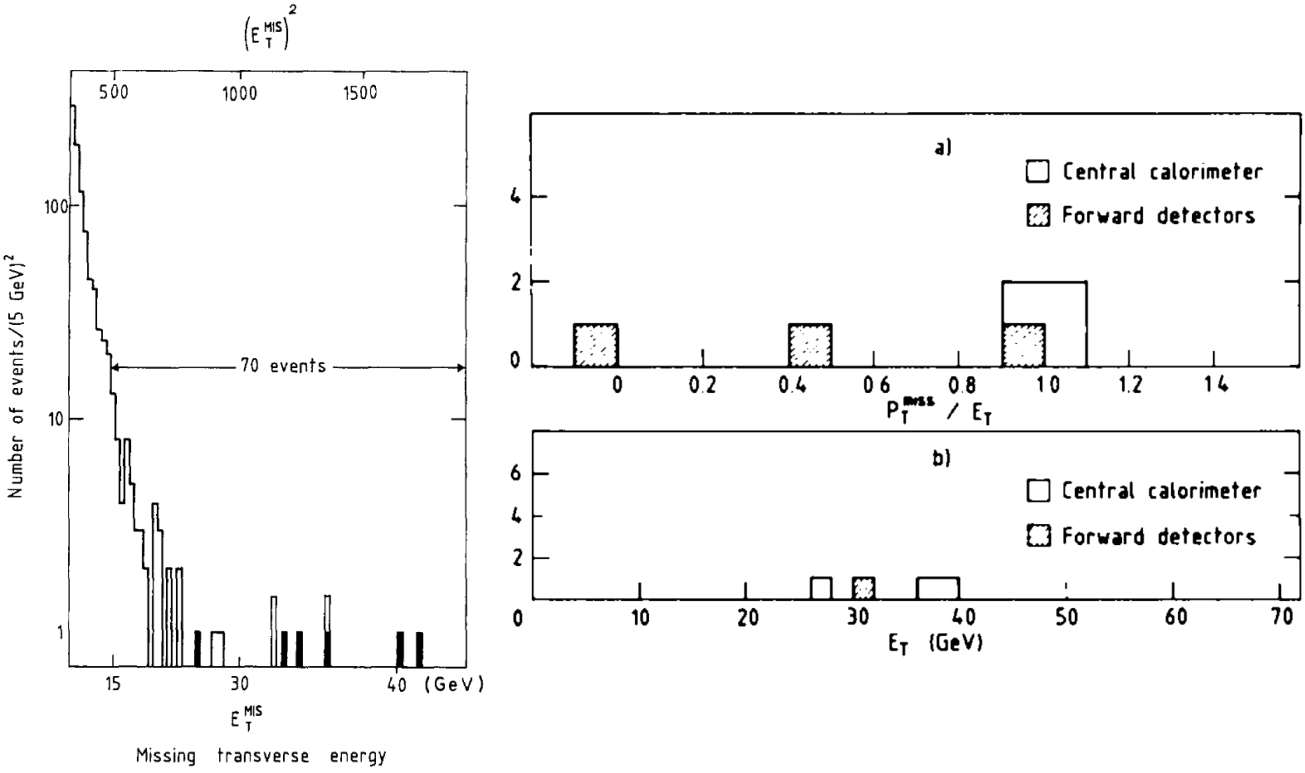


**Figure 3.1: Left**: UA1 distribution of the missing transverse energy for equal bins of $(E_{\mathrm{T}}^{\mathrm{MIS}})^2$. The events highlighted in black contain a high-$p_{\mathrm{T}}$ electron. Figure taken from Ref. [121]. **Right**: (a) ratio of the missing $p_{\mathrm{T}}$ to the electron $p_{\mathrm{T}}$ (called $E_{\mathrm{T}}$ in the publication) for six UA2 events containing an electron with $E_{\mathrm{T}} > 15$ GeV. (b) electron $p_{\mathrm{T}}$ distribution for the four UA2 events with the highest $|\vec{p}_{\mathrm{T}}^{\,\mathrm{miss}}|/E_{\mathrm{T}}$ ratio. Figure taken from Ref. [122].

the selection is refined by extending the previous selection to both clusters, leaving four events. They are consistent with a unique value of the $e^+e^-$ invariant mass, within the detector resolution. As the UA1 detector was able to detect muons, the collaboration found one extra event consistent with the $\mathrm{Z}^0 \to \mu^+\mu^-$ process. From the same collision period, the UA2 collaboration extracted eight events containing two isolated electrons with $E_{\mathrm{T}} > 25$ GeV [124], as displayed in the right panel of Figure 3.2. From these studies, the two collaborations were able to estimate the mass of the $\mathrm{Z}^0$ boson as:

$$m_{\mathrm{Z}^0}^{\mathrm{UA1}} = 95.2 \pm 2.5 \pm 3.0 \text{ GeV}/c^2, \qquad m_{\mathrm{Z}^0}^{\mathrm{UA2}} = 91.9 \pm 1.3 \pm 1.4 \text{ GeV}/c^2,$$

providing the first experimental observation of a signal consistent with the expectations for the $\mathrm{Z}^0$ boson.

By 1985, before the collider shutdown in 1986 for upgrade, the two collaborations had collected a sizeable amount of signal associated to $\mathrm{W}^\pm$ and $\mathrm{Z}^0$ leptonic decays. UA1 had recorded 290 signals for the $\mathrm{W}^\pm$ in the electronic channel and 57 in the muonic channel, as well as 33 (21) events

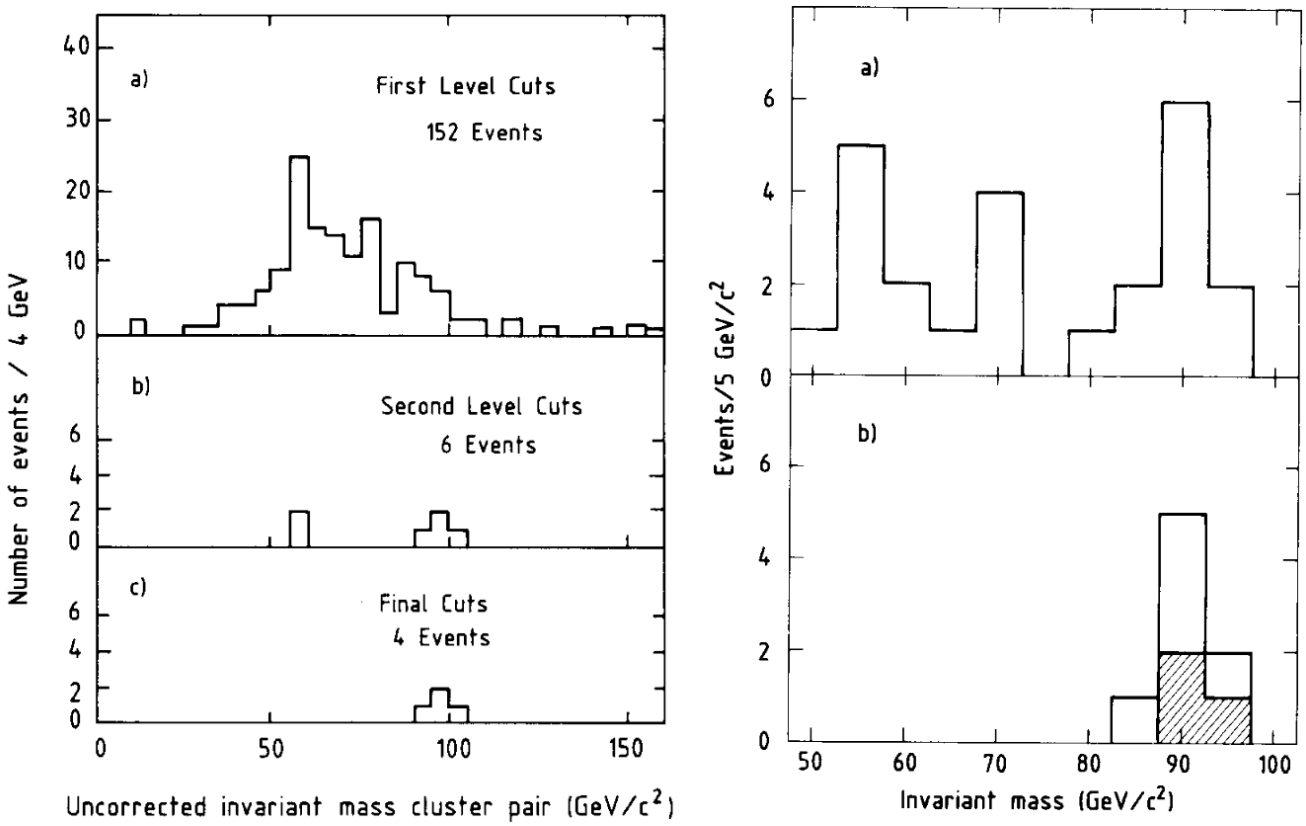


**Figure 3.2: Left**: search for the $Z^0 \to e^+e^-$ decay in UA1. The events are selected by requiring (a) two hits in the calorimeter with transverse energy $E_T > 25$ GeV with $p_T > 7$ GeV/$c$ for one (b) or two (c) of the associated tracks. Figure taken from Ref. [123]. **Right**: search for the $Z^0 \to e^+e^-$ decay in UA2. The top panel shows the invariant mass distribution of pairs of particle reconstructed from hits in the calorimeter with $E_T > 25$ GeV. The bottom panel shows the same distribution after requiring that one (white area) or two tracks (shaded area) are identified as isolated electrons. Figure taken from Ref. [124].

corresponding to $Z^0$ electronic (muonic) decays [125]. In the same years, the UA2 collaboration recorded samples of 251 $W^\pm \to e^\pm\nu$ and 39 $Z^0 \to e^+e^-$ events [126]. This allowed the two collaborations to precise their respective measurements for the masses of the weak bosons:

$$m_{W^\pm}^{UA1} = 82.7 \pm 1.0 \pm 2.7 \text{ GeV}/c^2, \qquad m_{W^\pm}^{UA2} = 80.2 \pm 0.8 \pm 1.3 \text{ GeV}/c^2,$$
$$m_{Z^0}^{UA1} = 93.1 \pm 1.0 \pm 3.1 \text{ GeV}/c^2, \qquad m_{Z^0}^{UA2} = 91.5 \pm 1.2 \pm 1.7 \text{ GeV}/c^2.$$

The experimental confirmation of the existence of the weak bosons was a striking confirmation of crucial aspects of the Standard Model of particle physics. The physics community was at that time already heavily committed to the theory, and the UA1 and UA2 results were highly expected. Nonetheless, they represent an extraordinary experimental triumph, coming from experiments designed, approved and built within a few years, along with the development of important experimental techniques that are still in use forty years later.

### 3.1.2 $W^{\pm}$ and $Z^0$ bosons in the Standard Model

In quantum electrodynamics (QED) [9], the Lagrangian for the photon $A^\mu$ coupled to an electron field $\psi$ reads:

$$\mathcal{L}_{\text{QED}} = -\frac{1}{4}F^{\mu\nu}F_{\mu\nu} + \overline{\psi}\left(i\gamma^\mu D_\mu - m_e\right)\psi, \tag{3.2}$$

where the adopted notations follow that of the QCD Lagrangian of Equation 1.2. This Lagrangian is invariant under independent redefinitions of the phase of the field $\psi$ at each space-time point,

$$\psi'(x) = \exp\left(i\theta(x)\right)\psi(x), \tag{3.3}$$

provided that the gauge field $A^\mu$ transforms as

$$A'_\mu(x) = A_\mu(x) - \frac{1}{e}\partial_\mu\theta(x). \tag{3.4}$$

The Lagrangian thus possesses a local gauge invariance under transformations of the field belonging to the U(1) gauge group. There is a single gauge coupling $e$ corresponding to this group.

The Standard Electroweak Model known as Glashow-Weinberg-Salam (GWS) [114, 115, 116] builds up on QED, extending it to the $\text{SU}(2)\otimes\text{U}(1)$ group. Initially, the Lagrangian of this model contains three massless bosons $W^i$ associated with the SU(2) group, and one massless boson $B$ associated with U(1), yielding the gauge boson Lagrangian:

$$\mathcal{L} = -\frac{1}{4}W^{i\,\mu\nu}W^i_{\mu\nu} - \frac{1}{4}B^{\mu\nu}B_{\mu\nu} \tag{3.5}$$

with the field strength tensors of the U(1) gauge field $B$ and the SU(2) gauge fields $W^i$:

$$W^i_{\mu\nu} = \partial_\mu W^i_\nu - \partial_\nu W^i_\mu - g_W\epsilon^{ijk}W^j_\mu W^k_\nu, \tag{3.6}$$

$$B_{\mu\nu} = \partial_\mu B_\nu - \partial_\nu B_\mu, \tag{3.7}$$

$g_W$ being the SU(2) gauge coupling. Analogously to gluons carrying colour charge in QCD, the $W^i$ vector bosons already have interactions because of the non-abelian nature of the symmetry group SU(2). The coupling of the gauge fields to fermionic matter fields is implemented using the covariant derivative:

$$D^\mu = \delta_{ij}\partial^\mu i g_W\left(T\cdot W^\mu\right)_{ij} + iY\delta_{ij}g'_W B^\mu \tag{3.8}$$

where $g'_W$ is the U(1) gauge coupling. The matrices $T$ are a representation of the SU(2) weak isospin algebra and the U(1) charge $Y$ is called the weak hypercharge. The tensor $\epsilon^{ijk}$ appears because its components are the structure constants of SU(2):

$$\left[T^i, T^j\right] = i\epsilon^{ijk}T^k \qquad \text{with} \qquad \epsilon^{123} = 1. \tag{3.9}$$

One can define $W^\pm_\mu = \left(W^1_\mu \mp iW^2_\mu\right)/\sqrt{2}$ and $T^\pm = T^1 \pm iT^2$ to obtain:

$$W_\mu\cdot T = W^3_\mu T_3 + \frac{1}{\sqrt{2}}W^+_\mu T^+ + \frac{1}{\sqrt{2}}W^-_\mu T^- \tag{3.10}$$

where the matrices $T^{\pm}$ and $T^3$ satisfy

$$\left[T^+, T^-\right] = 2T^3, \tag{3.11}$$

$$\left[T^3, T^{\pm}\right] = \pm T^{\pm}. \tag{3.12}$$

$T^+$ and $T^-$ are thus the weak isospin raising and lowering operators.

The presence of four massless bosons in Equation 3.5 is contradicted by experimental observations, as only one massless vector boson (the photon) is found in nature. The feebleness and short range of the weak interaction indicates that the mediating bosons are massive. It is then necessary to include in the theory a mechanism of spontaneous symmetry breaking that gives explicit mass terms for three of the bosons and retains only one conserved charge, the electric charge. In the Standard Model of the electroweak interaction, the fundamental $\mathrm{SU}(2) \otimes \mathrm{U}(1)$ symmetry is broken by the Higgs mechanism. The first implementation of this mechanism is due to P. W. Anderson in 1962 [127] (published in 1963), applied solely to non-relativistic theory. The relativistic model was developed in 1964 by three different groups[2]: François Englert and Robert Brout [129], Peter W. Higgs [130], and Gerald Guralnik, Carl Hagen and Tom Kibble [131]. A few years later, the theory was proved to be renormalisable even in the presence of massive bosons by Gerard 't Hooft and Martinus Veltman [132]. The LHC era provided a striking confirmation of the Higgs mechanism through the discovery of a particle consistent with the expectations on the Higgs boson by the ATLAS [133] and CMS [134] Collaborations in high-energy pp collisions.

The electric charge arises as a nontrivial linear combination of $Y_W$, the weak hypercharge, and the $T_3$ component of the weak isospin:

$$Q = T_3 + \frac{1}{2} Y_W \tag{3.13}$$

that does not couple to the Higgs boson. Said otherwise: the Higgs and electromagnetic fields have no effect on each other, at the tree level, while any other combination of the hypercharge and weak isospin will interact with the Higgs. As a consequence, one has an apparent separation between the weak force and electromagnetism. The U(1) symmetry group of electromagnetism is then defined by the group generated by this special linear combination. This spontaneous symmetry breaking makes the $W_3$ and $B$ bosons coalesce into two different physical bosons with different masses, corresponding to the neutral weak boson $\mathrm{Z}^0$ and the photon $\gamma$:

$$\begin{pmatrix} \gamma \\ \mathrm{Z}^0 \end{pmatrix} = \begin{pmatrix} \cos\theta_W & \sin\theta_W \\ -\sin\theta_W & \cos\theta_W \end{pmatrix} \begin{pmatrix} B \\ W_3 \end{pmatrix}, \tag{3.14}$$

where $\theta_W$ is the Weinberg or electroweak mixing angle parametrising the rotation of the axes in the ($W_3$, $B$) plane. It is fixed by the relative strength of the coupling constants:

$$\sin^2\theta_W = \frac{g'^2_W}{g^2_W + g'^2_W} \simeq 0.23. \tag{3.15}$$

[2]In 1965, two 20-year old Russian undergraduates, Alexander Migdal and Alexander Polyakov, derived the mechanism independently from the other groups [128]. As their work was not supported by leading scientists of their time, they saw their paper delayed by the editorial office of JTEP until its publication in 1966.

After this rotation the quadratic terms in the vector boson fields become

$$\mathcal{L} = \frac{g_W^2 v^2}{4} W_\mu^+ W^{-\,\mu} + \frac{(g_W^2 + g_W'^2) v^2}{8} Z_\mu Z^\mu \tag{3.16}$$

where $v$ is the Higgs vacuum expectation value. The $\mathrm{W}^\pm$ and $\mathrm{Z}^0$ bosons have therefore acquired a mass term given by:

$$m_{\mathrm{W}^\pm} = \frac{1}{2} v g_W, \qquad m_{\mathrm{Z}^0} = \frac{1}{2} v \sqrt{g_W^2 + g_W'^2} = \frac{m_{\mathrm{W}^\pm}}{\cos\theta_W}. \tag{3.17}$$

Thus, as the Higgs field acquires a non-zero vacuum expectation value, the symmetry of the SU(2) group is spontaneously broken. This does not give rise to Goldstone boson, as it was the case for the QCD symmetry breaking, but leads to the formation of the massive vector bosons $\mathrm{W}^\pm$ and $\mathrm{Z}^0$.

### 3.1.3 Properties of the $\mathrm{W}^\pm$ and $\mathrm{Z}^0$ bosons

The properties of the particles are listed and updated by the Particle Data Group [6] by using the full available data. For the weak bosons, the parameters are determined from a global fit of data coming from the LEP [135] and SLC [136] accelerators, designed in the 1980s to copiously produce $\mathrm{Z}^0$ bosons following their prediction and discovery at SPS. Both these experiments are lepton colliders, enabling the study the boson properties in a very clear environment. The $\mathrm{W}^\pm$ parameters (mass, width, branching fractions) are obtained by combining data from the LEP, Tevatron [137] and LHC [77] experiments.

The procedure for obtaining the $\mathrm{Z}^0$ mass and width follows that of the LEP Electroweak Working Group [138], relying on a global analysis of data through a fit using the $\mathrm{Z}^0$ mass, width, and hadronic cross section, the ratios of hadronic to leptonic partial widths, and the $\mathrm{Z}^0$ pole forward-backward lepton asymmetries. The mass and width come from the corresponding parameters in a Breit-Wigner distribution [139] in its relativistic form, commonly used to model resonances in high-energy physics. It has the probability density function:

$$f(E) = \frac{k}{\left(E^2 - M^2\right)^2 + M^2\Gamma^2}, \tag{3.18}$$

where $M$ and $\Gamma$ are the mass and width of the resonance, respectively, and $E$ is the centre-of-mass energy. $k$ is a constant of proportionality equal to:

$$k = \frac{2\sqrt{2} M \Gamma \gamma}{\pi\sqrt{M^2 + \gamma}} \qquad \text{with} \qquad \gamma = \sqrt{M^2\left(M^2 + \Gamma^2\right)}. \tag{3.19}$$

The Breit-Wigner distribution is also used for the determination of the $\mathrm{W}^\pm$ properties, based on studies from the LEP Electroweak working group [140], the Tevatron Working Group [141, 142] and the ATLAS Collaboration [143]. The world average procedure done by the Particle Data Group is

illustrated in Figure 3.3 for the mass and the width of the $W^{\pm}$ boson. The values labelled LEP2 are obtained by averaging the results obtained by the different collaborations at LEP: ALEPH, DELPHI, L3 and OPAL. The Tevatron values are averages of the CDF and D0 results. One can appreciate the progressive increase of precision of the measurements, as the top points correspond to the running years of LEP, up to 2000, followed by the Tevatron which operated until 2011, and for the mass of the $W^{\pm}$ the additional measurement provided by the ATLAS Collaboration in 2018.

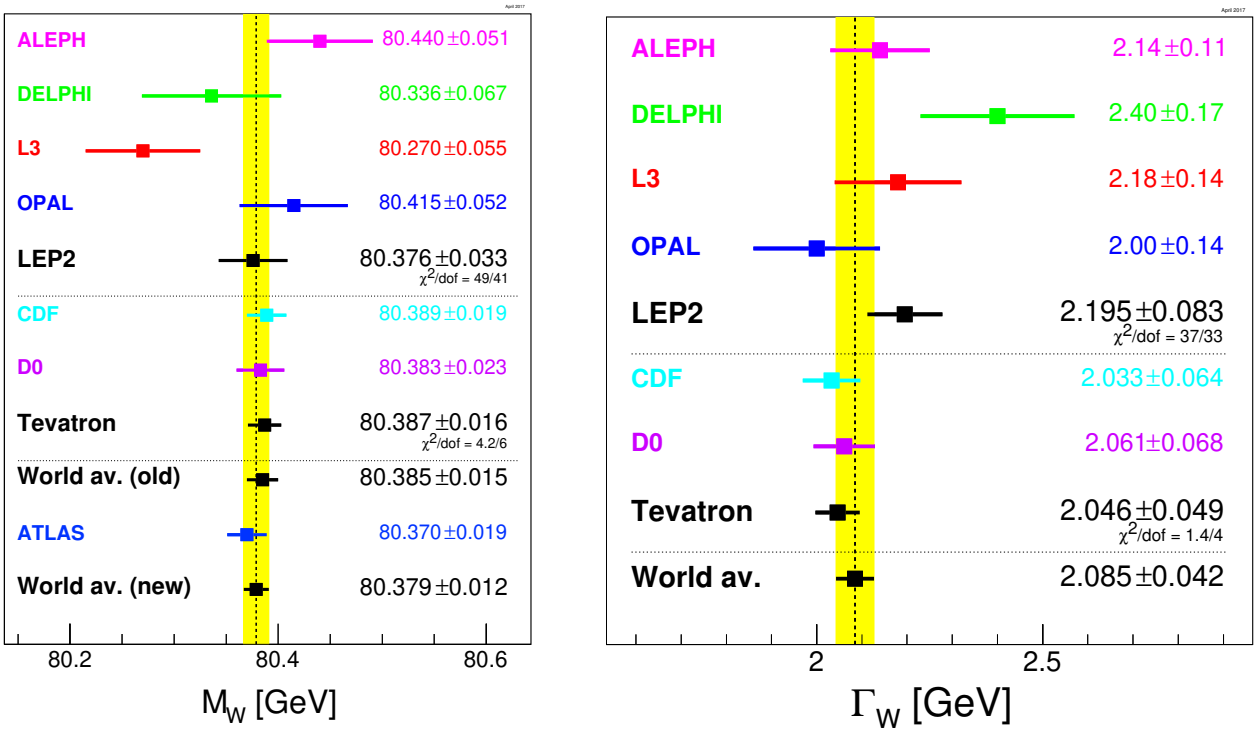


**Figure 3.3:** World averages of the mass (left) and the width (right) of the $W^{\pm}$ bosons from measurements from the LEP, Tevatron and, for the mass, LHC experiments. Figures taken from Ref. [6].

Table 3.2 presents the mass, width, and hadronic and leptonic branching ratios ($BR$) of the $W^{\pm}$ and $Z^0$ bosons. The electroweak sector provides several ways to test the Standard Model and look for signs of new physics. A recent review of electroweak precision tests of the Standard Model can be found in Ref. [144], where an emphasis is put on new developments since the discovery of the Higgs boson.

| Boson | Mass (GeV/$c^2$) | Full width (GeV/$c^2$) | Hadronic $BR$ (%) | Leptonic $BR$ (%) |
|---|---|---|---|---|
| $W^{\pm}$ | 80.379 ± 0.012 | 2.085 ± 0.042 | 67.41 ± 0.27 | 10.86 ± 0.09 |
| $Z^0$ | 91.1876 ± 0.0021 | 2.4952 ± 0.0041 | 69.911 ± 0.056 | 3.3658 ± 0.0023 |

**Table 3.2:** Mass, full width, and branching fractions of the hadronic and leptonic decays of the $W^{\pm}$ and $Z^0$ bosons. Adapted from Ref. [6].

## 3.2 Production and decay

### 3.2.1 The Drell-Yan process

One can consider the factorised expression of Equation 1.72 for the production of a lepton pair through quark-antiquark annihilation, and expand perturbatively the partonic cross section:

$$\sigma_{\mathrm{NN}}^{AB} = \sum_{i,j} \int \mathrm{d}x_1, \mathrm{d}x_2 f_i(x_1, Q^2) f_j(x_2, Q^2) \hat{\sigma}_{q\bar{q}\to\ell\bar{\ell}} \tag{3.20}$$

$$= \sum_{i,j} \int \mathrm{d}x_1, \mathrm{d}x_2 f_i(x_1, Q^2) f_j(x_2, Q^2) \times \left[ \hat{\sigma}_{\mathrm{LO}} + \frac{\alpha_s(Q^2)}{2\pi} \hat{\sigma}_{\mathrm{NLO}} + \left( \frac{\alpha_s(Q^2)}{2\pi} \right)^2 \hat{\sigma}_{\mathrm{NNLO}} + ... \right]. \tag{3.21}$$

The expression is general, and applies to a wide variety of hard-scattering processes, such as jets and heavy flavour production. Among these processes is the so-called Drell-Yan process, named after the suggestion of Sidney Drell and Tung-Mow Yan in 1970 [145] as a mean to describe the production of a lepton-antilepton pair in hadronic collisions. Experimentally, the process was first observed in proton-uranium collisions at the Alternating Gradient Synchrotron (AGS) [146]. Initially formulated for the creation of a lepton pair by the exchange of an off-shell photon, the Drell-Yan mechanism can be extended to the production of the $Z^0$ and $W^{\pm}$ bosons, thus covering the subprocesses:

$$\begin{array}{ccccc} q\bar{q} & \to & \gamma^* & \to & \ell^+\ell^- \\ q\bar{q} & \to & \mathrm{Z}^0 & \to & \ell^+\ell^- \\ q\bar{q}' & \to & \mathrm{W}^{\pm} & \to & \ell^{\pm}\nu \end{array}$$

The Drell-Yan process contributes to the PDF determination in the same way as the data from deep inelastic scatterings (DIS). Indeed, the Feynman diagram of the Drell-Yan process is obtained by simply rotating the diagram of DIS by 90°:

DIS: 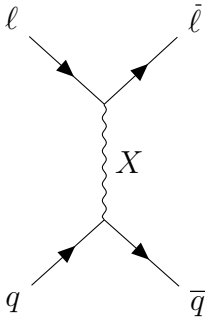


⇒ Drell-Yan: 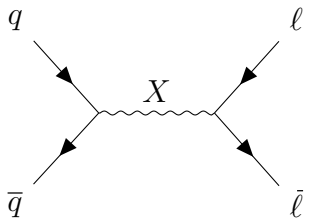

with $X = \gamma^*, \mathrm{Z}^0, \mathrm{W}^\pm$. A time-like electromagnetic boson is produced in the $s$-channel in the Drell-Yan process while a space-like boson is produced in the $t$-channel in DIS. The lowest-order partonic cross section for $q\overline{q}$ annihilation creating a lepton pair via the exchange of an off-shell photon is given by:

$$\hat{\sigma}\left(q(p_1)\overline{q}(p_2) \to \ell\bar{\ell}\right) = \frac{4\pi\alpha^2}{3\hat{s}}\frac{1}{N}Q_q^2, \tag{3.22}$$

where $\hat{s} = (p_1 + p_2)^2$. In general, the incoming quark and antiquark have a spectrum of collision energies $\sqrt{\hat{s}}$, it is then more convenient to consider the differential lepton pair invariant mass distribution. The subprocess cross section for producing a lepton pair of mass $M$ then reads:

$$\frac{\mathrm{d}\hat{\sigma}}{\mathrm{d}M^2} = \frac{4\pi\alpha^2}{3M^2}\frac{1}{N}Q_q^2\delta\left(\hat{s} - M^2\right). \tag{3.23}$$

In the centre-of-mass frame of the two hadrons, the 4-momenta of the incoming partons are:

$$p_1 = \frac{\sqrt{s}}{2}\left(x_1, 0, 0, x_1\right), \tag{3.24}$$

$$p_2 = \frac{\sqrt{s}}{2}\left(x_2, 0, 0, -x_2\right). \tag{3.25}$$

One can relate the $q\overline{q}$ collision energy $\hat{s}$ to the overall hadron-hadron collision energy by:

$$\hat{s} = (p_1 + p_2)^2 = x_1 x_2 s. \tag{3.26}$$

Substituting Equation 3.23 into Equation 3.21 gives the parton-model cross section for the process:

$$\frac{\mathrm{d}\sigma}{\mathrm{d}M^2} = \int_0^1 \mathrm{d}x_1\mathrm{d}x_2 \sum_q \left[f_q(x_1)f_{\overline{q}}(x_2) + f_{\overline{q}}(x_1)f_q(x_2)\right] \times \frac{\mathrm{d}\hat{\sigma}}{\mathrm{d}M^2}(q\overline{q} \to \ell\bar{\ell}) \tag{3.27}$$

$$= \frac{4\pi\alpha^2}{3M^2}\frac{1}{N}\int_0^1 \mathrm{d}x_1\mathrm{d}x_2\delta\left(x_1x_2s - M^2\right) \times \left\{\sum_q Q_q^2\left[f_q(x_1)f_{\overline{q}}(x_2) + f_{\overline{q}}(x_1)f_q(x_2)\right]\right\}. \tag{3.28}$$

In the parton model, the distribution functions $f_i(x)$ are independent of $M^2$, the lepton pair cross section multiplied by $M^4$ thus exhibits a scaling in the variable $\tau = M^2/s$:

$$M^4\frac{\mathrm{d}\sigma}{\mathrm{d}M^2} = \frac{4\pi\alpha^2}{3N}\tau\int_0^1 \mathrm{d}x_1\mathrm{d}x_2\delta\left(x_1x_2 - \tau\right) \times \left\{\sum_q Q_q^2\left[f_q(x_1)f_{\overline{q}}(x_2) + f_{\overline{q}}(x_1)f_q(x_2)\right]\right\} \tag{3.29}$$

$$= \frac{4\pi\alpha^2}{3N}\tau\mathcal{F}(\tau), \tag{3.30}$$

which is exactly analogous to the approximate Bjorken scaling of the DIS structure functions $F_i(x, Q^2)$. From the 4-momenta of the incoming parton, one derives the rapidity of the lepton pair in terms of the parton momentum fractions:

$$y = \frac{1}{2}\ln\left(\frac{x_1}{x_2}\right) \tag{3.31}$$

and thus:

$$x_1 = \sqrt{\tau}\exp(y), \qquad x_2 = \sqrt{\tau}\exp(-y). \tag{3.32}$$

The double-differential cross section therefore reads:

$$\frac{\mathrm{d}^2\sigma}{\mathrm{d}M^2\mathrm{d}y} = \frac{4\pi\alpha^2}{3M^2Ns}\left\{\sum_q Q_q^2\left[f_q(x_1)f_{\overline{q}}(x_2) + f_{\overline{q}}(x_1)f_q(x_2)\right]\right\}. \tag{3.33}$$

By measuring the distribution as a function of the mass and rapidity of the dilepton, one can thus directly measure the quark and antiquark distribution functions in the colliding hadrons. Figure 3.4 shows the flavour decomposition of the $\mathrm{Z}^0$ and $\mathrm{W}^\pm$ total cross sections in pp collisions [147] from the MRST PDF set [148]. In the evolution of the decomposition as a function of the collision energy, one can appreciate the relevance of increasing the energy for probing the inner structure of the nucleon. The contribution from *s*-*c* scatterings reaches 23% (17%) of the total $\mathrm{W}^-$ ($\mathrm{W}^+$) cross section at the LHC nominal energy of 14 TeV. This significant dependence on the strange and charm contributions makes the weak bosons valuable probes of the sea quark distributions.

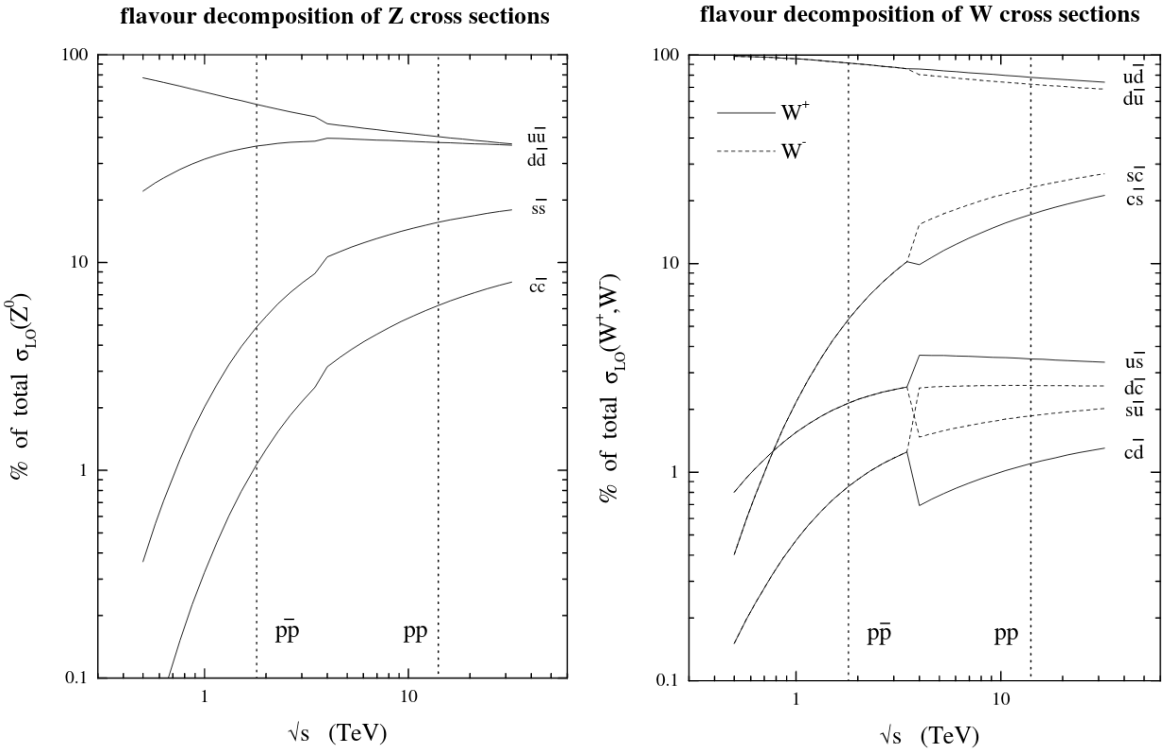


**Figure 3.4: Left**: parton flavour decomposition of the $\mathrm{Z}^0$ total cross section as a function of the collision energy. Individual contributions are shown as percentages of the total cross section. The vertical dashed lines, from left to right, correspond to the $\mathrm{p\overline{p}}$ collisions at $\sqrt{s} = 1.8$ TeV performed at Tevatron and pp collisions at $\sqrt{s} = 14$ TeV, the nominal collision energy at the LHC. **Right**: same as left, for $\mathrm{W}^+$ (solid lines) and $\mathrm{W}^-$ (dashed lines). In $\mathrm{p\overline{p}}$ collisions the decomposition is the same for $\mathrm{W}^+$ and $\mathrm{W}^-$. Figures taken from Ref. [147].

### 3.2.2 Higher order corrections

The usage of pQCD requires the evaluation of higher order corrections in order to determine at which order the contributions start to be negligible, such that the perturbative expansion can be truncated. Various studies were produced following the planification of the LHC, for the evaluation of NLO [149] and NNLO [150] corrections on the production of weak bosons. Figure 3.5 shows the $Z^0$ and $W^{\pm}$ cross sections as a function of rapidity, evaluated for various orders of the pertubative expansion [150], at the foreseen LHC nominal energy of $\sqrt{s} = 14$ TeV.

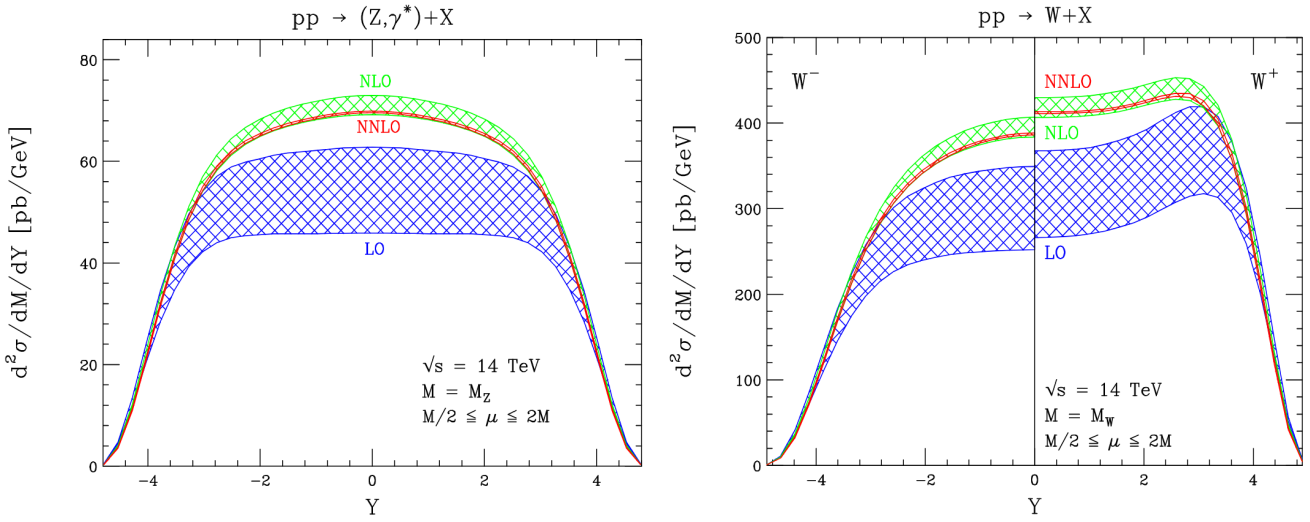


**Figure 3.5:** Rapidity distribution of the $Z^0$ (left) and $W^{\pm}$ (right) cross sections at LO, NLO and NNLO in pp collisions at the LHC nominal energy $\sqrt{s} = 14$ TeV with the MRST PDF set [151]. Since the production is symmetric in $y$, only half of the range is shown for $W^-$ and $W^+$. The uncertainty bands are obtained by varying the factorisation and renormalisation scales in the interval $m_{Z^0,W^{\pm}}/2 \leq \mu_{R,F} \leq 2m_{Z^0,W^{\pm}}$. Figures taken from Ref. [150].

For the $Z^0$ boson (left panel of Figure 3.5), the NLO corrections significantly increase the LO predictions by 15% at large rapidities up to 30% at midrapidity. One can notice as well a modification of the shape of the NLO distribution, which is more peaked at $y = 0$. Adding the NNLO corrections yields a very different conclusion, as the production is slightly decreased by only 1–2% compared to NLO, with which it is in agreement within uncertainties. This indicates that at NNLO, the predictions are already starting to converge and will be stable against higher-order QCD corrections. The associated uncertainty shows very little dependence on the factorisation and renormalisation scales, allowing one to use the $Z^0$ boson as a probe of the parton distributions and an efficient observable for discriminating among the various available PDF sets.

The same conclusion is derived from the study of the $W^+$ and $W^-$ bosons (right panel of Figure 3.5). Here as well the addition of NLO corrections yields an enhancement of the production, especially at midrapidity, while NNLO corrections bring rather small modifications to the distribution. Adding higher-order contributions drastically reduces the uncertainties, which ranges from about 0.6% at midrapidity to 3% for large rapidities. The production shows large differences for the

two charges of the boson, such that comparative studies can be foreseen to bring supplementary information and constraints on PDF models.

### 3.2.3 Muonic decay channel

As indicated in Table 3.2, the $Z^0$ and $W^{\pm}$ bosons mainly decay hadronically. However, this decay mode suffers from the large background created by jets, such that the leptonic decay provides a much cleaner environment. The dominant processes for the creation of weak bosons decaying into muons are then:

$$u\overline{u}(d\overline{d}) \to Z^0 \to \mu^+\mu^-, \qquad u\overline{d} \to W^+ \to \mu^+\nu_\mu, \qquad d\overline{u} \to W^- \to \mu^-\overline{\nu}_\mu,$$

with significant contributions from $s$-$c$ scatterings and higher order corrections including gluons and photons initial and final state radiations. The detection of the $Z^0$ boson is then straightforward, as the final state consists of two muons of large transverse momenta forming a dimuon of large invariant mass. The detection of the $W^{\pm}$ bosons, on the contrary, is complicated by the presence of a neutrino in the final state, which can not be directly detected, and the procedure for the signal extraction from data depends on the experimental condition. A hermetic detector enables the indirect characterisation of the neutrino by means of the missing energy and momentum in the event, whereas for an non-hermetic detector the signal has to be extracted from the single muon spectrum. In the latter case, the so-called template fit method can be used, relying on the generation of MC templates accounting for the various contributions to the inclusive spectrum, which are then combined in an appropriate manner and used to fit and reproduce the data. The specific contribution of muons from $W^{\pm}$ decays can then be isolated.

The vector-axial vector ($V - A$) nature of the $W^{\pm}$ decay conserves the correlation between the boson rapidity $y_W$ and the muon pseudorapidity $\eta_\mu$, and the decay of the muon is thus not isotropic. At the parton level, the cross section in the rest frame of the $W^{\pm}$ is proportional to the angle $\theta^*$ between the boson and the decay muon [10]:

$$\frac{d\sigma}{d\cos\theta^*} \propto (1 \pm \cos\theta^*)^2, \tag{3.34}$$

with the sign depending on the product of the $W^{\pm}$-boson and the decay-muon helicities. This relation creates a preferred angular orientation for the decay, as illustrated in Figure 3.6. The weak interaction only couples left-handed fermions and right-handed anti-fermions. From angular momentum conservation, the outgoing lepton $\ell$ (anti-lepton $\bar{\ell}$) will preferentially follow the direction of the incoming quark $q$ (anti-quark $\bar{q}$). This can have a strong effect for the detection of the signal at large rapidities: for a process where the lepton is emitted backward with respect to the $W^{\pm}$ boson, the detection of the lepton at large rapidity requires the emission of the boson at opposite and even larger rapidities, pushing the reach of the detection towards a kinematic region where the production quickly drops.

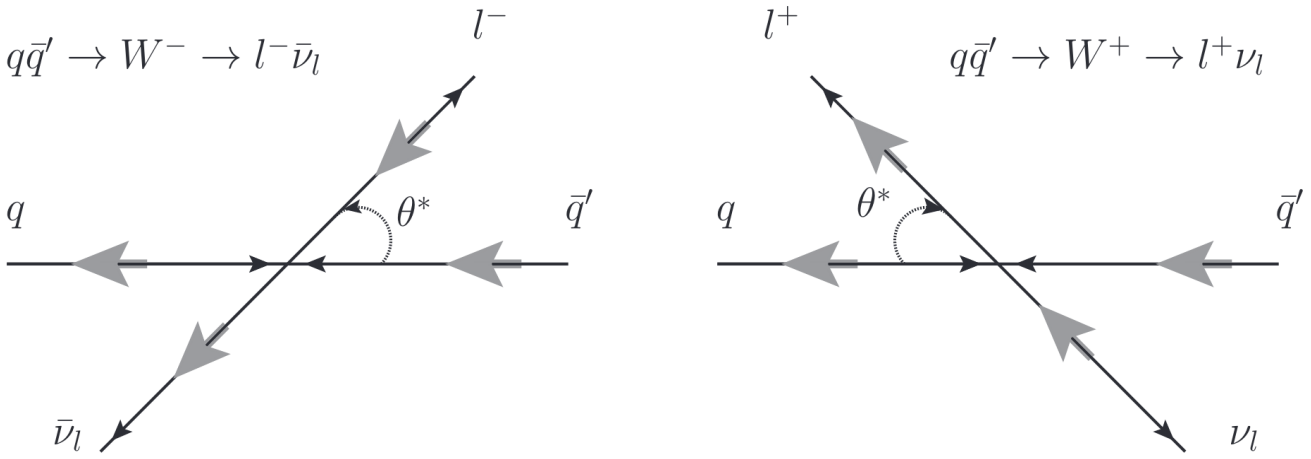


**Figure 3.6:** $W^{\pm}$ production and decay diagrams for $W^-$ (left) and $W^+$ (right) as seen in the boson rest frame. The small black arrows indicate the direction of motion of the particles, while the large grey arrows correspond to their spin, with the spin of the $W^{\pm}$ always pointing in direction of the incoming antiquark.

### 3.2.4 Production and study in proton–lead collisions

The production of weak bosons has not been studied in heavy-ion collisions before the LHC era, due to limitations in energies. Copious production at the LHC was foreseen, and triggered the interest of the theory community, for its impact on nPDF determination. As the valence quark distributions are rather well constrained by nuclear DIS, the production of weak bosons provides an efficient way to probe the sea quark PDF [152, 153]. The asymmetrical nature of p+A collisions, enabling to disentangle the measurements at forward and backward rapidities, were strong arguments in favour of the inclusion of a p–Pb program at the LHC [153, 90]. Figure 3.7 shows the calculated cross sections, as a function of rapidity, of the $Z^0$ and $W^{\pm}$ bosons, obtained from the CTEQ6.6 free-nucleon PDF [154], either used alone or paired with the EPS09 [98] nuclear modification function. The cross sections were calculated for p–Pb collisions at $\sqrt{s_{\mathrm{NN}}} = 8.8$ TeV, corresponding to the nominal LHC energy for this collision system.

The relevance of the measurement of the $Z^0$-boson production in p–Pb collisions is illustrated by the almost symmetric spectrum predicted in the absence of nuclear effects in the PDF. The residual asymmetry is due to the different relative content of $u$ and $d$ quarks in the proton and lead nuclei (the isospin effect), and can be shown to have a small effect on the $Z^0$-boson production [153] close to the $Z^0$ peak. The red dashed line in the left panel of Figure 3.7 illustrates this by showing the distributions obtained by only considering QED couplings, which correspond to the removal of the pure $Z^0$-exchange and $Z^0/\gamma^*$-interference terms in the computation, leaving only the virtual photon exchange. It is normalised by a factor 1100 for visibility. The large asymmetry seen for this process brings out the effects associated to the different isospin content of the two hadrons.

Applying the nuclear effects introduces a strong asymmetry in the rapidity-dependent cross

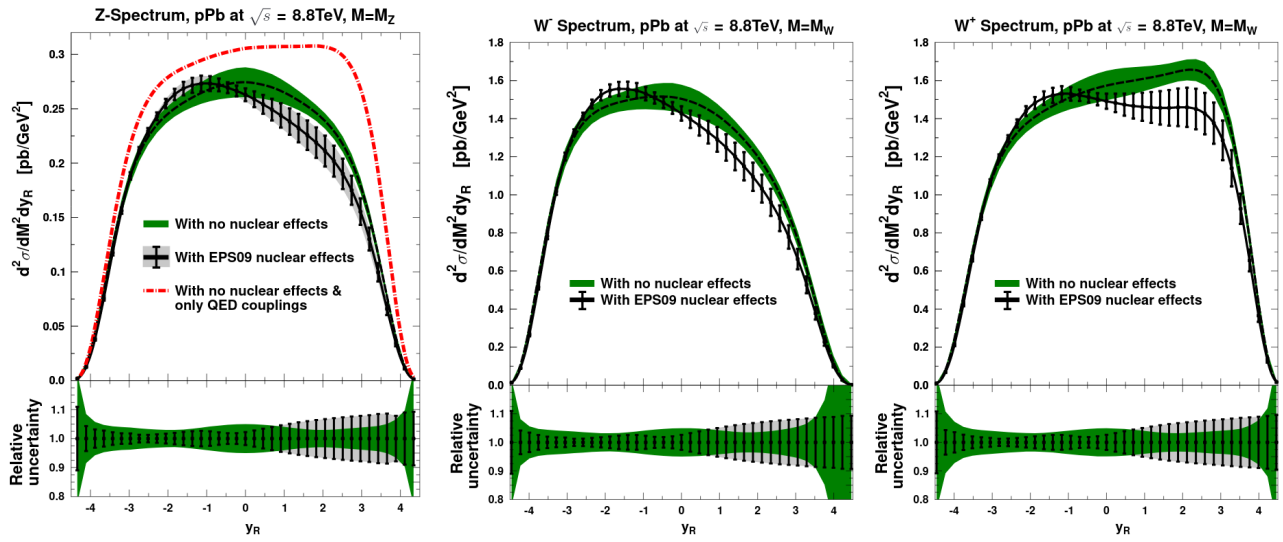


**Figure 3.7:** Production cross section of the $Z^0$ (left), $W^-$ (middle) and $W^+$ (right) bosons in p–Pb collisions at $\sqrt{s_{NN}} = 8.8$ TeV, calculated at the boson pole mass $M^2 = M^2_{Z^0,W^\pm}$. The dashed line and green uncertainty band correspond to predictions with the CTEQ6.6 [154] PDF set, without application of nuclear modifications. The full line corresponds to predictions with the CTEQ6.6 PDF, modified by the EPS09 [98] parametrisation of the nuclear modifications. The black vertical lines indicate the uncertainty from the nPDF. The lower panels show the relative uncertainties with the same colour code. The red dashed curve superimposed to the $Z^0$ distribution correspond to the cross section for virtual photon exchange only. The abscissae are labelled $y_R$ to indicate that the rapidity is the boson one, in the absence of final state radiations. Figures taken from Ref. [153].

section. The production at negative rapidities correspond to the high-$x$ region of the nPDF, assessing both enhancing (anti-shadowing) and suppressing (EMC) effects, while the production at positive rapidities is modified by the suppressive shadowing. This strikingly shows the advantage of p–Pb collisions, where the two regions can be disentangled and independently probed. One can still notice that the size of the error bars remains important, such that the predictions with and without nuclear modifications are often nearly, if not fully, compatible within uncertainties, even when the central values show significant discrepancies. Measuring the production of weak bosons does not only provide constraints for the determination of the nPDF, but also helps to shrink the model uncertainties, which remain sizeable.

The same distributions computed for the $W^-$ and $W^+$ bosons show drastic differences with respect to the $Z^0$ case, as illustrated in the middle and right panels of Figure 3.7. Here the predictions without nuclear modifications of the PDF are already highly asymmetrical, an effect arising from the different flavours responsible for the production. Nonetheless, significant deviations for the free-nucleon predictions can be seen, especially at positive rapidities in the interval $0 \lesssim y \lesssim 3$. The measurement of the $W^\pm$ can moreover be performed independently for the two charges, enabling the evaluation of a series of additional observables such as the charge ratio. In such ratios, part of the experimental and theoretical uncertainties can cancel, allowing for a better overall precision.

From this study one can derive the relevant quantities to be measured, which will provide meaningful inputs for the determination of the nuclear modifications. The first one is naturally the production cross section itself, which has been shown in the previous chapter to be directly proportional to the PDF of the partons in colliding hadrons:

$$\sigma_{\mathrm{AB}} \propto \sum_{q} \left[ f_q(x_1, Q^2) f_{\overline{q}}(x_2, Q^2) + f_{\overline{q}}(x_1, Q^2) f_q(x_2, Q^2) \right]. \tag{3.35}$$

The charge ratio $R$ provides information on the quark content of nucleus, and can constrain the PDF of the light quarks through its sensitivity to the $d$-to-$u$ ratio. It is defined as:

$$R = \frac{N_{\mu^+ \leftarrow \mathrm{W}^+}}{N_{\mu^- \leftarrow \mathrm{W}^-}}. \tag{3.36}$$

One can furthermore increase the sensitivity to the difference in production with respect to the charge by defining the lepton charge asymmetry $A_{\mathrm{ch}}$, a function of the charge ratio:

$$A_{\mathrm{ch}} = \frac{N_{\mu^+ \leftarrow \mathrm{W}^+} - N_{\mu^- \leftarrow \mathrm{W}^-}}{N_{\mu^+ \leftarrow \mathrm{W}^+} + N_{\mu^- \leftarrow \mathrm{W}^-}} = \frac{R-1}{R+1}. \tag{3.37}$$

The magnitude of the nuclear effects are estimated by means of the nuclear modification factor $R_{\mathrm{pPb}}$, defined as the ratio of the cross section in p–Pb collisions to that in pp, the latter being corrected for the number of nucleons in a lead ion:

$$R_{\mathrm{pPb}} = \frac{1}{208} \frac{\mathrm{d}\sigma_{\mathrm{p-Pb}}}{\mathrm{d}\sigma_{\mathrm{pp}}}. \tag{3.38}$$

In order to match what is experimentally accessible, the denominator is taken as the sum of independent pp collisions, such that measurements of the cross section at the same or similar energies can be used. As a consequence, in the study of weak boson production, the nuclear modification factor must be considered with care, as it includes effects such as the isospin which can significantly affect the production (notably that of $\mathrm{W}^{\pm}$ bosons). Even without nuclear modification of the PDFs, the $R_{\mathrm{pPb}}$ would deviate from unity, and this observable must not be mistaken for the nuclear modification function described in Section 1.2.4.

In the Glauber modelling of nuclear collisions, it is natural to assume that, for hard processes, the number of produced particles scales with the number of binary (nucleon–nucleon) collisions $N_{\mathrm{coll}}$. In this case the scattering processes are well localised and the interference effects between different collisions may be neglected. The cross section of a hard process without any strong final state effect, such as the leptonic decay of the $\mathrm{Z}^0$ and $\mathrm{W}^{\pm}$ bosons, are then expected to show the same dependence as $N_{\mathrm{coll}}$ to the collision geometry. Therefore, one expects:

$$\frac{\sigma_{\mathrm{AB}}(b)}{N_{\mathrm{coll}}(b)} = \text{const.}, \tag{3.39}$$

for all values of the impact parameter $b$. The experimental verification of the binary scaling requires an unbiased estimation of the centrality of the collisions, from which is estimated the geometry of the collision. A recent review of the theoretical and experimental progresses in the Glauber model, including studies of the binary scaling of hard processes, can be found in Ref. [155].

## 3.3 Measurements at the LHC

The production of the $Z^0$ and $W^{\pm}$ bosons has been measured in HIC by the four main experiments of the LHC, providing a variety of results for nPDF determination. The available results are summarised in Table 3.3. As for the work presented in this thesis, the results of these analyses are compared with predictions with and without nuclear modifications in order to evaluate their constraining power, as well as the ability of the models to reproduce the data.

| System | p–Pb | | | | Pb–Pb | | | |
|---|---|---|---|---|---|---|---|---|
| $\sqrt{s_{\mathrm{NN}}}$ | 5.02 TeV | | 8.16 TeV | | 2.76 TeV | | 5.02 TeV | |
| Boson | $Z^0$ | $W^{\pm}$ | $Z^0$ | $W^{\pm}$ | $Z^0$ | $W^{\pm}$ | $Z^0$ | $W^{\pm}$ |
| ALICE | [156] | [156] | **[157]** | **[158]** | | | [159, 157] | [158] |
| ATLAS | [160] | | | | [161] | [162] | [163] | [164] |
| CMS | [165] | [166] | | [167] | [168, 169] | [170] | [171] | |
| LHCb | [172] | | [173] | | | | | |

**Table 3.3:** References of the available measurements of the $Z^0$- and $W^{\pm}$-boson production performed in HIC at the LHC. The references indicated in bold correspond to the publications of the measurements presented in this thesis.

It is worth stressing that, due to the geometry of the various detector as well as their detection capabilities, the measurements are performed over a large range of kinematic regions. The ATLAS and CMS detectors lie at midrapidity, covering the range $|y| \lesssim 2.5 - 3.5$, while ALICE and LHCb cover large rapidities in the intervals $2.5 < y_{\mathrm{ALICE}} < 4$ and $2 < y_{\mathrm{LHCb}} < 4.5$. ATLAS and CMS can detect electrons and muons, and the measurements are often provided in both channels, if not combined. The large statistics available at midrapidity allows for a sharper selection on the transverse momentum of the lepton from $W^{\pm}$ decays, which is then typically higher than that of ALICE measurements at large rapidities.

### 3.3.1 Production in Pb–Pb collisions at midrapidities

The ATLAS and CMS Collaborations measured the production of the $Z^0$ and $W^{\pm}$ bosons through their leptonic decays in Pb–Pb collisions at $\sqrt{s_{\mathrm{NN}}} = 2.76$ TeV and 5.02 TeV. Both experiments cover the midrapidity region. Figure 3.8 shows the measurements done by ATLAS on the $Z^0$ boson at $\sqrt{s_{\mathrm{NN}}} = 2.76$ TeV [161]. On the left panel, the production is presented by means of the yield per event as a function of rapidity. This normalised yield of the $Z^0$ boson shows the well expected decrease of production towards large rapidities, and one can observe the good agreement with theoretical predictions, within uncertainties, over the whole $|y| < 2.5$ rapidity range.

On the right panel of Figure 3.8, the yield is presented normalised to the average number of binary nucleon-nucleon collisions $\langle N_{\mathrm{coll}} \rangle$, as a function of the average number of participants $\langle N_{\mathrm{part}} \rangle$ and for various $p_{\mathrm{T}}$ intervals. This measurement allows one to probe the scaling of hard processes with $N_{\mathrm{coll}}$ that one foresees from a Glauber modelling of the collision, from Equation 3.39. For all the $p_{\mathrm{T}}$ intervals considered, the scaling is observed. Indeed, although some deviations can be

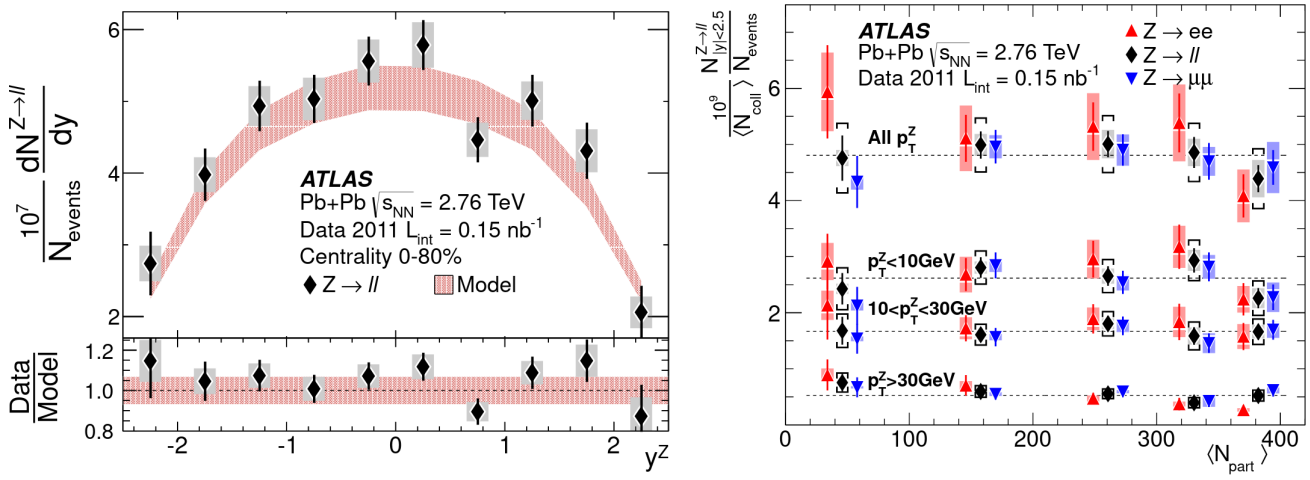


**Figure 3.8:** **Left**: per-event rapidity distribution of detected $Z^0$ bosons in Pb–Pb collisions at $\sqrt{s_{NN}}$ = 2.76 TeV measured by the ATLAS Collaboration. The model to which the data points are compared correspond to Pythia-simulated events normalised to the $Z^0 \to \ell\ell$ cross section in pp collisions at the same energy taken from NNLO calculations and scaled by $\langle T_{AA} \rangle$. The bars and boxes around the data points indicate the statistical and systematic uncertainties, respectively. **Right**: centrality dependence of the $Z^0$ boson yield divided by $\langle N_{coll} \rangle$ in Pb–Pb collisions at $\sqrt{s_{NN}}$ = 2.76 TeV. Measurement for the *ee* and $\mu\mu$ channels are horizontally shifted for better visibility. Bars and boxes around the data points correspond to statistical and systematic uncertainties, respectively. The bracket around the combined results show the total uncertainty, including that on $\langle N_{coll} \rangle$. The dashed lines are fits of the distributions with a constant. Figures taken from Ref. [161].

seen for the independent measurements in the $e^+e^-$ and $\mu^+\mu^-$, the combined measurements are consistent with constants, indicated on the plots as dashed lines corresponding to fits of the data.

ATLAS also measured the production of weak bosons in Pb–Pb collisions at $\sqrt{s_{NN}}$ = 5.02 TeV. The measured yields of the $Z^0$, $W^+$ and $W^-$, normalised to the average of the nuclear overlap function $\langle T_{AA} \rangle$, are reported in Figure 3.9. They are compared with theoretical predictions calculated with the EPPS16 [54] and nCTEQ15 [55] nPDF sets, as well as predictions from the free-nucleon CT14 [63] model, accounting for the isospin effect but without nuclear modifications. It is especially interesting to note here that the measurements in Pb–Pb collisions seem to favour the predictions without nuclear modification of the PDF. The $Z^0$ measurements are not consistent with predictions, although closer to free-nucleon than to nPDF models. The $W^\pm$ measurements are fully consistent with the CT14-only predictions.

The most recent measurements in Pb–Pb collisions brought the uncertainties on the electroweak boson productions down to a few-percent level, and shown peculiar discrepancies with theoretical predictions. This triggered several theoretical studies, aiming at benefiting from the new precision and explaining the deviation between the models and the measurements. In a study by K. Eskola et al. [174], the standard paradigm of taking the inelastic nucleon-nucleon cross section at a value

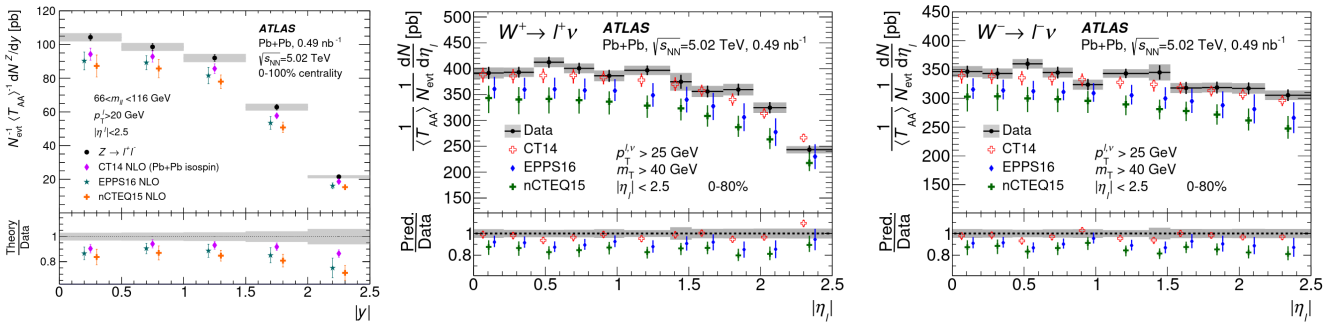


**Figure 3.9:** Normalised yields of the $Z^0$ (left), $W^+$ (middle) and $W^-$ (right) bosons as a function of the absolute rapidity ($Z^0$) or pseudorapidity ($W^{\pm}$) measured in Pb–Pb collisions at $\sqrt{s_{NN}} = 5.02$ TeV by the ATLAS Collaboration. The bars and boxes correspond to the statistical and systematic uncertainties, respectively. The measurement are compared with predictions from the EPPS16 [54] and nCTEQ15 [55] nPDF models, as well as prediction from the free-nucleon CT14 [63] PDF, accounting the isospin but without nuclear modifications. The bottom panels show the ratios of the predicted yields to the measured ones. Figures taken from Refs. [163, 164].

extrapolated from pp data is questioned as a potential source of bias. The alternative determination they propose leads to a nuclear-suppressed cross section that amounts to 60% of the standard value. Another study by F. Jonas and C. Loizides [175] investigates a possible effect from the centrality determination itself, as well as the relevance of the skin thickness in Pb which can play a significant role at the precision level attained by the most recent experimental measurements.

### 3.3.2 Production in Pb–Pb collisions at large rapidities

The production of $Z^0$ and $W^{\pm}$ bosons at large rapidities has been measured by the ALICE Collaboration. The left panel of Figure 3.10 shows the $Z^0$ invariant yield normalised to the average of the nuclear overlap $\langle T_{AA} \rangle$ measured in Pb–Pb collisions at $\sqrt{s_{NN}} = 5.02$ TeV [157]. This study is performed on the combined data samples from the 2015 and 2018 collision periods at the LHC, improving the previous ALICE measurement done on 2015 data only [159]. Comparing the two top points in the figure, one can appreciate the increase of precision brought by the supplementary statistics. The measured yield is compared with predictions from the EPS09 [98], EPPS16 [54] and nCTEQ15 [55] models, with which a good agreement is found. Comparison is also drawn with a calculation using the free-nucleon CT14 [63] PDF, including the isospin effect. This calculation is clearly not consistent with the measurement, showing a deviation of 3.4 $\sigma$. This study provides a significant observation of nuclear modifications. Its precision will also help reducing the uncertainties of the models.

Preliminary measurements of the $W^{\pm}$ production at large rapidities were recently released by the ALICE Collaboration. The right panel of Figure 3.10 shows the nuclear modification factor $R_{AA}$ of the $W^+$ and $W^-$ bosons in Pb–Pb collisions at $\sqrt{s_{NN}} = 5.02$ TeV as a function of the collision centrality. The factor is calculated from the invariant yield of the $\mu^{\pm} \leftarrow W^{\pm}$ process normalised to the average nuclear overlap function $\langle T_{AA} \rangle$, then divided by the centrality-independent pp cross

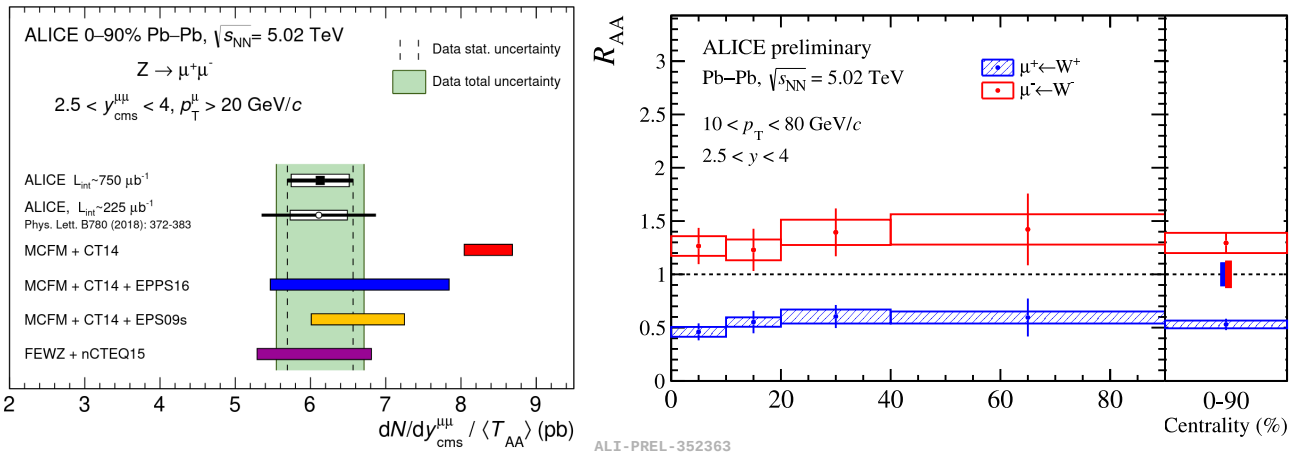


**Figure 3.10: Left**: invariant yield of the $Z^0 \rightarrow \mu^+\mu^-$ divided by $\langle T_{AA} \rangle$ measured inPb–Pb collisions at $\sqrt{s_{NN}} = 5.02$ TeV. The vertical dashed band represents the statistical uncertainty on the data while the green filled band corresponds to the quadratic sum of statistical and systematic uncertainties. The result is compared with the previous ALICE measurement in the same collision system [159] as well as theoretical predictions. Figure taken from Ref. [157]. **Right**: preliminary measurement of $W^-$ and $W^+$ nuclear modification factor in Pb–Pb collisions at $\sqrt{s_{NN}} = 5.02$ TeV. The pp reference is taken from pQCD calculations with the CT10 PDF set [176].

section taken from pQCD calculations with the CT10 [176] free-nucleon PDF. The flat behaviour observed for the $R_{AA}$ is therefore also seen for the normalised invariant yield itself, providing a confirmation of the binary scaling expected from the Glauber model. The $R_{AA}$ shows an increase of the $W^-$ production, and a decrease of that of $W^+$, a consequence of the isospin effect which affects differently the bosons depending on their charge. This measurement constitutes the first evaluation of the $W^{\pm}$ production in heavy-ion collision in this rapidity region. The finalised results will be published along the measurement in p–Pb collisions in Ref. [158], where they will be compared with theoretical calculations.

### 3.3.3 Production in p–Pb collisions at midrapidities

The production of $Z^0$ measured at midrapidity by ATLAS [160] is shown in Figure 3.11. The measurement is made on the combination of the dielectron and dimuon channels. The measurement cover the rapidity interval $|y^*| < 3.5$, with $y^*$ denoting the rapidity in the centre-of-mass frame. It is compared with predictions from the CT10 [176] and MSTW2008 [177] free-nucleon PDFs, the former being NLO and the latter NNLO. Comparisons are also made with predictions including the nuclear modifications of the PDF by applying the EPS09 [98] modification function to the CT10 baseline. The distribution is seen to be strongly asymmetric, following the expected trend observed in Figure 3.7. In order to evaluate the agreement between the models and data, the authors performed a $\chi^2$ test of compatibility. The unmodified CT10 and MSTW2008 calculations have $p$-values of 0.07 and 0.01, respectively, while the CT10+EPS09 combination gives a $p$-value of 0.79, pointing towards a preference for the observation of nuclear correction effects from the

study. The same conclusion was derived from a Kolmogorov-Smirnov test [178]. It should be noted that at midrapidity, the effect of nuclear corrections tends to be small, as the region cover several competing nuclear effects.

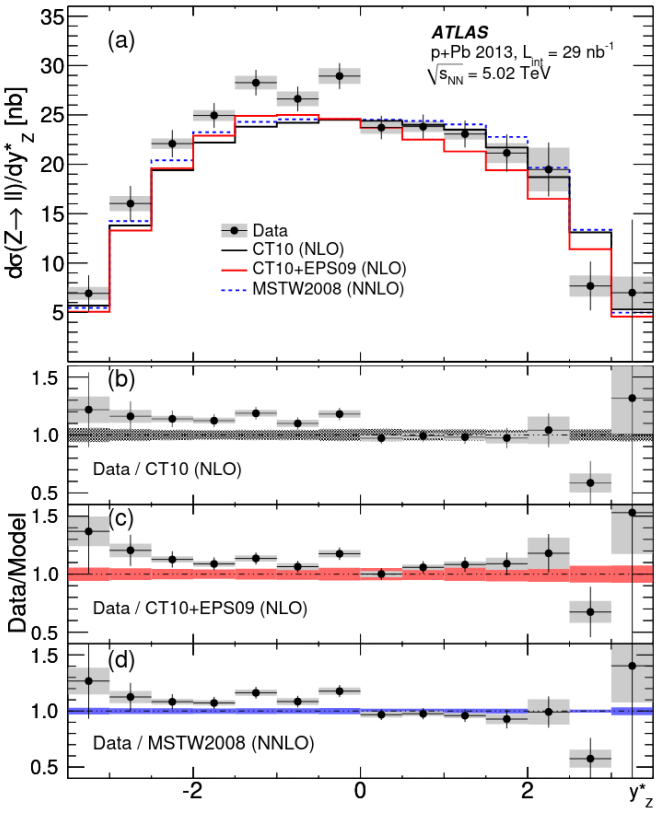


**Figure 3.11:** Rapidity-differential cross section of the $Z^0$ detected in the leptonic decay channel ($e + \mu$) in p–Pb collisions at $\sqrt{s_{NN}} = 5.02$ TeV with the ATLAS detector. The bars and boxes indicate the statistical and systematic uncertainties, respectively. The measurements are compared with calculations with the CT10 [176] and MSTW2008 [177] free-nucleon PDF, and with the EPS09 [98] nPDF set, using CT10 as baseline. The bottom panels shows the ratio of the data to the various models. Figure taken from [160].

The production of the $W^{\pm}$ boson was measured by CMS in p–Pb collisions at $\sqrt{s_{NN}} = 5.02$ TeV and 8.16 TeV [166, 167], in the electronic and muonic channels. As the signal is characterised by a high-$p_T$ lepton, a kinematic selection of $p_T > 25$ GeV/$c$ is applied to the data. The CMS detector enables the evaluation of the missing transverse energy due to the final-state neutrino. The cross sections for $W^+$ and $W^-$ are shown as a function of the lepton pseudorapidity in Figure 3.12. The results at $\sqrt{s_{NN}} = 5.02$ TeV are compared with predictions from the CT10+EPS09 nuclear model and standalone CT10 calculations. The measurement at $\sqrt{s_{NN}} = 8.16$ TeV are compared with more recent models, namely EPPS16 [54] and nCTEQ15 [55] for nuclear sets, and CT14 [63] for free nucleons. The two nPDF calculations use CT14 as well, although it should be remembered

that EPPS16 requires a baseline for the modelisation of the Pb ion, while nCTEQ15 is a full parametrisation of the nPDFs, and CT14 is then only used to model the incoming proton.

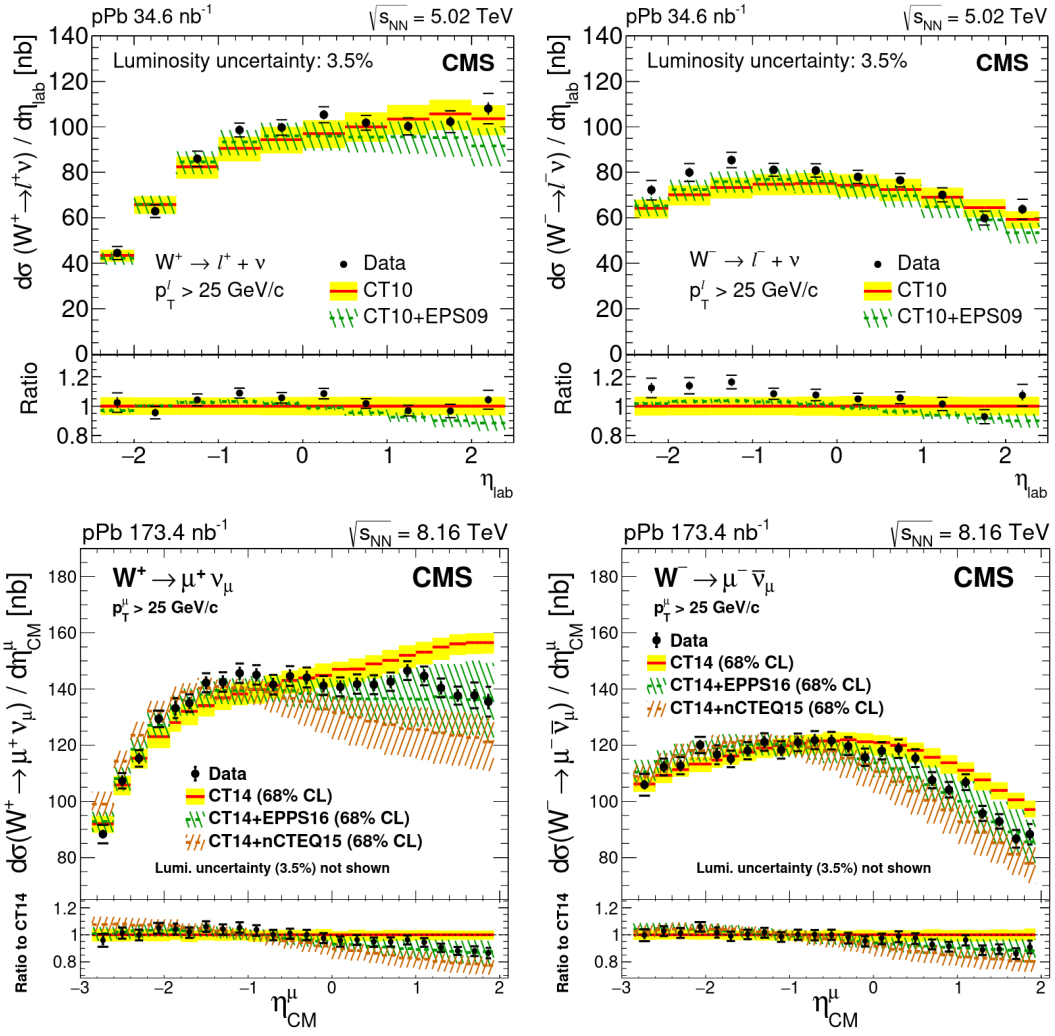


**Figure 3.12:** Production cross section of $W^+$ (left) and $W^-$ (right), as a function of the lepton pseudorapidity, in p–Pb collisions at $\sqrt{s_{NN}} = 5.02$ TeV (top) and 8.16 TeV (bottom) measured by the CMS Collaboration. The error bars represent the statistical uncertainty, while brackets show the statistical and systematic uncertainties summed in quadrature. The free-nucleon predictions from CT10 [176] and CT14 [63] are shown as full bands, the predictions including the nuclear corrections are displayed as dashed lines. They rely on the EPS09 [98], EPPS16 [54] or nCTEQ15 [55] parametrisation of the nPDFs. The bottom panels show the ratio of the data and nPDF calculations to that of the free-nucleon ones. Figures taken from [166, 167].

In the 5.02 TeV measurement, one finds the same lack of large difference between the predictions with and without nuclear corrections, as the size of the latter tend to be of the order of the corrections themselves. At 8.16 TeV, the comparison yields more meaningful results. In the negative rapidity region, the data are compatible with all calculations within uncertainties. At

forward rapidities, nuclear corrections are higher and large deviations from the CT14-only predictions are seen. The measurement follows the trend of the nPDF by showing a depletion in this region. Comparing EPPS16 and nCTEQ15, one sees that the shadowing effect is more pronounced in the latter, something which is not in agreement with the data. Over the whole rapidity range, the EPPS16 model appears to be favoured.

### 3.3.4 Production in p–Pb collisions at large rapidities

The measurements at large rapidities are possible thanks to the coverage of the LHCb detector and the muon spectrometer of ALICE. The measurement of the $Z^0$ boson in p–Pb collisions by LHCb is shown in Figure 3.13. The measurements are compared with NNLO predictions from the MSTW2008 [177] PDF set paired with EPS09 [98] for the nuclear corrections. Due to the short running time of heavy-ion collision at the LHC, and the low production cross section of the weak boson at large rapidities, the measurement was performed from a limited number of reconstructed $Z^0$: $4 \pm 2$ bosons at backward rapidities and $11 \pm 3$ at forward, explaining the large uncertainties seen in the plot. Nonetheless, one can see that the calculations at backward rapidity underestimate the production cross section. At forward rapidity the measured production rate is fully compatible with calculations.

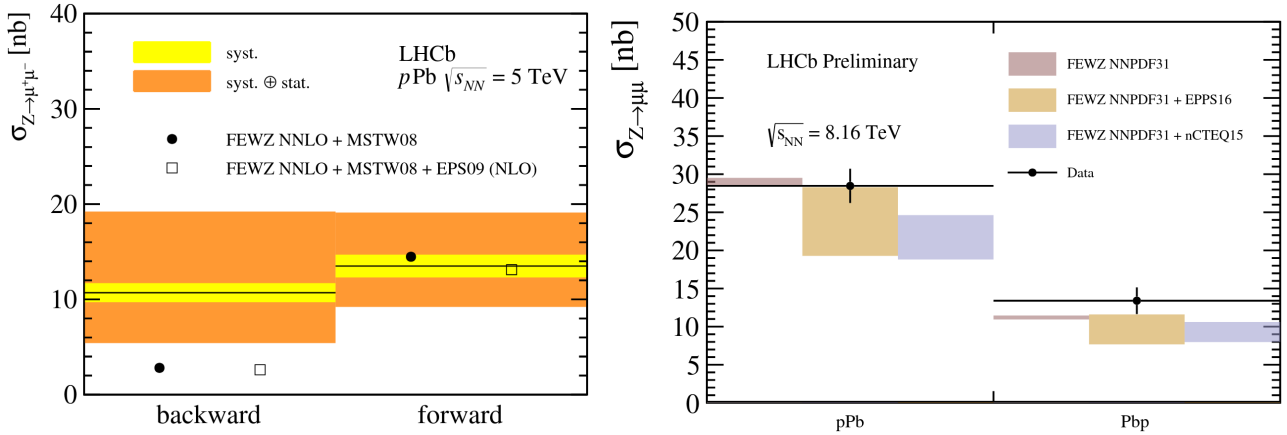


**Figure 3.13: Left**: $Z^0$-boson cross section measured in p–Pb collisions at $\sqrt{s_{\rm NN}} = 5.02$ TeV by the LHCb Collaboration, at backward and forward rapidities. The inner bands represent the systematic uncertainty, while the outer ones indicate the statistical and systematic uncertainties summed in quadrature. The measurements are compared with predictions from the MSTW2008 [177] PDF set, with and without including the nuclear corrections using EPS09 [98]. The uncertainties on the theoretical predictions are negligible compared to those on the experimental results, they are therefore not shown. Figure taken from Ref. [172]. **Right**: same measurements from p–Pb collisions at $\sqrt{s_{\rm NN}} = 8.16$ TeV. The error bars correspond to the total uncertainty. Predictions from the NNDPF3.1 [49] free-PDF set are shown, along with calculations including the nuclear corrections from the EPPS16 [54] and nCTEQ15 [55] models. Figure taken from Ref. [173].

The ALICE Collaboration measured the production of the $Z^0$ and $W^{\pm}$ bosons in p–Pb collisions at $\sqrt{s_{NN}} = 5.02$ TeV and 8.16 TeV. The measured cross sections are shown in Figure 3.14. Here as well, the limited statistics in the data leads to rather large uncertainties on the measurement, while the ability to control the detector misalignment created a significant amount of systematic uncertainty. It is interesting to note for the $W^{\pm}$ cross section the different behaviour of $W^+$ and $W^-$, and especially the large suppression of the $W^+$ production at backward rapidities. The measurements are compared with two free-PDF models, MSTW2008 [177] and CT10 [176], both with and without nuclear corrections using EPS09 [98]. The usage of different baselines may introduce sizeable differences, although this is not the case with more recent sets that tend to be compatible with one another. As seen at the edges of the rapidity intervals probed by CMS, the nuclear modifications are rather negligible at backward rapidity while they are not at forward. Yet, the uncertainties on the measurements does not allow for drawing any strong conclusion on the nuclear corrections, as they are generally compatible with predictions regardless of whether the nuclear corrections are implemented or not.

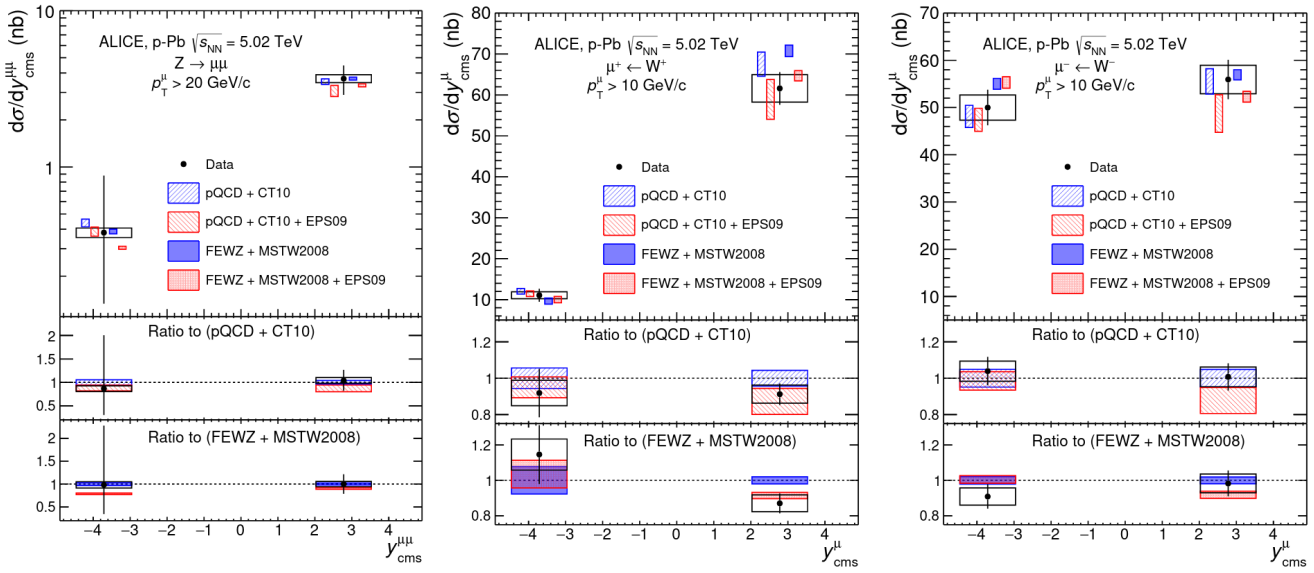


**Figure 3.14:** Cross sections of $Z^0$ (left), $W^+$ (middle) and $W^-$ (right) in the muonic decay channel, measured at forward and backward rapidities by the ALICE Collaboration in p–Pb collisions at $\sqrt{s_{NN}} = 8.16$ TeV. The bars and boxes represent the statistical and systematic uncertainties, respectively. The results are compared with theoretical calculations with the CT10 [176] and MSTW2008 [177] free-PDF sets, paired with the EPS09 [98] parametrisation of the nPDF. In the top panels, the predictions are horizontally shifted for better visibility. The bottom panels show the ratio of data and EPS09 to the free-nucleon predictions. Figures taken from Ref. [156].

The ALICE Collaboration also measured the $Z^0$ and $W^{\pm}$ productions in p–Pb collisions at $\sqrt{s_{NN}} = 8.16$ TeV [157, 158], which constitutes the topic of this work. The analyses and results are described in details in Chapters 8 and 9.

# Part II

# A Large Ion Collider Experiment

# Chapter 4

# The ALICE detector

This chapter presents the ALICE detector. A brief overview of ALICE in the context of the LHC at CERN is given, followed by an overview of the detector itself and a description of its so called global detectors and central barrel subsets. As the analysis presented in this thesis relies on data taken with the muon spectrometer, this part of the apparatus is described in detail in the dedicated following chapter.

## 4.1 The Large Hadron Collider

### 4.1.1 LHC at CERN

The Large Hadron Collider (LHC) is a large and powerful circular collider installed at the European Organization for Nuclear Research (CERN[1]), in the 26.7 km diameter tunnel previously occupied by the Large Electron-Positron collider (LEP). It sits at the end of the CERN accelerator complex, displayed in Figure 4.1. It delivered its first proton beam in 2009. The LHC is designed for very-high energy hadronic collisions, reaching the ultra-relativistic regime. Even before the construction of the LHC, the CERN had a long history of scientific achievements [179], such as the discovery of neutral currents, the first observation of the $W^{\pm}$ and $Z^0$ bosons, the creation and manipulation of antihydrogen atoms and the report of direct CP violation. In the LHC era, the peak achievement is the observation of a boson consistent with the Higgs boson predicted 40 years earlier. A detailed description of the LHC can be found in Ref. [180].

Along the LHC sit four main experiments, each targeting different physics goals and featuring different detection methods to reach them:

- **A Large Ion Collider Experiment (ALICE)** [181]: a multipurpose experiment optimised for the high-multiplicity environment created by heavy-ion collisions, and through them the study of the strongly interacting matter;

[1]The CERN acronym comes from the former name of the organisation, European Center for Nuclear Research, in french Centre Européen pour la Recherche Nucléaire.

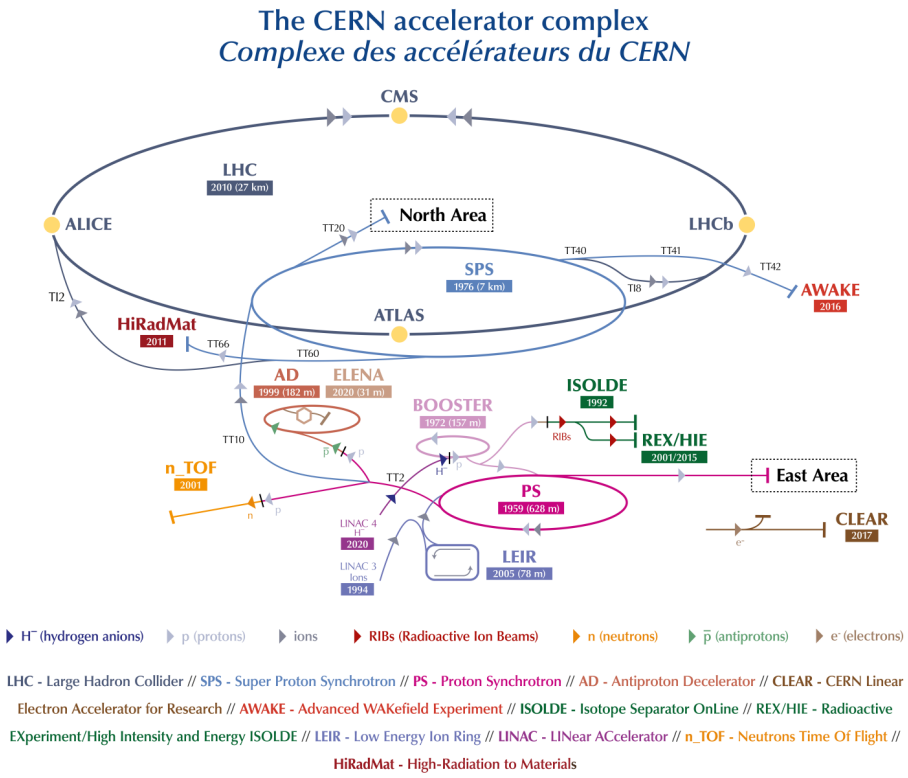


**Figure 4.1:** The CERN facility. The arrows indicate the path taken by the various particle beams, from their production site to the collision points.

- **A Toroidal LHC ApparatuS (ATLAS)** [182]: a multipurpose experiment, designed for high luminosity pp mode in order to search for new particles and physics beyond the Standard Model;
- **Compact Muon Solenoid (CMS)** [183]: another general purpose experiment, with the same goals as ATLAS but using different technical solutions;
- **LHC beauty (LHCb)** [184]: a fully instrumented forward spectrometer focusing on P violation, heavy-flavor CP violation and the matter-antimatter asymmetry, mainly through beauty physics.

Although ALICE is the only detector dedicated to heavy-ion collisions, all the experiments have an heavy-ion program. Following their respective designs and physics goals, they have various geometrical acceptances, allowing them to cover the phase space in a complementary way. A typical year of data taking at the LHC contains a lengthy time dedicated to pp mode, a few weeks for heavy-ion collisions, followed by a winter shutdown. Data taking happens several years in a row, after which a Long Shutdown (LS) takes place, allowing the collaborations to repair and upgrade their detectors, and the LHC teams the accelerator. Two shutdowns have happened since

the starting of the LHC, LS1 from 2013 to 2015 and LS2, started in 2018 and still ongoing at the time of writing of this thesis.

### 4.1.2 Injection and beams

The CERN accelerator complex relies on using previous accelerators as injectors for the new ones. The injection chain is sketched in Figure 4.2: before reaching the LHC itself, a particle is pre-accelerated in a chain of accelerators. The proton source is a simple bottle of hydrogen gas. The hydrogen atoms are stripped off their electron with an electric field, then injected into the Linear Accelerator 2 (LINAC2), the first accelerator of the chain, before moving to the circular Proton Synchrotron (PS) and Super Proton Synchrotron (SPS), reaching an energy of 50 MeV, 28 GeV and 450 GeV at each stage. The lead beam is obtained by evaporating Pb atoms, removing the 29 outermost electrons electrically. The resulting ions are accelerated by LINAC3, sent through a 1 $\mu$m-thin layer of carbon, removing 25 more electrons, and injected into and accelerated by the Low Energy Ion Ring (LEIR) then PS, from where they follow the same chain as the protons. The remaining 28 electrons are removed by an aluminium foil after PS. During these steps, the protons and lead are assembled in hundreds of bunches forming a train (a proton beam typically contains about 2 800 bunches with $10^{11}$ protons each at start). In such a train, the minimal bunch spacing, defined as the minimal time between two injections in the SPS, is about 25 ns.

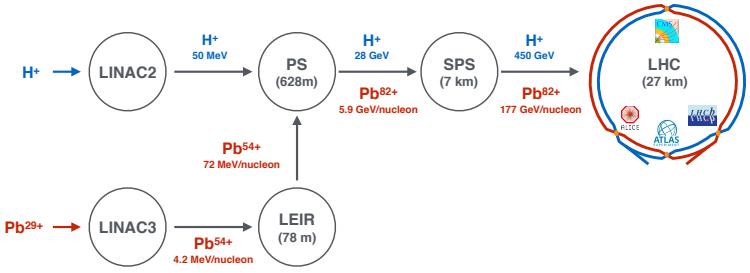


**Figure 4.2:** The LHC injection chain for proton and lead beams. The energy per nucleon attained after each accelerator and, for Pb, the ionisation, are indicated.

The two beams are finally sent in the two beam pipes of the LHC, one circulating clockwise and the other anticlockwise. They are accelerated using electromagnetic resonators, kept into circular orbits by means of dipole magnets, and brought to collision at four points where the main LHC experiments are installed. Under normal operation conditions, the beams can circulate several hours in the LHC, after which their intensity diminishes and the collision rate becomes too low. As to maximise the collision probability, they are collimated before the interaction points using quadrupole magnets. Table 4.1 indicates the nucleon-nucleon centre-of-mass energy $\sqrt{s_{\mathrm{NN}}}$, luminosity $\mathcal{L}$ and geometrical cross section $\sigma_{geom}$ under nominal running conditions for the three main collision configurations: proton-proton (pp), proton-lead (p–Pb) and lead-lead (Pb–Pb).

| Mode | $\sqrt{s_{\mathrm{NN}}}$ (TeV) | $\mathcal{L}$ ($\mathrm{cm^{-2}s^{-1}}$) | $\sigma_{geom}$ (b) |
|---|---|---|---|
| pp | 14.0 | $10^{34}$ | 0.07 |
| p–Pb | 8.8 | $10^{29}$ | 1.9 |
| Pb–Pb | 5.5 | $10^{27}$ | 7.7 |

**Table 4.1:** LHC nominal nucleon-nucleon centre-of-mass energy $\sqrt{s_{\mathrm{NN}}}$, luminosity $\mathcal{L}$ and geometrical cross section $\sigma_{geom}$ for pp, p–Pb and Pb–Pb collisions.

## 4.2 Overview of ALICE

At the time of writing of this thesis, the ALICE collaboration consisted in 1,975 members from 170 institutes in 40 countries. Its 300$^{\mathrm{th}}$ publication came out in 2020. The collaboration uses a 26 m long, 16 m wide and 16 m high detector, weighting 10 000 tons, buried 56 m underground at one of the LHC interaction points. The detector is designed to cope with the high particle multiplicities expected in the most central heavy-ion collisions ($\mathrm{d}N_{\mathrm{ch}}/\mathrm{d}y$ up to 8 000) while still being able to track and reconstruct particles from very low to fairly high transverse momentum ($p_{\mathrm{T}}$), between $\sim$ 100 MeV/$c$ and $\sim$ 100 GeV/$c$. Figure 4.3 shows a cross sectional view of the detector. In this chapter, the ALICE detector is presented in its configuration during the LHC Run 2, when the data used for the measurements presented in this thesis were collected. The configuration for the Run 3, accounting for the upgrade of LS2, will be described in Chapter 7.

The ALICE subdetectors can be regrouped in three main ensembles, whose composition and usage are described in more details in the next sections:

- a set of global detectors participating in the event triggering and providing general information on the collision, such as the collision centrality and multiplicity, and the event plane reconstruction;
- the central barrel, covering the mid-rapidity range, used for primary vertex reconstruction, tracking of charged particles, particle identification of electrons, photons and charged hadrons, and detection of jets;
- the muon spectrometer, aiming at detecting the muon decay products of low mass mesons ($\rho$, $\phi$, $\omega$), quarkonia, heavy-flavor hadrons and weak bosons at large rapidity.

The combination of the central barrel and muon spectrometer gives ALICE a large spatial coverage, illustrated in Figure 4.4 in which it is compared to the acceptance of the other LHC experiments.

The ALICE coordinate system [186] is a right-handed orthogonal Cartesian system with the origin at the collision point. The $z$ axis follows the beam line, with the muon spectrometer at negative $z$. The positive and negative sides are conventionally referred to as A-side and C-side, respectively. Table 4.2 summarises the names, acceptances, positions and roles of the various subparts of the detector. Complementary to what is presented in this thesis, one can refer to the

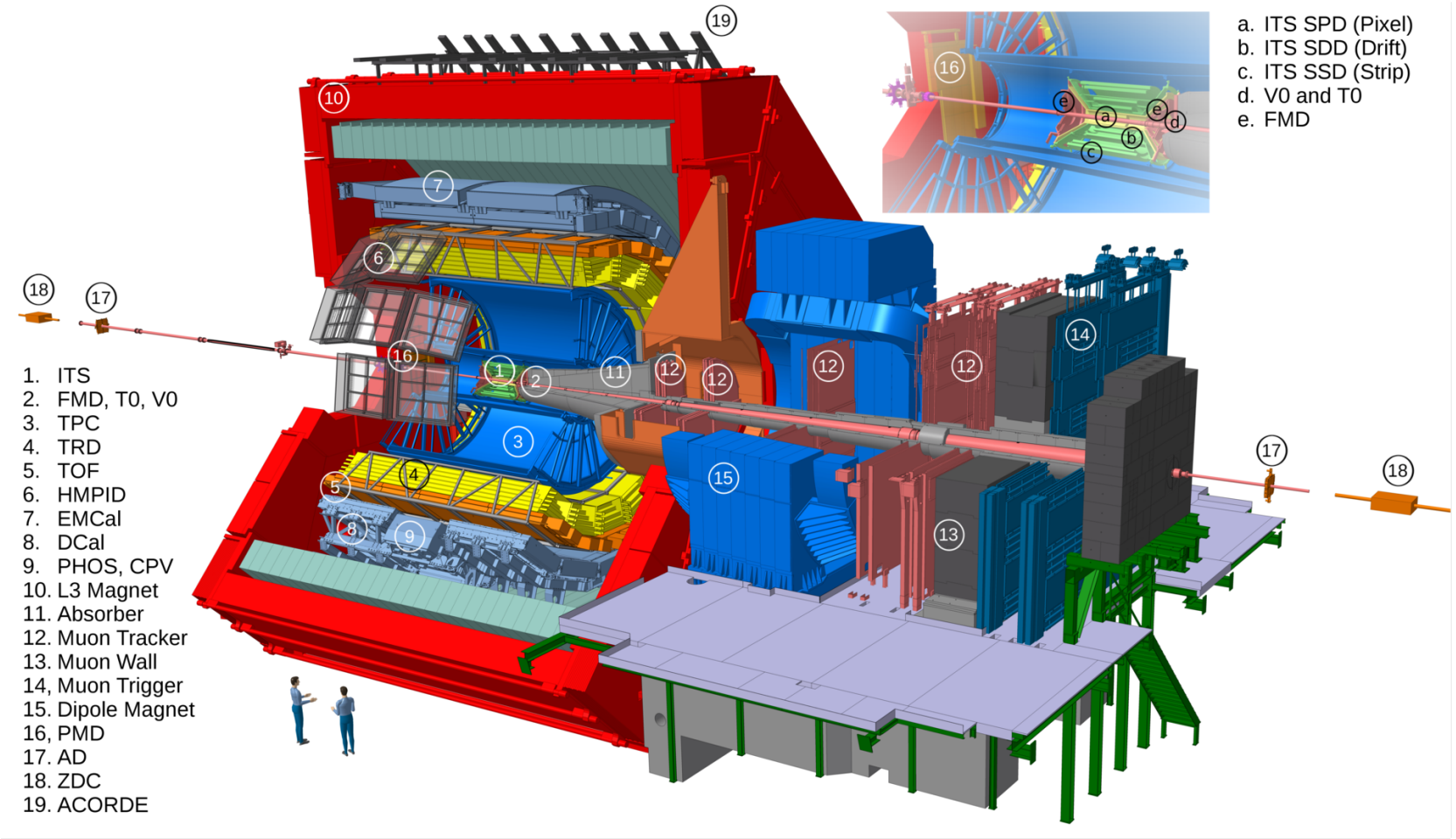


**Figure 4.3:** Schematics of the ALICE detector and its subparts. The region around the collision point is detailed in the top right panel.

| Detector | Acceptance | | Position | Main purpose |
|---|---|---|---|---|
| | Polar | Azimuthal | | |
| Global detectors | | | | |
| ZDC: ZN | $\|\eta\| > 8.8$ | full | $z = \pm 113$m | forward neutrons |
| ZDC: ZP | $6.5 < \|\eta\| < 7.5$ | $\|\phi\| < 10^\circ$ | $z = \pm 113$m | forward protons |
| ZDC: ZEM | $4.8 < \|\eta\| < 5.7$ | $\|2\phi\| < 32^\circ$ | $z = 7.3$m | photons |
| PMD | $2.3 < \eta < 3.9$ | full | $z = 367$cm | photons |
| FMD disc 1 | $3.6 < \eta < 5.0$ | full | $z = 320$cm | charged particles |
| FMD disc 2 | $1.7 < \eta < 3.7$ | | inner: $z = 83$cm<br>outer: $z = 75$cm | |
| FMD disc 3 | $-3.4 < \|\eta\| < -1.7$ | | inner: $z = -63$cm<br>outer: $z = -75$cm | |
| T0 | A-side: $4.6 < \eta < 4.9$<br>C-side: $-3.3 < \eta < -3.0$ | full | $z = 370$cm<br>$z = -70$cm | charged particles |
| V0 | A-side: $2.8 < \eta < 5.1$<br>C-Side: $-3.7 < \eta < -1.7$ | | $z = 340$cm<br>$z = -90$cm | time, vertex |
| AD | A-side: $4.8 < \eta < 6.3$<br>C-side: $-7.0 < \eta < -4.9$ | full | $z = 170$cm<br>$z = -195$cm | diffractive events |
| Central barrel | | | | |
| ITS layer 1,2 (SPD) | $\|\eta\| < 2.0$, $\|\eta\| < 1.4$ | full | $r = 3.9, 7.6$cm | tracking, vertex |
| ITS layer 3,4 (SDD) | $\|\eta\| < 0.9$, $\|\eta\| < 0.9$ | | $r = 15.0, 23.9$cm | tracking, PID |
| ITS layer 5,6 (SSD) | $\|\eta\| < 1.0$, $\|\eta\| < 1.0$ | | $r = 38, 43$cm | |
| TPC | $\|\eta\| < 0.9$ | full | $85 < r < 247$ | tracking, PID |
| TRD | $\|\eta\| < 0.8$ | full | $290 < r < 368$cm | tracking, $e^{\pm}$ identification |
| TOF | $\|\eta\| < 0.9$ | full | $370 < r < 399$cm | PID |
| HMPID | $\|\eta\| < 0.6$ | $1^\circ < \phi < 59^\circ$ | $r = 490$cm | PID |
| PHOS | $\|\eta\| < 0.12$ | $220^\circ < \phi < 320^\circ$ | $460 < r < 478$cm | photons |
| EMCAL | $\|\eta\| < 0.7$ | $80^\circ < \phi < 187^\circ$ | $430 < r < 455$cm | photons, jets |
| DCAL | $0.22 < \|\eta\| < 0.7$<br>$\|\eta\| < 0.7$ | $260^\circ < \phi < 320^\circ$<br>$320^\circ < \phi < 327^\circ$ | | |
| ACORDE | $\|\eta\| < 1.3$ | $30^\circ < \phi < 150^\circ$ | $r = 850$cm | cosmic rays, calibration |
| Muon spectrometer | | | | |
| Tracking station 1 | $-4.0 < \eta < -2.5$ | full | $z = -5.36$m | muon tracking |
| Tracking station 2 | | | $z = -6.86$m | |
| Tracking station 3 | | | $z = -9.83$m | |
| Tracking station 4 | | | $z = -12.92$m | |
| Tracking station 5 | | | $z = -14.22$m | |
| Trigger station 1 | $-4.0 < \eta < -2.5$ | full | $z = -16.12$m | muon triggering |
| Trigger station 2 | | | $z = -17.12$m | |

**Table 4.2:** Position, geometrical coverage and main purpose of the ALICE subdetectors. Adapted from [185].

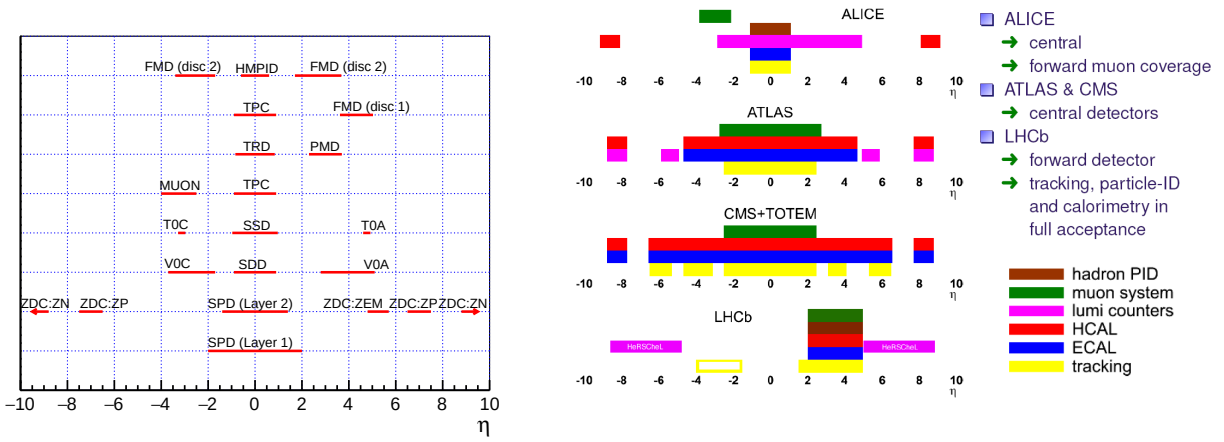


**Figure 4.4: Left**: Pseudorapidity coverage of the ALICE subdetectors. **Right**: Comparison of the geometrical acceptances of the main LHC experiments.

Technical Design Report [187] of the subdetectors and the various Physics Performance Reports [188, 189, 185] for more information.

## 4.3 Global detectors

The event characterisation in ALICE mostly relies on a set of detectors lying at large rapidities, both in the forward and backward regions. They provide general information on the event, such as the centrality, the reaction plane and the trigger decision. They participate as well in the evaluation of the luminosity, and the rejection of background induced by beam-gas interactions. A short description of these detectors is given here, along with selected examples of their usage and performances.

### 4.3.1 Constituents

- **Zero Degree Calorimeter (ZDC)** [190]: the ZDC is made of two identical sets of two hadronic calorimeters each: one for proton (ZP) and one for neutrons (ZN). The sets are located along the beam pipes, on both sides of the collision point, 113 m away from it. They aim at measuring the energy of the spectator nucleons for an estimation of the collision centrality. They are made of dense material slabs, in which silica optical fibres are embedded as active material, detecting the Cherenkov light produced by the charged particles of the shower created when a nucleon hits the calorimeter. The spectator protons are separated from the beam by the LHC beam optics, while spectator neutrons fly at zero degree without changing direction. The ZN have to sit in between the two beam pipes and have therefore the tightest geometrical constraints with a transverse dimension required to be smaller than 7 cm. A dense tungsten alloy was chosen as to maximise the shower containment. The ZP, sitting outside the pipes, is made of larger, less expensive brass absorbers.

The two sets are completed by an electromagnetic calorimeter, the ZEM, placed at large rapidity on the A-side. Made of lead and quartz fibres, it is used to remove ambiguities in the centrality determination: in peripheral collisions many nucleons remain bound in large nuclear fragments that continue to travel in the beam pipe without being detected by the ZDC, having a magnetic rigidity close to that of the beam. The ZEM helps resolving such ambiguities by providing an estimation of the number of participant nucleons. By comparing the energy measured by the ZEM with the one measured by ZN and ZP, one is comparing the number of participant and spectator nucleons from which the centrality of the collision can be evaluated.

- **Photon Multiplicity Detector (PMD)** [191]: the PMD is a particle shower detector, placed on the A-side at 3.6 m from the collision point. It is made of two identical planes of closely packed hexagonal proportional counters, filled with an Ar+$CO_2$ mixture and encompassing a thick lead converter. The plane behind the converter registers hits from photons and charged particles, while the plane in front of it is used for vetoing charged particles, as to disentangle the photon signal. The PMD enables the measurement of the photon multiplicity and spatial distribution (in the $\eta - \phi$ space) and helps providing an estimation of the transverse electromagnetic energy and reaction plane of the event.

- **ALICE Diffractive (AD)** [192]: the AD detector was installed during the first long shutdown of the LHC, between 2013 and 2014. It is composed of two stations installed on each side of the interaction point at very large rapidities. The stations contains two layers of 4 scintillators plastics of about $18 \times 21$ cm$^2$ each. The light generated by charged particles hitting the scintillators is converted by photomultipliers. The AD aims at extending the acceptance for low diffractive masses, it also improves the trigger efficiency for Minimum Bias events.

- **Forward detectors: Forward Multiplicity Detector (FMD), T0, V0** [193]: the conventional denomination of "forward detectors" actually regroups three apparatus, all sitting at large rapidities: the FMD, T0 and V0. They result from the splitting of the initially preferred solution of a unique device for fast triggering and multiplicity information in the forward and backward regions.

  **FMD** The FMD consists of five rings of silicon strip detectors, each containing 10 240 silicon sensors regrouped in 10 or 20 wafers. It aims at evaluating the charged particle multiplicity at large rapidities. Together with the Inner Tracking System of the central barrel, they provide an early multiplicity measurement, fully covering the $-3.4 < \eta < 5.1$ range and for all collision systems. The FMD also participates in the evaluation of correlations, the collective flow and the reaction plane of the event.

  **T0** The T0 is made of two arrays of 12 Cherenkov counters each, asymmetrically placed on the A- and C-side at $z = 375$ cm and $z = -72.7$ cm respectively. Its time resolution of about 50 ps makes it useful for fast triggering, providing a wake-up signal to the Transition

Radiation Detector and delivering a collision time reference to the Time-Of-Flight. The measurement of the vertex position with a precision of $\pm 1.5$ cm yields a fast trigger by confirming the position of the interaction point within pre-defined limits. Coupled to a measurement of the particle multiplicity, it generates three possible trigger signals: minimum bias, semi-central and central. The T0 is also used as a reference in Van Der Meer (vdM) scans for the evaluation of the visible cross section.

**V0** The V0 consists of two arrays of scintillator tiles, each segmented in 4 concentric rings and 8 sectors of 45° in azimuth, asymmetrically placed around the collision point at $z = 340$ cm (V0-A) and $z = -90$ cm (V0-C). The main goals of the V0 are to provide an online trigger through the coincidence of a signal in the two arrays, as well as background-rejection capabilities. It is used to provide a wake-up signal to the Transition Radiation Detector (TRD) of the central barrel. The measured signal amplitude is used for the determination of the centrality via a Glauber model fit, and the measurement of the particle time-of-flight between the two arrays helps to discriminate again beam-gas interactions. As for the T0, the V0 participates in the evaluation of the visible cross section by means of vdM scans.

### 4.3.2 V0-based triggering and beam-gas rejection

One of the main goal of the V0 is to provide a Minimum Bias (MB) trigger for all collision systems and centrality-based triggers in AA collisions. The V0-based triggers used throughout the ALICE operating since 2009 are listed in Table 4.3. The measurement of the time-of-flight between the two arrays allows as well an efficient rejection of background signals from beam-gas interactions.

| Trigger name | Condition |
|---|---|
| MB-`OR` | signals in V0 and SPD (obsolete) |
| MB-`AND` | signals in V0-A and V0-C |
| MBZ | MB and signal in both ZDC |

**Table 4.3:** Minimum Bias triggers provided by the V0.

In the 2009 and 2010 pp periods, the MB-`OR` trigger was used, requiring a signal in the central barrel Silicon Pixel Detector (SPD, corresponding to the two innermost layers of the ITS) or in either of the two arrays of the V0. With the increase of luminosity and background after 2010, the high-efficiency MB-`OR` was replaced by the high-purity MB-`AND`, requiring hits in both arrays. The triggering on MB events can be extended with the requirement of having also a signal from the two arrays of the ZDC. On top of the MB triggers, the V0 provides centrality-based triggers through the application of thresholds on the summed-up signals. Several amplitude triggers can be defined, corresponding to various centrality ranges of interest, among which the 0–10%, 0–50% and 30–50% ranges are commonly used. The left panel of Figure 4.5 shows the number of recorded events, for MB and two centrality classes, in Pb–Pb collisions at $\sqrt{s_{\mathrm{NN}}} = 5.02$ TeV in 2015 and 2018.

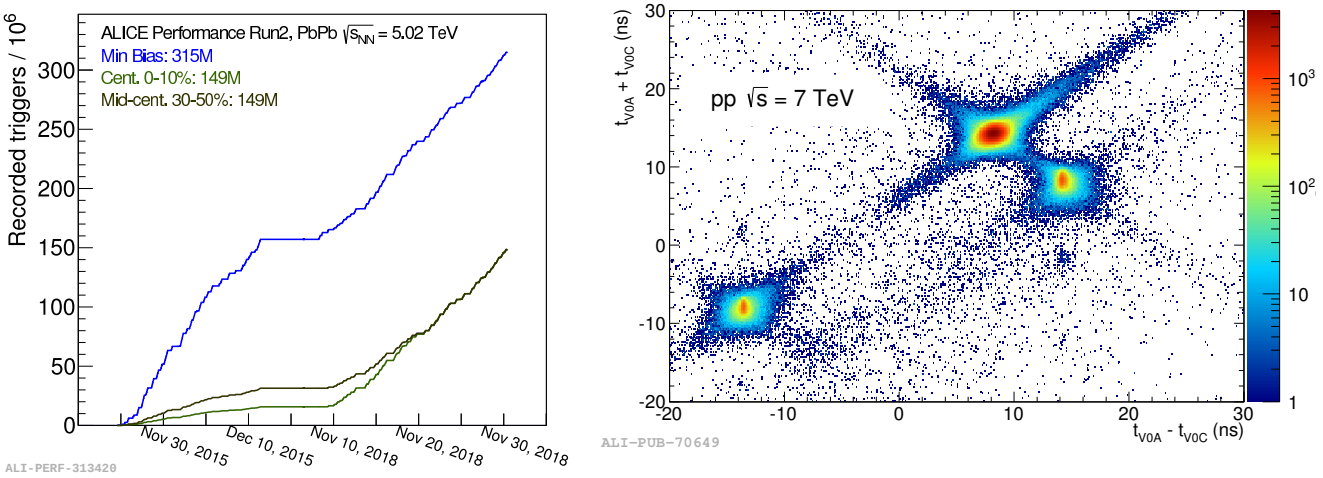


**Figure 4.5: Left**: Number of recorded events for MBZ and centrality-based triggers from the V0, as a function of time in Pb–Pb collisions at $\sqrt{s_{\rm NN}}$ = 5.02 TeV. **Right**: Correlation between the sum and difference of signal times in V0-A and V0-C in pp collisions at $\sqrt{s_{\rm NN}}$ = 7 TeV. The collision events at (8.3 ns, 14.3 ns) can be distinguished from the background from beam 1 at (-14.3 ns, -8.3 ns) and beam 2 at (14.3 ns, 8.3 ns). Figure taken from Ref. [185].

The LHC beam pipes feature a very high, yet non-perfect vacuum which constitutes a source of background through the interaction between the beams and the residual gas in the pipes. This source can be efficiently reduced thanks to the two arrays of the V0, by measuring the time-of-flight of particles on each side and applying an offline selection. This measurement, in pp collisions at $\sqrt{s_{\rm NN}}$ = 7 TeV, is shown in the right panel of Figure 4.5. At the front-end electronics level, a coincidence window of 8 ns is placed around the beam-beam timing in order to select beam-beam events and reject a great part of the beam-gas events. Since the 2012 run, this selection criterion is also partially applied at the hardware level.

### 4.3.3 Luminosity and visible cross sections

In scattering theory the luminosity $\mathcal{L}$ is the ratio of the number of events $N$ detected per unit of time ($\mathrm{d}N/\mathrm{d}t$) to the total inelastic cross section $\sigma_{\rm inel}$. It has the dimension of events per area per time ($\mathrm{m}^{-2}\mathrm{s}^{-1}$), often expressed with the non-SI units of barn: $\mathrm{b}^{-1}\mathrm{s}^{-1}$. The integral of $\mathcal{L}$ with respect to time defines the integrated luminosity $\mathcal{L}_{\rm int}$:

$$\mathcal{L} = \frac{1}{\sigma_{\rm inel}}\frac{\mathrm{d}N}{\mathrm{d}t}, \qquad \mathcal{L}_{\rm int} = \int \mathcal{L}\mathrm{d}t. \tag{4.1}$$

Its evaluation in ALICE for a given data sample is based on the visible cross section $\sigma_{\rm vis}$ seen by a detector. One needs to define a class of inelastic events satisfying a given trigger condition, hereafter referred to as the reference process. The visible cross section is a fraction of $\sigma_{\rm inel}$:

$$\sigma_{\rm vis} = \epsilon \times \sigma_{\rm inel}, \tag{4.2}$$

where $\epsilon$ is the fraction of inelastic events satisfying the trigger condition. Once $\sigma_{\rm vis}$ is measured, the luminosity can be evaluated as the ratio between the rate $R$ of the reference process and the visible cross section:

$$\mathcal{L} = \frac{R}{\sigma_{\rm vis}}. \tag{4.3}$$

With this procedure one does not need to know $\epsilon$, and the measurement of $\sigma_{\rm vis}$ provides an absolute normalisation factor for indirect luminosity determination in data analysis.

The visible cross section of a chosen reference process can be measured by means of vdM scans [194, 195], in which the two beams are moved across each other in the $x$ and $y$ directions (in the horizontal and vertical planes respectively). The $x$ and $y$ scans are performed separately, the beams being head-on in the other direction. At a circular collider, the measurement of the rate of the reference process as a function of the beam separation $\Delta x$ and $\Delta y$ allows one to determine the head-on luminosity for a pair of colliding bunches with particle intensities $n_1$ and $n_2$ as:

$$\mathcal{L} = \frac{n_1 n_2 f_{\rm rev}}{h_x h_y}, \tag{4.4}$$

where $f_{\rm rev}$ is the collider revolution frequency and $h_x$ and $h_y$ are the effective beam widths in the $x$ and $y$ directions. They are measured as the area below the $R(\Delta x, 0)$ and $R(0, \Delta y)$ curves normalised to the head-on rate $R(0, 0)$. Using the latter and the luminosity computed with Equation 4.4, and solving Equation 4.3, one can evaluate $\sigma_{\rm vis}$.

Coincidence between signals in the two arrays of the V0 (i.e. the MB-`AND` trigger) and the T0 provide useful reference processes for the evaluation of $\sigma_{\rm vis}$ [196]. In the T0 case, an additional criterion requests that the longitudinal coordinate of the interaction vertex is within $\pm$ 30 cm of the nominal collision point. This criterion is applied through the time difference of the signals in T0-A and T0-C, and aims at rejecting beam-gas and satellite background. Signal in one of the ZDC neutron calorimeters can also be used as reference, providing a sensitivity to both electromagnetic dissociation events with single- or double-sided neutron emission, and hadronic events. Figure 4.6 shows an example of visible cross section measurement in p–Pb collisions, using V0- and T0-based reference processes.

### 4.3.4 Centrality determination

The centrality $c$ is defined as the percentage of the total hadronic cross section, which experimentally corresponds to either a particle multiplicity $N_{\rm ch}$ or an energy deposition in the ZDC $E_{\rm ZDC}$, as measured by the detector, above or up to a certain threshold $N_{\rm ch}^{\rm thr}$ or $E_{\rm ZDC}^{\rm thr}$:

$$c \approx \frac{1}{\sigma_{\rm AA}} \int_{N_{\rm ch}^{\rm thr}}^{\infty} \frac{{\rm d}\sigma}{{\rm d}N_{\rm ch}} {\rm d}N_{\rm ch} \approx \frac{1}{\sigma_{\rm AA}} \int_{0}^{E_{\rm ZDC}^{\rm thr}} \frac{{\rm d}\sigma}{{\rm d}E_{\rm ZDC}} {\rm d}E_{\rm ZDC}. \tag{4.5}$$

The procedure for the centrality estimation in ALICE is briefly summarised here. More details can be found in Ref. [197] and references herein.

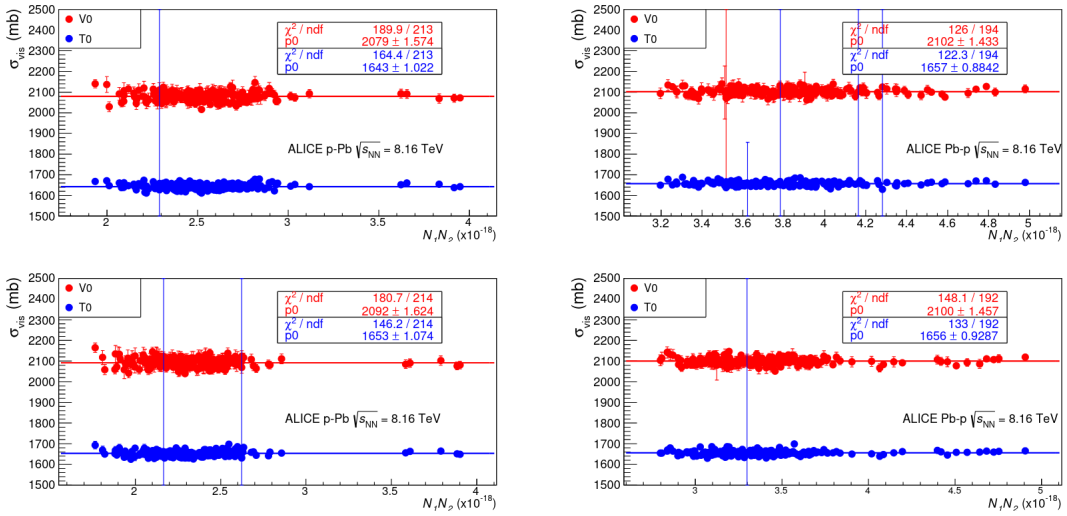


**Figure 4.6:** Visible cross sections for the V0 (red) and T0 (blue) processes measured in vdM scans in p–Pb (left) and Pb–p (right) collisions at $\sqrt{s_{\mathrm{NN}}} = 8.16$ TeV, as a function of the product of the colliding bunches intensities. The top and bottom plots correspond to two different scans, the solid line is a constant fit to the data. Figure taken from [196].

The centrality related geometrical quantities, $N_{\mathrm{part}}$ and $N_{\mathrm{coll}}$, corresponding to the number of participant nucleons and binary collisions respectively (see Section 2.3), are usually obtained by means of Monte Carlo implementations of the Glauber model [85]. The nucleon position $\rho(r)$ in the nucleus is modelised stochastically using a modified Woods-Saxon (or 2-parameter Fermi) distribution, and the Glauber MC is coupled to a Negative Binomial Distribution (NBD) [198] to ensure an adequate reproduction of the data. The parameters of the resulting, so called NBD-Glauber model are determined by fitting the amplitude of the signal collected in the V0, as illustrated in Figure 4.7. The mean number of participants $\langle N_{\mathrm{part}} \rangle$ and binary collisions $\langle N_{\mathrm{coll}} \rangle$ can then be calculated for centrality classes defined by sharp cuts in the simulated V0 distribution.

While this method provides an efficient evaluation of the centrality in Pb–Pb collisions, it suffers from an important caveat in p–Pb, namely the multiplicity fluctuations [200]. For p–Pb collisions, those fluctuations are sizeable compared to the width of the $N_{\mathrm{part}}$ distribution, a centrality selection based on multiplicity may then select a sample of nucleon-nucleon collisions which is biased compared to a sample defined by cuts on the impact parameter $b$. The NBD-Glauber fit itself allows one to quantify this effect. In the left panel of Figure 4.8 is shown the ratio between the average multiplicity per average participant to the average multiplicity of the NBD-Glauber fit as a function of centrality. As expected, the ratio does not deviate from unity when the classes are defined by a selection on $b$. In Pb–Pb, the ratio deviates for the most peripheral collisions only, reflecting the fact that the width of the plateau of the $N_{\mathrm{part}}$ distribution is large with respect to multiplicity fluctuations. On the contrary, in p–Pb collisions and for multiplicity-based estimators, large deviations are found both in the central and peripheral regions.

This motivated the development of the so-called hybrid method, aiming at providing an unbi-

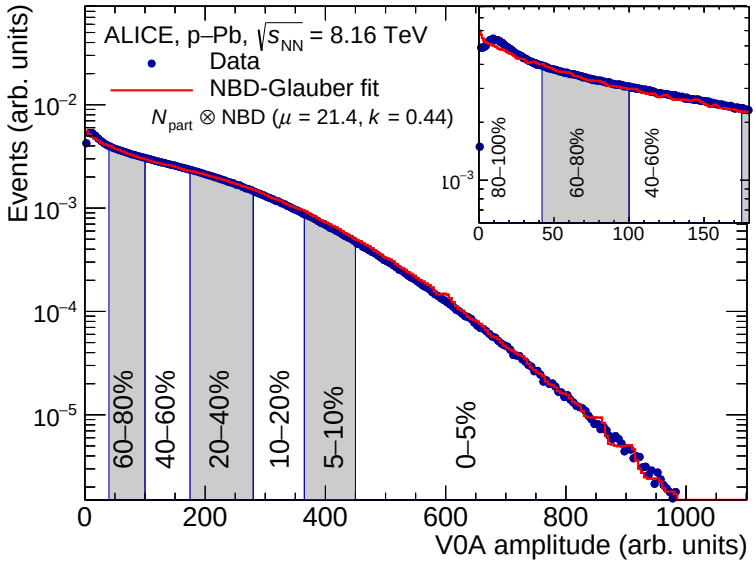


**Figure 4.7:** Distribution of the sum of amplitudes in V0-A (Pb-going side) for p–Pb collisions at $\sqrt{s_{\rm NN}}$ = 8.16 TeV. The distribution is fitted with the NBD-Glauber model, shown as a line. The insert shows a zoom of the most peripheral region. The failure of the NBD-Glauber fit at very low amplitude reflects the trigger inefficiencies in peripheral collisions. Figure taken from Ref. [199].

ased centrality estimator. The method, described in Ref. [200], relies on two assumptions:

- the energy deposited in the ZDC is free from the multiplicity bias,
- some observables scale linearly with $N_{\rm coll}$ and $N_{\rm part}$, according to the wounded nucleon model [201, 202].

Two such observables are used, either assuming that the charged-particle multiplicity at mid-rapidity is proportional to $N_{\rm part}$, or that the target-going (here the Pb ion) charged-particle multiplicity is proportional to the number of wounded target nucleon (with $N_{\rm part}^{\rm target} = N_{\rm part} - 1 = N_{\rm coll}$ in p–Pb). These two assumptions lead to the computation of two sets of $\langle N_{\rm coll} \rangle$: $\langle N_{\rm coll}^{\rm mult} \rangle$ in the former case and $\left\langle N_{\rm coll}^{\rm Pb-side} \right\rangle$ in the latter. In the right panel of Figure 4.8 is shown the effect of using the hybrid method for the centrality evaluation in p–Pb collisions. The charged-particle multiplicity, scaled to $\langle N_{\rm part} \rangle$, shows a flat trend which one can extrapolate to the pp measurement (black point). Table 4.4 reports the value of $\langle N_{\rm coll} \rangle$ obtained with the two methods for various centrality classes.

## 4.4 Central barrel

The central barrel of ALICE, sitting in the mid-rapidity region, contains three main ensembles. The tracking system (ITS and TPC) provides a measurement of the primary vertex position and enables the tracking and identification of charged particles. The particle identification system (TRD, TOF

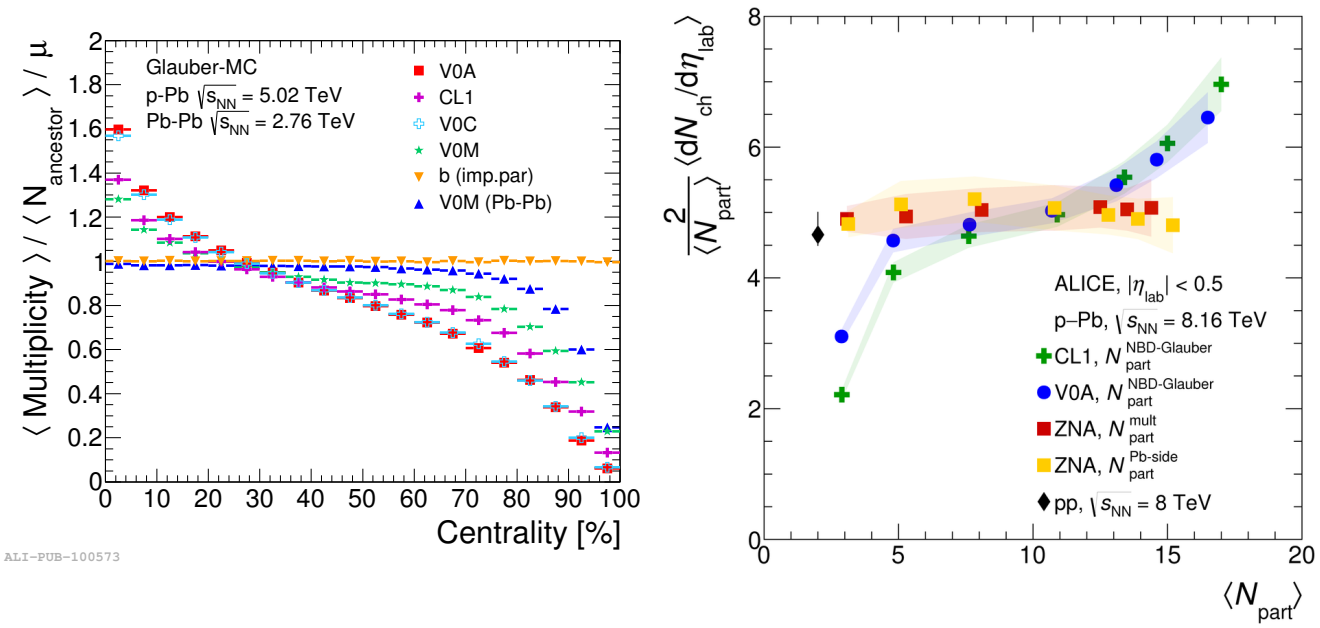


**Figure 4.8: Left**: Multiplicity fluctuation bias quantified as the mean multiplicity per average participant over the average multiplicity of the NBD-Glauber fit $\mu$ as a function of centrality. Figure taken from Ref. [200]. **Right**: Charged particle multiplicity normalised to the average number of participant $\langle N_{\rm coll} \rangle$ for different centrality estimators, in p–Pb collisions at $\sqrt{s_{\rm NN}} = 8.16$ TeV. The same quantity measured in pp collisions at $\sqrt{s_{\rm NN}} = 8$ TeV is given for reference. Figure taken from Ref. [199].

| Centrality (%) | $\langle N_{\rm coll}^{\rm mult} \rangle$ | $\left\langle N_{\rm coll}^{\rm Pb-side} \right\rangle$ | syst. (%) |
|---|---|---|---|
| 0–5 | 13.4 | 14.2 | 6.4 |
| 5–10 | 12.5 | 12.9 | 3.9 |
| 10–20 | 11.5 | 11.8 | 3.4 |
| 20–40 | 9.81 | 9.77 | 2.3 |
| 40–60 | 7.09 | 6.83 | 4.3 |
| 60–80 | 4.28 | 4.09 | 4.9 |
| 80–100 | 2.08 | 2.13 | 3.3 |

**Table 4.4:** Average number of collisions $\langle N_{\rm coll} \rangle$ evaluated from the multiplicity either at midrapidity or on the Pb-side ($\langle N_{\rm coll}^{\rm mult} \rangle$ and $\left\langle N_{\rm coll}^{\rm Pb-side} \right\rangle$ respectively) with the hybrid method, in p–Pb collisions at $\sqrt{s_{\rm NN}} = 8.16$ TeV. Table adapted from Ref. [197].

and HMPID) supports the PID capabilities of the tracking system, notably by improving the separation of protons, kaons, pions and electrons over a wide $p_{\rm T}$ range. Finally, the calorimetry system (PHOS, EMCAL and DCAL) extends the measurement in the central barrel to neutral particles. The central barrel is immersed in a low magnetic field ($\leq 0.5$ T) delivered by the L3 magnet.

### 4.4.1 Detector layout

- **Inner Tracking System (ITS)** [203]: the ITS consists of six layers of silicon detectors, covering $|\eta| < 2$ for the innermost layer and $|\eta| < 1.4$ for the outermost one, located at $r = 3.9$ cm and $r = 43$ cm respectively. The six layers are regrouped in three subsystems, from the inside out one finds: two layers of Silicon Pixel Detectors (SPD), two layers of Silicon Drift Detectors (SDD) and two layers of Silicon Strip Detectors (SSD). The ITS aims at measuring primary and secondary vertices, participating to the particle identification, supporting the tracking capabilities of the TPC at low momenta and providing a measurement of the multiplicity at mid-rapidity. Combined with the FMD, it allows for a continuous measurement of the multiplicity in the range $-3.4 < \eta < 5.1$. While the six layers operate together at a low frequency (100 Hz) to match the pace of the central barrel, the SPD can run at higher rate (1 kHz) in order to provide the vertex information to the faster-paced muon spectrometer.

- **Time-Projection Chamber (TPC)** [204]: the TPC is a 90 $m^2$ cylinder filled with an Ar+$CO_2$ gas mixture, divided into two drift sectors by a central electrode. The end caps are structured into 18 trapezoidal regions on each side, equipped with multi-wire proportional chamber with cathode pad readout. The magnetic field delivered by the L3 magnet, coupled to the size of the TPC which longitudinal extension amounts to about 500 cm, leads to a drift time of 88 $\mu$s, limiting the recording rate in the central barrel. The TPC is the main device for particle identification and charged particle tracking at mid-rapidity. In combination with the ITS, it provides as well a precise measurement of the vertex position, even in the large-multiplicity environment created in heavy-ion collisions.

- **Transition Radiation Detector (TRD)** [205]: the TRD is composed of 540 modules, each containing a 4.8 cm thick radiator and a multiwire proportional chamber with cathode pad readout. They are regrouped in 18 sectors of 6 layers with a 5-fold segmentation along the beam direction. The TRD was designed for electron identification through electron-pion discrimination, and in combination with the ITS and TPC it allows for the measurement of vector meson resonances and open heavy flavors.

- **Time-Of-Flight (TOF)** [206, 207]: the TOF detector consists of multigap resistive plate chambers arranged in 18 sectors in azimuth and 5 sectors along $z$. They feature a high and uniform electric field over the sensitive volume, such that any traversing particle immediately triggers an avalanche, generating signals picked-up by electrodes. With a time resolution better than 40 ps and an efficiency close to 1, the TOF is able to identify protons, pions and kaons in the intermediate momentum range.

- **High-Momentum Particle Identification Detector (HMPID)** [208]: the HMPID is composed of 7 proximity-focusing ring imaging Cherenkov counters of about 1.5 $\times$ 1.5 $m^2$ each, providing a partial azimuthal coverage of 58°. The Cherenkov radiation is emitted when a charged particle crosses the 15 mm thick perfluorohexane radiators and collected by photon counters made of multiwire pad chambers. The HMPID extends the TOF identification of protons, kaons and pions to higher momenta.

- **Calorimeters: PHOton Spectrometer (PHOS), ElectroMagnetic CALorimeter (EMCAL), Di-jet CALorimeter (DCAL)** [209, 210, 211]: outside of the HMPID sits a set of calorimeters with partial azimuthal coverages, extending the detection and tracking abilities of ALICE to photons and jets. Initially composed of the PHOS and EMCAL, the set was completed during the first long shutdown of the LHC (LS1) with the DCAL, installed back-to-back in azimuth with the EMCAL, to achieve correlation analysis.

  **PHOS** The PHOS is composed of an ElectroMagnetic Calorimeter (EMC) made of highly-segmented, dense lead-tungstate crystals. The electromagnetic shower created when a particle hits the EMC is detected by avalanche photodiodes. As to discriminate between charged and neutral particles, a Charged Particle Veto (CPV), made of multiwire proportional chambers with cathode pad readout, is installed in front of the EMC. The 99% efficiency of the CPV allows the PHOS to measure photons and neutral mesons in their photonic decays in a large momentum range.

  **EMCAL and DCAL** The EMCAL and DCAL (commonly referred to as EMCAL) are layered Pb-scintillators sampling calorimeters with alternating layers of 1.44 mm of lead and 1.76 mm of polystyrene scintillators, in which electromagnetic particles lose their energy via a combination of brehmsstrahlung radiation and pair creation. The EMCAL enhances ALICE's capabilities to measure jets and high-momentum photons and electrons. The addition of DCAL at opposite azimuth from EMCAL, thus forming a two-arm calorimeter, enables the study of back-to-back correlations where jets are involved. The EMCAL also serves for triggering on high-energy jets.

- **ALICE COsmic Ray DEtector (ACORDE)** [212]: on top of the $L_3$ magnet sits ACORDE, a scintillator array for triggering on cosmic rays. 60 modules are distributed on the three upper surfaces of the magnet. Each contains two $0.2 \times 2$ m$^2$ paddles of plastic scintillators arranger in a doublet configuration. The trigger hit is provided by a coincidence signal in the two paddles within a time window of 40 ns. The signal can be used for the calibration, alignment and performance studies of other ALICE tracking devices (ITS, TPC and TRD), which tracking precision enables the recording of interesting cosmic events with very high multiplicity of parallel muon tracks, the so-called muon bundles.

### 4.4.2 Primary vertex reconstruction

The determination of the primary vertex relies on the preliminary estimation made by the SPD, which is afterwards constrained using the tracks reconstructed by the tracking systems of the central barrel.

A first estimation is performed by looking at tracklets in the innermost layers of the ITS. Two hits in the SPD layers, having similar azimuthal angles, are assumed to come from the same source and define a tracklet. By linear extrapolation, a preliminary estimation of the corresponding

track is estimated. Due to the presence of the bending magnet, the linear extrapolation is an approximation, but the proximity of the SPD to the nominal collision point allow for a precise enough estimation with this procedure. For a given event, a first evaluation of the primary vertex is performed by fitting all the tracks for their crossover point. As to account for a possible pile-up, in which several collisions happen in a small enough time window such that they are mixed into a single event, the fitting procedure is iterated, discarding at each step the tracks participating to the determination of the previous vertex. By construction, the first vertex found has the largest number of contributing tracks and is taken as the primary one. As the SPD is able to operate at a rate higher than the one of the other ITS layers, its estimation of the vertex is available for the muon spectrometer. The precision of the estimation is high enough to be used as a constraint in the first tracking pass.

The position of the vertex is more precisely determined in a second step, from the tracks reconstructed by the TPC and the full ITS. The same procedure is followed, extrapolating the tracks to the collision region and fitting the distribution of validated tracks. Figure 4.9 shows the width of the luminous region (the region over which the events are distributed) in the transverse ($x$) and longitudinal ($z$) directions, in pp and Pb–Pb collisions. The precision on the vertex position

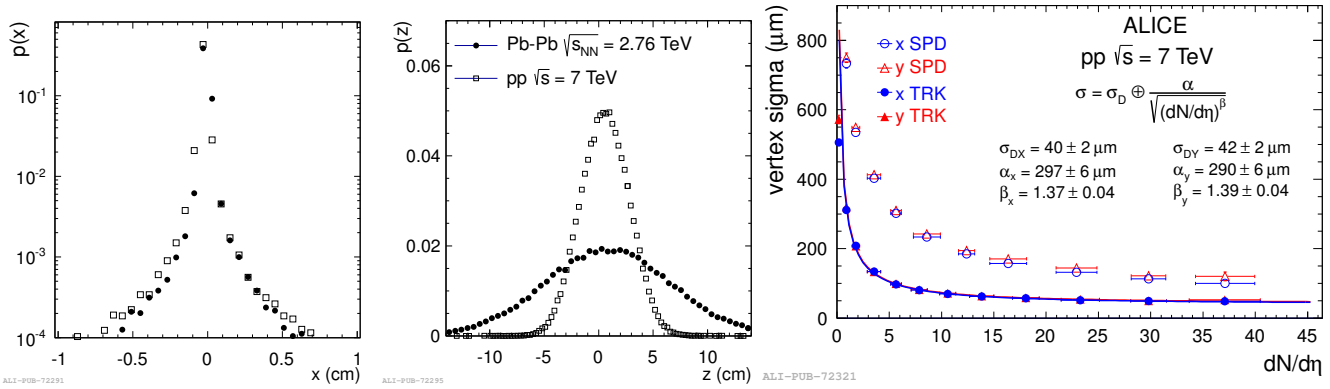


**Figure 4.9: Left and centre**: Transverse and longitudinal profiles of the luminous region obtained from the reconstructed vertices in pp and p–Pb collisions. **Right**: Widths of the final vertex distribution (solid points) in the transverse $(x, y)$ plane. For comparison, the width of the vertices evaluated by the SPD is shown as open points. All the figures are taken from Ref. [185].

depends on the finite size of the luminous region $\sigma_{\mathrm{D}}$ and the resolution on the vertex determination, itself depending on the particle multiplicity (indicating the number of tracks available for the determination) and the fit parameters:

$$\sigma_{\mathrm{vtx}} = \sigma_{\mathrm{D}} \oplus \frac{\alpha}{\sqrt{(\mathrm{d}N/\mathrm{d}\eta)^{\beta}}}. \tag{4.6}$$

The resolution, as a function of the particle multiplicity, is shown in the rightmost panel of Figure 4.9. The solid points correspond to the precision of the final vertex, determined from the tracks reconstructed in the central barrel. For comparison, the widths of the preliminary vertices estimated from the SPD tracklets is shown as open points.

### 4.4.3 Charged track reconstruction

The procedure for track reconstruction in the central barrel is illustrated in Figure 4.10. It relies on a three-stages inward-outward-refit sequence [213, 214], starting in the TPC and adding more and more information at each step, up to the precise determination of the track nature, spatial characteristics and quality.

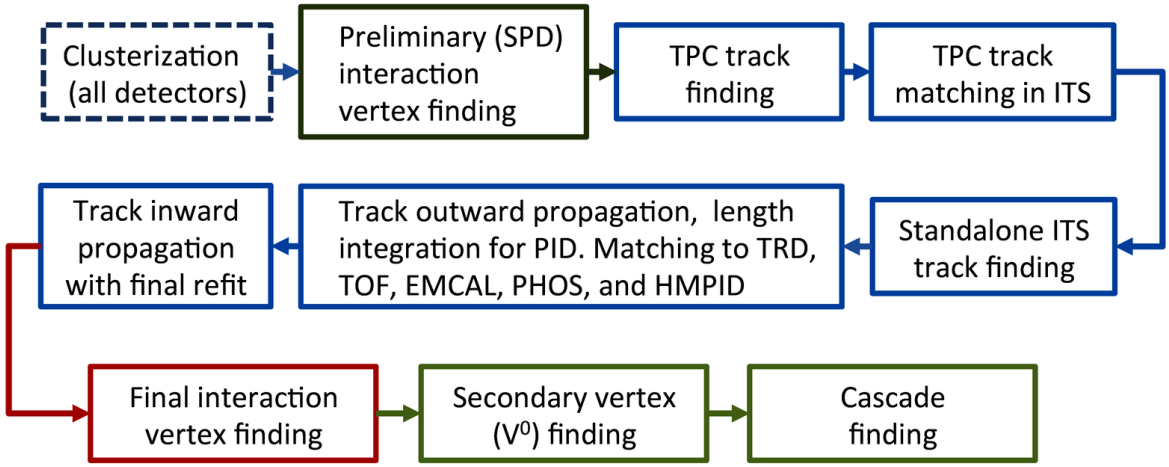


**Figure 4.10:** Event reconstruction flow in the central barrel.

The procedure starts with the clusterisation, in which the raw data of the detectors are converted into so-called clusters containing the position of the signal, its amplitude, time, etc. with the associated errors. In the TPC, at large radius, clusters are associated in order to build track seeds. A seed consists in either two points in the TPC associated to a constraint from the preliminary vertex evaluation by the ITS, or three points in the TPC without the vertex constraint. The track finding and fitting then employs the Kalman filter [215], starting from the outermost pads of the TPC and propagating the track candidate inwards by looking for hits in the nearest clusters fulfilling a proximity cut. The Kalman filter follows three steps at each stage:

1. take as input a track candidate as a state vector containing the track parameters and their covariance matrices, which are propagated to the next pad row in the TPC;

2. add to the inverted covariance matrix, representing the current state of knowledge on the track parameters at this point, a noise term accounting for the loss of information due to stochastic processes (multiple scatterings, energy loss fluctuations...);

3. update the track information if the point in the new pad is compatible with the track prolongation.

A first identification is performed at this stage thanks to the $\mathrm{d}E/\mathrm{d}x$ measurement. The TPC readout chambers contain 159 tangential pad rows, a track would ideally produce 159 hits when

crossing the active volume. After the first reconstruction pass, a quality selection is applied to the tracks, rejecting the ones without a minimum, pre-defined number of contributing pads (requiring typically 20 clusters, and more than 50% of the cluster expected for a given track position). The tracks reconstructed and validated in the TPC and then used as seeds for track reconstruction in the ITS. The procedure followed through the TPC readout pads is repeated for the 6 layers of the ITS. After all the layers have been considered, $\chi^2$-based checks are performed, aiming at resolving conflicts between tracks sharing one or several clusters, or selecting the best candidate among several hypotheses for a given track. Finally, the highest quality candidates are added to the reconstructed event. The left panel of Figure 4.11 shows the improvement of the resolution following the matching with ITS and application of the vertex constraint. The latter drastically improves the resolution of the TPC standalone tracks, while it has no effect on the ITS-TPC matched tracks.

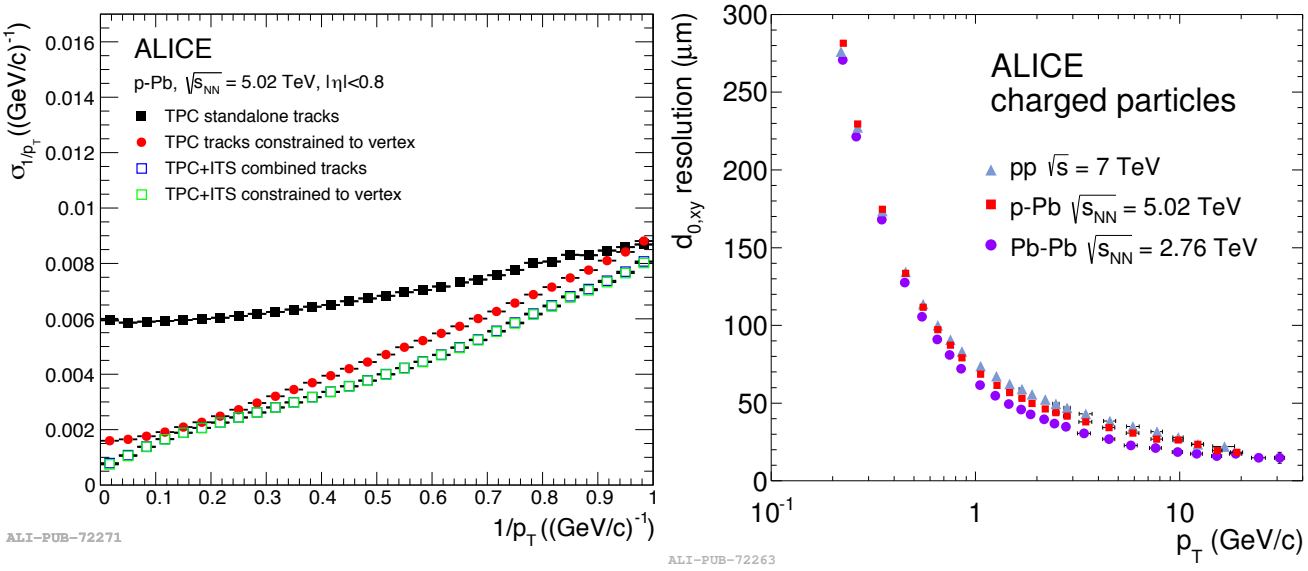


**Figure 4.11: Left**: $p_{\mathrm{T}}$ resolution for standalone TPC and ITS-TPC matched tracks with and without constraint to the vertex, in p–Pb collisions at $\sqrt{s_{\mathrm{NN}}} = 5.02$ TeV. The ITS-TPC matching and vertex constraint significantly improves the resolution. **Right**: Resolution of the transverse distance to the primary vertex for charged ITS-TPC matched tracks in pp, p–Pb and Pb–Pb collisions. Figures taken from Ref. [185].

After completion of the ITS tracking, the tracks are propagated to their point of closest approach to the preliminary interaction vertex, and the Kalman filter is reversed. Starting with much more precise parameters, the track are refitted in the outward direction, using the clusters found during the inward step. At this stage, some improperly assigned points can be discarded thanks to the precision. After reaching the TPC radius, an attempt is made to match the tracks with tracklets in the TRD and hits in the TOF and HMPID in order to refine the track identification, as well as EMCAL and PHOS. Finally, combining all the information, the tracks are propagated inwards and refitted one last time on the previously found clusters in the TPC and ITS. The

track's position, direction, inverse curvature and its associated covariance matrix are determined. The vertices are determined from this final set, the vertex producing the largest amount of tracks being considered as the primary vertex. The right panel of Figure 4.11 shows the final resolution of the transverse distance to the primary vertex for charged ITS-TPC matched tracks in pp, p–Pb and Pb–Pb collisions. One can notice the increase of precision in heavier systems, thanks to the higher multiplicity allowing for a better determination of the vertex.

### 4.4.4 Particle identification

The Particle IDentification (PID) in the central barrel proceeds in two steps. In the first one, the subdetectors, considered independently, are used to assign to each particle a set of probabilities, one for each type of particle. In a second step, those individual information are combined to improve the separation between particle species and assign a type to each track. The PID relies on different mechanism, depending on the detector and the particle species.

#### Hadrons

The hadron identification is performed using four subsystems, by means of three mechanisms:

- the specific energy loss $\mathrm{d}E/\mathrm{d}x$ in the ITS four outmost layers (SSD and SDD) and in the TPC, compared to predictions computed with the parametrised Bethe-Block equation,
- the measurement of the arrival time in the TOF, compared with the integral of the particle's time-of-flight computed for different mass hypotheses in the last tracking pass of the Kalman filter,
- the Cherenkov angle measurement in the HMPID, given by

$$\cos\theta = \frac{1}{n\beta}, \tag{4.7}$$

  where $\theta$ is the Cherenkov angle, $n$ the refractive index of the radiator and $\beta$ the particle velocity.

The PID through $\mathrm{d}E/\mathrm{d}x$ measurement in the TPC is illustrated in the left panel of Figure 4.12. The PID capabilities can be furthermore improved by combining several participating subdetectors. The right panel of Figure 4.12 shows the results of combining the difference between expected and measured PID signals in the TPC and the TOF. The kaon / pion separation can be extended by means of fits of the bidimensional distribution.

The usage of several subdetectors with different technical solutions allow for extending the hadron identification over a large momentum range. Figure 4.13 shows the $\mathrm{K}/\pi$ and $\mathrm{K/p}$ separation power of the four systems considered in this section, as a function of the particle $p_{\mathrm{T}}$, in Pb–Pb collisions. The separation is expressed as the distance $\Delta$ between the peaks divided by the Gaussian width $\sigma$ of the pion and kaon response. The lower panel in each figure shows the $p_{\mathrm{T}}$ range over which the detector have a separation power of more than $2\sigma$.

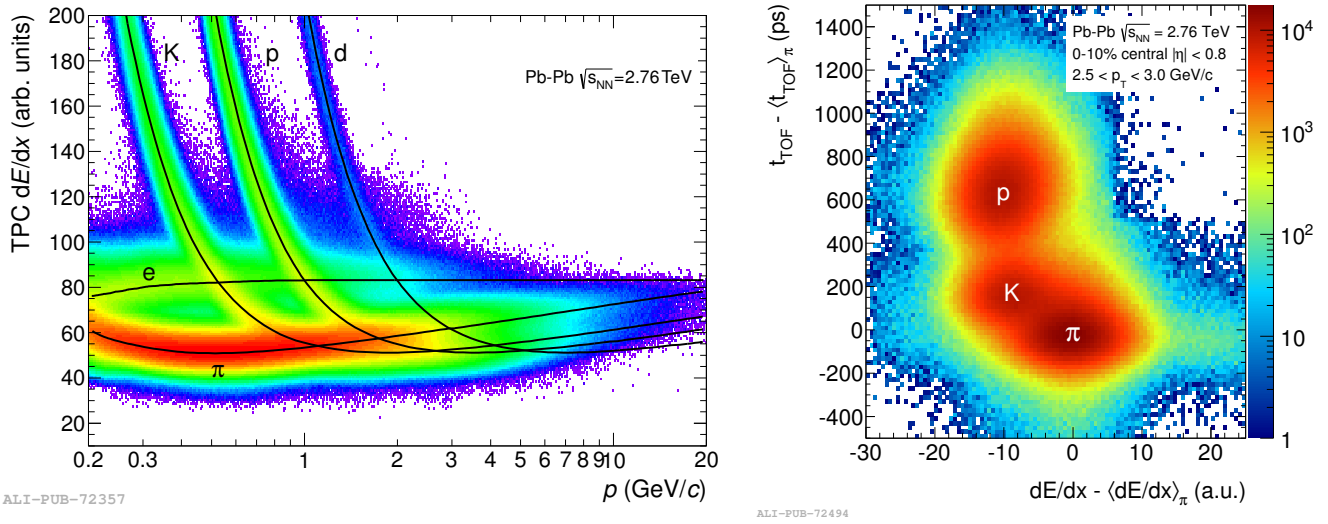


**Figure 4.12: Left**: Specific energy loss $\mathrm{d}E/\mathrm{d}x$ in the TPC as a function of the particle momentum, in Pb–Pb collisions at $\sqrt{s_{\mathrm{NN}}} = 2.76$ TeV. The lines correspond to parametrisations of the Bethe-Block equation. **Right**: K/$\pi$ separation by combining the arrival time measurement in TOF and $\mathrm{d}E/\mathrm{d}x$ in the TPC. Figures taken from Ref. [185].

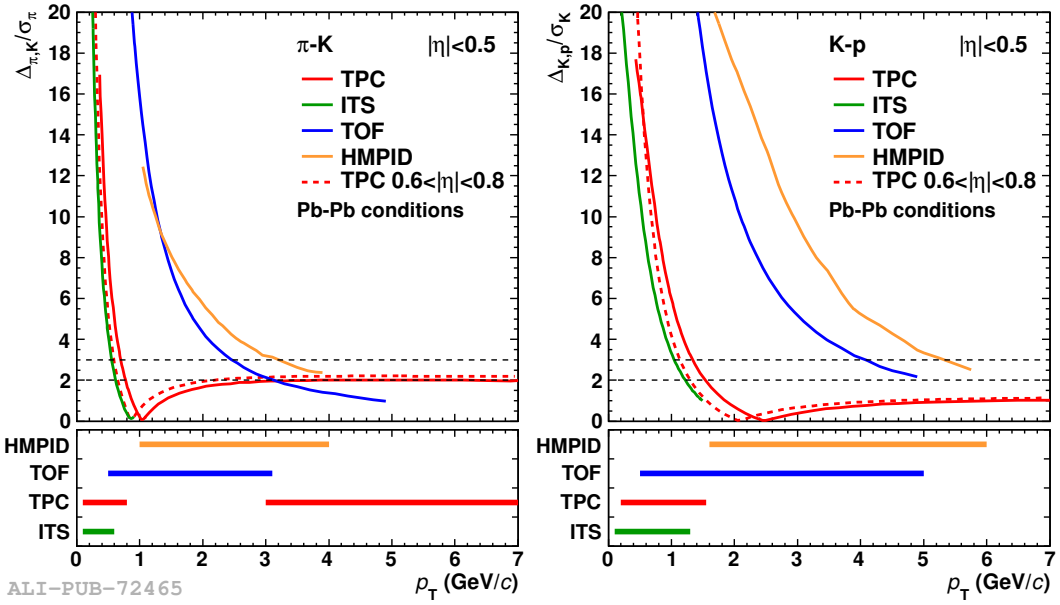


**Figure 4.13:** Kaon-pion (left) and kaon-proton (right) separation power of the ITS, TPC, TOF and HMPID systems as a function of the particle transverse momentum. The lower panels show the $p_{\mathrm{T}}$ range over which the system has a separation power higher than $2\sigma$. Figures taken from Ref. [185].

### Electrons

The detectors participating to the PID of hadrons also contribute to the identification of electrons. In addition, the EMCAL, PHOS and TRD have dedicated electron identification capabilities. The

electron PID in EMCAL and PHOS are based on the $E/p$ method, exploiting the fact that the electrons deposit their entire energy in calorimeters while hadrons only lose a small fraction of it. The ratio of the particle's energy to its momentum is therefore close to unity for electrons and much lower for hadrons, allowing one to disentangle the two signals. Figure 4.14 shows the $E/p$ distribution of the energy $E$ in the EMCAL clusters and the momentum $p$ of the reconstructed tracks from pp collisions at $\sqrt{s_{\rm NN}} = 7$ TeV in the intermediate $p_{\rm T}$ range, for electrons and pions. The measured distributions are compared to Pythia simulations of each process. As expected, the electrons signal is characterised by a peak close to 1, the lower tail expansion being due to brehmsstrahlung in the detector material in front of the EMCAL.

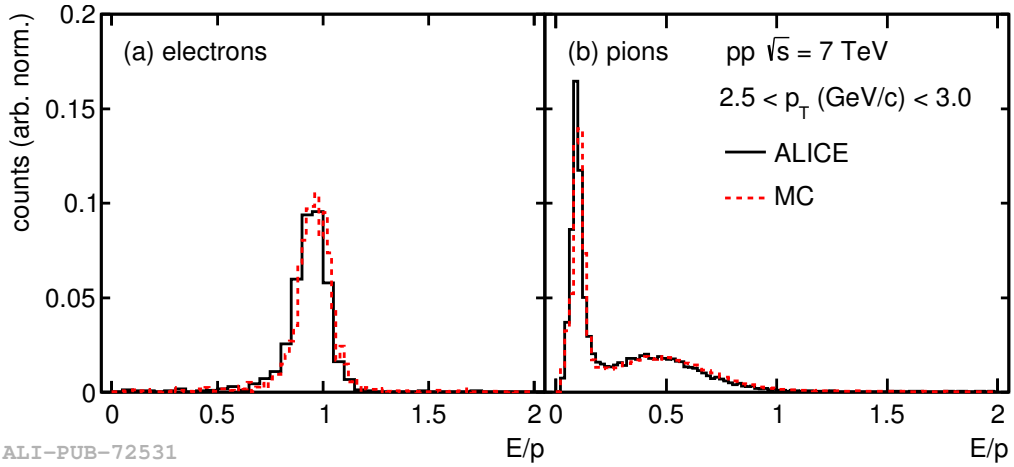


**Figure 4.14:** $E/p$ distribution for electrons (left) and pions (right) in the EMCAL, in pp collisions at $\sqrt{s} = 7$ TeV. The samples of identified electrons and pions are obtained from $\gamma$ conversion and $\Lambda/\mathrm{K}^0_{\mathrm{S}}$ decays respectively. The dotted lines correspond to Pythia simulations of each processes, with realistic detector configuration and full reconstruction. Figure taken from Ref. [185].

The electron identification in the TRD is based on $\mathrm{d}E/\mathrm{d}x$ measurement associated with their transition radiation, that is the emission of a radiation when a relativistic charged particle crosses the interface of two media with different dielectric constant. The emission is proportional to the relativistic Lorentz factor $\gamma$. At 1 GeV/$c$, $\gamma_e/\gamma_\pi \approx 2000/7$, enabling $e/\pi$ differentiation. The working principle of the TRD is illustrated in the left panel of Figure 4.15, while the right panel shows TRD signal, combining $\mathrm{d}E/\mathrm{d}x$ and transition radiation, in p–Pb collisions. The electron signal forms a bulk which is easily identified.

### Photons

Photon identification in the central barrel relies on two procedures: either the reconstruction of electromagnetic showers in the PHOS and EMCAL calorimeters, or the reconstruction of electron-positron pairs coming from the conversion of photons in the material of the inner detectors with the Photon Conversion Method (PCM).

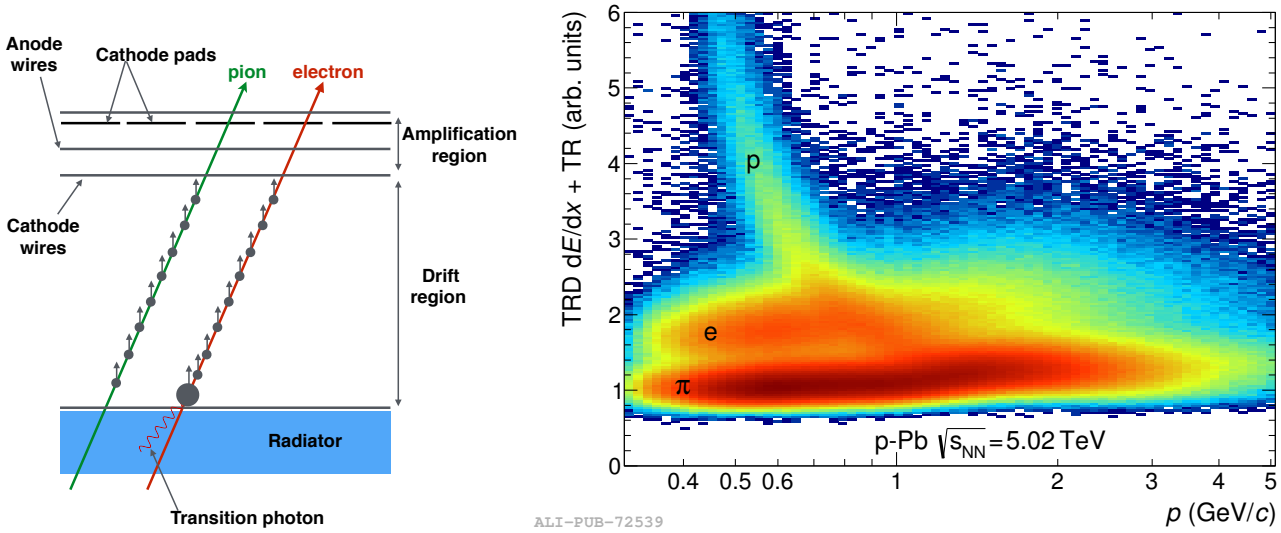


**Figure 4.15: Left**: Cross sectional view, in the $r - \phi$ plane, of one of the TRD layer, with the clusters produced by an electron and a pion track. **Right**: TRD signal ($\mathrm{d}E/\mathrm{d}x$ + transition radiation) as a function of the particle momentum, in p–Pb collisions at $\sqrt{s_{\mathrm{NN}}} = 5.02$ TeV, for protons from $\Lambda$ decays, charged pions from $\mathrm{K}^0_{\mathrm{S}}$ decays and electrons from $\gamma$ conversions. Figure taken from Ref. [185].

In the PHOS and EMCAL, the cluster finding algorithm starts from any cell measuring an energy deposit above a certain threshold. This threshold varies depending on the collision configuration, as to account for the probability of overlap being higher in Pb–Pb. Cells sharing a common edge with the first one, and measuring an energy above the noise level, are added to the cluster, until the full shower is isolated. A shower can be created either by a single electromagnetic or hadronic shower, or by an overlap of several ones. The latter case will be characterised by local maxima, i.e. several cells with large energy separated by at least one cell with lower energy. The presence of such a pattern initiates the so-called cluster unfolding algorithm, aiming at separating the various showers. Once the shower reconstruction is done, the photon identification in the calorimeters is performed following three criteria:

1. the shower should not match a charged-particle track reconstructed by the tracking system,
2. the shower shape parameters can be used to discriminate between photonic and hadronic showers,
3. the time-of-flight information should correspond to a fast particle and allow for the rejection of clusters produced by nucleons.

The application of several or all of these criteria depends on the requested purity of the sample, the procedure varies from one analysis to another.

Above 5 MeV, the interaction between photons and the detector material is dominated by conversion into electron-positron pairs, which can be precisely measured and reconstructed with

the ITS and TPC. As the conversion probability is highly dependent on the amount, geometry and composition of the material, an accurate knowledge of it is of utmost importance. The secondary vertex reconstruction, and the electron and positron detection and reconstruction, are performed as presented in the previous section. An extra selection is applied, requiring that the momentum vector of the leptons are almost parallel at the conversion point. The final candidates are selected following a constraint on the dilepton invariant mass and the opening angle between the reconstructed photon momentum vector and the vector joining the primary vertex and the conversion point. In the left panel of Figure 4.16, the invariant mass distribution of all secondary vertices, calculated with the electron mass hypothesis, is shown before and after the selection. The right panel of the figure shows, in the $(x, y)$ transverse plane, the distribution of the reconstructed conversion points, displaying a precise gamma-ray tomography of the inner detectors of ALICE.

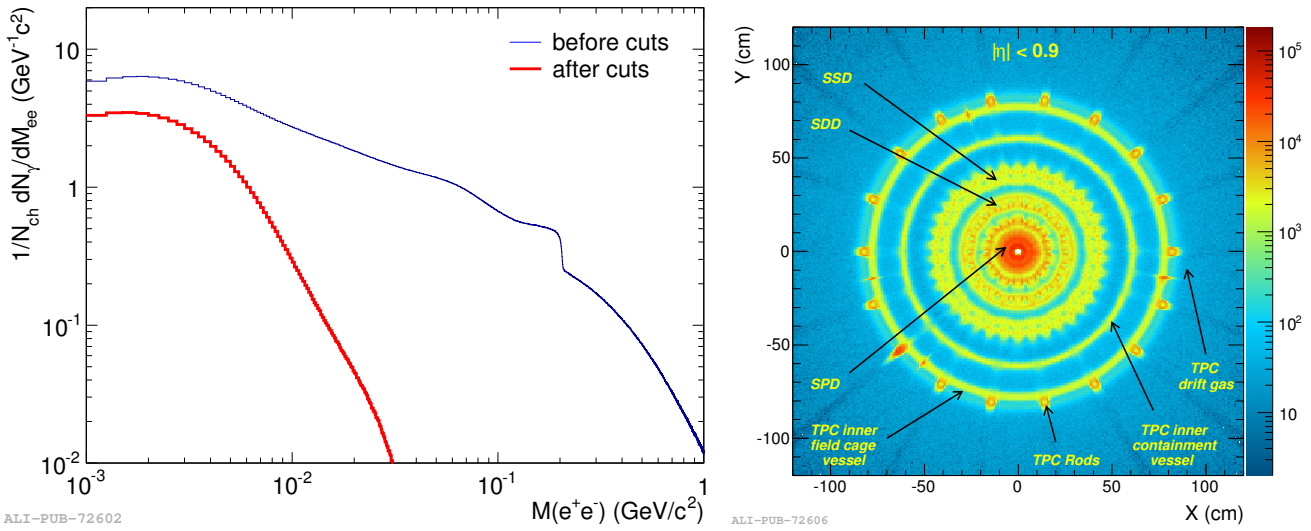


**Figure 4.16: Left**: Comparison between the dilepton invariant mass distribution before and after applying the selection. **Right**: Transverse distribution of the reconstructed photon conversion points for $|\eta| > 9$. The different layers of the ITS and inner parts of the TPC are clearly visible. Figures taken from Ref. [185].

### Jets

The measurement of jets in heavy-ion collisions offers an efficient way to probe the hot medium through the jet quenching phenomenon. As the initial parton travels through the medium before its fragmentation, it loses energy by means of brehmsstrahlung and collisional energy loss. The in-medium fragmentation and hadronisation may be modified as well. Following this, the energy and substructure of the jet is modified in heavy-ion collisions to that of pp collisions, providing a probe of the QGP properties [216].

Experimentally, a jet is specified in terms of a reconstruction algorithm [217, 218] that clusters hadrons within a cone of specified distance $R$ in the angular space. As to ensure that the algorithm

is applicable to both experimental data and theoretical calculations, it is expected to be collinear- and infrared-safe (respectively meaning that the jet measurement should not be affected by collinear splitting or soft emissions). In ALICE, the jet candidates are reconstructed using the anti-$k_{\mathrm{T}}$ [219] algorithm. The reconstruction can depend solely on charged tracks measurement by the ITS and TPC (charged jets) or combine them with the energy deposition in the EMCAL to include neutral particles (full jets). In the latter case, the energy deposition in the EMCAL by charged particles is subtracted as to avoid double counting.

The next step consists in correcting for the background contribution to the jet candidate measured energy. The standard method relies on event-by-event calculation of the average momentum density, which is multiplied by the jet area and the result subtracted from the measured energy. As this method leads to large residual fluctuations, an ongoing effort aims at developing new techniques allowing for a more precise measurement of the jet momentum, e.g. relying on machine learning [220].

# Chapter 5

# Forward muon spectrometer

The measurements presented in this thesis are performed on data recorded using the muon spectrometer of ALICE. The machinery is detailed in the first two sections, while the last two respectively describe the procedures for muon tracking and triggering. Considerations on the efficiency are given following their relevance for the study of weak bosons. Most of the information presented in this chapter is extracted from the ALICE paper [181], the spectrometer technical design reports and the ALICE performance paper [181, 221, 222, 185]. More details can be found in these documents, and references herein.

## 5.1 Overview

The ALICE detector is equipped with a muon spectrometer lying at large rapidities. It detects muons with full azimuthal coverage and polar angle $171^\circ < \theta < 178^\circ$, corresponding to pseudorapidity $-4 < \eta < -2.5$ in the ALICE convention. The spectrometer enables the measurement of the muon decays of light ($\rho$, $\omega$, $\phi$) and heavy (J/$\psi$ and $\Upsilon$ families) vector mesons, HF hadrons (B and D), and weak bosons ($W^{\pm}$ and $Z^0$). The large rapidity coverage is complementary to the central barrel and to other LHC experiments, such as ATLAS and CMS. It overlaps with the rapidity coverage of the LHCb detector ($-2 < \eta_{\mathrm{LHCb}} < -4.5$), but the technical conception and physics goal of the two apparatus lead them to probe different regimes: LHCb is designed for high luminosity pp mode but saturates for the most central heavy-ion events, while ALICE is fully efficient in the latter and suffers from the limitations of its recording rate in the former.

The spectrometer is composed of a set of tracking chambers assisted by a dipole magnet for momentum measurement, a triggering system, and a set of absorbers shielding the detector from various background sources. A detailed layout is shown in Figure 5.1, and Table 5.1 gives the main technical characteristics of the muon arm.

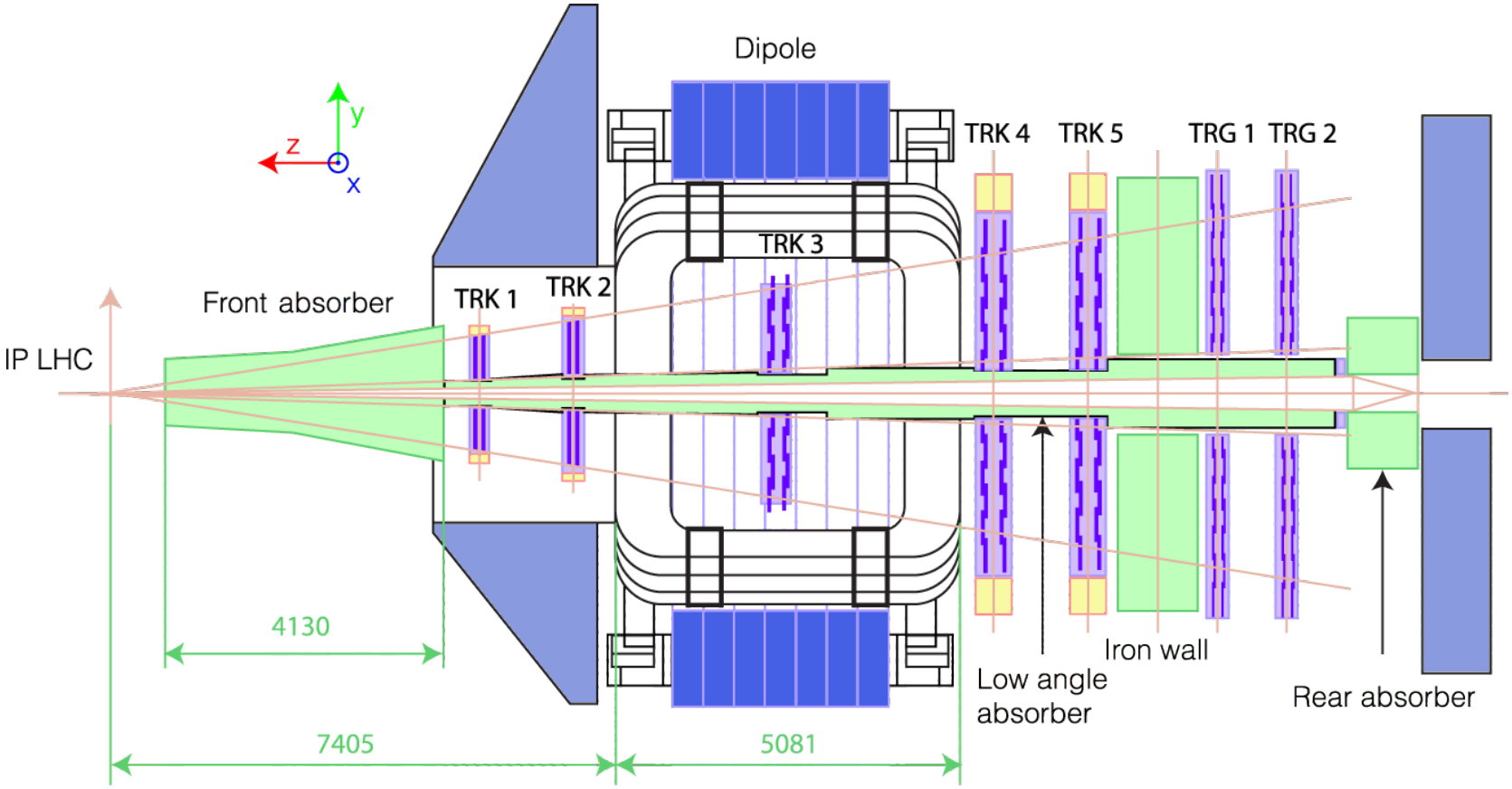


**Figure 5.1:** Cross sectional view, in the longitudinal plane, of the ALICE muon spectrometer. The five tracking chambers (TRK 1-5) are sitting in front of the two triggering stations (TRG 1-2). The third tracking chamber is embedded in the dipole magnet. The systems are shielded by a set of absorbers (front, rear, low angle absorbers and iron wall) for background filtering. The distances indicated on the figure are in unit of mm.

| Muon detection | |
|---|---|
| Polar angular coverage | $171^\circ < \theta < 178^\circ$ |
| Azimuthal angular coverage | full |
| Minimum muon momentum | 4 GeV/$c$ |
| Pseudorapidity coverage | $-4.0 < \eta < -2.5$ |
| **Front absorber** | |
| Longitudinal (from IP) | $-5\,030$ mm $\leq z \leq -900$ mm |
| Total thickness (material) | $\simeq 10\ \lambda_{\rm int}, \simeq 60\ X_0$ (carbon, concrete, steel) |
| **Dipole magnet** | |
| Nominal magnetic field, integrated field | 0.67 T, 3 Tm |
| Free gap between poles | 2.972 - 3.956 m |
| Overall magnet length | 4.97 m |
| Longitudinal position (from IP) | $-z = 9.94$ m (centre of the dipole coils) |
| **Tracking chambers** | |
| No. of stations, no. of planes per station | 5, 2 |
| Longitudinal position of stations | $-z = 5\,357$, 6 860, 9 830, 12 920, 14 221 mm |
| Anode-cathode gap (equal to wire pitch) | 2.1 mm for st. 1, 2.5 mm for st. 2-5 |
| Gas mixture | 80% Ar + 20% $CO_2$ |
| Pad size st. 1 (bending plane) | $4.2 \times 6.3$, $4.2 \times 12.6$, $4.2 \times 25.2$ mm$^2$ |
| Pad size st. 2 (bending plane) | $5 \times 7.5$, $5 \times 15$, $5 \times 30$ mm$^2$ |
| Pad size st. 3-5 (bending plane) | $5 \times 25$, $5 \times 50$, $5 \times 100$ mm$^2$ |
| Maximum hit density st. 1-5 (central Pb–Pb $\times$ 2) | 5.0, 2.1, 0.7, 0.5, 0.6 $\times$ 10 cm$^{-2}$ hits/cm$^2$ |
| Spatial resolution (bending plane) | $\simeq 70\ \mu$m |
| **Trigger chambers** | |
| No. of stations, no. of planes per station | 2, 2 |
| Longitudinal position of stations | $-z = 16\,120$, 17 120 m |
| Total no. of RPCs, total active surface | 72, about 140 m$^2$ |
| Gas gap | single, 2 mm |
| Electrode material and resistivity | Bakelite, $\rho = 3 - 8 \times 10^9 \Omega$ cm |
| Gas mixture | $C_2H_2F_4$ / i-butane / $SF_6$ (89.7%, 10%, 0.3%) |
| Pitch of readout strip (bending plane) | 10.6, 21.2, 42.5 mm (for trigger st.1) |
| Max. strip occupancy in bend. (non bend.) plane | 3% (10%) in central Pb–Pb |
| Maximum hit rate on RPCs | 3 Hz / cm$^2$ in Pb–Pb |
| **Trigger electronics** | |
| Total no. of FEE channels | $2.1 \times 10^4$ |
| No. of local trigger cards | 234 + 8 |

**Table 5.1:** Summary of the main characteristics of the ALICE muon spectrometer. The information in the table are adapted from Ref. [181].

## 5.2 Composition

### 5.2.1 Tracking system

The muon tracker is composed of five stations, each containing two planes of cathode pad chambers. The third station sits inside a 800-tons dipole magnet, delivering a integrated magnetic field of 3 Tm by means of resistive coils. The first two chambers have radii defined by the angular acceptance of the spectrometer (polar angle $171^\circ < \theta < 178^\circ$ with the origin at the collision point, in full azimuth), while the last three chambers are larger in order to account for the deviation of charged tracks in the magnetic field. They are arranged in a projective geometry from 2.5 to 20 $m^2$, for a total surface of about 100 $m^2$. The magnetic field generated by the dipole magnet lies in the horizontal plane, perpendicular to the beam line, from which one defines the bending $(y, z)$ and non-bending $(x, y)$ planes. Its polarity can be inverted in a short time, and Pb–Pb data are recorded using the two configurations.

The tracking system is required to attain a spatial resolution better than 100 $\mu$m, mainly driven by the mass resolution needed to disentangle the bottomonia states[1] and constrained by the particle multiplicity in Pb–Pb collisions. This requirement is fulfilled with Multi-Wire Proportional Chambers (MWPC) of high granularity. The chambers of the first two stations have a quadrant structure, with the readout electronics distributed on their surface. The three other chambers have a slat architecture with electronics on the side of the slats (Figure 5.2). The first station, having to cope with a very high particle density in the vicinity of the collision point, is composed of pads as small as $4.2 \times 6.3$ $mm^2$. Larger pads are used for the stations further away from the interaction point.

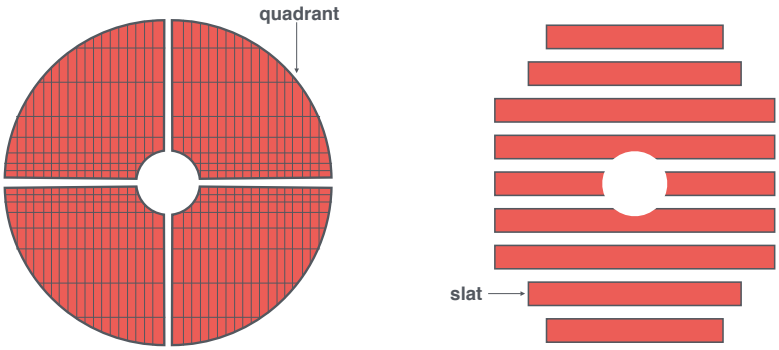


**Figure 5.2:** Schematic view of the quadrant structure (left) and slat architecture (right) of the two innermost and three outermost tracking stations respectively.

The working principle of the MWPC is illustrated on Figure 5.3. Each MWPC is composed

[1] Which requires a resolution of 100 MeV/$c^2$ at 10 GeV/$c^2$

of a central anode plane with equally spaced wires, sitting in-between two cathode planes whose segmentation aims at keeping the occupancy below 5%. The wires have a high voltage, of about 1650 V, while the cathode planes are grounded. This generates an electric field with increasing gradient towards the wires. The volume within the two cathodes is filled with a gaseous mixture of Ar+$CO_2$ at a 80% / 20% ratio. As to limit multiple scatterings in the chambers, low-Z materials such as carbon fibres are used, resulting in a chamber thickness of 0.03 radiation length ($X_0$).

A charged particle crossing the gaseous medium will ionise it, liberating electrons that drift towards the nearest anode wire due to the electric field, triggering an avalanche of secondary electrons. The resulting ion cloud creates a charge distribution on the cathode pads nearby. The cathode positions provide the $x$ and $y$ coordinates of the hit, while the $z$ coordinate is provided by the position of the chamber itself.

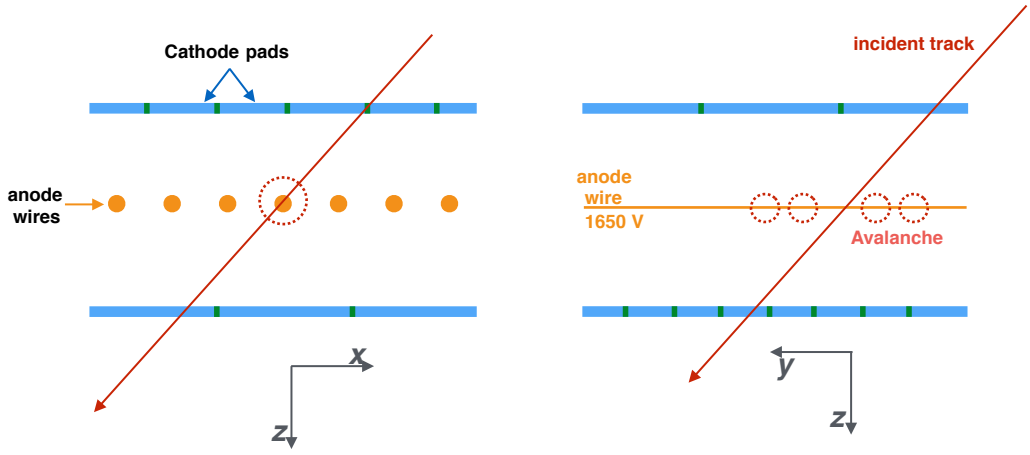


**Figure 5.3:** Layout and working principle of the MWPC composing the tracking chambers viewed in the $(x, z)$ and $(y, z)$ planes.

### 5.2.2 Trigger stations

The muon trigger system is composed of four $\sim 6 \times 6$ m$^2$ planes regrouped in two stations, located 16 and 17 m away from the nominal interaction point. Each planes contains 18 single-gap Resistive Plate Chambers (RPC) made of two high-resistivity Bakelite electrodes separated by a 2 mm gas gap (Figure 5.4). The outside faces of the plates are painted with graphite, one is kept under high voltage while the other is grounded. The signal is created by the avalanche of electrons triggered by a charged particle crossing the gas in-between the two electrodes.

The signal is picked-up by orthogonal readout strips, providing bi-dimensional information on the hit position. The strips are connected to the Front-End Electronics (FEE), which gather the

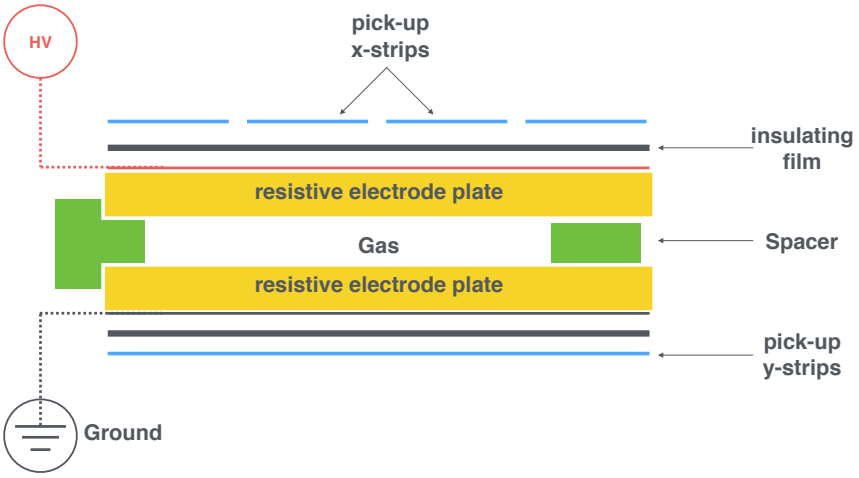


**Figure 5.4:** Schematics of a RPC composing the muon trigger planes.

signal from the four planes and pass it to the local trigger electronics. The system is divided into 234 detection areas, each associated to a local trigger board. The strip segmentation is finer at very large rapidity, where a high multiplicity is expected, and decreases when moving further away from the beam line. The chamber response is fast, with a signal rising in about 2 ns, and the trigger system attains a spatial resolution of $\sim$ 1 cm and time resolution of the order of 1-2 ns.

### 5.2.3 Absorbers

The ALICE spectrometer design was driven by the requirement of coping with the very high multiplicity environments created by heavy-ion collisions, applying an extra factor two to the multiplicity predicted by means of simulations with HIJING [223]. Several absorbers are meant to shield the muon chambers, reducing the detector occupancy and helping the background rejection. The filtering set is composed of four absorbers: the front absorber, between the interaction point and the muon chambers, the low-angle absorber, also called beam shield and lying along the beam pipe, the iron wall sitting between the tracking and triggering systems, and the rear absorber located after the trigger stations.

The front absorber is a 37-tons cone located inside the $L_3$ magnet, before the first tracking station and at 90 cm from the nominal interaction point. It aims at reducing the flux of charged particles by at least a factor two. Its length of 4.13 m correspond to about 60 $X_0 \simeq 10\ \lambda_{\text{int}}$. Besides filtering, the front absorber is required to limit multiple scatterings as to not compromise the resolution of the spectrometer. In this regard, the region close to the interaction is made of carbon, a low-Z material, followed by concrete. The carbon and concrete part is surrounded by high-Z material (lead and polyethylene) in order to absorb low-energy photons and neutrons, as well as secondary particles produced within the absorber itself.

The triggering stations are further protected by a 1.2 m thick iron wall filtering out hadrons and secondary particles punching through the front absorber. The whole spectrometer is protected

from the high background produced by the interactions with the beam pipe of particles (mainly pions and kaons) emitted at very small angle ($\theta < 2^{\circ}$) by the small-angle absorber and second iron wall. The small-angle beam shield is made of high-density material (tungsten and lead) enveloped with stainless steel. It surrounds the beam pipe throughout the muon arm in its entirety. The second iron wall protects the back of the trigger stations from the particle produced in beam-gas interactions.

## 5.3 Track reconstruction

### 5.3.1 Reconstruction algorithm

Following the passage of charged particles in the tracking chambers, clusters are determined by means of the Maximum Likelihood Expectation Maximisation (MLEM) algorithm [224], which allows one to find local maxima in a distribution for which equations are either not known or cannot be solved directly. The spatial location are determined by fitting the cathode-induced charged distribution with a 2D-Mathieson function [225], a single parameter function applicable for small anode-cathode separation:

$$\frac{\rho(\lambda)}{q_a} = K_1 \frac{1-\tanh^2(\mathrm{K}_2\lambda)}{1+K_3\cdot\tanh^2(\mathrm{K}_2\lambda)}, \qquad \text{with} \qquad \mathrm{K}_1 = \frac{\mathrm{K}_2\sqrt{\mathrm{K}_3}}{4\tanh^{-1}\sqrt{\mathrm{K}_3}}, \qquad \mathrm{K}_2 = \frac{\pi}{2}\left(1-\frac{\sqrt{\mathrm{K}_3}}{2}\right), \tag{5.1}$$

where $q_a$ is the net anode charge and $\lambda = x/h$ with $h$ the anode-cathode separation and $x$ the position along the $x$-axis, either parallel or normal to the anode wire direction. The single parameter $K_3$ can be determined from the chamber geometrical configuration, allowing for the evaluation of the cluster position $x$ with a fit. The cluster information is used as inputs for the track reconstruction algorithm, which is based on the Kalman filter [215] already presented for the track reconstruction in the central barrel (Section 4.4.3).

The algorithm builds track seeds starting from station 4 and 5, as they are less subject to background contamination from soft particles escaping the front absorber. In each station, a track segment is built by linking cluster pairs from the two planes, and joining them with a straight line. The seeds are extrapolated in the magnetic field to the preliminary vertex estimated by the ITS (usually SPD only), after which a first estimation of the track momentum can be performed using the standard Lorentz law:

$$\vec{F} = \frac{\mathrm{d}\vec{p}}{\mathrm{d}t} = q\left(\vec{E} + \vec{v}\times\vec{B}\right), \tag{5.2}$$

where $q$ is the charge of the track, $\vec{v}$ its velocity and $\vec{E}$ and $\vec{B}$ the electric and magnetic fields of the magnet. From this relation the guessed track momentum $p$ can be linked to the radius of the track curvature $R$ using:

$$p[\mathrm{GeV/c}] = 0.3[\mathrm{T}]\times \mathrm{R[cm]} = 0.3[\mathrm{T}]\times\frac{\mathrm{L[cm]}}{\theta_{\mathrm{d}}} \tag{5.3}$$

where $L$ is the length of the magnet and $\theta_d$ is the angle between the beam line and the track segment after the magnet. Here a first selection criterion is applied on the guessed track momentum, where tracks with $p < 3$ GeV/$c$ or $p > 3$ TeV/$c$ are rejected.

The second step of the track reconstruction algorithm starts back from the seeds built in station 4 or 5, and look for corresponding clusters in station 5 or 4. At least one cluster has to be found in the two planes of the other station, defining the second criterion of the tracking algorithm: a valid track needs to have at least three out of the four possible clusters in stations 4 and 5. The association of clusters between the two stations is based on a $\chi^2$ selection. The presence of several clusters passing the selection leads the track seed to become a tree with several hypotheses, which are all propagated. The Kalman algorithm reevaluates the track kinematic parameters using the new information, and the procedure is repeated down to the first station. At each station, a track hypothesis is discarded if no cluster can be associated to it. Additionally, at each recomputation of the track parameters a $\chi^2$-based cut aims at discarding tracks of poor quality. Therefore, the Kalman filter-based algorithm for track reconstruction features three selection criteria:

- the first estimation of the track momentum should yields 3 GeV/$c < p <$ 3 TeV/$c$,
- the track hypothesis has to pass $\chi^2$-based selections at both cluster and track levels,
- the track has to be built from at least one out of the two possible clusters in stations 1, 2 and 3, and three out of the possible four clusters in stations 4 and 5.

After the full reconstruction of the tracks in the tracking system, one gets the so-called uncorrected track parameters yielded by the Kalman filter. The tracks are finally extrapolated to the vertex position measured by the SPD, and their parameters are corrected for multiple scatterings and energy loss in the front absorber.

### 5.3.2 Alignment of the tracking chambers

The requirement of a mass resolution of 1% at the $\Upsilon$ mass introduces a strong constraint on the alignment of the tracking chambers. During the installation of the chambers, they are positioned with a spatial accuracy of a few tenth of millimetres by means of theodolite measurements and photogrammetry. At the beginning of each data taking period, dedicated runs are performed for the alignment, during which the dipole magnet is switched off. The ten chambers are aligned on straight tracks. This initial positioning is disturbed when switching on the magnet and electronics power supplies. The chamber supports suffer as well from thermal stress. Such deformations need to be accounted for, in order to correct the data and be able to reproduce the alignment conditions in the simulations.

The misalignment is monitored by means of the Geometry Monitoring System (GMS) [226], an array of about 460 optical sensors installed on platforms located at each corner of the tracking chambers. Two different optical devices are used, both recording with CCD sensors optical signals projected through a lens. The long range monitoring, corresponding to measurements between stations, in provided by Brandeis CCD Angle Monitor (BCAM). Each BCAM contains two or more light sources, and an electronic camera looking at light sources from other BCAM. The short range monitoring, measuring distance between the two planes within a station, is provided by Red Alignment System NIKHEF (RASNIK) based proximity systems, a single tube containing the lens and CCD, which focuses on a mask with coded squares attached to another layer. The information is gathered by the Long-Wire Data Acquisition System (LWDAQ).

The relative position of the planes is determined using a modified version of the MILLEPEDE package [227]. MILLEPEDE provides a way to include both global and local parameters, respectively referring to parameters contributing to all data (such as a chamber position) or relative to a single track (e.g. track curvature). Data recorded with and without magnetic field, as well as measurements from the GMS, can then be incorporated all at once in the determination of the relative misalignment, performed by a simultaneous fit of global and local parameters with a linear least square model. In this way, a precision of about 100 $\mu$m is reached.

While the method is sensitive to the relative misalignment of the detector elements, it does not account for a potential global displacement of the entire spectrometer. A data-driven method was hence developed, simulating the detector response with a parametrisation of the measured resolution of the clusters associated to a track, using extended Crystal Ball (CB) functions [228] to reproduce the distribution of the differences between the cluster and the track position in each chamber. The parameters of the Gaussian core and power law tails of the CB are tuned to data, then used to reproduce the smearing of the track parameters. A global displacement of the detector is mimicked by applying a systematic shift, in opposite direction for positively and negatively charged tracks, to the distribution of the angular deviation of the tracks in the magnetic field. This shift parameter is determined from simulations, reproducing the difference between positive and negative tracks observed in data.

### 5.3.3 Reconstruction efficiency

The efficiency of the tracking stations is calculated from data, taking advantage of the detector redundancy. The tracking algorithm requires only a subset of the chambers to be fired, enabling the evaluation of each chamber efficiency, which are then combined to determine the overall efficiency of the tracker. Let i and j be the two chambers of a station. One can face four configurations when a track goes through the station, as illustrated in Figure 5.5: the "ij" configuration when both chambers are fired, "i0" and "0j" if only the chamber i or j is fired, and "00" when no clusters are reconstructed in the station.

The total number of tracks $N_{\mathrm{tot}}$ is the sum of the four configurations:

$$N_{\mathrm{tot}} = N_{\mathrm{ij}} + N_{\mathrm{i0}} + N_{\mathrm{0j}} + N_{\mathrm{00}}. \tag{5.4}$$

Considering that the efficiency of chambers i and j (hereafter $\epsilon_{\mathrm{i}}$ and $\epsilon_{\mathrm{j}}$) are independent, one can write:

$$N_{\mathrm{ij}} = \epsilon_{\mathrm{i}} \cdot \epsilon_{\mathrm{j}} \cdot N_{\mathrm{tot}}, \qquad N_{\mathrm{i0}} = \epsilon_{\mathrm{i}} \cdot (1 - \epsilon_{\mathrm{j}}) \cdot N_{\mathrm{tot}}, \qquad N_{\mathrm{0j}} = (1 - \epsilon_{\mathrm{i}}) \cdot \epsilon_{\mathrm{j}} \cdot N_{\mathrm{tot}}, \tag{5.5}$$

from which follows:

$$\epsilon_{\mathrm{i}} = \frac{N_{\mathrm{ij}}}{N_{\mathrm{ij}} + N_{0j}}, \qquad \text{and} \qquad \epsilon_{\mathrm{j}} = \frac{N_{\mathrm{ij}}}{N_{\mathrm{ij}} + N_{i0}}, \tag{5.6}$$

the efficiency of each chamber can be evaluated without having to know $N_{00}$.

The efficiency of the tracking system is also affected by the presence of fake tracks. This can be dealt with by applying a selection on the $p \times DCA$, the product of the track momentum to its distance of closest approach (that is, the distance to the primary vertex of the track trajectory

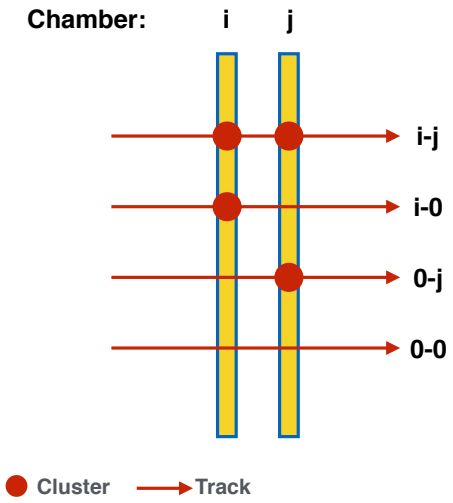


**Figure 5.5:** Possible configurations after the passage of a charged particle through a tracking station with chambers $i$ and $j$.

projected in the plane transverse to the beam axis), ensuring that the track points to the interaction vertex. At low $p_{\mathrm{T}}$, below 1-2 GeV/$c$, this cut is not fully efficient, a selection on the track normalised $\chi^2$ is then also applied ($\chi^2 < 3.5$) to further reduce the contamination. The amount of fake tracks is largely reduced by this selection, amounting to about 1.5% for the 0-10% central events in Pb–Pb.

## 5.4 Muon triggering

The muon trigger system aims at reducing, thanks to the iron wall, the probability of triggering, and therefore storing, events where no valid muon candidate for light vector mesons, open and closed HF hadrons, or weak boson is present. It provides as well muon identification through the matching of a track segment in the trigger stations to a track reconstructed in the tracking system. The trigger decision is taken by the muon chambers, at the electronics level. It is based on a fast selection (about 650 ns) of candidate muon and dimuon signals above a user-defined $p_{\mathrm{T}}$ threshold. The $p_{\mathrm{T}}$-based procedure is justified by the rejection of pions and kaons, expected to be dominant at low $p_{\mathrm{T}}$. It is illustrated in Figure 5.6.

The trigger decision is performed by comparing in station 2 the track segment reconstructed from hits in the two stations, to a "track with infinite momentum" defined as a straight line passing through the interaction vertex and the cluster in the first station, and extrapolated to the second. The difference in position between the two tracks defines the deviation $\delta y = y_2 - y_\infty$. The $p_{\mathrm{T}}$ selection can then be applied by cutting on $\delta y$, which is inversely proportional to $p_{\mathrm{T}}$. The $p_{\mathrm{T}}$ cut is not sharp, as the intrinsic trigger efficiency is not an ideal step function: it increases sharply before reaching a plateau of about 99% around 5 GeV/$c$. Two cuts are defined, serving different analysis purposes. A low-$p_{\mathrm{T}}$ cut enables the analysis of particle of low transverse momentum. As the signal rate in this region is high, and in order to cope with the recording rate and storing

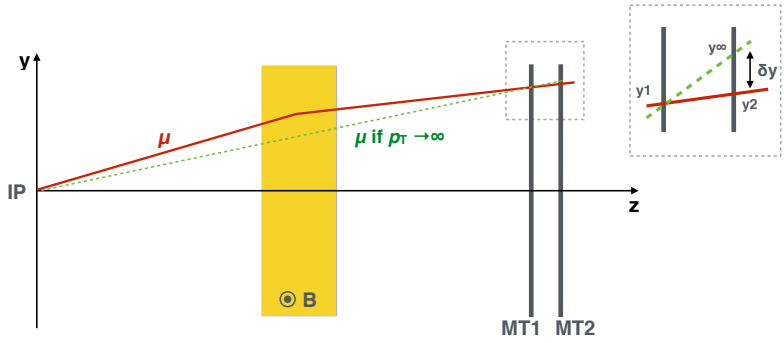


**Figure 5.6:** Sketch of the working principle of the muon trigger decision. The insert on the top right is a zoom-in of the dotted square. The MT1 and MT2 labels indicate the first and second trigger stations respectively.

capabilities, the low-$p_{\mathrm{T}}$ triggers are downscaled. As to maximise the statistics for intermediate to high $p_{\mathrm{T}}$ probes, a high-$p_{\mathrm{T}}$ cut, without downscaling factor, is also defined. The values of those $p_{\mathrm{T}}$ threshold are period dependent, ranging from 0.5 to 4.2 TeV/$c$. Combined with the charge of the track and the single muon / dimuon label, the muon trigger can produce six different trigger signals, summarised in Table 5.2.

| Trigger type | Trigger name | Condition |
|---|---|---|
| Muon-Single | `MSL` | single muon, low-$p_{\mathrm{T}}$ threshold |
| | `MSH` | single muon, high-$p_{\mathrm{T}}$ threshold |
| Muon-Pair | `MLL` | same-sign muon pair, low-$p_{\mathrm{T}}$ threshold |
| | `MLH` | same-sign muon pair, high-$p_{\mathrm{T}}$ threshold |
| | `MUL` | opposite-sign muon pair, low-$p_{\mathrm{T}}$ threshold |
| | `MUH` | opposite-sign muon pair, high-$p_{\mathrm{T}}$ threshold |

**Table 5.2:** Trigger types defined by the muon trigger system. For dimuon triggers, the $p_{\mathrm{T}}$ threshold is applied on individual tracks.

The efficiency of the trigger chambers is evaluated using the information redundancy, as for the tracking chambers. The trigger efficiency can also be affected by the occupancy. The detector contains 234 local boards, the resulting granularity creates a sizeable probability of having two tracks that are close enough to interfere with the trigger signal. This is evaluated by embedding technique. A simulated signal is embedded in real data, as to mimic the detector occupancy during data taking, and the trigger rate is compared to the one obtained from pure simulation, only using as input the chamber efficiencies. The loss of trigger signal evaluated with this method can reach 3.5% for the most central Pb–Pb collisions [185].

# Chapter 6

# Data taking in ALICE

This chapter introduces the online and offline systems of ALICE, constituting the two steps of the data treatment chain that was in place during the LHC Run 2. The online control system implements trigger selections and handles the flow of data from their detection in the sub-elements of the detector to the storage of the selected events on hard drives. The offline system performs the reconstruction of the event and encompasses the analysis and simulation frameworks, enabling data analysis.

## 6.1 Online Control System

ALICE aims at taking data during hadronic collisions performed at the LHC, focusing on but not restricting to heavy-ion collisions. It therefore operates in several running modes with significant differences. The Pb–Pb mode, primary focus of the experiment, features a relatively low interaction rate (of $\leq 10$ kHz at nominal luminosity $\mathcal{L} = 10^{27}$ cm$^{-2}$ s$^{-1}$), relatively short running time (a few weeks per year) but very high multiplicities and thus large event sizes. This requires a rather low trigger selectivity, but the trigger complexity is high and needs at least the partial reconstruction of the event in order to extract signals of interest. Handling and storing large-size events require sufficient bandwidth together with an efficient selection and compression of the data. On the contrary, in pp mode (and, to some extend, p–Pb), the interaction rate is much higher (up to 500 kHz) while the event size is small. The running time, in pp mode, is of several months a year. In this case, the requirements on the trigger complexity, bandwidth and data compression are less drastic, whereas the trigger selectivity becomes crucial.

These requirements are met using the Online Control System, composed of the Trigger system, the High-Level Trigger (HLT), the Data Acquisition (DAQ) and the Detector Control System (DCS). The four modules are interfaced with each other by the Experiment Control System (ECS) layer, as shown in Figure 6.1. These five parts, constituting the online control system, are summarised in the following subsections, more information can be found in the dedicated Technical Design Report [229].

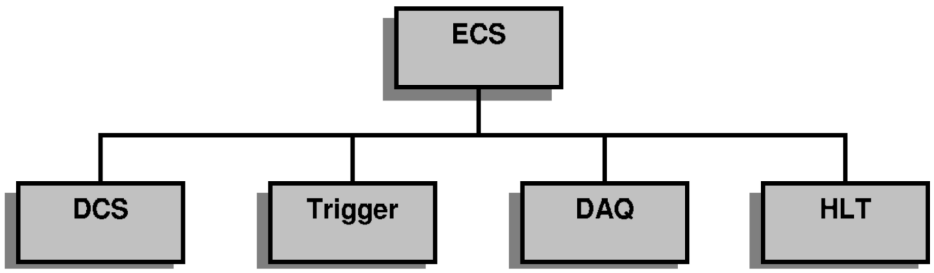


**Figure 6.1:** The ALICE online control system. The Trigger system, High-Level Trigger (HLT), Data Acquisition (DAQ) and Detector Control System (DCS) are monitored and interfaced by the Experiment Control System (ECS). Figure taken from Ref. [229].

### 6.1.1 Trigger

The triggering in ALICE is challenging, due to the widely varying relaxation time of the various subdetectors, and the differences between the particle multiplicities, event sizes, and interaction rates among the various running modes. This is optimised by the Central Trigger Processor (CTP), designed to select events having specific features at a rate that can be scaled as to account for the bandwidth restrictions.

The triggering procedure is based on logic trigger signals sent by the subdetectors. They are characterised by a specific measurement made by the detector itself, often following from a fast calculation, such as an evaluation of the multiplicity, a $p_{\mathrm{T}}$ threshold, the presence of a muon pair, etc. An example of such calculation is the one used to apply the $p_{\mathrm{T}}$ selection by the muon trigger presented in Section 5.4. These logical signals are sent to the CTP as trigger inputs, where they are combined using a Field-Programmable Gate Array (FPGA), an integrated circuit containing an array of programmable logic blocks. The FPGA combines the input signals following a user defined process in order to form the different physics triggers (e.g. 10% most central MB event, single muon with high-$p_{\mathrm{T}}$ threshold...). The CTP communicates independently with each detector, as they may have different triggering patterns, by means of Local Trigger Units (LTUs). There is one LTU per detector element, which sends the recorded signal to the CTP, receives its trigger decision, translates it following the detector needs, and forward it to the Front-End Electronics (FEE) of the detector. The detectors providing triggering capabilities, along with their functions, are listed in Table 6.1.

Following from the low latency of some of the detectors, the trigger decision is organised in three levels. The fastest level, L0, is delivered to the detector 1.2 $\mu$s after the collision, providing a alert to detectors whose electronics are not pipe-lined, but awaiting for a trigger decision to start processing signals. The L1 level arrives at the detector 6.5 $\mu$s after the interaction took place. At this stage, most of the trigger inputs are available, allowing for a major rate reduction to be applied when needed. The last trigger level, L2, comes after the end of the drift time of the TPC (about 88 $\mu$s), after which the past-future pile-up protection can be applied. In Pb–Pb mode, the past-future protection circuit monitors the number of interactions, characterised by their multiplicity. Pile-up of two central events will veto the trigger, while pile-up of an event with low multiplicity can be

| Detector | Functions | Level |
|---|---|---|
| SPD | hit-multiplicity and hit-topology based trigger | L0 |
| TRD | electron, high-$p_{\mathrm{T}}$ particle, charged jet | L1 |
| TOF | multiplicity, topology (back-to-back), cosmic ray | L0 |
| PHOS | photon | L0 |
| EMCAL | photon, neutral jet | L0/L1 |
| ACORDE | cosmic ray (single and multiple hits) | L0 |
| V0 | coincidence-based MB, centrality | L0 |
| T0 | event vertex selection, interaction trigger | L0 |
| ZDC | MB interaction, electromagnetic dissociation | L1 |
| MUON | single muon, dimuon | L0 |

**Table 6.1:** Trigger capabilities provided by the various ALICE detectors, with their trigger level (see text). Taken from Ref. [185].

tolerated up to a programmable level. After L2, the events are furthermore filtered following the decision of the HLT.

This organisation in terms of timing levels allows one to define and control differently partitions of the detector. A partition, also called a detector cluster, is a dynamically-defined subset of detectors participating in the readout of a given event. A cluster is defined for its relevance in terms of data analysis, and the trigger decision sent to this particular cluster can be adapted according to the recording rate of its constituents. For example, the muon spectrometer is able to record data at a much higher rate than the TPC. Along with other fast detectors (including e.g. the SPD for vertex measurement, the V0 and T0 arrays for the evaluation of the multiplicity), it is regrouped in the MUON cluster, improving the statistics available for this specific physics channel.

The input data handled by the CTP is usually global, meaning that it does not correlate specific geometrical regions in different detectors. For peculiar applications however, it might not be required to record the whole event, and a selection defining a specific azimuthal region can allow for physics analysis while providing an efficient way to reduce the amount of data needed to be processed and stored. This type of selection is especially fruitful when triggering on events in which the ALICE calorimetry system is involved, as it does not have a full azimuthal coverage. The boundaries of the azimuthal region can be imposed to the most central detectors, such as the ITS and TPC.

Finally, the CTP is designed to handle the rate of the various triggers. The data acquisition tends to saturate with high frequency triggers, leaving few to no bandwidth available for triggering on rare processes. In order to prioritise those events, of particular physics interest, the CTP is able to downscale the non-rare triggers to a predefined rate. The data acquisition monitors the occupancy of its buffers, sending a signal to the CTP when it exceeds a given threshold. The CTP responds by restricting triggering on common processes, ensuring continued available bandwidth for rare processes. When the occupancy of the buffers has lowered below a suitable threshold, another signal is sent to re-activate all the trigger types. The timing at which the non-rare triggers

are downscaled is precisely monitored as to be taken into account while evaluating the integrated luminosity.

A set of trigger inputs, output trigger cluster, past-future protection requirements, along with a few other control bits, define together a trigger class, the central concept for event selection in ALICE. Classes are named following a generic scheme:

`C<descriptor> - <BC mask> - <past-future protection> - <cluster>`,

where:

- the `descriptor` is a logical function of the input codes,
- the `BC mask` code is a letter describing for which bunch crossing category the trigger is active,
- the `past-future protection` code defines whether the past-future protection scheme is applied (and how) or not,
- the detector `cluster` code corresponds to the cluster read out in the trigger class.

For instance, the measurement of the W-boson production presented in this thesis uses as main trigger `CMSH7-B-NOPF-MUFAST`. The class corresponds to `MSH7` events: events where the muon trigger (`M`) reports the detection of a single muon (`S`) with a high $p_{\mathrm{T}}$ threshold (`H`), in combination with a MB signal from the V0 arrays (`7`). The class is active for the `B` bunch crossing categories (two filled bunches crossing), without past-future protection (`NOPF`), and read out data from the detectors of the `MUFAST` cluster, containing the SPD, T0, V0, AD, and the muon tracking and trigger systems. The major ALICE triggers are summarised in Table 6.2.

### 6.1.2 Data AcQuisition (DAQ)

The ALICE DAQ [230] is a vast computing system composed of hundreds of interconnected Personal Computers (PCs) aiming at organising and controlling the flow of data from its detection to the storage of the events. Along the chain is performed sub- and full event reconstruction, in association with the HLT farm. The DAQ also includes software packages for the monitoring of data quality and system performances. The architecture of the DAQ is shown in Figure 6.2. It relies on the parallelisation of the data treatment, with data streams working independently and concurrently, followed by stages of event building where data are merged and eventually recorded as a complete event. The LHC clock, having a precision of 25 ns corresponding to at most one bunch crossing, is used to associate a time tag to each fragment in order to identify fragments pertaining to the same event for the full reconstruction.

The chain starts at the level of the detectors read-out. The CTP forms a decision for every bunch crossing, which is sent to the LTU of each detector needed to be read out. The LTUs communicate the positive decisions by means of Timing, Trigger and Control (TTC) systems, associating to the raw data the LHC timing reference, first level trigger decision and the corresponding bunch and event number. Data are then pushed into the system by the detectors Front-End and

| Trigger | Description | Condition |
|---|---|---|
| MB-type triggers | | |
| MB`or` | minimum bias | signals in one of the V0s and SPD |
| MB`and` | minimum bias | signals in V0A and V0C |
| MBZ | minimum bias | MB and signals in both ZDCs |
| SPI | multiplicity | $n$ hits in SPD |
| Centrality triggers | | |
| CENT | central event | V0-based centrality trigger for Pb–Pb (0–10%) |
| SEMI | semicentral event | V0-based centrality trigger for Pb–Pb (0–50%) |
| EMCAL triggers | | |
| E0 | EMCAL L0 | EMCAL L0 shower trigger in coincidence with MB |
| EJE | neutral jet | EMCAL L1 jet algorithm following EMCAL L0 |
| EJE2 | neutral jet | like EJE but with lower threshold |
| EGA | photon/electron | EMCAL L1 photon algorithm following EMCAL L0 |
| EGA2 | photon/electron | like EGA but with lower threshold |
| TRD triggers | | |
| TJE | charged jet | $n$ charged particles in TRD chamber in coincidence with MB |
| TQU | electron for quarkonia | electron with $p_{\mathrm{T}} > 2$ GeV/$c$ in TRD in coincidence with MB |
| TSE | electron for open beauty | electron with $p_{\mathrm{T}} > 3$ GeV/$c$ in TRD in coincidence with MB |
| MUON triggers | | |
| MSL | single muon low | single muon in muon tracker in coincidence with MB |
| MSH | single muon high | like MSL but with higher threshold |
| MUL | dimuon unlike sign | two muons of opposite sign above low threshold, in coinc. with MB |
| MLL | dimuon like sign | two muons of same sign above low threshold, in coinc. with MB |
| Miscellaneous triggers | | |
| HM | high multiplicity | high multiplicity in SPD in coincidence with MB |
| PH | photon by PHOS | PHOS energy deposit in coincidence with MB |
| EE | single electron | electron signal in TRD (sector 6–8) and EMCAL |
| DG | diffractive | charged particle in SPD and no signal in V0 |
| CUP | barrel ultraperipheral | charged particle in SPD and no signal in V0, for Pb–Pb and p–Pb |
| MUP | muon ultraperipheral | (di)muon in muon trigger and no signal in V0A, for Pb–Pb and p–Pb |
| ZED | electromagnetic dissociation | signal in any of the neutron ZDCs |
| COS | cosmic event | signal in ACORDE |

**Table 6.2:** Descriptors of the major ALICE triggers. Adapted from Ref. [185].

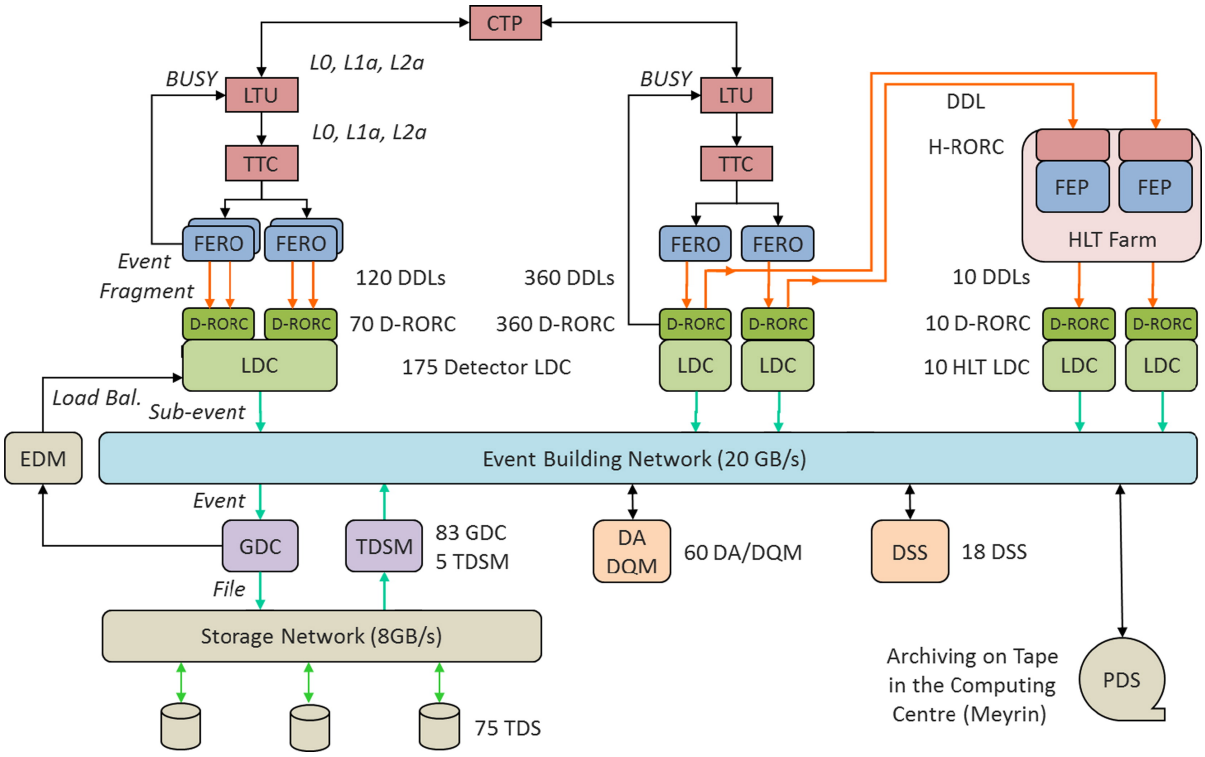


**Figure 6.2:** Overview of the ALICE DAQ system and its interface with the HLT system. The meaning of the acronyms is given in the text. Figure taken from Ref. [230].

Read-Out (FERO) electronics through about 500 optical Detector Data Links (DDLs). The signals conveyed by the DDL are collected by DAQ Read-Out Receiver Cards (D-RORCs), hosted by PCs called Local Data Concentrators (LDCs). In the LDCs the event fragments are getting assembled into sub-events according to their tagging. Some D-RORCs also send a copy of the data to the HLT farm where it is received by Common Read-Out Receiver Cards (C-RORCs)[1] and transferred to the Front-End Processor (FEP). The HLT performs a preliminary online reconstruction, from which a decision about the data to be recorded is taken (see Section 6.1.3). Upon positive decision, the sub-events assembled by the LDCs are shipped to the Global Data Collectors (GDCs) where they are furthermore combined. The distribution of the LDCs outputs to the GDCs is monitored by the Event Destination Manager (EDM) as to ensure an efficient repartition of the data and computing load. The full events are built by the GDCs, and written into data files which are stored in the Transient Data Storage (TDS), a temporary buffer big enough to store several hours worth of continuous data taking. The files are read by the TDS Managers (TDSMs) and finally migrated to the Permanent Data Storage (PDS) at the CERN computing centre, where they will be accessible for offline analysis.

The Data Acquisition and Test Environment (DATE) [231] is the DAQ software framework.

[1]During the LHC Run 1, the data were received by HLT Read-Out Receiver Cards (H-RORCs), before being changed for C-RORCs following the need for higher link rates.

Its functions cover the overall control of the system, as well as the system performance and data quality monitoring. The services needed by the DAQ system itself such as the control or the database are performed by the DAQ Services Servers (DSS). Additional servers are used to run the Detector Algorithms (DA) or the Data Quality Monitoring (DQM).

The DAs constitute a framework designed and implemented to achieve as much as possible the detector calibration directly online. Indeed, the systems are sensitive to configuration settings, mechanical geometry, changes in the environmental conditions, ageing of the components and defections in the sensors. The output of the calibration tasks may be needed to configure the detector electronics for data taking, enabling e.g. the production of zero-suppressed data or the masking of noisy channels, in order to reduce the volume of data. DAs are detector-specific calibration procedures, provided by the sub-detector teams and implemented in the global framework. Each DA collects the detector data and produces results online, which can be directly reused for example to configure the detector and contribute to the sub- and full event reconstruction performed by the DAQ. They can also be shipped offline, post-processed if necessary, and stored to be used in data analysis. Two types of DAs are defined, depending on whether they need a dedicated run (exclusive mode) or they are active during data taking (background mode). In the first case, so-called LDC DA, the data are collected during a dedicated, standalone (single detector running) and usually short-duration run, and recorded on the LDCs. At the end of the run, the DA is launched on the data and the calibration results are directly available. These runs are also used to fine-tune or debug the DA behaviour itself. In background modes, called MON DA, dedicated monitoring machines are used to run single DA processes. The data are then picked-up from the normal data flow in a non-intrusive way, and processed on the fly. Each DA focuses on a given type of event (calibration, physics) and the source it uses to monitor it (a detector or set of detectors). A post-processing phase follows the end of the run as to finalise the results. A MON DA can typically aim at filling an histogram event by event, then compute a fit and extract some key value. MON DAs are used as well to map dead channels. The full mapping of the detector may need a large amount of events, in which case intermediate results are saved at the end of a run and re-loaded for the next run.

The DQM is ensured by the Automatic MOnitoRing Environment (AMORE) framework developed by and used in ALICE. It is mainly written in C++ and interfaced with the ROOT [232] data analysis framework, whilst the use of AliRoot [233], the ALICE offline framework described in section 6.2, is used when offline analysis is needed. It was designed to be flexible and modular, such that each detector team is able to develop specific code that is built into dynamic libraries called modules.

The modules use the DATE monitoring libraries to access the raw data, collect data from the LDCs and GDCs, or read data from files. AMORE is based on a publisher-subscriber paradigm, as illustrated in Figure 6.3. On the publisher side, large number of processes, called agents, contain user-defined code to be executed depending on the DAQ environment status (start or end of run, ongoing data taking...) and producing output objects to be published. An output typically contains the resulting quantities, often in the form of histograms (although there is no restriction on their type) associated to metadata allowing for a proper and coherent handling by the framework. All

is encapsulated into Monitor Objects (MOs) and published into a pool. Each MO has a quality associated to it, which is stored within the object. The quality is a flag that can take different values:

- `kNULLFLAG`: no quality, used for transient objects or when associating a quality it not applicable (e.g. for the transport of error messages),
- `kINFO`: good quality,
- `kWARNING`: the object should be checked,
- `kERROR`: the object is clearly of bad quality,
- `kFATAL`: the object is so incorrect it calls for an immediate intervention.

Depending on user needs, the MOs can be discarded at the end of the running period, after a defined period of time, or stored permanently in a MySQL database for future access.

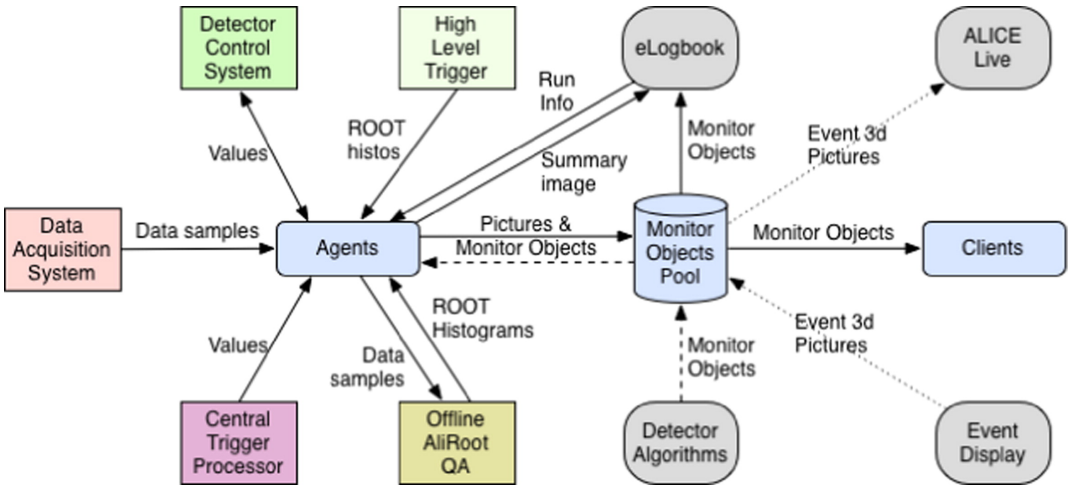


**Figure 6.3:** The publisher-subscriber paradigm of AMORE. On the publisher side, agents communicate with the various part of the online system in order to produce MOs published in a pool. The pool is the accessed by clients (the subscribers) for visualisation in the control room. Figure taken from Ref. [230].

The subscriber part uses clients to connect to the pool, retrieve the MOs and display them in the ALICE control room through a customisable Graphical User Interface (GUI) (see the left panel of Figure 6.4). Since most of the detector teams have similar needs and requirements, a generic GUI has been developed, allowing one to choose and display MOs among the thousand of objects produced by the agents. Custom GUIs were also developed by the teams following their specific requirements for commissioning, testing and monitoring purposes. Custom GUIs also allow one to use custom object types that could not be handled properly by the generic GUI. The DQM is interfaced with the ALICE DAQ bookkeeping facility, the Electronic Logbook (eLogbook), with which it communicates in both ways. The eLogbook provides the DQM with information about

the run, such as its type (physics, calibration...) or the detectors involved. In return, it can read the pool and give a worldwide access to the MOs through a web client, while the subscriber clients are only accessible from within the ALICE control room. The right panel of Figure 6.4 shows an example of MOs retrieved and displayed through the eLogbook.

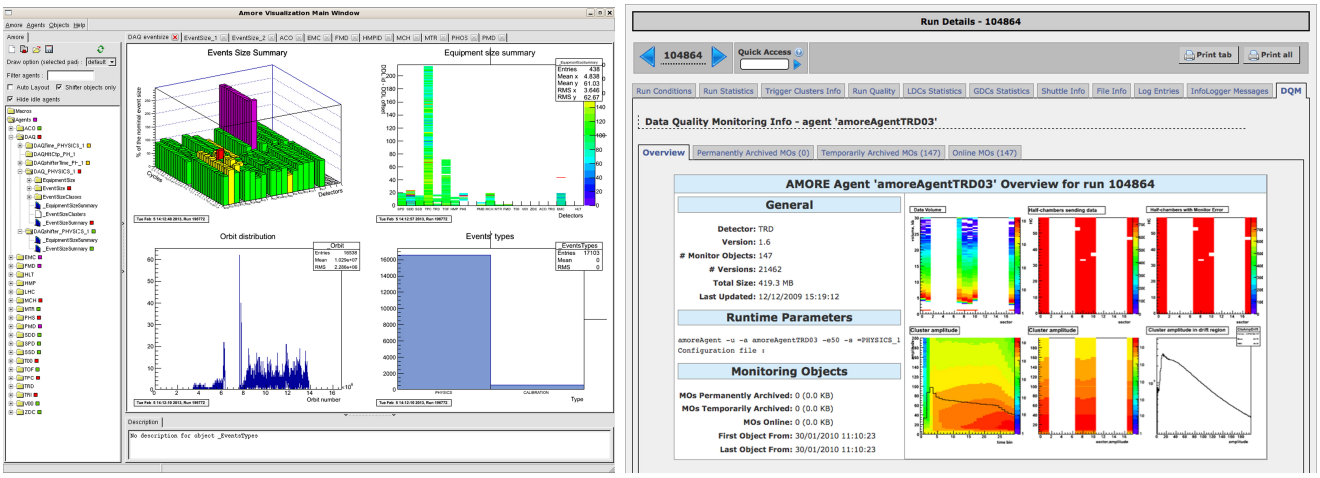


**Figure 6.4:** Examples of MOs visualisation, using the AMORE generic GUI (left) or accessed through the eLogbook (right). Figures taken from Ref. [230].

### 6.1.3 High-Level Trigger (HLT)

The HLT [234] is a large PC farm supporting the ALICE DAQ. Its main purposes are to emit a software trigger decision and provide efficient data compression as to reduce the amount of space needed for data storage. By performing a real-time, full-event reconstruction, the HLT enables the application of efficient compression algorithms. The complete reconstruction allows as well one to perform a direct, high-level evaluation of the quality of the data, immediately revealing problems that arise during data taking. The precise reconstruction of the event requires a calibration of the detectors, which in turns relies on a first reconstruction as input. By performing a fast, online reconstruction, the HLT contributes to the calibration procedures and helps reducing the required offline resources. In summary the HLT participates to triggering, online reconstruction, calibration, quality monitoring and data compression. The architecture of the HLT is described in Figure 6.5.

Since the TPC produces more than 90% of the data volume, it constitutes the main target for data compression and provides the HLT with its most intensive computing tasks. The processing of the TPC data starts with the clusterisation of the raw data, which happens on-the-fly as the data flow received by the C-RORCs is pushed into FPGAs. The cluster finder of the HLT extracts the hits from the raw data, looks for time-separated bunches of neighbouring signals in the TPC detection plane, and calculates the coordinates using the weighted mean of the signals (i.e. their centre of gravity) along with the computation of other quantities such as the total charge and the cluster width. The data compression is then achieved in two ways:

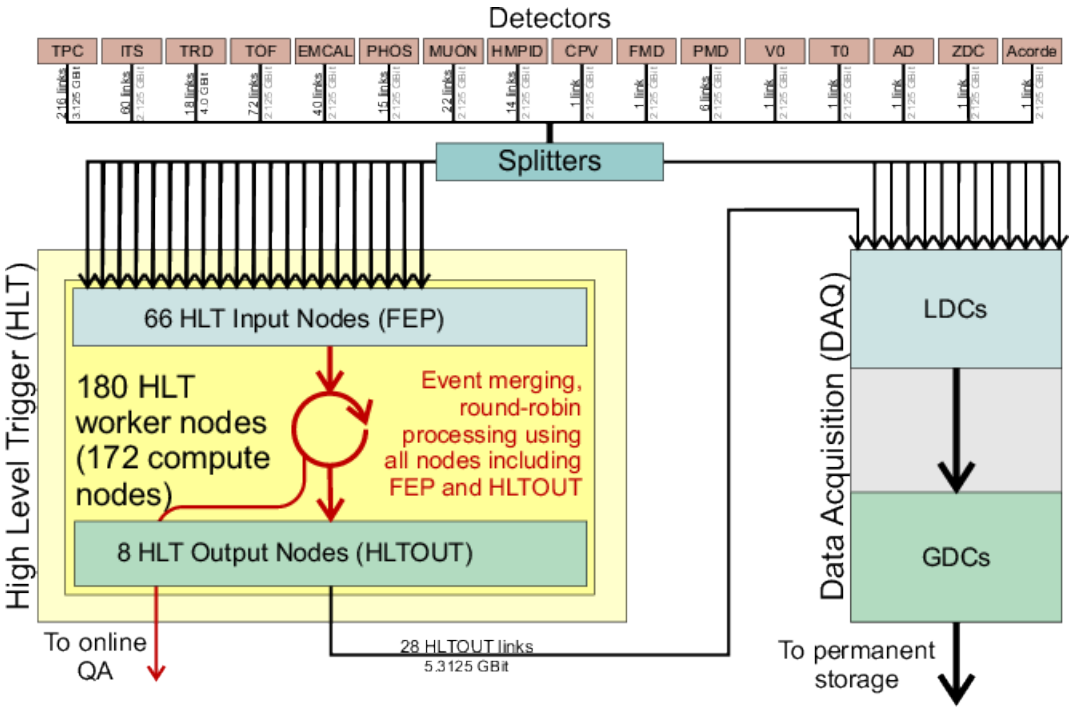


**Figure 6.5:** The ALICE HLT in the data readout scheme. The HLT output (HLTOUT) is sent back to the DAQ at the LDC level. In parallel, Quality Assurance (QA) and calibration data are shipper via dedicated interfaces. Figure taken from Ref. [234].

1. the computed floating point properties are converted into fixed point integers, with the last significant digit corresponding to the detector resolution;

2. the fixed size properties are furthermore compressed using Huffman entropy encoding [235].

The compression of the raw data themselves would yield a maximum compression factor of two, lower than what is achievable at the cluster level. Figure 6.6 shows the compression rate, as a function of the number of TPC clusters, achieved during pp collisions at $\sqrt{s_{\mathrm{NN}}} = 13$ TeV in 2017. An average compression factor of 7.3 was achieved. The TPC raw data are eventually replaced by the HLT compressed data.

Following the clusterisation, a real-time track reconstruction is performed. As to cope with the performance requirements of the HLT, the online track-reconstruction algorithm differs from the offline one, still based on the Kalman filter technique [215] but with a more heuristic approach, first looking at each individual TPC sectors independently, then combining them. The algorithm does not employ decision trees or multiple track hypotheses, a cluster shared among track candidates is immediately assigned to the one satisfying best the track quality criteria. The HLT track finder is shown to achieve a resolution comparable to that of the offline finder, while running an order of magnitude faster.

In a second, independent branch, the reconstruction process for other individual detectors starts with the clusterisation of the raw data, and continues with the track finding. This, combined with the reconstructed TPC tracks, leads to the creation of the Event Summary Data (ESD), a complex

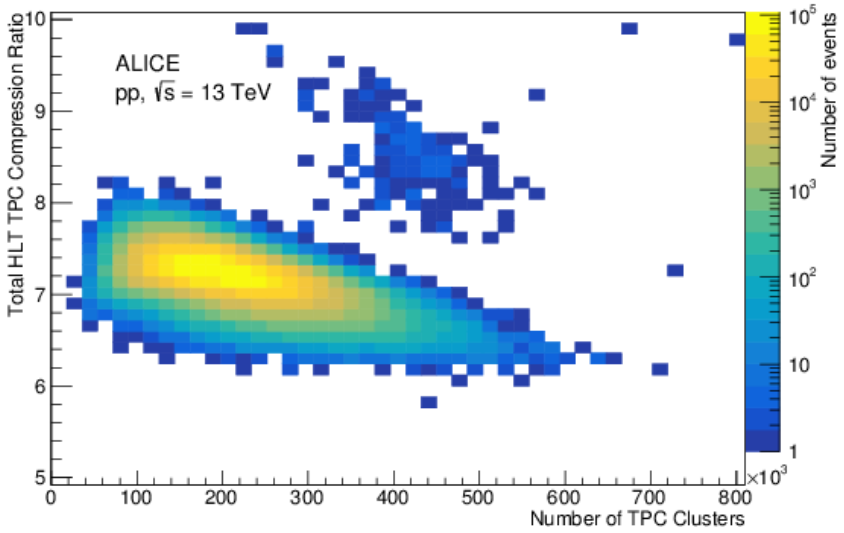


**Figure 6.6:** HLT compression factor achieved for TPC data, as a function of the input data size expressed in terms of the number of TPC clusters, in pp collisions at $\sqrt{s_{\mathrm{NN}}} = 13$ TeV in 2017. The average compression factor over the whole period amounts to 7.3. Figure taken from Ref. [234].

ROOT data structure holding all of the reconstruction information for a given event. The HLT sends its output back to the DAQ via dedicated optical links. In addition, it forms a trigger decision, containing a readout list specifying the detector output to be stored or discarded. The DAQ buffers the event fragments locally, waiting for the HLT decision to arrive. Upon positive decision, the event is accepted if all the detector links are able to store data, rejected if none of them can. A negative decision can be issued for some detector links, in which case the corresponding data may be replaced by the HLT ones.

The TPC, being a drift detector, is very sensitive to changes in the environmental conditions such as the pressure or the temperature, through their effects on the properties of the gas inside the drift chamber. The tracking quality is also affected by the geometrical misalignment between the TPC and the ITS. In order to account for the latter, calibration maps are computed online from the received data by comparing independently fitted TPC track parameters with those found in the ITS. The maps are then used to correct the clusters. As no data are available at the beginning of the run, the HLT starts from a default calibration. Then, after the collection of a sufficient amount of data (roughly 3 000 Pb–Pb events, which takes about two minutes), a map is established and replaces the previous one. The calibration maps are updated every 15 minutes, corresponding to the time window during which the drift time calibration is stable. Currently, the HLT has access to the value of the pressure at the beginning of the run, and no access to the temperature at all[2]. On the contrary, pressure and temperature as a function of time is available for offline calibration.

[2] A fact that will change in Run 3, during which the temperature at the beginning of the run will be communicated to the HLT.

On average, the difference in position along the $z$ axis evaluated with online and offline calibrations lies around 0.5 mm, which is of the order of the intrinsic TPC space point resolution.

Finally, the access to the raw data from all the detectors, and the subsequent reconstruction of the event fragments, allow the HLT to participate in the data quality monitoring. User-defined quantities are collected or evaluated for each event and used to fill histograms on-the-fly, which can the be accessed at any time during the run or displayed by the monitoring stations in the control room.

### 6.1.4 Detector and Experiment Control Systems (DCS and ECS)

As shown in Figure 6.7, the ALICE control system includes all control activities of the online systems: the ECS, the DCS, and the control of the DAQ, Trigger and HLT.

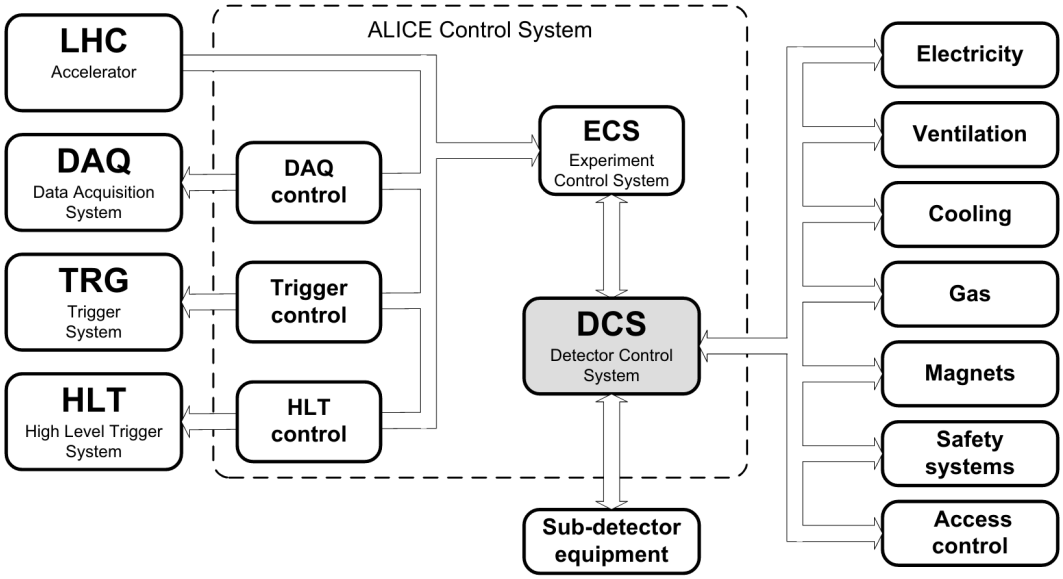


**Figure 6.7:** The ALICE control system put in context. Figure taken from Ref. [229].

The DCS is responsible for the safe and correct operation of the ALICE experiment. It aims at ensuring the highest possible running efficiency by reducing downtime to a minimum and maximising the number of readout channels operational at any time. It contributes as well to the efficiency of physics analysis by storing all the necessary parameters. A strong emphasis was put on its availability and reliability, as it is meant to be operational, sometimes unattended, throughout all the phases of the experiment, including shutdowns. The core of the DCS is a commercial Supervisory Control And Data Acquisition (SCADA), which controls and monitors the detector devices (such as the high voltage set to the muon tracking chambers, for instance), provides configuration data from the configuration database and archives relevant data into an archival database.

The hardware architecture relies on a 3-layers organisation. The lowest-level, so-called field layer consists of devices connected to the about 150 sub-systems of ALICE, collecting information

from the sub-detectors and providing services to them. The intermediate-level controls layer, composed of about 100 PCs and a number of Programmable Logic Controllers (PLCs), collects the information sent by the field layer and send control commands to the devices. The top-level supervisory layer provides the user interface and the connection to the disk servers or to the ALICE external systems.

The software architecture is a tree-like structure mimicking the structure of the sub-detectors and their own sub-systems and devices. The framework enables the communication with external devices and systems through a standardised set of interfaces. The basic building blocks are the Control Units, modelling the behaviour and interactions between components, and the Device Units driving the equipment to which they correspond. At the end of the run, the critical parameters for physics analysis are exported from the archival database to the Offline Condition DataBase (OCDB), a set of files containing the alignment and calibration data.

The ECS is the top level of control in ALICE, providing a unified view of the experiment and a central point from where all the operations are initiated and controlled. It also allows for independent, concurrent activities on parts of the experiment by different operators through a splitting of the experiment, at the detector level, into partitions. The ECS then performs the configuration of the partitions, manages the resources allocated to them, and handles potential conflicts between them. The architecture of the ECS is illustrated in Figure 6.8.

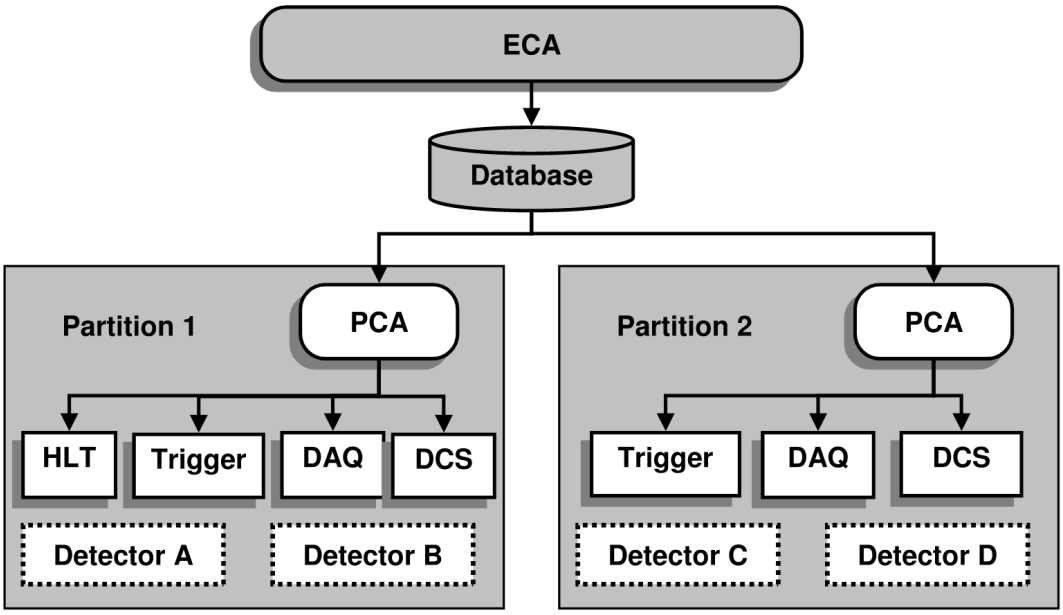


**Figure 6.8:** Schematics of the ECS architecture. Figure taken from Ref. [229].

At the heart of the system lies the database, where all resources are described. Its manipulation is facilitated by an utility, the Experiment Control Agent (ECA). Resources are allocated by the Partition Control Agent (PCA), creating an environment in which only the allocated resources are visible to the online systems. Within a partition, the ECS manages the specific control systems

active at a lower level (DCS and controls of the Trigger, DAQ and HLT) and the communication and synchronisation with the LHC machine.

## 6.2 ALICE Offline

The ALICE offline framework [236, 237] is a set of softwares used by the ALICE collaboration for data processing. Except for some legacy FORTRAN code, it is based on the Object Oriented (OO) paradigm through the use of the C++ programming language [238]. Using ROOT [232] as a baseline framework, it provides an environment for event generation and reconstruction, detector simulation, as well as data acquisition and analysis. The framework has three main objectives:

- the simulation of various processes featured in hadronic collisions,
- the reconstruction of physics data from simulated and real interactions, including the detector response,
- the analysis of the reconstructed data.

It is the end point of the experimental activity, in which the physics content is extracted from the data.

### 6.2.1 The LHC computing grid

During Run 2, CERN was storing around 8 Gb of data per second, while seeing global transfer rates of over 60 Gb/s. This amount of data produced, processed and stored during running time requires massive computing and transfer capabilities. Providing the global resources for storage, distribution and analysis of the data is the role of the Worldwide LHC Computing Grid (WLCG) [239], a network of about 900 000 computer cores from over 170 sites in 42 countries. The general layout of the grid was formalised in the hierarchical, so-called MONARC model [240] and is illustrated in Figure 6.9.

MONARC is a distributed system in which the computing centres are organised in Tiers. Tier 0 is the CERN data centre itself (which is also part of the Tier 1 and 2 levels), located in Geneva, Switzerland. It represents about 20% of the total computing capacity, and is responsible for the storage of the raw data, the running of first reconstruction passes, and the distribution of the raw and reconstructed outputs to the Tier 1 centres. The Tier 1 level regroups thirteen major computing centres with high storage capacity and permanent support for the grid. Tier 1 centres outside of CERN collectively store a copy of the raw and reconstructed data, providing a natural backup. They participate to the large-scale reprocessing of the data, and ensure safe-keeping and distribution of the corresponding output to Tier 2 centres. Tier 2s are smaller regional computing centres, typically universities and other scientific institutes. They can provide sufficient computing power and storage capacities for specific analysis tasks. One of the major difference between the Tiers is the Quality of Service (QoS) and the reliability of the computing resources, the highest level being offered by Tiers 0 and 1. Outside of the grid model, one can also consider Tiers 3 and

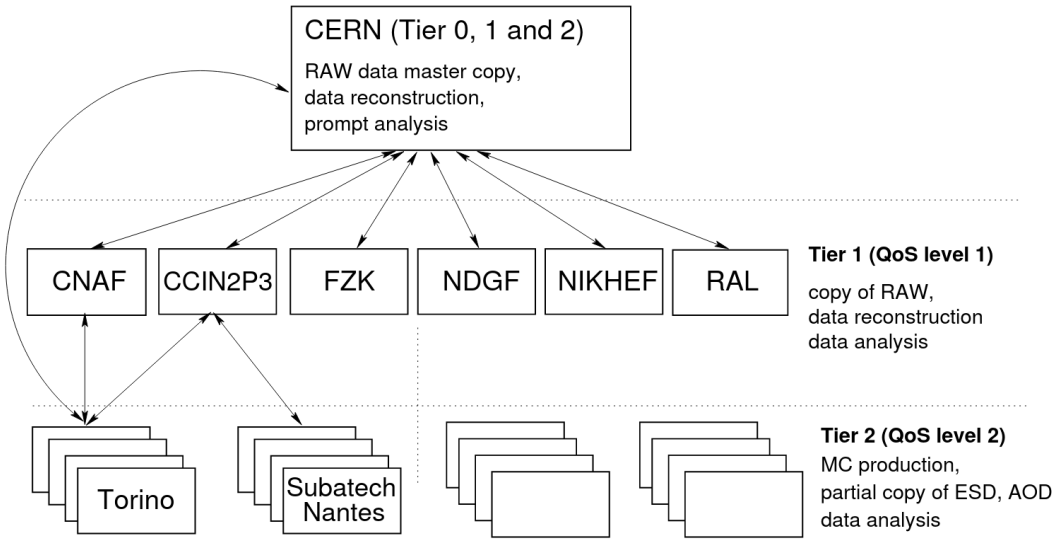


**Figure 6.9:** Schematic view of the computing grid hierarchy in the framework of the tiered MONARC model. Figure taken from Ref. [236].

4, corresponding to university departmental centres and user workstations, respectively.

The user interacts with the grid by means of the User Interface (UI) provided by the ALICE Environment (AliEn) system [241]. AliEn was conceived as the ALICE user entry point into the grid, shielding him from the underlying complexity and heterogeneity. The authentication in AliEn allows the user to access the grid, retrieve data and submit jobs for simulation and analysis using Job Agents (JAs). Users describe their jobs via the Job Description Language (JDL). The submitted jobs are collected on the AliEn servers and distributed among the computing centres, taking into account the grid and centres workload and the availability of the requested files. AliEn also provides an interface in ROOT using Application Programming Interface (API) services, as well as the Information and Monitoring services used to check and publish the status of the grid under the MonALISA framework [242]. Through the MonALISA interface, the user can monitor the jobs and collect several parameters such as the job status, its running and cpu times or its memory consumption.

### 6.2.2 ROOT and AliRoot

AliRoot is the name of the ALICE offline framework for Run 1 and 2. It is based on ROOT, an OO program and library developed by CERN, optimised for an efficient handling of very large quantities of data. Originally dedicated to high-energy physics, and containing therefore several features specific to this field, it is now used in many other applications such as astrophysics and data mining. Key features of ROOT include its Input/Output (I/O) subsystem, allowing one to store and retrieve C++ objects, and its data containers called ROOT `trees`, with its substructures `branches` and `leaves`. The ROOT framework offers a number of important elements which are

exploited in AliRoot, including a complete data analysis framework, with a large set of utility functions such as commonly used mathematical functions, random number generators, and multi-parametric and minimisation procedures. The inclusion of a C++ compiler (initially CINT, now Cling) makes it versatile, allowing one to use it to execute C++ scripts and command line inputs. The Parallel ROOT Facility (PROOF) [243] extends ROOT capabilities on parallel computing systems and clusters, providing a distributed, parallel computing platform for large-scale production and analysis.

The AliRoot framework is illustrated in Figure 6.10. The central part of the framework is the STEER module, which provides steering of program execution for simulation, reconstruction and analysis, general run management, creation and destruction of data structures, and base classes for simulation, reconstruction, and detector elements. To each detector corresponds an independent module containing the necessary code for simulation and reconstruction. AliRoot was designed with two basic principles in mind: modularity and re-usability, as to maximise the participation of physicists in the code development and minimise the amount of unused or rewritten code.

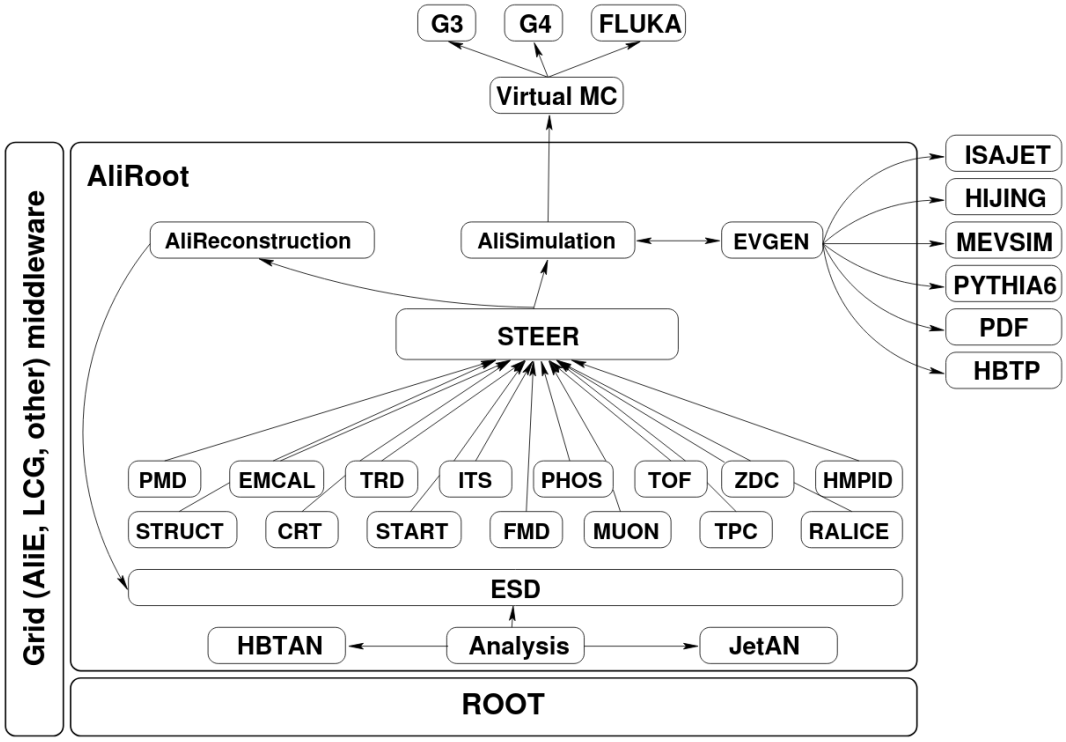


**Figure 6.10:** Schematic view of the AliRoot framework. Figure taken from Ref. [236].

Modularity allows for the replacement of part of the system with minimal to no impact on the rest. Elements of the framework are made modular by defining an abstract interface to them. This provides, for example, the possibility to use different transport Monte Carlo's, via a set of virtual interfaces that are part of the ROOT system, called Virtual Monte Carlo (Virtual MC). Several event generators can also be used, either independently or in combination, by means of

the EVGEN interface. The standardisation of the output through the interfaces allows one to make such changes without affecting the user code. Re-usability protects the investment made by programmers, ensuring the maximum amount of backward compatibility as the system evolves.

### 6.2.3 Simulation and reconstruction

The role of the AliRoot framework for simulation and reconstruction is shown schematically in Figure 6.11. An event generator, by means of MC techniques, produces a set of particles with the associated kinematic information. A kinematic tree is build following the production history, in the form of mother-daughter relationships and from the knowledge of the production vertex. The generated tracks are then transported through the detector via detector simulation packages such as GEANT 3 [244], GEANT 4 [245] or FLUKA [246]. The package transports the particle through the set of simulated detectors and produces hits, which in the terminology inherited from GEANT3 indicates the energy deposition at a given point. At the next step, the detector response is taken into account. The hits are dis-integrated, the generated track information is removed from the hits and the MC information is only kept in labels attached to the hits, as to be retrieved at the end of the chain for comparison. In the digitisation process, hits are first transformed into an ideal detector response, then a real detector response, accounting for the electronic manipulation of the signals, and replicating the running conditions taken from the OCDB. If one needs to superimpose different simulated events, an intermediate high-resolution, zero-threshold format called summable digits can be used. This enables for example event merging, where a signal event is embedded into a signal-free underlying event as to include the occupancy in the evaluation of the detector response. Eventually, the digits are converted into raw data, a format corresponding to the actual output of the detector during data taking. From here on the processing of simulated data is indistinguishable from the processing of the real ones.

The data produced by the event generator contain the full information on the particles, including their identification and momentum. Along the processing chain, the information is dis-integrated and reduced to that generated by particles crossing the detector. The reconstruction algorithms used on the real raw data are applied to the simulated ones in order to reconstruct the full event in a similar way. The presence of the labels allows one to link the reconstructed information with the information taken directly from the MC generation, from which the detector performances can be evaluated, e.g. through the so-called acceptance-times-efficiency ($A \times \epsilon$) factor estimated by taking the ratio of reconstructed to generated signal for a given process.

Fast simulations, indicated by the arrows in Figure 6.11, are shortcuts of the whole chain, increasing the speed of the simulation by bypassing some steps. The AliRoot framework implements several algorithms for such simulations. A typical need for fast simulation comes from low cross-section observables, for which high-statistics simulations are required, above the computing resources generally available. In this case the full detector response can be replaced with a meaningful parametrisation of the acceptance, efficiency and resolution. The parameters are to be evaluated once, through a detailed simulation, and can then be reused during analysis. The systematic error introduced by the fast simulation procedures is in general small compared to the reduction in statistical uncertainty. The AliRoot framework for fast simulations is highly modula-

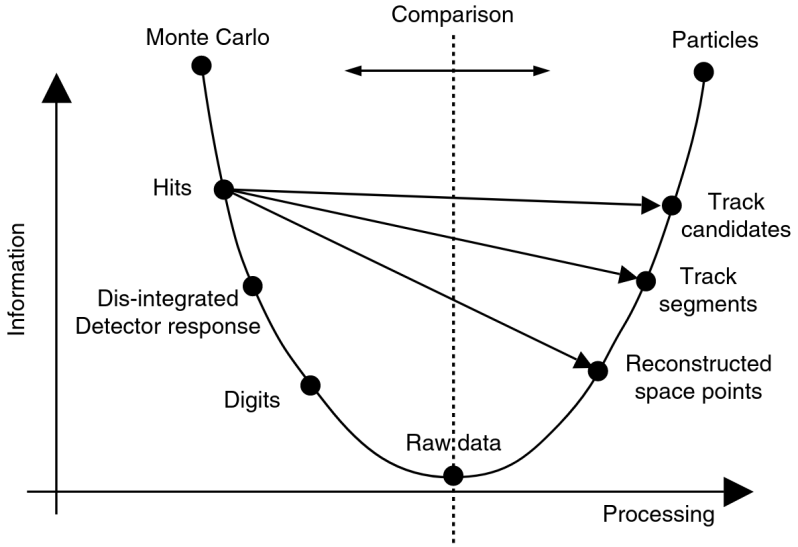


**Figure 6.11:** Schematic depiction of the data processing framework in AliRoot. The vertical dashed line separates the simulation part (left) from the reconstruction one (right). The curve follows the full simulation and reconstruction chain, the arrows indicate the possibilities for fast simulations (see text for details). Figure taken from Ref. [188].

ble, allowing the user to define and implement methods specific to a given analysis task.

The output of the reconstruction procedure is the ESD, a ROOT file including all the necessary information for physics studies, such as global event properties, PID, track momenta, etc. The size of the ESD is already about one order of magnitude smaller than that of the raw data. This can be further reduced by a train of user-defined analysis tasks, producing Analysis Object Data (AOD) after the filtering of the ESD following the needs of specific physics objectives. After each collision period, so-called scheduled analyses are planed and prioritised in order to produce general AOD for a given physics channel, following the needs of the various Physics Working Groups (PWGs). A typical example is the AOD for muon analysis, containing only events where a muon-related trigger was fired and removing data of some of the central barrel detectors. This extra step of filtering reduces even more the size of the files needed to be read, ensuring a scalable economy of computing time and resources.

# Chapter 7

# ALICE in the LHC Run 3

This chapter presents the upgrade of the ALICE detector that is ongoing thanks to the LHC long shutdown. The upgrade aims at providing the experimental apparatus and continuous readout capabilities necessary to fully benefit from the high p–Pb and Pb–Pb collision rate delivered by the LHC after its restart, scheduled for the first semester of 2022. During Run 3, a total luminosity of $\sim 10$ nb$^{-1}$ is foreseen in Pb–Pb collisions. The physics motivation for the upgrade is summarised in Section 7.1. It is followed by a description of the detector upgrades in Sections 7.2 and 7.3 for the central barrel and the muon spectrometer, respectively. The unprecedented collision and recording rates that are foreseen require, in addition to the detector upgrade, a significant modification of the software environment, leading to the development of the Online-Offline framework described in Section 7.4. In this last section, the module for the Quality Control of the Muon Identifier data is presented, as its development constituted the Service Task of this thesis work.

## 7.1 Physics motivation

QCD is the established gauge theory of the strong interaction. However, several of its fundamental aspects are not well understood, such as the parton-hadron transition, the nature of confinement, and the nature of the QCD matter at high temperature. The main objectives of ALICE are the experimental verification of the phase transitions and the investigation of the properties of the strongly-interacting matter. In order to fulfil its scientific program, and fully exploit the potential of the LHC run 3, the ALICE collaboration is upgrading its hardware and software environment, aiming at extending the precision of the current measurements and enabling new ones. The main part of the physics program, which defines the requirements for the detector, concerns the production of heavy-flavour hadrons, quarkonia and low-mass dileptons. The upgraded ALICE detector can also bring significant contributions to jet measurements and searches for heavy nuclear states. A short description of the main physics motivation is given below, a detailed description can be found in the ALICE upgrade Letter of Intent [247].

**Heavy flavours** The high-precision measurement of charm and beauty production in HIC is one of the main physics motivations for the upgrade of the ALICE detector. Two topics that need high-precision and high-statistics measurements are foreseen:

- the study of the thermalisation of heavy quarks in the medium, through the determination of the baryon-to-meson ratio for $c$ and $b$ particles, the azimuthal anisotropies, and possible in-medium thermal production of charm quarks,
- the evaluation of the parton-mass and colour-charge dependencies of the in-medium energy loss, by measuring the $p_{\mathrm{T}}$-dependencies of the nuclear modification factors separately for D and B mesons and comparing them with those for light-flavour particles.

The capability of studying yields and spectra of particles containing heavy quarks is given by the performance of secondary-vertex isolation close to the primary interaction vertex. Removing the high background affecting such measurements, especially at low $p_{\mathrm{T}}$, requires excellent particle identification (PID) capabilities, beyond what can be achieved with the present detector.

**Quarkonia** Measurements of the charmonium family will be a key objective of the LHC run 3. Charmonia are the first hadrons for which a clear suppression mechanism in QGP was proposed, based on a colour-charge analogue of Debye screening [248]. Further extensions of the model were proposed following the difficulties or reproducing the observed suppression patterns, notably that of $\psi(2S)$. One of the main alternative is the statistical hadronisation model, in which the charm quarks produced in the initial hard collisions thermalise in the QGP and are distributed into hadrons at chemical freeze-out. The model then takes as input the charm-production cross section, thus requiring its precise determination. Another model for charmonium production is the kinetic transport model, in which a continuous dissociation and regeneration of charmonium takes place in the QGP over its entire lifetime. Besides the charm-production cross section, this model requires the knowledge of the time dependence of the temperature, as well as other relevant cross sections and assumptions on the melting scenarii of charmonium states.

The measurement of the production of different charmonium states in Pb–Pb collisions at the LHC should provide a definitive answer on the question of the production mechanism in the QGP. The published results from the LHC runs 1 and 2 indicate the importance of measurements down to zero $p_{\mathrm{T}}$. Statistically significant measurements of the different charmonium states is also mandatory, the excited $\psi(2S)$ and $\psi(3S)$ being prime examples calling for high statistics, and the expected integrated luminosity of run 3 will bring the measurement of the yield, nuclear modification factor and elliptic flow up to new precision levels. Other measurements are expected to benefit from the ALICE upgrade, such as the $J/\psi$ polarisation and production at low $p_{\mathrm{T}}$, where an excess, possibly coming from photo-production, has already been observed.

The upgrade will also enable a more precise measurement of the $\Upsilon$ family, bringing additional and complementary information on the QCD colour force with respect to the charmonium family. The bottomonium production is sensitive to the same phenomena as the charmonium system. However, the binding energies in vacuum and the dissociation temperatures in a heat bath differ significantly, the measurement then allows for the access of different regions of the in-medium heavy-quark potential.

**Low-mass dileptons** The measurement of low-mass dileptons gives an insight into the bulk properties and space-time evolution of the hot and dense QCD matter formed in ultra-relativistic HIC, and provides an access to the hadronic excitation spectrum in the medium. Such measurements assess:

- the spontaneous breaking of chiral symmetry, through the distortion of the vector and axial-vector spectral functions, and which is related to the masses of the light-quark particles. Such modifications, in particular for the $\rho$ meson, should be observable in dilepton spectra,
- the temperature reached by the system, evaluated by measurements of the dilepton invariant-mass and $p_{\mathrm{T}}$ spectra,
- the lifetime of the phases of the system and its overall space-time evolution, by disentangling early and late contributions allowing one to access the evolution of collectivity and the fundamental properties related to it, such as the transport coefficients, the viscosity, and the equation of state which become potentially accessible.

The measurement of low-mass dileptons with the upgraded ALICE detector will exploit the $\mathrm{e}^+$ $\mathrm{e}^-$ channel. The detection capabilities must go down to 0.1–0.2 GeV/$c$ in order to reach dilepton invariant masses and transverse momenta as low as the critical temperature $T_c \simeq 150$ MeV. Measurements in this region are challenged by the rejection of different backgrounds, such as electrons from Dalitz decays, charm decays and photon conversion in the detector material. In order to achieve this goal, the upgrade aims at improving the tracking capabilities at very-low momenta, enhancing the vertexing capabilities through which the photon-conversion and charm-decay background are suppressed, and lowering the material budget for a reduction of the conversion probability. It is also important to increase the integrated luminosity, by achieving a high-rate event detection and storage.

**Jets** The study of jets enables to map out the energy loss of hard scattered partons in the QGP, giving an access to the properties of the medium. On their way out of the medium, partons interact with the QGP, losing energy through both radiative and elastic processes. The observed energy loss, referred to as jet quenching, strongly depends on the colour-charge density in the medium. It softens the fragmentation function of the jet, which results in an enhancement of low-momentum hadron multiplicity and a depletion of the high-$p_{\mathrm{T}}$ region. The measurement of jet quenching opens the probing of the medium at the hottest, densest stage of the collision. Precise measurements of the jet substructure and of its modification in terms of energy flow, of the modification of jet-energy patterns, and of the broadening of jets due to interactions in the hot matter promise to offer new fundamental insights into the underlying theory. ALICE provides tools for differential studies of the jet structure through the track reconstruction and separation down to low momentum, and the PID including that of heavy flavours. The high-rate upgrade will also provide substantial benefits for photon-jet correlation studies, which are typically limited by the small cross section of electromagnetic processes and the challenge of extracting isolated photons in HIC.

**Heavy nuclear states** Another area where the ALICE measurements are unique is the search for exotic objects. The PID capabilities benefit from the combination of different detectors and techniques, which has lead for example to the successful search for the $\overline{^4\mathrm{He}}$ antinuclei. The expected high rate will enable the inspection of as many as $10^{10}$ Pb–Pb events, allowing for a systematic study of the production of nuclei and antinuclei, bringing within reach the detection of light multi-hyper-nuclei such as ${}^{5}_{\Lambda\Lambda}\mathrm{H}$. Other exotic objects to search for include bound states of $(\Lambda\Lambda)$ or the H dibaryon, a possible $(\Lambda\mathrm{n})$ bound state, as well as bound states involving multi-strange baryons. The important point to note here is that, using the ALICE apparatus, in addition to search for the existence of these states, one can also study their decay properties. The presence of strangeness in these objects, making them more flavour symmetric than ordinary matter, may increase their stability. Such observations would give access to completely new information on hyper-nuclei and other heavy-nuclear bound states.

## 7.2 Central barrel and global detectors

### 7.2.1 Inner Tracking System

The present ITS [203] consists of six cylindrical layers of silicon detectors placed coaxially around the beam pipe, at radii from 39 to 430 mm and covering the pseudorapidity range $|\eta| < 0.9$. The number, position and segmentation of the layers were designed to achieve the highest possible precision in the determination of charged particles distance of closest approach ($DCA$) to the primary vertex and efficient track finding in combination with the TPC. The inner radius is the minimum allowed by the beam pipe, while the outer radius is required to match tracks with those from the TPC. A crucial limitation of the present ITS detector is given by its limited readout capabilities. Although only marginally dependent on the detector occupancy, the ITS can run up of a maximum of about 1 kHz. For the physics observables aimed at by the upgrade physics program, for which selective triggers cannot be applied, this rate limitation would restrict ALICE to use only a small fraction of the full Pb–Pb collision rate.

The upgrade of the ITS [249] aims at solving these issues, by modifying the layout, the segmentation and the readout of the detector. The new ITS, ITS2, is fully based on the CMOS Monolithic Active Pixel Sensors (MAPS) technology, which combines sensitive volume and front-end readout logic in the same piece of silicon. Such a technology allows for the reduction the material budget thanks to the thin sensors (50 to 100 $\mu$m) and limited need of cooling, in combination with light-material interconnection circuits and support structures. The ITS2 layout is shown in Figure 7.1. It includes seven cylindrical layers grouped in two sub-systems: the Inner Barrel (IB), with three 27 cm-long layers with radii of 2.3, 3.1 and 3.9 cm, and the Outer Barrel (OB) composed of two 84 cm-long middle layers at 24 and 30 cm from the interaction point, and two 148 cm-long outer layers at 42 and 48 cm. The seven layers cover a total surface of about 10 m$^2$ with 12.5 gigapixels.

The ITS2 design characteristics will lead to a sizeable improvement of the ALICE tracking performances, especially for low-$p_{\mathrm{T}}$ particles, below 1 GeV/$c$. The material budget of the three innermost layers, as low as 0.35% of a radiation length $X_0$, combined with a spatial resolution

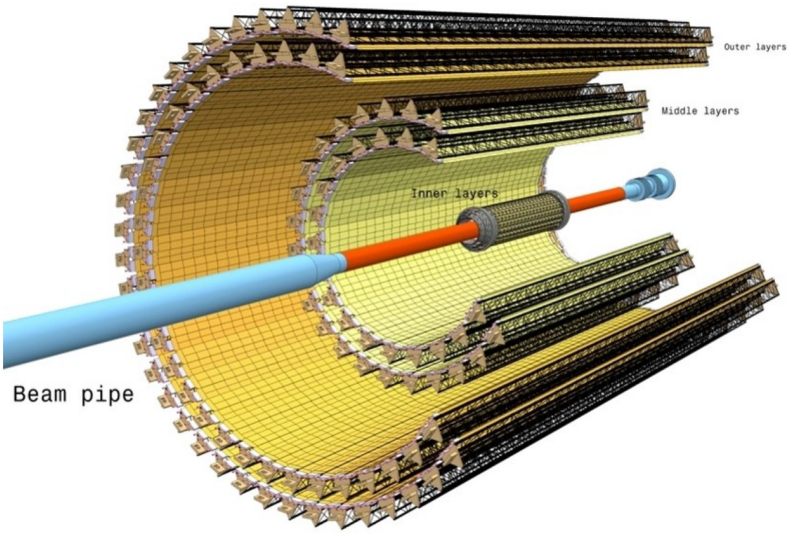


**Figure 7.1:** The ITS2 layout, with three inner layers close to the beam pipe, two middle layers and two outer layers.

of about 5 $\mu$m (measured in beam tests) and the 2.3 cm radius of the innermost layer, will drive the expected track impact parameter resolution at $p_{\mathrm{T}} \sim 500$ MeV/$c$ down to about 40 $\mu$m, which improves the original tracker performance by a factor $\sim 3$ in the transverse plane and $\sim 6$ in the beam direction. This will enable the separation of prompt and secondary $c$ and $b$ quarks. The new detector will also allow for an efficient track reconstruction down to very low $p_{\mathrm{T}}$. Simulations, displayed in Figure 7.2, show that the tracking efficiency at $p_{\mathrm{T}} \sim 0.1$ GeV/$c$ will be improved by about a factor 6. The readout electronics will also enables the recording of events at a typical rate of 50 kHz and a few 100 kHz for minimum bias Pb–Pb and pp collisions, respectively.

### 7.2.2 Time Projection Chamber

The TPC [204] is the main charged-particle tracking and PID device of the ALICE detector. It was optimised to provide high precision momentum and d$E$/d$x$ measurements in the high density of charged particles in central Pb–Pb collisions. The current design of the readout is based on Multi-Wire Proportional Chambers (MWPC) with cathode pad readout. The size of the readout pads is chosen to minimise the detector occupancy and optimise the position resolution and two-track separation, resulting in a total of 557,568 readout channels and an active readout area of about 32 m$^2$. The readout chambers employ a commonly used scheme of wire grids, including a plane of anode wires, cathode wires and a gating grid. In the absence of a trigger, the gating grid wires are biased by a voltage that prevents electrons to enter the amplification region and ions from previous events to penetrate into the drift volume. The maximum drift time of ions from the amplification region to the gating grid is about 180 $\mu$s. In order to provide efficient ion gating, the gating grid must therefore be closed for 180 $\mu$s after the end of the electron drift, Additionally, a 100 $\mu$s past protection is applied to avoid event pile-up. This sets a first limitation of about 3.5 kHz to the maximum readout rate of the present TPC. Another limitation is given by the

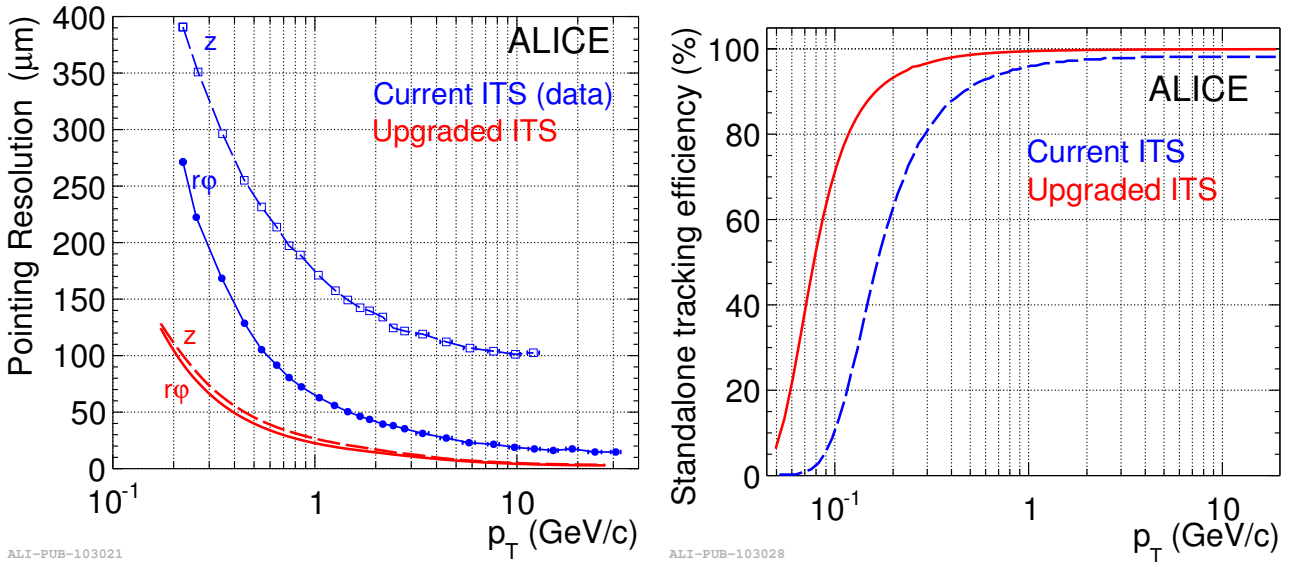


**Figure 7.2:** Simulated performances of the ITS2 (red) compared with measured performances of the original ITS (blue). The track pointing resolution (left) and the tracking efficiency (right) are shown as a function of the tracked particle transverse momentum.

readout electronics that is capable of sustaining a maximum rate of minimum-bias events of 520 Hz. Operating the TPC in ungated mode, i.e. leaving the gating grid continuously open, would result in a severe buildup of space charge in the drift volume due to back-drifting ions.

The goal of the upgrade is to operate in an ungated mode while keeping the distortions of the drift field induced by the ion space charge at a tolerable level. In particular, the excellent tracking and PID capabilities as provided by the present system must be preserved. The upgraded detector will operate continuously and triggerless without the use of a gating grid. This is achieved by using new readout chambers based on multi-stage Gas Electron Multipliers (GEM) [250]. GEMs have been proven to operate reliably in high-rate applications and provide intrinsic ion blocking capabilities, thus enabling the TPC to operate in a continuous, ungated readout mode at collision rates of 50 kHz. The TPC upgrade increases the readout rate by about two orders of magnitude compared to the present system, giving access to previously inaccessible physics observables. As an example, the low-mass dielectron invariant mass spectrum is shown in Figure 7.3, as it would be accumulated in a typical yearly heavy-ion run at an integrated luminosity of about 3 $\mathrm{nb}^{-1}$, with the current and upgraded TPC. A detailed description of the design, construction and installation of the TPC upgrade is given in Ref. [251].

### 7.2.3 Readout and trigger

The ALICE upgrade aims at reaching the readout of 50 kHz Pb–Pb collisions and 200 kHz pp and p–Pb collisions at nominal performances, as well as implementing a new online system that is capable of receiving and processing the full detector information. This requires a general modification and improvement of the detector readout and trigger systems [252]. With this program,

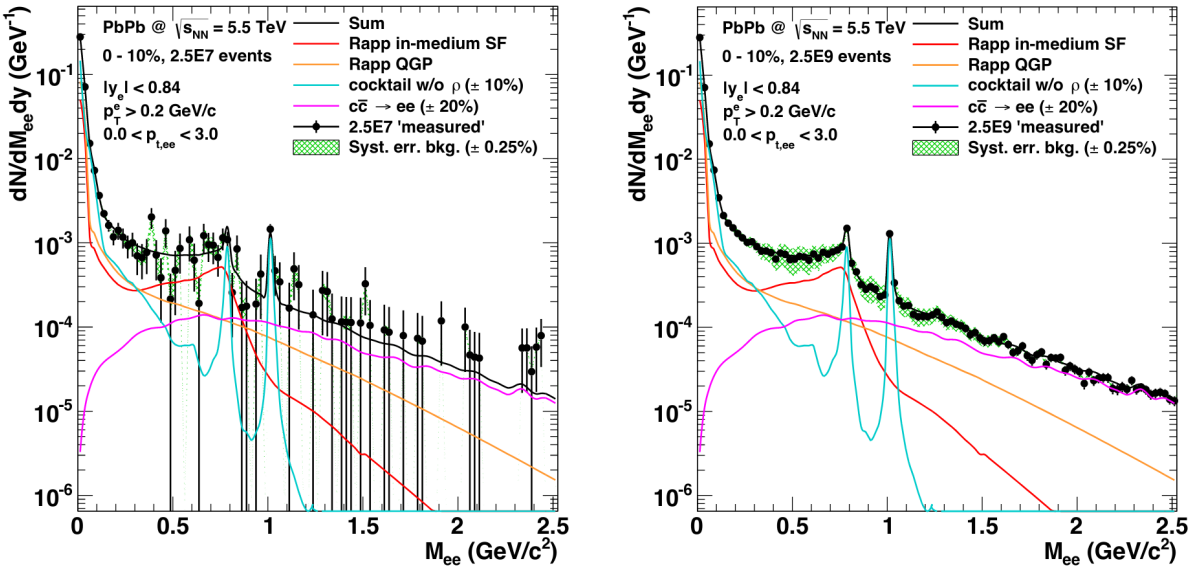


**Figure 7.3:** Simulations of the inclusive $e^+$ $e^-$ invariant mass spectrum for the 10% most central events in Pb–Pb collisions at $\sqrt{s_{\rm NN}} = 5.5$ TeV, assuming $2.5 \times 10^7$ events (left) and $2.5 \times 10^9$ events (right) corresponding to the collected data with the current and upgraded TPC, respectively. Figures taken from Ref. [247].

the statistics for the aforementioned physics topics will be increased by a factor $\sim 100$ (10) for MB events at mid- (large) rapidities over the numbers achievable with the ALICE detector up to LS2. The idea of reading the full detector information, either upon a MB trigger or in a continuous fashion, requires one single trigger signal based on an interaction trigger detector only. However, in order to keep flexibility and to allow trigger contributions for the elimination of possible background signals as well as triggers for calibration and commissioning, a Central Trigger Processor (CTP) delivering several trigger signals will be employed.

**Upgrade architecture** Figure 7.4 shows the ALICE upgraded readout scheme. The on-detector electronics systems connect via front-end links to either the ALICE Common Readout Unit (CRU) or, when the readout electronics is not upgraded, to detector-specific readout systems. The CRU, a computing unit based on high-performance Field-Programmable Gate Array (FPGA) processors, acts as the interface between the on-detector systems, the Online-Offline ($O^2$) computing system and the CTP. The readout systems are connected to the Detector Control System (DCS) via standard optical detector data links. In this scheme, three general readout configurations exist:

1. In the first configuration, the Local Trigger Unit (LTU) uses the fast serial trigger link protocol to transmit the timing and trigger information directly to the CRU located in the counting room, via a trigger distribution module. The CRU modules forward the data to the detector front-end electronics via the GBT front-end links.

2. The second configuration is used for detectors needing a minimum latency trigger path and also uses the CRU for the readout. The LTUs connect directly to the on-detector electronics,

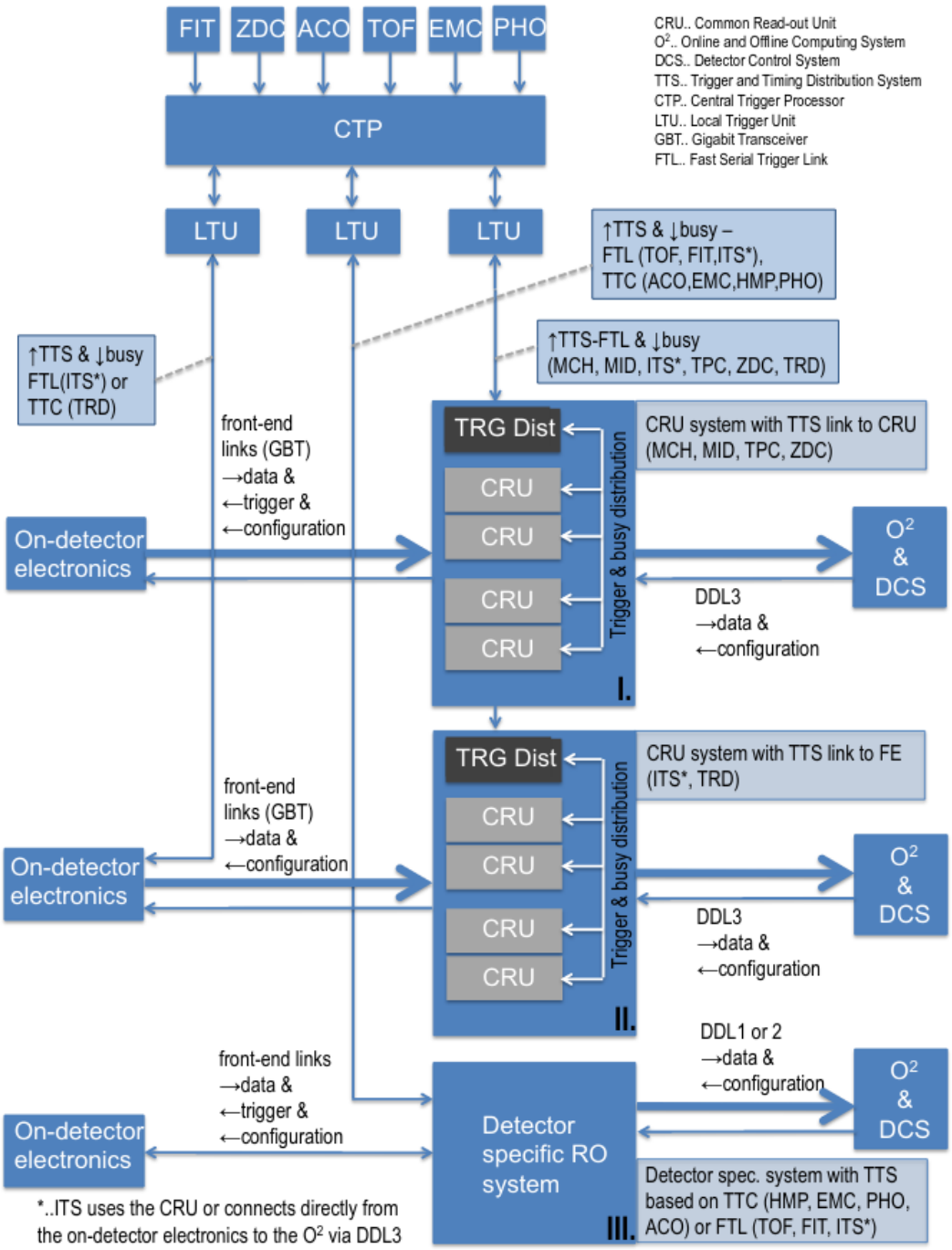


**Figure 7.4:** Upgraded readout scheme of ALICE. Configuration I: CRU is used as readout processor and trigger distribution system. Configuration II: CRU is used as readout processor, the trigger distribution is done from the CTP/LTU directly to the on-detector electronics. Configuration III: CRU is not used as the detectors do not upgrade their electronics and use detector-specific readout systems. Figure taken from Ref. [252].

bypassing the CRU, for trigger signals.

3. The third configuration does not use the CRU to read out the detector, and relies on the detector-specific systems when they are not upgraded.

**Fast Interaction Trigger (FIT)** As part of the upgrade, the cluster of ALICE forward detectors will be replaced by a single trigger detector, the Fast Interaction Trigger (FIT). The FIT will be the main forward trigger, luminometer, and detector for the measurement of the collision time. It will as well determine the event multiplicity, and the collision centrality and event plane. The FIT system is composed of three subdetectors, the FV0, FT0 and FDD, which are respectively the upgrades of the V0, T0 and AD. They are all located in the large rapidity regions, and integrated in a common front end electronics and DCS. A schematic view of the FIT sub-systems is shown in Figure 7.5, with the position, coverage and technology of each sub-detector given in Table 7.1. The diversity of the detection techniques and the scattered positions are needed in order to fulfil the many required functionalities.

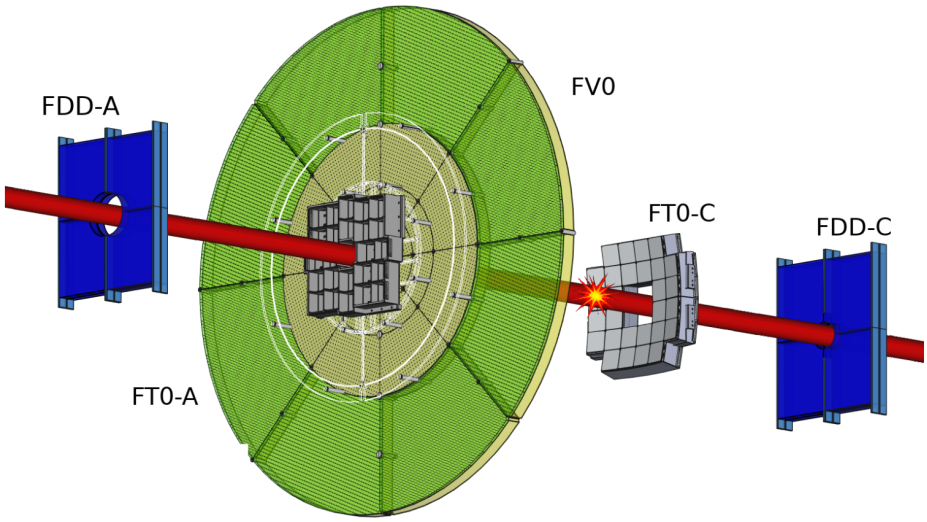


**Figure 7.5:** Schematics of the FIT layout, with the relative locations of the FV0, FT0 and FDD arrays (not to scale). Figure taken from Ref. [253].

Among the three components of the FIT detector, the FT0 is the fastest: comprising 208 optically separated quartz radiators, its expected time resolution for high-multiplicity HIC is about 7 picoseconds, ranking FIT among the fastest detectors in high-energy physics experiments. This precise timing is crucial for online vertex determination and for identifying charged lepton and hadron species using time-of-flight measurement. The FV0 is the largest component, consisting in five concentrical rings for a total radius of about 68 cm. Its size provides an optimal acceptance, which is of utmost importance for extracting the centrality and determining the event plane. Finally, the FDD uses two nearly identical scintillator arrays to tag photon-induced or diffractive processes by recognising the absence of activity in the forward direction. It will also provide a background monitoring tool.

| | $z$ position (m) | Radius (mm) | Pseudorapidity | Technology |
|---|---|---|---|---|
| FT0-A | 3.3 | $47.5 < r < 205.6$ | $3.5 < \eta < 4.9$ | Cherenkov quartz radiators |
| FT0-C | -0.819 | $63.3 < r < 211.1$ | $-3.3 < \eta < -4.9$ | |
| FV0 - ring 1 | 3.16 | $41 < r < 72.1$ | $4.5 < \eta < 5.0$ | Segmented scintillator |
| FV0 - ring 2 | | $73.9 < r < 128.1$ | $3.9 < \eta < 4.5$ | |
| FV0 - ring 3 | | $129.9 < r < 211.6$ | $3.4 < \eta < 3.9$ | |
| FV0 - ring 4 | | $213.4 < r < 386.1$ | $2.8 < \eta < 3.4$ | |
| FV0 - ring 5 | | $387.9 < r < 720.25$ | $2.2 < \eta < 2.8$ | |
| FDD-A | 17 | $62 < r < 211.1$ | $4.8 < \eta < 6.3$ | Scintillator arrays |
| FDD-C | -19 | $37 < r < 282$ | $-7.0 < \eta < -4.9$ | |

**Table 7.1:** Position, radial and pseudorapidity coverages, and technology of the sub-systems of FIT.

**Trigger system** The upgraded ALICE trigger system supports the readout of triggered and continuously read out detectors. Some sub-systems not upgrading their readout electronics will not be capable of reading the full event rate. These detectors will therefore be read out whenever they are not busy. The information is merged with the data from the other sub-detectors in the online system. Figure 7.6 shows how the physics and so-called heartbeat triggers will be used for the continuous and triggered readout. As the online system supports the continuous read-out of

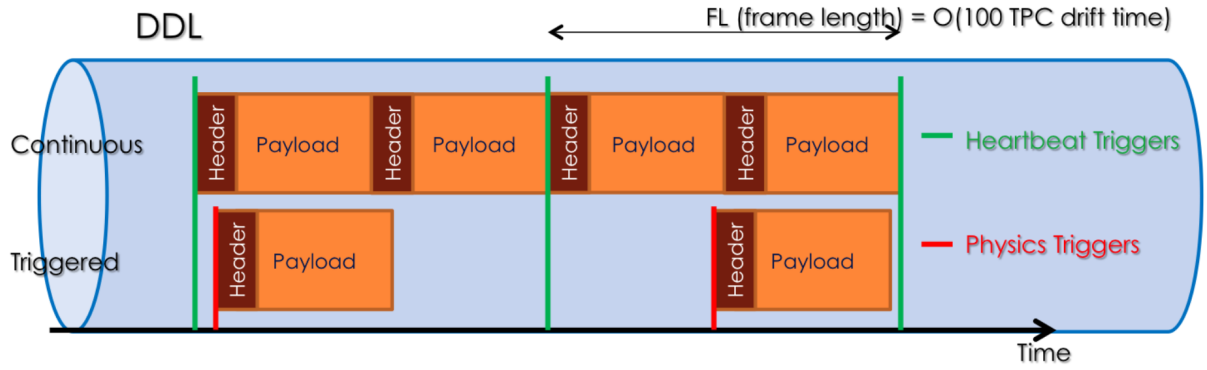


**Figure 7.6:** Illustration of the usage of physics and heartbeat triggers for the corresponding readout modes. Figure taken from Ref. [252].

detectors, the event building is based on the assembly of data recorded during a time frame of configurable length common to all detectors. The time frame boundaries are communicated to the detector readout electronics via the transmission of non-physics heartbeat triggers, allowing for the separation of the data stream into pieces for the event building. The heartbeat trigger is scheduled by the CTP to run with the highest possible priority and with a fixed period. The detector readout systems implement copies of the bunch crossing, orbit and trigger counters, The hardware compares these counters with the LHC counters only transmitted in full during a heartbeat event. In case of a discrepancy, the detector electronics re-aligns the counters and communicates the error to the online system. Each readout unit generates a heartbeat event containing no physics data

but indicating the bunch crossing and orbit counter information at which the heartbeat trigger arrived. These events are used by the online system for data segmentation, fault finding and recovery procedures. The electronics of the existing detectors are or will be upgraded to handle this combination of physics and heartbeat triggers.

The CTP will manage a system of detectors with different properties. The majority of the detectors will read out at the nominal interaction rate, dead-time free. However, in order to provide backward compatibility to detectors not being upgraded, the trigger system must cope with detectors which will have dead-time during the readout. The strategy for the upgraded ALICE system is to select and read out all interactions and apply an online data reduction in the online computing system. Trigger inputs are collected to satisfy three different latencies, given three different levels denoted as LM, L0 and L1. The LM latency is suitable for generating a wake-up signal for the TRD electronics, and is provided by the FIT detector. It will not, however, be possible to generate a trigger signal from the EMCal early enough for this trigger level, for which reason the L0 signal is retained. The trigger levels of the various sub-systems, and corresponding readout rate in 50 kHz Pb–Pb collisions, are summarised in Table 7.2.

| Group | Detector | Triggered by | Pb–Pb readout rate (kHz) | CRU used |
|---|---|---|---|---|
| Global and cosmic | FIT | L0 or L1 | 100 | no |
| | ZDC | L0 | $> 100$ | yes |
| | ACORDE | L0 or L1 | 100 | no |
| Central barrel | ITS | L0 | 100 | yes |
| | TPC | (L0 or L1) | 50 | yes |
| | TRD | LM & (L0 or L1) | 39 | yes |
| | TOF | L0 or L1 | $> 100$ | no |
| | HMPID | L0 & L1 | 2.5 | no |
| | PHOS | L0 & L1 | 42 | no |
| | EMCal | L0 & L1 | 42 | no |
| Muon | MFT | (L0 or L1) | 50 | yes |
| | MCH | (L0 or L1) | 100 | yes |
| | MID | (L0 or L1) | $> 100$ | yes |

**Table 7.2:** Readout parameter overview for Pb–Pb beam operation at 50 kHz interaction rate. Triggers in parentheses are optional. Adapted from Ref. [252].

## 7.3 Muon spectrometer

### 7.3.1 Motivation for the upgrade

The main limitation of the run 2 muon spectrometer comes from the multiple scattering effects induced on the muon tracks by the hadron absorber, resulting in the inability to determine precisely the muon production vertex. This prevents the disentanglement of open charm and open beauty

production at forward rapidity without making assumptions relying on physics models. It is impossible to separate prompt and displaced $J/\psi$ mesons, thereby losing an important source for the study of beauty production. Additionally, there are significant statistical uncertainties, especially for low masses and low $p_{\mathrm{T}}$, in single muon and dimuon analyses due to the high background coming from semi-muonic decays of pions and kaons. Also, there is limited mass resolution for the light neutral resonances. Apart from these, the readout of the present system is not designed to cope with the high rates foreseen in Runs 3 and 4. The upgrade for the muon spectrometer thus include a modification of the readout electronics [247] and the addition of a new silicon pixel tracker, the Muon Forward Tracker (MFT) [254].

### 7.3.2 Muon identifier and tracking system

The muon trigger system is upgraded to become the Muon Identifier (MID), which will operate in continuous readout mode. The readout rate will be more than two orders of magnitude larger compared to the previous design. To reduce ageing effects in the Resistive Plate Chambers (RPC), the charge per hit must be limited. This is realised by using the same types of RPCs at lower gain with a new front-end chip, called FEERIC, that provides signal amplification contrary to the previous chips. The upgrade plan includes a replacement of the RPCs closest to the beam line, as they have accumulated an already large integrated charge during Runs 1 and 2. The performance of the RPCs with the new electronics was tested to be similar to the precedent configuration. The efficiency of the FEERIC-equipped RPCs is displayed in Figure 7.7. In both the bending and non-bending planes, it is typically measured to be higher that 97%.

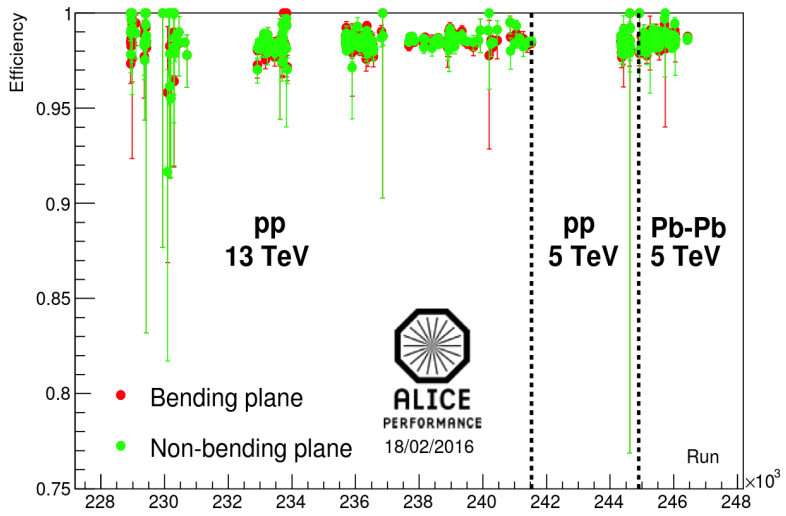


**Figure 7.7:** Efficiency of the MID RPCs equipped with FEERIC cards, measured in ALICE in 2015 for pp and Pb–Pb collisions.

The upgraded MID readout architecture is shown in Figure 7.8. The architecture features 16 crates containing one regional board and 16 local ones. The eight half-planes of the MID are segmented into 7 columns and 9 lines each, a column-line intersection is treated by up to 4 local

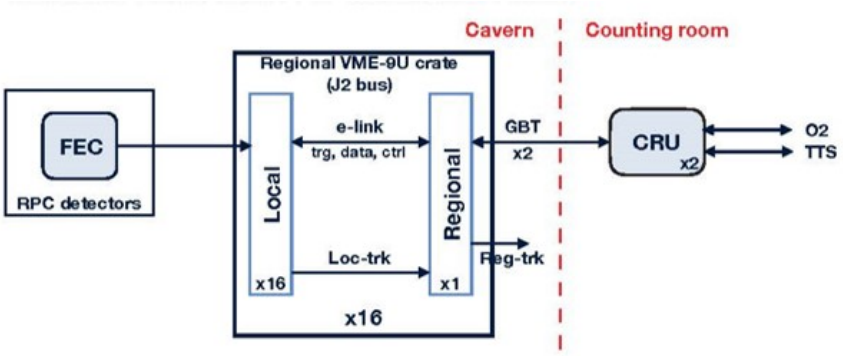


**Figure 7.8:** MID readout electronics architecture.

cards. In order to reduce the design and production effort, the hardware implementation of the regional and local boards is identical, the FPGA firmware they contain being adapted depending on the usage. The local card receives the binary chamber signal indicating whether the corresponding channel has been fired for each bunch crossing. The signal is processed by the FPGA in the local card, applying e.g. a user-defined mask of noisy channels or a reduction of the data volume through zero-suppression, providing as well a 16-bit counter for monitoring the detector counting rate and a trigger, clock, control and data interface to the regional card. The regional card receives the local information via 16 serial links, merges the raw events in their final format and add the trigger information. The regional cards contains two GBT links to send the data to the CRUs in the counting room, which then forward the MID data to the $O^2$ computing system.

The muon chambers (MCH) constituting the tracking system consist of 156 MWPC with cathode pad readout, the so-called cathode pad chambers, with more than one million electronic channels. In order to support the interaction rate of 50 kHz, the design readout rate has been set to 100 kHz as safety margin. Approximately 34,000 front-end ASICs and 17,000 front-end cards need to be replaced and are connected via about 500 GBT optical links to the CRU. The data transmission between the Front-End Electronics (FEE) and the CRU is based on optical GBT links.

The detector implementation is not modified, thus the location, physical layout and connections to the chambers of the FEE boards remain unchanged. A new front-end chip called SAMPA [255] has been developed in common with the TPC upgrade project. The previous FE boards are replaced by new Dual SAMPA (DS) boards, each hosting two SAMPA chips providing a total of 64 readout channels. The data from the DS boards are shipped out through FE links implemented on printed circuit boards. New concentrator boards accumulate data from several DS boards and send them to the CRU.

### 7.3.3 Muon Forward Tracker

The role of the MFT [254] is to measure charged tracks with high spatial resolution in front of the muon spectrometer and inside its acceptance. The MFT surrounds the beam pipe, being positioned inside the ITS outer barrel and between the ITS inner barrel and the front absorber of the muon

spectrometer. The layout and position of the MFT is shown in Figure 7.9. The MFT consists of

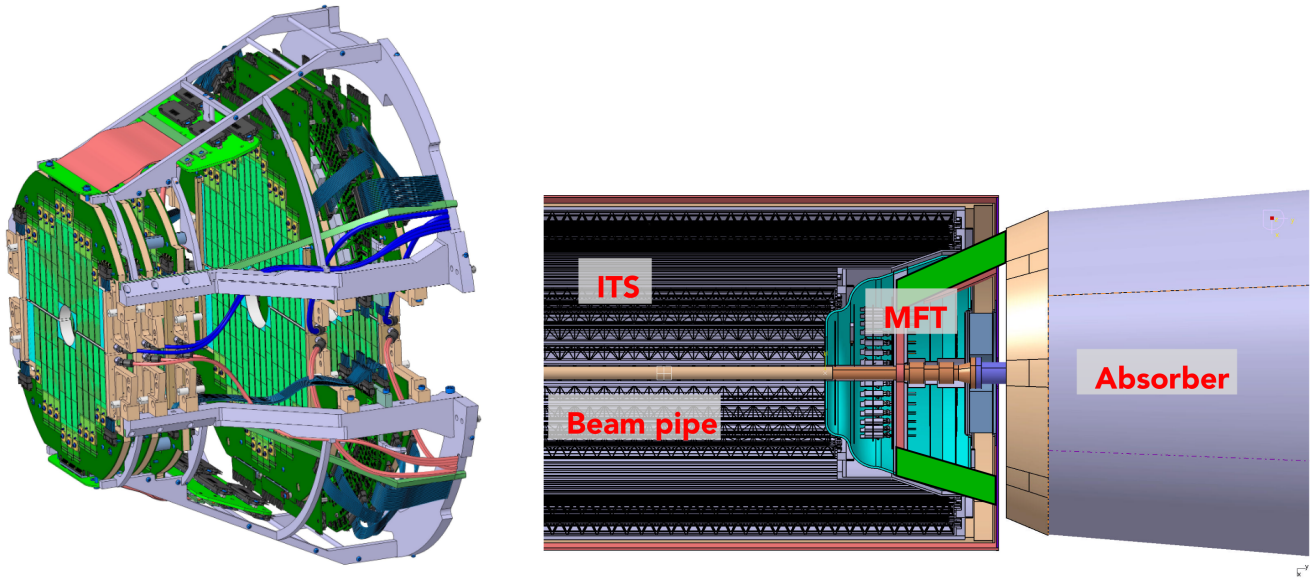


**Figure 7.9: Left**: 3-dimensional view of the MFT detector. **Right**: schematics of the MFT position between the ITS and the front absorber of the muon spectrometer.

two half-cones, each containing five half-disks. Conventionally, the half-disks are denoted HD-0 to HD-4, starting from the disk closest to the interaction point. The MFT covers the pseudorapidity acceptance $-3.6 < \eta < -2.45$. In this range, the probability for a particle to hit at least four of the five disks is greater than 90%, considering a Gaussian distribution for the interaction vertex in the $z$ direction with $\sigma \simeq 60$ mm, a value slightly superior to what has been measured during Runs 1 and 2. A half-disk consists of a disk spacer, a support, two printed circuit boards and the sensor ladders. A sensor ladder consists of between one and five silicon pixel sensors soldered to a printed circuit with aluminium strips. The geometrical parameters of the MFT and of each half-disk are reported in Table 7.3.

| | HD-0 | HD-1 | HD-2 | HD-3 | HD-4 | Full MFT |
|---|---|---|---|---|---|---|
| Inner radius (mm) | 25.0 | 25.0 | 25.0 | 38.2 | 39.2 | – |
| Outer radius (mm) | 92.6 | 98.0 | 104.3 | 130.1 | 143.5 | – |
| $z$-position (mm) | $-460$ | $-493$ | $-531$ | $-687$ | $-768$ | – |
| Number of sensors | 64 | 64 | 76 | 112 | 132 | 896 |

**Table 7.3:** Geometrical parameters of the MFT, and number of sensors per half-disk and in the full MFT. Adapted from Ref. [254].

An example of the expected effect of the MFT is shown in Figure 7.10 for the study of the $\psi(2S)$ through the dimuon invariant mass spectra. The matching between tracks in the MFT and the tracking chambers of the spectrometer will allow one to disentangle prompt and non-prompt charm and beauty production. It will gives access to the measurement of $\psi(2S)$ by enhancing the

signal-to-background ratio by a factor 5 or 6, enabling the test of dissociation and recombination models by comparing the nuclear modification factors of $J/\psi$ and $\psi(2S)$ down to zero $p_{\mathrm{T}}$.

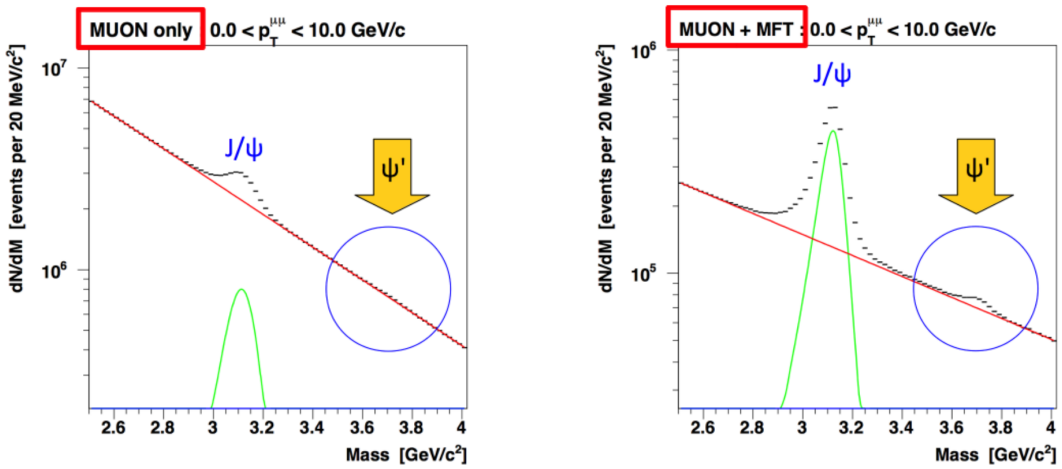


**Figure 7.10:** Dimuon invariant mass distribution in the $J/\psi$ family region for $p_{\mathrm{T}}^{\mu\mu} < 10$ GeV/$c$, in Pb–Pb collisions, without (left) and with (right) including information from the MFT.

## 7.4 Software upgrade

### 7.4.1 The Online-Offline framework

The ALICE upgrade addresses the challenge of reading out and inspecting Pb–Pb collisions at rates of 50 kHz, and sampling pp and p–Pb collisions at up to 200 kHz. This results in the collection and inspection of a data volume significantly higher than that of Runs 1 and 2. This requires the development of a new computing framework, the Online-Offline ($\mathrm{O}^2$) computing system [256]. The computing architecture is shown in Figure 7.11. The total throughput from the detector will increase up to 3TB/s, to be then reduced to 500 GB/s after an initial compression by a farm of about 150 parallel First Level Processors (FLP) computing nodes. Raw data are splitted in chunks, so-called uncompressed time frames, up to 23 ms long. A many-to-many network setup then recomposes all the parts belonging to the same time frame on one of the Event Processing Node (EPN) in a round robin manner. Each time frame is on average 10 GB in size, and each EPN is expected to perform reconstruction on it. The derived quantities, such as the track parameters, are then used as a mean to compress raw data related information and reduce the size of each compressed time frame to an average of 2 GB, with an aggregate rate of 100 GB/s, to persistent storage. A later asynchronous (relative to data taking) step then uses the EPN farm to reprocess all the data taken in the synchronous processing, using final calibrations and reconstructing the part of the detectors that can afford late reconstruction. A major difference between Run 3 and Run 1-Run 2 data processing is therefore the blending of traditional roles of the online and offline frameworks, which now share the same algorithms.

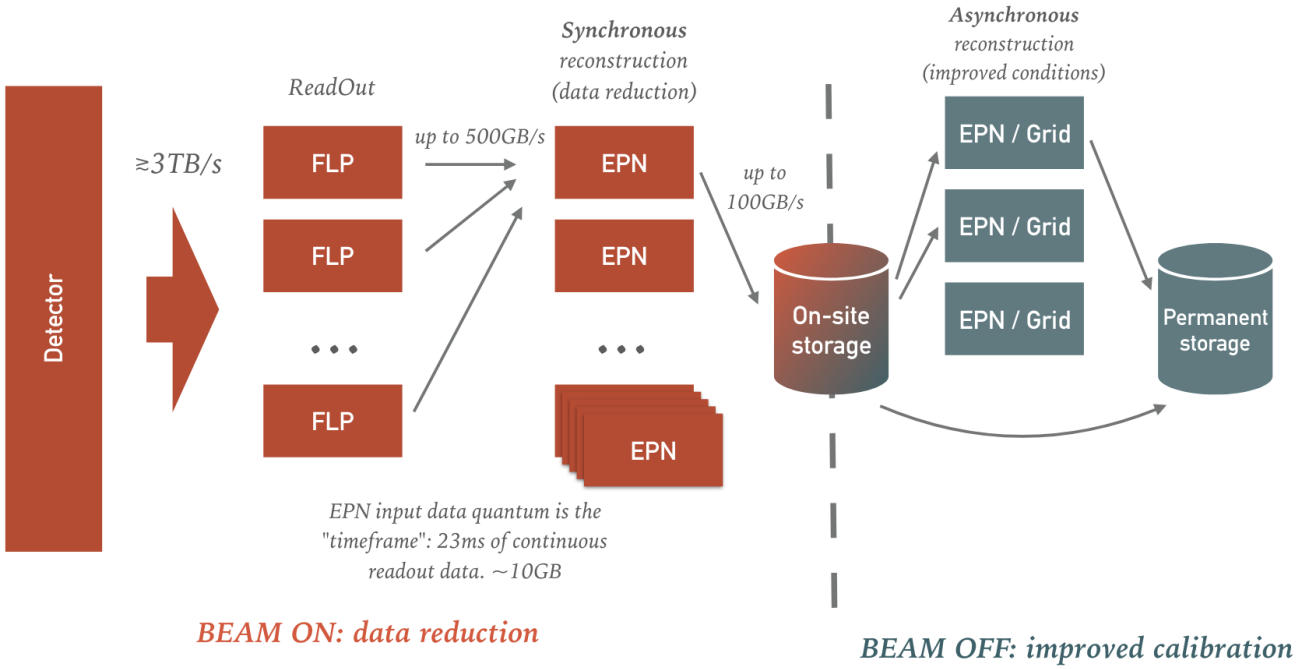


**Figure 7.11:** The computing architecture of ALICE in Run 3.

In order to cope with the challenges of Run 3, and in particular to ensure components reusage between the synchronous and asynchronous phases, the $O^2$ framework is developed in collaboration with the FAIR software group at the GSI institute. The ALICE $O^2$ architecture derives from the current Run 1-Run 2 architecture of the High Level Trigger (HLT), and can be considered subdivided into three major parts:

- the transport layer, FairMQ,
- the $O^2$ data model,
- the Data Processing Layer (DPL).

### The transport layer: FairMQ

The so-called transport layer is implemented using the FairMQ [257] message passing toolkit developed at GSI. It defines the core building blocks of the architecture in terms of so-called `FairMQDevices`, and implements how they communicate among each other. This abstracts away from the user the interaction with the network fabric itself. Moreover, for the case in which two devices work on the same node, shared-memory-backed message passing is also supported. Effectively FairMQ is an implementation of the actor model [258] for concurrent processing.

### The $O^2$ data model

On top of the transport layer, ALICE builds the $O^2$ data model, a specific description of the messages being exchanged by the various devices. The data model is designed with three key

features: being computer language agnostic, being extensible, and allowing for an efficient transport between nodes and mapping of the data objects in shared memory or the GPU memory where required.

Each message is expected to be composed of two parts, a header and a payload. The header contains by default information such as the data origin (i.e. the detector or process creating it), a mnemonic data description (i.e. the type of data contained in the payload) and other ancillary information like a spatial index or the serialisation method used to encode the payload. While a base header is required for every message, user code can attach extra headers allowing the construction of a veritable type system to describe the payloads.

Multiple data formats and serialisation methods are supported for the different payloads. For all the cases where serialisation of complex objects can be afforded, for example for Quality Control and Assurance, native serialisation of C++ objects, such as histograms, is assured via native ROOT `TMessage` serialisation.

### The Data Processing Layer

By construction, the transport layer provided by FairMQ is generic and experiment agnostic, hiding lower level implementation details of the transport but still providing very basic abstractions to the end user who wants to write algorithms. On the other hand, the $O^2$ data model provides a simplified type system to describe the objects being exchanged by the framework, but it does not monitor how the data exchange concretely happens. For these two reasons, relying only on the two would leave a lot of standards to be written by the end user. In particular, it would be needed to take care of creating a proper configuration that connects all the devices required to perform a given computation, making sure there are no pathological cases in the configuration such as missing or circular dependencies between modules. This would require to keep track of all the in-flight parts relative to a computation, potentially coming from different sources, and dispatch the computation only when all the inputs are available.

Thus a third layer, the DPL, is introduced, allowing one to describe the computation as a set of data processors implicitly organised in a logical dataflow describing how the data is transformed. The DPL configuration is expressed by the user in a declarative and implicit manner. Each data processor needs to declare upfront its input types (e.g. clusters), as well as its outputs (e.g. tracks). The DPL creates a topology that connects the producer of some kind of data to all its consumers. This removes from the user the need of managing the topology, allows for the composition of smaller workflows into larger ones, and leaves to the framework the role of optimising the logical dataflow description to a physical topology. Such a dataflow is implemented by providing a callback that fills the model representing the workflow.

Once a dataflow is described, the user can run it by simply starting a single executable, called the DPL driver. Depending on the deployment environment, such a driver will map the dataflow to a concrete topology and from there to a set of processes running FairMQ devices. While doing so, it makes sure the configuration matches the development environment. For example, on a laptop it will use a simple debug GUI to display logs and metrics aggregated during the processing. On the other hand, when deployed in the online cluster, it will make sure it connects to the production logging and monitoring infrastructure. Once the configuration to be deployed is fully determined,

the driver launches the process itself or generate a configuration for third party deployment tools.

### 7.4.2 Data Quality Control

The aim of data Quality Control (QC) is to provide a prompt feedback on the quality of the data being recorded and on the processes underlying the handling and transformation of this data, such as reconstruction and calibration. It is also of great importance to control the quality of subsequent reconstruction/calibration steps performed asynchronously to the data taking. As a consequence, the QC covers what is known as quality assurance and data quality monitoring. The output of the QC chain consists of an assessment of the data quality, usually computed automatically. The QC decision is used to check the transition from uncompressed to fully compressed data. The QC system can be described by a workflow as in Figure 7.12.

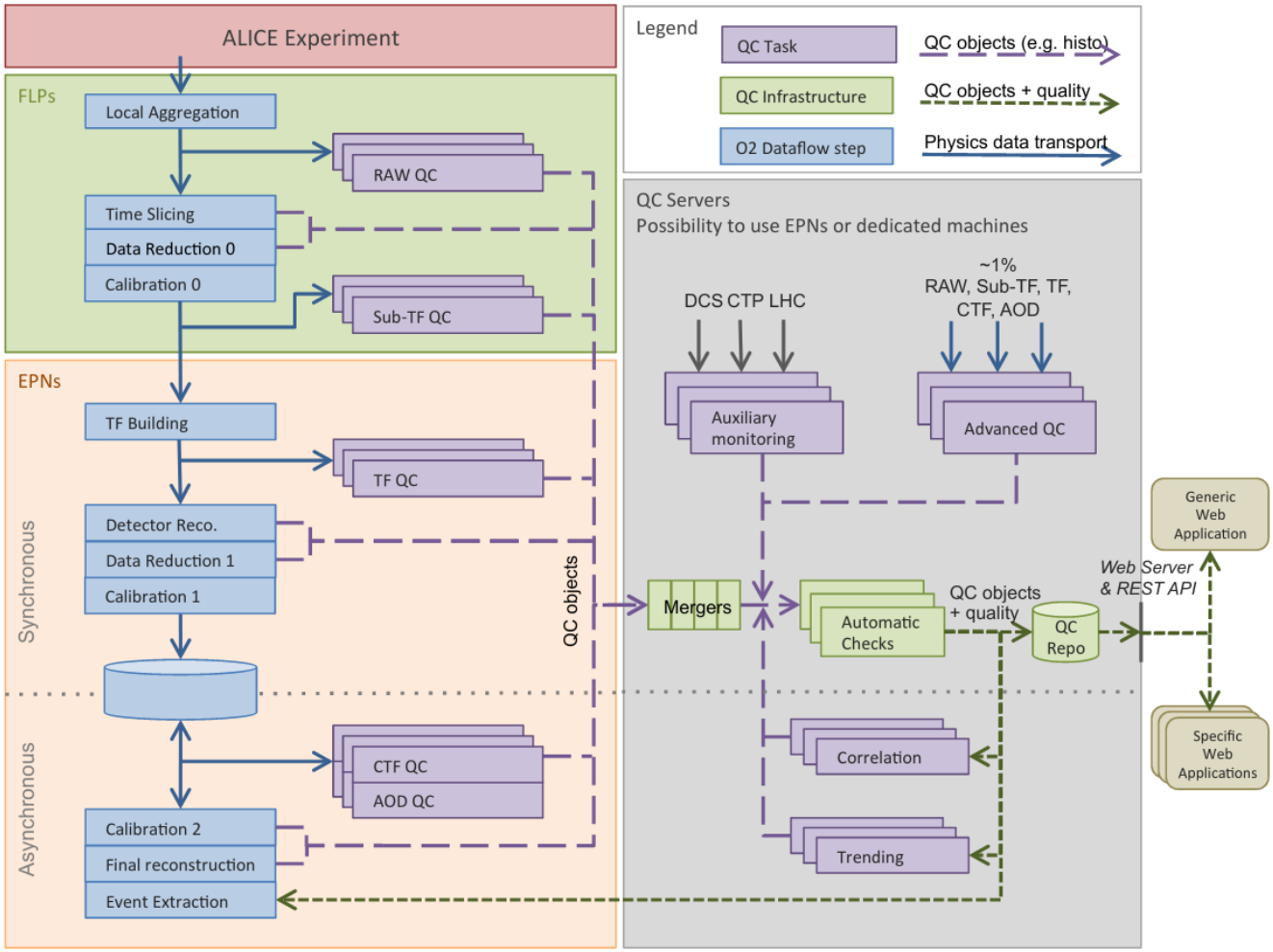


**Figure 7.12:** Quality Control and assessment general design in $O^2$.

### QC objects production

The QC system receives data at different stages of the online data flow or from the offline data storage. Information about the conditions under which these data were collected and the associated calibration, is also made available to this system. The QC provides objects (e.g. histograms, graphs or values) and a quality assessment for nearly all of them. The quality assessment is provided by the setting of different quality flags. In order to assess or refine the quality of an object, different types of monitoring can be carried out, depending on the time and information available. In addition, the QC output objects will require metadata to index the monitoring information and reduce the need for collecting such information from other systems.

The QC objects are produced in three different places:

1. Within other processes from the data taking pipeline. This case applies in priority to the tasks which would anyway produce QC objects during their execution. It is also used when monitoring the decoding, calibration or reconstruction processes themselves. It has the advantage of saving resources by not duplicating the work, but can affect the data taking.

2. As independent processes on the EPN/FLP. Within the synchronous data flow, these processes can have shared memory access to the data going through the nodes and will process as much as they can while the data are still accessible in the buffers, without slowing down the data taking.

3. As independent processes in dedicated QC nodes. These processes have less constraints, as they cannot affect the data taking, at the cost of receiving less samples, possibly around 1% of the full data. This approach is favoured for QC tasks that consume many resources, in terms of memory or CPU.

The system is flexible enough to manage QC object producers with different needs in terms of resources, performance, stability and data sample quality. It can also accept objects produced in non-QC processes.

### Merging

Most of the QC objects which are produced on the FLP and EPN nodes need to be merged. As far as the FLPs are concerned, as QC is often by detector, merging could happen for a subset of the FLPs which serve a given detector but not all of them. The merging procedure can be done either by embedding QC results in the data stream as separate blocks, or using a scalable merging procedure as will be done for the QC objects of the EPNs. On the EPNs, the QC objects will be produced while processing aggregated Time Frames. Since successive Time Frames will be reconstructed by different EPN nodes, the merging process will have to collect the QC objects from all EPNs. This merging can be executed synchronously for the fraction of data needed for fast quality assessment and asynchronously for the rest of the data. It means that the QC objects can still be populated and produced even though the mergers might not be able to cope with the amount of data.

Given the high number of inputs (up to 1 per EPN, i.e. 1500) a multi-level approach, such as Map-Reduce, is used. Mergers and producers are decoupled and each is unaware of the existence of the others. Producers populate objects and make them available whenever possible. Mergers pull the latest version of the QC objects at regular intervals and merge them.

### Automatic checks

Automatic checks usually consist in the comparison of the QC data with a reference value, such as a threshold or a distribution. In general, references may change according to the run and data taking conditions, including detector hardware status, beam conditions or the collision system. For this reason, the QC is able to set and modify the reference online. For the sake of the reproductibility of quality assessment and for asynchronous use, the reference is stored and versioned in a database.

There is a dual interaction with the Condition and Calibration Data Base (CCDB[1]): the system allows for the reference data set online to be written in the database, the previously set reference and thresholds but also the variables related to data taking conditions are read from the database by the QC processes. Both synchronous and asynchronous QC processes need to access the reference in the database. Separating the generation of QC objects from the quality assessment means that the latter can be done asynchronously and even iteratively if the reference data or the evaluation procedure were to be modified.

### Correlation and trending

Some QC processes need to take as input the merged, and often time-aggregated, output of other QC processes. This is true for correlation and trending which can be considered as standard QC processes running within the QC farm. Despite the fact that they run asynchronously and should not need any merging, automatic check procedures need to be done and quality rated.

### Storage

Merged QC objects and their associated quality are stored for future reference and in view of correlation and trending. The storage is able to handle the foreseen load which consists of an average of 5000 objects, peaking at 10000, updated every 60 seconds while serving the clients. A relational database is typically capable of such performance. Moreover, the limiting factor for such a system has been demonstrated to be bandwidth. For a pessimistic average size of 1 MB per monitoring object, a 10 GB/s input connection would be far enough even for the peaks. Finally, such a system is able to cache seamlessly the data in case of congestions.

### QC results

The QC objects and their associated quality are used to check the transition from compressed to fully compressed data in the asynchronous part of the data flow. During data taking operations, the QC results are accessed by shifters and experts, inside and outside the control room, via one

[1]The CCDB is the ALICE O2 experiment parameter manager for Run 3. It replaces the OCDB used for this purpose in Run 1 and 2. More information can be found in Ref. [256].

or several dedicated web applications. The system provides a web API to enable an individual access to the necessary information for tool building.

A generic application is provided which meets the needs of the shifter and the common needs of the users in general. This application is also web-based and allows for the display and manipulation of objects in a dynamic way. This implies the ability to transfer and display ROOT-based objects in a web browser. It uses the recent developments in ROOT which provides the serialisation of ROOT objects and files either in binary or in a JSON format. Most of the application is done client-side in javascript. As the visualisation clients connect via a web server to the database, they cannot affect other QC processes. The web server can even limit the number of requests going to the database which could indirectly impact the QC chain.

### 7.4.3 MID raw data QC

A typical QC task contains files for the task itself, files for the checkers, and a `json` file for the configuration. The QC requires a number of configuration items in the configuration file:

- `config`: contains the global configuration of the QC which applies to any component, such as the links to the required databases and paths to repositories for the output objects,
- `tasks`: contains the declaration of the QC tasks, with the name of the task, module and detector, the class used for the initialisation and running of the task, and possibly a set of user-defined parameters that will be propagated throughout the workflow,
- `externalTasks`: contains the declaration of external devices which sends objects to the QC to be checked and stored,
- `checks`: contains the declaration of the QC checks, associated to a task and defining the user-defined class containing the checks to be performed,
- `dataSamplingPolicies`: provides a way to sample the data in the DPL workflow based on given conditions, such as a fraction of randomly selected data or a size limit to the payload.

If needed, the configuration file can also contain the declaration of aggregators and post-processing tasks.

The QC of the MID raw data is performed by the `RawQcTask` of the MID module. The raw data are organised in pages, each page containing a Raw Data Header (RDH) and the payload, constituting altogether the HeartBeat Frame (HBF). Each page corresponds to an orbit trigger. Whenever the CRU receives an orbit trigger, it closes the current page by sending an HBF with empty payload. The HBFs themselves are organised into Time Frames (TFs), containing a user-defined number of HBF. Initially, TFs were composed of 256 HBFs, which was reduced to 128 to cope with processing limitations of the TPC. TFs are sent to the QC, and used as inputs for the `RawQcTask::monitorData` function containing the QC algorithm. The input raw data are parsed with `DPLRawParser`, allowing one to read the TF HBF per HBF. The information contained in the HBF is decoded, then read by the task.

The first version of the QC MID module was meant to read the raw data and produce an output object showing the number of hits in each RPC of the detector. Figure 7.13 shows this distribution obtained by running this initial version of the QC on simulated data. A unique identifier is attributed to each of the 72 RPCs of the MID, the eight peak observed in the distribution corresponding to the eight half-planes of the detector. It is worth stressing that this peculiar pattern is created by the nonphysical template used for MC simulations of muons, which is only used for testing purposes and does not reflect the expected pattern in data taking. The task is associated

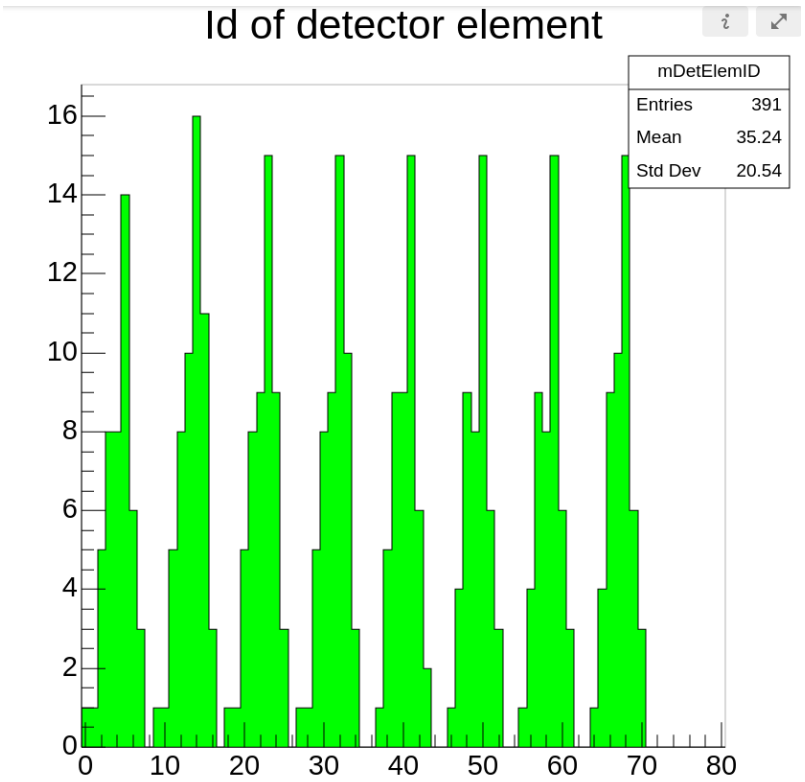


**Figure 7.13:** Event distribution as a function of the detector element, obtained from the QC MID module ran on simulated data.

to a QC check, whose output is colour-encoded in the histogram of Figure 7.13. The MID contains four planes arranged in two stations, creating a redundancy of the information, from which one can evaluate the efficiency of the detector, and build tracklets that can be match to tracks reconstructed in the tracking system. The failure of part of the detector would thus deteriorate the quality of the data and that of the reconstruction. The QC check implemented verifies that information is collected from the four planes of the MID. The distribution in Figure 7.13 is splitted by the QC check in four parts, each containing the 18 RPCs of a given plane of the MID. The QC check collects the signal in these four regions and returns a `Quality` object that can have values:

- `good`: all four planes send information,
- `medium`: one plane in at least one of the station does not send information,

- `bad`: the two planes in at least one station do not send information.

The module was tested as a continuous workflow by pairing it to a data producer continuously sending raw data, mimicking real data taking. The output object of the QC task is then filled on the fly, and the histogram is regularly updated, allowing one to verify the detector status as a function of time.

The module was further completed for extending checks of the raw data. The reading is extended in order to check each GBT link individually, and look for inconsistencies in the data. One can for example force an error by modifying the electronics delay between local and regional cards. Manually setting this delay at a non-nominal value leads the local and regional responses to not arrive at the same bunch crossing, producing errors. The output is a file containing a list of possible problems, if any, as well as a summary containing the number of processed and faulty events. The list of problems is provided per interaction record. An entry in the output file typically reads:

```
BCid: 0x71c Orbit: 0xf   [in  page: 542  (line: 277505)  ]
loc-reg inconsistency: fired locals (00010000) != expected from reg (00000000);
Crate ID: 15  Loc ID:  4  status: 0xc0  trigger: 0x 0 firedChambers: [...]
```

The event can be identified through the bunch crossing (BC) and orbit identifiers. The next line provides information on the origin of the error. In this example, following the nature of the error that was forced, the entry is tagger as `loc-reg inconsistency`. The last line allows to locate the error in terms of the crate and local board identifiers, and contains the coordinates of the fired chambers, enabling the monitoring of the status of each RPC individually. The checker produces a summary of the error detection after each TF, in the form:

```
Fraction of faulty events: 232 / 4296
```

The fraction of faulty events represents the ratio of the number of processed events where an error was found, to the total number of processed events. This information can be sent to a standard QC output object, such as a histogram, which is then filled on-the-fly as the TFs are received and processed by the task. An example is shown in Figure 7.14.

For now the module was tested locally, on simulated data, and consists in the QC of raw data only. The next step will require its testing in the full $O^2$ framework, and the inclusion of further checks such as noisy channels, occupancy, digits and clusters.

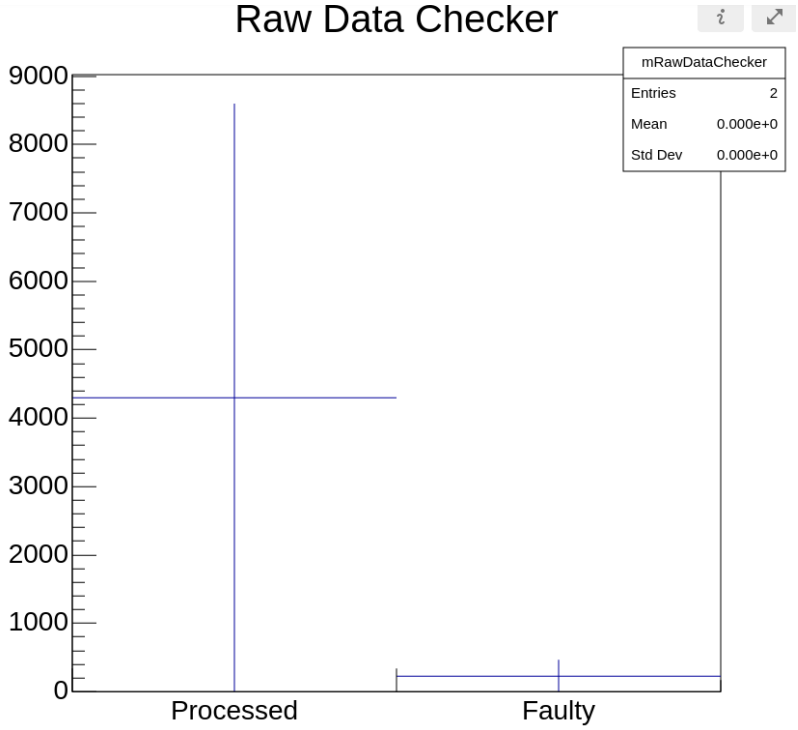


**Figure 7.14:** Event distribution as a function of the detector element, obtained from the QC MID module ran on simulated data.

# Part III

# $\mathrm{Z}^0$- and $\mathrm{W}^{\pm}$-boson measurements in p–Pb collisions at $\sqrt{s_{\mathrm{NN}}} = 8.16$ TeV

# Chapter 8

# Data analysis

The the performance of the measurement of the weak-boson production in heavy-ion collisions (HIC) at large rapidities, with the ALICE muon spectrometer, was studied in Ref. [259]. Their measurements in p–Pb collisions at $\sqrt{s_{\rm NN}} = 5.02$ TeV by the ALICE Collaboration [156] showed that, although feeble, the signal can be extracted, and with the energy increase at 8.16 TeV one can expect a significantly higher production for a precise measurement. This chapter presents the analysis methodology and the intermediary results that lead to the measurements presented in the next chapter. The chapter starts with a presentation of the data sample in Section 8.1, describing the event and track selections along with the evaluation of the integrated luminosity and the event centrality. Section 8.2 focuses on the signal extractions of the $\rm Z^0$ and $\rm W^{\pm}$ bosons, with considerations on the background evaluation. The procedure for the efficiency correction is described in Section 8.3. The chapter ends with information on the computation for differential studies in Section 8.4 and a summary of the systematic uncertainties affecting the measurements in Section 8.5.

## 8.1 Data samples and selection

### 8.1.1 Collision system and LHC periods

The data samples analysed in this work correspond to two p–Pb collision periods and were collected in November and December 2016 by the ALICE detector at the LHC. Because of the single magnet design at the LHC, the proton and Pb beams have the same magnetic rigidity. The energy per nucleon in the Pb beam is therefore smaller than that of the proton beam by a factor $\frac{82}{208} \sim 0.4$. The centre-of-mass energy per nucleon-nucleon collision $\sqrt{s_{\rm NN}}$ in a HIC is related to the centre-of-mass energy of pp collisions $\sqrt{s}$ with the same accelerating conditions as:

$$\sqrt{s_{\rm NN}} = \sqrt{s} \times \sqrt{\frac{Z_1 Z_2}{A_1 A_2}}, \tag{8.1}$$

where $A_1$ ($Z_1$) and $A_2$ ($Z_2$) are the atomic (charge) numbers of the first (second) colliding ion. In the 2016 p–Pb collision period, the equivalent centre-of-mass energy in pp collisions is $\sqrt{s} = 13$

TeV, from which one gets:

$$\left.\begin{array}{ll} Z_1 = 1 & Z_2 = 82 \\ A_1 = 1 & A_2 = 208 \end{array}\right\} \quad \Rightarrow \quad \sqrt{s_{\mathrm{NN}}} = 13 \times \sqrt{\frac{82}{208}} = 8.16 \text{ TeV}. \tag{8.2}$$

Since the collision system is asymmetrical, the rapidity in the centre-of-mass frame is shifted with respect to that of the laboratory frame by:

$$\Delta y = \frac{1}{2} \ln \left( \frac{Z_{\mathrm{p}}/A_{\mathrm{p}}}{Z_{\mathrm{Pb}}/A_{\mathrm{Pb}}} \right) \approx 0.465 \tag{8.3}$$

towards the proton beam. The muon spectrometer of ALICE covers the pseudorapidity interval $-4 < \eta_{\mathrm{lab}} < -2.5$ in the ALICE coordinate system[1], such that the angular coverage correspond to different values of Bjorken-$x$ depending on whether the proton beam moves towards the spectrometer or away from it. For convenience, the former configuration is called the p-going configuration, or p–Pb collisions, the latter Pb-going or Pb–p. As the spectrometer does not cover both positive and negative rapidities, the two configurations are realised by swapping the beam directions. If one adopts the convention that the proton beam travels towards positive rapidities, the rapidity intervals in the centre-of-mass frame are then:

- p–Pb collisions: $2.03 < y_{\mathrm{cms}} < 3.53$,
- Pb–p collisions: $-4.46 < y_{\mathrm{cms}} < -2.96$.

The corresponding Bjorken-$x$ intervals are given in Table 8.1. They are calculated at LO with Equation 3.32, which reads, for p–Pb collisions:

$$x_{1,2} = \frac{M_{\mathrm{Z,W}}}{\sqrt{s_{\mathrm{NN}}}} \exp\left(-y\right). \tag{8.4}$$

| | $-4.46 < y_{\mathrm{cms}} < -2.96$ | $2.03 < y_{\mathrm{cms}} < 3.53$ |
|---|---|---|
| $\mathrm{Z}^0$ | $2.16 \times 10^{-1} < x < 9.66 \times 10^{-1}$ | $3.27 \times 10^{-4} < x < 1.47 \times 10^{-3}$ |
| $\mathrm{W}^{\pm}$ | $1.90 \times 10^{-1} < x < 8.51 \times 10^{-1}$ | $2.89 \times 10^{-4} < x < 1.29 \times 10^{-3}$ |

**Table 8.1:** Bjorken-$x$ intervals assessed by the measurement of $\mathrm{Z}^0$ and $\mathrm{W}^{\pm}$ bosons with the ALICE muon spectrometer in p–Pb collisions at $\sqrt{s_{\mathrm{NN}}} = 8.16$ TeV. The calculations are performed at LO with the masses of the bosons set at the PDG values [6].

The data taking is divided into periods, conventionally denoted as

`LHC + year + sequential letters`.

[1]The ALICE coordinate system is an orthogonal right-handed basis with the origin at the collision point, the $\vec{e}_x$ pointing to the centre of the accelerator and $\vec{e}_y$ pointing upwards.

Following this naming scheme, the data from p–Pb and Pb–p collisions correspond to the LHC16r and LHC16s periods, respectively. After data taking, a Quality Assurance (QA) procedure is performed in order to select runs of good quality from a set of appropriate selections. The main tasks of the QA are: the detection of problems with sub-detectors that were not spotted during data taking, the evaluation of the quality of the reconstruction, the investigation of the severity of the problems and possibility to fix them (e.g. by running the reconstruction algorithms once more), the classification of each run as `good` or `bad` for physics analyses. This last step is done for all the detector clusters, such that issues found with a given sub-detector does not rule out the run for physics analyses that do not make use of it. The QA may be needed to be performed several times, producing several sets of Analysis Object Data (AOD) from different reconstruction passes. The last passes used for the LHC16r and LHC16s periods are respectively `muon_calo_pass2` and `muon_calo_pass3`[2], which produced the AOD191 set. The analyses were performed with AliRoot version v5-08-11a-1 for the $Z^0$ measurement and v5-09-44-1 for the $W^{\pm}$ one. The list of good runs for muon analyses are given in Table 8.2. After QA, 57 and 80 runs are valid for muon analyses in the LHC16r and LHC16s period, respectively.

| LHC16r (57 runs) | | | | LHC16s (80 runs) | | | | | |
|---|---|---|---|---|---|---|---|---|---|
| 265594 | 265742 | 266023 | 266197 | 266437 | 266525 | 266618 | 266775 | 266942 | 267077 |
| 265596 | 265744 | 266025 | 266208 | 266438 | 266533 | 266621 | 266776 | 266943 | 267109 |
| 265607 | 265746 | 266034 | 266234 | 266439 | 266534 | 266630 | 266800 | 266944 | 267110 |
| 265691 | 265754 | 266074 | 266235 | 266441 | 266539 | 266657 | 266805 | 266988 | 267130 |
| 265694 | 265756 | 266076 | 266296 | 266470 | 266543 | 266658 | 266807 | 266993 | 267131 |
| 265696 | 265785 | 266081 | 266299 | 266472 | 266549 | 266659 | 266857 | 266994 | |
| 265697 | 265787 | 266084 | 266300 | 266479 | 266584 | 266665 | 266878 | 266997 | |
| 265698 | 265788 | 266085 | 266304 | 266480 | 266587 | 266668 | 266880 | 266998 | |
| 265700 | 265789 | 266086 | 266305 | 266487 | 266588 | 266669 | 266882 | 267020 | |
| 265701 | 265792 | 266117 | 266312 | 266514 | 266591 | 266674 | 266883 | 267022 | |
| 265709 | 265795 | 266187 | 266316 | 266516 | 266593 | 266676 | 266885 | 267062 | |
| 265713 | 265797 | 266189 | 266318 | 266518 | 266595 | 266702 | 266886 | 267063 | |
| 265714 | 265840 | 266190 | | 266520 | 266613 | 266703 | 266912 | 267067 | |
| 265740 | 265841 | 266193 | | 266522 | 266614 | 266706 | 266915 | 267070 | |
| 265741 | 266022 | 266196 | | 266523 | 266615 | 266708 | 266940 | 267072 | |

**Table 8.2:** Runs from the LHC16r and LHC16s periods that passed the QA.

### 8.1.2 Event selection

On the data that passed the QA, a first selection is applied as to retain the events relevant for the analyses. The first selection is the Physics Selection (PS), which is automatically performed by

[2]The `muon_calo` passes are meant to provide a fast reconstruction for detectors involved in the muon and calorimetry analyses, bypassing for example the reconstruction in the TPC. The involved detectors are: the muon tracking and trigger systems, SPD, V0, T0, ZDC, AD, EMCAL and PHOS.

the `AliPhysicsSelectionTask`. At its lowest level, the PS performs basic checks on V0 and ZDC timings to ensure that the event correspond to a collision at the interaction point. The task also enables a rejection of events affected by the bunch-crossing pile-up (corresponding to events with two or more collisions occurring in the same bunch crossing) and out-of-bunch pile-up (where one or more collisions occurred in bunch crossings different from the one that trigger the acquisition). The events are furthermore required to have a good vertex reconstructed by the SPD, asking for a non-zero number of contributors in the SPD, and a longitudinal vertex position estimated within $\pm$10 cm from the nominal interaction point. For the muon analyses presented here, the rejection of pile-up events removes about 10% of the data sample, while the selection on the vertex has a very small effect.

The last event selection relies on the trigger classes fired during data taking. In this work, four triggers were used:

- **Minimum Bias (MB) trigger**: `INT`, corresponding to a logical `AND` between signals from V0A and V0C. The trigger used is `CINT7-B-NOPF-CENT`. Given the smaller downscaling factor with respect to the `CINT7-B-NOPF-MUFAST` trigger class, it allows for a higher statistics for the offline normalisation,

- **Single Muon Low trigger**: `MSL`, requiring one muon track fired in the trigger system with a $p_{\mathrm{T}} \gtrsim 0.5$ GeV/$c$ threshold in addition to the MB trigger. The trigger class used is the `CMSL7-B-NOPF-MUFAST`,

- **Single Muon High trigger**: `MSH`, same as `MSL`, with a $p_{\mathrm{T}}$ threshold at $\sim 4.2$ GeV/$c$. The trigger class used is `CMSH7-B-NOPF-MUFAST`,

- **Dimuon Unlike-sign Low trigger**: `MUL`, which requires a muon pair of opposite charge sign, each with $p_{\mathrm{T}} \gtrsim 0.5$ GeV/c, in addition to the MB trigger. The trigger class used is `CMUL7-B-NOPF-MUFAST`.

The last two triggers are meant to provide the data samples containing dimuons and single muons of high $p_{\mathrm{T}}$, which characterise the signal of the $\mathrm{Z}^0$ and $\mathrm{W}^{\pm}$ bosons. The `MSL` trigger is used for an alternative computation for the luminosity determination, as explained in the next section. Table 8.3 summarises the main characteristics of the two analysed periods.

| Period | System | Nb of runs | Rapidity | $\mathrm{N}_{\texttt{CMSH}}$ | $\mathrm{N}_{\texttt{CMUL}}$ |
|---|---|---|---|---|---|
| LHC16r | p–Pb | 57 | $2.03 < y_{\mathrm{cms}} < 3.53$ | $18.5 \times 10^6$ | $25.8 \times 10^6$ |
| LHC16s | Pb–p | 80 | $-4.46 < y_{\mathrm{cms}} < -2.96$ | $35.1 \times 10^6$ | $72.0 \times 10^6$ |

**Table 8.3:** Main characteristics of the periods analysed in this study, from p–Pb collisions at $\sqrt{s_{\mathrm{NN}}} = 8.16$ TeV.

### 8.1.3 Luminosity

The integrated luminosity for each period, and the associated statistical uncertainty, are calculated as:

$$\mathcal{L}_{\rm int} = \frac{N_{\rm MB}}{\sigma_{\rm V0}} = \frac{F^{\rm MB}_{\rm norm} \times N_{\texttt{CTRIG}}}{\sigma_{\rm V0}}, \qquad \left(\frac{\sigma^{\mathcal{L}_{\rm int}}_{\rm stat}}{\mathcal{L}_{\rm int}}\right)^2 = \sum_i \left(\frac{\sigma_i}{x_i}\right)^2, \tag{8.5}$$

where TRIG is MUL for the $Z^0$ measurement and MSH for the $W^{\pm}$ one. $\sigma_{\rm V0}$ is the visible cross-section estimated by means of van-der-Meer scans of the V0-based MB trigger signal. For the LHC16r and LHC16s periods it amounts to $2.09 \pm 0.04$ b and $2.10 \pm 0.04$ b respectively, where the quoted errors are systematics, the statistical ones being negligible [196]. The $x_i$ ($\sigma_i$) in the formula for the statistical uncertainty correspond to the quantities (statistical uncertainty on the quantities) used for the evaluation of the luminosity, with $i = \{F^{\rm MB}_{\rm norm}, N_{\texttt{CTRIG}}, \sigma_{\rm MB}\}$.

$F^{\rm MB}_{\rm norm}$ is a normalisation factor used to obtain the number of MB events $N_{\rm MB}$ corresponding to the number of CTRIG triggered events $N_{\texttt{CTRIG}}$. It can be computed using two methods, and has to be corrected for pile-up.

**Offline method** The first method to compute $F_{\rm norm}$ is based on recorded triggers at the offline level, in AODs. One can compute the offline normalisation factor for each run $i$ with the direct offline method (off1):

$$F^{{\rm off1},i}_{\rm norm} = \frac{N^i_{\rm MB}}{N^i_{\rm MB\&0TRIG}} \times PU^i, \tag{8.6}$$

where $N^i_{\rm MB}$ is the total number of MB events, and $N^i_{\rm MB\&0TRIG}$ is the total number of MB events where one 0TRIG input is recorded, that is, a TRIG input at the L0 level. $PU^i$ is the pile-up correction (see below) that accounts for the probability to have more than one interaction in an event.

The precision can be increased by defining an indirect offline method (off2), adding an extra step in which an intermediate trigger with higher statistics is used. In this work the single muon CMSL trigger is used. The offline factor then becomes

$$F^{{\rm off2},i}_{\rm norm} = \frac{N^i_{\rm MB}}{N^i_{\rm MB\&0MSL}} \times \frac{N^i_{\texttt{CMSL}}}{N^i_{\texttt{CMSL\&0TRIG}}} \times PU^i, \tag{8.7}$$

where $N^i_{\texttt{CMSL}}$ is the total number of MSL events and $N^i_{\rm MB\&0MSL}$ ($N^i_{\texttt{CMSL\&0TRIG}}$) is the number of MB (CTRIG) events where one 0MSL (0TRIG) event is recorded.

**Online method** The $F_{\rm norm}$ factor can also be computed using a so-called online method, based on the online L0b trigger scalers. It corresponds to L0 inputs sent from the trigger to the CTP. The normalisation factor is computed for each run as:

$$F^{{\rm on},i}_{\rm norm} = \frac{{\rm L0b}^i_{\rm MB}}{{\rm L0b}^i_{\texttt{TRIG}}} \times \frac{P^i_{\rm MB}}{P^i_{\texttt{TRIG}}} \times PU^i, \tag{8.8}$$

where $\mathrm{L0b}^i_{\mathrm{MB}}$ and $\mathrm{L0b}^i_{\texttt{TRIG}}$ are the measured trigger counts of the L0b inputs for MB and TRIG triggers, both taken from the MUFAST[3] trigger cluster, and $P^i_{\mathrm{MB}}$ and $P^i_{\texttt{MUL}}$ are the purity factors computed offline in order to correct the L0b taken directly from the OCDB where the physics selection is not yet applied.

**Purity** The purity factors $P^i_{\mathrm{MB},\texttt{TRIG}}$ are corrections applied to account for MB or TRIG events that do not pass the PS. They are defined as

$$P^i_{\mathrm{MB},\texttt{TRIG}} = \frac{N^i_{\mathrm{MB},\texttt{TRIG}}(PS)}{N^i_{\mathrm{MB},\texttt{TRIG}}(ALL)}, \tag{8.9}$$

where $N^i_{\mathrm{MB},\texttt{TRIG}}(ALL)$ and $N^i_{\mathrm{MB},\texttt{TRIG}}(PS)$ are the number of events recorded by the MB or TRIG trigger during the run $i$ before and after PS, respectively. The $P^i_{\mathrm{MB}}$, $P^i_{\texttt{CMUL}}$ and $P^i_{\texttt{CMSH}}$, as a function of the run number, are displayed in Fig. 8.1.

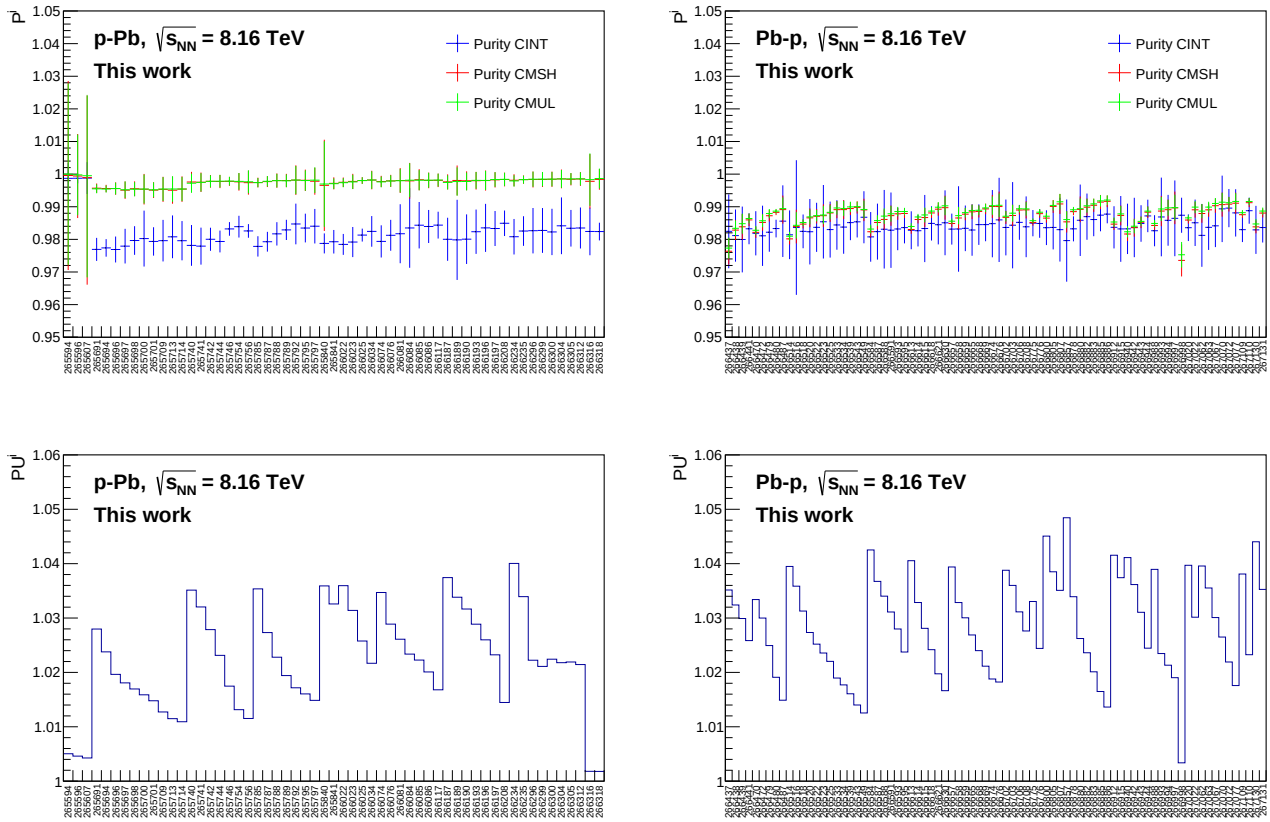


**Figure 8.1:** Evolution of the purity (top) and pile-up (bottom) factors as a function of the run number, in p–Pb (left) and Pb–p (right) collisions.

[3]The MUFAST cluster contains the muon trigger and tracking systems, as well as the SPD, V0, T0 and AD.

**Pile-up factor** The pile-up factor $PU^i$ for run $i$ is calculated using

$$PU^i = \frac{\mu^i}{1 - e^{-\mu^i}}. \tag{8.10}$$

$\mu^i$ is the mean number of collisions per bunch crossing, assuming a poissonian distribution, for the run $i$:

$$\mu^i = -\ln\left(1 - \frac{P^i_{\mathrm{MB}} \times \mathrm{L0bRate}^i_{\mathrm{MB}}}{n^i_b \times f_{\mathrm{LHC}}}\right), \tag{8.11}$$

where $P^i_{\mathrm{MB}}$ is the MB purity factor for run $i$, $\mathrm{L0bRate}^i_{\mathrm{MB}}$ is the number of MB events recorded by the L0b counter per data taking time, $n^i_b$ is the number of colliding bunches and $f_{\mathrm{LHC}} = 11245$ Hz is the revolution frequency of the LHC. The evolution of the pile-up factor as a function of the run number is shown in Fig. 8.1. The factor is not used in the $\mathrm{W}^{\pm}$ analysis, as the pile-up is already accounted for at the Physics Selection level.

**Luminosities** For each method, the total $F_{\mathrm{norm}}$ and its statistical uncertainty are computed as the weighted average of the run-per-run contributions:

$$F_{\mathrm{norm}} = \frac{\sum_{i=1}^{N_{\mathrm{runs}}} F^i_{\mathrm{norm}} \times N^i_{\texttt{CTRIG}}}{\sum_{i=1}^{N_{\mathrm{runs}}} N^i_{\texttt{CTRIG}}}, \tag{8.12}$$

The evolution of the $F^i_{\mathrm{norm}}$ factors, as a function of the run number, is displayed in Fig. 8.2, and Table 8.4 summarises the numerical values obtained with the two methods for the two periods. The direct offline method is neglected compared to the indirect one, as the latter provides a much more precise evaluation of the normalisation factor. The final $F_{\mathrm{norm}}$ is taken as the average between the online and indirect offline methods, the difference between the two is taken as systematic uncertainty.

| | CMUL trigger | | CMSH trigger | |
|---|---|---|---|---|
| Method | p-going | Pb-going | p-going | Pb-going |
| $F^{\mathrm{off1}}_{\mathrm{norm}}$ | $679.8 \pm 5.4$ | $373.0 \pm 1.0$ | $765.9 \pm 14.4$ | $596.9 \pm 2.3$ |
| $F^{\mathrm{off2}}_{\mathrm{norm}}$ | $678.7 \pm 1.4$ | $371.5 \pm 0.4$ | $755.0 \pm 1.7$ | $596.9 \pm 0.8$ |
| $F^{\mathrm{on}}_{\mathrm{norm}}$ | $683.3 \pm 0.5$ | $372.2 \pm 0.3$ | $765.3 \pm 0.6$ | $603.4 \pm 0.5$ |
| Total | $681.0 \pm 1.0 \pm 4.6$ | $371.9 \pm 0.4 \pm 0.7$ | $760.2 \pm 1.2 \pm 10.3$ | $600.2 \pm 0.7 \pm 6.5$ |

**Table 8.4:** Normalisation factors obtained from the direct offline (off1), indirect offline (off2) and online (on) methods for the dimuon (CMUL) and single muon (CMSH) triggers. The quoted uncertainties in the different methods are the statistical uncertainties. The ones quoted for the total values are statistical and systematic uncertainties, respectively.

The integrated luminosity is then computed using Equation 8.5. At this stage, the $\mathrm{Z}^0$ and $\mathrm{W}^{\pm}$ measurements followed two different approaches. At the time when the $\mathrm{Z}^0$ measurement

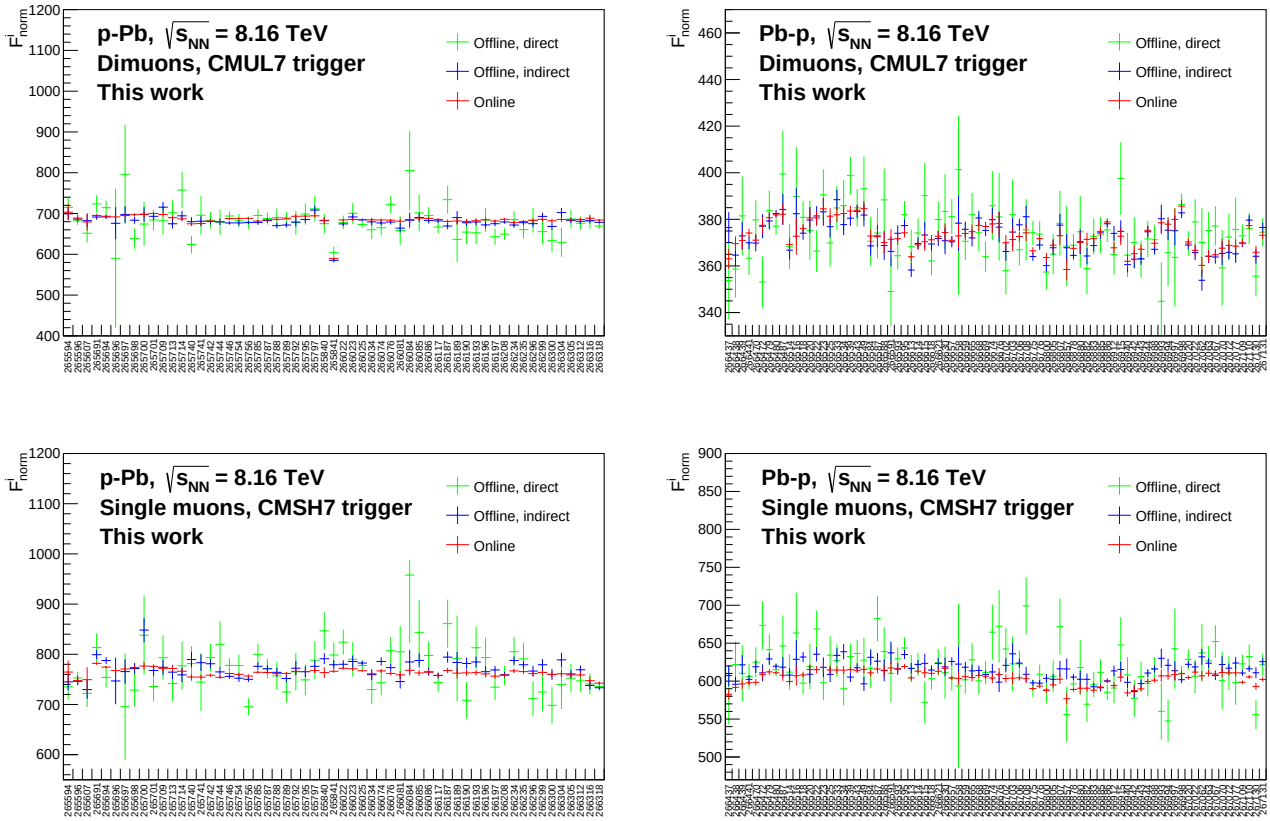


**Figure 8.2:** $F_{\text{norm}}$ as a function of the run number, for `MUL` (top) and `MSH` triggered events, in p–Pb (left) and Pb–p (right) collisions.

was performed, the `AliPhysicsSelectionTask` did not offer the possibility to exclude the pile-up events, such that they were included in the data sample from which the luminosity is computed. It was verified afterwhile that the pile-up effect is negligible for this measurement at the cross section level, as the reduction in the luminosity comes with a reduction of the number of extracted dimuons from $\mathrm{Z}^0$ decays, the two effects ending up cancelling each other out. For the $\mathrm{W}^{\pm}$, performed more recently, the pile-up events are rejected by the PS task, leading to a lower value for the luminosity as events are rejected much earlier in the analysis flow. It was also verified that the two analyses, having the same MB condition, are consistent with one another when the same procedure is followed for both `CMUL` and `CMSH` triggered events. For the luminosity, one gets:

- without pile-up rejection:

$$\mathcal{L}_{\text{int}} = \begin{cases} 8.40 \pm 0.01\ (\text{stat}) \pm 0.17\ (\text{syst})\ \text{nb}^{-1} & \text{at forward,} \\ 12.74 \pm 0.01\ (\text{stat}) \pm 0.26\ (\text{syst})\ \text{nb}^{-1} & \text{at backward,} \end{cases} \tag{8.13}$$

- with pile-up rejection:

$$\mathcal{L}_{\text{int}} = \begin{cases} 6.73 \pm 0.01\ (\text{stat}) \pm 0.16\ (\text{syst})\ \text{nb}^{-1} & \text{at forward,} \\ 10.0 \pm 0.01\ (\text{stat}) \pm 0.22\ (\text{syst})\ \text{nb}^{-1} & \text{at backward.} \end{cases} \tag{8.14}$$

### 8.1.4 Centrality

The event multiplicity is obtained using the `AliMultSelection` task. No selection on the multiplicity is applied, such that the full 0–100% range is covered. The events passing the PS and good vertex selection are classified in multiplicity bins, an example of such a classification is shown in Figure 8.3 for single-muon triggered events and V0M (the combination of signals in the two V0 arrays) as multiplicity estimator.

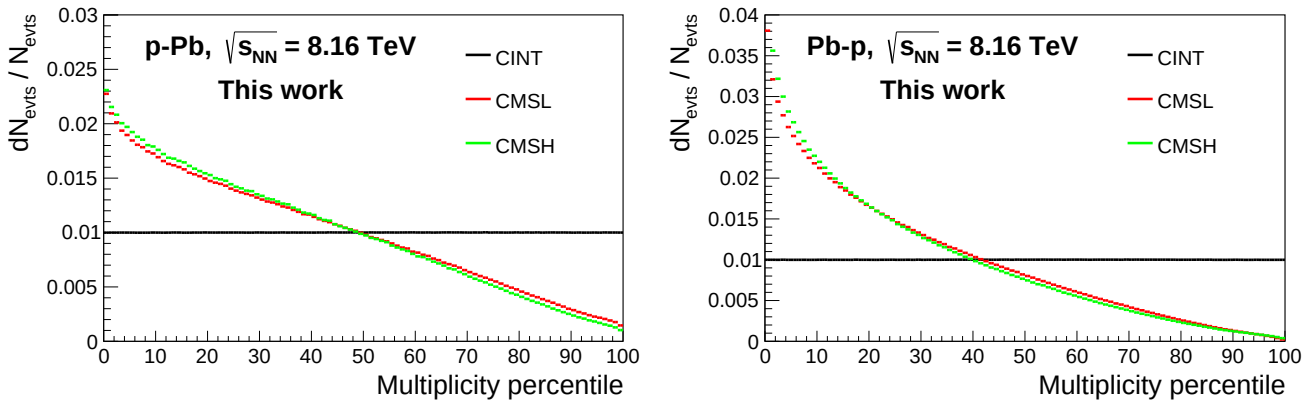


**Figure 8.3:** Multiplicity distribution of MB, `MSL` and `MSH` triggered events measured by V0M in p–Pb (left) and Pb–p (right) collisions.

As discussed in Section 4.3.4, evaluating the centrality of the collision using multiplicity-based estimators such as V0 or CL1 (the outer layer of the SPD) is biased in p–Pb collisions due to the size of the multiplicity fluctuations. The ZDC provides an alternative and unbiased measurement of the collision centrality through the measurement of the energy deposited at beam rapidity by the spectator neutrons in the ZDC calorimeters. The calorimeter lying on the Pb-fragment side is ZNA in p-going collisions, ZNC in Pb-going.

The centrality is expressed as $\langle N_{\text{coll}} \rangle$, the average number of binary nucleon–nucleon collisions obtained from the hybrid method described in Refs. [200, 197]. The method relies on the assumption that the charged-particle multiplicity measured at mid-rapidity is proportional to the average number of nucleons participating in the interaction $\langle N_{\text{part}} \rangle$. The values of $\langle N_{\text{part}} \rangle$ for a given ZN-centrality class is calculated by scaling the average number of participants in MB collisions $\langle N_{\text{part}}^{\text{MB}} \rangle$, estimated by means of Glauber Monte Carlo (MC) [89], with the ratio of the average charged-particle multiplicity measured at mid-rapidity for the ZN-centrality class to that in MB collisions. In the following, these values are denoted $\langle N_{\text{part}}^{\text{mult}} \rangle$ to indicate this assumption. The corresponding number of binary collisions is then obtained as $\langle N_{\text{coll}}^{\text{mult}} \rangle = \langle N_{\text{part}}^{\text{mult}} \rangle - 1$. The associated

| Centrality class | 0–100% | 0–20% | 20–40% | 40–60% | 60–100% |
|---|---|---|---|---|---|
| $\langle N_{\rm coll}^{\rm mult} \rangle$ | $7.09 \pm 0.28$ | $12.2 \pm 0.52$ | $9.81 \pm 0.17$ | $7.09 \pm 0.29$ | $3.17 \pm 0.09$ |

**Table 8.5:** Average number of binary collisions $\langle N_{\rm coll}^{\rm mult} \rangle$ estimated with the hybrid ZN method in p–Pb collisions at $\sqrt{s_{\rm NN}} = 8.16$ TeV. Table adapted from Ref. [197].

uncertainty is evaluated using different approaches as described in Ref. [197]. The resulting values of $\langle N_{\rm coll}^{\rm mult} \rangle$ and their uncertainties are summarised in Table 8.5.

### 8.1.5 Track selection

The selected events should contain at least one or two muon tracks, following the selection on the trigger condition. In order to extract them, and select the tracks relevant for the analyses, a number of selection criteria is applied. A first set aims at ensuring a clean sample of muon track candidates:

- the **trigger-tracker matching** requires that each track reconstructed in the muon tracking system matches a track segment in the trigger chambers. The selection is based on a $\chi^2$ test of the quality of the matching. The matching serves as muon identification, as the shielding of the trigger system is expected to stop all particles but muons,
- a selection of the **polar angle at the end of the front absorber** $\theta_{\rm abs}$ requires $170^\circ < \theta_{\rm abs} < 178^\circ$. Equivalently, the same selection can be applied to the **radial transverse position** at the end of the front absorber $R_{\rm abs}$, asking it to be in the interval $17.5 < R_{\rm abs} < 89.5$ cm. This aims at removing the tracks crossing the high-density region of the front absorber, where they experience significant multiple scatterings,
- the **product of the track momentum to its distance of closest approach** $p \times DCA$ provides an efficient rejection of the contamination by tracks not pointing to the interaction vertex. It exploits the correlation between the track momentum $p$ and its $DCA$, corresponding to the distance to the primary vertex of the track trajectory extrapolated to the plane transverse to the beam axis. Indeed, following the multiple scatterings in the front absorber, the $DCA$ distribution of particles produced in the collision follows a Gaussian distribution, with a width dependent on the material crossed and which is proportional to the inverse momentum of the tracks. Background tracks, on the other hand, have on average a $DCA$ larger than about 40 cm, independently from their momentum. A Gaussian fit of the distribution is performed, allowing one to apply the selection $p \times DCA < 6\ \sigma$ for the rejection of this background source.

Supplementary to this selection, a fiducial region is defined following the detection capabilities and to increase the efficiency of the signal extraction:

- a selection on the track **pseudorapidity**, $-4 < \eta_{\rm lab} < -2.5$, ensures that the track is within the spectrometer acceptance and avoids edge effects,

- a low boundary is set on the track **transverse momentum** as both the $Z^0$ and $W^{\pm}$ signals are characterised by high-$p_T$ muons. The limit is set at $p_T > 10$ GeV/$c$ in the $W^{\pm}$ measurement, and $p_T > 20$ GeV/$c$ for $Z^0$. In this second case, the selection is applied on the individual tracks and not on the dimuon $p_T$,
- in the $Z^0$ analysis, the **invariant mass** interval over which the signal is extracted is $60 < m_{\mu\mu} < 120$ GeV/$c^2$ as to fully encompass the $Z^0$ peak while excluding as much background as possible.

The effects of the selections are illustrated in Figure 8.4.

The top panels show the evolution of the single muon $p_T$ distribution for muon track candidates in the `MSH` triggered events, as the selection criteria are sequentially applied. One sees a large difference in the effects of the selection between p–Pb and Pb–p collisions. In the latter, the spectrometer lies on the side of the Pb fragments, and receives a large amount of supplementary background compared to p–Pb collisions. The number of tracks in the distributions is given in Table 8.6.

| **Period** | after PS | + good vertex | + $\eta$ | + $\theta_{abs}$ | + matching | + pDCA |
|---|---|---|---|---|---|---|
| **LHC16r** | 16,691,304 | 15,368,669 | 14,211,023 | 14,126,091 | 10,283,041 | 10,247,955 |
| **LHC16s** | 30,931,163 | 28,531,664 | 25,850,779 | 25,587,821 | 15,995,207 | 15,714,934 |

**Table 8.6:** Number of tracks after physics and vertex selection and the application of the cuts.

The middle panels of Figure 8.4 show the final distribution, after application of the full selection, of the single muon $p_T$ spectrum for positively and negatively charged tracks, as well as the combined distribution. A bulk of production is seen around $\sim 40$ GeV/$c$, half of the $W^{\pm}$ boson mass, corresponding to the characteristic signal of its muonic decay (the Jacobian peak). There is a significant difference between the $\mu^+$ and $\mu^-$ distribution, following from the quark content of the nucleus that affect in opposite manner the production of $W^+$ and $W^-$ bosons. This difference is striking when looking at the charge ratio as a function of $p_T$, shown in the bottom panels of the figure.

## 8.2 Signal extraction

### 8.2.1 Overview

The evaluation of the production starts from the extraction of the number of $Z^0$ and $W^{\pm}$ bosons from the data. The former is characterised by two muons of opposite charges, each with high $p_T$, forming a dimuon of invariant mass close to the mass of the boson itself, around 90 GeV/$c^2$. The invariant mass is calculated as:

$$m_{\mu\mu} = \sqrt{(E_1 + E_2)^2 - (p_{x,1} + p_{x,2})^2 - (p_{y,1} + p_{y,2})^2 - (p_{z,1} + p_{z,2})^2}, \tag{8.15}$$

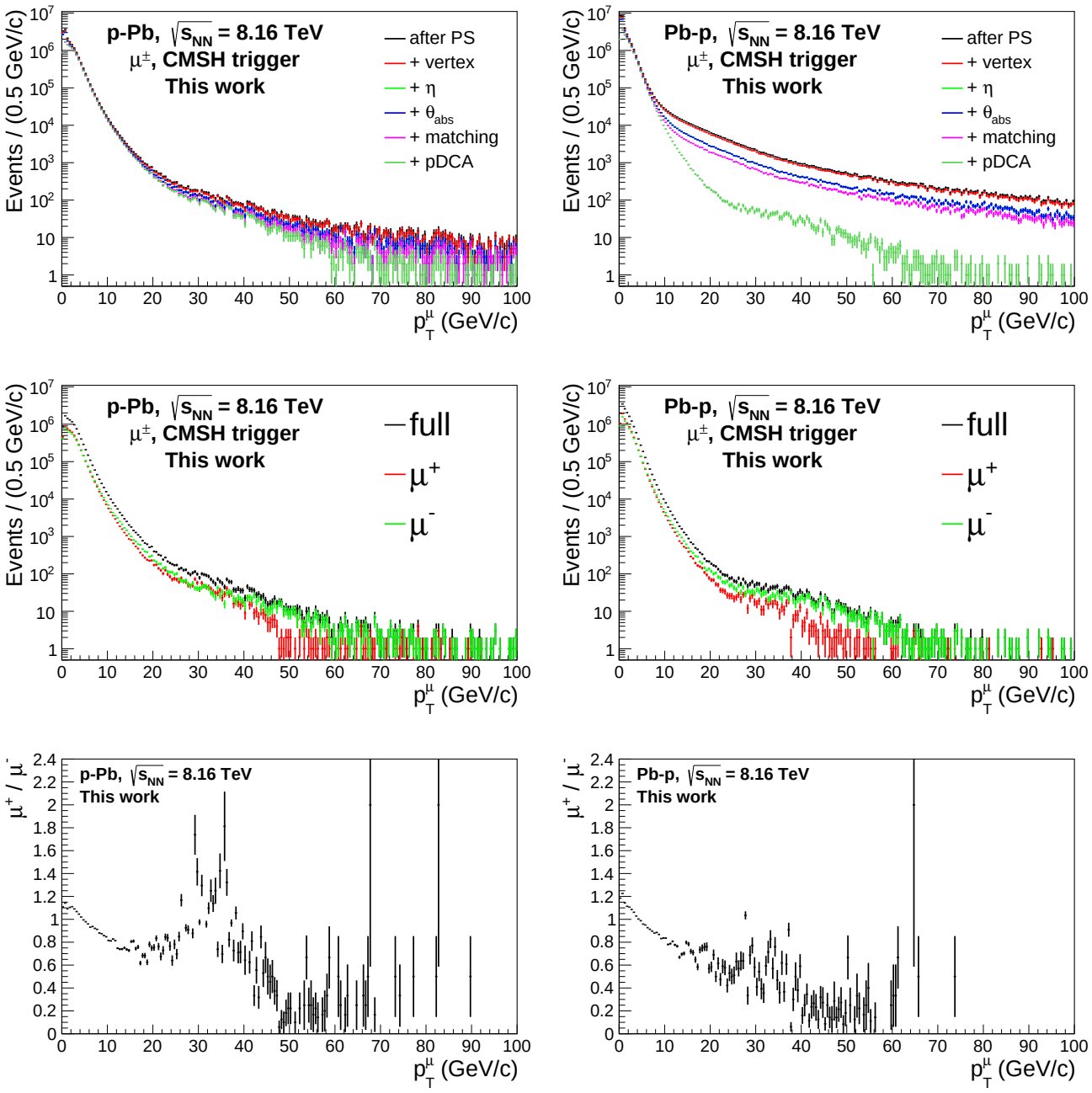


**Figure 8.4: Top**: evolution of the $p_{\mathrm{T}}$ distribution of muon track candidates from MSH-triggered events during the application of the event and track selections. **Middle**: $p_{\mathrm{T}}$ distribution of $\mu^+$, $\mu^-$ and $\mu^{\pm}$ (full) tracks after the full event and track selections. **Bottom**: charge ratio $\mu^+/\mu^-$ as a function of $p_{\mathrm{T}}$. The left column correspond to p–Pb collisions, the right one to Pb–p collisions.

where $E$ are the measured energies of the two muons and the $p_i$ are the $x$, $y$ and $z$ components of their momenta. The transverse momentum and pseudorapidity of the dimuon can also be evaluated

following:

$$p_{\mathrm{T}}^{\mu\mu} = \sqrt{\left(p_{x,1} + p_{x,2}\right)^2 + \left(p_{y,1} + p_{y,2}\right)^2}, \qquad \eta_{\mu\mu} = \frac{1}{2}\ln\left(\frac{E_1 + E_2 + p_{z,1} + p_{z,2}}{E_1 + E_2 - (p_{z,1} + p_{z,2})}\right). \tag{8.16}$$

The extraction of the $\mathrm{W}^{\pm}$ boson is complicated by the presence of a neutrino in the final state. Moreover, as ALICE is not a hermetic detector, the missing energy or transverse mass in the event cannot be estimated. The signal extraction procedure then relies on the inclusive single muon $p_{\mathrm{T}}$ distribution, in which three main contributions are expected: the large $p_{\mathrm{T}}$ region is populated by muons coming from $\mathrm{W}^{\pm}$ and $\mathrm{Z}^0$ bosons, while at low $p_{\mathrm{T}}$ a large number of muons coming from the decay of heavy-flavour hadrons (HF) is expected. The inclusive spectrum is reproduced from simulations with the template fit method. MC simulations are performed for each contribution, then combined with:

$$f(p_{\mathrm{T}}) = N_{\mathrm{bkg}} \cdot f_{\mathrm{bkg}}(p_{\mathrm{T}}) + N_{\mu^{\pm}\leftarrow\mathrm{W}^{\pm}} \cdot \left(f_{\mu^{\pm}\leftarrow\mathrm{W}^{\pm}}(p_{\mathrm{T}}) + R \cdot f_{\mu^{\pm}\leftarrow\mathrm{Z}^0}(p_{\mathrm{T}})\right), \tag{8.17}$$

where:

- $f_{\mathrm{bkg}}$, $f_{\mu^{\pm}\leftarrow\mathrm{W}^{\pm}}$ and $f_{\mu^{\pm}\leftarrow\mathrm{Z}^0}$ are the templates, constructed following the simulation procedure explained below,
- $N_{\mathrm{bkg}}$ and $N_{\mu^{\pm}\leftarrow\mathrm{W}^{\pm}}$ are the numbers of muons from HF decays and $\mathrm{W}^{\pm}$ decays respectively,
- $R$ is the ratio of the cross section of muons from $\mathrm{Z}^0$ decays to that of $\mathrm{W}^{\pm}$ decays estimated by the MC generator.

Equation 8.17 is used to fit the single muon inclusive spectrum, with $N_{\mathrm{bkg}}$ and $N_{\mu^{\pm}\leftarrow\mathrm{W}^{\pm}}$ as free parameters, while $R$ is fixed. The yield of muons from $\mathrm{W}^{\pm}$ decays is then directly given by the value of $N_{\mu^{\pm}\leftarrow\mathrm{W}^{\pm}}$ after the fit.

### 8.2.2 MC simulations

The signal extraction for the $\mathrm{W}^{\pm}$ relies on MC simulations of contributions from $\mathrm{W}^{\pm}$ and $\mathrm{Z}^0$ bosons and HF hadrons. As these simulations are meant to reproduce the experimental spectrum, it needs to include a reproduction of the particle transport through the detector, as well as its running conditions and detection capabilities. The simulations will also be used for the evaluation of the detector efficiency. All simulations are performed run-by-run, with a number of events proportional to the number of `MSH`- or `MUL`-triggered events in the data.

#### HF hadrons

The simulation of HF-hadron production and muonic decay is estimated in the Fixed-Order Next-to-Leading-Log (FONLL) framework [95, 96], from production cross sections obtained with [260]. The cross sections are obtained as a function of $p_{\mathrm{T}}$ and $y$, with the NNPDF3.0 [261] PDF set, and summing over the various possible decay chains:

$$b \to B \to \ell,$$
$$b \to B \to D \to \ell,$$
$$c \to (0.7D^0 + 0.3D^+) \to \ell.$$

As prediction cannot be made directly for p–Pb collisions at $\sqrt{s_{\rm NN}} = 8.16$ TeV from the web interface, they were derived from pp collisions at 8 TeV, without accounting for the nuclear corrections. Such corrections are expected to be negligible in the region of interest of this work, as they only affect the $p_{\rm T}$ region below $\sim 5$ GeV/$c$ [262]. The rapidity shift and energy difference are accounted for by:

- obtaining the $\mathrm{d}\sigma/\mathrm{d}y$ distributions in $2.03 < y < 3.53$ and $-4.46 < y < -2.96$,
- shifting the distributions from the initial ranges to $-4 < y < -2.5$ to manually implement the rapidity,
- performing a bin-by-bin scaling to increase the production for the energy difference, with a scaling factor given by:
$$\frac{\sqrt{s_{\rm NN}}(\text{p–Pb})}{\sqrt{s}(\text{pp})} = \frac{8.16}{8} = 1.02. \tag{8.18}$$
assuming that the deviation from linearity over such a small range is negligible [263].

The resulting distributions are fitted with phenomenological functions:

$$f(p_{\rm T}) = p_0 \frac{\exp\left(-p_1 \times \sqrt{p_{\rm T}}\right)}{p_{\rm T}^{p_2}}, \qquad f(y) = p_0 + p_1 \times y^2, \tag{8.19}$$

where the $p_i$, $i = 0, 1, 2$ are free parameters. The results of the fits are shown in Figure 8.5. They are used for the parametrisation for MC generation of muons from HF hadron decays with PYTHIA 6 [264].

After the generation with PYTHIA 6, the events are passed to a GEANT3 [265] simulation of the detector, anchored to the corresponding files in the OCDB. The GEANT3 code reproduces the running condition during data taking, including the misalignment, and simulates the particle transport through the material. This reproduction of the running condition is not perfect, such that other corrections need to be applied.

The simulations must be corrected for the cluster resolution of the muon chambers, which has to be degraded in order to match the resolution observed during data taking. The standard reconstruction parametrises the cluster resolution with a distribution having Gaussian tails. A more realistic description can be achieved using Crystal Ball (CB) functions instead [266]. A CB has a Gaussian core that models the detector resolution, and power-law tails with independent parameters on both sides. The low-mass tail accounts for energy loss effects, while the high-mass tail is attributed to multiple Coulomb scatterings in the front absorber and momentum resolution. The CB function reads:

$$f(x; N, \overline{x}, \sigma, t_1, t_2, p_1, p_2) = N \cdot \begin{cases} A \cdot (B - t)^{-p_1}, & t \le t_1, \\ \exp\left(-\frac{1}{2}t^2\right), & t_1 \le t \le t_2, \\ C \cdot (D + t)^{-p_2}, & t \ge t_2. \end{cases} \tag{8.20}$$

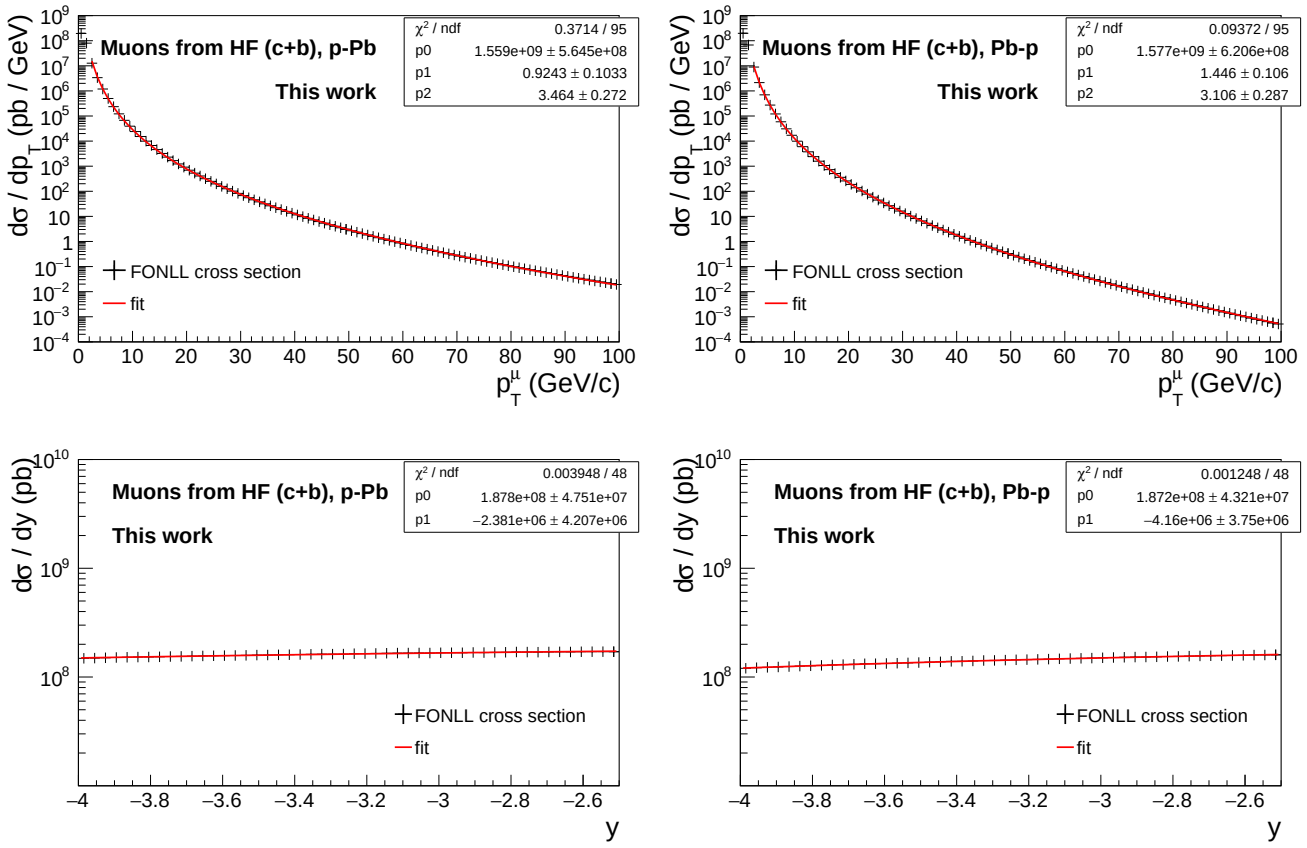


**Figure 8.5:** FONLL [95] cross sections for the leptonic decay of HF hadrons as a function of $p_{\mathrm{T}}$ (top) and $y$ (bottom) in p–Pb (left) and Pb–p (right) collisions. The lines correspond to fits with phenomenological functions.

where:

$$t = \frac{x - \overline{x}}{\sigma}, \qquad A = \left(\frac{p_1}{|t_1|}\right)^{p_1} \cdot \exp\left(-\frac{|t_1|^2}{2}\right), \qquad B = \frac{p_1}{|t_1|} - |t_1|, \tag{8.21}$$

$$C = \left(\frac{p_2}{|t_2|}\right)^{p_2} \cdot \exp\left(-\frac{|t_2|^2}{2}\right), \qquad D = \frac{p_2}{|t_2|} - |t_2|. \tag{8.22}$$

$N$, $\overline{x}$ and $\sigma$ are the normalisation, mean and width of the Gaussian core while $p_i$ and $t_i$ $(i = 1, 2)$ are the parameters of the tails. The $A$, $B$, $C$ and $D$ terms are defined as to ensure that both the function and its first derivative are continuous. The parameters are tuned on data, using the CB as a fit function for various experimental observables.

The anchoring to the OCDB, and the usage of the alignment files it contains, allows for taking into account the relative displacement of the detector elements with respect to one another. In addition, one may face as well a misalignment of the spectrometer in its entirety. This effect

is mimicked by applying a systematic shift to the track deviation in the magnetic field, shifting the $\mu^+$ and $\mu^-$ tracks in opposite directions. The magnitude of this shift can be tuned using an initialisation parameter of the `AliTaskMuonTrackSmearing` task, this parameter being the number of $\sigma$ by which the mean value of the CB function used for the cluster resolution is shifted. Its evaluation has to be performed by comparing some variable of interest between distributions from data and simulation.

In this work, the global shift was tuned by looking at the single muon $p_{\mathrm{T}}$ distribution. Between 10 and 20 GeV/$c$, one can assume that the distribution is only coming from the muonic decay of HF hadrons. The FONLL-based simulations of HF hadron decays are analysed using various tuning factors and the $\mu^+/\mu^-$ ratio is computed and compared to the one measured in the data. Table 8.7 shows the experimentally measured ratio, and the one obtained for various values of the tuning parameter. A parameter of 2.4 is found to best reproduce the ratio in p–Pb collisions, while the best match is found for a tuning parameter 2.3 in Pb–p. As the tuning parameter is expected to be the same for the two periods, which were taken one after the other and without any access to the ALICE cavern in between, a value of 2.4 is chosen, since:

- it is computed from a higher number of muons: in the [10;20] GeV/$c$ interval, there are about 70,000 muons in the p–Pb data sample, 40,000 in Pb–p,
- the global agreement for both periods is better: the ratio in p–Pb (Pb–p) simulations is at $0.2\sigma$ ($1\sigma$) from that of data with a tuning at 2.4, at $1.2\sigma$ ($0.3\sigma$) with a tuning at 2.3.

| **System** | Data | 2.2 | 2.3 | 2.4 | 2.5 | 2.6 |
|---|---|---|---|---|---|---|
| **p–Pb** | $0.781 \pm 0.006$ | $0.794 \pm 0.003$ | $0.787 \pm 0.002$ | $0.780 \pm 0.002$ | $0.772 \pm 0.002$ | $0.767 \pm 0.002$ |
| **Pb–p** | $0.766 \pm 0.007$ | $0.774 \pm 0.002$ | $0.768 \pm 0.002$ | $0.759 \pm 0.002$ | $0.751 \pm 0.001$ | $0.745 \pm 0.001$ |

**Table 8.7:** Charge ratio $\mu^+/\mu^-$ for $p_{\mathrm{T}}$ between 10 and 20 GeV/$c$ measured in data and FONLL-based simulations for various values of the global misalignment tuning parameter in p–Pb and Pb–p collisions.

Although the value of 2.4 is taken as the central value of the shift, one can see in Table 8.7 that all tuning parameters between 2.2 and 2.6 are still leading to a charge ratio in simulations that agrees with the experimental one within $3\sigma$. The 2.2–2.6 range is therefore taken as the uncertainty interval on the tuning parameter of the smearing task.

### $\mathbf{Z^0}$ and $\mathbf{W^{\pm}}$ bosons

The generation of the weak bosons is performed using POWHEG [267] as the particle generator. POWHEG generates hard events for various processes where heavy quarks, Higgs and electroweak bosons are involved. It implements NLO calculations and includes the $\mathrm{Z}^0/\gamma^*$ interference. CT10 [176] at NLO is used for the free-nucleon PDF and EPS09 [98], also at NLO, serves for the implementation of the nuclear corrections. As POWHEG is only a hard event generator, it needs to be interfaced with a shower MC program such as PYTHIA6 [264]. The detector response is simulated using GEANT3 [265], with corrections for the cluster resolution and the global misalignment

parametrised in the same way as for the HF simulations. The isospin effect, which has a significant effect on the $W^{\pm}$ bosons, is accounted for by simulating separately pp and pn binary collisions, then combining the results together with the formula:

$$\frac{1}{N_{\mathrm{pPb}}}\frac{\mathrm{d}N_{\mathrm{pPb}}}{\mathrm{d}p_{\mathrm{T}}} = \frac{Z}{A}\frac{1}{N_{\mathrm{pp}}}\frac{\mathrm{d}N_{\mathrm{pp}}}{\mathrm{d}p_{\mathrm{T}}} + \frac{A-Z}{A}\frac{1}{N_{\mathrm{pn}}}\frac{\mathrm{d}N_{\mathrm{pn}}}{\mathrm{d}pt}, \tag{8.23}$$

where $A = 208$ and $Z = 82$ are the atomic and charge number of Pb, respectively. The above formula is valid for the $W^{\pm}$ simulations, the merging for the $Z^0$ is done at the invariant mass level instead of the transverse momentum. The output of the simulations is shown in Figure 8.6. The figures show the MC truth distributions, i.e. the simulations at the generation level, before particle transport, for the $p_{\mathrm{T}}$ distribution of single muon tracks from $W^{\pm}$ decays, and the dimuon invariant mass distribution of muon pairs from $Z^0$ decays.

In Equation 8.17, the number of muons coming from the decays of $Z^0$ bosons is not a free parameter, it is set to be proportional to the number of muons from $W^{\pm}$ following the ratio of their respective cross sections as predicted by POWHEG (the parameter $R$ in the equation). The procedure is the following:

- the $\mathrm{d}N/\mathrm{d}p_{\mathrm{T}}$ distribution is obtained from the simulations, applying the full event and track selections,
- the resulting distribution is scaled by a factor $\sigma_{4\pi}/N_{\mathrm{trials}}$, where $\sigma_{4\pi}$ is the total POWHEG cross section of the process in the full phase space, and $N_{\mathrm{trials}}$ is the total number of events that were generated in order to get the required statistics after the selection. This scaling transforms the $\mathrm{d}N/\mathrm{d}p_{\mathrm{T}}$ distribution into $\mathrm{d}\sigma/\mathrm{d}p_{\mathrm{T}}$,
- the cross sections for the $W^{\pm}$ and $Z^0$ bosons, are obtained by integration over the region of interest, which allows for the evaluation of their ratio $R = \sigma_{Z^0}/\sigma_{W^{\pm}}$.

The ratios computed for the two collision systems and both muon electrical charges are given in Table 8.8.

| System | p–Pb | | Pb–p | |
|---|---|---|---|---|
| Muon charge | – | + | – | + |
| $R$ | 0.34 | 0.22 | 0.21 | 0.48 |

**Table 8.8:** Ratio $R$ of the $\mu^{\pm} \leftarrow Z^0$ cross section to that of $\mu^{\pm} \leftarrow W^{\pm}$ estimated in p–Pb and Pb–p collisions at $\sqrt{s_{\mathrm{NN}}} = 8.16$ TeV from simulations with POWHEG [267].

### 8.2.3 $Z^0$-boson signal extraction

The signal extraction of the $Z^0$ boson in its muonic decay is performed from the dimuon invariant mass distribution obtained after applying the event and track selection detailed in Section 8.1.

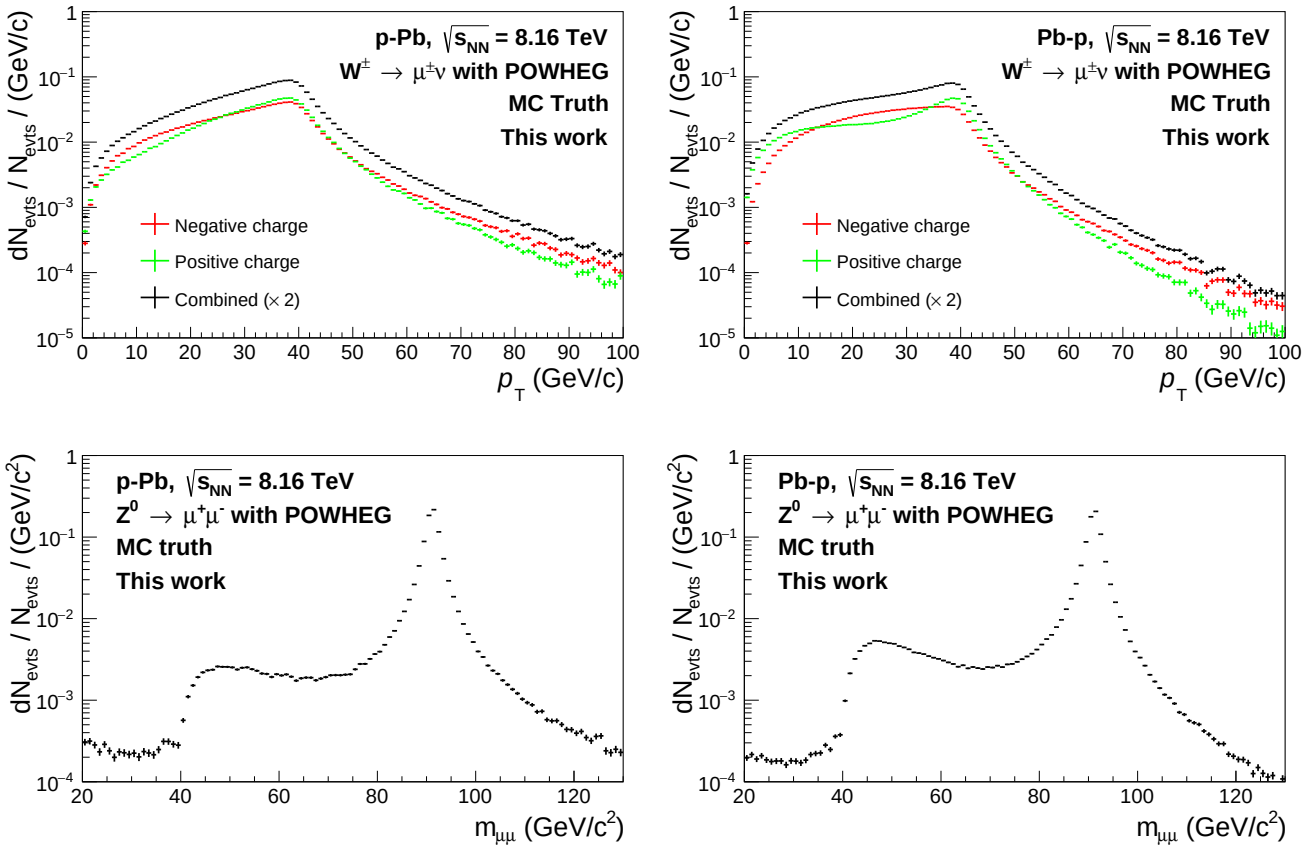


**Figure 8.6: Top**: $p_{\mathrm{T}}$ distribution of the single muons from $\mathrm{W}^{\pm}$ decays, for positively and negatively charged muons, and their combination with Equation 8.23. All the distribution are normalised to 1, the combined distribution is furthermore scaled by a factor 2 for visibility. **Bottom**: invariant mass distribution of dimuons from $\mathrm{Z}^0$ decays, normalised to 1. In the four plots, the distributions are the MC truth, obtained at NLO with the POWHEG [267] generator paired with PYTHIA6 [264], using CT10 [176] and EPS09 [98] and PDF and nPDF sets, respectively. The left (right) panels correspond to p–Pb (Pb–p) collisions.

The resulting distributions in p–Pb and Pb–p collisions show a typical peak around the mass of the $\mathrm{Z}^0$, as illustrated in Figure 8.7. The experimental distributions are compared to the fully reconstructed simulations presented in this section, the latter being normalised to the number of events in the data. A good agreement is found between the data ans simulations, when comparing the dimuon invariant mass, transverse momentum and rapidity distributions of the $\mathrm{Z}^0$. Counting the entries of the invariant mass spectrum between 60 and 120 GeV/$c^2$, one finds:

$$\begin{cases} 64 \pm 8 \ \mathrm{Z}^0 \text{ candidates}, & \text{p–Pb collisions}, \\ 34 \pm 6 \ \mathrm{Z}^0 \text{ candidates}, & \text{Pb–p collisions}. \end{cases}$$

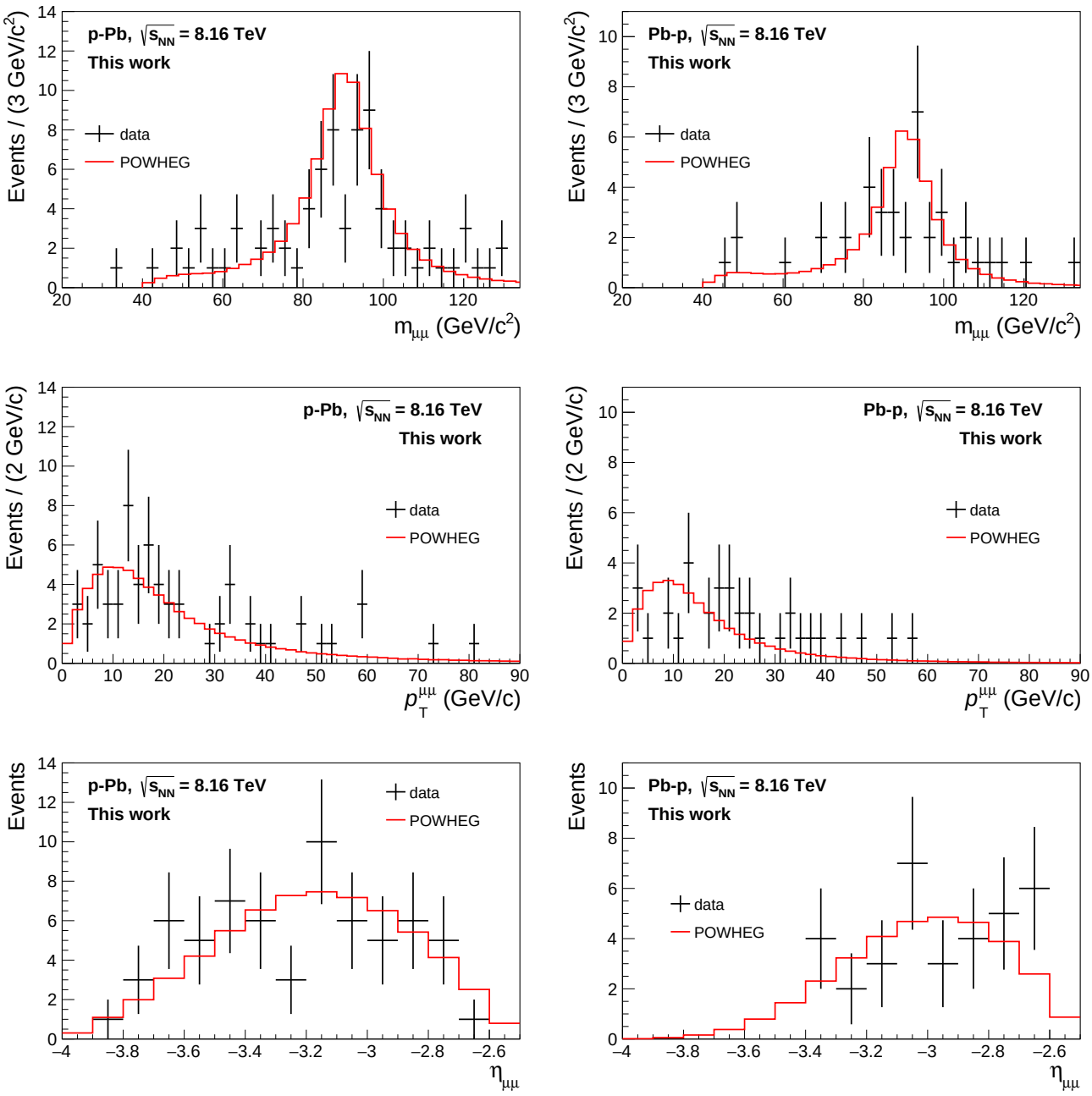


**Figure 8.7:** Invariant mass (top), $p_{\mathrm{T}}$ (middle) and $\eta$ (bottom) distributions of dimuons from $\mathrm{Z}^0$ candidates in p–Pb (left) and Pb–p (right) collisions at $\sqrt{s_{\mathrm{NN}}} = 8.16$ TeV. The lines correspond to fully reconstructed simulations of the $\mathrm{Z}^0 \to \mu^+\mu^-$ process at NLO, generated with POWHEG, using CT10 and EPS09 as PDF and nPDF, respectively. The particle transport and detector response is accounted for using the GEANT3 code.

The fiducial region over which the measurement is performed,

$$\begin{cases} p_{\mathrm{T}}^{\mu} > 20 \text{ GeV}/c, \\ -4 < y_{\mu} < -2.5, \\ 60 < m_{\mu\mu} < 120 \text{ GeV}/c^2, \end{cases}$$

is defined such that the signal region is isolated from background as much as possible. However, several sources can create a muon pair of opposite sign and high invariant mass that will contaminate the signal. In this study, the following sources were considered:

- the muonic decays of HF hadrons: $c\overline{c} \to \mu^+\mu^-$ and $b\overline{b} \to \mu^+\mu^-$,
- the muonic decays of top-antitop pairs: $t\overline{t} \to \mu^+\mu^-$,
- indirect $\mathrm{Z}^0$ decays through a $\tau$ pair, which then decay into two muons (and neutrinos): $\mathrm{Z}^0 \to \tau^+\tau^- \to \mu^+\mu^-\nu_{\mu}\overline{\nu}_{\mu}$,
- uncorrelated pairs formed from muons that do not originate from the same physics process.

The first source is estimated with POWHEG simulations of the $c\overline{c}(b\overline{b}) \to \mu\mu$ process. The MC truth distributions are scaled to the cross section predicted by the generator, then scaled again to the luminosity of the corresponding collision period. This yields a realistic estimation of the contribution of these processes to the experimental invariant mass spectrum. The simulations were performed in the full phase space, the same selection as for the signal extraction is then applied in order to reach the same fiducial region. Figure 8.8 shows the evolution of the invariant mass distribution of dimuons from $c$ and $b$ decays. One can see that after the full selection is applied, the significant amount of dimuons initially found in the region of interest is completely removed. It is worth reminding that the selection applied to the data contains no selection on the dimuon rapidity, the one shown in the figures is only given for reference. Following this study, the contribution from the muonic decays of HF hadrons to the background is neglected.

The $t\overline{t}$ and $\tau^+\tau^-$ contributions are estimated using simulations with POWHEG, applying again the same selection as in the data. The distributions are then scaled to the $\mathrm{Z}^0 \to \mu\mu$ distribution following the ratio of their cross sections predicted by POWHEG. The comparison is shown in the bottom panels of Figure 8.8. The contamination from each source is estimated as the ratio of the background source integrated in the region of interest, to that of the signal. These ratios are found to be negligible, except for the $t\overline{t} \to \mu^+\mu^-$ process in p–Pb collisions, which yields a 1% contribution in the fiducial region. The fact that it is not contributing in Pb–p collisions can be explained by the rapidity shift, which pushes the rapidity in the centre-of-mass towards large negative rapidity. The rapidity distribution of dimuons from top-antitop decays being narrower than that of $\mathrm{Z}^0$ decays, the production is more suppressed.

The last source that was considered is the uncorrelated background, coming from muons pairs artificially constructed from muons that do not come from the same process. Since the probability to have such a pair is the same for muons of same or opposite charge, the uncorrelated background can be estimated by looking at the like-sign dimuon invariant mass distribution in the data, applying the same selection as for the signal extraction. Figure 8.9 shows the invariant mass

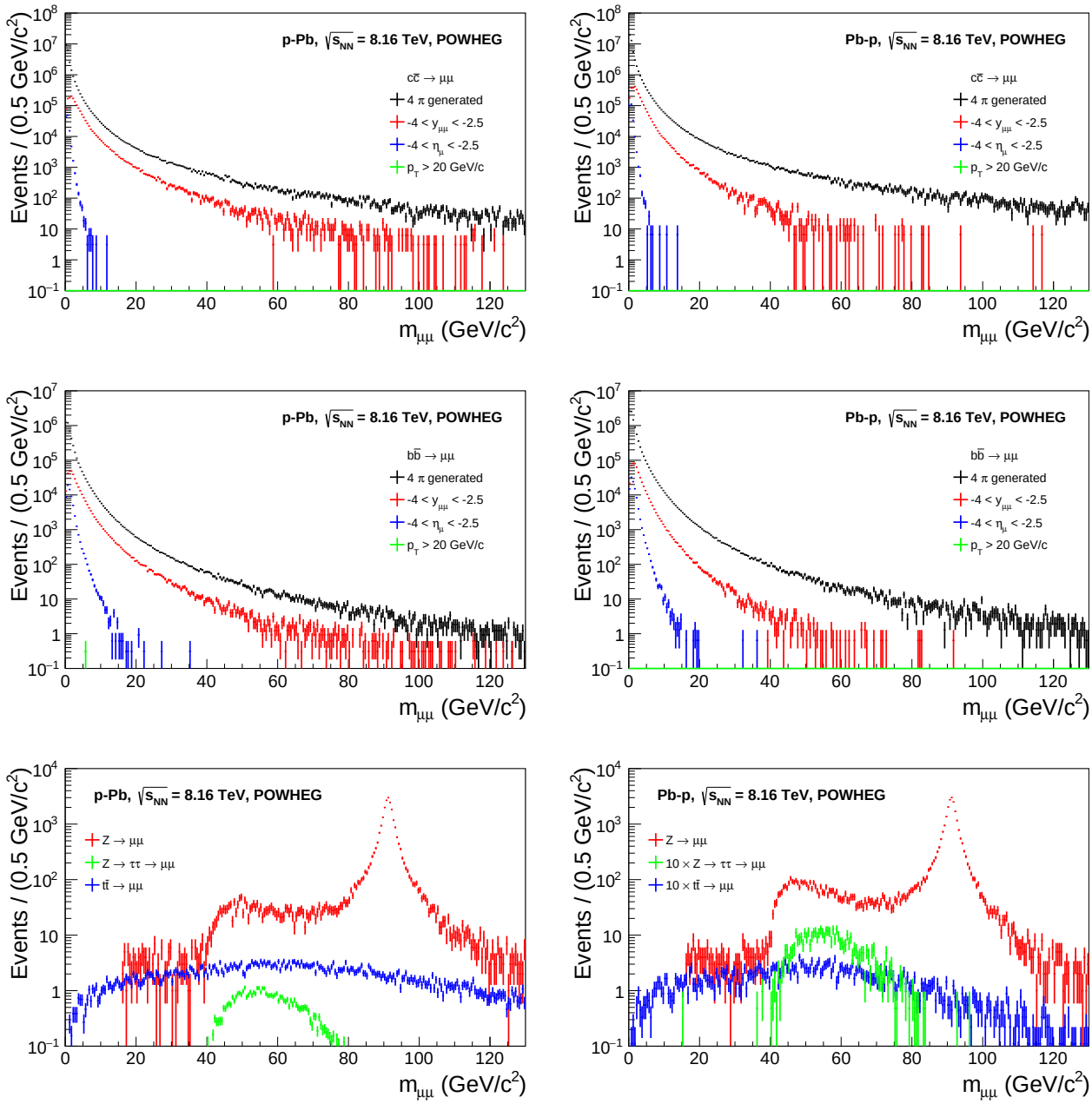


**Figure 8.8:** Estimation of the contamination to the $Z^0$ signal from several background sources in p–Pb (left) and Pb–p (right) collisions. **Top and middle**: POWHEG simulations of the contribution of $c$ (top) and $b$ (middle) hadron decays, scaled to the cross section of the process and to the integrated luminosity of the corresponding collision period. **Bottom**: relative yield of the $t\bar{t} \to \mu^+\mu^-$ and $Z^0 \to \tau^+\tau^- \to \mu^+\mu^-\nu_\mu\overline{\nu}_\mu$ processes to that of $Z^0 \to \mu\mu$ following the ratio of the POWHEG cross sections. The distributions from $t$ and $\tau$ in Pb–p collisions are scaled by a factor 10 for visibility.

distribution of same-sign muon pairs obtained from MSH-triggered events, for various values of the $p_{\mathrm{T}}$ selection. When a selection at 20 GeV/$c$ is applied, no entry is left in the spectrum, both in p–Pb and Pb–p collisions. An upper limit to this contribution can be obtained by releasing the $p_{\mathrm{T}}$ selection, fitting the distribution and extrapolate to the $60 < m_{\mu\mu} < 120$ GeV/$c^2$ region. Several functions were tested: a single tail CB, the ATLAS function, a power law (PL) and a double exponential (expo):

$$f_{\mathrm{CB}} = N \cdot \begin{cases} \exp\left(-\frac{(x-\overline{x})^2}{2\sigma^2}\right) & \text{if } \frac{x-\overline{x}}{\sigma} < p_0 \\ A \cdot \left(B - \frac{x-\overline{x}}{\sigma}\right)^{-p_1} & \text{otherwise} \end{cases}, \qquad f_{\mathrm{ATLAS}} = p_0 \cdot \frac{\exp(-p_1\sqrt{x})}{x^{p_2}},$$
$$f_{\mathrm{expo}} = p_0 \exp(p_1 x) + p_2 \exp(p_3 x), \qquad f_{\mathrm{PL}} = \frac{p_0}{\left(1+(x/p_1)^2\right)^{p_2}}, \tag{8.24}$$

where the $p_i$ are free parameters and the notations for the CB follows the ones of the two-tails version given in Equation 8.20. The results of the fits with the CB and PL functions are shown in Figure 8.9, the CB function yielding the lowest $\chi^2$/ndf, the PL function giving the highest estimation of the contribution in the fiducial region of interest. In all the trials, the integral in the region of interest is negligible, with a maximum of $10^{-3}$ "counts".

Combining all these considerations, the total amount of background is 1% in p–Pb collisions while it is negligible in Pb–p. This allows one to take the background as a systematic uncertainty on the signal extraction, which can then be performed by simply counting the entries in the fiducial region of interest defined by the selections on the muon $p_{\mathrm{T}}$ and $y$, and the dimuon invariant mass.

### 8.2.4 $\mathrm{W}^{\pm}$-boson signal extraction

The signal extraction of the $\mathrm{W}^{\pm}$ boson is done by fitting the inclusive single muon $p_{\mathrm{T}}$ spectrum with a combination of MC templates accounting for the various contributions, using Equation 8.17. Figure 8.10 shows examples of such fits for the four possible combinations of charges and collision systems. The templates used here were obtained with the central values of the FONLL predictions for HF, CT10nlo and EPS09nlo in POWHEG for weak bosons, and were corrected for the cluster resolution and global misalignment as described in Section 8.2.2. The fits are performed in the 15–65 GeV/$c$ interval, then extrapolated to the full $p_{\mathrm{T}} > 10$ GeV/$c$ region. In the four cases, the fit is observed to well reproduce the inclusive spectrum. The number of muons coming from $\mathrm{W}^{\pm}$ decays is extracted as the $N_{\mu\leftarrow\mathrm{W}}$ parameter in Equation 8.17.

Despite the agreement, one has to consider the dependence of the signal extraction procedure on the various inputs for the fits and the parametrisation of the simulations used for generating the templates. This dependence can be investigated by varying these inputs, and performing the fit with an alternative set up in order to evaluate the difference it makes in the signal extraction. The variations that were considered for this study are listed here and described below:

- the interval over which the fit is performed,
- the PDF and nPDF sets used for the generation of the $\mathrm{W}^{\pm}$ and $\mathrm{Z}^0$ templates, and the order at which the simulations are performed,

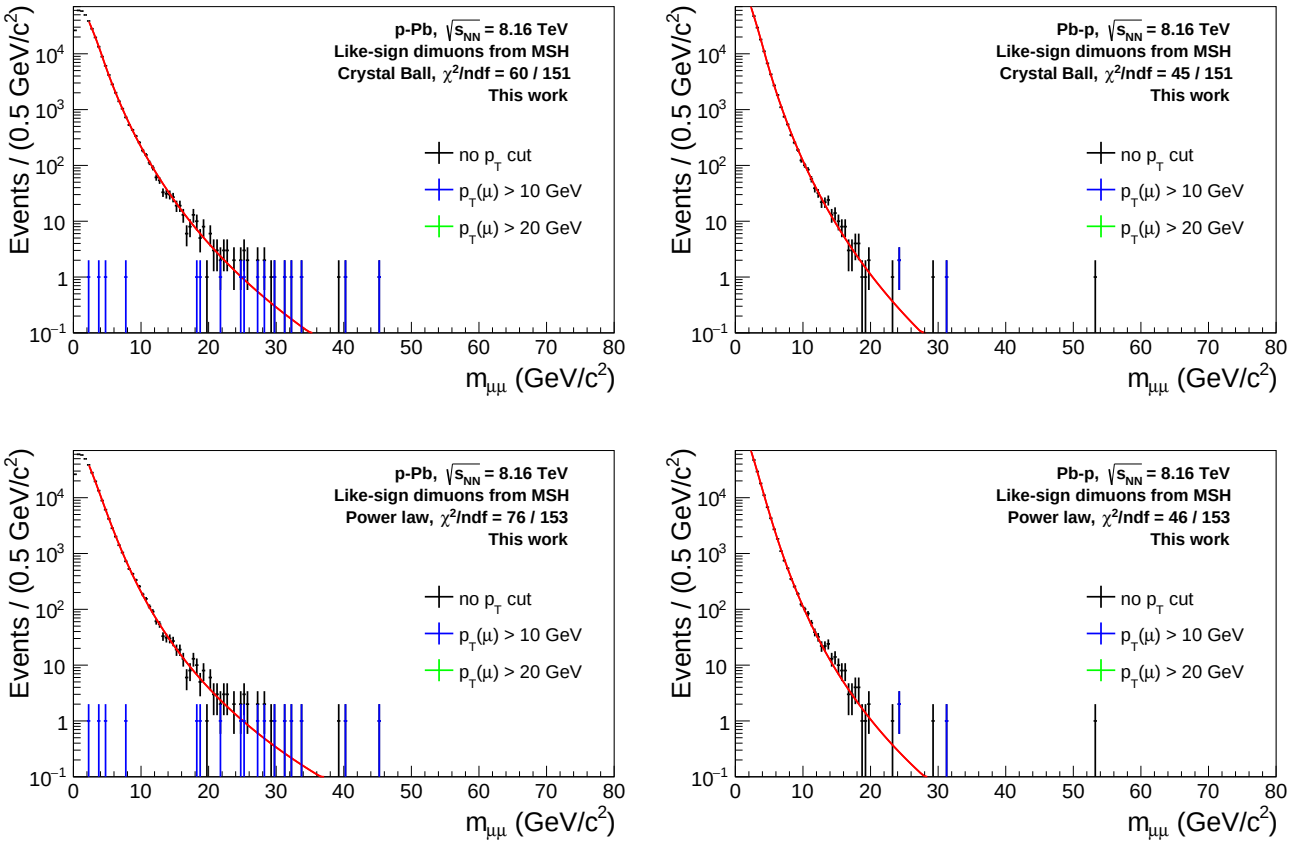


**Figure 8.9:** Invariant mass distribution of same sign muon pairs in p–Pb (left) and Pb–p (right) collisions, for various values of the muon $p_{\mathrm{T}}$ selection. The curves correspond to fits of distributions without $p_{\mathrm{T}}$ selection, using a Crystal Ball (top) or power law (bottom) function.

- the FONLL predictions used for the generation of the HF template,
- the correction for the cluster resolution,
- the correction for the global misalignment of the spectrometer.

**Fit range** The fits shown in Figure 8.10 are performed between 15 and 65 GeV/$c$. Varying the boundaries of the interval will change the weight of each template in the determination of the best fit parameter, which can impact the fit stability and the signal extraction. In order to take this effect into account, the low limit is varied between 10 and 20 GeV/$c$ with steps of 2 GeV/$c$, and the high limit is varied between 50 and 80 GeV/$c$ with steps of 6 GeV/$c$. The two variations are not done independently, instead each configuration of low and high boundaries is used, for a total of 36 possibilities.

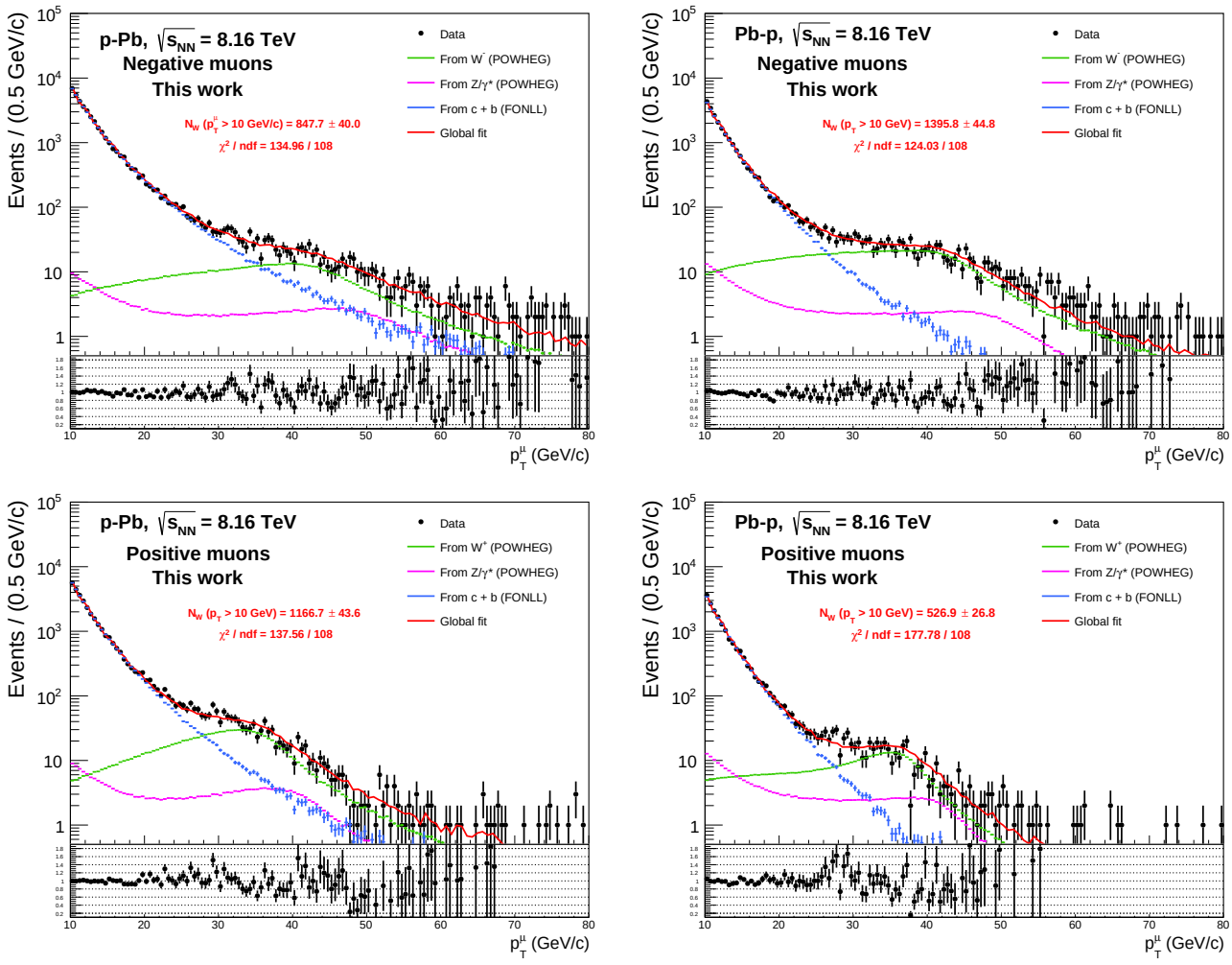


**Figure 8.10:** Global fits of the single muon $p_{\mathrm{T}}$ distribution in p–Pb (top) and Pb–p (bottom) collisions for negatively (left) and positively (right) charged muons. The bottom panel in each plot shows the ratio of the data to the fit result, after extrapolation of the latter to the full $p_{\mathrm{T}}$ range.

**Coupling constant and perturbative order** The generation of the weak boson templates with POWHEG uses CT10 and EPS09, both at NLO, with a value of the strong coupling constant taken as the PDG world average of $\alpha_s = 0.118$. The CT10 PDF set comes with several subsets, among which two are determined with the most extreme variations of $\alpha_s$ within its uncertainty, ranging from 0.112 to 0.127. These subsets can be used by calling the `CT10nlo_as_0112` and `CT10nlo_as_0127` PDFs. The order at which the PDF and nPDF are determined can also be tested by using the LO version of CT10 and EPS09, rather than the NLO one. The $p_{\mathrm{T}}$ distribution of muons from $\mathrm{W}^{\pm}$ decays is shown in Figure 8.11 for simulations at LO, and with the variations of $\alpha_s$, compared to the nominal parametrisation with CT10nlo + EPS09nlo and $\alpha_s = 0.118$. These variations can have a non-negligible effect on the predicted production of muons from $\mathrm{W}^{\pm}$ decays. But since these simulations are meant to build templates, one only has to consider the shape and

they were then normalised to unity for comparison. The effect of these variations is found to be negligible.

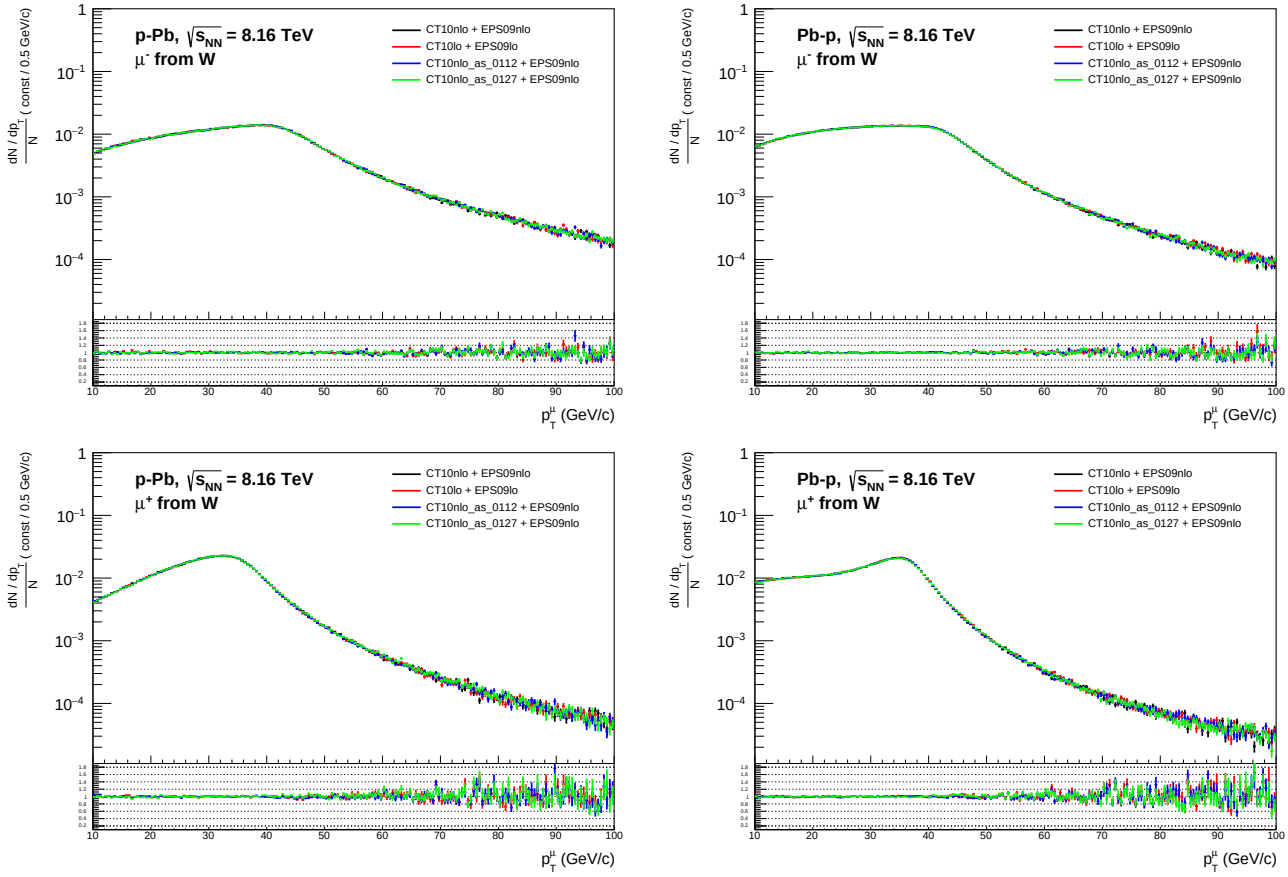


**Figure 8.11:** $p_{\mathrm{T}}$ distribution of negative (top) and positive (bottom) muon from $\mathrm{W}^{\pm}$ decays in p–Pb (left) and Pb–p (right) collisions simulated at LO and for variations of $\alpha_s$, compared to the nominal parametrisation. In each plot, the bottom panel shows the ratio of the modified distribution to the central one.

**nPDF set** The dependence on the nPDF was accounted for by replacing EPS09 with EKS98 [268] in the POWHEG simulations. The distributions, once normalised to unity, are found to be in very good agreement. Yet, contrary to what was observed for $\alpha_s$ and the perturbative order, changing the nPDF has a significant effect on the ratio $R$ of Equation 8.17, such that this source is included in the pool of variations considered in this study.

**FONLL predictions** The predictions for the cross section of muons from HF hadron decays come with an uncertainty emanating from the knowledge of the mass of the heavy quark, the baseline PDF and the factorisation and renormalisation scales. The distributions taken at the edge of the uncertainty intervals show a non-negligible difference in the shape of the predicted

production, as the uncertainty is $p_{\mathrm{T}}$-dependent. This effect was accounted for by fitting the high and low edges of the uncertainty band, instead of the central values. The initial template was then weighted by the ratio of these fits to the central one, accounting for the correlation between the generated and reconstructed tracks.

**Cluster resolution** The procedure for the correction of the cluster resolution in simulations, described in Section 8.2.2, relies on the determination of the CB parameters. The initial set is determined by matching the simulations to data, an alternative set can be fully obtained from simulations, yielding different parameters for the CB function that will introduce a difference in the reconstruction. The $p_{\mathrm{T}}$ distribution of muons obtained with the two sets are compared in Figure 8.12. This variation creates a narrower peak when the MC-tuned parameters are used,

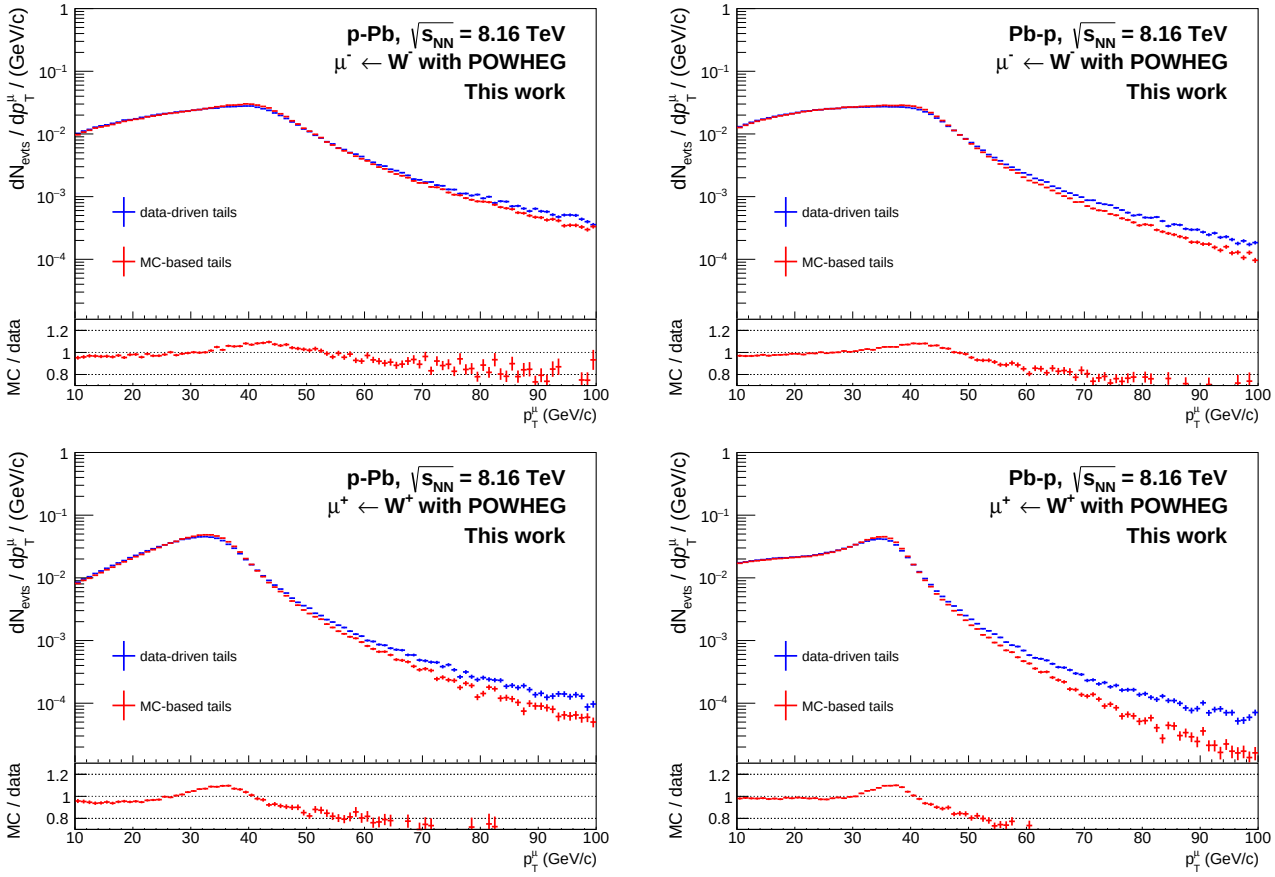


**Figure 8.12:** $p_{\mathrm{T}}$ distribution of negative (top) and positive (bottom) muon from $\mathrm{W}^{\pm}$ decays in p–Pb (left) and Pb–p (right) collisions simulated with the nominal (data-based) and alternative (MC-tuned) sets of parameters for the cluster resolution correction. The bottom panel in each plot shows the ratio of the distribution obtained with the alternative set to that with the nominal one.

which impacts the weight of the HF and $\mathrm{Z}^0$ templates at low and high $p_{\mathrm{T}}$.

**Global misalignment** The tuning parameter of the task mimicking the global misalignment, determined by following the procedure described in Section 8.2.2, was estimated to be:

$$n_{\text{shift}} = 2.4 \pm 0.2\ \sigma_{\text{CB}}. \tag{8.25}$$

The uncertainty can have a significant effect on the simulated distributions, the fits were then performed with three values of the parameter: its central value, and the low and high limits if the uncertainty interval, 2.2 and 2.6. The $p_{\text{T}}$ distribution of single muons obtained using these three values are compared in Figure 8.13.Variations in $n_{\text{shift}}$ induce a significant shift of the distribution, and the Jacobian peak is displaced by a few GeV/$c$.

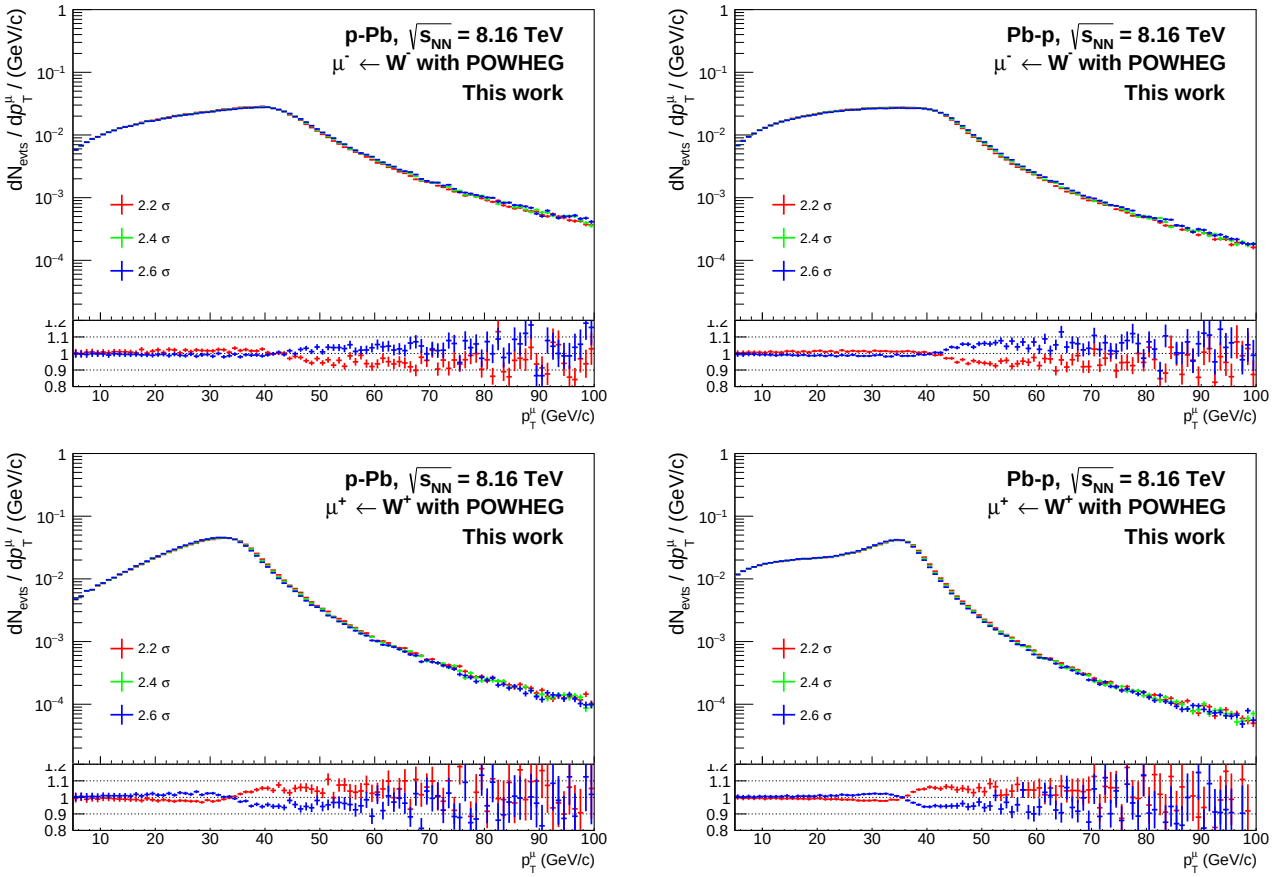


**Figure 8.13:** $p_{\text{T}}$ distribution of negative (top) and positive (bottom) muon from $\text{W}^{\pm}$ decays in p–Pb (left) and Pb–p (right) collisions simulated with the three values of the tuning parameter accounting for the global misalignment of the spectrometer. In each plot, the bottom panel shows the ratio of the modified distributions (with a tuning at 2.2 and 2.6) to the central one (tuning at 2.4).

The signal extraction is finally performed by considering all these variations, combining them in every way possible. The variations include the fit range (36 possibilities), the nPDF (2 possibilities),

the FONLL inputs (3 possibilities), the parameters for the cluster resolution (2 possibilities) and the tuning parameter for the global misalignment (3 possibilities). In total, 1296 configurations are used to construct the templates and fit the experimental spectrum. For each fit, a selection is defined and it determines whether the configuration is kept or not:

- the fit result must be valid (`TFitResult::IsValid() == kTRUE`),
- the covariant matrix must be accurate (`TFitResult::CovMatStatus() == 3`).

As the variations are applied to both $\mu^+$ and $\mu^-$ spectra, a combined $\chi^2$ test was defined as:

$$\frac{\chi^2_{\text{tot}}}{\text{ndf}_{\text{tot}}} = \frac{\chi^2_{\mu^-} + \chi^2_{\mu^+}}{\text{ndf}_{\mu^-} + \text{ndf}_{\mu^+}}. \tag{8.26}$$

The fit result of a given configuration is kept if $\chi^2_{\text{tot}}/\text{ndf}_{\text{tot}} < 2$, ensuring that the configuration is able to reproduce the inclusive spectrum despite the independent analysis of negatively and positively charged muons.

The final value for $N_{\text{W}}$, and its associated statistical uncertainty, is taken as the average of all the values obtained with different input parameters and fit ranges. Their dispersion, evaluated as the standard deviation, is taken as the systematic uncertainty on the signal extraction:

$$\left\langle N_{\text{W}} \right\rangle = \frac{\sum_{i=1}^{n} N_{\text{W}}^i}{n}, \qquad \sigma^{\text{stat}}_{N_{\text{W}}} = \frac{\sum_{i=1}^{n} \sigma^{\text{stat}}_{N_{\text{W}}^i}}{n}, \qquad \sigma^{\text{syst}}_{N_{\text{W}}} = \sqrt{\frac{\sum_{i=1}^{n} \left( N_{\text{W}}^i - \left\langle N_{\text{W}} \right\rangle \right)^2}{n-1}}, \tag{8.27}$$

where $n$ is the number of configurations that passed the fit quality selection. Figure 8.14 shows the number of $\text{W}^{\pm}$ extracted from each trial, with the corresponding average and associated statistical and systematic uncertainties, along with the $\chi^2_{\text{tot}}/\text{ndf}_{\text{tot}}$ of each trial that passed the selection. The combinations of the variations tend to be able to reproduce the data, as only 1% of the configurations are discarded in p–Pb collisions, and 0.5% in Pb–p. The fit results show rather large fluctuations in p–Pb collisions for the $\text{W}^-$ yield, leading to a higher systematic uncertainty (about 9%) than for the other configurations. Table 8.9 shows the raw signals for muons from $\text{W}^{\pm}$ decays extracted from the data, with the corresponding statistical and systematic uncertainties.

| | p–Pb | Pb–p |
|---|---|---|
| $\mu^- \leftarrow \text{W}^-$ | $824.1 \pm 43.9 \pm 72.8$ | $1388.4 \pm 48.5 \pm 53.3$ |
| $\mu^+ \leftarrow \text{W}^+$ | $1105.8 \pm 47.3 \pm 65.4$ | $493.0 \pm 28.3 \pm 35.8$ |

**Table 8.9:** Raw number of muons from $\text{W}^{\pm}$ decays, extracted from a global fit of the inclusive single muon $p_{\text{T}}$ distributions for $p_{\text{T}}^{\mu} > 10$ GeV/$c$ and $-4 < y_{\text{lab}}^{\mu} < -2.5$. The quoted errors correspond to the statistical and systematic uncertainties, respectively.

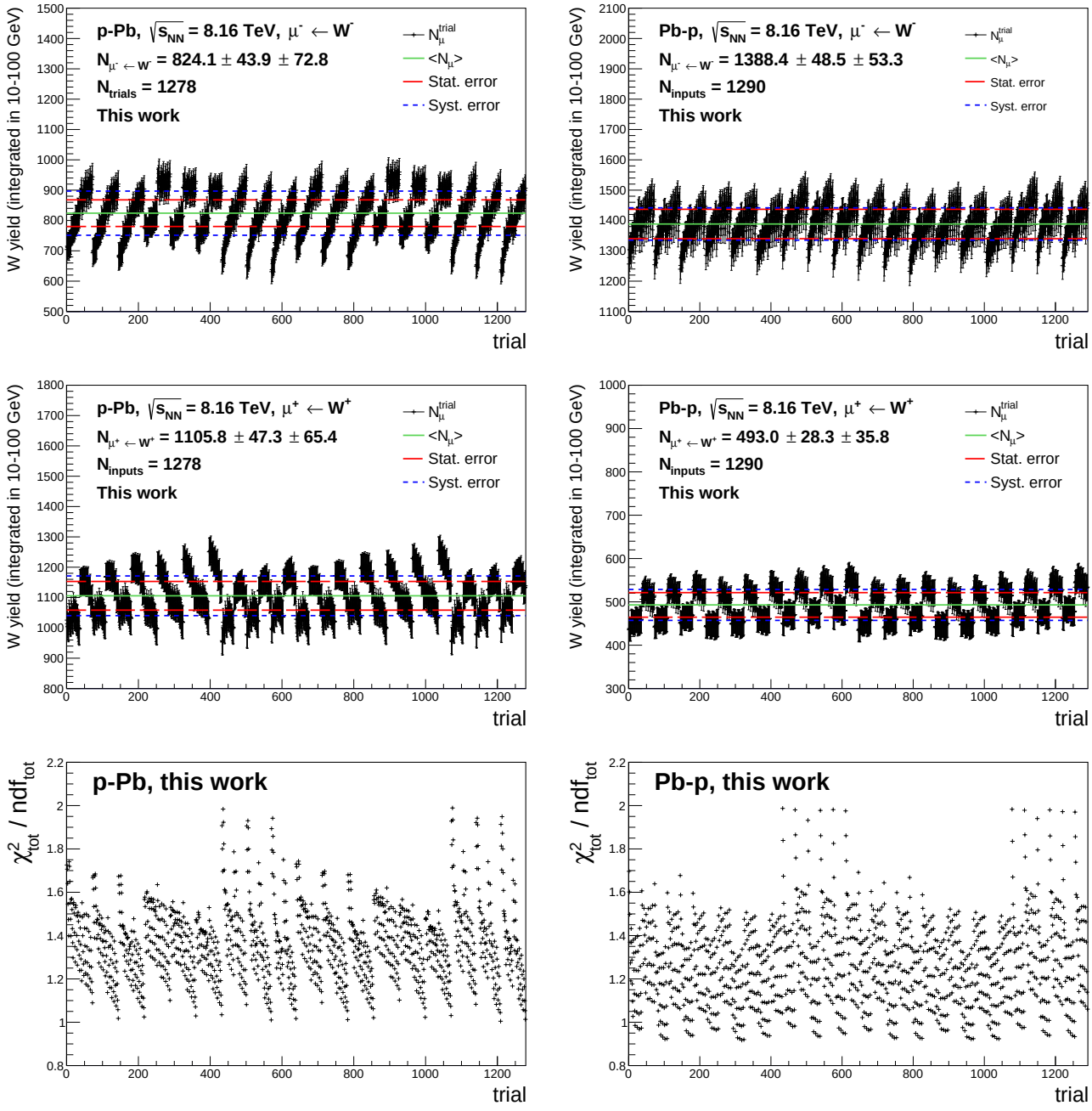


**Figure 8.14:** Extraction of the $W^{\pm}$ signal in p–Pb (left) and Pb–p (right) collisions. **Top and middle**: raw number of muons from $W^{\pm}$ decays as a function of the trial, for negative (top) and positive (middle) muons. The solid line represents the average of the distribution, while the long-dashed (short-dashed) line represents the statistical (systematic) uncertainty. **Bottom**: $\chi^2_{\rm tot}/{\rm ndf}_{\rm tot}$ distributions for the fits that passed the quality selection.

## 8.3 Efficiency correction

In order to evaluate the real production of the $Z^0$ and $W^{\pm}$ bosons, one needs to correct the raw yield for the efficiency of the detector. The latter is evaluated by means of simulations, using the same simulations that were presented above, with POWHEG for the generation of hard events, paired with PYTHIA6 for parton shower. The CT10 and EPS09 PDF and nPDF sets are used, both at NLO, with the isospin effect included by simulating pp and pn binary collisions combined with Equation 8.23. The particle transport and detector response are monitored by a detector simulation with the GEANT3 transport code. The simulations are anchored to the LHC16r and LHC16s OCDB. The cluster resolution is corrected using CB functions with the data-driven parameters, and the global misalignment is parametrised with a 2.4 $\sigma$ deviation. The simulations are performed run-by-run, with a number of generated events proportional to the number of `CMUL` and `CMSH` events for the computation of the efficiency of muons from $Z^0$ and $W^{\pm}$ decays, respectively.

The efficiency $\epsilon$ for each run $i$ is calculated as the ratio of the number of reconstructed events in the spectrometer $N^i_{\text{rec}}$ to the number of generated events in the fiducial region $N^i_{\text{gen}}$ taken from the MC truth:

$$\epsilon_i = \frac{N^i_{\text{rec}}}{N^i_{\text{gen}}}. \tag{8.28}$$

The overall efficiency of the period, and associated statistical uncertainty, are computed through an averaging over the run efficiencies, weighted by $w_i$ the fraction of `MUL`- or `MSH`-triggered events in run $i$:

$$\langle\epsilon\rangle = \frac{\sum_{i=1}^{n} w_i \times \epsilon_i}{\sum_{i=1}^{n} w_i}, \qquad \sigma_{\langle\epsilon\rangle} = \frac{\sqrt{\sum_{i=1}^{n} w_i \times \sigma_{\epsilon_i}}}{\sum_{i=1}^{n} w_i}. \tag{8.29}$$

The systematic uncertainty on the efficiency is evaluated by varying the simulation environment. Variations on the PDF and nPDF sets were considered, but the effects on the total efficiency itself are negligible. The same conclusion was derived from variations of the transport code, replacing GEANT3 by GEANT4. The only significant source of systematic uncertainty on the efficiency comes from the corrections for the cluster resolution and global misalignment. In the $Z^0$ analysis, it was evaluated by computing the efficiency with and without the corrections. Figure 8.15 shows the dimuon invariant mass distribution simulated with and without the corrections for cluster resolution and global misalignment. Including the corrections smears the peak in the distribution. Since the measurement is performed in a limited range in invariant mass, this smearing pushes part of the events outside of the boundaries, such that the total efficiency decreases, by 8% in p–Pb collisions and 6% in Pb–p collisions. In the $Z^0$ analysis this source of uncertainty is the largest contribution to the overall systematic uncertainty on the measurements. In the $W^{\pm}$ study, as a second alternative set of parameters for the cluster resolution became available, the uncertainty was evaluated independently for the cluster resolution and tuning of the global misalignment, by varying one while fixing the other at its nominal value. Computing the efficiency from simulations parametrised with CB functions, using either the data-driven set of parameters or the MC-tuned one, yields a difference below 1% which is taken as the associated uncertainty. With a cluster resolution parametrised with CB functions with the data-driven parameters, the global misalign-

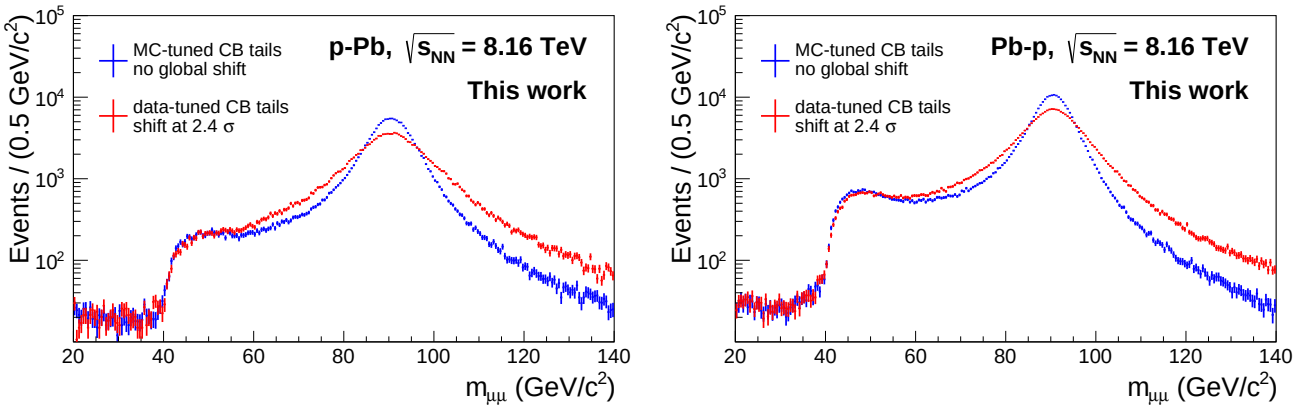


**Figure 8.15:** Invariant mass distribution of dimuons from $Z^0$ decays.

ment was varied between the boundaries of its uncertainty, at 2.2 and 2.6 $\sigma$. Even by taking the largest estimation, that is, the full difference between the two, the effect is found to be negligible compared to the one from the cluster resolution.

The efficiencies of muons from $W^-$, $W^+$ and $Z^0$ decays are shown in Figure 8.16. A similar trend is found for the three bosons in a given collision system, with a stable detector efficiency in LHC16r while several drops are seen in LHC16s. This feature originates from face-to-face high-voltage trips in the third and fourth stations of the tracking system, decreasing the overall tracking capabilities of the spectrometer. The efficiency for dimuons is lower than that of single muons, due to the need of detecting two muons instead of one, but also following from the smearing effect of the cluster resolution correction described above, explaining why the fraction of missed dimuons is more that twice that of single muons. The efficiencies computed in the full fiducial region are given in Table 8.10, with the systematic uncertainties corresponding to the corrections for cluster resolution and global misalignment.

| | p–Pb | Pb–p |
|---|---|---|
| $\epsilon(\mu^- \leftarrow W^-)$ | $0.905 \pm 0.007$ (syst) | $0.878 \pm 0.006$ (syst) |
| $\epsilon(\mu^+ \leftarrow W^+)$ | $0.907 \pm 0.005$ (syst) | $0.886 \pm 0.003$ (syst) |
| $\epsilon(\mu^+\mu^- \leftarrow Z^0)$ | $0.724 \pm 0.001$ (stat) $\pm 0.057$ (syst) | $0.723 \pm 0.001$ (stat) $\pm 0.041$ (syst) |

**Table 8.10:** Efficiencies of $\mu^\pm$ from $W^\pm$ decays and $\mu^+\mu^-$ from $Z^0$ decays in p–Pb and Pb–p collisions. The statistical uncertainties on the efficiency correction for the $W^\pm$ bosons are negligible. The systematic uncertainties come from the cluster resolution correction and global misalignment, the other sources being negligible.

## 8.4 Differential studies

So far, the procedure and intermediate results have been presented from computations in the full fiducial region. Due to the large statistics of the $W^{\pm}$ analysis, results were also obtained in several bins of rapidity and collision centrality. It is worth stressing that the whole analysis procedure was done for all the considered bins. In the laboratory frame, the rapidity interval was splitted in three bins of width 0.4, 0.4 and 0.7 from central to large rapidities, yielding in the centre-of mass

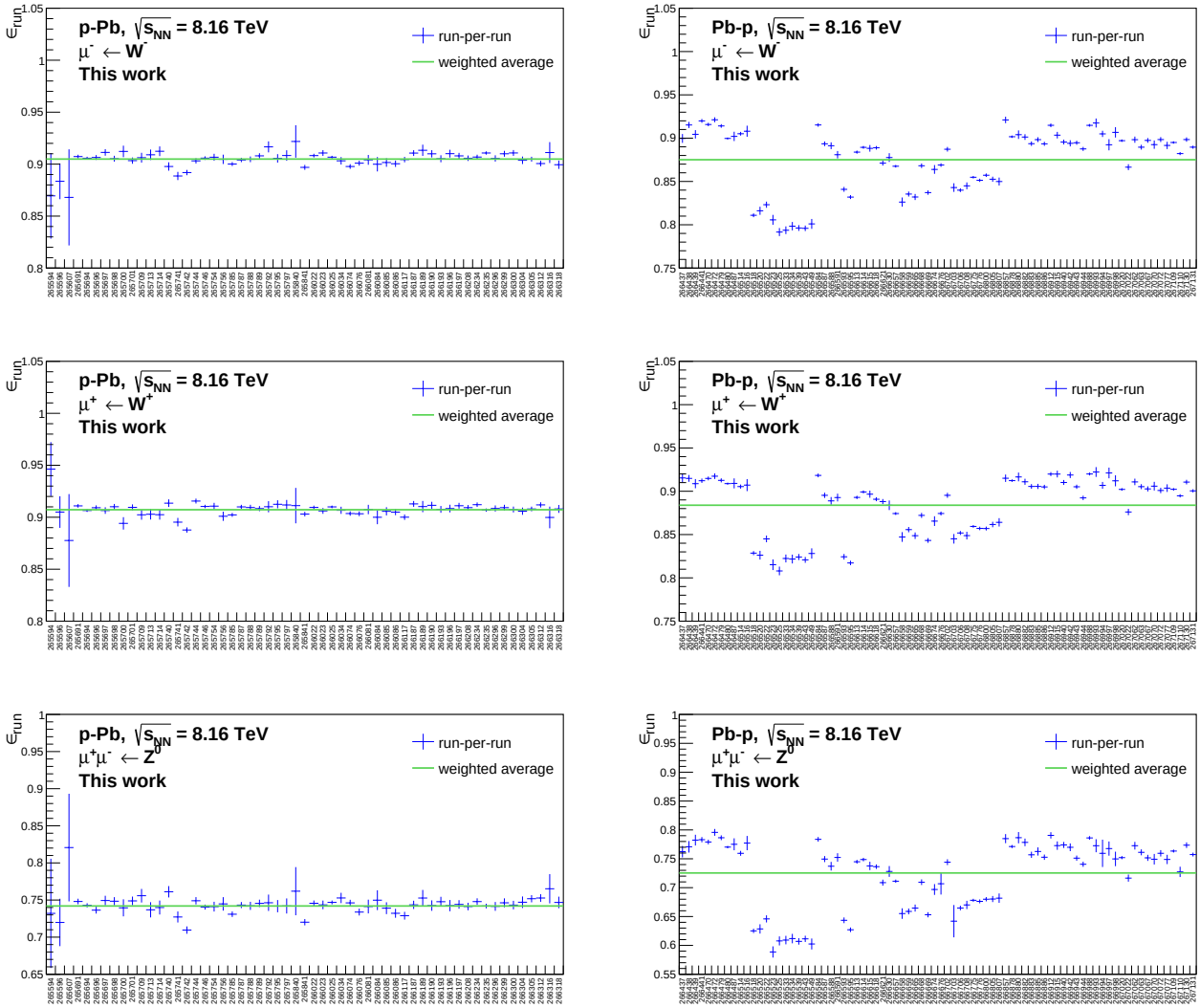


**Figure 8.16:** Run-by-run efficiencies in p–Pb (left) and Pb–p (right) collisions for single muons from $W^-$ (top) and $W^+$ (middle) decays, and dimuons from $Z^0$ decays (bottom). The horizontal lines correspond to the weighted averages of the whole periods.

frame:

$$\begin{cases} y_{\rm cms} \in [+2.03, +2.43]; [+2.43, +2.83]; [+2.83, +3.53] & \text{in p–Pb collisions,} \\ y_{\rm cms} \in [-4.46, -3.76]; [-3.76, -3.36]; [-3.36, -2.96] & \text{in Pb–p collisions.} \end{cases} \tag{8.30}$$

These bins were considered for all the observables measured for muons from $\mathrm{W}^{\pm}$ decays. Along with the rapidity-dependent measurements, an evaluation of the normalised yield as a function of the collision centrality was performed, considering four centrality intervals: 0–20%, 20–40%, 40–60% and 60–100%. The larger width of the largest rapidity and lowest centrality intervals were required as to have a sufficient amount of signal for the measurements. The available statistics being too low in the $\mathrm{Z}^0$ measurement, differential studies were not considered.

## 8.5 Summary of systematic uncertainties

The systematic uncertainties on the luminosity, signal extraction and efficiency are described in the corresponding sections of this chapter. Three supplementary sources were included. The uncertainty on the tracking efficiency is obtained by considering the difference between the efficiencies obtained from data and MC simulations, using the redundancy between the tracking chambers [185] as described in Section 5.3.3. The uncertainty on the muon trigger efficiency is determined by propagating the uncertainty on the intrinsic efficiency of the individual trigger chambers, which is evaluated in a similar manner as for the tracking system, with a data-driven method using the redundancy of the trigger chamber information. Finally, the muon identification introduces an additional uncertainty, which reflects the differences observed between data and simulations when applying different values of the $\chi^2$ selection on the matching between tracks reconstructed in the tracking system with track segments in the trigger chambers. It should be noted that these last sources were not evaluated for this work, but taken from the $\Upsilon$ analysis in p–Pb collisions at $\sqrt{s_{\rm NN}} = 8.16$ TeV [269]. The uncertainties on single muons are half that of dimuons. The sources of systematic uncertainties, and their values, are summarised in Table 8.11. The total systematic for an observable is obtained by summing in quadrature the relevant sources.

| *in %* | p–Pb collisions | | | Pb–p collisions | | |
|---|---|---|---|---|---|---|
| | $W^-$ | $W^+$ | $Z^0$ | $W^-$ | $W^+$ | $Z^0$ |
| Signal extraction | 8.8 | 5.9 | 1.0 | 3.8 | 7.3 | — |
| – vs rapidity | 4.4 – 14.3 | 3.9 – 10.7 | — | 2.5 – 9.5 | 3.9 – 21.6 | — |
| – vs centrality | 3.6 – 12.8 | 3.6 – 12.8 | — | 3.6 – 12.8 | 3.6 – 12.8 | — |
| Tracking efficiency | 0.5 | | 1.0 | 1.0 | | 2.0 |
| Trigger efficiency | 0.5 | | 1.0 | 0.5 | | 1.0 |
| Trigger-tracker matching | 0.5 | | 1.0 | 0.5 | | 1.0 |
| Cluster resolution and alignment | 0.7 | 0.6 | 7.7 | 0.7 | 0.3 | 5.7 |
| Normalisation factor | 1.4 | | 0.7 | 1.0 | | 0.2 |
| V0 cross section | 1.9 | | 1.9 | 2.0 | | 2.0 |
| $\langle N_{\rm coll}^{\rm mult} \rangle$ | 2.8 – 4.3 | | — | 2.8 – 4.3 | | — |

**Table 8.11:** Summary of the systematic uncertainties affecting the measurements of muons from $W^{\pm}$ and $Z^0$ decays in p–Pb and Pb–p collisions. Ranges are indicated for differential studies, corresponding to the extrememost values. A horizontal bar indicates that the source is not applicable, either because the analysis is not concerned by the source, or it was found to be negligible.

# Chapter 9

# Results and physics interpretation

This chapter presents the measurements of the $\mathrm{Z}^0$ and $\mathrm{W}^{\pm}$ productions studied via their muonic decays in p–Pb collisions at $\sqrt{s_{\mathrm{NN}}} = 8.16$ TeV. The productions are presented through the production cross section in Section 9.1, the lepton charge asymmetry in Section 9.2 and the nuclear modification factor in Section 9.3. Throughout the chapter, the results are given both in the full acceptance of the muon spectrometer and in several rapidity intervals. The measured productions are compared with the measurements performed by the ALICE Collaboration in p–Pb collisions at $\sqrt{s_{\mathrm{NN}}} = 5.02$ TeV [156] at large rapidity, and with measurements of the CMS Collaboration in p–Pb collisions at $\sqrt{s_{\mathrm{NN}}} = 8.16$ TeV at midrapidity [167]. They are also compared with theoretical calculations from various models, with and without nuclear modifications. The $y$-integrated cross sections of the $\mathrm{W}^{\pm}$ bosons, normalised to the average number of binary collisions, are presented in Section 9.4.

## 9.1 $\mathrm{Z}^0$ and $\mathrm{W}^{\pm}$ production cross sections in p–Pb collisions

### 9.1.1 Measured production

The production cross sections of electroweak bosons in their muonic decays are experimentally measured as:

$$\frac{\mathrm{d}\sigma_{\mu^+\mu^-\leftarrow\mathrm{Z}^0}}{\mathrm{d}y} = \frac{N_{\mu^+\mu^-\leftarrow\mathrm{Z}^0}}{\Delta y \times \mathcal{L}_{\mathrm{int}} \times \varepsilon}, \qquad \frac{\mathrm{d}\sigma_{\mu^\pm\leftarrow\mathrm{W}^\pm}}{\mathrm{d}y} = \frac{N_{\mu^\pm\leftarrow\mathrm{W}^\pm}}{\Delta y \times \mathcal{L}_{\mathrm{int}} \times \varepsilon}, \tag{9.1}$$

where $N_{\mu^+\mu^-\leftarrow\mathrm{Z}^0}$ and $N_{\mu^\pm\leftarrow\mathrm{W}^\pm}$ are the number of dimuons from $\mathrm{Z}^0$ decays and single muons from $\mathrm{W}^{\pm}$ decays extracted from the data, respectively, $\Delta y$ is the width of the rapidity interval, $\mathcal{L}_{\mathrm{int}}$ is the integrated luminosity and $\varepsilon$ is the detector efficiency. The cross sections are by convention uncorrected for the muonic decay branching fraction. They are measured in the fiducial regions defined by the track selections:

$$\mathrm{Z}^0: \quad \begin{cases} -4 < \eta_\mu < -2.5, \\ p_{\mathrm{T}}^\mu > 20 \text{ GeV}/c, \\ 60 < m_{\mu^+\mu^-} < 120 \text{ GeV}/c^2, \end{cases} \qquad \mathrm{W}^{\pm}: \quad \begin{cases} -4 < \eta_\mu < -2.5, \\ p_{\mathrm{T}}^\mu > 10 \text{ GeV}/c. \end{cases}$$

The production cross sections measured in the full acceptance of the spectrometer are shown in the top panels of Figure 9.1, and the values are summarised in Table 9.1.

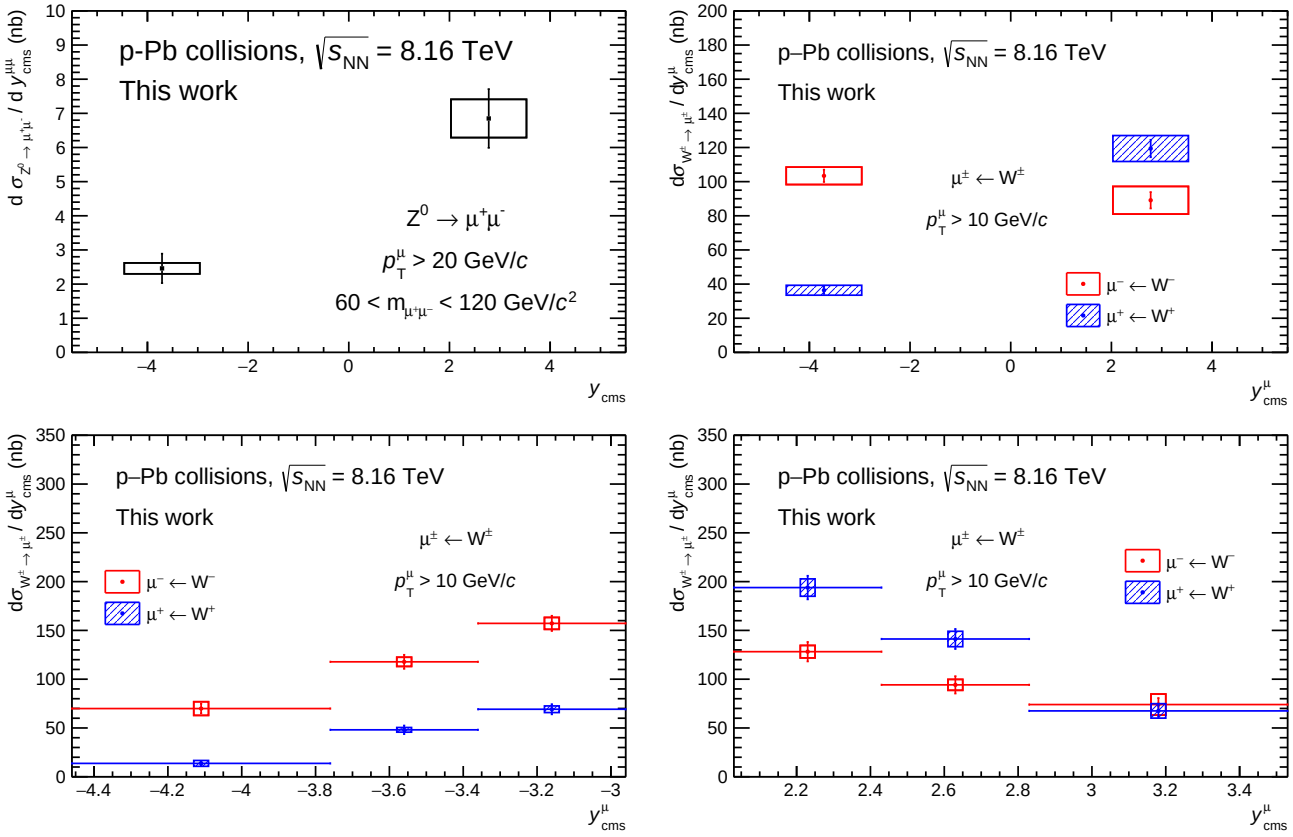


**Figure 9.1:** Production cross sections of the muonic decays of $Z^0$ and $W^\pm$ bosons measured in p–Pb collisions at $\sqrt{s_{NN}} = 8.16$ TeV. The top panels show the cross sections integrated in the full acceptance of the muon spectrometer, while the bottom panels display the cross sections of the $\mu^\pm \leftarrow W^\pm$ processes in several rapidity bins. The data points are at the centre of the intervals, their horizontal extension corresponds to the width of the rapidity ranges. The vertical bars and boxes indicate the statistical and systematic uncertainties, respectively.

The top left panel shows the cross section of the $Z^0 \rightarrow \mu^+\mu^-$ process. The large difference seen between backward and forward rapidities comes from the rapidity shift, which pushes the forward region towards higher production while moving the backward region to the tail of the bell-shaped cross section distribution. One can notice that, due to the rather low amount of signal, the measurements are dominated by the statistical uncertainties, which amount to 13% (17%) in p–Pb (Pb–p) collisions while the systematics is 8% (7%). The top right panel of Figure 9.1 shows the same observable for the $\mu^- \leftarrow W^-$ and $\mu^+ \leftarrow W^+$ processes. Several effects act differently for the four combinations of rapidities and charge. The rapidity shift has the same consequence of increasing the production at forward rapidities and decreasing it at backward. The isospin effect significantly impacts the productions of $W^-$ and $W^+$, it favours the former and suppresses the latter. Finally, the considerations on helicities developed in Section 3.2.3 and their consequences

| | Pb–p, $-4.46 < y_{\rm cms} < -2.96$ | p–Pb, $2.03 < y_{\rm cms} < 3.53$ |
|---|---|---|
| $\mathrm{d}\sigma_{\mu^+\mu^-\leftarrow \mathrm{Z}^0}/\mathrm{d}y$ | $2.46 \pm 0.43 \pm 0.16$ nb | $6.85 \pm 0.86 \pm 0.56$ nb |
| $\mathrm{d}\sigma_{\mu^-\leftarrow \mathrm{W}^-}/\mathrm{d}y$ | $105.4 \pm 3.7 \pm 5.2$ nb | $90.2 \pm 4.8 \pm 8.2$ nb |
| $\mathrm{d}\sigma_{\mu^+\leftarrow \mathrm{W}^+}/\mathrm{d}y$ | $37.1 \pm 2.1 \pm 2.9$ nb | $120.8 \pm 5.2 \pm 7.7$ nb |

**Table 9.1:** Production cross sections of the $\mathrm{Z}^0$ and $\mathrm{W}^{\pm}$ bosons in their muonic decays in p–Pb collisions at $\sqrt{s_{\rm NN}} = 8.16$ TeV. The quoted errors correspond to the statistical and systematic uncertainties, respectively.

on the kinematics of the process yield a sizeable modification of the production, especially visible for the $\mu^+ \leftarrow \mathrm{W}^+$ process at negative rapidities, which is significantly suppressed.

The amount of muons from $\mathrm{W}^{\pm}$ decays extracted from the data enabled the possibility of differential measurements, splitting the rapidity acceptance of the spectrometer into three bins. The production cross sections measured in this configuration are displayed in the bottom panels of Figure 9.1. The choice of a three-bin division was driven by the requirement to have a statistical uncertainty of the order of the systematic one. The width of the bins were taken as to roughly divide the raw yield into three equivalent samples. This allows for the measurement of the evolution of the cross section as a function of rapidity in a statistically significant manner, providing an accurate description of the behaviour of the production at large rapidities. One can especially notice the more drastic decrease of the $\mathrm{W}^+$ production at positive rapidities compared to that of $\mathrm{W}^-$. The measured values in all rapidity bins are given in Table 9.2.

| | | $-4 < y_{\rm lab} < -3.3$ | $-3.3 < y_{\rm lab} < -2.9$ | $-2.9 < y_{\rm lab} < -2.5$ |
|---|---|---|---|---|
| Pb–p | $\mathrm{d}\sigma_{\mu^-\leftarrow \mathrm{W}^-}/\mathrm{d}y$ | $71.3 \pm 4.9 \pm 7.1$ nb | $120.1 \pm 7.3 \pm 4.6$ nb | $160.4 \pm 8.0 \pm 5.8$ nb |
| | $\mathrm{d}\sigma_{\mu^+\leftarrow \mathrm{W}^+}/\mathrm{d}y$ | $13.9 \pm 2.4 \pm 3.0$ nb | $49.1 \pm 4.5 \pm 2.4$ nb | $70.5 \pm 5.3 \pm 3.3$ nb |
| p–Pb | $\mathrm{d}\sigma_{\mu^-\leftarrow \mathrm{W}^-}/\mathrm{d}y$ | $74.8 \pm 6.8 \pm 10.9$ nb | $95.4 \pm 9.0 \pm 5.7$ nb | $129.7 \pm 10.2 \pm 6.6$ nb |
| | $\mathrm{d}\sigma_{\mu^+\leftarrow \mathrm{W}^+}/\mathrm{d}y$ | $68.3 \pm 6.0 \pm 7.6$ nb | $142.9 \pm 10.4 \pm 8.1$ nb | $195.6 \pm 12.2 \pm 9.0$ nb |

**Table 9.2:** Production cross sections of the $\mu^- \leftarrow \mathrm{W}^-$ and $\mu^+ \leftarrow \mathrm{W}^+$ processes in p–Pb collisions at $\sqrt{s_{\rm NN}} = 8.16$ TeV for various centrality intervals. The quoted errors correspond to the statistical and systematic uncertainties, respectively.

### 9.1.2 Comparison with measurements at $\sqrt{s_{\rm NN}} = 5.02$ TeV

These measurements extend at higher energies the study of the $\mathrm{Z}^0$- and $\mathrm{W}^{\pm}$-boson production at $\sqrt{s_{\rm NN}} = 5.02$ TeV previously published by the ALICE Collaboration [156] from a lower integrated luminosity of $5.81 \pm 0.20$ nb$^{-1}$ for Pb–p collisions and $5.03 \pm 0.18$ nb$^{-1}$ for p–Pb collisions. The production cross sections at both energies are compared in Figure 9.2. The comparison of the two measurements shows the expected increase of the production as a function of the collision energy. Apart from this, the cross sections at both energies show the same trends. The increase in statistics allow for a much more precise measurement at 8.16 TeV, especially for the $\mathrm{Z}^0$, as the statistical

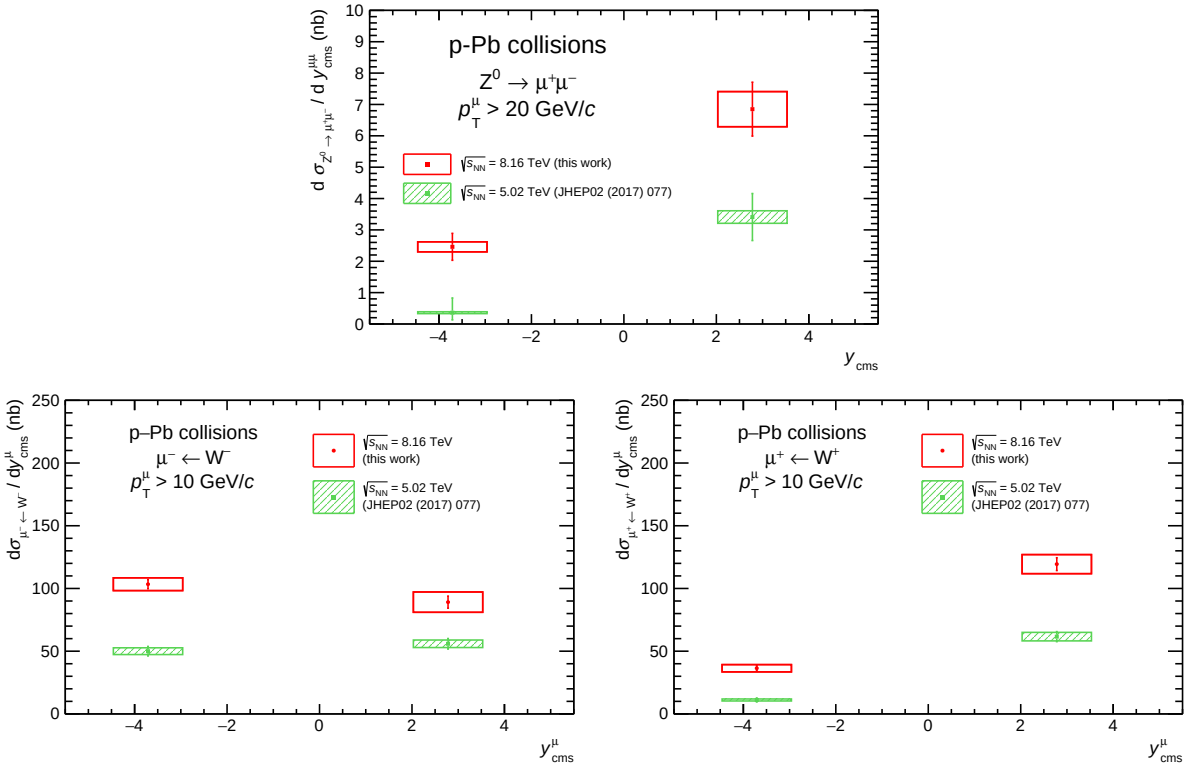


**Figure 9.2:** Production cross sections of the muonic decays of $Z^0$ (top), $W^-$ (bottom left) and $W^+$ (bottom right) bosons measured in p–Pb collisions at $\sqrt{s_{NN}} = 8.16$ TeV (this work) and $\sqrt{s_{NN}} = 5.02$ TeV from Ref. [156]. The bars and boxes indicate the statistical and systematic uncertainties, respectively.

uncertainty at 5.02 TeV amounts to 20% in p–Pb collisions and more than 100% in Pb–p, as the cross section was estimated from two $Z^0$ candidates. With the forthcoming increase of luminosity at the LHC, one can expect the measurements of weak bosons in heavy-ion collisions to attain a very high precision, providing strong constraints on nPDF models.

### 9.1.3 Comparison with theoretical calculations

The measurements of the $Z^0$-boson production are compared to theoretical calculations in Figure 9.3. The calculations were obtained at NLO from the EPPS16 [54] and nCTEQ15 [55] nuclear models, using CT14 [63] as baseline PDF in the former case, and for the modelisation of the proton beam. Calculations were also obtained from standalone CT14, including the isospin effect but no nuclear modification of the PDF. The comparison of the nuclear- and free-PDF predictions allows one to evaluate the effect of the nuclear modifications themselves. One can see that at backward rapidity, as the Bjorken-$x$ region overlaps the EMC and anti-shadowing regions, the net effect is small and predictions with and without nuclear modifications are indistinguishable. At forward rapidity, where the Bjorken-$x$ region is fully immersed in the suppressing shadowing region,

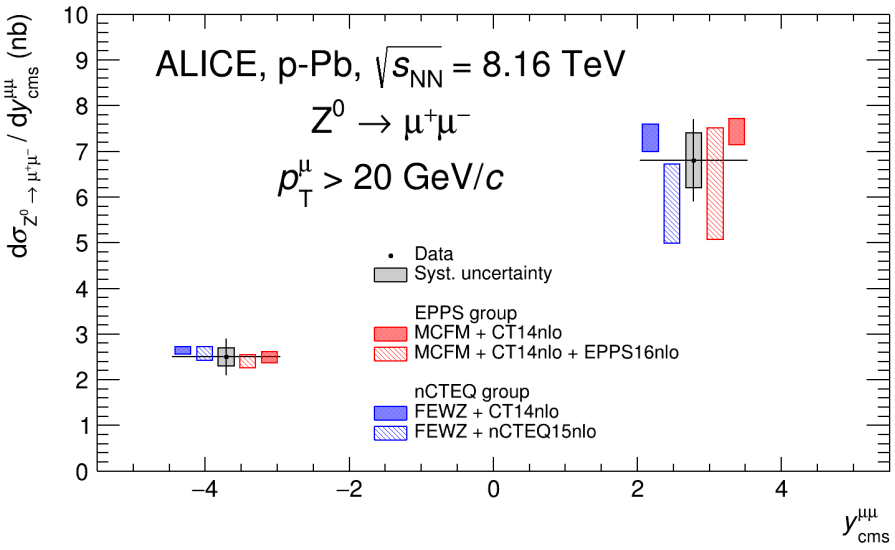


**Figure 9.3:** Production cross section of the $Z^0 \rightarrow \mu^+\mu^-$ process in p–Pb collisions at $\sqrt{s_{NN}} = 8.16$ TeV, compared with theoretical predictions with the EPPS16 [54] and nCTEQ15 [55] nPDF sets, as well as the free-nucleon CT14 PDF [63], accounting for the isospin effect but without nuclear modification of the PDF. The bars and boxes around the data points correspond to the statistical and systematic uncertainties. The theory points are horizontally shifted for better readability.

the nuclear effects are more sizeable. The nCTEQ15 calculations foresee a significant deviation from the free-PDF predictions while, due to larger uncertainties, the EPPS16 prediction partly encompasses the CT14 calculation. A small difference is seen between the free-nucleon calculations provided by the two groups, although they are consistent with one another. This discrepancy is explained by the different approaches followed by the two groups. They used different generators for the computation, with the EPPS16 predictions being performed with MCFM [270] while the nCTEQ15 calculations were done with FEWZ [271], although this is not expected to have a large effect. The second source of difference comes from the factorisation and renormalisation scales. In the nCTEQ15 calculation, they were fixed at the $Z^0$ mass taken from the PDG review [6], for all events. In the EPPS16 calculations, they were set event-by-event, at the dilepton invariant mass, which is on average significantly lower than the $Z^0$ mass due to the $\gamma^*$ interference. This explains the difference between the free-nucleon calculations from the two groups, despite the usage of the same PDF set.

Comparing the measurements with the predictions, one sees that the data are well reproduced by the theory. The uncertainty on the measurement prevents to derive any further conclusion on the nuclear modifications, as they are in agreement with both nuclear and free-nucleon calculations. Yet, one can note that the uncertainty of the measurement at forward rapidity is smaller than that of the EPPS16 calculation. With the higher statistics provided by the high-luminosity LHC, this measurement will become a valuable addition to the data pool used for nPDF determination.

The $W^{\pm}$ cross sections were also compared with model calculations. By the time the analysis was completed, two new nPDF sets became available: the nCTEQ15 model was extended by the inclusion of $Z^0$ and $W^{\pm}$ data from the LHC, leading to the nCTEQ15WZ [272] determination. The nNNPDF2.0 [56] model includes flavour decomposition, which enables the evaluation of electroweak boson production. The comparison of the differential cross sections with various theoretical models is shown in Figure 9.4. In the theory points, the same pattern is seen as for the prediction on the $Z^0$ production, with small to no nuclear effects predicted at backward rapidities and significant suppression due to nuclear modifications at forward. Comparing the nCTEQ15 and nCTEQ15WZ models, one sees the benefits of including $Z^0$ and $W^{\pm}$ data at the LHC, as the latter model features largely reduced uncertainties compared to the pristine version. While the EPPS16, nCTEQ15 and nCTEQ15WZ models tend to agree with each other, within uncertainties, the nNNPDF2.0 model shows large discrepancies in the predicted production and evolution as a function of rapidity, especially for $W^-$. Here one especially notices the predictions at positive rapidities, which follow a flat behaviour. It should be stressed that the nNNPDF model is still under development, and is yet to include part of the available data which can have a significant impact on the calculation of the $W^{\pm}$ production. The methodology of the nNNPDF collaboration, relying on neural networks for the determination of the interpolants, leads this model to have much smaller uncertainties.

The evolution of the measured production as a function of rapidity deviates from what is predicted by the models in the $W^-$ analysis, especially for the most central bins where the data are higher than the models, regardless of whether they include the nuclear modifications or not. At larger rapidities an agreement is found with the EPPS16, nCTEQ15 and nCTEQ15WZ models, while the peculiar behaviour predicted by nNNPDF2.0 does not catch the measurement. In the $W^+$ case, the general agreement with nuclear models is better. The measured cross section in the most central positive rapidity bin seems to favour the free-nucleon PDF, although still being in agreement with several nuclear models within uncertainties. In the five other rapidity bins, the measurements favour the inclusion of nuclear modifications in the calculations. This observation is particularly valid for the $2.83 < y_{\mathrm{cms}} < 3.53$ bin, where the data is in agreement with nPDF calculations while showing a 3.5 $\sigma$ deviation from the CT14-only prediction. It is worth recalling that this bin covers the lowest Bjorken-$x$ region, around $10^{-4}$, where it is especially useful to provide constraints to the model. Interestingly enough, one can notice that the nNNPDF2.0 model provides the best reproduction of the measurement in this region. Finally, the measurements at positive rapidities, for both $W^-$ and $W^+$, have much lower uncertainties than that of most of the calculations, following from the lack of constraints in the corresponding Bjorken-$x$ interval. These measurements can therefore be particularly useful for the determination of nPDF, in helping reducing the model uncertainties at low-$x$.

### 9.1.4 Comparison with CMS measurement at midrapidity

The CMS Collaboration has measured the production of $W^{\pm}$ boson in the muonic decay channel at midrapidity, in between the forward and backward rapidity intervals accessible from the ALICE muon spectrometer. The measurements in p–Pb collisions at $\sqrt{s_{\mathrm{NN}}} = 8.16$ TeV are published in Ref. [167]. The data sample has a corresponding luminosity of $173.4 \pm 6.1$ nb$^{-1}$, and the

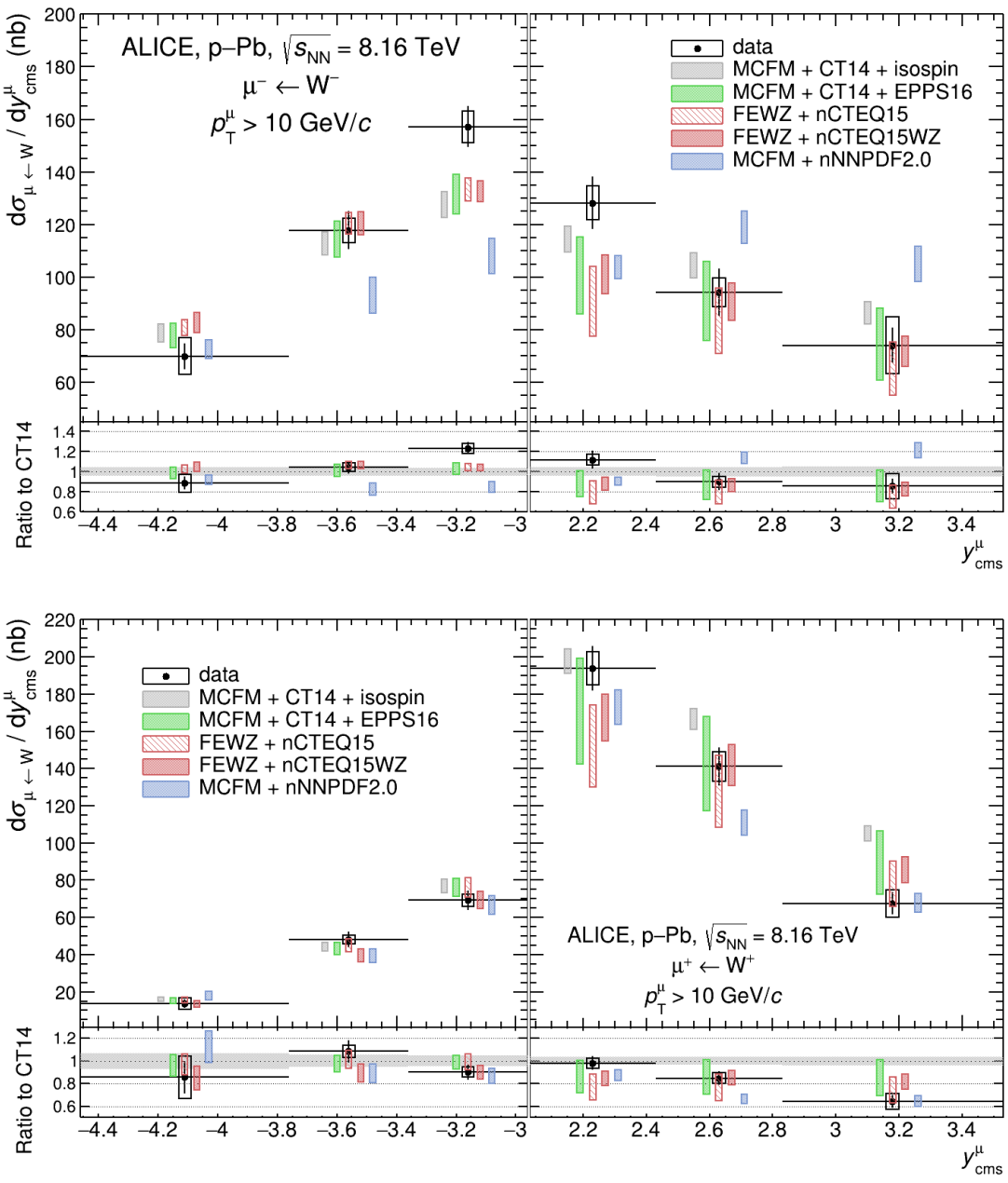


**Figure 9.4:** Production cross section of the $W^\pm \to \mu^\pm \nu_\mu$ process for $W^-$ (top) and $W^+$ (bottom) as a function of rapidity for muons with $p_T > 10$ GeV/$c$ in p–Pb collisions at $\sqrt{s_{NN}} = 8.16$ TeV. The measurements are compared with predictions from several nPDF sets, as well as with calculations based on the CT14 PDF [63], accounting for the isospin effect but without nuclear modifications of the PDF. The bottom panels show the ratio to the CT14 calculations. The horizontal bars correspond to the width of the rapidity intervals. The vertical bars and boxes indicate the statistical and systematic uncertainties, respectively, and the grey band in the bottom panels represent the uncertainty of the CT14 predictions. The data points are centered in the rapidity intervals, while the theory predictions are horizontally shifted for better readability.

measurement is performed in the fiducial region:

$$\begin{cases} |\eta^{\mu}_{\rm lab}| < 2.4, \\ p^{\mu}_{\rm T} > 25 \text{ GeV}/c. \end{cases}$$

Apart from a gap of 0.1 units of rapidity, the combination of the CMS and ALICE acceptances are fully complementary, which leads to cover the pseudorapidity range $|\eta^{\mu}_{\rm lab}| < 4$, providing a exhaustive measurement of the nuclear effects over four orders of magnitude of Bjorken-$x$. Since the $p_{\rm T}$ selection is different in the two analyses, a direct comparison can not be drawn. The contribution of the two measurements can efficiently be compared by looking at the ratio of data to theory, and taking the free-nucleon calculation as a reference allows one to highlight the nuclear modifications. In Figure 9.5 is shown the ratio of the ALICE and CMS measurements to CT14 [63] calculations accounting for the isospin effect but without implementation of the nuclear modifications. For comparison purposes, the ratio of EPPS16 [54] to CT14 is also shown.

The ALICE measurements extend the trend seen at the edges of the CMS acceptance, with a ratio close to or even at unity at negative rapidities while rather significant suppressing nuclear effects are seen at positive rapidities. The EPPS16 model seems to well reproduce the evolution of the measurements from both collaborations. A striking feature of the ALICE measurements at large rapidities are the size of the uncertainties compared to that of the EPPS16 calculations, pointing once more the ability of these measurement to provide further constraining inputs for the nPDF determination.

## 9.2 Lepton charge asymmetry

The lepton charge asymmetry $A_{\rm ch}$ is measured as:

$$A_{\rm ch} = \frac{N^{\rm corr}_{\mu^+\leftarrow {\rm W}^+} - N^{\rm corr}_{\mu^-\leftarrow {\rm W}^-}}{N^{\rm corr}_{\mu^+\leftarrow {\rm W}^+} + N^{\rm corr}_{\mu^-\leftarrow {\rm W}^-}}, \tag{9.2}$$

where $N^{\rm corr}_{\mu^+\leftarrow {\rm W}^+}$ and $N^{\rm corr}_{\mu^-\leftarrow {\rm W}^-}$ are respectively the number of muons from $\rm W^+$ and $\rm W^-$ decays extracted from the data and corrected for the efficiency of the detector. This ratio is an interesting observable for its sensitivity to the down-to-up quark ratio in the nucleus. It also allows for the reduction of the uncertainties, as some sources such as the trigger and tracking efficiencies cancel in the calculation. The theoretical calculations have reduced uncertainties as well, due to the cancellation of sources such as the choice of the factorisation and renormalisation scales. In this work, the lepton charge asymmetry was measured in the full acceptance of the spectrometer, as well as in the same rapidity bins as those considered for the evaluation of the differential cross section. In the full acceptance, the measured $A_{\rm ch}$ amounts to:

$$A^{\rm Pb-p}_{\rm ch} = -0.479 \pm 0.046 \pm 0.056, \qquad A^{\rm p-Pb}_{\rm ch} = 0.145 \pm 0.014 \pm 0.021, \tag{9.3}$$

where the quoted uncertainties are statistical and systematic, respectively. The measured values in the rapidity bins are given in Table 9.3.

The measured $A_{\rm ch}$ are shown in Figure 9.6. In the top panel, the measurement performed in

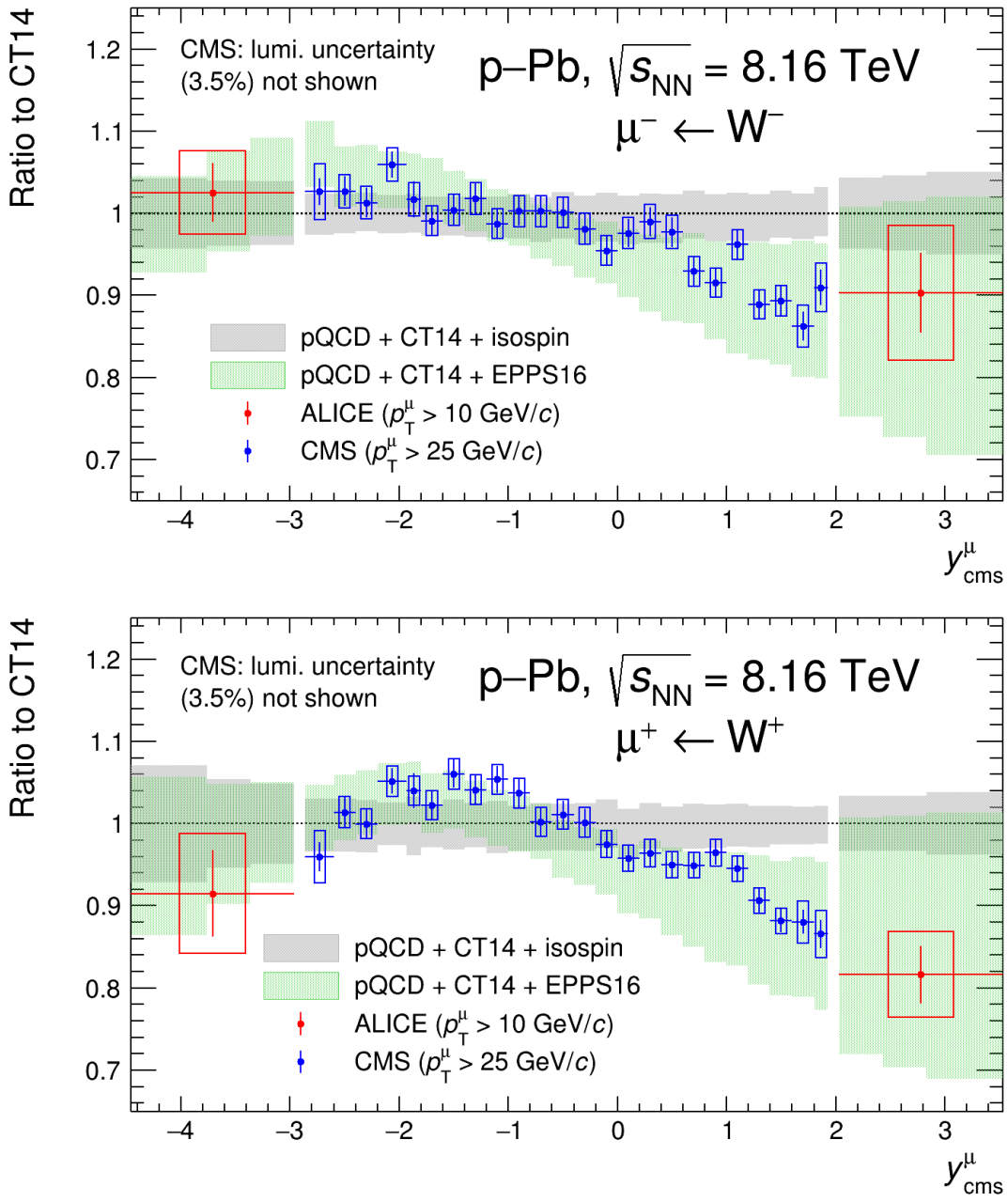


**Figure 9.5:** Ratio to CT14 [63] predictions of the production cross section of muons from $W^-$ (top) and $W^+$ (bottom) decays measured by the ALICE (this work) and CMS [167] Collaborations in p–Pb collisions at $\sqrt{s_{NN}}$ = 8.16 TeV. The measured ratio is compared to the one obtained from pQCD calculations with CT14 + EPPS16 [54]. All calculations include the isospin effect. The grey band around the line at unity corresponds to the uncertainty on the free-PDF prediction, the bars and boxes around the data points indicate the statistical and systematic uncertainties, respectively.

| | $-4 < y_{\rm lab} < -3.3$ | $-3.3 < y_{\rm lab} < -2.9$ | $-2.9 < y_{\rm lab} < -2.5$ |
|---|---|---|---|
| $A_{\rm ch}^{\rm Pb-p}$ | $-0.647 \pm 0.175 \pm 0.229$ | $-0.420 \pm 0.066 \pm 0.029$ | $-0.389 \pm 0.049 \pm 0.025$ |
| $A_{\rm ch}^{\rm p-Pb}$ | $-0.047 \pm 0.006 \pm 0.012$ | $0.200 \pm 0.034 \pm 0.019$ | $0.203 \pm 0.029 \pm 0.017$ |

**Table 9.3:** Lepton charge asymmetry of muons from $\rm W^{\pm}$ decays, measured in p–Pb collisions at $\sqrt{s_{\rm NN}} = 8.16$ TeV. The quoted errors are the statistical and systematic uncertainties, respectively.

the full acceptance of the spectrometer is compared with the ALICE measurement made in p–Pb collisions at $\sqrt{s_{\rm NN}} = 5.02$ TeV [156]. From the comparison, one can derive the same conclusions as for the cross sections. The increase of statistics yields a more precise result, which is not dominated by the statistical uncertainty anymore. The measured asymmetry increases as a function of the collision energy. At forward rapidity, the measurement at $\sqrt{s_{\rm NN}} = 8.16$ TeV is not consistent with zero as it was the case for the measurement at 5.02 TeV, highlighting the different evolution of the

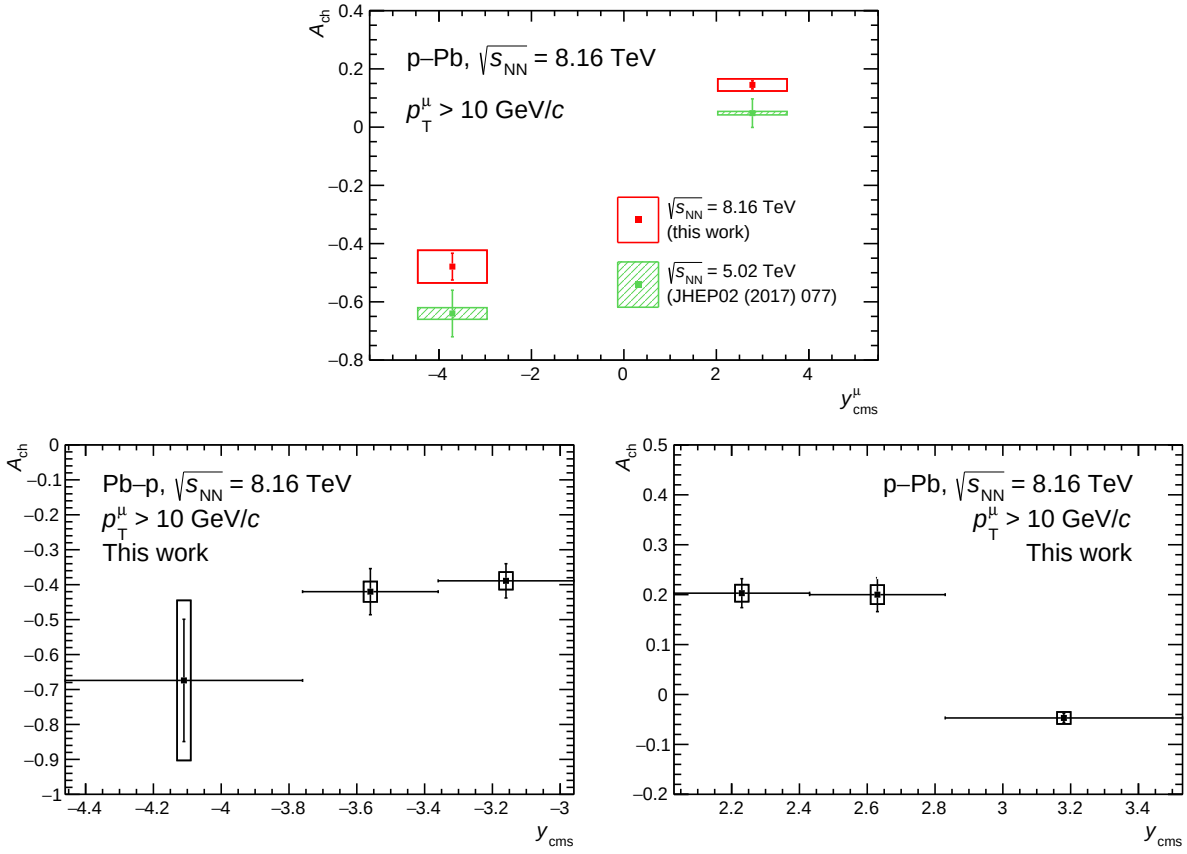


**Figure 9.6:** Lepton charge asymmetry of muons from $\rm W^{\pm}$ decays in p–Pb collisions at $\sqrt{s_{\rm NN}} = 8.16$ TeV. The top panel shows the measurement in the full acceptance of the spectrometer, along with the measurement in p–Pb collisions at $\sqrt{s_{\rm NN}} = 5.02$ TeV from Ref. [156]. The bottom panel shows the differential measurement performed in p–Pb collisions at $\sqrt{s_{\rm NN}} = 8.16$ TeV. The bars and boxes indicate the statistical and systematic uncertainties, respectively.

$u$- and $d$-quark PDFs as the energy increases. The differential evaluation, shown in the bottom panels of Figure 9.6, predicts a sharp drop of the asymmetry at large rapidities, with a sign reversal at forward. At backward, the small amount of positive muons from $W^+$ decays leads to a large uncertainty in the bin at the largest rapidity, preventing to firmly conclude on the decrease.

Figure 9.7 shows the comparison of the $A_{ch}$ with various theoretical calculations. The predictions were obtained with the EPPS16 [54] and nNNPDF2.0 [56] nuclear models, as well as free-PDF predictions relying on CT14 [63] for reference. It is interesting to note that at both negative and positive rapidities, the EPPS16 model does not predict any deviation of the $A_{ch}$ from free-PDF calculations, such that the observable would be more sensitive to the proton PDF than to the nuclear modifications. On the contrary, the nNNPDF2.0 model shows a very large deviation at positive rapidity. Interestingly enough, the measurement lies between the two models, by showing a decrease of the ratio towards higher rapidities, although not as large as what is predicted by nNNPDF2.0.

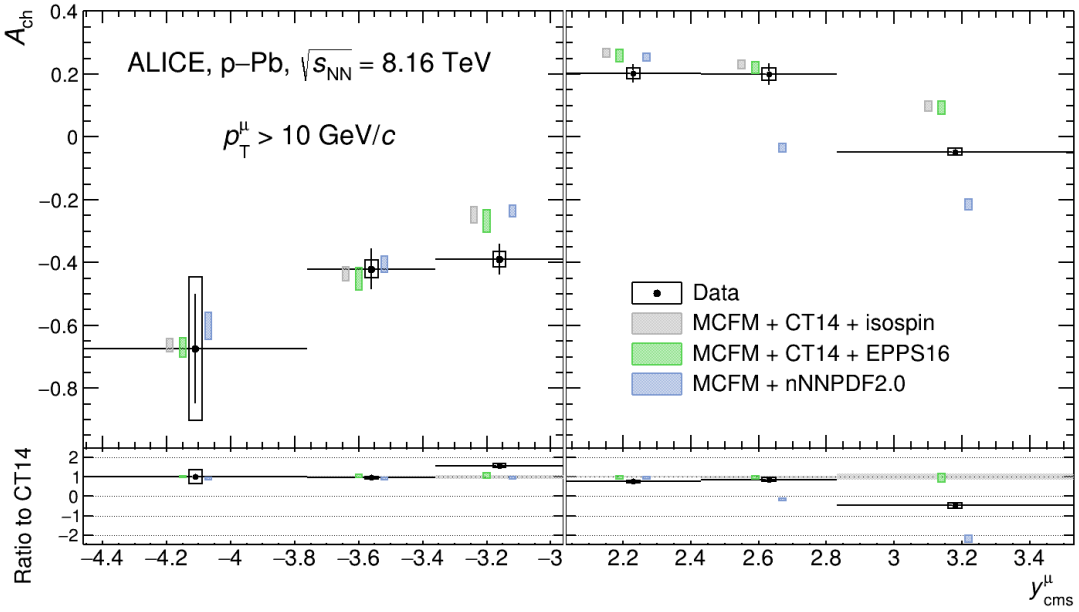


**Figure 9.7:** Lepton charge asymmetry $A_{ch}$ as a function of rapidity of muons from $W^\pm$ decays in p–Pb collisions at $\sqrt{s_{NN}}$ = 8.16 TeV. The measurements are compared with predictions from the EPPS16 [54] and nNNPDF2.0 [56] nPDF sets, as well as CT14-only [63] predictions including the isospin effect but without nuclear modifications. The bottom panels show the ratio to the CT14 calculations.The bars and boxes indicate the statistical and systematic uncertainties, respectively. The theory points are horizontally shifted for better readability.

## 9.3 Nuclear modification factor

The nuclear modification factor $R_{\rm pPb}$ is calculated as:

$$R_{\rm pPb} = \frac{1}{208}\frac{\sigma^{\rm p\text{–}Pb}_{\mu^{\pm}\leftarrow {\rm W}^{\pm}}}{\sigma^{\rm pp}_{\mu^{\pm}\leftarrow {\rm W}^{\pm}}}. \tag{9.4}$$

$\sigma^{\rm p\text{–}Pb}_{\mu^{\pm}\leftarrow {\rm W}^{\pm}}$ corresponds to the production cross sections measured in p–Pb collisions and presented in Section 9.1. $\sigma^{\rm pp}_{\mu^{\pm}\leftarrow {\rm W}^{\pm}}$ is the reference cross section in pp collisions at the same energy. Since such a measurement has not been made, due to the lack of pp collisions at $\sqrt{s} = 8.16$ TeV, the reference cross section must either be extrapolated from a similar measurement, or be estimated via theoretical calculations. The LHCb Collaboration has measured the production of $\rm W^{\pm}$ boson in pp collisions at $\sqrt{s} = 8$ TeV [273]. The lower energy of the collision, the difference in acceptance, and a $p_{\rm T}$ selection set at 20 GeV/$c$ in the LHCb study, would necessitate to perform simulations in order to correct the measurements before using them for the evaluation of the $R_{\rm pPb}$. It was therefore decided to adopt the second option, and obtain the reference cross section fully from simulations. The calculations were performed with the same simulation environment as the one used for the signal extraction, using POWHEG [267] as hard event generator, paired with PYTHIA6 [264] for parton shower, and CT10 [176] as proton PDF. The LHCb study has shown that CT10 is able to well reproduce the measurement of $\rm W^{\pm}$ bosons over the acceptance of the ALICE muon spectrometer and at similar collision energy. Two sources of uncertainties were considered:

- the uncertainty from the knowledge on the PDF was evaluated by replacing CT10 with CTEQ6.6 [154], taking as uncertainty half the difference between the cross sections computed with the two models,
- the uncertainty from the knowledge of $\alpha_s$, which was varied between its boundaries at 0.112 and 0.127, taking the difference between the cross sections computed with these values with the one computed with the central value $\alpha_s = 0.118$, providing the lower and upper limit of the uncertainty interval.

The two sources are eventually combined quadratically to determine the full uncertainty on the calculation.

The measured $R_{\rm pPb}$ are shown in Figure 9.8. The values of the $R_{\rm pPb}$ measured in the full acceptance of the muon spectrometer are indicated in Table 9.4. The nuclear modification factor of weak bosons assesses the combination of the nuclear modifications and isospin effect. The net effect is rather small at positive rapidities, where the $R_{\rm pPb}$ are close to one for both $\rm W^{-}$ and $\rm W^{+}$. On the contrary, the effect is important at backward rapidities, where the $R_{\rm pPb}$ deviates significantly from unity. The measured values for various rapidity bins are given in Table 9.5. When going towards large rapidities, the $R_{\rm pPb}$ follow a decreasing trend, indicating that the production cross section is wider in pp collisions and decreases less rapidly than the production in p–Pb collisions. The exception to this trend is the $R_{\rm pPb}$ for $\rm W^{+}$ at negative rapidities, where fluctuations in the measurement seem to suggest a flat behaviour.

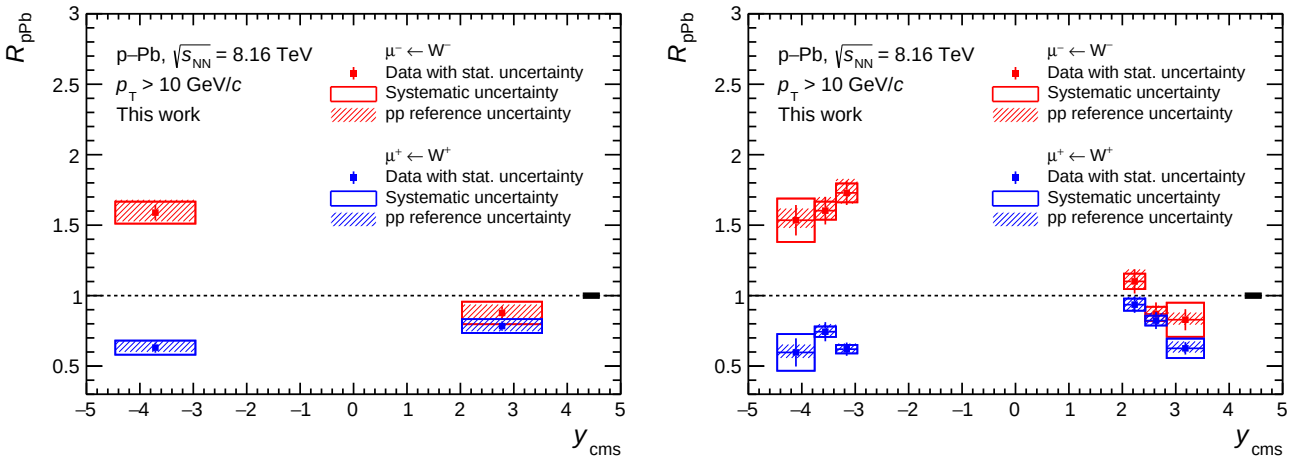


**Figure 9.8:** Nuclear modification factor $R_{\mathrm{pPb}}$ of muons from $\mathrm{W}^{\pm}$ decays measured in p–Pb collisions at $\sqrt{s_{\mathrm{NN}}} = 8.16$ TeV, in the full acceptance of the muon spectrometer (left) and in various rapidity bins (right). The reference pp cross section is taken from calculations with the CT10 [176] proton PDF. The bars and open boxes indicate the statistical and systematic uncertainties on the cross section in p–Pb, respectively. The hashed boxes represent the uncertainty on the reference cross section. The systematic uncertainty on the luminosity is shown as a black box around the line $R_{\mathrm{pPb}} = 1$.

| | Pb–p, $-4.46 < y_{\mathrm{cms}} < -2.96$ | p–Pb, $2.03 < y_{\mathrm{cms}} < 3.53$ |
|---|---|---|
| $R_{\mathrm{pPb}}^{\mu^- \leftarrow \mathrm{W}^-}$ | $1.620 \pm 0.057 \pm 0.079^{+0.092}_{-0.062}$ | $0.888 \pm 0.047 \pm 0.080^{+0.060}_{-0.039}$ |
| $R_{\mathrm{pPb}}^{\mu^+ \leftarrow \mathrm{W}^+}$ | $0.643 \pm 0.036 \pm 0.051^{+0.046}_{-0.031}$ | $0.793 \pm 0.034 \pm 0.051^{+0.048}_{-0.037}$ |

**Table 9.4:** Nuclear modification factor of muons from $\mathrm{W}^{\pm}$ decays in p–Pb collisions at $\sqrt{s_{\mathrm{NN}}} = 8.16$ TeV in the full acceptance of the muon spectrometer. The quoted errors correspond to the statistical and systematic uncertainties from the p–Pb cross section, and the upper and lower bound of the systematic uncertainty from the pp cross section, respectively.

The measured $R_{\mathrm{pPb}}$ are compared with theoretical calculations in Figure 9.9 obtained with the EPPS16 [54] and nNNPDF2.0 [56] models. The calculations show interesting behaviours as a function of rapidity. The $R_{\mathrm{pPb}}$ of muons from $\mathrm{W}^-$ decays is predicted by both models to increase as a function of rapidity, while the opposite trend is seen in the measurement. In the three other configurations, the EPPS16 model predicts very small to no evolution of the nuclear modification factor, which is consistent with the measurement of $\mathrm{W}^+$ at negative rapidities but contradicts what is experimentally observed at positive rapidities. Discrepancies are also seen when comparing the measurements with nNNPDF2.0 calculations. The behaviour of the $\mathrm{W}^-$ nuclear modification factor follows opposite trends than that of the measurements, increasing towards large rapidities while the measured $R_{\mathrm{pPb}}$ decreases. The agreement seems better for the $\mathrm{W}^+$ boson. At negative rapidities, the nNNPDF2.0 is in agreement with the measurement within uncertainties, although it predicts a slight increase at very large rapidity while the data seems to favour the opposite.

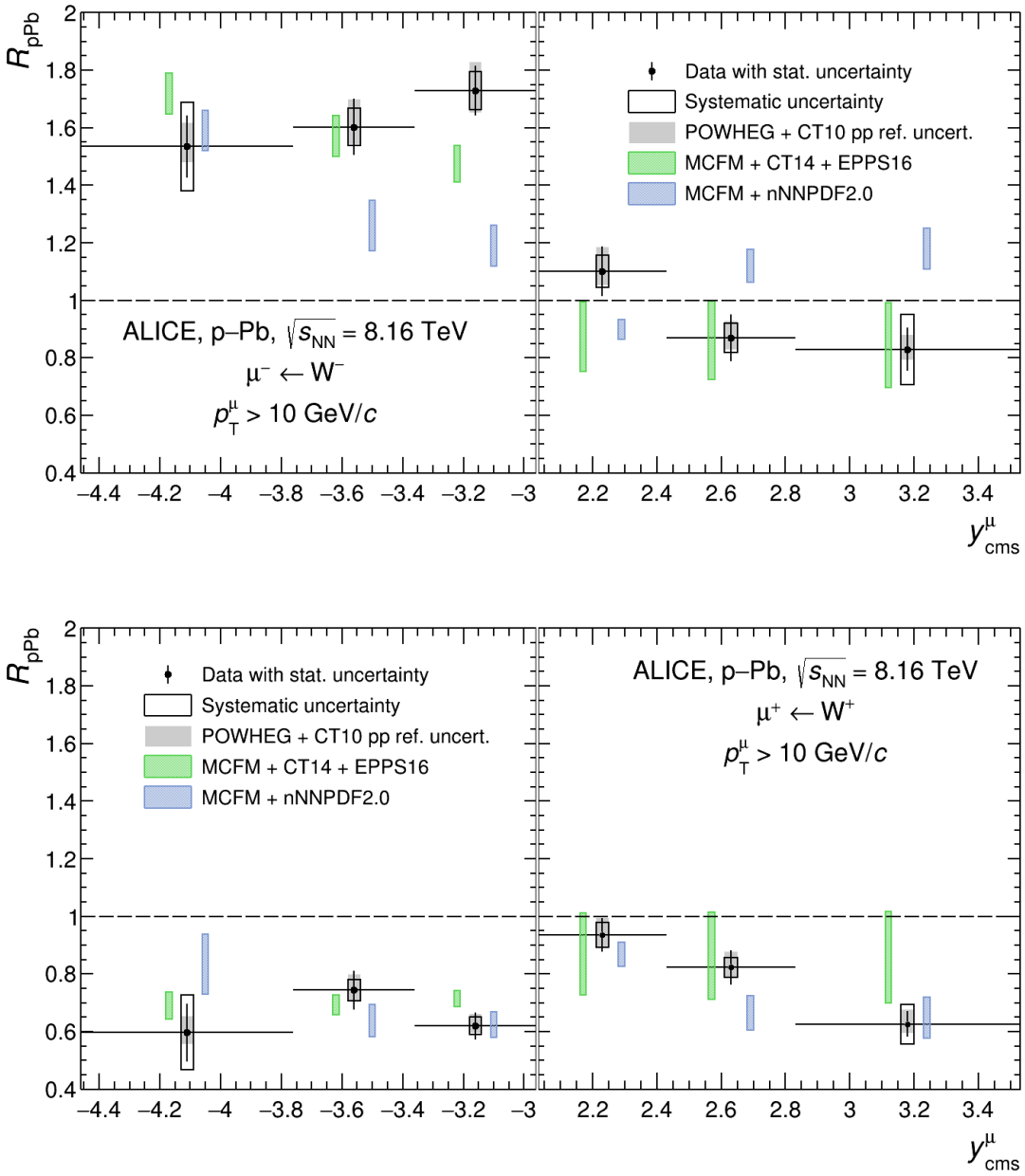


**Figure 9.9:** Nuclear modification factor $R_{\mathrm{pPb}}$ of muons from $\mathrm{W}^-$ (top) and $\mathrm{W}^+$ (bottom) decays, as a function of rapidity, in p–Pb collisions at $\sqrt{s_{\mathrm{NN}}} = 8.16$ TeV. The measurements are compared with predictions from the EPPS16 [54] and nNNPDF2.0 [56] models, using CT14 [63] and NNPDF3.1 [49] proton PDF sets for the reference cross section, respectively. The bars and boxes indicate the statistical and systematic uncertainties on the cross section in p–Pb collisions, respectively. The uncertainty on the reference cross section is indicated as a grey band around the data points. The theory points are horizontally shifted for better readability.

| | | $-4 < y_{\rm lab} < -3.3$ | $-3.3 < y_{\rm lab} < -2.9$ | $-2.9 < y_{\rm lab} < -2.5$ |
|---|---|---|---|---|
| Pb–p | $R_{\rm pPb}^{\mu^-\leftarrow {\rm W}^-}$ | $1.566 \pm 0.107 \pm 0.155^{+0.085}_{-0.053}$ | $1.635 \pm 0.099 \pm 0.062^{+0.098}_{-0.060}$ | $1.765 \pm 0.088 \pm 0.064^{+0.100}_{-0.076}$ |
| | $R_{\rm pPb}^{\mu^+\leftarrow {\rm W}^+}$ | $0.606 \pm 0.105 \pm 0.132^{+0.056}_{-0.039}$ | $0.760 \pm 0.070 \pm 0.036^{+0.054}_{-0.034}$ | $0.632 \pm 0.047 \pm 0.030^{+0.040}_{-0.029}$ |
| p–Pb | $R_{\rm pPb}^{\mu^-\leftarrow {\rm W}^-}$ | $0.838 \pm 0.076 \pm 0.122^{+0.052}_{-0.035}$ | $0.882 \pm 0.083 \pm 0.053^{+0.058}_{-0.041}$ | $1.111 \pm 0.087 \pm 0.057^{+0.086}_{-0.049}$ |
| | $R_{\rm pPb}^{\mu^+\leftarrow {\rm W}^+}$ | $0.621 \pm 0.055 \pm 0.069^{+0.032}_{-0.032}$ | $0.833 \pm 0.061 \pm 0.047^{+0.056}_{-0.037}$ | $0.943 \pm 0.059 \pm 0.043^{+0.058}_{-0.041}$ |

**Table 9.5:** Nuclear modification factor of muons from $\rm W^{\pm}$ decays in p–Pb collisions at $\sqrt{s_{\rm NN}} = 8.16$ TeV in various rapidity bins. The quoted errors correspond to the statistical and systematic uncertainties from the p–Pb cross section, and the upper and lower bound of the systematic uncertainty from the pp cross section, respectively.

At positive rapidities, the same decreasing tendency is seen in both the experimental data and nNNPDF2.0 calculations, although disagreeing on the gradient. One can generally conclude that the theory faces difficulties in reproducing the $R_{\rm pPb}$ data, stressing the importance of providing new inputs for the determination of the nuclear models.

## 9.4 Binary scaling

The production of $\rm W^{\pm}$ was finally studied as a function of centrality, in order to verify the expected scaling of hard processes with the number of binary nucleon-nucleon collisions. The study of the centrality-dependent yield can also serve as test bench for the centrality estimation. In order to maximise the amount of signal in each bin, the yields of $\rm W^-$ and $\rm W^+$ are combined. Four centrality classes were considered: 0–20%, 20–40%, 40–60% and 60–100%. The centrality is expressed as the average number of binary nucleon-nucleon collisions $\langle N_{\rm coll}^{\rm mult} \rangle$, the correspondence between $\langle N_{\rm coll}^{\rm mult} \rangle$ and the centrality classes was given in Table 8.5. The normalised invariant yield is evaluated as:

$$\frac{1}{\langle N_{\rm coll}^{\rm mult} \rangle} \times \frac{N^i_{\rm W^{\pm}}}{\mathcal{L}_{\rm int} \times f^i_{\rm MB} \times \varepsilon}, \tag{9.5}$$

where $N^i_{\rm W^{\pm}}$ is the number of muons from $\rm W^{\pm}$ decays in a given centrality class $i$, $f^i_{\rm MB}$ is the fraction of MB-triggered events in the centrality class $i$ to that in 0–100%, $\mathcal{L}_{\rm int}$ is the integrated luminosity and $\varepsilon$ is the detector efficiency.

The bias of multiplicity-based estimators was observed in this study, as seen in Figure 9.10 (the computation of the cross section is described below). The expected scaling of the $\rm W^{\pm}$ production with the average number of binary nucleon-nucleon collisions $\langle N_{\rm coll}^{\rm mult} \rangle$ is realised when using the ZDC as centrality estimators, but large deviations are seen when the centrality is estimated with the multiplicity-based V0 and CL1.

The normalised cross section in the full centrality range is measured to be:

$$\text{Pb–p} : 30.2 \pm 2.0 \pm 2.8 \text{ nb}, \qquad \text{p–Pb} : 44.6 \pm 3.3 \pm 5.1 \text{ nb}.$$

The measured evolution of the normalised invariant yield as a function of $\langle N_{\rm coll}^{\rm mult} \rangle$ is shown in Figure 9.11. The centrality-dependent yield is found to be consistent with a constant within uncertainties.

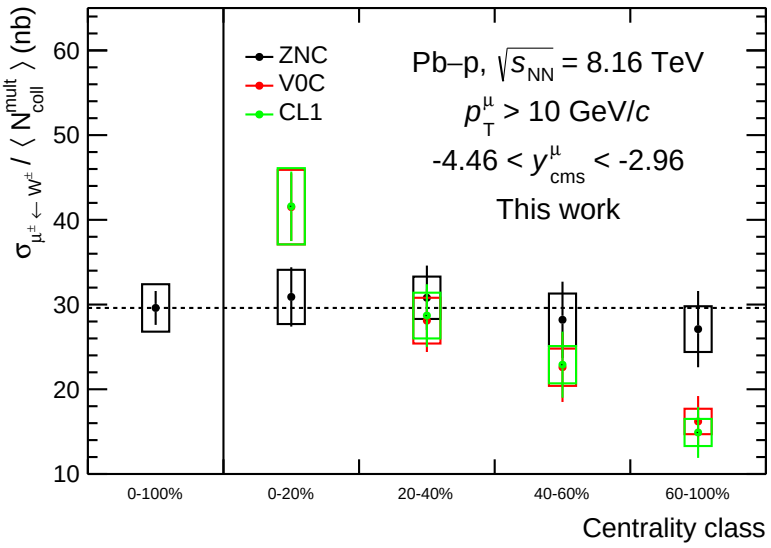


**Figure 9.10:** Production of $W^\pm$ boson normalised to the average number of binary collision $\langle N_{coll}^{mult} \rangle$ for various centrality estimators and centrality intervals. A dashed line is drawn at the value for 0–100% centrality to guide the eye.

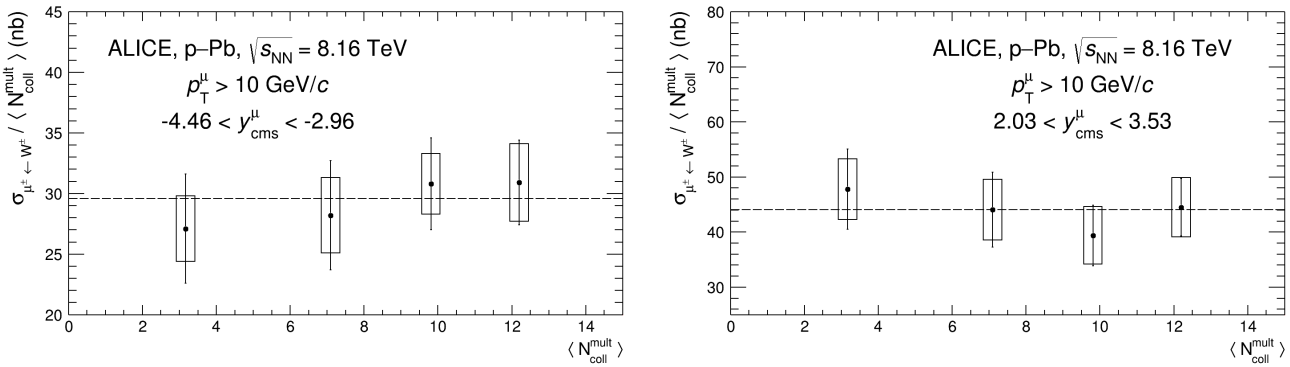


**Figure 9.11:** Combined yields of muons from $W^\pm$ decays in p–Pb collisions at $\sqrt{s_{NN}} = 8.16$ TeV, normalised to the average number of binary nucleon-nucleon collisions $\langle N_{coll}^{mult} \rangle$, for Pb–p (left) and p–Pb (right) collisions. The bars and boxes correspond to the statistical and systematic uncertainties, respectively. The horizontal dashed lines correspond to the normalised yield measured for the 0–100% centrality.

It should be stressed that the dashed line in the figure is not a linear fit of the distribution, but rather indicate the value measured in the 0–100% centrality range. A separate evaluation of the invariant yield from $W^-$ and $W^+$ was tested, leading the same conclusion. The resulting statistical uncertainties prevent to see any charge-dependent effect on the normalised yield.

# Conclusion

In this thesis, the measurements of the $Z^0$- and $W^{\pm}$-boson production in p–Pb collisions at $\sqrt{s_{NN}} = 8.16$ TeV with ALICE are reported. The electroweak bosons are detected through their leptonic decays, using data collected with the muon spectrometer of the experiment. Two data samples were used, corresponding to p–Pb and Pb–p collisions, with an integrated luminosity of $6.81 \pm 0.15$ nb$^{-1}$ and $10.2 \pm 0.27$ nb$^{-1}$, respectively. For each analysis, a fiducial region was define as to ensure a clean data sample and measurements at the highest precision:

$$Z^0: \quad \begin{cases} -4 < \eta_\mu < -2.5, \\ p_T^\mu > 20 \text{ GeV}/c, \\ 60 < m_{\mu^+\mu^-} < 120 \text{ GeV}/c^2, \end{cases} \qquad W^{\pm}: \quad \begin{cases} -4 < \eta_\mu < -2.5, \\ p_T^\mu > 10 \text{ GeV}/c. \end{cases}$$

Accounting for the rapidity shift in p–Pb collisions, the rapidity intervals in the centre-of-mass frame covered by the spectrometer are $-4.46 < y_{cms}^{Pb\text{-}p} < -2.96$ and $2.03 < y_{cms}^{p\text{-}Pb} < 3.53$, corresponding to high ($\sim 10^{-1}$) and low ($\sim 10^{-3}$–$10^{-4}$) Bjorken-$x$ regions, respectively. The production of the $Z^0$ boson was presented as the production cross section at negative and positive rapidities, measured in the full acceptance of the muon spectrometer. The $W^{\pm}$ production was reported through the production cross section, lepton charge asymmetry and nuclear modification factor, and was evaluated in the full acceptance and in several rapidity intervals.

The measurements were compared to similar studies at the LHC. Comparisons with the same analyses performed in p–Pb collisions at $\sqrt{s_{NN}} = 5.02$ TeV by the ALICE Collaboration highlighted the benefits of increasing the energy of the collisions and luminosity of the periods. The measurements at $\sqrt{s_{NN}} = 8.16$ TeV were indeed found to be much more precise, although the $Z^0$ yields was still facing statistical limitations. The combination of the CMS and ALICE measurements of the $W^{\pm}$ cross sections shown the complementarity of the LHC experiments, as the combined measurements assess the full $|y_{lab}| < 4$ interval, over eight units of rapidity.

The measurements were compared to theoretical predictions, from the EPPS16, nCTEQ15 and nNNPDF2.0 nPDF models, as well as reference calculations with the free-nucleon CT14 PDF, accounting for the isospin effect but without nuclear modifications. The production cross section of the $Z^0$ boson was found to be well reproduced by the models. No conclusion could be derived on the nuclear modifications, as the measurements were consistent with all predictions, regardless of whether they include the nuclear corrections or not. The $W^{\pm}$ cross sections were also generally well reproduced by the models, at the exception of $W^-$ in the most central bins at both forward and backward rapidities where disagreements are observed. The $W^+$ cross section at positive rapidities

shows a strong preference for predictions including the nuclear modifications. The deviation from the free-PDF calculation goes up 3.5 $\sigma$ for the largest rapidity interval. The recent nNNPDF2.0 model is overall less efficient at reproducing the measurements.

Comparison of the lepton charge asymmetry yielded interesting differences between the EPPS16 and nNNPDF2.0 models at forward rapidity, where the EPPS16 predictions does not show any significant nuclear effects, while nNNPDF2.0 predicts a large drop towards larger rapidities. The measured asymmetry lies in between the two models, showing a decrease of the asymmetry although not as strong as what is foreseen by the nNNPDF2.0 calculation. The two models are also strongly disagreeing on the nuclear modification factor. Yet, no strong preference can be seen when comparing with the measurements.

The normalised yield of $\mathrm{W}^{\pm}$ bosons was also present as a function of the average number of binary nucleon-nucleon collisions. The study shown the important bias of multiplicity-based estimators of the centrality. With the unbiased estimation provided by the ZDC detector, the distribution of the normalised yield is found to be consistent with a constant, as expected from a Glauber modelling of the collision.

This study provides important constraints for the nPDF determination, in a Bjorken-$x$ region where the available data are scarce. Significant tensions are observed between the measured production and the theoretical calculations. The precision of the measurements is often found to be better than that of the calculations, such that even when an agreement if found this study will help for nPDF determination by participating in the reduction of the model uncertainties. By including all the measurements of weak boson production provided by the LHC experiments, including the ones obtained in this work, nPDF determination groups will be able to provide a new generation of sets with drastically improved accuracy and precision.

The high luminosity foreseen at the LHC after its restart in 2022 will provide another increase in the precision of electroweak boson measurements. The statistics will enable differential studies of the $\mathrm{Z}^0$-boson production, and a higher granularity for that of the $\mathrm{W}^{\pm}$ bosons. It should also allow one to measure backward-forward asymmetries in p–Pb collisions with the ALICE muon spectrometer, despite the small overlap of the centre-of-mass rapidity intervals due to the rapidity shift, which only covers $2.96 < |y_{\mathrm{cms}}| < 3.53$. These measurements during the LHC Runs 3 and 4 will pursue the iterations between the experimental and theoretical communities towards the determination of nPDF.

# List of Figures


1.1 Summary of measurements of $\alpha_s(Q^2)$ as a function of the energy scale $Q$. . . . . 13
1.2 Constituent quark masses as a function of the squared momentum for the $u/d$, $s$, $c$ and $b$ quarks. . . . . 16
1.3 Schematic view of the phases of the QCD matter in the plane of temperature $T$ and baryon-chemical potential $\mu_B$. . . . . 17
1.4 **Left**: pseudo-critical temperature $T_c(0)$ as a function of the lattice volume $N_\tau$ using several parametrisation of $C^\Sigma$, $C^\chi$ and $\chi^\Sigma$. **Right**: phase boundary of $2+1$ flavour QCD. . . . . 19
1.5 Feynman diagram for the deep inelastic lepton-hadron scattering. . . . . 21
1.6 Feynman diagram for the deep inelastic lepton-hadron scattering, preceded by a gluon radiation. . . . . 22
1.7 The NNPDF3.1 NNLO PDF set. . . . . 30
1.8 Illustration of the EPPS16 fit function $R_i^A(x, Q_0^2)$. . . . . 32
1.9 The nNNPDF2.0 nPDF set. . . . . 34

2.1 Light cone and space-time evolution of a HIC. . . . . 38
2.2 Temperature $T$ and baryon chemical potential $\mu_B$ as a function of the beam energy. 41
2.3 Optical limit of the Glauber model. . . . . 43
2.4 Glauber-MC event simulated in Au–Au collisions at $\sqrt{s_{\mathrm{NN}}} = 200$ GeV in the transverse and longitudinal planes. . . . . 46
2.5 EPPS16 nuclear modifications for Pb at the parametrisation scale $Q_0^2 = 10$ GeV$^2$, for the $u_\mathrm{V}$, $d_\mathrm{V}$ and $g$ PDFs. . . . . 48
2.6 **Left**: nuclear modification factors for the charm and bottom quarks in p–Pb collisions at $\sqrt{s_{\mathrm{NN}}} = 8.8$ TeV from the EPS09 nPDF model. **Right**: inclusive jet nuclear modification factor $R^*_{\mathrm{pPb}}$ as a function of the jet $p_\mathrm{T}$, in p–Pb collisions at $\sqrt{s_{\mathrm{NN}}} = 5.02$ TeV, measured by the CMS collaboration. . . . . 48
2.7 Near-side ridge measured in pp, p–Pb and Pb–Pb collisions at the LHC. . . . . 50

3.1 $\mathrm{W}^\pm$ measurements by the UA1 and UA2 Collaborations. . . . . 56
3.2 $\mathrm{Z}^0$ measurements by the UA1 and UA2 Collaborations. . . . . 57
3.3 World average of the mass and width of the $\mathrm{W}^\pm$ bosons. . . . . 61
3.4 Flavour decomposition of the $\mathrm{Z}^0$ and $\mathrm{W}^\pm$ production cross sections as a function of the collision energy. . . . . 64

3.5 Rapidity distribution of the $Z^0$ and $W^{\pm}$ cross sections at LO, NLO and NNLO in pp collisions at the LHC nominal energy $\sqrt{s} = 14$ TeV with the MRST PDF set. . . 65
3.6 Production and decay diagrams of the $W^{\pm}$ bosons in the rest frame. . . . . 67
3.7 Production cross sections of the $Z^0$ and $W^{\pm}$ bosons in p–Pb collisions at $\sqrt{s_{NN}} =$ 8.8 TeV from the EPS09 model. . . . . 68
3.8 Measurement of $Z^0$-boson production in Pb–Pb collisions at $\sqrt{s_{NN}} = 2.76$ TeV by the ATLAS Collaboration. . . . . 71
3.9 Measurement of $Z^0$- and $W^{\pm}$-boson production in Pb–Pb collisions at $\sqrt{s_{NN}} = 5.02$ TeV by the ATLAS Collaboration. . . . . 72
3.10 Measurement of $Z^0$- and $W^{\pm}$-boson production in Pb–Pb collisions at $\sqrt{s_{NN}} = 5.02$ TeV by the ALICE Collaboration. . . . . 73
3.11 Rapidity-differential cross section of the $Z^0$ detected in the leptonic decay channel $(e + \mu)$ in p–Pb collisions at $\sqrt{s_{NN}} = 5.02$ TeV with the ATLAS detector. . . . . 74
3.12 Production cross section of $W^+$ and $W^-$, as a function of the lepton pseudorapidity, in p–Pb collisions at $\sqrt{s_{NN}} = 5.02$ TeV and 8.16 TeV measured by the CMS Collaboration. . . . . 75
3.13 $Z^0$-boson production cross section measured in p–Pb collisions at $\sqrt{s_{NN}} = 5.02$ TeV and 8.16 TeV by the LHCb Collaboration. . . . . 76
3.14 Production cross sections of the $Z^0$ and $W^{\pm}$ bosons in p–Pb collisions at $\sqrt{s_{NN}} = 5.02$ TeV measured by the ALICE Collaboration. . . . . 77

4.1 The CERN facility. . . . . 82
4.2 The LHC injection chain for proton and lead beams. . . . . 83
4.3 Schematics of the ALICE detector. . . . . 85
4.4 **Left**: Pseudorapidity coverage of the ALICE subdetectors. **Right**: Comparison of the geometrical acceptances of the main LHC experiments. . . . . 87
4.5 **Left**: Number of recorded events for the V0-based triggers in Pb–Pb collisions. **Right**: Correlation between the sum and difference of signal times in V0-A and V0-C in pp collisions. . . . . 90
4.6 Visible cross sections for the V0 and T0 processes measured in vdM scans in p–Pb collisions. . . . . 92
4.7 Sum of amplitudes in V0-A for p–Pb collisions. . . . . 93
4.8 Multiplicity bias in p–Pb collisions. . . . . 94
4.9 **Left and centre**: Transverse and longitudinal profiles of the luminous region. **Right**: Widths of the final vertex distribution in the transverse plane. . . . . 97
4.10 Event reconstruction flow in the central barrel. . . . . 98
4.11 Resolution for standalone TPC and ITS-TPC matched tracks. . . . . 99
4.12 **Left**: Specific energy loss $\mathrm{d}E/\mathrm{d}x$ in the TPC as a function of the particle momentum, in Pb–Pb collisions. **Right**: $K/\pi$ separation by combining the arrival time measurement in TOF and $\mathrm{d}E/\mathrm{d}x$ in the TPC. . . . . 101
4.13 Kaon-pion and kaon-proton separation power of the ITS, TPC, TOF and HMPID systems as a function of the particle transverse momentum. . . . . 101

4.14 $E/p$ distribution for electrons and pions in the EMCAL, in pp collisions at $\sqrt{s} = 7$ TeV. . . . 102
4.15 **Left**: Cross sectional view of one of the TRD layer. **Right**: TRD signal as a function of the particle momentum, in p–Pb collisions at $\sqrt{s_{\rm NN}} = 5.02$ TeV, for protons from $\Lambda$ decays, charged pions from $\rm K^0_S$ decays and electrons from $\gamma$ conversions. . . . 103
4.16 **Left**: Comparison between the dilepton invariant mass distribution before and after applying the selection. **Right**: Transverse distribution of the reconstructed photon conversion points for $|\eta| > 9$. . . . 104

5.1 Cross sectional view, in the longitudinal plane, of the ALICE muon spectrometer. . 108
5.2 Schematic view of the quadrant structure and slat architecture of the two innermost and three outermost tracking stations. . . . 110
5.3 Layout and working principle of the MWPC composing the tracking chambers. . . . 111
5.4 Schematics of a RPC composing the muon trigger planes. . . . 112
5.5 Possible configurations after the passage of a charged particle through a tracking station. . . . 116
5.6 Sketch of the working principle of the muon trigger decision. . . . 117

6.1 The ALICE online control system. . . . 120
6.2 Overview of the ALICE DAQ system and its interface with the HLT system. . . . 124
6.3 The publisher-subscriber paradigm of AMORE. . . . 126
6.4 Examples of MOs visualisation, using the AMORE generic GUI or accessed through the eLogbook. . . . 127
6.5 The ALICE HLT in the data readout scheme. . . . 128
6.6 HLT compression factor achieved for TPC data, in pp collisions. . . . 129
6.7 The ALICE control system put in context. . . . 130
6.8 Schematics of the ECS architecture. . . . 131
6.9 Schematic view of the computing grid hierarchy in the framework of the tiered MONARC model. . . . 133
6.10 Schematic view of the AliRoot framework. . . . 134
6.11 Schematic depiction of the data processing framework in AliRoot. . . . 136

7.1 The ITS2 layout. . . . 141
7.2 Simulated performances of the ITS2 compared with measured performances of the original ITS. . . . 142
7.3 Simulations of the inclusive $\rm e^+$ $\rm e^-$ invariant mass spectrum for the current and upgraded TPC. . . . 143
7.4 Upgraded readout scheme of ALICE. . . . 144
7.5 Schematics of the FIT layout. . . . 145
7.6 Illustration of the usage of physics and heartbeat triggers for the corresponding readout modes. . . . 146
7.7 Efficiency of the MID RPCs equipped with FEERIC cards. . . . 148
7.8 MID readout electronics architecture. . . . 149

7.9 3-dimensional view of the MFT detector and schematics of the its position in the muon spectrometer. . . . 150
7.10 Dimuon invariant mass distribution in the $J/\psi$ family region, in Pb–Pb collisions, without and with including information from the MFT. . . . 151
7.11 The computing architecture of ALICE in Run 3. . . . 152
7.12 Quality Control and assessment general design in $O^2$. . . . 154
7.13 Event distribution as a function of the detector element, obtained from the QC MID module ran on simulated data. . . . 158
7.14 Event distribution as a function of the detector element, obtained from the QC MID module ran on simulated data. . . . 160

8.1 Evolution of the purity and pile-up factors as a function of the run number, in p–Pb and Pb–p collisions. . . . 168
8.2 $F_{\mathrm{norm}}$ as a function of the run number in p–Pb and Pb–p collisions. . . . 170
8.3 Multiplicity distribution of MB, `MSL` and `MSH` triggered events measured by V0M in p–Pb and Pb–p collisions. . . . 171
8.4 **Top**: evolution of the $p_{\mathrm{T}}$ distribution of muon track candidates from `MSH`-triggered events during the application of the event and track selections. **Middle**: $p_{\mathrm{T}}$ distribution of $\mu^+$, $\mu^-$ and $\mu^\pm$ tracks after the full event and track selections. **Bottom**: charge ratio $\mu^+/\mu^-$ as a function of $p_{\mathrm{T}}$. . . . 174
8.5 FONLL cross sections for the leptonic decay of HF hadrons as a function of $p_{\mathrm{T}}$ and $y$ in p–Pb and Pb–p collisions. . . . 177
8.6 **Top**: $p_{\mathrm{T}}$ distribution of the single muons from $W^\pm$ decays, for positively and negatively charged muons, and their combination. **Bottom**: invariant mass distribution of dimuons from $Z^0$ decays, normalised to 1, in p–Pb and Pb–p collisions. . . . 180
8.7 Invariant mass, $p_{\mathrm{T}}$ and $\eta$ distributions of dimuons from $Z^0$ candidates in p–Pb and Pb–p collisions at $\sqrt{s_{\mathrm{NN}}} = 8.16$ TeV. . . . 181
8.8 Estimation of the contamination to the $Z^0$ signal from several background sources in p–Pb and Pb–p collisions. . . . 183
8.9 Invariant mass distribution of same sign muon pairs in p–Pb and Pb–p collisions, for various values of the muon $p_{\mathrm{T}}$ selection. . . . 185
8.10 Global fits of the single muon $p_{\mathrm{T}}$ distribution in p–Pb and Pb–p collisions for negatively and positively charged muons. . . . 186
8.11 $p_{\mathrm{T}}$ distribution of negative and positive muon from $W^\pm$ decays in p–Pb and Pb–p collisions simulated at LO and for variations of $\alpha_s$, compared to the nominal parametrisation. . . . 187
8.12 $p_{\mathrm{T}}$ distribution of negative and positive muon from $W^\pm$ decays in p–Pb and Pb–p collisions simulated with the nominal (data-based) and alternative (MC-tuned) sets of parameters for the cluster resolution correction. . . . 188
8.13 $p_{\mathrm{T}}$ distribution of negative and positive muon from $W^\pm$ decays in p–Pb and Pb–p collisions simulated with the three values of the tuning parameter accounting for the global misalignment of the spectrometer. . . . 189
8.14 Extraction of the $W^\pm$ signal in p–Pb and Pb–p collisions. . . . 191

8.15 Invariant mass distribution of dimuons from $Z^0$ decays. . . . . 193
8.16 Run-by-run efficiencies in p–Pb and Pb–p collisions for single muons from $W^-$ and $W^+$ decays, and dimuons from $Z^0$ decays. . . . . 194

9.1 Production cross sections of the muonic decays of $Z^0$ and $W^\pm$ bosons measured in p–Pb collisions at $\sqrt{s_{NN}} = 8.16$ TeV. . . . . 198
9.2 Production cross sections of the muonic decays of $Z^0$, $W^-$ and $W^+$ bosons measured in p–Pb collisions at $\sqrt{s_{NN}} = 8.16$ TeV and $\sqrt{s_{NN}} = 5.02$ TeV. . . . . 200
9.3 Production cross section of the $Z^0 \to \mu^+\mu^-$ process in p–Pb collisions at $\sqrt{s_{NN}} = 8.16$ TeV, compared with theoretical predictions. . . . . 201
9.4 Production cross section of the $W^\pm \to \mu^\pm\nu_\mu$ process for $W^-$ and $W^+$, in p–Pb collisions at $\sqrt{s_{NN}} = 8.16$ TeV, compared with theoretical predictions. . . . . 203
9.5 Ratio to CT14 predictions of the production cross section of muons from $W^-$ and $W^+$ decays measured by the ALICE and CMS Collaborations in p–Pb collisions at $\sqrt{s_{NN}} = 8.16$ TeV. . . . . 205
9.6 Lepton charge asymmetry of muons from $W^\pm$ decays in p–Pb collisions at $\sqrt{s_{NN}} = 8.16$ TeV. 206
9.7 Lepton charge asymmetry $A_{ch}$ as a function of rapidity of muons from $W^\pm$ decays in p–Pb collisions at $\sqrt{s_{NN}} = 8.16$ TeV. . . . . 207
9.8 Nuclear modification factor $R_{pPb}$ of muons from $W^\pm$ decays measured in p–Pb collisions at $\sqrt{s_{NN}} = 8.16$ TeV. . . . . 209
9.9 Nuclear modification factor $R_{pPb}$ of muons from $W^-$ and $W^+$ decays, as a function of rapidity, in p–Pb collisions at $\sqrt{s_{NN}} = 8.16$ TeV. . . . . 210
9.10 Production of $W^\pm$ boson normalised to the average number of binary collision $\langle N_{coll}^{mult} \rangle$ for various centrality estimators and centrality intervals. . . . . 212
9.11 Combined yields of muons from $W^\pm$ decays in p–Pb collisions at $\sqrt{s_{NN}} = 8.16$ TeV, normalised to the average number of binary nucleon-nucleon collisions $\langle N_{coll}^{mult} \rangle$, for Pb–p and p–Pb collisions. . . . . 212

# List of Tables


1.1 Charge, isospin, additive quantum numbers and mass of the known quarks. . . . . 8
1.2 Key specifications of the nCTEQ15, EPPS16 and nNNPDF2.0 nPDF sets. . . . . 35

2.1 Heavy-ion accelerators. . . . . 42

3.1 Centre-of-mass energy, instantaneous and integrated luminosity delivered by the CERN proton-antiproton collider from 1981 to 1990. . . . . 55
3.2 Mass, full width, and branching fractions of the hadronic and leptonic decays of the $W^{\pm}$ and $Z^0$ bosons. . . . . 62
3.3 References of the available measurements of the $Z^0$- and $W^{\pm}$-boson production performed in HIC at the LHC. . . . . 70

4.1 LHC nominal nucleon-nucleon centre-of-mass energy, luminosity and geometrical cross section for pp, p–Pb and Pb–Pb collisions. . . . . 84
4.2 Position, geometrical coverage and main purpose of the ALICE subdetectors. . . . . 86
4.3 Minimum Bias triggers provided by the V0. . . . . 89
4.4 Average number of collisions $\langle N_{\rm coll} \rangle$ evaluated in p–Pb collisions. . . . . 94

5.1 Summary of the main characteristics of the ALICE muon spectrometer. . . . . 109
5.2 Trigger types defined by the muon trigger system. . . . . 117

6.1 Trigger capabilities provided by the various ALICE detectors. . . . . 121
6.2 Descriptors of the major ALICE triggers. . . . . 123

7.1 Position, radial and pseudorapidity coverages, and technology of the sub-systems of FIT. . . . . 146
7.2 Readout parameter overview for Pb–Pb beam operation at 50 kHz interaction rate. 147
7.3 Geometrical parameters of the MFT, and number of sensors per half-disk and in the full MFT. . . . . 150

8.1 Bjorken-$x$ intervals assessed by the measurement of $Z^0$ and $W^{\pm}$ bosons with the ALICE muon spectrometer in p–Pb collisions at $\sqrt{s_{\rm NN}} = 8.16$ TeV. . . . . 164
8.2 Runs from the LHC16r and LHC16s periods that passed the QA. . . . . 165
8.3 Main characteristics of the periods analysed in this study, from p–Pb collisions at $\sqrt{s_{\rm NN}} = 8.16$ TeV. . . . . 166

8.4 Normalisation factors obtained from the direct offline, indirect offline and online methods for the dimuon and single muon triggers. . . . 169
8.5 Average number of binary collisions $\langle N_{\rm coll}^{\rm mult} \rangle$ estimated with the hybrid ZN method in p–Pb collisions at $\sqrt{s_{\rm NN}} = 8.16$ TeV. . . . 172
8.6 Number of tracks after physics and vertex selection and the application of the cuts. 173
8.7 Charge ratio $\mu^+/\mu^-$ for $p_{\rm T}$ between 10 and 20 GeV/$c$ measured in data and FONLL-based simulations for various values of the global misalignment tuning parameter in p–Pb and Pb–p collisions. . . . 178
8.8 Ratio $R$ of the $\mu^\pm \leftarrow {\rm Z}^0$ cross section to that of $\mu^\pm \leftarrow {\rm W}^\pm$ estimated in p–Pb and Pb–p collisions at $\sqrt{s_{\rm NN}} = 8.16$ TeV from simulations with POWHEG. . . . 179
8.9 Raw number of muons from $\rm W^\pm$ decays, extracted from a global fit of the inclusive single muon $p_{\rm T}$ distributions for $p_{\rm T}^\mu > 10$ GeV/$c$ and $-4 < y_{\rm lab}^\mu < -2.5$. . . . 190
8.10 Efficiencies of $\mu^\pm$ from $\rm W^\pm$ decays and $\mu^+\mu^-$ from $\rm Z^0$ decays in p–Pb and Pb–p collisions. . . . 193
8.11 Summary of the systematic uncertainties affecting the measurements of muons from $\rm W^\pm$ and $\rm Z^0$ decays in p–Pb and Pb–p collisions. . . . 195

9.1 Production cross sections of the $\rm Z^0$ and $\rm W^\pm$ bosons in their muonic decays in p–Pb collisions at $\sqrt{s_{\rm NN}} = 8.16$ TeV. . . . 199
9.2 Production cross sections of the $\mu^- \leftarrow {\rm W}^-$ and $\mu^+ \leftarrow {\rm W}^+$ processes in p–Pb collisions at $\sqrt{s_{\rm NN}} = 8.16$ TeV for various centrality intervals. . . . 199
9.3 Lepton charge asymmetry of muons from $\rm W^\pm$ decays, measured in p–Pb collisions at $\sqrt{s_{\rm NN}} = 8.16$ TeV. . . . 206
9.4 Nuclear modification factor of muons from $\rm W^\pm$ decays in p–Pb collisions at $\sqrt{s_{\rm NN}} = 8.16$ TeV in the full acceptance of the spectrometer. . . . 209
9.5 Nuclear modification factor of muons from $\rm W^\pm$ decays in p–Pb collisions at $\sqrt{s_{\rm NN}} = 8.16$ TeV in various rapidity bins. . . . 211

# Bibliography


[1] M. D. Schwartz, *Quantum Field Theory and the Standard Model*. Cambridge University Press, Cambridge, 2014.

[2] M. Gell-Mann, "A schematic model of baryons and mesons," *Physics Letters* **8** (1964) 214–215.

[3] G. Zweig, "An $SU_3$ model for strong interaction symmetry and its breaking,". `https://cds.cern.ch/record/570209`. Published in: *Developments in the Quark Theory of Hadrons. Vol. 1: 1964 - 1978*, ed. D. Lichtenberg and S. Rosen, Hadronic Press, Nonantum MA, 1980. pp. 22-101.

[4] T. Nakano and K. Nishijima, "Charge Independence for $V$- particles," *Progress of Theoretical Physics* **10** (1953) 581–582.

[5] M. Gell-Mann, "The interpretation of the new particles as displaced charge multiplets," *Il Nuovo Cimento (1995-1965)* **4** (1956) 848–866.

[6] **Particle Data Group**, P. Zyla, *et al.*, "Review of Particle Physics," *Progress of Theoretical and Experimental Physics* **2020** (2020) 083C01. `https://pdg.lbl.gov/`. Updated in 2021.

[7] M. Fierz, "Über die relativische Theorie kräftefreier Teilchen mit beliebigem Spin," *Helvetica Physica Acta* **12** (1939) 3–37.

[8] O. W. Greenberg, "Spin and Unitary-Spin Independence in a Paraquark Model of Baryons and Mesons," *Physical Review Letters* **13** (1964) 598.

[9] M. E. Peskin and D. V. Schroeder, *An Introduction to Quantum Field Theory*. Advanced Book Program, Boudler, CO, 1995.

[10] R. Ellis, W. Stirling, and B. Webber, *QCD and Collider Physics*. Cambridge Monographs on Particle Physics, Nuclear Physics and Cosmology. Cambridge University Press, Cambridge, 1996.

[11] C. G. Callan, "Broken Scale Invariance in Scalar Field Theory," *Physical Review D* **2** (1970) 1541.

[12] K. Symanzik, "Small distance behaviour in field theory and power counting," *Communications in Mathematical Physics* **18** (1970) 227–246.

[13] K. Symanzik, "Small-distance-behaviour analysis and Wilson expansion," *Communications in Mathematical Physics* **23** (1971) 49–86.

[14] W. A. Baarden, A. J. Buras, D. Duke, and T. Muta, "Deep-inelastic scattering beyong the leading order in asymptotically free gauge theories," *Physical Review D* **18** (1978) 3998.

[15] G. Altarelli, *The Development of Perturbative QCD*. World Scientific Publishing Company, Singapore, 1994. Ch. 6: Polarized Electroproduction and the Spin of the Quarks inside the Proton. pp. 294-307.

[16] E. Noether, "Invariante Variationprobleme," *Nachrichten der Königlichen Gesellschaft der Wissenschaften zu Göttingen* **2** (1918) 235–257.

[17] S. Hands, "The phase diagram of QCD," *Contemporary Physics* **42** (2001) 209–225, `arXiv:physics/0105022 [phys.ed-ph]`.

[18] K. Langfeld, H. Markum, R. Pullirsch, C. Robers, and S. Schmidt, "Concerning the quark condensate," *Physical Review C* **67** (2003) 065206, `arXiv:nucl-th/0301024 [nucl-th]`.

[19] G. Ecker, "Chiral perturbation theory," *Progress in Particle and Nuclear Physics* **35** (1995) 1–80, `arXiv:hep-ph/9501357 [hep-ph]`.

[20] X. Zhang, *Study of Heavy Flavours from Muons Measured with the ALICE Detector in Proton-Proton and Heavy-Ion Collisions at the CERN-LHC*. PhD thesis, Université Blaise Pascal – Clermont-Ferrand II, 2012. tel-00786269.

[21] C. Fischer and R. Alkofer, "Nonperturbative propagators, running coupling, and the dynamical quark mass of Landau gauge QCD," *Physical Review D* **67** (2003) 094020, `arXiv:hep-ph/0301094 [hep-ph]`.

[22] A. Chodos, R. Jaffe, K. Johnson, C. Thorn, and V. Weisskopf, "New extended model of hadrons," *Physical Review D* **9** (1974) 3471.

[23] T. DeGrand, R. L. Jaffe, K. Johnson, and J. Kiskis, "Masses and other parameters of the light hadrons," *Physical Review D* **12** (1975) 2060.

[24] K. Johnson, "The M.I.T. bag model," *Acta Physica Polonica B* **6** (1975) 865–892.

[25] G. E. Brown and M. Rho, "The little bag," *Physics Letters B* **82** (1979) 177–180.

[26] L. Vepstas, A. D. Jackson, and A. S. Goldhaber, "Two-phase model of baryons and the chiral Casimir effect," *Physics Letters B* **140** (1984) 280–284.

[27] M. G. Alford, A. Schmitt, K. Rajagopal, and T. Schäfer, "Color superconductivity in dense quark matter," *Reviews of Modern Physics* **80** (2008) 1455, `arXiv:0709.4635 [hep-ph]`.

[28] J. B. Kogut, "The lattice gauge theory approach to quantum chromodynamics," *Reviews of Modern Physics* **55** (1983) 775.

[29] **HotQCD** Collaboration, A. Bazavov *et al.*, "Chiral crossover in QCD at zero and non-zero chemical potentials," *Physics Letters B* **795** (2019) 15–21, arXiv:1812.08235 [hep-lat].

[30] J. N. Guenther, "Overview of the QCD phase diagram. Recent progress from the lattice," *The European Physical Journal A* **57** (2021) 136, arXiv:2010.15503 [hep-lat].

[31] K. Yagi, T. Hatsuda, and Y. Miake, *Quark-Gluon Plasma*. Cambridge Monographs on Particle Physics, Nuclear Physics and Cosmology. Cambridge University Press, Cambridge, 2005.

[32] R. Pasechnik and M. Sumbera, "Phenomenological Review on Quark-Gluon Plasma: Concepts vs. Observations," *Universe* **3** (2017) 7, arXiv:1611.01533 [hep-ph].

[33] R. P. Feynman, "Very High-Energy Collisions of Hadrons," *Physical Review Letters* **23** (1969) 1415.

[34] R. P. Feynman, "The behavior of hadron collisions at extreme energies," *Conference Proceedings C* **690905** (1969) 237–258. First usage of the term parton.

[35] J. D. Bjorken and E. A. Paschos, "Inelastic Electron-Proton and $\gamma$-Proton Scattering and the Structure of the Nucleon," *Physical Review* **185** (1969) 1975.

[36] J. Collins, *Foundations of Perturbative QCD*. Cambridge Monographs on Particle Physics, Nuclear Physics and Cosmology. Cambridge University Press, Geneva, 2011.

[37] C. G. Callan and D. J. Gross, "High-Energy Electroproduction and the Constitution of the Electric Current," *Physical Review Letters* **22** (1969) 156.

[38] V. N. Gribov and L. N. Lipatov, "Deep inelastic e p scattering in perturbation theory," *Soviet Journal of Nuclear Physics* **15** (1972) 438–450.

[39] H. D. Politzer, "Reliable Perturbative Results for Strong Interactions?," *Physical Review Letters* **30** (1973) 1346.

[40] G. Altarelli and G. Parisi, "Asymptotic freedom in parton language," *Nuclear Physics B* **126** (1977) 298–318.

[41] J. C. Collins, D. E. Soper, and G. Sterman, *Perturbative Quantum Chromodynamics*, ch. Factorization of Hard Processes in QCD, pp. 1–91. World Scientific Publishing Company, Singapore, 1989. arXiv:hep-ph/0409313 [hep-ph].

[42] K. Kovarik, P. M. Nadolsky, and D. E. Soper, "Hadron structure in high-energy collisions," *Reviews of Modern Physics* **92** (2020) 045003, arXiv:1905.06957 [hep-ph].

[43] J. J. Ethier and E. R. Nocera, "Parton Distributions in Nucleons and Nuclei," *Annual Review of Nuclear and Particle Science* **70** (2020) 43–76, arXiv:2001.07722 [hep-ph].

[44] S. Alekhin, J. Blümlein, S. Moch, and R. Placakyte, "Parton Distribution Functions, $\alpha_s$ and Heavy-Quark Masses for LHC Run II," *Physical Review D* **96** (2017) 014011, arXiv:1701.05838 [hep-ph].

[45] **CTEQ** Collaboration, "The Coordinated Theoretical-Experimental Project on QCD." https://www.physics.smu.edu/scalise/cteq/.

[46] T.-J. Hou *et al.*, "New CTEQ global analysis of quantum chromodynamics with high-precision data from the LHC," *Physical Review D* **103** (2021) 014013, arXiv:1912.10053 [hep-ph].

[47] **JAM** Collaboration, N. Sato, C. Andres, E. J. Ethier, and W. Melnitchouk, "Strange quark suppression from a simultaneous Monte Carlo analysis of parton distributions and fragmentation functions," *Physical Review D* **101** (2020) 074020, arXiv:1905.03788 [hep-ph].

[48] S. Bailey, T. Cridge, L. A. Harland-Lang, A. D. Martin, and R. S. Thorne, "Parton distributions from LHC, HERA, Tevatron and fixed target data: MSHT20 PDFs," *The European Physical Journal C* **81** (2020) 341, arXiv:2012.04684 [hep-ph].

[49] **NNPDF** Collaboration, R. D. Ball *et al.*, "Parton distributions from high-precision collider data," *The European Physical Journal C* **77** (2017) 663, arXiv:1706.00428 [hep-ph].

[50] J. Pumplin, D. Stump, R. Brock, D. Casey, J. Huston, J. Kalk, H. L. Lai, and W. K. Tung, "Uncertainties of predictions from parton distribution functions II: the Hessian method," *Physical Review D* **65** (2001) 014013, arXiv:hep-ph/0101032 [hep-ph].

[51] A. Buckley, J. Ferrando, S. Lloyd, K. Nordstrom, B. Page, M. Ruefenacht, M. Schoenherr, and G. Watt, "LHAPDF6: parton density access in the LHC precision era," *The European Physical Journal C* **75** (2015) 132, arXiv:1412.7420 [hep-ph].

[52] "LHAPDF 6.3.0." https://lhapdf.hepforge.org/.

[53] **PDF4LHC** Collaboration, J. Butterworth *et al.*, "PDF4LHC recommendations for LHC Run II," *Journal of Physics G* **43** (2015) 023001, arXiv:1510.03865 [hep-ph].

[54] K. J. Eskola, P. Paakkinen, H. Paukkunen, and C. A. Salgado, "EPPS16: Nuclear parton distributions with LHC data," *The European Physics Journal C* **77** (2017) 163, arXiv:1612.05741 [hep-ph].

[55] K. Kovarik, A. Kusina, T. Jezo, D. B. Clark, C. Keppel, F. Lyonnet, J. G. Morfin, F. I. Olness, J. F. Owens, I. Schienbein, and J. Y. Yu, "nCTEQ15 - Global analysis of nuclear parton distributions with uncertainties in the CTEQ framework," *Physical Review D* **93** (2016) 085037, arXiv:1509.00792 [hep-ph].

[56] R. A. Khalek, J. J. Ethier, J. Rojo, and G. van Weelden, "nNNPDF2.0: Quark Flavor Separation in Nuclei from LHC Data," *Journal of High-Energy Physics* **09** (2020) 183, arXiv:2006.14629 [hep-ph].

[57] D. de Florian, R. Sassot, M. Stratmann, and P. Zurita, "Global Analysis of Nuclear Parton Distributions," *Physical Review D* **85** (2011) 074028, arXiv:1112.6324 [hep-ph].

[58] H. Khapour and S. Atashbar Tehrani, "Global analysis of nuclear parton distribution functions and their uncertainties at next-to-next-to-leading order," *Physical Review D* **93** (2016) 014026, arXiv:1601.00939 [hep-ph].

[59] M. Walt, I. Helenius, and W. Vogelsang, "Open-source QCD analysis of nuclear parton distribution functions at NLO and NNLO," *Physical Review D* **100** (2019) 096015, arXiv:1908.03355 [hep-ph].

[60] S. Alekhin *et al.*, "HERAFitter - Open Source QCD Fit Project," *The European Physical Journal C* **75** (2015) 304, arXiv:1410.4412 [hep-ph].

[61] N. Armesto, "Nuclear shadowing," *Journal of Physics G* **32** (2006) R367–R394, arXiv:hep-ph/0604108 [hep-ph].

[62] S. Malace, D. Gaskell, D. W. Higinbotham, and I. Cloet, "The Challenge of the EMC Effect: existing data and future directions," *International Journal of Modern Physics E* **23** (2014) 1430013, arXiv:1405.1270 [nucl-ex].

[63] S. Dulat, T. J. Hou, J. Gao, M. Guzzi, J. Huston, P. Nadolsky, J. Pumplin, C. Schmidt, D. Stump, and C. P. Yuan, "New parton distribution functions from a global analysis of quantum chromodynamics," *Physical Review D* **93** (2016) 033006, arXiv:1506.07443 [hep-ph].

[64] H.-L. Lai, J. Huston, Z. Li, P. Nadolsky, J. Pumplin, D. Stump, and C.-P. Yuan, "Uncertainty induced by QCD coupling in the CTEQ global analysis of parton distributions," *Physical Review D* **82** (2010) 054021, arXiv:1004.4624 [hep-ph].

[65] J. F. Owens, J. Huston, C. E. Keppel, S. Kuhlmann, J. G. Morfin, F. Olness, J. Pumplin, and D. Stump, "The impact of new neutrino DIS and Drell-Yan data on large-$x$ parton distributions," *Physical Review D* **75** (2007) 054030, arXiv:hep-ph/0702159 [hep-ph].

[66] W. Busza, K. Rajagopal, and W. van der Shee, "Heavy Ion Collisions: The Big Picture and the Big Questions," *Annual Review of Nuclear and Particle Science* **68** (2018) 339–376, arXiv:1802.04801 [hep-ph].

[67] M. Strickland, "Anisotropic Hydrodynamics: Three Lectures," *Acta Physica Polonica B* **45** (2014) 2355, arXiv:1410.5786 [nucl-th].

[68] L. V. Gribov, E. M. Levin, and M. G. Ryskin, "Semihard processes in QCD," *Physics Reports* **100** (1983) 1–150.

[69] A. H. Mueller and J. Qiu, "Gluon recombination and shadowing at small values of $x$," *Nuclear Physics B* **268** (1986) 427–452.

[70] F. Gelis, E. Iancu, J. Jalilian-Marian, and R. Venugoplan, "The Color Glass Condensate," *Annual Review of Nuclear and Particle Science* **60** (2010) 463–489, arXiv:1002.0333 [hep-ph].

[71] X.-G. Huang and J. Liao, "Kinetic evolution of the glasma and thermalization in heavy-ion collisions," *International Journal of Modern Physics E* **23** (2014) 1430003, arXiv:1402.5578 [nucl-th].

[72] E. G. Ferreiro, "Excited charmonium suppression in proton-nucleus collisions as a consequence of comovers," *Physics Letters B* **749** (2015) 98–103.

[73] J. Cleymans, "Status of the thermal model and chemical freeze-out," *EPJ Web of Conferences* **95** (2015) 03004.

[74] W. Florkowski, M. P. Heller, and M. Spalinski, "New theories of relativistic hydrodynamics in the LHC era," *Reports on Progress in Physics* **81** (2017) 046001, arXiv:1707.02282 [hep-ph].

[75] P. Romatschke, "Do nuclear collisions create a locally equilibrated quark-gluon plasma?," *The European Physical Journal C* **77** (2017) 21, arXiv:1609.02820 [nucl-th].

[76] P. Romatschke, "Relativistic Fluid Dynamics Far From Local Equilibrium," *Physical Review letters* **120** (2018) 012301, arXiv:1704.08699 [hep-th].

[77] L. Evans and P. Bryant, "LHC Machine," *Journal of Instrumentation* **3** (2008) S08001.

[78] M. Harrison, S. Peggs, and T. Roser, "The RHIC Accelerator," *Annual Review of Nuclear and Particle Science* **52** (2002) 425–469.

[79] E. Syresin *et al.*, "NICA Accelerator Complex at JINR," in *Proceedings of the 10th International Particle Accelerator Conference (IPAC'19), Melbourne, Australia, 19-24 May 2019*, pp. 452–454. Jun., 2019.

[80] P. Spiller *et al.*, "The FAIR Heavy Ion Synchrotron SIS100," *Journal of Instrumentation* **15** (2020) T12013.

[81] A. Accardi *et al.*, "Electron Ion Collider: The Next QCD Frontier - Understanding the glue that binds us all," 2014.

[82] **NA50** Collaboration, M. C. Abreu *et al.*, "Evidence for deconfinement of quarks and gluons from the J/$\psi$ suppression pattern measured in Pb–Pb collisions at the CERN-SPS," *Physics Letters B* **477** (2000) 28–36.

[83] **NA61/SHINE** Collaboration, N. Abgrall *et al.*, "NA61/SHINE facility at the CERN SPS: beams and detector systems," *Journal of Instrumentation* **9** (2014) P06005, arXiv:1401.4399 [physics.ins-det].

[84] **NA60+ Collaboration** Collaboration, T. Dahms, E. Scomparin, and G. Usai, "Expression of Interest for a new experiment at the CERN SPS: NA60+," tech. rep., CERN, Geneva, May, 2019. https://cds.cern.ch/record/2673280.

[85] M. L. Miller, K. Reygers, S. J. Sanders, and P. Steinberg, "Glauber Modeling in High Energy Nuclear Collisions," *Annual Review of Nuclear and Particle Science* **57** (2007) 205–243, arXiv:nucl-ex/0701025 [nucl-ex].

[86] A. Bialas, M. Bleszynski, and W. Czyz, "Multiplicity distributions in nucleus-nucleus collisions at high energies," *Nuclear Physics B* **111** (1976) 461–476.

[87] T. Ludlam, A. Pfoh, and A. Shor, "HIJET: a Monte Carlo event generator for p-nucleus and nucleus-nucleus collisions," 1985. https://www.osti.gov/biblio/6195452. BNL-51921.

[88] A. Shor and R. Longacre, "Effects of secondary interactions in proton-nucleus and nucleus-nucleus collisions using the hijet event generator," *Physics Letters B* **218** (1989) 100–104.

[89] C. Loizides, J. Kamin, and D. d'Enterria, "Improved Monte Carlo Glauber predictions at present and future nuclear colliders," *Physical Review C* **97** (2018) 054910, arXiv:1710.07098 [nucl-ex]. Erratum: Phys.Rev.C**99**(2019)019901.

[90] C. A. Salgado and other, "Proton-Nucleus Collisions at the LHC: Scientific Opportunities and Requirements," *Journal of Physics G* **39** (2012) 015010, arXiv:1105.3919 [hep-ph].

[91] **STAR** Collaboration, J. Adams, "Evidence from $d$ + Au Measurements for Final-State Suppression of High-$p_{\mathrm{T}}$ Hadrons in Au+Au Collisions at RHIC," *Physical Review Letters* **91** (2003) 072304, arXiv:nucl-ex/0306024 [nucl-ex].

[92] **PHENIX** Collaboration, S. S. Adler *et al.*, "Absence of Suppression in Particle Production at Large Transverse Momentum in $\sqrt{s_{\mathrm{NN}}} = 200$ GeV $d$ + Au Collisions," *Physical Review Letters* **91** (2003) 072303, arXiv:nucl-ex/0306021 [nucl-ex].

[93] **STAR** Collaboration, C. Adler *et al.*, "Centrality dependence of high pT hadron suppression in Au+Au collisions at $\sqrt{s_{\mathrm{NN}}} = 130$ GeV," *Physical Review Letters* **89** (2002) 202301, arXiv:nucl-ex/0206011 [nucl-ex].

[94] **PHENIX** Collaboration, S. S. Adler *et al.*, "Suppressed $\pi^0$ Production at Large Transverse Momentum in Central Au+Au Collisions at $\sqrt{s_{\mathrm{NN}}} = 200$ GeV," *Physical Review Letters* **91** (2003) 072301, arXiv:nucl-ex/0304022 [nucl-ex].

[95] M. Cacciari, M. Greco, and P. Nason, "The $p_T$ spectrum in heavy-flavour hadroproduction," *Journal of High Energy Physics* **05** (1998) 007, arXiv:hep-ph/9803400 [hep-ph].

[96] M. Cacciari, S. Frixione, and P. Nason, "The $p_T$ spectrum in heavy-flavour photoproduction," *Journal of High Energy Physics* **03** (2001) 006, arXiv:hep-ph/0102134 [hep-ph].

[97] **CMS** Collaboration, V. Khachatryan *et al.*, "Measurement of inclusive jet production and nuclear modifications in pPb collisions at $\sqrt{s_{\mathrm{NN}}} = 5.02$ TeV," *The European Physical Journal C* **76** (2016) 372, arXiv:1601.02001 [nucl-ex].

[98] K. J. Eskola, H. Paukkunen, and C. A. Salgado, "EPS09 – A new generation of NLO and LO nuclear parton distribution functions," *Journal Of High Energy Physics* **04** (2009) 065, arXiv:0902.4154 [hep-ph].

[99] S. Cao and X.-N. Wang, "Jet quenching and medium response in high-energy heavy-ion collisions: a review," *Reports on Progress in Physics* **84** (2021) 024301, arXiv:2002.04028 [hep-ph].

[100] V. Khachatryan *et al.*, "Observation of long-range, near-side angular correlations in proton-proton collisions at the LHC," *Journal of High Energy Physics* **09** (2010) 91, arXiv:1009.4122 [hep-ex].

[101] **STAR** Collaboration, B. I. Abelev *et al.*, "Long range rapidity correlations and jet production in high energy nuclear collisions," *Physical Review C* **80** (2009) 064912, arXiv:0909.0191 [nucl-ex].

[102] **PHOBOS** Collaboration, B. Alver *et al.*, "High Transverse Momentum Triggered Correlations over a Large Pseudorapidity Acceptance in Au + Au Collisions at $\sqrt{s_{\mathrm{NN}}} = 200$ GeV," *Physical Review Letters* **104** (2010) 062301, arXiv:0903.2811 [nucl-ex].

[103] **ALICE** Collaboration, K. Aamodt *et al.*, "Harmonic decomposition of two particle angular correlations in Pb–Pb collisions at $\sqrt{s_{\mathrm{NN}}} = 2.76$ TeV," *Physics Letters B* **708** (2012) 249–264, arXiv:1109.2501 [nucl-ex].

[104] **CMS** Collaboration, S. Chatrchyan *et al.*, "Observation of long-range, near-side angular correlations in pPb collisions at the LHC," *Physics Letters B* **718** (2013) 795–814, arXiv:1210.5482 [nucl-ex].

[105] **ATLAS** Collaboration, G. Aad *et al.*, "Observation of Long-Range Elliptic Azimuthal Anisotropies in $\sqrt{s} = 13$ and 2.76 TeV *pp* Collisions with the ATLAS Detector," *Physical Review Letters* **116** (2016) 172301, arXiv:1509.04776 [hep-ex].

[106] J. L. Nagle and W. A. Zajc, "Small System Collectivity in Relativistic Hadronic and Nuclear Collisions," *Annual Review of Nuclear and Particle Science* **68** (2018) 1–36, arXiv:1801.03477 [nucl-ex].

[107] E. Fermi, "Versuch einer Theorie der $\beta$-Strahlen," *Zeitschrift für Physik* **88** (1934) 161–177. Preliminary notes: *La ricerca scientifica* **2** (1933) 12.

[108] H. Yukawa, "On the Interaction of Elementary Particles," *Progress of Theoretical Physics Supplement* **1** (1955) 1–10.

[109] C. M. G. Lattes, G. P. S. Occhialini, and C. F. Powell, "Observations of the Tracks of Slow Mesons in Photographic Emulsions," *Nature* **160** (1947) 453–456.

[110] R. P. Feynman and M. Gell-mann, "Theory of the Fermi Interaction," *Physical Review* **109** (1958) 193.

[111] E. C. G. Sudarshan and R. E. Marshak, "The nature of the four-fermion interaction," in *Proceedings of the Padua-Venice Conference on Mesons and Newly-Discovered Particles*, pp. 22–27. 1957. `https://web2.ph.utexas.edu/~gsudama/pub/1958_005.pdf`. Reprinted in: P.K. Kabir, *The Development of Weak Interaction Theory*, Gordon and Breach, New York 1963, pp. 118-128.

[112] J. J. Sakurai, "Mass reversal and weak interactions," *Il Nuovo Cimento (1955-1965)* **7** (1958) 649–660.

[113] J. Leite Lopes, "A model of the universal fermi interaction," *Nuclear Physics* **8** (1958) 234–236.

[114] S. L. Glashow, "The renormalizability of vector meson interactions," *Nuclear Physics* **10** (1959) 107–117.

[115] A. Salam and J. C. Ward, "Weak and electromagnetic interactions," *Il Nuovo Cimento (1955-1965)* **11** (1959) 568–577.

[116] S. Weinberg, "A Model of Leptons," *Physical Review Letters* **19** (1967) 1264.

[117] C. Rubbia, P. McIntyre, and D. Cline, "Producing Massive Neutral Intermediate Vector Bosons with Existing Accelerators," in *Proceedings of the International Neutrino Conference, Aachen 1976*, pp. 683–687. 1976.

[118] **UA1** Collaboration, A. Astbury *et al.*, "A $4\pi$ solid angle detector for the SPS used as a proton-antiproton collider at a centre of mass energy of 540 GeV," Tech. Rep. CERN-SPSC-78-06. SPSC-P-92, CERN, Geneva, 1978. `https://cds.cern.ch/record/319371`.

[119] **UA1** Collaboration, M. Barranco Lunque *et al.*, "The construction of the central detector for an experiment at the CERN p-p collider," *Nuclear Instruments and Methods* **176** (1980) 175–180.

[120] **UA2** Collaboration, M. Banner *et al.*, "Proposal to study antiproton-proton interactions at 540 GeV cm energy," Tech. Rep. CERN-SPSC-78-8. SPSC-P-93, CERN, Geneva, 1978. `https://cds.cern.ch/record/596804`.

[121] **UA1** Collaboration, G. Arnison *et al.*, "Experimental observation of isolated large transverse energy electrons with associated missing energy at s=540 GeV," *Physics Letters B* **122** (1983) 103–116.

[122] **UA2** Collaboration, M. Banner *et al.*, "Observation of single isolated electrons of high transverse momentum in events with missing transverse energe at the CERN pp collider," *Physics Letters B* **122** (1983) 476–485.

[123] **UA1** Collaboration, G. Arnison *et al.*, "Experimental observation of lepton pairs of invariant mass around 95 GeV/$c^2$ at the CERN SPS collider," *Physics Letters B* **126** (1983) 398–410.

[124] **UA2** Collaboration, P. Bagnaia *et al.*, "Evidence for $Z^0 \to e^+e^-$ at the CERN pp collider," *Physics Letters B* **129** (1983) 130–140.

[125] **UA1** Collaboration, C. Albajar *et al.*, "Studies of intermediate vector boson production and decay in UA1 at the CERN proton-antiproton collider," *Zeitschrift für Physik C* **44** (1989) 15–61. `https://cds.cern.ch/record/193391`.

[126] **UA2** Collaboration, B. Adeva *et al.*, "A determination of the properties of the neutral intermediate vector boson $Z^0$," *Physics Letters B* **231** (1989) 509–518.

[127] P. W. Anderson, "Plasmons, Gauge Inveriance, and Mass," *Physical Review* **130** (1963) 439.

[128] A. A. Migdal and A. M. Polyakov, "Spontaneous Breakdown of Strong Interaction Symmetry and Absence of Massless Particles," *Soviet Physics - Journal of Experimental and Theoretical Physics* **51** (1966) 135–146. `http://jetp.ac.ru/cgi-bin/dn/e_024_01_0091.pdf`.

[129] F. Englert and R. Brout, "Broken Symmetry and the Mass of Gauge Vector Mesons," *Physical Review Letters* **13** (1964) 321.

[130] P. W. Higgs, "Broken Symmetries and the Masses of Gauge Bosons," *Physical Review Letters* **13** (1964) 508.

[131] G. S. Guralnik, C. R. Hagen, and T. Kibble, "Global Conservation Laws and Massless Particles," *Physical Review Letters* **13** (1964) 585.

[132] G. 't Hooft and M. Veltman, "Regularization and renormalization of gauge fields," *Nuclear Physics B* **44** (1972) 189–213.

[133] **ATLAS** Collaboration, G. Aad *et al.*, "Observation of a new particle in the search for the Standard Model Higgs boson with the ATLAS detector at the LHC," *Physics Letters B* **716** (2012) 1–29, `arXiv:1207.7214 [hep-ex]`.

[134] **CMS** Collaboration, S. Chatrchyan *et al.*, "Observation of a new boson at a mass of 125 GeV with the CMS experiment at the LHC," *Physics Letters B* **716** (2012) 30–61, `arXiv:1207.7235 [hep-ex]`.

[135] S. Myers and E. Picasso, "The design, construction and commissioning of the CERN large Electron-Positron collider," *Contemporary Physics* **31** (1990) 387–403.

[136] "SLAC Linear Collider Conceptual Design Report," Tech. Rep. SLAC-229, Stanford Linear Accelerator Center, Jun, 1980.

[137] S. Holmes, R. S. Moore, and V. Shiltsev, "Overview of the Tevatron collider complex: goals, operations and performance," *Journal of Instrumentation* **6** (2011) T08001, arXiv:1106.0909 [physics.acc-ph].

[138] **ALEPH** Collaboration, **DELPHI** Collaboration, **L3** Collaboration, **OPAL** Collaboration, **SLD** Collaboration, **LEP Electroweak** Working Group, **SLD Electroweak** and **Heavy Flavour** groups, "Precision electroweak measurements on the Z resonance," *Physics Reports* **427** (2006) 257–454, arXiv:hep-ex/0509008 [hep-ex].

[139] G. Breit and E. Wigner, "Capture of Slow Neutrons," *Physical Review* **49** (1936) 519.

[140] **ALEPH** Collaboration, **DELPHI** Collaboration, **L3** Collaboration, **OPAL** Collaboration, **SLD** Collaboration, **LEP Electroweak** Working Group, **SLD Electroweak** and **Heavy Flavour** groups, "Electroweak measurements in electron-positron collisions at W-boson-pair at LEP," *Physics Reports* **532** (2013) 119–244, arXiv:1302.3415 [hep-ex].

[141] **CDF, D0** Collaboration, T. A. Aaltonen *et al.*, "Combination of CDF and D0 $W$-Boson Mass Measurements," *Physical Review D* **88** no. 5, (2013) 052018, arXiv:1307.7627 [hep-ex].

[142] The **Tevatron Electroweak** Working Group, "Combination of CDF and D0 Results on the Width of the W boson," arXiv:1003.2826 [hep-ex]. FERMILAB-TM-2460-E.

[143] **ATLAS** Collaboration, M. Aaboud *et al.*, "Measurement of the $W$-boson mass in pp collisions at $\sqrt{s} = 7$ TeV with the ATLAS detector," *The European Physical Journal C* **78** (2018) 110, arXiv:1701.07240 [hep-ex]. Erratum: EPJC **78**(2018)898.

[144] J. Erler and M. Schott, "Electroweak Precision Tests of the Standard Model after the Discovery of the Higgs Boson," *Progress in Particle and Nuclear Physics* **106** (2019) 68–119, arXiv:1902.05142 [hep-ph].

[145] S. D. Drell and T.-M. Yan, "Massive Lepton-Pair Production in Hadron-Hadron Collisions at High Energies," *Physical Review Letters* **25** (1970) 316. Erratum: PRL **25**(1970)902.

[146] J. H. Christenson *et al.*, "Observation of Massive Muon Pairs in Hadron Collisions," *Physical Review Letters* **25** (1970) 1523.

[147] A. D. Martin, R. G. Roberts, W. J. Stirling, and R. S. Thorne, "Parton Distributions and the LHC: W and Z Production," *The European Physical Journal C* **14** (2000) 133–145, arXiv:hep-ph/9907231 [hep-ph].

[148] A. D. Martin, R. G. Roberts, W. J. Stirling, and R. S. Thorne, "Parton distributions: a new global analysis," *The European Physical Journal C* **4** (1998) 463–496, arXiv:hep-ph/9803445 [hep-ph].

[149] S. Frixione and M. L. Mangano, "How accurately can we measure the $W$ cross section?," *Journal of High Energy Physics* **05** (2005) 056, arXiv:hep-ph/0405130 [hep-ph].

[150] C. Anastasiou, L. Dixon, K. Melnikov, and F. Petriello, "High-precision QCD at hadron colliders: electroweak gauge boson rapidity distributions at NNLO," *Physical Review D* **69** (2004) 094008, arXiv:hep-ph/0312266 [hep-ph].

[151] A. D. Martin, R. G. Roberts, W. J. Stirling, and R. S. Thorne, "NNLO global parton analysis," *Physics Letters B* **531** (2002) 216–224, arXiv:hep-ph/0201127 [hep-ph].

[152] R. Vogt, "Shadowing effects on vector boson production," *Physical Review C* **64** (2001) 044901, arXiv:hep-ph/0011242 [hep-ph].

[153] H. Paukkunen and C. A. Salgado, "Constraints for the nuclear parton distributions from $Z$ and $W^{\pm}$ production at the LHC," *Journal of High Energy Physics* **03** (2011) 71, arXiv:1010.5392 [hep-ph].

[154] P. M. Nadolsky, H.-L. Lai, Q.-H. Cao, J. Huston, J. Pumplin, D. Stump, W.-K. Tung, and C.-P. Yuan, "Implications of CTEQ global analysis for collider observables," *Physical Review D* **78** (2008) 013004, arXiv:0802.0007 [hep-ph].

[155] D. d'Enterria and C. Loizides, "Progress in the Glauber model at collider energies.". To appear in Annual Review of Nuclear and Particle Science. arXiv:2011.14909 [hep-ph].

[156] **ALICE** Collaboration, J. Adam *et al.*, "W and Z boson production in p-Pb collisions at $\sqrt{s_{\mathrm{NN}}} = 5.02$ TeV," *Journal of High Energy Physics* **02** (2017) 077, arXiv:1611.03002 [nucl-ex].

[157] **ALICE** Collaboration, S. Acharya *et al.*, "Z-boson production in p–Pb collisions $\sqrt{s_{\mathrm{NN}}} = 8.16$ TeV and Pb–Pb collisions at $\sqrt{s_{\mathrm{NN}}} = 5.02$ TeV," *Journal of High Energy Physics* **09** (2020) 076, arXiv:2005.11126 [nucl-ex].

[158] **ALICE** Collaboration, S. Acharya *et al.*, "$\mathrm{W}^{\pm}$-boson production in p–Pb collisions $\sqrt{s_{\mathrm{NN}}} = 8.16$ TeV and Pb–Pb collisions at $\sqrt{s_{\mathrm{NN}}} = 5.02$ TeV.". To be published.

[159] **ALICE** Collaboration, S. Acharya *et al.*, "Measurement of $\mathrm{Z}^0$-boson production at large rapidities in Pb-Pb collisions at $\sqrt{s_{\mathrm{NN}}} = 5.02$ TeV," *Physics Letters B* **780** (2018) 372–383, arXiv:1711.10753 [nucl-ex].

[160] **ATLAS** Collaboration, G. Aad *et al.*, "$Z$ boson production in $p$+Pb collisions at $\sqrt{s_{NN}} = 5.02$ TeV measured with the ATLAS detector," *Physical Review C* **92** (2015) 044915, arXiv:1507.06232 [hep-ex].

[161] **ATLAS** Collaboration, G. Aad *et al.*, "Measurement of $Z$ boson Production in Pb+Pb Collisions at $\sqrt{s_{NN}} = 2.76$ TeV with the ATLAS Detector," *Physical Review Letters* **110** (2013) 022301, arXiv:1210.6486 [hep-ex].

[162] **ATLAS** Collaboration, G. Aad *et al.*, "Measurement of the production and lepton charge asymmetry of $W$ bosons in Pb+Pb collisions at $\sqrt{s_{NN}} = 2.76$ with the ATLAS detector," *European Physics Journal C* **75** (2015) 23, arXiv:1408.4674 [hep-ex].

[163] **ATLAS** Collaboration, G. Aad *et al.*, "$Z$ boson production in Pb+Pb collisions at $\sqrt{s_{\mathrm{NN}}}$= 5.02 TeV measured by the ATLAS experiment," *Physics Letters* **B802** (2020) 135262, arXiv:1910.13396 [nucl-ex].

[164] **ATLAS** Collaboration, G. Aad *et al.*, "Measurement of $\mathrm{W}^{\pm}$ boson production in Pb+Pb collisions at $\sqrt{s_{\mathrm{NN}}} = 5.02$ TeV with the ATLAS detector," *European Physical Journal C* **79** (2019) 935, arXiv:1907.10414 [nucl-ex].

[165] **CMS** Collaboration, V. Khachatryan *et al.*, "Study of Z boson production in pPb collisions at $\sqrt{s_{NN}} = 5.02$ TeV," *Physics Letters B* **759** (2016) 36, arXiv:1512.06461 [hep-ex].

[166] **CMS** Collaboration, V. Khachatryan *et al.*, "Study of W boson production in pPb collisions at $\sqrt{s_{\mathrm{NN}}} = 5.02$ TeV," *Physics Letters B* **750** (2015) 565, arXiv:1503.05825 [nucl-ex].

[167] **CMS** Collaboration, A. M. Sirunyan *et al.*, "Observation of nuclear modifications in $\mathrm{W}^{\pm}$ boson production in pPb collisions at $\sqrt{s_{\mathrm{NN}}} = 8.16$ TeV," *Physics Letters B* **800** (2020) 135048, arXiv:1905.01486 [hep-ex].

[168] **CMS** Collaboration, S. Chatrchyan *et al.*, "Study of Z boson production in PbPb collisions at $\sqrt{s_{NN}} = 2.76$ TeV," *Physical Review Letters* **106** (2011) 212301, arXiv:1102.5435 [nucl-ex].

[169] **CMS** Collaboration, S. Chatrchyan *et al.*, "Study of Z production in PbPb and pp collisions at $\sqrt{s_{\mathrm{NN}}} = 2.76$ TeV in the dimuon and dielectron decay channels," *Journal of High Energy Physics* **03** (2015) 022, arXiv:1410.4825 [nucl-ex].

[170] **CMS** Collaboration, S. Chatrchyan *et al.*, "Study of $W$ boson production in PbPb and $pp$ collisions at $\sqrt{s_{NN}} = 2.76$ TeV," *Physics Letters B* **715** (2012) 66, arXiv:1205.6334 [nucl-ex].

[171] **CMS** Collaboration, A. M. Sirunyan *et al.*, "High precision measurements of Z boson production in PbPb collisions at $\sqrt{s_{\mathrm{NN}}} = 5.02$ TeV," 2021. CMS-HIN-19-003, CERN-EP-2021-039. To be published.

[172] **LHCb** Collaboration, R. Aaij *et al.*, "Observation of $Z$ production in proton-lead collisions at LHCb," *Journal of High Energy Physics* **09** (2014) 030, arXiv:1406.2885 [hep-ex].

[173] **LHCb** Collaboration, R. Aaij *et al.*, "Measurement of $Z$ production cross-sections in proton-lead collisions at $\sqrt{s_{\rm NN}} = 8.16$ TeV," 2019. https://cds.cern.ch/record/2700245. LHCb-CONF-2019-003.

[174] K. J. Eskola, I. Helenius, M. Kuha, and H. Paukkunen, "Shadowing in Inelastic Nucleon-Nucleon Cross Section?," *Physical Review Letters* **125** (2020) 212301, arXiv:2003.11856 [hep-ph].

[175] F. Jonas and C. Loizides, "Centrality dependence of electroweak boson production in PbPb collisions at the LHC.". To be published. arXiv:2104.14903 [nucl-ex].

[176] H.-L. Lai, M. Guzzi, J. Huston, Z. Li, P. Nadolsky, J. Pumplin, and C.-P. Yuan, "New parton distributions for collider physics," *Physical Review D* **82** (2010) 074024, arXiv:1007.2241 [hep-ph].

[177] A. D. Martin, W. J. Stirling, R. S. Thorne, and G. Watt, "Parton distributions for the LHC," *The European Physical Journal C* **63** (2009) 189–285, arXiv:0901.0002 [hep-ph].

[178] C. A. Pruneau, *Data Analysis Technique for Physical Scientists*. Cambridge University Press, Cambridge, 2014.

[179] H. Schopper and L. Di Lella, *60 Years of CERN Experiments and Discoveries*, vol. 23 of *Advanced Series on Directions in High Energy Physics*. World Scientific, 2015. https://www.worldscientific.com/doi/abs/10.1142/9441.

[180] O. S. Brüning, P. Collier, P. Lebrun, S. Myers, R. Ostojic, J. Poole, and P. Proudlock, *LHC Design Report*. CERN Yellow Reports: Monographs. CERN, Geneva, 2004. http://cds.cern.ch/record/782076.

[181] **ALICE** Collaboration, K. Aamodt *et al.*, "The ALICE experiment at the CERN LHC," *Journal of Instrumentation* **3** (2008) S08002. http://cds.cern.ch/record/1129812. Also published by CERN Geneva in 2010.

[182] **ATLAS** Collaboration, G. Aad *et al.*, "The ATLAS Experiment at the CERN Large Hadron Collider," *Journal of Instrumentation* **3** (2008) S08003. https://cds.cern.ch/record/1129811. Also published by CERN Geneva in 2010.

[183] **CMS** Collaboration, S. Chatrchyan *et al.*, "The CMS experiment at the CERN LHC," *Journal of Instrumentation* **3** (2008) S08004. https://cds.cern.ch/record/1129810. Also published by CERN Geneva in 2010.

[184] **LHCb** Collaboration, A. A. Alves *et al.*, "The LHCb Detector at the LHC," *Journal of Instrumentation* **3** (2008) S08005. https://cds.cern.ch/record/1129809. Also published by CERN Geneva in 2010.

[185] **ALICE** Collaboration, B. B. Abelev *et al.*, "Performance of the ALICE Experiment at the CERN LHC," *International Journal of Modern Physics* **A29** (2014) 1430044, arXiv:1402.4476 [nucl-ex].

[186] **ALICE** Collaboration, L. Betev and P. Chochula, "Definition of the ALICE coordinate System and Basic Rules for Subdetector Components Numbering," 2003. https://edms.cern.ch/document/406391/2. ALICE-INT-2003-038.

[187] **ALICE** Collaboration, "Technical design reports." https://alice-collaboration.web.cern.ch/documents/tdr/index.html.

[188] **ALICE** Collaboration, P. Cortese *et al.*, "ALICE: Physics performance report, volume I," *Journal of Physics G* **30** (2004) 1517–1763. https://cds.cern.ch/record/643556.

[189] **ALICE** Collaboration, C. W. Fabjan *et al.*, "ALICE: Physics performance report, volume II," *Journal of Physics G* **32** (2006) 1295–2040. https://cds.cern.ch/record/879894.

[190] **ALICE** Collaboration, G. Dellacasa *et al.*, "ALICE Zero-Degree Calorimeter (ZDC): Technical Design Report," Tech. Rep. CERN-LHCC-99-005. ALICE-TDR-3, CERN, Mar, 1999. https://cds.cern.ch/record/381433.

[191] **ALICE** Collaboration, G. Dellacasa *et al.*, "ALICE Photon Multiplicity Detector (PMD): Technical Design Report," Tech. Rep. CERN-LHCC-99-032. ALICE-TDR-6, CERN, Sep, 1999. https://cds.cern.ch/record/451099.

[192] A. V. Tello, "AD, the ALICE diffractive detector," in *Proceedings of the 9th International Workshop on Diffraction in High Energy Physics (Diffraction 2016)*, vol. 1, p. 04002. 2017.

[193] **ALICE** Collaboration, P. Cortese *et al.*, "ALICE forward detectors: FMD, T0 and V0: Technical Design Report," Tech. Rep. CERN-LHCC-2004-025. ALICE-TDR-11, CERN, Sep, 2004. https://cds.cern.ch/record/781854.

[194] S. van der Meer, "Calibration of the effective beam height in the ISR," Tech. Rep. CERN-ISR-PO-68-31. ISR-PO-68-31, CERN, Geneva, 1968. https://cds.cern.ch/record/296752.

[195] V. Balagura, "Notes on van der Meer Scan for Absolute Luminosity Measurement," *Nuclear Instruments and Methods in Physics Research A* **654** (2011) 634–638, arXiv:1103.1129 [physics.ins-det].

[196] **ALICE** Collaboration, A. Acharya *et al.*, "ALICE luminosity determination for p-Pb collisions at $\sqrt{s_{\mathrm{NN}}} = 8.16$ TeV," Tech. Rep. ALICE-PUBLIC-2018-002, CERN, Apr, 2018. https://cds.cern.ch/record/2314660.

[197] **ALICE** Collaboration, A. Acharya *et al.*, "Centrality determination in heavy ion collisions," Tech. Rep. ALICE-PUBLIC-2018-011, CERN, Aug, 2018. https://cds.cern.ch/record/2636623.

[198] **UA5 Collaboration** Collaboration, G. J. Alner *et al.*, "Multiplicity distributions in different pseudorapidity intervals at a CMS energy of 540 GeV," *Physics Letters B* **160** (Apr, 1985) 193–198. 25 p. https://cds.cern.ch/record/159457.

[199] **ALICE** Collaboration, S. Acharya *et al.*, "Charged-particle pseudorapidity density at mid-rapidity in p–Pb collisions at $\sqrt{s_{\rm NN}} = 8.16$ TeV," *The European Physical Journal C* **79** (2019) 307, arXiv:1812.01312 [nucl-ex].

[200] **ALICE** Collaboration, J. Adam *et al.*, "Centrality dependence of particle production in p–Pb collisions at fivenn," *Physical Review C* **91** (2015) 064905, arXiv:1412.6828 [nucl-ex].

[201] A. Bialas, M. Bleszynski, and W. Czyz, "Multiplicity Distributions in Nucleus-Nucleus Collisions at High-Energies," *Nuclear Physyics B* **111** (1976) 461–476.

[202] A. Bialas and A. Bzdak, "Wounded quarks and diquarks in high energy collisions," *Physical Review C* **77** no. 3, (Mar, 2008) 034908.

[203] **ALICE** Collaboration, G. Dellacasa *et al.*, "ALICE Inner Tracking System (ITS): Technical Design Report," Tech. Rep. CERN-LHCC-99-012. ALICE-TDR-4, CERN, Jun, 1999. http://cds.cern.ch/record/391175.

[204] **ALICE** Collaboration, G. Dellacasa *et al.*, "ALICE time projection chamber: Technical Design Report," Tech. Rep. CERN-LHCC-2000-001. ALICE-TDR-7, CERN, Jan, 2000. https://cds.cern.ch/record/451098.

[205] **ALICE** Collaboration, P. Cortese *et al.*, "ALICE transition-radiation detector: Technical Design Report," Tech. Rep. CERN-LHCC-2001-021. ALICE-TDR-9, CERN, Oct, 2001. https://cds.cern.ch/record/519145.

[206] **ALICE** Collaboration, G. Dellacasa *et al.*, "ALICE Time-Of-Flight system (TOF): Technical Design Report," Tech. Rep. CERN-LHCC-2000-012. ALICE-TDR-8, CERN, Feb, 2000. https://cds.cern.ch/record/430132.

[207] **ALICE** Collaboration, P. Cortese *et al.*, "ALICE Time-Of Flight system (TOF): addendum to the Technical Design Report," Tech. Rep. CERN-LHCC-2002-016. ALICE-TDR-8-add-1, CERN, Apr, 2002. https://cds.cern.ch/record/545834.

[208] **ALICE** Collaboration, S. Beole *et al.*, "ALICE high-momentum particle identification: Technical Design Report," Tech. Rep. CERN-LHCC-98-019. ALICE-TDR-1, CERN, Aug, 1998. https://cds.cern.ch/record/381431.

[209] **ALICE** Collaboration, G. Dellacasa *et al.*, "ALICE Photon Spectrometer (PHOS): Technical Design Report," Tech. Rep. CERN-LHCC-99-004. ALICE-TDR-2, CERN, Mar, 1999. https://cds.cern.ch/record/381432.

[210] **ALICE** Collaboration, P. Cortese *et al.*, "ALICE Electromagnetic Calorimeter Technical Design Report," Tech. Rep. CERN-LHCC-2008-014. ALICE-TDR-14, CERN, Aug, 2008. http://cds.cern.ch/record/1121574.

[211] **ALICE** Collaboration, J. Allen *et al.*, "ALICE DCal: An Addendum to the EMCal Technical Design Report Di-Jet and Hadron-Jet correlation measurements in ALICE," Tech. Rep. CERN-LHCC-2010-011. ALICE-TDR-14-add-1, CERN, Jun, 2010. http://cds.cern.ch/record/1272952.

[212] **ACORDE** Collaboration, A. Fernández *et al.*, "ACORDE a Cosmic Ray Detector for ALICE," *Nuclear Instruments and Methods in Physics Research A* **572** (2006) 102–103. https://cds.cern.ch/record/957722.

[213] M. Ivanov, I. Belikov, P. Hristov, T. Kuhr, and K. Safarik, "Track reconstruction in high density environment," *Nuclear Instrumentation and Methods in Physics Research A* **566** (2006) 70.

[214] Y. Belikov, M. Ivanov, K. Safarik, and B. J, "TPC tracking and particle identification in high density environment," *eConf* **C0303241** (2003) TULT011, arXiv:physics/0306108 [physics].

[215] R. Fruhwirth, "Application of Kalman filtering to track and vertex finding," *Nuclear Instrumentation and Methods in Physics Research A* **262** (1987) 444.

[216] A. Majumder and M. Van Leeuwen, "The Theory and Phenomenology of Perturbative QCD Based Jet Quenching," *Progress in Particle and Nuclear Physics* **66** (2011) 41, arXiv:1002.2206 [hep-ph].

[217] M. Connors, C. Nattrass, R. Reed, and S. Salur, "Jet measurements in heavy ion physics," *Reviews of Modern Physics* **90** (2018) 025005, arXiv:1705.01974 [nucl-ex].

[218] M. Cacciari, G. P. Salam, and G. Soyez, "FastJet user manual," *The European Physical Journal C* **72** no. 3, (2012) 1896, arXiv:1111.6097 [hep-ph].

[219] M. Cacciari, G. P. Salam, and G. Soyez, "The anti-kt jet clustering algorithm," *Journal of High Energy Physics* **2008** no. 04, (2008) 063, arXiv:0802.1189 [hep-ph].

[220] R. Haake, "Machine Learning based jet momentum reconstruction in Pb-Pb collisions measured with the ALICE detector," in *Proceedings of European Physical Society Conference on High Energy Physics — PoS(EPS-HEP2019)*, vol. 364, p. 312. 2020. arXiv:1909.01639 [nucl-ex].

[221] **ALICE** Collaboration, G. Dellacasa *et al.*, "Technical Design Report of the Dimuon Forward Spectrometer," Tech. Rep. CERN-LHCC-99-022. ALICE-TDR-5, CERN, Aug, 1999. http://cds.cern.ch/record/401974.

[222] **ALICE** Collaboration, G. Dellacasa *et al.*, "ALICE dimuon forward spectrometer: addendum to the Technical Design Report," Tech. Rep. CERN-LHCC-2000-046. ALICE-TDR-5-add-1, CERN, Dec, 2000. http://cds.cern.ch/record/494265.

[223] X.-N. Wang and M. Gyulassy, "HIJING 1.0: A Monte Carlo Program and Particle Production in High Energy Hadronic and Nuclear Collisions," *Computer Physics Communications* **83** (1994) 307–331, arXiv:nucl-th/9502021 [nucl-th].

[224] A. Zinchenko and G. Chabratova, "A new approach to cluster finding and hit reconstruction in cathode pad chambers and its development for the forward muon spectrometer of ALICE," *Nuclear Instrumentation and Methods in Physics Research A* **502** (2003) 778–780.

[225] E. Mathieson, "Cathode charge distributions in multiwire chambers: 4. Empirical formula for small anode-cathode separation," *Nuclear Instrumentation and Methods in Physics Research A* **270** (1988) 602–603.

[226] A. Grigoryan *et al.*, "The Geometry Monitoring System of the ALICE Dimuon spectrometer - Overview," 2005. http://cds.cern.ch/record/960453. ALICE-INT-2005-009.

[227] V. Blobel and C. Kleinwort, "A New Method for the High-Precision Alignment of Track Detectors," in *Contribution to the Conference on Advanced Statistical Techniques in Particle Physics, Durham, 18-22 March 2002*. 2002. arXiv:hep-ex/0208021 [hep-ex].

[228] J. E. Gaiser, *Charmonium Spectroscopy from Radiative Decays of the J/Psi and Psi-Prime*. PhD thesis, SLAC - Stanford University, 1982. www.slac.stanford.edu/cgi-bin/getdoc/slac-r-255.pdf.

[229] **ALICE** Collaboration, P. Cortese *et al.*, "Technical Design Report of the Trigger, Data Acquisition, High-Level Trigger and Control System," Tech. Rep. CERN-LHCC-2003-062. ALICE-TDR-10, CERN, Nov, 2003. http://cds.cern.ch/record/684651.

[230] **ALICE** Collaboration, F. Carena *et al.*, "The ALICE data acquisition system," *Nuclear Instruments and Methods in Physics Research A* **741** (2014) 130–162.

[231] **ALICE** Collaboration, W. Carena *et al.*, "ALICE DAQ and ECS User's guide," Tech. Rep. ALICE-INT-2005-015, CERN, Jun, 2006. http://edms.cern.ch/document/616039/2.

[232] R. Brun and F. Rademakers, "ROOT – An object oriented data analysis framework," *Nuclear Instruments and Methods in Physics Research A* **389** (1997) 81–86.

[233] **ALICE** Collaboration, "AliRoot, ALICE Off-line framework for simulation, reconstruction and analysis." http://aliceinfo.cern.ch/Offline.

[234] **ALICE** Collaboration, S. Acharya *et al.*, "Real-time data processing in the ALICE High Level Trigger at the LHC," *Computer Physics Communications* **242** (2019) 25–48, arXiv:1812.08036 [physics.ins-det].

[235] D. A. Huffman, "A Method for the Construction of Minimum-Redundancy Codes," in *Proceedings of the IRE*, vol. 40, pp. 1098–1101. 1952.

[236] **ALICE** Collaboration, P. Cortese *et al.*, "Technical Design Report of the Computing," Tech. Rep. CERN-LHCC-2005-018. ALICE-TDR-12, CERN, Jun, 2005. http://cds.cern.ch/record/832753.

[237] **ALICE** Collaboration, "Alice offline." http://alice-offline.web.cern.ch.

[238] ISO/IEC, "ISO/IEC 14882:1998: Programming languages — C++," 1998. https://isocpp.org/std/the-standard.

[239] CERN, "WLCG — Worlwide LHC Computing Grid." https://wlcg.web.cern.ch.

[240] CERN, "The MONARC Project: Models Of Networked Analysis at Regional Centers for LHC Experiments." https://monarc.web.cern.ch/MONARC/.

[241] **ALICE** Collaboration, P. Saiz, L. Aphecetche, P. Buncic, R. Piskac, J.-E. Revsbech, and V. Sego, "AliEn — ALICE environment on the GRID," *Nuclear Instruments and methods in Physics Research A* **502** (2003) 437–440.

[242] I. Legrand *et al.*, "MonALISA: An agent based dynamic system to monitor, control and optimize distributed systems," *Computer Physics Communications* **180** (2009) 2472–2498.

[243] M. Ballintjin, R. Brun, F. Rademakers, and G. Roland, "The PROOF Distributed Parallel Analysis Framework based on ROOT," in *Proceedings of the 13th International Conference on Computing in High-Energy and Nuclear Physics, La Jolla, March 2003*, vol. C0303241, p. TUCT004. 2003. arXiv:physics/0306110 [physics].

[244] R. Brun, F. Bruyant, M. Maire, A. C. McPherson, and P. Zanarini, "GEANT3: user's guide Geant 3.10, Geant 3.11 rev. version," 1987. https://cds.cern.ch/record/1119728. CERN-DD-EE-84-01.

[245] **GEANT4** Collaboration, S. Agostinelli *et al.*, "Geant4 — a simulation toolkit," *Nuclear Instruments and Methods in Physics Research A* **506** (2003) 250–303.

[246] A. Ferrari, P. R. Sala, A. Fasso, and J. Ranft, "FLUKA: a multi-particle transport code (program version 2005)," 2005. https://cds.cern.ch/record/898301. CERN-2005-010; INFN-TC-2005-11; SLAC-R-773.

[247] **ALICE** Collaboration, B. Aabelev *et al.*, "Upgrade of the ALICE Experiment: Letter Of Intent," *Journal of Physics G* **41** (2014) 087001.

[248] T. Matsui and H. Satz, "$J/\psi$ suppression by quark-gluon plasma formation," *Physics Letters B* **178** (1986) 416–422.

[249] **ALICE** Collaboration, B. Abelev *et al.*, "Technical Design report for the Upgrade of the ALICE Inner Tracking System," Tech. Rep. CERN-LHCC-2013-024. ALICE-TDR-017, CERN, Nov, 2013. https://cds.cern.ch/record/1625842.

[250] F. Sauli, "GEM: A new concept for electron amplification in gas detectors," *Nuclear Instruments and Methods in Physics Research A* **386** (1997) 531–534.

[251] **ALICE TPC** Collaboration, J. Adolfsson *et al.*, "The upgrade of the ALICE TPC with GEMs and continuous readout," *Journal of Instrumentation* **16** (2021) P03022, arXiv:2012.09518 [physics.ins-det].

[252] **ALICE** Collaboration, B. Abelev *et al.*, "Upgrade of the ALICE Readout & Trigger System," Tech. Rep. CERN-LHCC-2013-019. ALICE-TDR-015, CERN, Sep, 2015. https://cds.cern.ch/record/1603472.

[253] S. Rojas-Torres, "The Forward Diffractive Detector for ALICE," in *Proceedings of the 8th Annual Conference on Large Hadron Collider Physics — PoS(LHCP2020)*, vol. 382, p. 221. 2020.

[254] **ALICE** Collaboration, J. Adam *et al.*, "Technical Design Report for the Muon Forward Tracker," Tech. Rep. CERN-LHCC-2015-001. ALICE-TDR-018, CERN, Jan, 2015. https://cds.cern.ch/record/1981898.

[255] S. H. I. Barboza *et al.*, "SAMPA chip: a new ASIC for the ALICE TPC and MCH upgrades," *Journal of Instrumentation* **11** (2016) C02088.

[256] **ALICE** Collaboration, J. Adam *et al.*, "Technical Design Report for the Upgrade of the Online-Offline Computing System," Tech. Rep. CERN-LHCC-2015-006. ALICE-TDR-019, CERN, Apr, 2015. https://cds.cern.ch/record/2011297.

[257] M. Al-Turany, D. Klein, A. Manafov, A. Rybalchenko, and F. Uhlig, "Extending the FairRoot framework to allow for simulation and reconstruction of free streaming data," *Journal of Physics: Conference Series* **513** (2014) 022001.

[258] C. Hewitt, P. Bishop, and R. Steiger, "A Universal Modular ACTOR Formalism for Artificial Intelligence," in *Proceedings of the 3rd Internation Joint Conference on Artificial Intelligence IJCAI'73*, pp. 235–245. 1973.

[259] Z. Conesa del Valle, *Performance of the ALICE muon spectrometer. Weak boson production and measurement in heavy-ion collisions at LHC.* PhD thesis, Université de Nantes, Universitat Autónoma de Barcelona, 2007. tel-00198703.

[260] "FONLL Heavy Quark Production," 2007. http://www.lpthe.jussieu.fr/~cacciari/fonll/fonllform.html.

[261] **NNPDF** Collaboration, R. D. Ball *et al.*, "Parton distributions for the LHC Run II," *Journal of High Energy Physics* **04** (2015) 040, arXiv:1410.8849 [hep-ph].

[262] S. Acharya *et al.*, "Production of muons from heavy-flavour hadron decays in p–Pb collisions at $\sqrt{s_{\rm NN}} = 5.02$ TeV," *Physics Letters B* **770** (2017) 459–472, arXiv:1702.01479 [nucl-ex].

[263] M. Cacciari. Private communication.

[264] T. Sjostran, S. Mrenna, and P. Skands, "PYTHIA 6.4 physics and manual," *Journal of High Energy Physics* **05** (2006) 026, arXiv:hep-ph/0603175 [hep-ph].

[265] R. Brun, F. Bruyant, F. Carminati, S. Giani, M. Maire, A. McPherson, G. Patrick, and L. Urban, "GEANT: Detector Description and Simulation Tool," 1994. https://cds.cern.ch/record/1082634. CERN-W-5013.

[266] **ALICE** Collaboration, J. Adam *et al.*, "Quarkonium signal extraction in ALICE," Tech. Rep. ALICE-PUBLIC-2015-006, CERN, Oct, 2015. https://cds.cern.ch/record/2060096.

[267] S. Aioli, P. Nason, C. Oleari, and E. Re, "A general framework for implementing NLO calculations in shower Monte Carlo programs: the POWHEG BOX," *JHEP* **06** (2010) 43, arXiv:1002.2581 [hep-ph].

[268] K. J. Eskola, V. J. Kolhinen, and C. A. Salgado, "The scale dependent nuclear effects in parton distributions for practical applications," *The European Physical Journal C* **9** (1999) 61–68, arXiv:hep-ph/9807297 [hep-ph].

[269] **ALICE** Collaboration, S. Acharya *et al.*, "$\Upsilon$ production in p–Pb collisions at $\sqrt{s_{\mathrm{NN}}} = 8.16$ TeV," *Physics Letters B* **806** (2020) 135486, arXiv:1910.14405 [nucl-ex].

[270] R. Boughezal, J. M. Campbell, K. Ellis, C. Focke, W. Giele, X. Liu, F. Petriello, and C. Williams, "Color-singlet production at NNLO in MCFM," *The European Physical Journal C* **77** (2017) 7, arXiv:1605.08011 [hep-ph].

[271] R. Gavin, F. Petriello, and S. Quackenbush, "FEWZ 2.0: A code for hadronic $Z$ production at next-to-next-to-leading order," *Computer Physics Communications* **182** (2011) 2388–2403, arXiv:1011.3540 [hep-ph].

[272] A. Kusina, T. Jezo, D. B. Clark, P. Duwentäster, E. Godat, T. J. Hobbs, J. Kent, M. Klasen, K. Kovarík, F. Lyonnet, K. F. Muzaffa, F. I. Olness, I. Schienben, and J. Y. Yu, "Impact of LHC vector boson production in heavy ion collisions on strange PDFs," *The European Physical Journal C* **80** (2020) 968, arXiv:2007.09100 [hep-ph].

[273] **LHCb** Collaboration, R. Aaij *et al.*, "Measurement of forward $W$ and $Z$ boson production in $pp$ collisions at $\sqrt{s} = 8$ TeV," *Journal of High-Energy Physics* **01** (2016) 155, arXiv:1511.08039 [hep-ex].